Breakthrough Hydrogel Technology

- Less Retreatment Compared to Platinum[1,2]
- Less Recurrence Compared to Platinum[1,2]
- High Progressive Occlusion[1,2]

For more information or a product demonstration, contact your local MicroVention representative:

MicroVention®
TERUMO

MicroVention, Inc.
Worldwide Headquarters **PH +1.714.247.8000**
1311 Valencia Avenue
Tustin, CA 92780 USA
MicroVention UK Limited PH +44 (0) 191 258 6777
MicroVention Europe, S.A.R.L PH +33 (1) 39 21 77 46
MicroVention Deutschland GmbH PH +49 211 210 798-0
microvention.com

stryker

NEW

Indication for Trevo® Retrievers

A New Standard of Care in Stroke

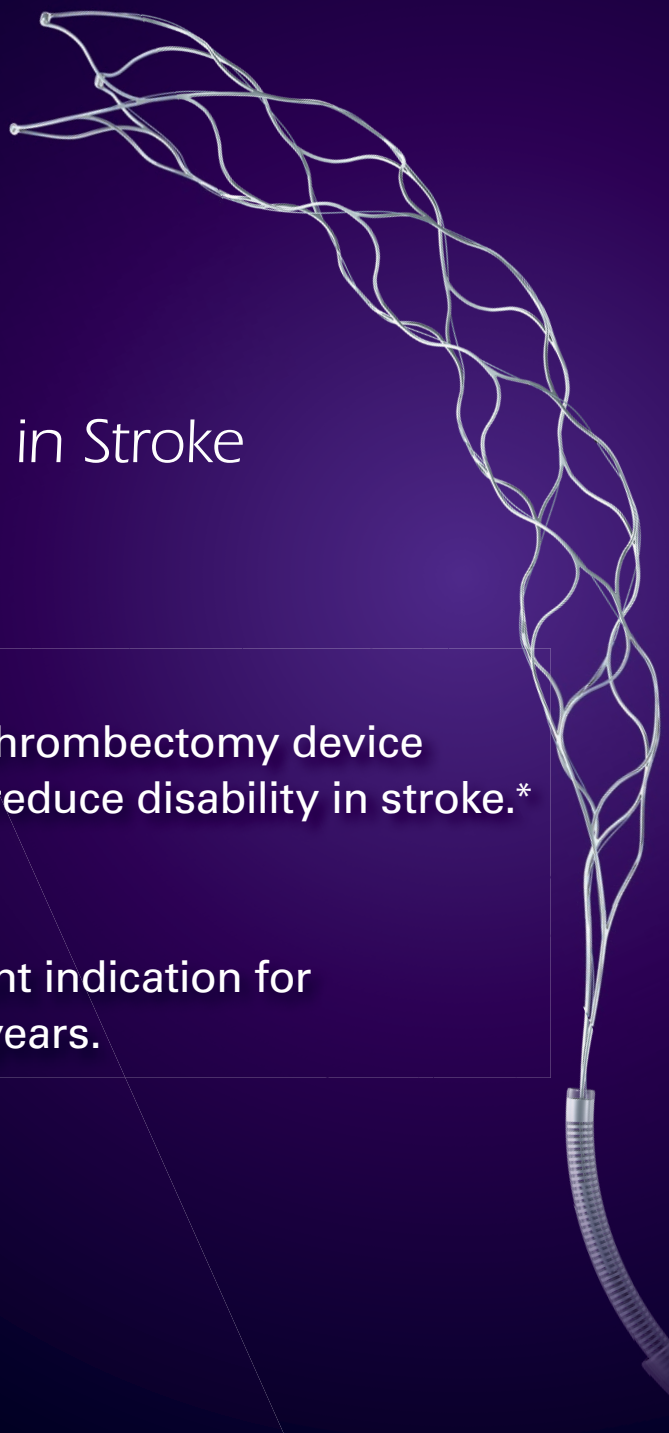

1st

FIRST
mechanical thrombectomy device indicated to reduce disability in stroke.*

FIRST
new treatment indication for stroke in 20 years.

Trevo XP
PROVUE RETRIEVER

Success accelerated.

*The Trevo Retriever is indicated for use to restore blood flow in the neurovasculature by removing thrombus for the treatment of acute ischemic stroke to reduce disability in patients with a persistent, proximal anterior circulation, large vessel occlusion, and smaller core infarcts who have first received intravenous tissue plasminogen activator (IV t-PA). Endovascular therapy with the device should start within 6 hours of symptom onset.

Magic

BALT

FLOW-DEPENDENT MICROCATHETER

NOW AVAILABLE THROUGH BLOCKADE™ MEDICAL

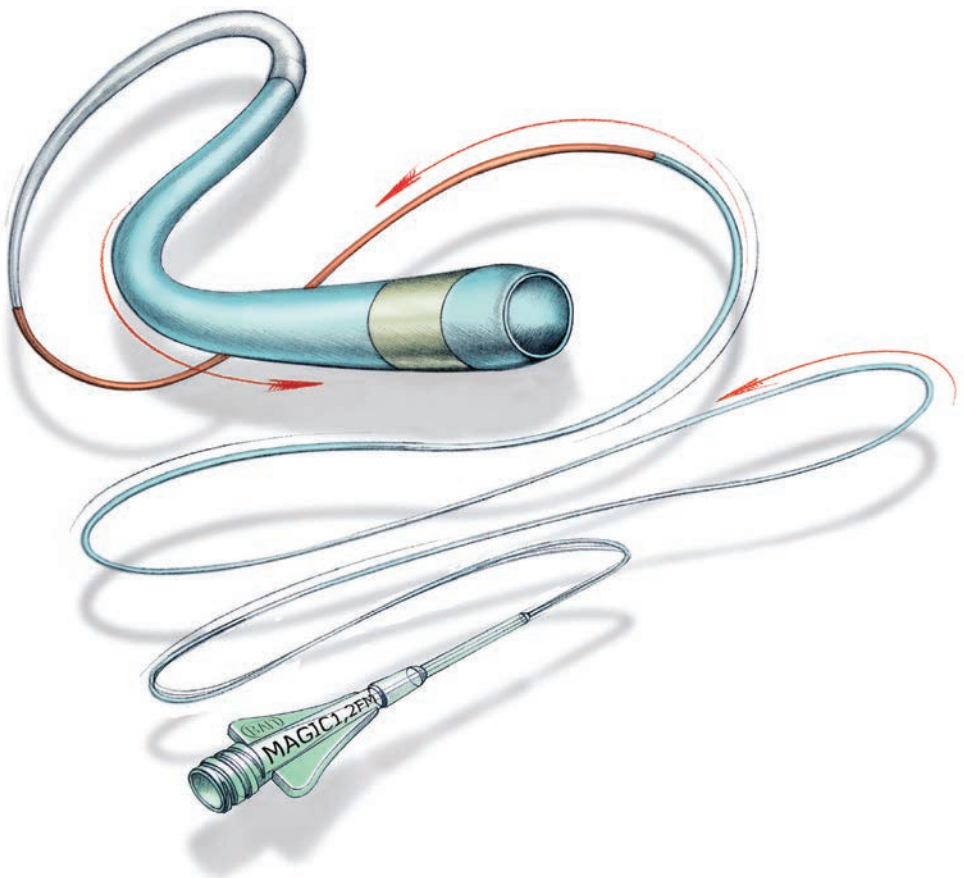

ORDERMAGICS@BLOCKADEMEDICAL.COM

MAGIC catheters are designed for general intravascular use. They may be used for the controlled, selective regional infusion of therapeutic agents or embolic materials into vessels.[1]

1. Magic Catheters IFU – Ind 19

MKTG-068 Rev. A

18 Technology Drive #169, Irvine Ca 92618
P 949.788.1443 | **F** 949.788.1444

BLOCKADE MEDICAL
A BALT Company

The brain at your fingertips

Rapid Medical

www.rapid-medical.com > tigertriever

ASNR 56th Annual Meeting & The Foundation of the ASNR Symposium 2018

June 2 - 7, 2018 | Vancouver, B.C., CANADA

The Vancouver Convention Centre East

Welcome and Greetings

Please join us in Vancouver, CANADA for the **56th Annual Meeting of the American Society of Neuroradiology** on June 2–7, 2018 at the Vancouver Convention Centre East. Surrounded by the coastal mountains and located on the waterfront, you can enjoy these spectacular views in the heart of downtown Vancouver. With its undeniable charm and friendly atmosphere, Vancouver is known around the world as both a popular tourist attraction and one of the best places to live.

ASNR enthusiastically presents **Neuroradiology: Adding Value and Improving Healthcare** at the Symposium of the Foundation of the ASNR, as well as the common thread throughout the Annual Meeting. Implementing a value-based strategy in imaging has grasped the attention of nearly every healthcare provider; in particular with Radiologists understanding that the future will demand their imaging practices deliver better value. Value in healthcare is typically defined as those imaging strategies that yield improved outcomes, lower costs, or both. As payment transitions from a fee-for-service to a value-based system, thus creating a fundamentally different marketplace dynamic, measuring good outcomes are at the center of this changeover. At this time of uncertainty what little remains clear is that without a well-defined knowledge of their outcomes, no medical specialty will be able to succeed in the future value-based system. The Symposium will feature how Neuroradiology, in its many subspecialty areas, adds value to clinical care pathways by directing healthcare practice towards better outcomes. The annual meeting programming will continue on this theme emphasizing imaging that improves health outcomes, while considering costs, thus adding value. Our discussions will incorporate many innovative approaches to how neuroimaging currently does and will continue to improve overall healthcare performance.

As the Program Chair for ASNR 2018, it is my pleasure and honor to welcome you to Vancouver, CANADA for our annual meeting! Vancouver is known for being a very walkable city with a compact downtown core hosting many places to enjoy. So pack your comfortable walking shoes and let's tour together with our colleagues and friends!

Pina Sanelli

Pina C. Sanelli, MD, MPH, FACR
ASNR 2018 Program Chair/President-Elect

NEURORADIOLOGY
Adding Value & Improving Healthcare

ASNR 2018 ▪ VANCOUVER

ASFNR ASHNR ASPNR ASSR SNIS

THE FOUNDATION OF THE ASNR

Pina C. Sanelli, MD, MPH, FACR
ASNR 2018 Program Chair/President-Elect

Programming developed in cooperation with the…

American Society of Functional Neuroradiology (ASFNR)
Max Wintermark, MD

American Society of Head and Neck Radiology (ASHNR)
Deborah R. Shatzkes, MD

American Society of Pediatric Neuroradiology (ASPNR)
Ashok Panigrahy, MD

American Society of Spine Radiology (ASSR)
John D. Barr, MD, FACR, FSIR, FAHA

Society of NeuroInterventional Surgery (SNIS)
Mahesh V. Jayaraman, MD

ASNR Health Policy (HPC) Committee
Robert M. Barr, MD, FACR

ASNR Computer Sciences & Informatics (CSI) Committee
John L. Go, MD, FACR

ASNR Research Scientist Programming Committee
Dikoma C. Shungu, PhD, Timothy P.L. Roberts, PhD

The International Hydrocephalus Imaging Working Group (IHIWG) / CSF Flow Group
William G. Bradley, Jr., MD, PhD, FACR, Harold L. Rekate, MD and Bryn A. Martin, PhD

Fairmont Waterfront Hotel

Pan Pacific Hotel

ASNR 56th Annual Meeting
c/o American Society of Neuroradiology
800 Enterprise Drive, Suite 205
Oak Brook, Illinois 60523-4216
Phone: 630-574-0220 + Fax: 630 574-0661
2018.asnr.org

ASHNR
American Society of
Head & Neck Radiology

51st Annual Meeting

American Society of

Head & Neck Radiology

Head and Neck Imaging in the City of Lights

Caesars Palace • Las Vegas, NV

September 16 – 20, 2017
(Saturday - Wednesday)

Please contact Educational Symposia at 813-806-1000 or ASHNR@edusymp.com or visit www.ASHNR.org for additional information.

We're Inside Every Great Neuroradiologist!

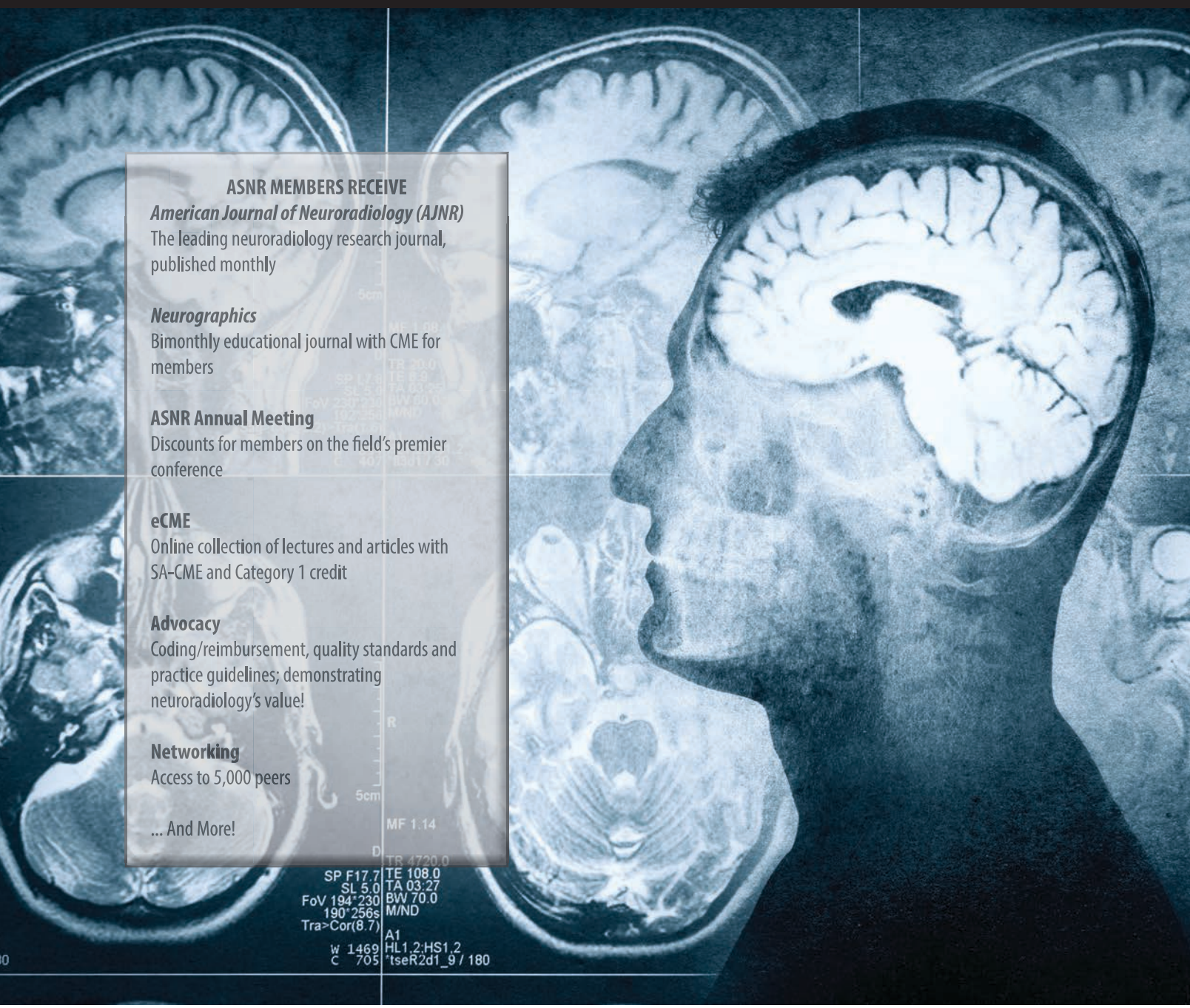

Join the leaders in neuroradiology today!
Learn more at www.asnr.org/join

ASNR
American Society of Neuroradiology

800 Enterprise Dr., Suite 205, Oak Brook, IL 60523 • (630)574-0220 • membership@asnr.org • www.asnr.org

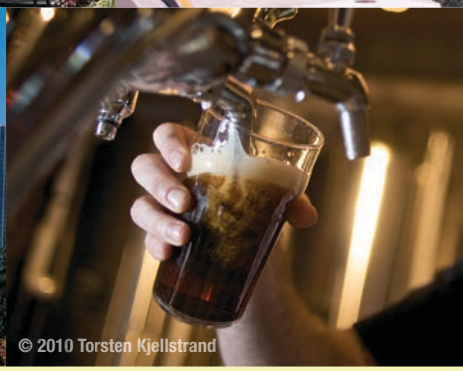

WE'VE MOVED TO FALL 2017!

11th Annual Meeting of the

American Society of

FUNCTIONAL NEURORADIOLOGY

October 9-11, 2017 • the Nines • Portland, Oregon

Optional Hands-on BOLD fMRI Workshop • October 8, 2017

PLEASE CONTACT EDUCATIONAL SYMPOSIA AT
813-806-1000 or ASFNR@edusymp.com or visit www.ASFNR.org for additional information.

Simplify
the MOC Process

Manage
your CME Credits Online

CMEgateway.org

Available to Members of Participating Societies

- American Board of Radiology (ABR)
- American College of Radiology (ACR)
- American Roentgen Ray Society (ARRS)
- American Society of Neuroradiology (ASNR)
- Commnission on Accreditation of Medical Physics Educational Programs, Inc. (CAMPEP)
- Radiological Society of North America (RSNA)
- Society of Interventional Radiology (SIR)
- SNM
- The Society for Pediatric Radiology (SPR)

It's Easy and Free!

Log on to CME Gateway to:

- View or print reports of your CME credits from multiple societies from a single access point.
- Print an aggregated report or certificate from each participating organization.
- Link to SAMs and other tools to help with maintenance of certification.

American Board of Radiology (ABR) participation!

By activating ABR in your organizational profile, your MOC–fulfilling CME and SAM credits can be transferred to your own personalized database on the ABR Web site.

Sign Up Today!

go to CMEgateway.org

Strengthen ASNR's representation at the national level.

Your membership in the American Medical Association strengthens ASNR's representation in the AMA House of Delegates—the policymaking body of the AMA that brings forth the views and interests of all physicians to establish national policy on health, medical, professional and governance matters.

Please activate your 2017 AMA membership, visit ama-assn.org or call AMA Member Relations at (800) 262-3211. If you are currently a member, thank you.

AMA member benefits and resources include:

- Unlimited access to **The JAMA Network®** which brings together *JAMA* and all 11 specialty journals with CME.
  jamanetwork.com
- **STEPS Forward™**, the AMA's new practice transformation series designed to help physicians achieve the Quadruple Aim: better patient experience, better population health and lower overall costs with improved professional satisfaction.
  stepsforward.org
- Free 18-month trial of ***DynaMed Plus®***, an evidence-based, clinical support tool that features thousands of images and provides immediate answers to clinical questions.
  offers.jamanetwork.com

AMA AMERICAN MEDICAL ASSOCIATION

ASNR American Society of Neuroradiology

Trevo® XP ProVue Retrievers

See package insert for complete indications, complications, warnings, and instructions for use.

INDICATIONS FOR USE

1. The Trevo Retriever is indicated for use to restore blood flow in the neurovasculature by removing thrombus for the treatment of acute ischemic stroke to reduce disability in patients with a persistent, proximal anterior circulation, large vessel occlusion, and smaller core infarcts who have first received intravenous tissue plasminogen activator (IV t-PA). Endovascular therapy with the device should start within 6 hours of symptom onset.
2. The Trevo Retriever is intended to restore blood flow in the neurovasculature by removing thrombus in patients experiencing ischemic stroke within 8 hours of symptom onset. Patients who are ineligible for intravenous tissue plasminogen activator (IV t-PA) or who fail IV t-PA therapy are candidates for treatment.

COMPLICATIONS

Procedures requiring percutaneous catheter introduction should not be attempted by physicians unfamiliar with possible complications which may occur during or after the procedure. Possible complications include, but are not limited to, the following: air embolism; hematoma or hemorrhage at puncture site; infection; distal embolization; pain/headache; vessel spasm, thrombosis, dissection, or perforation; emboli; acute occlusion; ischemia; intracranial hemorrhage; false aneurysm formation; neurological deficits including stroke; and death.

COMPATIBILITY

3x20mm retrievers are compatible with Trevo® Pro 14 Microcatheters (REF 90231) and Trevo® Pro 18 Microcatheters (REF 90238). 4x20mm retrievers are compatible with Trevo® Pro 18 Microcatheters (REF 90238). 4x30mm retrievers are compatible with Excelsior® XT-27® Microcatheters (150cm x 6cm straight REF 275081) and Trevo® Pro 18 Microcatheters (REF 90238). 6x25mm Retrievers are compatible with Excelsior® XT-27® Microcatheters (150cm x 6cm straight REF 275081). Compatibility of the Retriever with other microcatheters has not been established. Performance of the Retriever device may be impacted if a different microcatheter is used.

Balloon Guide Catheters (such as Merci® Balloon Guide Catheter and FlowGate® Balloon Guide Catheter) are recommended for use during thrombus removal procedures.

Retrievers are compatible with the Abbott Vascular DOC® Guide Wire Extension (REF 22260).

Retrievers are compatible with Boston Scientific RHV (Ref 421242).

SPECIFIC WARNINGS FOR INDICATION 1

- The safety and effectiveness of the Trevo Retrievers in reducing disability has not been established in patients with large core infarcts (i.e., ASPECTS ≤ 7). There may be increased risks, such as intracerebral hemorrhage, in these patients.
- The safety and effectiveness of the Trevo Retrievers in reducing disability has not been established or evaluated in patients with occlusions in the posterior circulation (e.g., basilar or vertebral arteries) or for more distal occlusions in the anterior circulation.

WARNINGS APPLIED TO BOTH INDICATIONS

- Administration of IV t-PA should be within the FDA-approved window (within 3 hours of stroke symptom onset).
- Contents supplied STERILE, using an ethylene oxide (EO) process. Nonpyrogenic.
- To reduce risk of vessel damage, adhere to the following recommendations:
  - Take care to appropriately size Retriever to vessel diameter at intended site of deployment.
  - Do not perform more than six (6) retrieval attempts in same vessel using Retriever devices.
  - Maintain Retriever position in vessel when removing or exchanging Microcatheter.
- To reduce risk of kinking/fracture, adhere to the following recommendations:
  - Immediately after unsheathing Retriever, position Microcatheter tip marker just proximal to shaped section. Maintain Microcatheter tip marker just proximal to shaped section of Retriever during manipulation and withdrawal.
  - Do not rotate or torque Retriever.
  - Use caution when passing Retriever through stented arteries.
- Do not resterilize and reuse. Structural integrity and/or function may be impaired by reuse or cleaning.
- The Retriever is a delicate instrument and should be handled carefully. Before use and when possible during procedure, inspect device carefully for damage. Do not use a device that shows signs of damage. Damage may prevent device from functioning and may cause complications.
- Do not advance or withdraw Retriever against resistance or significant vasospasm. Moving or torquing device against resistance or significant vasospasm may result in damage to vessel or device. Assess cause of resistance using fluoroscopy and if needed resheath the device to withdraw.
- If Retriever is difficult to withdraw from the vessel, do not torque Retriever. Advance Microcatheter distally, gently pull Retriever back into Microcatheter, and remove Retriever and Microcatheter as a unit. If undue resistance is met when withdrawing the Retriever into the Microcatheter, consider extending the Retriever using the Abbott Vascular DOC guidewire extension (REF 22260) so that the Microcatheter can be exchanged for a larger diameter catheter such as a DAC® catheter. Gently withdraw the Retriever into the larger diameter catheter.
- Administer anti-coagulation and anti-platelet medications per standard institutional guidelines.

PRECAUTIONS

- Prescription only – device restricted to use by or on order of a physician.
- Store in cool, dry, dark place.
- Do not use open or damaged packages.
- Use by "Use By" date.
- Exposure to temperatures above 54°C (130°F) may damage device and accessories. Do not autoclave.
- Do not expose Retriever to solvents.
- Use Retriever in conjunction with fluoroscopic visualization and proper anti-coagulation agents.
- To prevent thrombus formation and contrast media crystal formation, maintain a constant infusion of appropriate flush solution between guide catheter and Microcatheter and between Microcatheter and Retriever or guidewire.
- Do not attach a torque device to the shaped proximal end of DOC® Compatible Retriever. Damage may occur, preventing ability to attach DOC® Guide Wire Extension.

Concentric Medical
301 East Evelyn Avenue
Mountain View, CA 94041

Stryker Neurovascular
47900 Bayside Parkway
Fremont, CA 94538

strykerneurovascular.com

Date of Release: SEP/2016

EX_EN_US

NV00018973.AB

Target® Detachable Coil

See package insert for complete indications, contraindications, warnings and instructions for use.

INTENDED USE / INDICATIONS FOR USE

Target Detachable Coils are intended to endovascularly obstruct or occlude blood flow in vascular abnormalities of the neurovascular and peripheral vessels.

Target Detachable Coils are indicated for endovascular embolization of:

- Intracranial aneurysms
- Other neurovascular abnormalities such as arteriovenous malformations and arteriovenous fistulae
- Arterial and venous embolizations in the peripheral vasculature

CONTRAINDICATIONS

None known.

POTENTIAL ADVERSE EVENTS

Potential complications include, but are not limited to: allergic reaction, aneurysm perforation and rupture, arrhythmia, death, edema, embolus, headache, hemorrhage, infection, ischemia, neurological/intracranial sequelae, post-embolization syndrome (fever, increased white blood cell count, discomfort), TIA/stroke, vasospasm, vessel occlusion or closure, vessel perforation, dissection, trauma or damage, vessel rupture, vessel thrombosis. Other procedural complications including but not limited to: anesthetic and contrast media risks, hypotension, hypertension, access site complications.

WARNINGS

- Contents supplied STERILE using an ethylene oxide (EO) process. Do not use if sterile barrier is damaged. If damage is found, call your Stryker Neurovascular representative.
- For single use only. Do not reuse, reprocess or resterilize. Reuse, reprocessing or resterilization may compromise the structural integrity of the device and/or lead to device failure which, in turn, may result in patient injury, illness or death. Reuse, reprocessing or resterilization may also create a risk of contamination of the device and/or cause patient infection or cross-infection, including, but not limited to, the transmission of infectious disease(s) from one patient to another. Contamination of the device may lead to injury, illness or death of the patient.
- After use, dispose of product and packaging in accordance with hospital, administrative and/or local government policy.
- **This device should only be used by physicians who have received appropriate training in interventional neuroradiology or interventional radiology and preclinical training on the use of this device as established by Stryker Neurovascular.**
- Patients with hypersensitivity to 316LVM stainless steel may suffer an allergic reaction to this implant.
- MR temperature testing was not conducted in peripheral vasculature, arteriovenous malformations or fistulae models.
- The safety and performance characteristics of the Target Detachable Coil System (Target Detachable Coils, InZone Detachment Systems, delivery systems and accessories) have not been demonstrated with other manufacturer's devices (whether coils, coil delivery devices, coil detachment systems, catheters, guidewires, and/or other accessories). Due to the potential incompatibility of non Stryker Neurovascular devices with the Target Detachable Coil System, the use of other manufacturer's device(s) with the Target Detachable Coil System is not recommended.
- To reduce risk of coil migration, the diameter of the first and second coil should never be less than the width of the ostium.
- In order to achieve optimal performance of the Target Detachable Coil System and to reduce the risk of thromboembolic complications, it is critical that a continuous infusion of appropriate flush solution be maintained between a) the femoral sheath and guiding catheter, b) the 2-tip microcatheter and guiding catheters, and c) the 2-tip microcatheter and Stryker Neurovascular guidewire and delivery wire. Continuous flush also reduces the potential for thrombus formation on, and crystallization of infusate around, the detachment zone of the Target Detachable Coil.
- Do not use the product after the "Use By" date specified on the package.
- Reuse of the flush port/dispenser coil or use with any coil other than the original coil may result in contamination of, or damage to, the coil.
- Utilization of damaged coils may affect coil delivery to, and stability inside, the vessel or aneurysm, possibly resulting in coil migration and/or stretching.
- The fluoro-saver marker is designed for use with a Rotating Hemostatic Valve (RHV). If used without an RHV, the distal end of the coil may be beyond the alignment marker when the fluoro-saver marker reaches the microcatheter hub.
- If the fluoro-saver marker is not visible, do not advance the coil without fluoroscopy.
- Do not rotate delivery wire during or after delivery of the coil. Rotating the Target Detachable Coil delivery wire may result in a stretched coil or premature detachment of the coil from the delivery wire, which could result in coil migration.
- Verify there is no coil loop protrusion into the parent vessel after coil placement and prior to coil detachment. Coil loop protrusion after coil placement may result in thromboembolic events if the coil is detached.
- Verify there is no movement of the coil after coil placement and prior to coil detachment. Movement of the coil after coil placement may indicate that the coil could migrate once it is detached.
- Failure to properly close the RHV compression fitting over the delivery wire before attaching the InZone® Detachment System could result in coil movement, aneurysm rupture or vessel perforation.
- Verify repeatedly that the distal shaft of the catheter is not under stress before detaching the Target Detachable Coil. Axial compression or tension forces could be stored in the 2-tip microcatheter causing the tip to move during coil delivery. Microcatheter tip movement could cause the aneurysm or vessel to rupture.
- Advancing the delivery wire beyond the microcatheter tip once the coil has been detached involves risk of aneurysm or vessel perforation.
- The long term effect of this product on extravascular tissues has not been established so care should be taken to retain this device in the intravascular space.

Damaged delivery wires may cause detachment failures, vessel injury or unpredictable distal tip response during coil deployment. If a delivery wire is damaged at any point during the procedure, do not attempt to straighten or otherwise repair it. Do not proceed with deployment or detachment. Remove the entire coil and replace with undamaged product.

- After use, dispose of product and packaging in accordance with hospital, administrative and/or local government policy.

CAUTIONS / PRECAUTIONS

- Federal Law (USA) restricts this device to sale by or on the order of a physician.
- Besides the number of InZone Detachment System units needed to complete the case, there must be an extra InZone Detachment System unit as back up.
- Removing the delivery wire without grasping the introducer sheath and delivery wire together may result in the detachable coil sliding out of the introducer sheath.
- Failure to remove the introducer sheath after inserting the delivery wire into the RHV of the microcatheter will interrupt normal infusion of flush solution and allow back flow of blood into the microcatheter.
- Some low level overhead light near or adjacent to the patient is required to visualize the fluoro-saver marker; monitor light alone will not allow sufficient visualization of the fluoro-saver marker.
- Advance and retract the Target Detachable Coil carefully and smoothly without excessive force. If unusual friction is noticed, slowly withdraw the Target Detachable Coil and examine for damage. If damage is present, remove and use a new Target Detachable Coil. If friction or resistance is still noted, carefully remove the Target Detachable Coil and microcatheter and examine the microcatheter for damage.
- If it is necessary to reposition the Target Detachable Coil, verify under fluoroscopy that the coil moves with a one-to-one motion. If the coil does not move with a one-to-one motion or movement is difficult, the coil may have stretched and could possibly migrate or break. Gently remove both the coil and microcatheter and replace with new devices.
- Increased detachment times may occur when:
  - Other embolic agents are present.
  - Delivery wire and microcatheter markers are not properly aligned.
  - Thrombus is present on the coil detachment zone.
- Do not use detachment systems other than the InZone Detachment System.
- Increased detachment times may occur when delivery wire and microcatheter markers are not properly aligned.
- Do not use detachment systems other than the InZone Detachment System.

Stryker Neurovascular
47900 Bayside Parkway
Fremont, CA 94538

strykerneurovascular.com

Date of Release: MAR/2016

EX_EN_US

NV00018669.AB

A Complete Coil Portfolio

MicroVention's comprehensive portfolio features clinically proven Hydrogel coils, which can be used exclusively or in combination with our trusted Platinum coils to treat a wide range of aneurysms and neurovascular lesions.

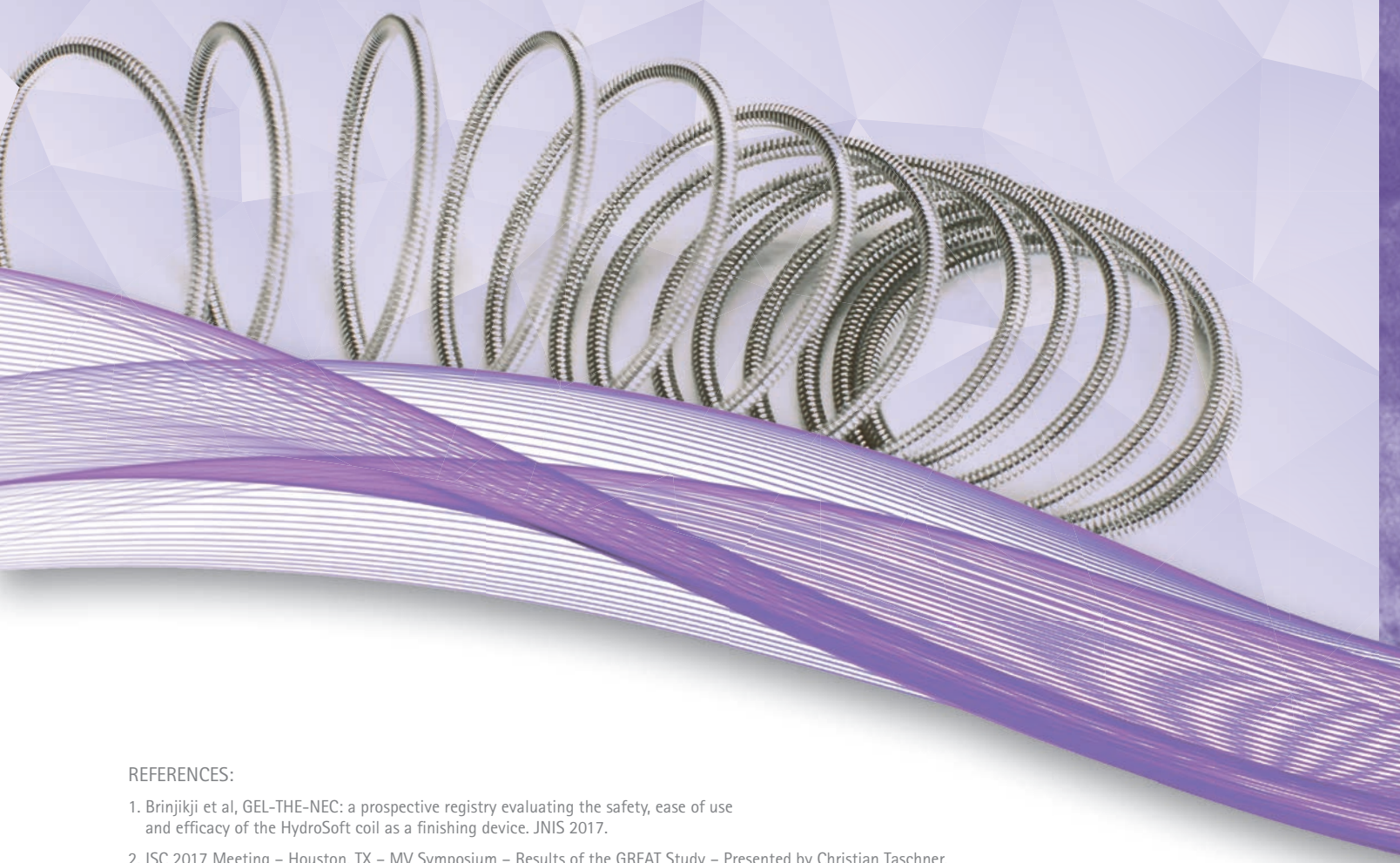

REFERENCES:

1. Brinjikji et al, GEL-THE-NEC: a prospective registry evaluating the safety, ease of use and efficacy of the HydroSoft coil as a finishing device. JNIS 2017.
2. ISC 2017 Meeting – Houston, TX – MV Symposium – Results of the GREAT Study – Presented by Christian Taschner, MD, Department of Neuroradiology, Medical Centre – University of Freiburg, Germany

INDICATIONS FOR USE:

The HydroCoil® Embolic System (HES) and MicroPlex Coil System (MCS) are intended for the endovascular embolization of intracranial aneurysms and other neurovascular abnormalities such as arteriovenous malformations and arteriovenous fistulae. The HES and MCS are also intended for vascular occlusion of blood vessels within the neurovascular system to permanently obstruct blood flow to an aneurysm or other vascular malformation and for arterial and venous embolizations in the peripheral vasculature.

The device should only be used by physicians who have undergone pre-clinical training in all aspects of HES/MCS procedures as prescribed by MicroVention.

stryker®
Neurovascular

Purposeful innovation in mind.

Smooth and stable.

Target Detachable Coils deliver consistently smooth deployment and exceptional microcatheter stability. Designed to work seamlessly together for framing, filling and finishing. Target Coils deliver the high performance you demand.

For more information, please visit www.strykerneurovascular.com/Target or contact your local Stryker Neurovascular sales representative.

Target®
DETACHABLE COILS

NV00018669.AA

THE PROVEN LEADER

The STAR™ Tumor Ablation System is the proven leader in spine RF ablation with thousands of patients treated.

Dual thermocouples for active temperature monitoring on a single instrument

Steerable and navigational RF ablation instrument

SpineSTAR® delivers RF energy directly to the tumor

Tumor is debulked

STAR Clinical Studies Demonstrate[1-4]:

- Fast, durable pain relief
- Rapid improvement in mobility and quality of life
- Reduction or discontinuation of pain medication
- Site-specific ablation zones and real time temperature monitoring
- May be combined with radiation and/or chemotherapy

MERITMEDICAL®

Merit.com/star

Indications for Use: The STAR™ Tumor Ablation System is indicated for palliative treatment in spinal procedures by ablation of metastatic malignant lesions in a vertebral body. As with most surgical procedures, there are risks associated with the STAR procedure, including serious complications. For complete information regarding risks, contraindications, warnings, precautions, and adverse events please review the System's Instructions for Use.

References
1 Pain Physician 2014 Jul-Aug; 17(4):317-27 2 Radiology 2014 Oct; 273 (1): 261-7 3 J. Vasc Interv Radiol 2015; 18: 573-581 4 Pain Physician 2015; 18: 573-581

402549001/A ID 102016

JUNE 2017

AJNR

VOLUME 38 • PP 1069–1273

AJNR

AMERICAN JOURNAL OF NEURORADIOLOGY

JUNE 2017
VOLUME 38
NUMBER 6
WWW.AJNR.ORG

THE JOURNAL OF DIAGNOSTIC AND INTERVENTIONAL NEURORADIOLOGY

Synthetic MRI in clinical neuroimaging

Autoimmune encephalitis

MR biomarker of spinal cord white matter injury

Official Journal ASNR • ASFNR • ASHNR • ASPNR • ASSR

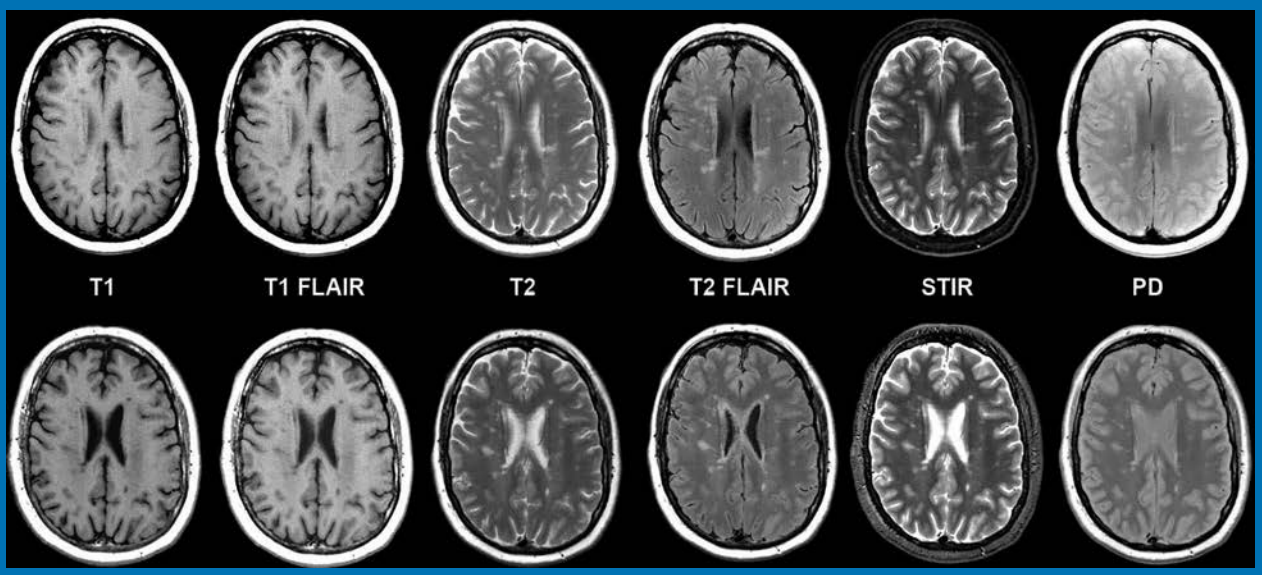

AJNR

AMERICAN JOURNAL OF NEURORADIOLOGY

JUNE 2017
VOLUME 38
NUMBER 6
WWW.AJNR.ORG

Publication Preview at www.ajnr.org features articles released in advance of print. Visit www.ajnrblog.org to comment on AJNR content and chat with colleagues and AJNR's News Digest at http://ajnrdigest.org to read the stories behind the latest research in neuroimaging.

AJNR (Am J Neuroradiol ISSN 0195–6108) is a journal published monthly, owned and published by the American Society of Neuroradiology (ASNR), 800 Enterprise Drive, Suite 205, Oak Brook, IL 60523. Annual dues for the ASNR include $170.00 for journal subscription. The journal is printed by Cadmus Journal Services, 5457 Twin Knolls Road, Suite 200, Columbia, MD 21045; Periodicals postage paid at Oak Brook, IL and additional mailing offices. Printed in the U.S.A. POSTMASTER: Please send address changes to American Journal of Neuroradiology, P.O. Box 3000, Denville, NJ 07834, U.S.A. Subscription rates: nonmember $390 ($460 foreign) print and online, $310 online only; institutions $450 ($520 foreign) print and basic online, $895 ($960 foreign) print and extended online, $370 online only (basic), extended online $805; single copies are $35 each ($40 foreign). Indexed by PubMed/Medline, BIOSIS Previews, Current Contents (Clinical Medicine and Life Sciences), EMBASE, Google Scholar, HighWire Press, Q-Sensei, RefSeek, Science Citation Index, and SCI Expanded.

ONLINE FEATURES

LETTERS

BOOK REVIEWS *R.M. Quencer, Section Editor*

Please visit www.ajnrblog.org to read and comment on Book Reviews.

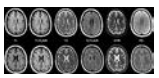

MS lesions shown both on coventional imaging (upper row) and synthetic (lower row) imaging sets.

Indicates Editor's Choices selection

Indicates Fellows' Journal Club selection

Indicates open access to non-subscribers at www.ajnr.org

Indicates article with supplemental on-line table

Indicates article with supplemental on-line photo

Indicates article with supplemental on-line video

Evidence-Based Medicine Level 1

Evidence-Based Medicine Level 2

AJNR

AMERICAN JOURNAL OF NEURORADIOLOGY

Publication Preview at www.ajnr.org features articles released in advance of print. Visit www.ajnrblog.org to comment on AJNR content and chat with colleagues and AJNR's News Digest at http://ajnrdigest.org to read the stories behind the latest research in neuroimaging.

JUNE 2017 • VOLUME 38 • NUMBER 6 • WWW.AJNR.ORG

Title: M42. The Orion nebula (M42) (left), and the adjacent Running Man nebula (NGC 1973) (right) are visible to the naked eye, but a tough photographic target because they combine a very bright central core with extended diffuse nebulosity. This image is a combination of 3 RGB photographs shot at different time intervals (60, 180, and 300 seconds) and combined using the high dynamic range (HDR) feature of PixInsight software. Registration, integration, channel combination, color correction, and HDR transform were done in PixInsight and slight touch-ups in Photoshop. The images were shot with Takahashi FSQ 106 from New Mexico and Australia and the total time of acquisition was 5.2 hours.

Jeffrey S. Ross, Mayo Clinic, Phoenix, Arizona

Autoimmune Encephalitis: Pathophysiology and Imaging Review of an Overlooked Diagnosis

B.P. Kelley, S.C. Patel, H.L. Marin, J.J. Corrigan, P.D. Mitsias, and B. Griffith

ABSTRACT

SUMMARY: Autoimmune encephalitis is a relatively new category of immune-mediated disease involving the central nervous system that demonstrates a widely variable spectrum of clinical presentations, ranging from the relatively mild or insidious onset of cognitive impairment to more complex forms of encephalopathy with refractory seizure. Due to its diverse clinical features, which can mimic a variety of other pathologic processes, autoimmune encephalitis presents a diagnostic challenge to clinicians. Imaging findings in patients with these disorders can also be quite variable, but recognizing characteristic findings within limbic structures suggestive of autoimmune encephalitis can be a key step in alerting clinicians to the potential diagnosis and ensuring a prompt and appropriate clinical work-up. In this article, we review antibody-mediated encephalitis and its various subtypes with a specific emphasis on the role of neuroimaging in the diagnostic work-up.

ABBREVIATIONS: NMDA = *N*-methyl D-aspartate; NMDAr = *N*-methyl D-aspartate receptor; VGKC = voltage-gated potassium channel

Autoimmune encephalitis is an important cause of new-onset altered mental status, the scope of which has only recently begun to be recognized in the medical literature.[1-3] Despite this increased recognition, it has yet to become an established diagnostic consideration outside of large tertiary referral centers.[1-5] The term "autoimmune encephalitis" generally refers to a family of closely related disease processes that share overlapping clinical features and neuroimaging findings but are ultimately differentiated by the specific antibody subtypes driving the underlying immune-mediated attack on different CNS structures.[6-8] This antibody-mediated attack on neuronal structures results in a localized inflammatory response. Thus, the clinical and imaging manifestations are dictated by the specific location of the underlying immune response within the nervous system, which leads to substantial variability. While limbic dysfunction is the single most consistent finding in autoimmune encephalitis, varying degrees of involvement are seen within the neocortex, striatum, hindbrain, spine, and peripheral nervous system based on the unique antibody profile.[3,9-12] In addition, certain antibody subtypes consistently lack imaging manifestations, while others characteristically demonstrate prominent "extralimbic" involvement.[3,7,13-15]

Although it was initially thought to be relatively rare, there is growing consensus that autoimmune encephalitis is responsible for a subset of altered mental status previously considered idiopathic.[3-5] Despite its growing recognition as a rare cause of altered mental status, autoimmune encephalitis remains a diagnosis of exclusion with more common causes often identified during the standard diagnostic evaluation.[16,17] However, more complex presentations of altered mental status may display atypical features without a clear etiology identified after routine testing.[16,17] In these situations, recognition of potential cases of autoimmune encephalitis by the radiologist can be the first step to optimizing clinical outcomes through ensuring that a prompt and appropriate clinical work-up is performed, including the use of specialized serum/CSF antibody panels, with the ultimate goal of establishing an effective treatment regimen before the onset of devastating complications.[3,5,8,18]

The purpose of this article is to discuss the subset of immune-mediated CNS conditions with features of autoimmune encephalitis (ie, antibody-mediated inflammation of the brain), provide a framework for radiologists to understand the relevant neuroimmunology, review the major antibody subtypes, and describe the constellation of clinical and imaging features that are most suggestive of this diagnosis.

From the Departments of Neuroradiology (B.P.K., S.C.P., H.L.M., J.J.C., B.G.), and Neurology (P.D.M.), Henry Ford Hospital, Detroit, Michigan.

Paper previously presented, in part, at: Annual Meeting of the American Society of Neuroradiology and the Foundation of the ASNR Symposium, May 23–26, 2016; Washington, DC.

Please address correspondence to Brendan P. Kelley, MD, MSc, Department of Radiology, Henry Ford Hospital, 2799 W Grand Blvd, Detroit, MI 48202; e-mail: brendank@rad.hfh.edu; @brendanpkelley

Indicates open access to non-subscribers at www.ajnr.org

Indicates article with supplemental on-line table.

http://dx.doi.org/10.3174/ajnr.A5086

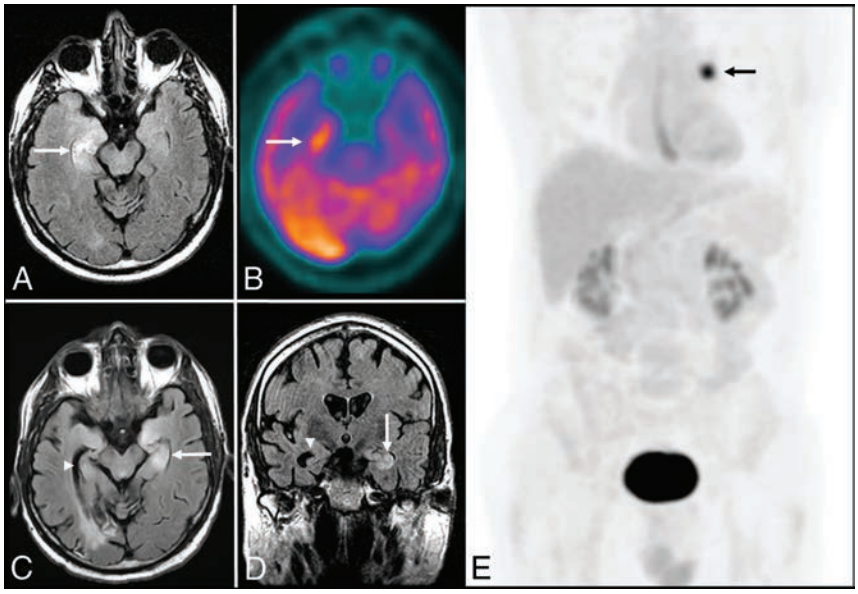

FIG 1. Anti-Hu encephalitis. A 68-year-old man with chronic obstructive pulmonary disease presented with gradually worsening memory deficits and confusion, with subclinical seizures. MR imaging of the brain demonstrates T2-FLAIR hyperintensity and mild expansion in the right medial temporal lobe (*A*), right insular cortex (not shown), and left dorsal thalamus (not shown), without restricted diffusion (not shown) or postcontrast enhancement (not shown). FDG-PET of the brain demonstrates a hypermetabolic focus within the right medial temporal lobe lesion (*B*). PET of the body demonstrates a hypermetabolic focus in the left lung (*E*), consistent with biopsy-proved small-cell lung cancer. The patient was in remission following treatment with intravenous immunoglobulin infusions, oral steroids, and chemotherapy, but he presented approximately 2.5 years later with worsening memory decline. MR imaging at that time (*C* and *D*) shows new T2-FLAIR hyperintensity in the left medial temporal lobe (*white arrow*) with volume loss within the right medial temporal lobe (*white arrowhead*). An old right occipital lobe infarct is also incidentally noted.

Pathophysiology: Models for Disease Classification

Antibody-mediated CNS disorders can be classified into 2 broad categories, paraneoplastic or nonparaneoplastic, based on the presence or absence of an underlying malignancy, respectively.[18-20] Paraneoplastic syndromes affecting the CNS are generally thought to develop in cancer when antigens shared by tumor cells and native nonneoplastic neuronal cells result in an antibody-mediated attack on previously immune-privileged neuronal structures.[2,6-8,19] Initially thought to occur in <1% of patients with cancer, more recent data suggest that the true incidence is likely much higher.[3-6] Paraneoplastic syndromes are most often seen in small-cell lung cancer but can also be seen in a variety of other cancers as well, such as neuroblastoma, germ cell tumor of the testis, breast cancer, Hodgkin lymphoma, thymoma, and immature ovarian teratomas.[19-22]

Regardless of the etiology and antibody profile, there is a clear predilection in autoimmune encephalitis for antigens within the limbic system (Figs 1 and 2).[3,10,23,24] Paraneoplastic limbic encephalitis, a specific paraneoplastic syndrome affecting the temporal lobe and limbic structures, was first described by the British neuropathologists Corsellis et al[25] in 1968 after identifying postinflammatory changes in the mesial temporal lobes of patients with progressive memory loss after being diagnosed with lung cancer. Kohler et al[26] later correlated these inflammatory changes with T2-weighted hyperintense signal changes on MR imaging of the brain. These characteristic neuroimaging findings were later validated by a larger study of 50 patients with paraneoplastic limbic encephalitis across different antibody profiles that found that 39 of 50 patients (79%) had similar T2-FLAIR hyperintense signal changes in their temporal lobes and limbic structures.[19] This study, conducted by Gultekin et al[19] in 2000, proposed the first diagnostic criteria for paraneoplastic limbic encephalitis, which included the following: 1) short-term memory loss, seizures, or psychiatric symptoms; 2) <4 years between symptom onset and cancer diagnosis; 3) exclusion of metastases, infection, metabolic, or other causes; and 4) one of the following: inflammatory CSF findings, temporal lobe T2 or FLAIR hyperintensity on MR imaging, or electroencephalogram abnormality in the temporal lobes.[19] Tüzün and Dalmau[27] subsequently modified these criteria in 2007 to account for the growing subset of nonparaneoplastic forms of autoimmune encephalitis, which also demonstrated prominent limbic involvement.

In addition to the "paraneoplastic-versus-nonparaneoplastic" categorization, antibody-mediated encephalitides can also be characterized as either group I or group II according to the location of their neuronal antigens (On-line Table), with group I antibodies targeting intracellular antigens and group II antibodies targeting antigens on the cell surface.[1,2,6,7,9,27] This distinction is clinically relevant because it has implications for treatment response, association with an underlying malignancy, and overall long-term prognosis.[9,20,22,28]

Group I Antibodies: Autoimmune Encephalitis with Intracellular Antigens

Group I antibodies target intracellular neuronal antigens, are more closely associated with an underlying malignancy, and use the same cytotoxic T-cell mechanisms when targeting the intracellular neuronal antigens and onconeuronal antigens as part of the immune response to cancer.[1,7,9,29] Group I antibodies are also associated with poor clinical outcomes, characterized by a decreased response to immunomodulatory therapy and an increased prevalence of "irreversible" neuronal damage, and often have the additional burden of an underlying malignancy.[9,19,21] Compared with group II antibodies, group I antibodies are less specific clinical markers of disease for autoimmune encephalitis and can also be seen in patients with cancer without paraneoplastic syndromes.[29,30]

Anti-Hu

Anti-Hu (anti-neuronal nuclear antibody 1) encephalitis is the most common paraneoplastic form of autoimmune encephalitis, has a relatively poor prognosis compared with other subtypes, and is associated with small-cell lung cancer in most cases (75%).[19,31] Anti-Hu syndrome is a distinct clinical phenotype described in

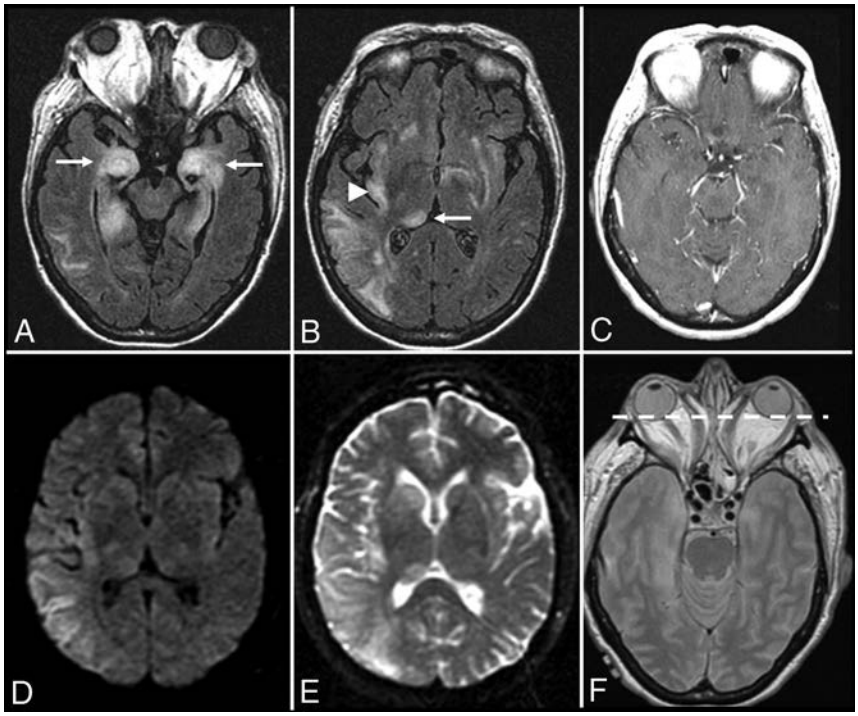

FIG 2. Graves ophthalmopathy with anti-Hu encephalitis. A 63-year-old woman with severe encephalopathy and diffuse enlargement of the extraocular muscles developed fatal autonomic dysfunction. MR imaging of the brain demonstrates prominent T2-FLAIR abnormalities in the mesial temporal lobes (*A*), right thalamus (*B*), right > left insular cortex (*B*), and posterior right temporal lobe (*B*), without enhancement (*C*) and with T2 shinethrough but no restricted diffusion on DWI (*D*) and the corresponding ADC map (*E*). There is also diffuse symmetric enlargement of the extraocular muscles, resulting in exophthalmos (*F*).

patients with cancer expressing anti-Hu antibodies and has features of paraneoplastic encephalomyelitis, paraneoplastic subacute sensory neuropathy, and paraneoplastic cerebellar degeneration.[19,31,32] While anti-Hu encephalitis is not as closely associated with seizures as some of the other major subtypes of autoimmune encephalitis, a subset of patients with anti-Hu encephalitis can present with epilepsia partialis continua, a specific seizure disorder characterized by extended focal motor epileptic seizures prominently involving the face and distal extremities that recur every few seconds/minutes.[32,33] MR imaging findings correlate with clinical features and typically include T2-FLAIR hyperintense lesions in the medial temporal lobes with variable involvement of the cerebellum and brain stem (Figs 1 and 2).[3,19,21,23]

Anti-Ma/Ta

Anti-Ma (Ma1/Ma2/Ma3) encephalitis has a better prognosis than anti-Hu and is strongly associated with testicular tumors in young men and small-cell lung cancer or breast cancer in older patients.[7,9,34,35] The association with testicular tumors in young men is so strong that some authors have advocated empiric orchiectomy in refractory cases of severe anti-Ma encephalitis for presumed microscopic neoplastic testicular tumors if certain diagnostic criteria are met and no other etiology is found.[36] According to a review of 38 patients with anti-Ma encephalitis, most patients (62%) presented with neurologic symptoms before the identification of their malignancy, which included any combination of limbic, diencephalic, or brain stem dysfunction.[13] Notably, only a minority of patients (26%) had classic symptoms of limbic encephalitis, and most patients with brain stem involvement had ophthalmoplegia (92%).[13] Abnormal findings on brain MR imaging were common (74%) and often involved classic T2-FLAIR hyperintense lesions in the medial temporal lobes with variable involvement of the thalamus and brain stem.[13] Although not classic, nodular postcontrast enhancement that can mimic tumor or infection has also been described.[13,35,36]

Anti-CV2

Anti-CV2 (collapsin response mediator protein 5) encephalitis is a unique subtype associated with small-cell lung cancer and malignant thymoma that has prominent T2-FLAIR hyperintense lesions in the striatum and clinically resembles choreiform movement disorders.[3,37] MR imaging features are also atypical compared with other types of autoimmune encephalitis in that there is less prominent involvement of the medial temporal lobe.[3,37] Most important, there is typically no restricted diffusion or T2-FLAIR hyperintense lesions in the striatum, which can help differentiate this condition from prion diseases like Creutzfeldt-Jakob disease.[3,16] When one considers this relatively rare diagnosis, it is important to first rule out more common toxometabolic disorders such as hyperammonemia, carbon monoxide poisoning, and hypoglycemia.

Anti-Glutamic Acid Decarboxylase

Glutamic acid decarboxylase (GAD) is an intracellular enzyme that catalyzes the synthesis of γ-aminobutyric acid, the major inhibitory neurotransmitter in the CNS. Anti-glutamic acid decarboxylase antibodies are unique because they are a group I antibody not typically associated with malignancy and are also associated with other nonneoplastic autoimmune conditions such as type 1 diabetes mellitus.[9,38] The anti-glutamic acid decarboxylase antibody subtype can cause a form of autoimmune encephalitis with classic temporal lobe lesions on MR imaging with the expected clinical findings of limbic encephalitis plus additional features of stiff person syndrome with early and prominent development of seizures (Fig 3).[9,38]

Additional Type I Antibody Subtypes

Amphiphysin antibodies are most often seen in breast cancer and small-cell lung cancer with associated clinical features of stiff person syndrome, myelopathy, myoclonus, and encephalomyelitis.[7,39] Ri (anti-neuronal nuclear antibody 2) antibodies are also most often seen in breast cancer and small-cell lung cancer, with features of brain stem encephalitis and opsoclonus-myoclonus syndrome.[7,39] Yo (pa-

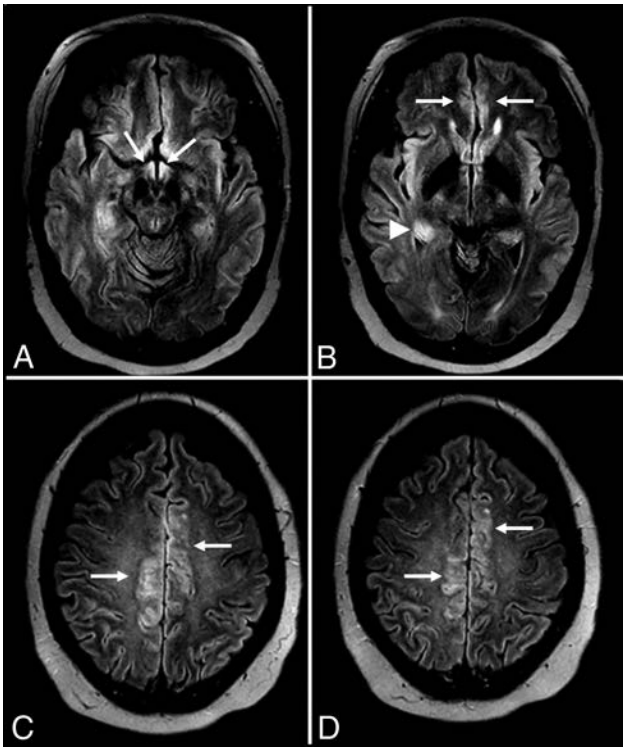

FIG 3. Anti-glutamic acid decarboxylase encephalitis. A 61-year-old woman presented with headaches, mild confusion, and nystagmus without development of psychosis, severe encephalopathy, or seizures. MR imaging of the brain demonstrates T2-FLAIR hyperintensity in the right > left hippocampus (*A* and *B*), right > left insular cortex (*B*), and bilateral cingulate gyrus (*C* and *D*) without restricted diffusion (not shown), hemorrhage (not shown), or postcontrast enhancement (not shown).

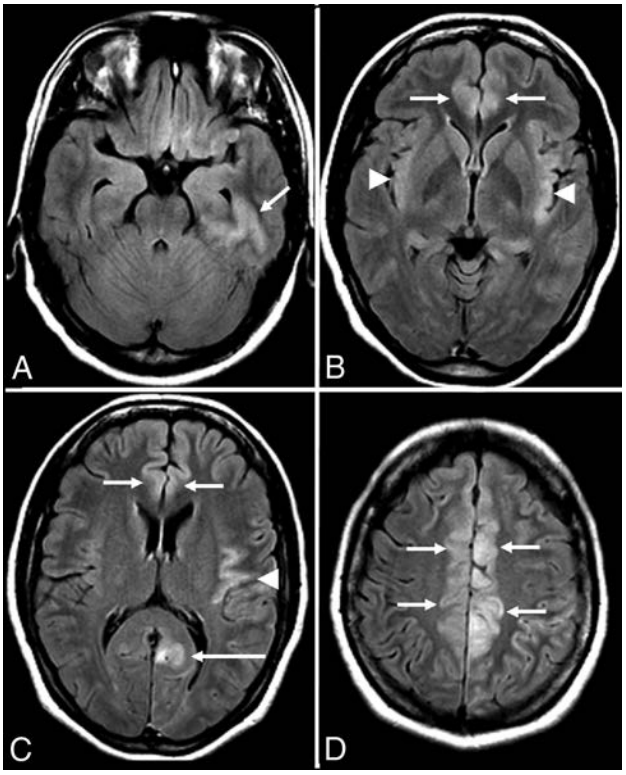

FIG 4. Anti-*N*-methyl D-aspartate receptor encephalitis. A 32-year-old woman presented with headaches, vertigo, and psychosis with subsequent development of encephalopathy and seizures. MR imaging of the brain performed after the onset of seizures 2 weeks after initial presentation demonstrates T2-FLAIR hyperintensity in the left inferior temporal lobe (*A*), left > right insular cortex (*B* and *C*), and left > right cingulate gyrus (*B–D*), without restricted diffusion (not shown), hemorrhage (not shown), or postcontrast enhancement (not shown).

rietal cell autoantibodies 1) antibodies are most often seen in ovarian cancer and breast cancer, with characteristic features of paraneoplastic cerebellar degeneration, but they can also demonstrate features of autoimmune encephalitis.[7,39,40]

Group II Antibodies: Autoimmune Encephalitis with Cell-Surface Antigens

Group II antibodies target cell-surface neuronal antigens, are less likely to be associated with an underlying malignancy, and use more "restricted" humoral immune mechanisms of neurotoxicity that typically respond better to early immunomodulatory therapy.[9,20,41] Group II antibodies also represent a more specific clinical marker of disease for antibody-mediated encephalitis, with reduction in serum antibody titers following treatment directly associated with improved neurologic outcomes.[41,42] Group II antibodies often target synaptic proteins and can result in the downregulation of receptors that leads to altered synaptic transmission associated with epileptiform activity.[9,11,15] Patients with nonneoplastic forms of autoimmune encephalitis associated with group II antibodies may have an underlying systemic autoimmune disorder or can develop symptoms following a viral infection or vaccination, but in many cases, no clear etiology is identified.[1,4,11,43] The current list of group II antibodies will likely continue to grow on the basis of the number of case reports in the medical literature of "suspected autoimmune encephalitis" or "steroid-responsive limbic encephalitis," in which a specific antibody or malignancy is not identified but the diagnosis is strongly suggested by a combination of characteristic clinical features, typical neuroimaging findings, good empiric treatment response, and no convincing alternative diagnosis.[43-45]

N-*Methyl D-Aspartate Receptor*

N-methyl D-aspartate receptor (NMDAr) encephalitis is one of the most common and best characterized subtypes of autoimmune encephalitis classically seen in young women and children with autoimmunity not associated with cancer (Fig 4).[20,28,46] This subtype is mediated by immunoglobulin G antibodies against the GluN1 subunit of the neuronal NMDAr, with inflammatory neuronal dysfunction that is thought to be initially reversible but potentially progresses to permanent neuronal destruction if untreated, due to prolonged inflammation and *N*-methyl D-aspartate (NMDA)-mediated glutamate excitotoxicity.[9,47,48] NMDAr encephalitis has a well-characterized progression of features characterized by an initial viral-like prodrome (fever, malaise, headaches, and anorexia), followed by psychiatric symptoms (anxiety, depression, schizophrenia, and psychosis), which progress to include temporal lobe dysfunction (amnesia and seizures) and ultimately culminate in severe neurologic deficits, including autonomic dysfunction, dystonia/dyskinesia, and profound encephalopathy.[3,20,49,50] There are many cautionary reports in the medical literature of young women with NMDAr encephalitis and

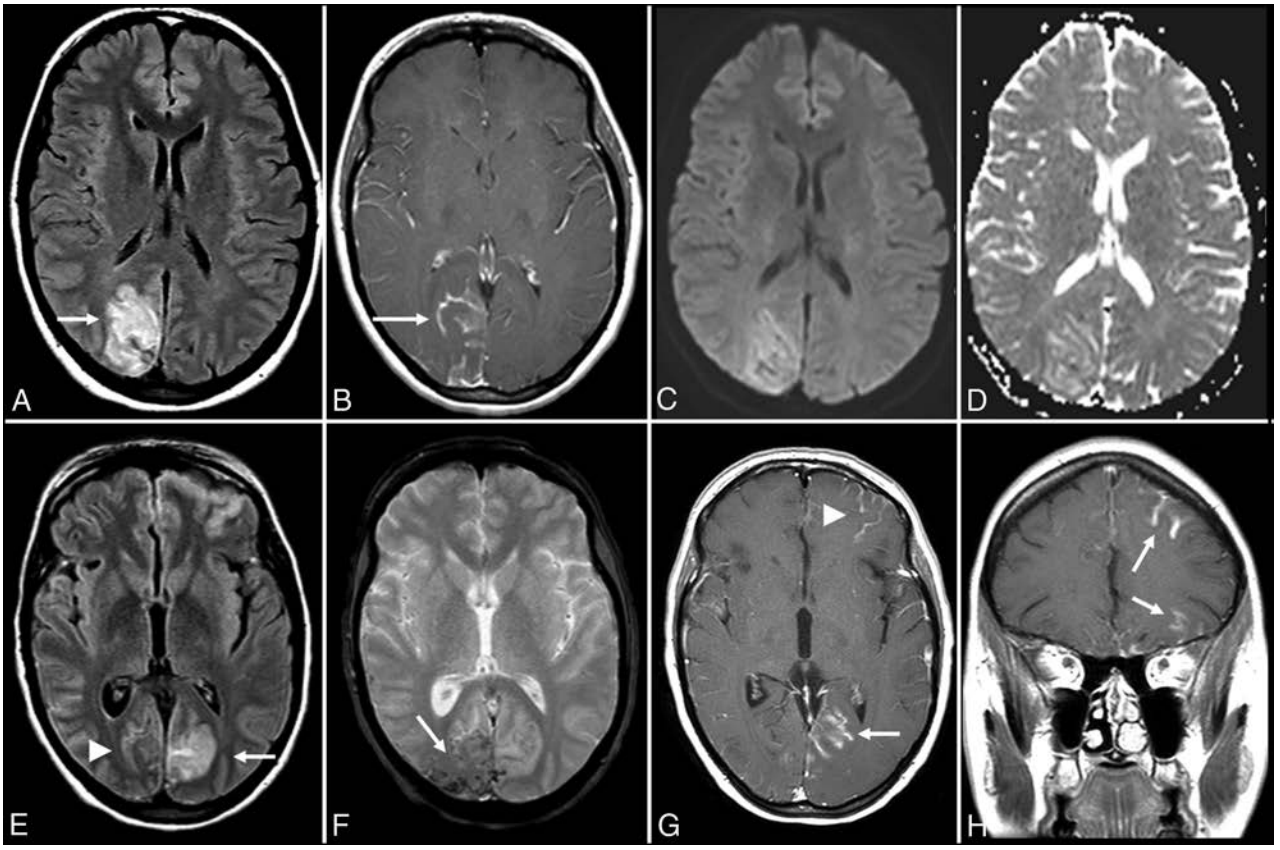

FIG 5. Anti-voltage-gated calcium channel encephalitis. A 39-year-old woman presented with left-sided weakness and left visual field deficits with subsequent development of encephalopathy and seizures. Initial MR imaging of the brain (*A–D*) demonstrates multifocal T2-FLAIR hyperintense lesions in the right parieto-occipital region (*A*), with associated pial/sulcal enhancement (*B*) and mild cortical restricted diffusion and T2 shinethrough within the subcortical white matter on DWI (*C*) and the corresponding ADC map (*D*). Follow-up MR imaging of the brain performed 34 days later (*E–H*) demonstrates decreased T2-FLAIR hyperintensity (*E*) with cortical laminar necrosis and petechial hemorrhage (*F*) at the original lesion, with progressive development on subsequent examinations of similar cortical lesions in the contralateral frontal, parietal, and occipital lobes (*E–H*).

no significant medical history who present with initial psychiatric symptoms that prompt admission to a psychiatric facility but later require transfer to the intensive care unit after development of the more severe neurologic deficits associated with this condition.[18,20,48,51]

With early diagnosis and treatment, patients with NMDAr encephalitis have a relatively good prognosis and can experience a return to their baseline functional status with complete resolution of neuroimaging abnormalities on follow-up examinations.[20,41,49] Relapsing forms of nonparaneoplastic NMDAr encephalitis have been reported, and long-term prophylaxis with steroid-sparing agents like rituximab may be required in a subset of cases.[42,48,50] A minority of cases of NMDAr encephalitis can be associated with an underlying malignancy, especially in older patients.[20,52,53] According to 1 study, 45% of adult women with NMDAr encephalitis had an underlying ovarian teratoma but only 9% of young girls had this finding.[53] In women older than 45 years of age, this same study found that 23% of women had an ovarian carcinoma instead of a teratoma.[53] This finding highlights the need to screen all patients with autoimmune encephalitis for an underlying malignancy, regardless of the antibody profile, and even to consider the possibility of a contralateral or concurrent tumor with a poor response to treatment despite removal of a tumor.[27,49] NMDAr encephalitis is an especially important diagnosis to consider in young patients with limbic encephalitis because the California Encephalitis Project found that the number of young patients in the study with NMDAr encephalitis was greater than those with any single viral etiology.[54] Anti-NMDAr antibodies have even been found in patients with herpes simplex virus encephalitis[55] and Rasmussen encephalitis,[56] which can further complicate the diagnostic work-up.

One unique feature of the NMDAr encephalitis subtype is that it is unlikely to have associated neuroimaging abnormalities on initial presentation (89%) or follow-up MR imaging of the brain (79%).[14] The lack of neuroimaging findings in NMDAr encephalitis is consistent across the medical literature, with another study reporting that most patients with NMDAr encephalitis (66%) had normal brain MR imaging findings, and the remaining 44% had wide variation in the distribution and degree of T2-FLAIR hyperintense signal changes throughout the brain.[53] Recognizing this established progression of specific symptoms and a lack of neuroimaging findings is essential to prospectively consider the diagnosis in the appropriate clinical setting, particularly when patients demonstrate characteristic electroencephalogram findings.[57] When brain MR imaging abnormalities are present, these T2-FLAIR hyperintense lesions can typically demonstrate mild transient cortical enhancement without restricted diffusion or hemorrhage (Fig 4).[3,14,53] When brain MR imaging findings are absent but the clinical findings suggest the possibility of an auto-

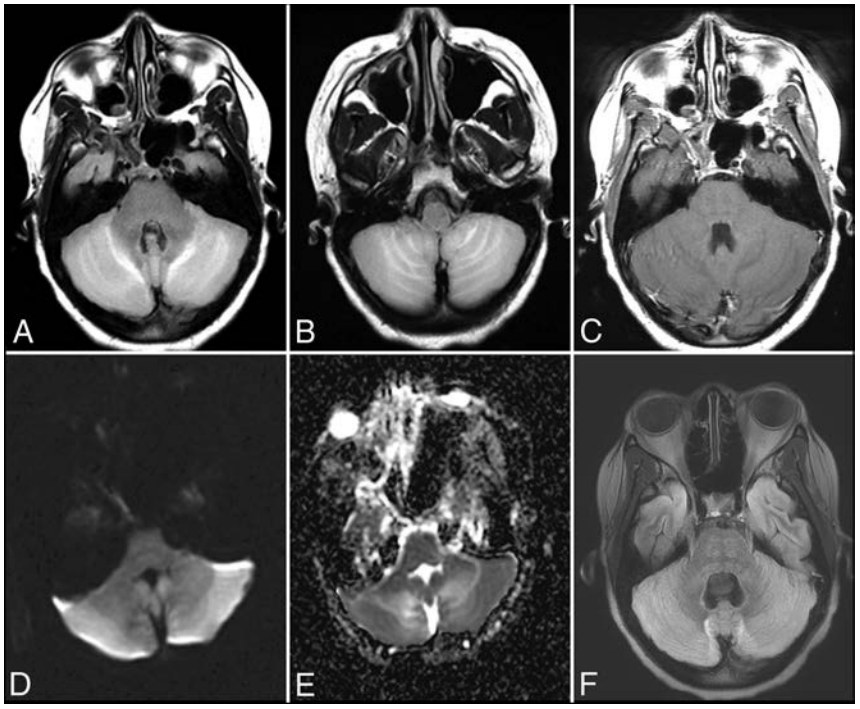

FIG 6. Anti-voltage-gated calcium channel cerebellitis. A 23-year-old woman with a history of autoimmune hepatitis presented with altered mental status. Initial brain MR imaging (*A–E*) demonstrates T2-FLAIR hyperintensity within the bilateral cerebellar hemispheres with mass effect on the fourth ventricle (*A* and *B*), without evidence of postcontrast enhancement (*C*) and with mild restricted diffusion on DWI (*D*) and the corresponding ADC map (*E*). A follow-up scan 1 month later (*F*) demonstrates resolution of the T2-FLAIR hyperintensity and associated mass effect on the fourth ventricle following a steroid taper.

immune encephalitis, brain FDG-PET imaging may be indicated, especially early in the disease process if clinical suspicion for autoimmune encephalitis is high, because it appears to be a more sensitive imaging technique for detecting temporal lobe abnormalities with normal brain MR imaging findings.[29,40,44,58]

Voltage-Gated Potassium Channel

Voltage-gated potassium channel (VGKC) encephalitis is one of the most common group 2 subtypes of autoimmune encephalitis, which can demonstrate classic features of limbic encephalitis but is primarily defined by the early and prominent development of medically intractable epilepsy.[24] The near-universal development of seizures in patients with VGKC encephalitis is partially explained by the high concentration of potassium channels in the limbic structures, and the epileptogenic potential of these antibodies is further supported by the observation that up to 6% of patients with a long-standing history of epilepsy were found to have circulating VGKC autoantibodies.[59] It remains unclear whether VGKC antibodies directly contribute to neuronal dysfunction independent of seizure activity, but there is growing consensus that a genetic predisposition to VGKC autoimmunity is probably an independent risk factor for the development of temporal lobe epilepsy.[9,59]

According to a recent review of 42 patients with VGKC encephalitis, most (69%) demonstrated MR imaging findings classic for autoimmune encephalitis in the acute setting (T2-FLAIR hyperintense lesions in 1 or both medial temporal lobes) and had an increased propensity to develop chronic findings of mesial temporal sclerosis on follow-up imaging (48%).[24] A subset of patients with medial temporal lobe lesions demonstrated additional findings of restricted diffusion and postcontrast enhancement (21%) that was highly associated with the development of mesial temporal sclerosis (66%).[24] Another important finding was that "extralimbic" involvement in VGKC encephalitis was exceedingly rare (5%).[24] The number of specific antibodies within the spectrum of VGKC encephalitis continues to grow, with distinction now being made for antibodies to particular antigens like leucine-rich glioma-inactivated 1, contactin-associated protein-like 2, and dipeptidyl-peptidase-like protein-6, which represent distinct subtypes of autoimmune encephalitis because these antibodies bind not to the Kv1 neuronal antigens of the VGKC but to other juxtaparanodal proteins with a different clinical profile.[6,60-63]

Voltage-Gated Calcium Channel

Voltage-gated calcium channel (VGCC) encephalitis is a relatively rare subtype described in women and young children, which is associated with the classic clinical progression of symptoms described in group II antibodies (viral prodrome → neuropsychiatric symptoms → limbic dysfunction → seizures) and can have prominent "migratory" extralimbic involvement with gyriform postcontrast enhancement and cortical laminar necrosis (Figs 5 and 6).[64,65]

γ-Aminobutyric Acid Receptor

γ-aminobutyric acid encephalitis (GABAr) has 2 subtypes that both have clinical features similar to those of VGKC encephalitis but are less common and have a better overall prognosis.[3,15,43,66] The 2 γ-aminobutyric acid receptor subtypes have different clinical profiles and are characterized by antibodies to either the γ-aminobutyric acid A-receptor or B-receptor subunits.[3,15,43,66] Patients with antibodies to the γ-aminobutyric acid B-receptor present with classic features of limbic encephalitis defined by early and frequent seizures with the development of T2-FLAIR hyperintense signal changes in 1 or both temporal lobes.[3,43,66] Patients with γ-aminobutyric acid B-receptor antibodies have a higher association with cancer than most other group II antibodies and are more often seen with small-cell lung cancer or pulmonary neuroendocrine tumors.[3,43,66] The development of autoimmune encephalitis in these patients usually precedes the diagnosis of cancer but responds well to immunosuppression and removal of the underlying tumor.[66] Patients with γ-aminobutyric acid A-receptors also have a good prognosis with adequate treatment, are not associated with cancer, and are unique because in addition to classic MR imaging findings, these patients often demonstrate

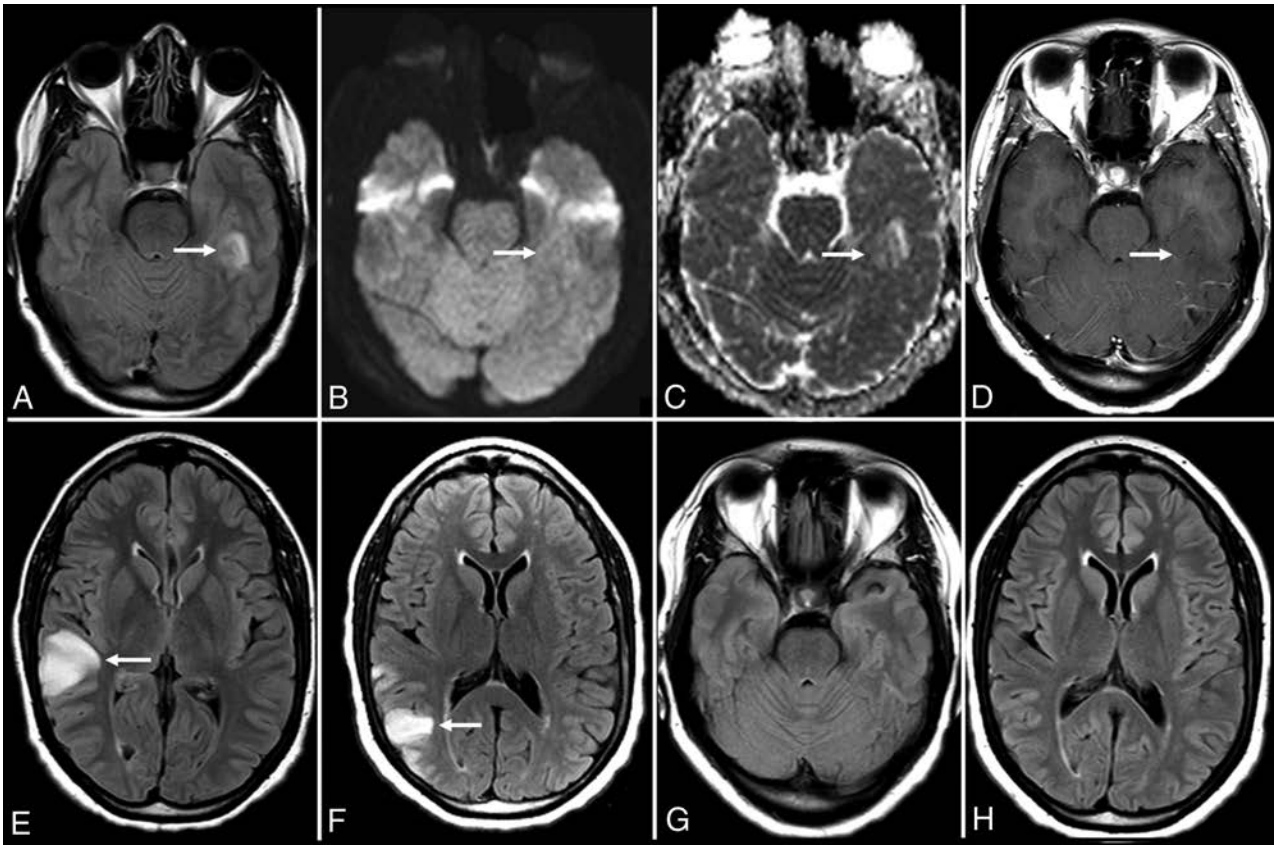

FIG 7. Hashimoto encephalitis. A 41-year-old woman presented with gradually worsening headaches and memory impairment without the development of psychosis or seizures. MR imaging of the brain (time, 0) demonstrates T2-FLAIR hyperintensity in the inferior left temporal lobe (*A*) without evidence of restricted diffusion (*B* and *C*). MR imaging of the brain (time, 21 days) demonstrates enlargement of the lesion on T2-FLAIR (not shown) without postcontrast enhancement (*D*). MR imaging of the brain (time, 3 months) demonstrates resolution of the prior lesion (not shown) but development of similar T2-FLAIR hyperintensity in the right frontoparietal junction (*E*). A subsequent scan at approximately 5 months shows near-complete resolution of that lesion with a new T2-FLAIR hyperintense lesion more posteriorly (*F*). A follow-up scan (*G* and *H*) nearly 1 year from onset shows complete resolution of the imaging abnormalities.

extensive T2-FLAIR hyperintense lesions outside of the limbic system.[3,15]

Alpha-Amino-3-Hydroxy-5-Methyl-4-Isoxazolepropionic Acid Receptor

Alpha-amino-3-hydroxy-5-methyl-4-isoxazolepropionic acid receptor (AMPAr) encephalitis is an uncommon subtype characterized by the subacute onset of purely psychiatric symptoms with T2-FLAIR hyperintensities isolated to the hippocampus. This subtype has a higher association with cancer than other cell-surface antibody subtypes and is most often seen in women with lung, breast, or thymic tumors.[3,67]

Additional Type II Antibody Subtypes

Anti-glutamate receptor 3 (GluR3) antibodies have been associated with Rasmussen encephalitis.[7] Anti-metabotropic glutamate receptor 1 (mGluR1) antibodies have been described in patients with lymphoma with cerebellar ataxia.[7] Anti-metabotropic glutamate receptor 5 (mGluR5) antibodies have been linked to limbic encephalitis associated with Hodgkin lymphoma (Ophelia syndrome).[7] Anti-D2 dopamine receptor antibodies represent a rare subtype associated with basal ganglia encephalitis.[8] Anti-glyoxylate reductase 1 (GlyR1) antibodies can be seen in 3 related groups distinguished by having dominant clinical features of stiff leg syndrome, stiff person syndrome, or progressive encephalomyelitis with rigidity and myoclonus.[6]

Systemic Autoimmunity with Encephalopathy

Neuropsychiatric manifestations of systemic autoimmune conditions such as systemic lupus erythematosus can occur and may be mediated by an antibody profile that includes antiphospholipid antibodies and anti-glutamate receptor antibodies.[68] Catastrophic antiphospholipid antibody syndrome is a condition that can present with strokelike symptoms and multifocal petechial hemorrhages throughout the brain, which are best seen on susceptibility-weighted MR imaging sequences.[68] Patients with thyroid dysfunction and antithyroid antibodies in conditions like Graves disease or Hashimoto thyroiditis can develop encephalopathy associated with their autoimmune thyroid disease that has a characteristic "migratory pattern" of neuroimaging findings with cortical T2-FLAIR lesions in different regions of the brain on sequential MR imaging examinations (Fig 7).[11,69] Hashimoto encephalopathy, in particular, is closely associated with autoimmune encephalitis, given its propensity for the combination of encephalopathy, psychiatric symptoms, and seizures.[69,70] MR imaging findings in Hashimoto encephalopathy often have more prominent fea-

tures of leukoencephalopathy (patchy and confluent T2-FLAIR hyperintense lesions in the subcortical, periventricular, and deep white matter).[2,43,70]

CONCLUSIONS

Autoimmune encephalitis is an important diagnostic consideration in patients presenting with new onset of altered mental status of unclear etiology. It includes a myriad of clinical conditions that have a common pathophysiology (ie, antibodies directed against CNS structures). The 2 distinct groups (group I, intracellular directed antibodies, and group II, cell-surface directed antibodies) have overlapping clinical and imaging features. Neuroimaging findings will most often involve the limbic structures, but involvement of the striatum, diencephalon, or rhombencephalon can be seen. A subset of patients with autoimmune encephalitis will have no neuroimaging findings despite profound neuropsychiatric dysfunction, but serum antibody testing can still ultimately lead to the diagnosis of autoimmune encephalitis. While there is no single diagnostic feature that can make this diagnosis in isolation, recognizing a certain constellation of findings during the work-up of complex and atypical cases of new-onset altered mental status is crucial to confirm the diagnosis with serologic testing and initiate treatment in a timely fashion.

ACKNOWLEDGMENTS

We are grateful to our clinical colleagues in the Department of Neurology within the Henry Ford Health System for their role in diagnosing and treating patients with autoimmune encephalitis at our institution. We would specifically like to acknowledge Dr Daniel Newman, Director of the Henry Ford Hoenselaar ALS Clinic, for his enthusiastic clinical support and expertise. We would also like to thank Dr Chunhai Hao, Chief of Neuropathology in the Department of Pathology and Laboratory Medicine at Henry Ford Hospital, for his work characterizing the histopathology of brain biopsy specimens in cases of suspected autoimmune encephalitis at our institution.

REFERENCES

1. Dalmau J, Rosenfeld MR. **Autoimmune encephalitis update.** *Neuro Oncol* 2014;16:771–78 CrossRef Medline
2. Caselli RJ, Drazkowski JF, Wingerchuk DM. **Autoimmune encephalopathy.** *Mayo Clin Proc* 2010;85:878–80 CrossRef Medline
3. da Rocha AJ, Nunes RH, Maia AC Jr, et al. **Recognizing autoimmune-mediated encephalitis in the differential diagnosis of limbic disorders.** *AJNR Am J Neuroradiol* 2015;36:2196–205 CrossRef Medline
4. Glaser CA, Gilliam S, Schnurr D, et al; California Encephalitis Project, 1998–2000. **In search of encephalitis etiologies: diagnostic challenges in the California Encephalitis Project, 1998–2000.** *Clin Infect Dis* 2003;36:731–42 CrossRef Medline
5. Armangue T, Leypoldt F, Dalmau J. **Autoimmune encephalitis as differential diagnosis of infectious encephalitis.** *Curr Opin Neurol* 2014;27:361–68 CrossRef Medline
6. Vincent A. **Autoimmune channelopathies: new antibody-mediated disorders of the central nervous system.** *F1000 Biol Rep* 2009;1:61 CrossRef Medline
7. Graus F, Saiz A, Dalmau J. **Antibodies and neuronal autoimmune disorders of the CNS.** *J Neurol* 2010;257:509–17 CrossRef Medline
8. Ramanathan S, Mohammad SS, Brilot F, et al. **Autoimmune encephalitis: recent updates and emerging challenges.** *J Clin Neurosci* 2014;21:722–30 CrossRef Medline
9. Bien CG, Vincent A, Barnett MH, et al. **Immunopathology of autoantibody-associated encephalitides: clues for pathogenesis.** *Brain* 2012;135:1622–38 CrossRef Medline
10. Demaerel P, Van Dessel W, Van Paesschen W, et al. **Autoimmune-mediated encephalitis.** *Neuroradiology* 2011;53:837–51 CrossRef Medline
11. Moscato EH, Jain A, Peng X, et al. **Mechanisms underlying autoimmune synaptic encephalitis leading to disorders of memory, behavior and cognition: insights from molecular, cellular and synaptic studies.** *Eur J Neurosci* 2010;32:298–309 CrossRef Medline
12. Oyanguren B, Sánchez V, González FJ, et al. **Limbic encephalitis: a clinical-radiological comparison between herpetic and autoimmune etiologies.** *Eur J Neurol* 2013;20:1566–70 CrossRef Medline
13. Dalmau J, Graus F, Villarejo A, et al. **Clinical analysis of anti-Ma2-associated encephalitis.** *Brain* 2004;127:1831–44 CrossRef Medline
14. Irani SR, Bera K, Waters P, et al. **N-methyl-D-aspartate antibody encephalitis: temporal progression of clinical and paraclinical observations in a predominantly non-paraneoplastic disorder of both sexes.** *Brain* 2010;133:1655–67 CrossRef Medline
15. Petit-Pedrol M, Armangue T, Peng X, et al. **Encephalitis with refractory seizures, status epilepticus, and antibodies to the GABAA receptor: a case series, characterisation of the antigen, and analysis of the effects of antibodies.** *Lancet Neurol* 2014;13:276–86 CrossRef Medline
16. Degnan AJ, Levy LM. **Neuroimaging of rapidly progressive dementias, part 1: neurodegenerative etiologies.** *AJNR Am J Neuroradiol* 2014;35:418–23 CrossRef Medline
17. Degnan AJ, Levy LM. **Neuroimaging of rapidly progressive dementias, part 2: prion, inflammatory, neoplastic, and other etiologies.** *AJNR Am J Neuroradiol* 2014;35:424–31 CrossRef Medline
18. Mittal MK, Rabinstein AA, Hocker SE, et al. **Autoimmune encephalitis in the ICU: analysis of phenotypes, serologic findings, and outcomes.** *Neurocrit Care* 2016;24:240–50 CrossRef Medline
19. Gultekin SH, Rosenfeld MR, Voltz R, et al. **Paraneoplastic limbic encephalitis: neurological symptoms, immunological findings and tumour association in 50 patients.** *Brain* 2000;123(pt 7):1481–94 CrossRef Medline
20. Dalmau J, Lancaster E, Martinez-Hernandez E, et al. **Clinical experience and laboratory investigations in patients with anti-NMDAR encephalitis.** *Lancet Neurol* 2011;10:63–74 CrossRef Medline
21. Rees JH. **Paraneoplastic syndromes: when to suspect, how to confirm, and how to manage**. *J Neurol Neurosurg Psychiatry* 2004; 75(suppl 2):ii43–50 Medline
22. de Beukelaar JW, Sillevis Smitt PA. **Managing paraneoplastic neurological disorders.** *Oncologist* 2006;11:292–305 CrossRef Medline
23. Urbach H, Soeder BM, Jeub M, et al. **Serial MRI of limbic encephalitis.** *Neuroradiology* 2006;48:380–86 CrossRef Medline
24. Kotsenas AL, Watson RE, Pittock SJ, et al. **MRI findings in autoimmune voltage-gated potassium channel complex encephalitis with seizures: one potential etiology for mesial temporal sclerosis.** *AJNR Am J Neuroradiol* 2014;35:84–89 CrossRef Medline
25. Corsellis JA, Goldberg GJ, Norton AR. **"Limbic encephalitis" and its association with carcinoma.** *Brain* 1968;91:481–96 CrossRef Medline
26. Kohler J, Hufschmidt A, Hermle L, et al. **Limbic encephalitis: two cases.** *J Neuroimmunol* 1988;20:177–78 CrossRef Medline
27. Tüzün E, Dalmau J. **Limbic encephalitis and variants: classification, diagnosis and treatment.** *Neurologist* 2007;13:261–71 CrossRef Medline
28. Suleiman J, Brilot F, Lang B, et al. **Autoimmune epilepsy in children: case series and proposed guidelines for identification.** *Epilepsia* 2013;54:1036–45 CrossRef Medline
29. Dalmau J, Bataller L. **Clinical and immunological diversity of limbic encephalitis: a model for paraneoplastic neurologic disorders.** *Hematol Oncol Clin North Am* 2006;20:1319–35 CrossRef Medline
30. Pittock SJ, Kryzer TJ, Lennon VA. **Paraneoplastic antibodies coexist and predict cancer, not neurological syndrome.** *Ann Neurol* 2004; 56:715–19 CrossRef Medline
31. Graus F, Keime-Guibert F, Reñe R, et al. **Anti-Hu-associated para-**

neoplastic encephalomyelitis: analysis of 200 patients. *Brain* 2001; 124:1138–48 CrossRef Medline
32. Rudzinski LA, Pittock SJ, McKeon A, et al. **Extratemporal EEG and MRI findings in ANNA-1 (anti-Hu) encephalitis.** *Epilepsy Res* 2011; 95:255–62 CrossRef Medline
33. Jacobs DA, Fung KM, Cook NM, et al. **Complex partial status epilepticus associated with anti-Hu paraneoplastic syndrome.** *J Neurol Sci* 2003;213:77–82 CrossRef Medline
34. Rosenfeld MR, Eichen JG, Wade DF, et al. **Molecular and clinical diversity in paraneoplastic immunity to Ma proteins.** *Ann Neurol* 2001;50:339–48 CrossRef Medline
35. Hoffmann LA, Jarius S, Pellkofer HL, et al. **Anti-Ma and anti-Ta associated paraneoplastic neurological syndromes: 22 newly diagnosed patients and review of previous cases.** *J Neurol Neurosurg Psychiatry* 2008;79:767–73 CrossRef Medline
36. Mathew RM, Vandenberghe R, Garcia-Merino A, et al. **Orchiectomy for suspected microscopic tumor in patients with anti-Ma2-associated encephalitis.** *Neurology* 2007;68:900–05 CrossRef Medline
37. Crespo-Burillo JA, Hernando-Quintana N, Ruiz-Palomino P, et al. **Chorea secondary to striatal encephalitis due to anti-CV2/CRMP5 antibodies: case description and review of the literature.** *Neurologia (Barcelona, Spain)* 2015;30:451–53 CrossRef Medline
38. Malter MP, Helmstaedter C, Urbach H, et al. **Antibodies to glutamic acid decarboxylase define a form of limbic encephalitis.** *Ann Neurol* 2010;67:470–78 CrossRef Medline
39. Ko MW, Dalmau J, Galetta SL. **Neuro-ophthalmologic manifestations of paraneoplastic syndromes.** *J Neuroophthalmol* 2008;28: 58–68 CrossRef Medline
40. Younes-Mhenni S, Janier MF, Cinotti L, et al. **FDG-PET improves tumour detection in patients with paraneoplastic neurological syndromes.** *Brain* 2004;127:2331–38 CrossRef Medline
41. Nunez-Enamorado N, Camacho-Salas A, Belda-Hofheinz S, et al. **Fast and spectacular clinical response to plasmapheresis in a paediatric case of anti-NMDA encephalitis** [in Spanish]. *Rev Neurol* 2012; 54:420–24 Medline
42. Gresa-Arribas N, Titulaer MJ, Torrents A, et al. **Antibody titres at diagnosis and during follow-up of anti-NMDA receptor encephalitis: a retrospective study.** *Lancet Neurol* 2014;13:167–77 CrossRef Medline
43. Saraya A, Mahavihakanont A, Shuangshoti S, et al. **Autoimmune causes of encephalitis syndrome in Thailand: prospective study of 103 patients.** *BMC Neurol* 2013;13:150 CrossRef Medline
44. Ances BM, Vitaliani R, Taylor RA, et al. **Treatment-responsive limbic encephalitis identified by neuropil antibodies: MRI and PET correlates.** *Brain* 2005;128:1764–77 CrossRef Medline
45. von Rhein B, Wagner J, Widman G, et al. **Suspected antibody negative autoimmune limbic encephalitis: outcome of immunotherapy.** *Acta Neurol Scand* 2017;135:134–41 Medline
46. Matoq AA, Rappoport AS, Yang Y, et al. **Anti-NMDA-receptor antibody encephalitis in infants.** *Epilepsy Behav Case Rep* 2015;4:99–101 CrossRef Medline
47. Bravo-Oro A, Acosta-Yebra D, Grimaldo-Zapata IP, et al. **Reversible cortical atrophy secondary to anti-NMDA receptor antibody encephalitis** [in Spanish]. *Rev Neurol* 2015;60:447–52 Medline
48. Kayser MS, Titulaer MJ, Gresa-Arribas N, et al. **Frequency and characteristics of isolated psychiatric episodes in anti-N-methyl-d-aspartate receptor encephalitis.** *JAMA Neurol* 2013;70:1133–39 CrossRef Medline
49. Irani SR, Vincent A. **NMDA receptor antibody encephalitis.** *Curr Neurol Neurosci Rep* 2011;11:298–304 CrossRef Medline
50. Gabilondo I, Saiz A, Galán L, et al. **Analysis of relapses in anti-NMDAR encephalitis.** *Neurology* 2011;77:996–99 CrossRef Medline
51. Titulaer MJ, McCracken L, Gabilondo I, et al. **Treatment and prognostic factors for long-term outcome in patients with anti-NMDA receptor encephalitis: an observational cohort study.** *Lancet Neurol* 2013;12:157–65 CrossRef Medline
52. Tüzün E, Zhou L, Baehring JM, et al. **Evidence for antibody-mediated pathogenesis in anti-NMDAR encephalitis associated with ovarian teratoma.** *Acta Neuropathol* 2009;118:737–43 CrossRef Medline
53. Florance NR, Davis RL, Lam C, et al. **Anti-N-methyl-D-aspartate receptor (NMDAR) encephalitis in children and adolescents.** *Ann Neurol* 2009;66:11–18 CrossRef Medline
54. Gable MS, Sheriff H, Dalmau J, et al. **The frequency of autoimmune N-methyl-D-aspartate receptor encephalitis surpasses that of individual viral etiologies in young individuals enrolled in the California Encephalitis Project.** *Clin Infect Dis* 2012;54:899–904 CrossRef Medline
55. Prüss H, Finke C, Höltje M, et al. **N-methyl-D-aspartate receptor antibodies in herpes simplex encephalitis.** *Ann Neurol* 2012;72: 902–11 CrossRef Medline
56. Takahashi Y, Mori H, Mishina M, et al. **Autoantibodies and cell-mediated autoimmunity to NMDA-type GluRepsilon2 in patients with Rasmussen's encephalitis and chronic progressive epilepsia partialis continua.** *Epilepsia* 2005;46(suppl 5):152–58 Medline
57. Gitiaux C, Simonnet H, Eisermann M, et al. **Early electro-clinical features may contribute to diagnosis of the anti-NMDA receptor encephalitis in children.** *Clin Neurophysiol* 2013;124:2354–61 CrossRef Medline
58. Baumgartner A, Rauer S, Mader I, et al. **Cerebral FDG-PET and MRI findings in autoimmune limbic encephalitis: correlation with autoantibody types.** *J Neurol* 2013;260:2744–53 CrossRef Medline
59. Majoie HJ, de Baets M, Renier W, et al. **Antibodies to voltage-gated potassium and calcium channels in epilepsy.** *Epilepsy Res* 2006;71: 135–41 Medline
60. Boronat A, Gelfand JM, Gresa-Arribas N, et al. **Encephalitis and antibodies to dipeptidyl-peptidase-like protein-6, a subunit of Kv4.2 potassium channels.** *Ann Neurol* 2013;73:120–28 CrossRef Medline
61. Lai M, Huijbers MG, Lancaster E, et al. **Investigation of LGI1 as the antigen in limbic encephalitis previously attributed to potassium channels: a case series.** *Lancet Neurol* 2010;9:776–85 CrossRef Medline
62. Irani SR, Alexander S, Waters P, et al. **Antibodies to Kv1 potassium channel-complex proteins leucine-rich, glioma inactivated 1 protein and contactin-associated protein-2 in limbic encephalitis, Morvan's syndrome and acquired neuromyotonia.** *Brain* 2010;133: 2734–48 CrossRef Medline
63. Lancaster E, Huijbers MG, Bar V, et al. **Investigations of caspr2, an autoantigen of encephalitis and neuromyotonia.** *Ann Neurol* 2011; 69:303–11 CrossRef Medline
64. Finkel L, Koh S. **N-type calcium channel antibody-mediated autoimmune encephalitis: an unlikely cause of a common presentation.** *Epilepsy Behav Case Rep* 2013;1:92–96 CrossRef Medline
65. Kaira K, Okamura T, Takahashi H, et al. **Small-cell lung cancer with voltage-gated calcium channel antibody-positive paraneoplastic limbic encephalitis: a case report.** *J Med Case Rep* 2014;8:119 CrossRef Medline
66. Lancaster E, Lai M, Peng X, et al. **Antibodies to the GABA(B) receptor in limbic encephalitis with seizures: case series and characterisation of the antigen.** *Lancet Neurol* 2010;9:67–76 CrossRef Medline
67. Joubert B, Kerschen P, Zekeridou A, et al. **Clinical spectrum of encephalitis associated with antibodies against the α-amino-3-hydroxy-5-methyl-4-isoxazolepropionic acid receptor: case series and review of the literature.** *JAMA Neurol* 2015;72:1163–69 CrossRef Medline
68. Gerosa M, Poletti B, Pregnolato F, et al. **Antiglutamate receptor antibodies and cognitive impairment in primary antiphospholipid syndrome and systemic lupus erythematosus.** *Front Immunol* 2016; 7:5 CrossRef Medline
69. Tamagno G, Celik Y, Simó R, et al. **Encephalopathy associated with autoimmune thyroid disease in patients with Graves' disease: clinical manifestations, follow-up, and outcomes.** *BMC Neurol* 2010; 10:27 CrossRef Medline
70. Rosenbloom MH, Smith S, Akdal G, et al. **Immunologically mediated dementias.** *Curr Neurol Neurosci Rep* 2009;9:359–67 CrossRef Medline

Thalamic Iron Differentiates Primary-Progressive and Relapsing-Remitting Multiple Sclerosis

A. Burgetova, P. Dusek, M. Vaneckova, D. Horakova, C. Langkammer, J. Krasensky, L. Sobisek, P. Matras, M. Masek, and Z. Seidl

ABSTRACT

BACKGROUND AND PURPOSE: Potential differences between primary progressive and relapsing remitting multiple sclerosis are the subject of ongoing controversial discussions. The aim of this work was to determine whether and how primary-progressive and relapsing-remitting multiple sclerosis subtypes differ regarding conventional MR imaging parameters, cerebral iron deposits, and their association with clinical status.

MATERIALS AND METHODS: We analyzed 24 patients with primary-progressive MS, 80 with relapsing-remitting MS, and 20 healthy controls with 1.5T MR imaging for assessment of the conventional quantitative parameters: T2 lesion load, T1 lesion load, brain parenchymal fraction, and corpus callosum volume. Quantitative susceptibility mapping was performed to estimate iron concentration in the deep gray matter.

RESULTS: Decreased susceptibility within the thalamus in relapsing-remitting MS compared with primary-progressive MS was the only significant MR imaging difference between these MS subtypes. In the relapsing-remitting MS subgroup, the Expanded Disability Status Scale score was positively associated with conventional parameters reflecting white matter lesions and brain atrophy and with iron in the putamen and caudate nucleus. A positive association with putaminal iron and the Expanded Disability Status Scale score was found in primary-progressive MS.

CONCLUSIONS: Susceptibility in the thalamus might provide additional support for the differentiation between primary-progressive and relapsing-remitting MS. That the Expanded Disability Status Scale score was associated with conventional MR imaging parameters and iron concentrations in several deep gray matter regions in relapsing-remitting MS, while only a weak association with putaminal iron was observed in primary-progressive MS suggests different driving forces of disability in these MS subtypes.

ABBREVIATIONS: BPF = brain parenchymal fraction; CCV = corpus callosum volume; CN = caudate nucleus; DGM = deep gray matter; EDSS = Expanded Disability Status Scale; GP = globus pallidus; HC = healthy controls; Put = putamen; QS = quantitative susceptibility; QSM = quantitative susceptibility mapping; PPMS = primary-progressive multiple sclerosis; RRMS = relapsing-remitting multiple sclerosis; RR_{EM} = relapsing-remitting EDSS-matched group; T1LL = T1 lesion load; T2LL = T2 lesion load

Pathologic cerebral iron accumulation in multiple sclerosis is a consistent finding in MR imaging and neuropathologic studies. Abnormal iron deposits were detected particularly in the deep gray matter (DGM)—that is, in the putamen, caudate nucleus (CN), and globus pallidus (GP) with iron-sensitive MR imaging techniques such as R2* relaxometry, magnetic field correlation imaging, phase imaging, and quantitative susceptibility mapping (QSM).[1-8] Neuropathologic studies in MS confirmed increased iron content in both glial cells and neurons in DGM associated with degenerative changes,[9] while overall iron loss was observed in normal-appearing white matter.[10] An increase in iron concentration appears to be an early phenomenon, with the highest amounts of accumulation occurring during the transitions from clinically isolated syndrome to definite MS.[11]

Received August 25, 2016; accepted after revision January 26, 2017.

From the Departments of Radiology (A.B., M.V., J.K., P.M., M.M., Z.S.) and Neurology (P.D., D.H.), Center of Clinical Neuroscience, First Faculty of Medicine, Charles University and General University Hospital in Prague, Prague, Czech Republic; Institute of Neuroradiology (P.D.), University Medicine Göttingen, Göttingen, Germany; Department of Neurology (C.L.), Medical University of Graz, Graz, Austria; and Department of Statistics and Probability (L.S.), University of Economics, Prague, Czech Republic.

This study was supported by the grants RVO VFN64165, 15-25602A Czech Ministry of Health, and GA CR 16-03322S. L.S. was supported by the Faculty of Informatics and Statistics, University of Economics, Prague.

Please address correspondence to Andrea Burgetova, MD, Department of Radiology, First Faculty of Medicine, Charles University and General University Hospital in Prague, Katerinska 30, 128 08 Prague 2, Czech Republic; e-mail: andrea.burgetova@vfn.cz

http://dx.doi.org/10.3174/ajnr.A5166

Currently, little information is available on the differences in iron content in various MS subtypes. Primary-progressive MS (PPMS) is a subtype characterized by a steady progression without relapses and worse response to immunosuppressant drugs. It has been postulated that underlying mechanisms and measures of disability progression in PPMS may be different from those in relapsing-remitting MS (RRMS). In particular, inflammation may be less prominent compared with neurodegeneration in the PPMS subtype. However, neuroimaging studies supporting this theory are lacking. It remains unclear whether PPMS and RRMS subtypes differ in iron accumulation in the DGM. Differences in demographic and clinical data cause difficulties in the comparison of these 2 subtypes. PPMS affects older age groups than RRMS, with a peak incidence in the fifth and sixth decades; the male-to-female ratio is typically 1:1 compared with 1:3 reported in most RRMS trials. Additionally, the Expanded Disability Status Scale (EDSS) score is higher in patients with PPMS than in those with RRMS, with the same disease duration indicating faster disease progression in PPMS.[12]

The primary goal of this study was to compare iron content and conventional MR imaging parameters such as T2 lesion load (T2LL), T1 lesion load (T1LL), brain parenchymal fraction (BPF), and corpus callosum volume (CCV) in RRMS and PPMS. We were particularly interested in whether these MS subtypes differ in iron concentration and whether iron accumulation has a different impact on disability in PPMS compared with RRMS. From several MR imaging–based techniques enabling the assessment of iron concentration in the brain,[13] we chose quantitative susceptibility mapping (QSM). Postmortem validation studies have demonstrated that QSM in the DGM is tightly correlated with iron concentration.[14] QSM has been shown to correlate with R2 and R2* relaxometry, but compared with these techniques, it does not require multiecho data, has a higher dynamic range, and might be more sensitive to smaller tissue-susceptibility changes.[15-18]

The secondary goal was to investigate the correlation between quantitative MR imaging parameters and clinical disability measured by the EDSS in both MS subtypes.

MATERIALS AND METHODS

Research Subjects

Twenty-four patients with PPMS, 20 age- and sex-matched healthy controls (HC), and 303 patients with RRMS were investigated. Patients with RRMS and PPMS were diagnosed according to the clinical classification of Lublin et al.[19] Of the total 28 patients with PPMS from the data base of our MS center, 4 patients were excluded due to contraindications to MR imaging, refusal to participate in this study, moving away, and incomplete set of data, respectively. Patients with RRMS who had routine MR imaging examinations from September 2013 to September 2015 were asked to participate in this study; 303 patients were investigated. From the whole sample of 303 patients with RRMS, 2 groups have been identified by distributional matching to the PPMS group by using the MatchIt Library (Version 2.4–21),[20] as implemented in the R Statistical and Computing Software (http://www.r-project.org/). The first RRMS group consisting of 80 patients was obtained by matching RRMS to PPMS according to age and sex. The second RRMS group was obtained by an independent procedure of matching RRMS to PPMS according to age, sex, and EDSS score. This additional EDSS matching, performed to control for higher disease severity in the PPMS group, yielded a group of 40 patients, referred to as $RR_{EDSS\text{-}Matched}$ (RR_{EM}); RRMS and RR_{EM} groups are partially overlapping with 29 patients included in both groups. Seventy-nine percent of patients from the RRMS group, 75% from the RR_{EM} group, and 29% from the PPMS group were on a long-term MS-specific treatment (On-line Table 1). Written informed consent was obtained from all patients, and the research was approved by the local medical ethics committee at First Faculty of Medicine, Charles University and General University Hospital in Prague, Czech Republic.

MR Imaging Acquisition and Image Processing

The examinations were performed by using a 1.5T MR imaging system (Gyroscan NT; Philips Healthcare, Best, the Netherlands); a standard quadratic head coil was used. The protocol included FLAIR (150 axial sections, TR = 1000 ms, TE = 140 ms, TI = 2600 ms, spatial resolution = $1 \times 1 \times 1$ mm^3, scan duration = 10 minutes 16 seconds), T1-weighted imaging (fast-field echo/3D, 150 axial sections, TR = 25 ms, TE = 5.01 ms, spatial resolution = $1 \times 1 \times 1$ mm^3, scan duration =12 minutes 48 seconds), and susceptibility-weighted imaging (fast-field echo/3D, 100 axial sections, TR = 48.1 ms, TE = 33.2 ms, spatial resolution = $0.8 \times 0.8 \times 2.0$ mm^3, scan duration = 6 minutes 30 seconds) pulse sequences.

Automated volumetric image analysis was performed with the in-house-developed ScanView software (http://www.scanview.cz/) as described previously.[21-23] In brief, after standard image processing, image signal intensity was normalized (peak = 10,000, WM = 5000 artificial units) and the volume of T2 lesions (T2LL) was measured in homogenized and filtered FLAIR images as the area exceeding 140% of the WM intensity and the size of 11 voxels. Next, T2 hyperintensities were transformed to the T1-weighted image and the volume of hypointensities (T1LL) was calculated as the area with signal below 70% of the WM. In addition, the number of thalamic lesions was counted by a single rater on FLAIR images. BPF (volume of the brain parenchyma divided by the volume of the brain parenchyma and CSF space) and CCV were measured on the T1-weighted image. For CCV measurement, transversal sections were reconstructed to the sagittal plane. After smoothing and edge-enhancing, we applied filters and the area of the corpus callosum was outlined automatically on 7 sections, including the midsagittal section and 3 adjacent sections to the left and to the right. The resulting areas bounded by the curve were then recorded in all 7 sagittal reconstructions, and average value was calculated. The corpus callosum volume was calculated as mean area multiplied by the total thickness of 7 sections.

The reproducibility of T1LL, T2LL, BPF, and CCV measurements was evaluated by using MR imaging data of 164 patients with MS who were examined every 8 weeks throughout 1 year. Interclass correlation coefficients of 2 measurements performed within 8 weeks were 0.9983 for T1/T2LL, 0.9920 for BPF, and 0.9985 for CCV. The estimated reproducibility error of the automatic WM lesion segmentation algorithm was calculated to be 10% for small lesions (<1 cm^3) and 2%–3% for larger lesions.

QSM images were reconstructed by using a total generalized

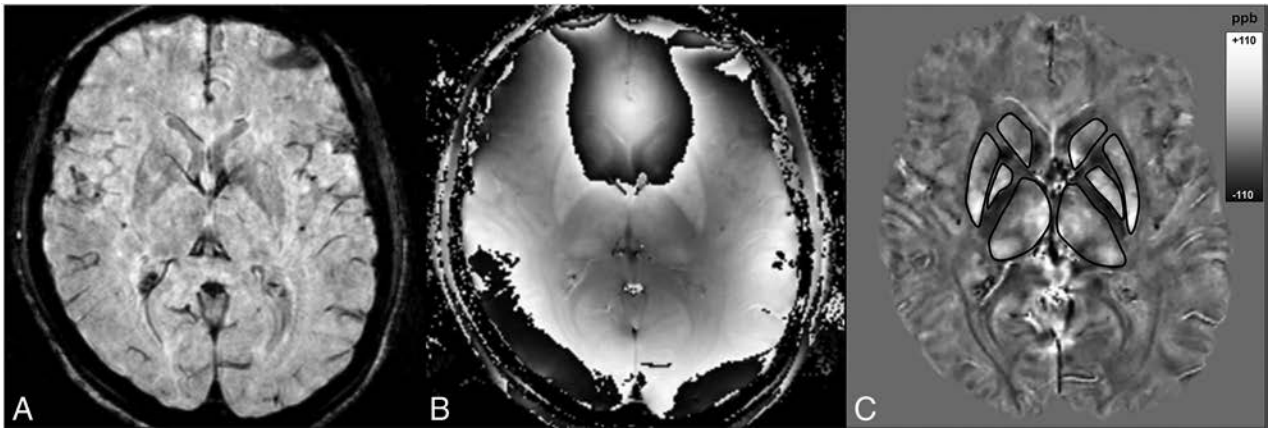

FIG 1. Sample MR image section depicting gradient-echo magnitude (*A*), raw phase (*B*), and quantitative susceptibility map (*C*) with ROIs outlined in the caudate nucleus, putamen, globus pallidus, and thalamus.

variation method as previously described.[24] Briefly, the reconstruction consisted of Laplacian unwrapping, background field removal, and dipole inversion by using the total generalized variation regularization in a single integrated step. Susceptibility was measured in the following ROIs: CN, putamen (Put), GP, and thalamus. ROIs were determined by using automated segmentation of the T1-weighted image with FreeSurfer, Version 4.5 (http://surfer.nmr.mgh.harvard.edu/). QSM images were rigidly aligned with the T1-weighted images, and subsequently regional median susceptibilities in parts per billion were measured (Fig. 1).

To check the performance of the automatic segmentation algorithm, we compared it with manual segmentation, which was considered ground truth. The extent of spatial overlap between the manual and automatic segmentations was evaluated by using comparative DICE scores. The CN, Put, GP, and thalamus outlines were manually segmented by a single rater in 3 randomly selected healthy subjects by using ITK-SNAP software (www.itksnap.org/).[25] The CN and Put were segmented on T1-weighted image; the GP and thalamus were segmented while simultaneously using coregistered T1-weighted and QSM images. The mean comparative DICE scores (1.0 is perfect alignment) were 0.76 (range, 0.71–0.80) for the CN, 0.79 (range, 0.79–0.80) for the Put, 0.74 (range, 0.68–80) for the GP, and 0.79 (range, 0.77–0.81) for the thalamus.

Because thalamic iron distribution is inhomogeneous, we have additionally performed manual segmentation of the entire thalamic outline and pulvinar outline in all subjects with QSM and T1-weighted images. Consequently, susceptibility in parts per billion was measured in the thalamus, pulvinar, and thalamus without the pulvinar.

Statistical Analysis

We used *t* tests or nonparametric Mann-Whitney *U* tests with a nonpooled SD to compare between-group differences in mean or median values of demographic, clinical, and MR imaging characteristics and median susceptibilities. Age was used as a covariate in the analysis to correct for age-related increases in cerebral iron concentration.[26] The Benjamini-Hochberg procedure with $P < .05$ was used to minimize the false discovery rate. The relations between EDSS and MR imaging metrics within each group were investigated by the Spearman correlation coefficient. Additionally, interaction analysis by using the multivariate general linear model was performed to examine whether the association between conventional MR imaging parameters and susceptibility in DGM nuclei differs by MS subtype. Interaction between MR imaging parameters and EDSS by MS subtype was also tested. Thus, patients were categorized into 1 of 4 classes according to EDSS category and MS subtype (ie, PPMS with EDSS ≤ 4, PPMS with EDSS > 4, RRMS with EDSS ≤ 4, RRMS with EDSS > 4). ANOVA and paired *t* tests were used to compare differences in means of MR imaging parameters among these subgroups. All analyses were performed with the statistical software R (www.r-project.org/); reported *P* values are 2-tailed.

RESULTS

Clinical and Conventional MR Imaging Parameters: Comparison of RRMS, PPMS, and Controls

MR imaging metrics in RRMS were compared with those in the PPMS and HC groups. The clinical disability (EDSS) distribution of patients with RRMS differs significantly from that in patients with PPMS ($P < .001$). The PPMS group was, therefore, also compared with the RR_{EM} MS subgroup, consisting of 40 patients matched for EDSS scores. Subject demographic and clinical data and comparison of conventional MR imaging parameters among RRMS, PPMS, and HC are listed in Table 1. The PPMS group showed significantly higher T1LL ($P = .023$) relative to the RRMS group, while no significant differences were found between PPMS and RR_{EM} MS groups in conventional MR imaging metrics.

Comparison of Susceptibility among MS Subtypes and HC

Compared with HC, both MS groups had significantly increased quantitative susceptibility (QS) values in the putamen (HC versus RRMS, $P = .042$, and PPMS, $P = .009$, respectively) (Fig. 2*A*). Regional susceptibility was significantly lower in the thalamus in the RRMS group compared with HC ($P = .004$). In contrast, there was no such decrease in thalamic susceptibility in the PPMS group compared with HC ($P = .757$). The only significant difference between MS subtypes found was lower regional susceptibility in the thalamus in the RRMS compared with the PPMS group ($P = .007$) (Table 2 and Fig. 2*B*). Lower QS values in the thalamus were also observed in the RR_{EM} group compared with PPMS ($P = .007$). Thalamic QS values were likely not influenced by demyelinating lesions

Table 1: Demographic and clinical data and conventional MRI metrics in HC, RRMS, RR_{EM}, and PPMS groups[a]

					P Value[b]		
	HC 20 (8/12)	RRMS 80 (32/48)	RR_{EM} MS 40 (16/24)	PPMS 24 (9/15)	PPMS vs RRMS (RR_{EM})	HC vs RRMS (RR_{EM})	HC vs PPMS
Age (yr)	48.0 (7.3)	46.9 (7.0)	48.6 (7.0)	47.4 (6.8)	.72 (.72)	.72 (.72)	.72
Disease duration (yr)	–	12.4 (10.7)	13.2 (11.0)	7.7 (3.3)	.006[c] (.006)[c]	–	–
EDSS[d]	–	2.5 (2.5)	4 (0.6)	4.5 (1.6)	<.001[c] (.173)	–	–
T1LL[d]	–	1.1 (1.1)	1.4 (1.6)	1.8 (3.3)	.023[c] (.276)	–	–
T2LL[d]	–	2.1 (4.9)	3.6 (7.2)	2.8 (10.6)	.431 (.923)	–	–
BPF (%)	86.2 (1.5)	84.2 (2.4)	83.8 (2.4)	84.7 (3.0)	.490 (.490)	<.001 (<.001)	.08
CCV (cm^3)	4.6 (0.6)	4.1 (0.7)	4.0 (0.7)	4.1 (0.8)	.690 (.690)	.004 (.001)	.013

Note:— – indicates not relevant.

[a] The number of participants and the female/male ratio are reported for each group. Unless otherwise indicated, data are reported as mean (SD). Numbers in parentheses in the headers of columns 2–5 are No. of subjects in groups (F/M).

[b] Pair-wise comparison (*P* value). Differences among HC, PPMS, and RRMS (RR_{EM}) groups were tested using a *t* test or Mann-Whitney *U* test with nonpooled SD (Benjamini-Hochberg correction).

[c] Significant.

[d] Mann-Whitney *U* test with nonpooled SD (Benjamini-Hochberg correction) (median and interquartile range).

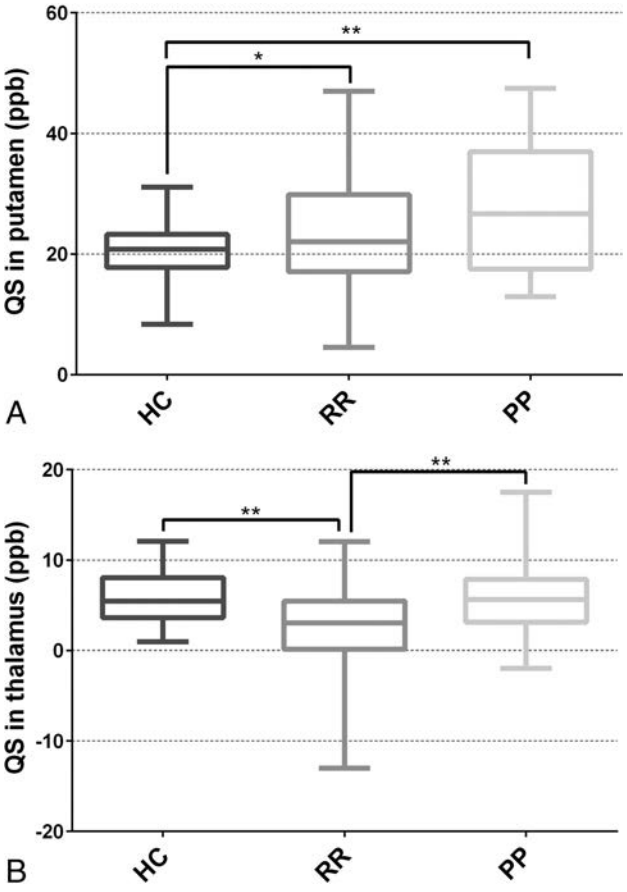

FIG 2. Quantitative susceptibility values in the putamen (*A*) and thalamus (*B*) across healthy controls and multiple sclerosis subtypes. Lower thalamic susceptibility values are observed in the RRMS compared with PPMS and HC groups. ppb indicates parts per billion.

because a single thalamic lesion was present in only 9 patients with RRMS (11%) and 3 with PPMS (12.5%).

Results from manual segmentation of the entire thalamus confirmed these findings, showing significantly lower QS values in RRMS compared with PPMS ($P = .026$) and a trend toward lower values in RRMS compared with HC ($P = .057$). When we analyzed thalamic substructures, the difference in QS among RRMS, PPMS, and HC groups was most pronounced in the thalamus without the pulvinar; in this region lower QS values were found in RRMS compared with HC ($P = .035$) and PPMS ($P = .035$) groups. No significant differences were found in the pulvinar (RRMS versus HC, $P = .28$; RRMS versus PPMS, $P = .28$) (On-line Table 2 and On-line Fig 1).

Correlations of QS Values with Conventional MR Imaging Metrics

In the RRMS group, we identified negative correlations between QS values in the thalamus and T2LL as well as T1LL and a positive correlation with BPF and CCV. In the PPMS group, QS values did not correlate with any conventional MR imaging parameter (Table 3).

Interaction analysis between each combination of dependent (QS in CN, GP, Put, thalamus) and independent (T1LL, T2LL, BPF, CCV) variables in PPMS and RRMS confirmed significant interaction between MS subtypes and the T1LL/T2LL effect on thalamic QS ($P < .05$). In the RRMS group, a strong negative linear relationship between T1LL/T2LL and QS in the thalamus was detected, while no such relationship was observed in the PPMS group (On-line Table 3 and On-line Fig 2).

Association between MR Imaging Metrics and Disability (EDSS) in MS Subtypes

In RRMS, the EDSS score was associated with all conventional MR imaging parameters: T1LL, T2LL, BPF, and CCV (Table 4). The strongest association was found for T1LL (Spearman correlation coefficient = 0.458, $P < .0001$). In addition, we identified a positive association between EDSS and QS values in the putamen (Fig 3*A*) and the CN. A negative association between the EDSS score and thalamic QS values was observed in the RRMS group (Fig 3*C*). In contrast, no association was found between the EDSS score and conventional MR imaging parameters in the PPMS group; there was only a positive association between EDSS and putaminal QS values observed in this group (Fig 3*B*, -*D*).

Interaction analysis comparing patients with EDSS ≤ 4 and EDSS > 4 in each MS subtype confirmed significant differences in mean thalamic susceptibility between RRMS with greater EDSS scores and PPMS regardless of EDSS scores ($P < .001$) (On-line Tables 4 and 5). Statistical differences in T1LL and T2LL were observed only between RRMS with greater EDSS scores and

Table 2: Quantitative susceptibility within deep GM structures[a]

DGM Structure QS (ppb)	HC	RRMS	RR_{EM} MS	PPMS	Pair-wise Comparison (*P* Value)[b]		
					PPMS vs RRMS (RR_{EM})	HC vs RRMS (RR_{EM})	HC vs PPMS
CN	32.6 (9.5)	35.0 (9.6)	38.3 (10.1)	36.8 (6.8)	.390 (.470)	.390 (.230)	.230
GP	66.7 (8.5)	71.9 (14.0)	72.4 (14.1)	70.8 (13.0)	.860 (.860)	.170 (.170)	.420
Put	20.3 (5.4)	24.3 (10.7)	27.7 (10.3)	28.1 (10.5)	.158 (.899)	.042[c] (.003)[c]	.009[c]
Thal	5.9 (3.3)	2.6 (4.9)	2.0 (5.7)	5.6 (3.9)	.007[c] (.007)[c]	.004[c] (.004)[c]	.757

Note:—Thal indicates thalamus.
[a] All values are means (SD).
[b] Pair-wise comparisons (*P* value) were tested using *t* tests with nonpooled SD (Benjamini-Hochberg correction).
[c] Significant.

Table 3: Correlations of QS values in DGM with conventional MRI parameters in the RRMS and PPMS groups

DGM Region	T1LL		T2LL		BPF		CCV	
	r_s	*P* Value	r_s	*P* Value	r_s	*P* Value	r_s	*P* Value
RRMS								
CN	−0.09	.44	−0.07	.56	−0.01	.96	−0.05	.63
GP	0.02	.85	0.07	.53	−0.00	.99	−0.10	.37
Put	0.14	.23	0.12	.30	−0.20	.08	−0.21	.06
Thal	−0.36	.001[a]	−0.35	.001[a]	0.23	.04[a]	0.25	.02[a]
PPMS								
CN	−0.13	.55	−0.16	.46	0.05	.80	0.02	.93
GP	0.07	.75	0.09	.69	−0.03	.86	0.06	.79
Put	0.25	.25	0.36	.09	−0.28	.18	−0.16	.47
Thal	−0.04	.85	0.03	.90	0.14	.52	0.11	.60

Note:—r_s indicates Spearman correlation coefficient; Thal, thalamus.
[a] Significant.

Table 4: Associations of EDSS with conventional MRI metrics and QS values

	RRMS		PPMS	
	r_s	*P* Value	r_s	*P* Value
Conventional MRI metrics				
T1LL	0.458	<.001[a]	0.195	.361
T2LL	0.336	.002[a]	0.237	.265
BPF	−0.281	.012[a]	−0.001	.995
CCV	−0.267	.017[a]	−0.089	.680
QS				
CN	0.234	.037[a]	0.127	.554
GP	−0.106	.350	−0.059	.785
Put	0.298	.007[a]	0.464	.022[a]
Thal	−0.251	.024[a]	0.119	.581

Note:—Thal indicates thalamus.
[a] Significant.

RRMS with lower EDSS scores ($P = .004$, $P = .027$, respectively) (On-line Tables 4, 6, and 7).

DISCUSSION

Comparing iron concentration in DGM between PPMS and RRMS subtypes, we identified QS values in the thalamus as the only significant difference between age- and sex-matched RRMS and PPMS groups. EDSS was associated with conventional MR imaging parameters, indicating disease severity in the RRMS group. Additionally, the EDSS score was positively associated with iron concentration in the putamen and CN and negatively associated with thalamic iron. No associations between EDSS and conventional MR imaging metrics were found in the PPMS group.

Previous MR imaging studies detected similarities but also several differences between PPMS and RRMS. Lesion morphology (iron deposition, the presence of the central vein), lesion count, and the proportion of cortical-to-total lesion counts were similar in PPMS and RRMS groups.[27] In PPMS, more diffuse abnormalities in the brain and spinal cord along with smaller caudate volume were apparent compared with RRMS.[28] In PPMS, clinicoradiologic correlation was weak for cerebral T1LL/T2LL but was stronger between spinal cord symptoms and spinal cord MR imaging parameters.[29,30]

In MS, increased iron levels seem to be already present in the clinically isolated syndrome group, and further buildup can be observed in the early stage after the transition to RRMS.[16,31,32] We confirmed significantly increased iron content in the putamen in both MS subtypes compared with HC, in agreement with previous studies.[4,6,7,33-35] While iron concentration was increased within the basal ganglia in patients with RRMS, the opposite (ie, lower iron concentration) was found in the thalamus. This result is consistent with findings in several previous MR R2* relaxometry studies showing lower thalamic iron in MS compared with HC.[6,7] On the contrary, other MR imaging studies with R2*, QSM, magnetic field correlation imaging, or phase imaging showed no significant difference[1,36] or even higher iron concentration in the thalamus in patients with RRMS.[2,8,37,38]

The cause of these contradictory findings is not clear. Because the disease duration of the RRMS group included in our study was rather long compared with other studies and thalamic iron content was negatively correlated with EDSS, one can speculate that iron may accumulate in the early MS stage, while its concentration may decrease in the later stage of the disease. However, another study indicated that the loss of thalamic iron in MS has already begun in patients with clinically isolated syndrome with further decrease after the conversion to definite MS.[11] In normal aging, total thalamic iron shows a very different pattern from that in all other DGM structures, with an accumulation until the fourth decade, followed by a mild decrease.[26] A histochemical study has shown that iron distribution in the thalamus is uneven, with the

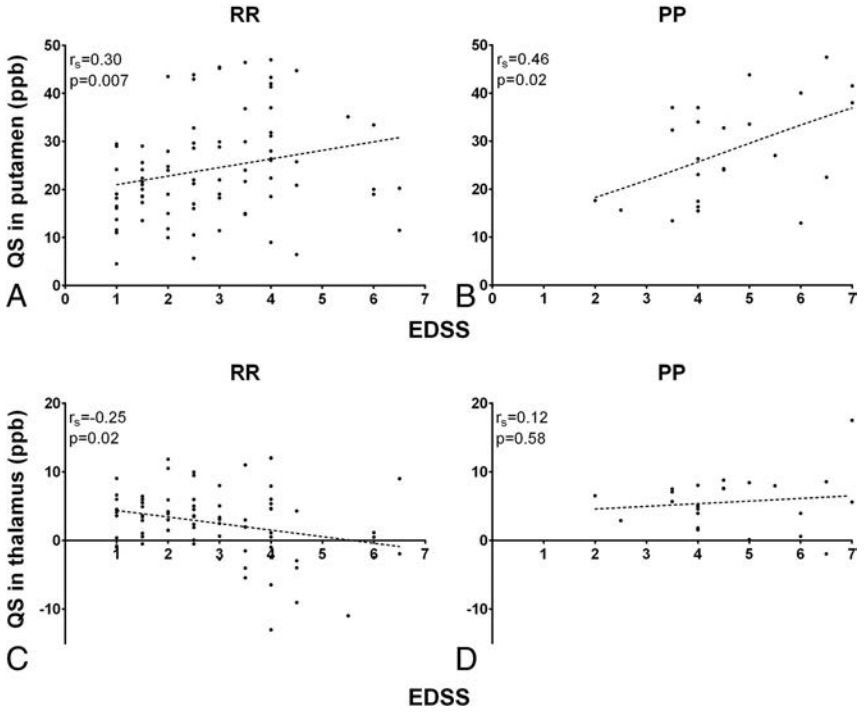

FIG 3. The relationship between clinical disability and quantitative susceptibility values in the putamen and thalamus across PPMS and RRMS groups. X-axes indicate EDSS, while y-axes indicate quantitative susceptibility values in parts per billion. A positive correlation between EDSS and putaminal quantitative susceptibility values is present in both the RRMS (*A*) and PPMS (*B*) groups. In the thalamus, a negative correlation between EDSS and quantitative susceptibility is present only in the RRMS group (*C*), while no correlation is observed in the PPMS group (*D*).

anterior nuclear group, dorsomedial group, and pulvinar having the highest iron reactivity.[39] It is thus possible that the temporal pattern of iron concentration change in individual thalamic nuclei is different. Indeed, a cross-sectional MR imaging study with R2* and QSM showed that iron in the thalamic pulvinar may increase with aging, while there was no age-related change in other thalamic nuclei.[40] In our study, the difference in thalamic QS values between RRMS on one hand and PPMS and HC on the other hand was mostly driven by variance in thalamic nuclei beyond the pulvinar, which is suggestive of diffuse iron loss within the thalamus.

Thalamic QS values in the PPMS group were significantly higher compared with the RRMS group; this finding indicates different regulation of thalamic iron concentration in these MS subtypes. However, the causes and consequences of different thalamic iron levels in RRMS and PPMS cannot be clarified from this cross-sectional study design. QS values in the thalamus were negatively correlated with T2LL and T1LL and with EDSS in the RRMS groups; this finding suggests an association between decreasing thalamic iron concentration and increasing WM impairment. This association between thalamic susceptibility and EDSS was not observed in the PPMS group. Susceptibility decrease may be due to lower (paramagnetic) iron or higher (diamagnetic) myelin content.[14,41] Higher myelin content is not plausible in the context of MS; thus, our finding of negative thalamic susceptibility values in patients with RRMS and higher EDSS scores is rather consistent with the loss of iron content. Moreover, the T2LL in the thalamus, which could potentially affect susceptibility, was very low, and the difference in lesion count was insignificant in the RRMS and PPMS groups.

When we investigated the conventional MR imaging metrics, T1LL was higher in the PPMS compared with the RRMS group. This T1LL difference could be related to higher clinical severity in the PPMS group, and it was not observed when patients with PPMS and RRMS were matched for EDSS scores. T1 hypointense lesions often represent the final destructive tissue changes, and T1LL may better correlate with disease progression and disability.[42] Di Perri et al[43] have shown that T1LL was similar in PPMS and RRMS subtypes matched for disease duration. However, the T1LL-to-T2LL ratio, along with clinical disability, was significantly higher in PPMS compared with RRMS. In other studies, on the contrary, the incidence of all brain lesion types has been reported to be reduced and brain atrophy increased in patients with PPMS compared with other MS subtypes, though there is a wide variability.[12,29,44-46] The low number of patients with PPMS in our study and in other studies precludes firm conclusions, and further studies with larger PPMS cohorts are needed.

Examining associations between clinical severity and MR imaging parameters in the PPMS group, we only found a positive association between EDSS and iron concentration in the putamen. The correlation between iron concentration in the putamen and CN and clinical severity is well-established in MS,[47,48] and it appears to be invariable regardless of the clinical subtype. Ropele et al[4] included 7 patients with PPMS and 7 with secondary-progressive MS, in addition to 83 with RRMS in their cohort. They identified the EDSS score as an independent predictor of iron accumulation in the DGM. However, the results were likely driven by RRMS, while there were a limited number of patients with PPMS and SPMS.[4] No significant association between conventional MR imaging metrics and EDSS has been detected in PPMS, which is consistent with findings in previous studies.[43,49] In RRMS, there was a correlation between EDSS and conventional MR imaging parameters, which reflects WM lesions and brain atrophy. The correlation of EDSS with T1LL was stronger than with T2LL. These findings are in the line with previous studies[23,42,50-55] showing that T1LL and T2LL provide a useful marker for disease progression and long-term therapeutic effect in RRMS.

To our best knowledge, this is the first study comparing iron concentration in DGM and its correlations with EDSS score between PPMS and RRMS subtypes. However, there are some limitations. Our PPMS group was rather small, and no MR imaging data were collected from the spinal cord, which could also contribute to the explanation of clinical disability. Cross-sectional

design provides no information regarding the temporal dynamics of iron accumulation. Future work using a larger PPMS cohort in a longitudinal setting is needed. Likewise, spinal cord pathology, iron deposition within WM, and demyelinating lesions should be the focus of further investigations.

CONCLUSIONS

Our findings support the concept that PPMS is a part of the MS disease spectrum, not a separate entity. When patients with RRMS are matched to those with PPMS for age, sex, and EDSS, these groups do not differ regarding conventional MR imaging metrics. Decreased susceptibility within the thalamus was the only significant MR imaging difference between PPMS and RRMS groups, suggesting different thalamic iron metabolism according to the underlying MS subtype.

On the other hand, there are significant differences in the extent of correlation of MR imaging parameters and clinical severity between PPMS and RRMS subtypes. In RRMS, EDSS is significantly associated with conventional parameters and, additionally, with iron concentration in the striatum. In contrast, no association was found in PPMS, except a weak correlation with putaminal iron. These findings suggest that different driving forces of disability take effect in RRMS and PPMS subtypes.

Disclosures: Andrea Burgetova—*RELATED*: *Grant*: RVO VFN64165 (Czech Ministry of Health), *Comments*: Money went to the institution and a part of it to me*. Petr Dusek—*RELATED*: *Grant*: Czech Ministry of Health, 15–25602A. Manuela Vaneckova—*RELATED*: *Grant*: Czech Ministries of Health, RVO-VFN64165*; *UNRELATED*: *Consultancy*: Biogen Idec, Novartis, Merck Serono, Teva Pharmaceutical Industries; *Payment for Lectures Including Service on Speakers Bureaus*: Biogen Idec, Novartis, Merck Serono, Teva Pharmaceutical Industries; *Travel/Accommodations/Meeting Expenses Unrelated to Activities Listed*: Biogen Idec, Genzyme. Dana Horakova—*UNRELATED*: *Consultancy*: Biogen Idec, Sanofi-Genzyme; *Grants/Grants Pending*: grants GA CR 16–03322S and PRVOUK P26/LF1/4*; *Payment for Lectures Including Service on Speakers Bureaus*: Biogen Idec, Novartis, Merck, Bayer HealthCare Pharmaceuticals, Sanofi-Genzyme, and Teva Pharmaceutical Industries. Jan Krasensky—*RELATED*: *Grant:* Ministry of Health, RVO-VFN-64165*; *UNRELATED*: *Travel/Accommodations/Meeting Expenses Unrelated to Activities Listed*: Biogen Idec, Novartis. Lukas Sobisek—*RELATED*: *Grant*: Czech Ministry of Education project PRVOUK-P26/LF1/4; *Other*: Novartis; *UNRELATED*: *Employment*: University of Economics in Prague, *Comments*: assistant in Department of Statistics and Informatics. Zdenek Seidl—*RELATED*: *Grant*: Ministry of Health, RVO-VFN64165.* *Money paid to the institution.

REFERENCES

1. Raz E, Branson B, Jensen JH, et al. **Relationship between iron accumulation and white matter injury in multiple sclerosis: a case-control study.** *J Neurol* 2015;262:402–09 CrossRef Medline
2. Cobzas D, Sun H, Walsh AJ, et al. **Subcortical gray matter segmentation and voxel-based analysis using transverse relaxation and quantitative susceptibility mapping with application to multiple sclerosis.** *J Magn Reson Imaging* 2015;42:1601–10 CrossRef Medline
3. Stankiewicz JM, Neema M, Ceccarelli A. **Iron and multiple sclerosis.** *Neurobiol Aging* 2014;35(suppl 2):S51–58 CrossRef Medline
4. Ropele S, Kilsdonk ID, Wattjes MP, et al. **Determinants of iron accumulation in deep grey matter of multiple sclerosis patients.** *Mult Scler* 2014;20:1692–98 CrossRef Medline
5. Ropele S, de Graaf W, Khalil M, et al. **MRI assessment of iron deposition in multiple sclerosis.** *J Magn Reson Imaging* 2011;34:13–21 CrossRef Medline
6. Khalil M, Langkammer C, Ropele S, et al. **Determinants of brain iron in multiple sclerosis: a quantitative 3T MRI study.** *Neurology* 2011;77:1691–97 CrossRef Medline
7. Burgetova A, Seidl Z, Krasensky J, et al. **Multiple sclerosis and the accumulation of iron in the basal ganglia: quantitative assessment of brain iron using MRI t(2) relaxometry.** *Eur Neurol* 2010;63:136–43 CrossRef Medline
8. Ge Y, Jensen JH, Lu H, et al. **Quantitative assessment of iron accumulation in the deep gray matter of multiple sclerosis by magnetic field correlation imaging.** *AJNR Am J Neuroradiol* 2007;28:1639–44 CrossRef Medline
9. Haider L, Simeonidou C, Steinberger G, et al. **Multiple sclerosis deep grey matter: the relation between demyelination, neurodegeneration, inflammation and iron.** *J Neurol Neurosurg Psychiatry* 2014;85:1386–95 CrossRef Medline
10. Hametner S, Wimmer I, Haider L, et al. **Iron and neurodegeneration in the multiple sclerosis brain.** *Ann Neurol* 2013;74:848–61 CrossRef Medline
11. Khalil M, Langkammer C, Pichler A, et al. **Dynamics of brain iron levels in multiple sclerosis: a longitudinal 3T MRI study.** *Neurology* 2015;84:2396–402 CrossRef Medline
12. Antel J, Antel S, Caramanos Z, et al. **Primary progressive multiple sclerosis: part of the MS disease spectrum or separate disease entity?** *Acta Neuropathol* 2012;123:627–38 CrossRef Medline
13. Dusek P, Dezortova M, Wuerfel J. **Imaging of iron.** *Int Rev Neurobiol* 2013;110:195–239 CrossRef Medline
14. Langkammer C, Schweser F, Krebs N, et al. **Quantitative susceptibility mapping (QSM) as a means to measure brain iron? A post mortem validation study.** *Neuroimage* 2012;62:1593–99 CrossRef Medline
15. Schmalbrock P, Prakash RS, Schirda B, et al. **Basal ganglia iron in patients with multiple sclerosis measured with 7T quantitative susceptibility mapping correlates with inhibitory control.** *AJNR Am J Neuroradiol* 2016;37:439–46 CrossRef Medline
16. Al-Radaideh AM, Wharton SJ, Lim SY, et al. **Increased iron accumulation occurs in the earliest stages of demyelinating disease: an ultra-high field susceptibility mapping study in clinically isolated syndrome.** *Mult Scler* 2013;19:896–903 CrossRef Medline
17. Wang Y, Liu T. **Quantitative susceptibility mapping (QSM): decoding MRI data for a tissue magnetic biomarker.** *Magn Reson Med* 2015;73:82–101 CrossRef Medline
18. Schweser F, Deistung A, Lehr BW, et al. **Differentiation between diamagnetic and paramagnetic cerebral lesions based on magnetic susceptibility mapping.** *Med Phys* 2010;37:5165–78 CrossRef Medline
19. Lublin FD, Reingold SC, Cohen JA, et al. **Defining the clinical course of multiple sclerosis: the 2013 revisions.** *Neurology* 2014;83:278–86 CrossRef Medline
20. Ho DE, Imai K, King G, et al. **MatchIt: nonparametric preprocessing for parametric causal inference.** *J Stat Soft* 2011;42:1–28
21. Horakova D, Kalincik T, Dolezal O, et al. **Early predictors of non-response to interferon in multiple sclerosis.** *Acta Neurol Scand* 2012;126:390–97 CrossRef Medline
22. Kalincik T, Vaneckova M, Tyblova M, et al. **Volumetric MRI markers and predictors of disease activity in early multiple sclerosis: a longitudinal cohort study.** *PLoS One* 2012;7:e50101 CrossRef Medline
23. Vaneckova M, Kalincik T, Krasensky J, et al. **Corpus callosum atrophy: a simple predictor of multiple sclerosis progression—a longitudinal 9-year study.** *Eur Neurol* 2012;68:23–27 CrossRef Medline
24. Langkammer C, Bredies K, Poser BA, et al. **Fast quantitative susceptibility mapping using 3D EPI and total generalized variation.** *Neuroimage* 2015;111:622–30 CrossRef Medline
25. Yushkevich PA, Piven J, Hazlett HC, et al. **User-guided 3D active contour segmentation of anatomical structures: significantly improved efficiency and reliability.** *Neuroimage* 2006;31:1116–28 CrossRef Medline
26. Hallgren B, Sourander P. **The effect of age on the non-haemin iron in the human brain.** *J Neurochem* 1958;3:41–51 CrossRef Medline
27. Kuchling J, Ramien C, Bozin I, et al. **Identical lesion morphology in primary progressive and relapsing-remitting MS: an ultrahigh field MRI study.** *Mult Scler* 2014;20:1866–71 CrossRef Medline
28. Jonkman LE, Rosenthal DM, Sormani MP, et al. **Gray matter corre-**

lates of cognitive performance differ between relapsing-remitting and primary-progressive multiple sclerosis. *PLoS One* 2015;10: e0129380 CrossRef Medline
29. Galego O, Gouveia A, Batista S, et al. **Brain atrophy and physical disability in primary progressive multiple sclerosis: a volumetric study.** *Neuroradiol J* 2015;28:354–58 CrossRef Medline
30. Nijeholt GJ, van Walderveen MA, Castelijns JA, et al. **Brain and spinal cord abnormalities in multiple sclerosis: correlation between MRI parameters, clinical subtypes and symptoms.** *Brain* 1998; 121(pt 4):687–97 CrossRef Medline
31. Hagemeier J, Heininen-Brown M, Poloni GU, et al. **Iron deposition in multiple sclerosis lesions measured by susceptibility-weighted imaging filtered phase: a case control study.** *J Magn Reson Imaging* 2012;36:73–83 CrossRef Medline
32. Quinn MP, Gati JS, Klassen ML, et al. **Increased deep gray matter iron is present in clinically isolated syndromes.** *Mult Scler Relat Disord* 2014;3:194–202 CrossRef Medline
33. Hammond KE, Metcalf M, Carvajal L, et al. **Quantitative in vivo magnetic resonance imaging of multiple sclerosis at 7 Tesla with sensitivity to iron.** *Ann Neurol* 2008;64:707–13 CrossRef Medline
34. Khalil M, Enzinger C, Langkammer C, et al. **Quantitative assessment of brain iron by R(2)* relaxometry in patients with clinically isolated syndrome and relapsing-remitting multiple sclerosis.** *Mult Scler* 2009;15:1048–54 CrossRef Medline
35. Zivadinov R, Heininen-Brown M, Schirda CV, et al. **Abnormal subcortical deep-gray matter susceptibility-weighted imaging filtered phase measurements in patients with multiple sclerosis: a case-control study.** *Neuroimage* 2012;59:331–39 CrossRef Medline
36. Du S, Sah SK, Zeng C, et al. **Iron deposition in the gray matter in patients with relapse-remitting multiple sclerosis: a longitudinal study using three-dimensional (3D)-enhanced T2*-weighted angiography (ESWAN).** *Eur J Radiol* 2015;84:1325–32 CrossRef Medline
37. Hagemeier J, Yeh EA, Brown MH, et al. **Iron content of the pulvinar nucleus of the thalamus is increased in adolescent multiple sclerosis.** *Mult Scler* 2013;19:567–76 CrossRef Medline
38. Modica CM, Zivadinov R, Dwyer MG, et al. **Iron and volume in the deep gray matter: association with cognitive impairment in multiple sclerosis.** *AJNR Am J Neuroradiol* 2015;36:57–62 CrossRef Medline
39. Morris CM, Candy JM, Oakley AE, et al. **Histochemical distribution of non-haem iron in the human brain.** *Acta Anat (Basel)* 1992;144: 235–57 CrossRef Medline
40. Acosta-Cabronero J, Betts MJ, Cardenas-Blanco A, et al. **In vivo MRI mapping of brain iron deposition across the adult lifespan.** *J Neurosci* 2016;36:364–74 CrossRef Medline
41. Fukunaga M, Li TQ, van Gelderen P, et al. **Layer-specific variation of iron content in cerebral cortex as a source of MRI contrast.** *Proc Natl Acad Sci U S A* 2010;107:3834–39 CrossRef Medline
42. Truyen L, van Waesberghe JH, van Walderveen MA, et al. **Accumulation of hypointense lesions ("black holes") on T1 spin-echo MRI correlates with disease progression in multiple sclerosis.** *Neurology* 1996;47:1469–76 CrossRef Medline
43. Di Perri C, Battaglini M, Stromillo ML, et al. **Voxel-based assessment of differences in damage and distribution of white matter lesions between patients with primary progressive and relapsing-remitting multiple sclerosis.** *Arch Neurol* 2008;65:236–43 Medline
44. Miller DH, Leary SM. **Primary-progressive multiple sclerosis.** *Lancet Neurol* 2007;6:903–12 CrossRef Medline
45. Stevenson VL, Miller DH, Rovaris M, et al. **Primary and transitional progressive MS: a clinical and MRI cross-sectional study.** *Neurology* 1999;52:839–45 CrossRef Medline
46. Thompson AJ, Montalban X, Barkhof F, et al. **Diagnostic criteria for primary progressive multiple sclerosis: a position paper.** *Ann Neurol* 2000;47:831–35 Medline
47. Zhang Y, Metz LM, Yong VW, et al. **3T deep gray matter T2 hypointensity correlates with disability over time in stable relapsing-remitting multiple sclerosis: a 3-year pilot study.** *J Neurol Sci* 2010; 297:76–81 CrossRef Medline
48. Tjoa CW, Benedict RH, Weinstock-Guttman B, et al. **MRI T2 hypointensity of the dentate nucleus is related to ambulatory impairment in multiple sclerosis.** *J Neurol Sci* 2005;234:17–24 CrossRef Medline
49. Ruggieri S, Petracca M, Miller A, et al. **Association of deep gray matter damage with cortical and spinal cord degeneration in primary progressive multiple sclerosis.** *JAMA Neurol* 2015;72:1466–74 CrossRef Medline
50. Bergsland N, Horakova D, Dwyer MG, et al. **Subcortical and cortical gray matter atrophy in a large sample of patients with clinically isolated syndrome and early relapsing-remitting multiple sclerosis.** *AJNR Am J Neuroradiol* 2012;33:1573–78 CrossRef Medline
51. Bermel RA, Bakshi R. **The measurement and clinical relevance of brain atrophy in multiple sclerosis.** *Lancet Neurol* 2006;5:158–70 CrossRef Medline
52. Bodini B, Battaglini M, De Stefano N, et al. **T2 lesion location really matters: a 10-year follow-up study in primary progressive multiple sclerosis.** *J Neurol Neurosurg Psychiatry* 2011;82:72–77 CrossRef Medline
53. Ciccarelli O, Brex PA, Thompson AJ, et al. **Disability and lesion load in MS: a reassessment with MS functional composite score and 3D fast FLAIR.** *J Neurol* 2002;249:18–24 CrossRef Medline
54. Kearney H, Rocca MA, Valsasina P, et al. **Magnetic resonance imaging correlates of physical disability in relapse onset multiple sclerosis of long disease duration.** *Mult Scler* 2014;20:72–80 CrossRef Medline
55. Zivadinov R, Stosic M, Cox JL, et al. **The place of conventional MRI and newly emerging MRI techniques in monitoring different aspects of treatment outcome.** *J Neurol* 2008;255(suppl 1):61–74 CrossRef Medline

Heterogeneity of Cortical Lesion Susceptibility Mapping in Multiple Sclerosis

M. Castellaro, R. Magliozzi, A. Palombit, M. Pitteri, E. Silvestri, V. Camera, S. Montemezzi, F.B. Pizzini, A. Bertoldo, R. Reynolds, S. Monaco, and M. Calabrese

ABSTRACT

BACKGROUND AND PURPOSE: Quantitative susceptibility mapping has been used to characterize iron and myelin content in the deep gray matter of patients with multiple sclerosis. Our aim was to characterize the susceptibility mapping of cortical lesions in patients with MS and compare it with neuropathologic observations.

MATERIALS AND METHODS: The pattern of microglial activation was studied in postmortem brain tissues from 16 patients with secondary-progressive MS and 5 age-matched controls. Thirty-six patients with MS underwent 3T MR imaging, including 3D double inversion recovery and 3D-echo-planar SWI.

RESULTS: Neuropathologic analysis revealed the presence of an intense band of microglia activation close to the pial membrane in subpial cortical lesions or to the WM border of leukocortical cortical lesions. The quantitative susceptibility mapping analysis revealed 131 cortical lesions classified as hyperintense; 33, as isointense; and 84, as hypointense. Quantitative susceptibility mapping hyperintensity edge found in the proximity of the pial surface or at the white matter/gray matter interface in some of the quantitative susceptibility mapping–hyperintense cortical lesions accurately mirrors the microglia activation observed in the neuropathology analysis.

CONCLUSIONS: Cortical lesion susceptibility maps are highly heterogeneous, even at individual levels. Quantitative susceptibility mapping hyperintensity edge found in proximity to the pial surface might be due to the subpial gradient of microglial activation.

ABBREVIATIONS: CL = cortical lesion; DIR = double inversion recovery; EDSS = Expanded Disability Status Scale; MHC = major histocompatibility complex; MOG = myelin oligodendrocyte glycoprotein; NAGM = normal-appearing gray matter; nQSM = QSM value in the NAGM; $nQSM_{contra}$ = median value of susceptibility from the reference tissue mask in the contralateral hemisphere; $nQSM_{surr}$ = median value of susceptibility from the reference tissue mask surrounding the lesion; QSM = quantitative susceptibility mapping; RRMS = relapsing-remitting multiple sclerosis; SPMS = secondary-progressive multiple sclerosis

In recent years, it has become increasingly clear that cortical and deep gray matter are not spared in multiple sclerosis.[1,2] Several neuropathologic studies have consistently demonstrated that cortical gray matter lesions (CLs) are frequent in MS and that their accumulation strongly correlates with long-term disability measures.[3] These observations have been confirmed and extended by imaging studies showing that CLs correlate with both physical and cognitive disability.[4,5] Unfortunately, despite these data, little is known about the pathogenetic mechanisms underlying CL development.

Neuropathologic studies have highlighted the lack of substantial focal immune infiltrates, complement deposition, and blood-brain barrier damage in MS CLs[6,7] and have suggested that meningeal inflammation and activated microglia may have a key role in GM damage.[3,8] In particular, most of the examined CLs in postmortem brain samples exhibit a chronic inflammatory phenotype and rims of activated microglia close to the pial surface or the lesion edge.[3,8,9]

In a previous MR imaging/histopathologic combined study,[10] hypointense rings on T2*, representing activated microglia or

Received June 23, 2016; accepted after revision January 21, 2017.

From the Department of Information Engineering (M. Castellaro, A.P., E.S., A.B.), University of Padova, Padova, Italy; Neurology B (M. Castellaro, R.M., M.P., V.C., S.M., M. Calabrese), Department of Neurological, Biomedical and Movement Sciences, University of Verona, Verona, Italy; Division of Brain Sciences (R.M., R.R.), Faculty of Medicine, Imperial College London, Hammersmith Hospital, London, UK; and Neuroradiology and Radiology Units (S.M., F.B.P.), Department of Diagnostics and Pathology, Verona University Hospital, Verona, Italy.

M. Castellaro and R. Magliozzi contributed equally to the article.

Dr Calabrese had full access to all data in the study and takes responsibility for the integrity of the data and the accuracy of the data analysis. Dr Calabrese received honoraria for speaking from Sanofi-Aventis, Novartis Pharmaceuticals, Bayer Shering Pharma, Merck Serono, and Biogen Idec and funds for travel from Sanofi-Aventis, Genzyme, and Merck Serono. Dr Magliozzi was supported by the GR-2010–2313255 grant from Italian Ministry of Health. Drs Calabrese and Reynolds were supported by a Progressive Multiple Sclerosis Alliance grant (PA 0124). No other disclosures were reported.

Please address correspondence to Massimiliano Calabrese, MD, Neurology B, Department of Neurological, Biomedical and Movement Sciences, University of Verona, Italy, Policlinico "G.B. Rossi" Borgo Roma, Piazzale L.A. Scuro, 10, 37134 Verona, Italy; e-mail: massimiliano.calabrese@univr.it

Indicates open access to non-subscribers at www.ajnr.org

http://dx.doi.org/10.3174/ajnr.A5150

macrophages, were observed at the edge of chronic active CLs. Similar rings have been reported in white matter lesions by using T2* phase imaging.[11] These results, in line with those by Kooi et al,[12] showed that some patients with MS had rims of activated microglia at the border of the CLs, whereas others did not. More recently, a study on ultra-high-field MR imaging on postmortem specimens of 2 patients with MS[13] did not find rings of activated iron-laden microglia within CLs, and all CLs appeared darker in R2* images and brighter in magnitude images.

Magnetic susceptibility is a fundamental physical tissue property, which is known to reflect clinically relevant tissue characteristics, such as tissue iron content. During the last decades, phase imaging,[14] SWI,[15] and T2* imaging[16] have been used to qualitatively assess magnetic susceptibility variations in cerebral tissue, including deep and cortical gray matter.[17] Increased paramagnetic susceptibility-weighted filtered phase values were observed in the putamen in patients with clinically isolated syndrome compared with healthy controls.[18] Thus, this finding suggests that susceptibility is sensitive to MS even in the early phase of the disease. In this context, quantitative susceptibility mapping (QSM),[19] which overcomes several nonlocal restrictions of susceptibility-weighted and phase imaging, could shed some light on the pathologic process taking place in the cortical GM of patients with MS. A recent study has investigated MS, using QSM in the basal ganglia,[20] showing that iron accumulation correlated with disease progression even in a patient with clinically isolated syndrome. Moreover, another group showed how WM MS lesions could be investigated longitudinally with QSM; the investigation could provide insight into the pathogenesis of those lesions.[21] However, limited quantitative susceptibility data of cortical GM and, especially, of CLs are available. Indeed, only a recent study at 7T showed,[22] in a restricted cohort of patients with MS, heterogeneity in CLs, with a predominant iron loss hypothesis.

In the present study, the characteristics of CLs were first determined with an analysis of microglial/macrophage activity in the postmortem MS brain, followed by the analysis of similar lesions in patients. 3D echo-planar imaging, which uses phase data to quantify local tissue susceptibility, was combined with a 3D double inversion recovery (DIR) at 3T to characterize the in vivo susceptibility of CLs in patients with MS.

MATERIALS AND METHODS

Neuropathologic Analysis

This study was performed on postmortem brain tissues from 16 patients with secondary-progressive multiple sclerosis (SPMS) (mean age at death, 44.4 ± 6.2 years, Table 1; disease duration, 23.31 ± 8.55 years; time to wheelchair [from onset to Expanded Disability Status Scale {EDSS} 7], 41.21 ± 7.83 years; relapse rate in the first 2 years of the disease, 2.6 ± 1.3) selected for the presence of widespread cortical demyelination associated with meningeal inflammation and by more rapid and severe disease outcome associated with intense inflammatory activity among a larger group of 48 patients with SPMS previously extensively characterized for the presence and levels of inflammatory features and the extent of gray and white matter demyelination.[23] Postmortem brain tissues from 8 controls, with no neurologic diseases, were also examined. In 3 snap-frozen tissue blocks for each SPMS and control case, the presence and extent of demyelination and characterization of CL activity were determined by immunostaining with monoclonal antibodies for myelin oligodendrocyte glycoprotein (MOG) and major histocompatibility complex (MHC class II).[3,24] CLs were classified, as previously described[8] into leukocortical type I, intracortical type II, or subpial type III.

Table 1: Neuropathologic details of postmortem brain tissue used in the study

	Sex/Age at Death (yr)	Postmortem Delay (hr)	Age at Onset (yr)
SPMS cases			
MS92	F/38	26	21
MS121	F/49	24	36
MS154	F/35	12	23
MS160	F/44	18	29
MS176	M/37	12	10
MS180	F/44	9	26
MS229	M/53	13	37
MS230	F/42	31	22
MS234	F/39	15	23
MS286	M/45	7	29
MS289	M/45	9	27
MS317	F/48	21	18
MS330	F/59	24	19
MS356	F/45	10	28
MS408	M/39	21	29
MS517	F/48	12	23
Control cases			
C14	F/64	18	
C25	M/35	22	
C28	F/60	13	
C30	M/75	17	
C36	M/68	30	
C41	M/51	22	
C48	M/68	10	
C54	M/66	16	

In Vivo Study Population

Thirty-six patients with MS[25] having at least 1 MR imaging–visible CL were studied (Table 2). Twenty-one had relapsing-remitting MS (RRMS), and 15 had secondary-progressive MS. At study entry, most patients were under immunomodulatory therapy: Twelve were treated with interferon β1a/bβ1b or glatiramer acetate; 6, with fingolimod; 4, with natalizumab; 3, with azathioprine; and 3, with dimethyl fumarate; and 8 were untreated.

Each patient was assessed with the Expanded Disability Status Scale[26] and underwent 3T MR imaging as described below. The study was approved by the University of Verona ethics committee, and informed consent was obtained from all patients.

MR Imaging Acquisition and Analysis

All patients were scanned with an Achieva 3T MR imaging scanner (Philips Healthcare, Best, the Netherlands). Isotropic 3D DIR (1 × 1 × 1 mm, 10 minutes 49 seconds), 3D T1-MPRAGE (1 × 1 × 1 mm, 5 minutes 50 seconds), and 3D EPI-SWI (0.55 × 0.55 × 0.55 mm, 5 minutes 51 seconds) images were acquired. Quantification of susceptibility maps was performed by using the recently introduced total generalized variation framework.[27]

After coregistration with 3D EPI, 3D DIR images were visually

Table 2: Demographic, clinical, and QSM-related characteristics of the patient population

	RRMS	SPMS	Whole Group
No.	21	15	36
Age (yr)	36.2 ± 5.8	49.5 ± 9.2	40.5 ± 8.0
Disease duration (yr)	9.7 ± 6.3	16.9 ± 7.0	12.7 ± 7.5
Sex (F/M)	16:5	9:6	25:11
EDSS (mean) (range)	2.0 (1.0–5.5)	5.0 (4.0–7.0)	3.0 (1.0–7.0)
No. of intracortical lesions (mean)			
Total	4.5 ± 3.6	2.1 ± 2.6	3.5 ± 3.4
QSM-hyperintense	2.8 ± 2.3	0.9 ± 1.2	2.0 ± 2.1
QSM-isointense	0.6 ± 0.7	0.1 ± 0.4	0.4 ± 0.6
QSM-hypointense	1.1 ± 1.5	0.9 ± 1.8	1.0 ± 1.6
No. of leukocortical lesions (mean)			
Total	2.6 ± 3.1	5.0 ± 3.5	3.6 ± 3.5
QSM-hyperintense	1.5 ± 1.8	1.9 ± 1.5	1.7 ± 1.7
QSM-isointense	0.5 ± 0.9	0.6 ± 1.3	0.5 ± 1.1
QSM-hypointense	0.5 ± 0.9	2.4 ± 2.4	1.3 ± 1.9
No. of total lesions (mean)			
Total	7.1 ± 5.2	7.1 ± 5.0	7.1 ± 5.1
QSM-hyperintense	4.2 ± 3.4	2.8 ± 2.3	3.6 ± 3.0
QSM-isointense	1.0 ± 1.2	0.7 ± 1.3	0.9 ± 1.3
QSM-hypointense	1.6 ± 1.8	3.3 ± 3.7	2.3 ± 2.8

inspected and CLs were identified as intracortical or leukocortical lesions. Each CL was identified following the recent recommendations for CL scoring in patients with MS.[28] All DIR images were assessed by consensus of experienced observers who were blinded to patient identity.

The appearance of CLs (identified with the DIR) on the QSM map was then evaluated. Each lesion was manually segmented on the DIR and then moved on the QSM. T1 was segmented to obtain a normal-appearing gray matter (NAGM) map.[29,30] A threshold of $P > .9$ was used to ensure including mainly GM. The NAGM mask was then moved to the QSM space. The obtained GM mask was then used to segment a portion of the NAGM surrounding the lesion. Each CL mask was dilated (a circle of 7 pixels was used as the kernel) and was used to reduce the whole GM mask to the surrounding NAGM tissue. The surrounding mask was then refined by subtracting a dilated mask of the CL (circle of 3 pixels) to exclude the proximity of the lesion. We repeated the procedure, choosing a contralateral area of the brain as a reference (including only NAGM tissue). The median values of susceptibility from the reference tissue mask surrounding the lesion ($nQSM_{surr}$) and in the contralateral hemisphere ($nQSM_{contra}$) were subtracted from the QSM estimates within the CL. The distributions of both $nQSM_{surr}$ and $nQSM_{contra}$ were then tested with a *t* test versus a zero-mean distribution. If both test results were statistically significant, the CL was classified as not isointense; otherwise, it was considered isointense. If the mean of both $nQSM_{surr}$ and $nQSM_{contra}$ was greater (lesser) than zero, the CL was classified as hyperintense (hypointense). If the mean value was discordant between the 2 references, the CL was discarded from the evaluation.

Statistical Analysis

Differences between RRMS and SPMS were assessed with ANOVA. The Pearson χ^2 was applied to test the difference between the 2 patient groups in terms of categoric data (percentage of lesions). The Pearson correlation coefficient was used to assess the correlation between disease duration and lesion-counting metrics, whereas the Spearman coefficient was used to analyze the correlation with the EDSS. When we calculated correlations, a false discovery rate (with a false-positive rate of 0.05) correction technique was used to address multiple comparison correction issues. Each statistical test was considered significant with a level of .05 when not otherwise specified.

RESULTS

Neuropathologic Analysis of Microglia Activity in CLs

To evaluate the microglia/macrophage activation in the different types of CLs, we performed immunostaining for MHC class II and CD68 on tissue blocks from 16 SPMS cases. The activity of all 127 CLs identified in the examined SPMS cases was analyzed: the largest proportion (45.0%) was chronic active, identified as cortical areas with MHC-II+ cells mainly localized at the lesion edge (Fig 1*A*), in agreement with previous studies.[3,8] This type of CL was more abundant compared with both chronic inactive (25.9%), with very low MHC II+ cell density through the entire lesion, and active (29.1%) CLs, characterized by numerous MHC-II+ lesions in the lesion core and borders (Fig 1*A*).

Examination of the inflammatory activity of large CLs (Fig 1*B*) showed that MHC class II immunostaining was mainly restricted to activated microglia with ramified morphology, with a higher density in the most external cortical layers close to the pial membrane in subpial type III CLs (Fig 1*C*) or close to the WM portion in type I CLs (Fig 1*D*), either in actively demyelinating or chronic active lesions. In chronic inactive lesions, a lower density of MHC-II+ cells was present, scattered in all demyelinated areas (Fig 1*E*, *-F*). Furthermore, for each of the examined patients with MS, all the different types of CL activity were found. Large CLs (Fig 1*B*) sometimes contained, simultaneously, rims of activated microglia either close to the pial surface (Fig 1*C*) or toward the WM lesion border (Fig 1*D*).

Imaging Data

Two hundred fifty-five CLs were identified in the living population. On the basis of the DIR sequence, 126 CLs were pure intracortical and 129 CLs were leukocortical; on the basis of QSM, 131 were hyperintense, 33 were isointense, and 84 were hypointense (Fig 2). Seven CLs were discarded from the analysis because discordant results of the *t* test between $nQSM_{surr}$ and $nQSM_{contra}$ were found. Among the 36 patients with MS, 32 showed at least 1 QSM-hyperintense CL, 16 showed at least 1 QSM-isointense CL, and 23 showed at least 1 QSM-hypointense CL. Twenty-six patients (72.22%) showed at least 2 QSM subtypes of CLs, and 11 patients showed all QSM subtypes of CLs at the same time. Table 2 shows the differences between intracortical and mixed GM/WM lesions.

The number of hyperintense CLs was higher in RRMS (mean, 4.1 ± 1.4; range, 0–14) compared with SPMS (mean, 2.2 ± 1.5; range, 0–5), while the number of hypointense CLs was higher in patients with SPMS (mean, 0.8 ± 1.1; range, 0–4 in RRMS; mean, 3.5 ± 3.5; range, 0–11 in SPMS). Indeed, in RRMS, 61.4% of CLs were hyperintense and 23.4% were hypointense, whereas in SPMS, 40.7% of CLs were hyperintense and 48.5% were hypointense.

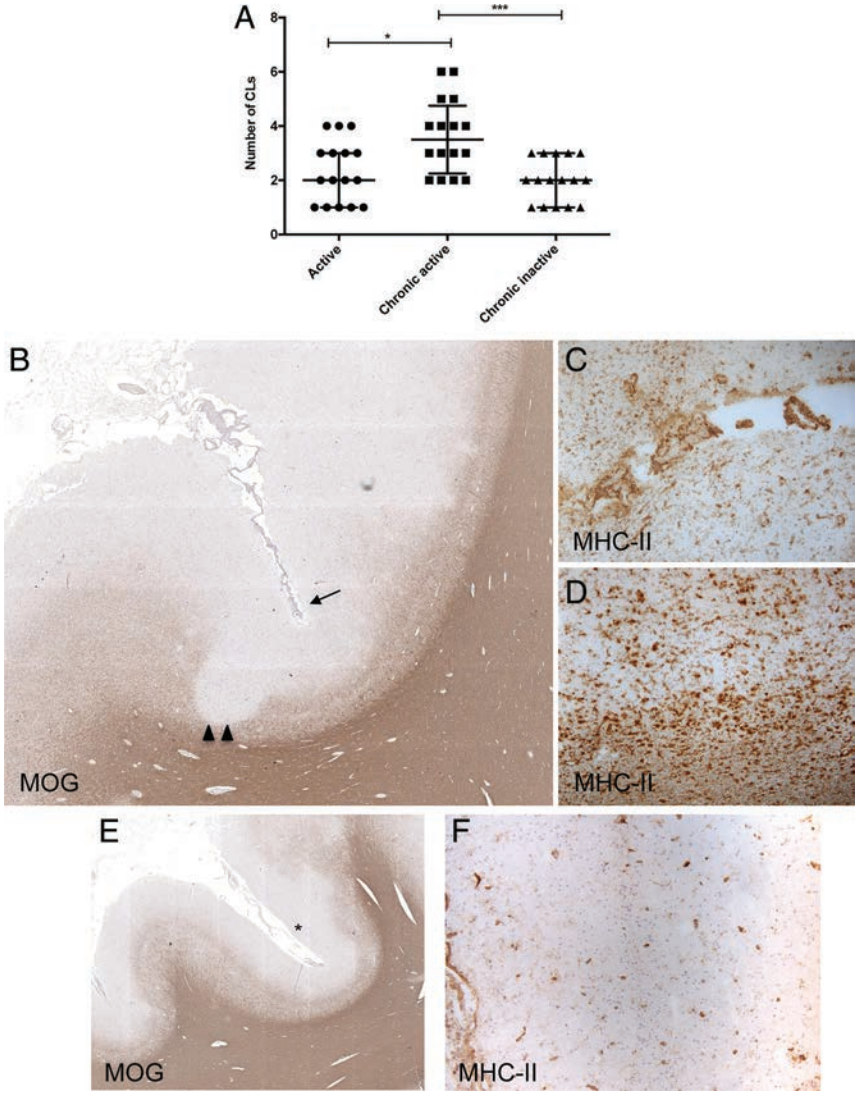

FIG 1. Neuropathologic assessment of cortical lesion activity. The number of active, chronic active, and chronic inactive GM lesions was evaluated with MHC class II immunostaining in 3 snap-frozen tissue blocks (*A*) for each of the examined 16 postmortem MS cases. A significant increased level of chronic active CL has been found compared with both active and chronic inactive CL. MOG immunostaining (*B*) shows an extensive chronic active subpial type III GM lesion, also reaching the WM (*arrowheads*). Combined MHC class II immunostaining of serial sections (*C* and *D*) demonstrates the high density of activated MHC-II+ cells close to the pial surface of the lesion (*arrow* in *B*, higher magnification in *C*) and toward the WM edge of the lesion (*arrowheads* in *B*, higher magnification in *D*). In a chronic inactive subpial CL (*D*), minimal density of MHC-II+ cells (*E*) has been found. In extensive chronic inactive lesions shown by MOG immunostaining loss (*E*), the lower density of MHC-II+ cells was present and scattered in all the demyelinated area, also close to the pial surface (*asterisk* in *E*, and higher magnification in *F*). Original magnifications ×25 (*B* and *E*),×200 (*C*, *D*, and *F*).

A moderate inverse correlation was observed between hyperintense intracortical CLs and disease duration ($r = -0.48$), while no correlation was observed between disease duration and hypointense or isointense CLs.

The total number of CLs correlated with EDSS ($r = 0.51$). In patients with RRMS, the correlation between both total QSM-hyperintense CLs and intracortical hyperintense CLs with EDSS was marked ($r = 0.63$ and 0.71, $P < .05$), while no correlation was observed between EDSS and QSM-hypointense or isointense CLs. Moreover, no correlation was found among hyperintense, hypointense, or isointense CLs and EDSS in patients with SPMS.

Neuropathology/Imaging Comparison

The QSM hyperintensity edge found in proximity to the pial surface in some examined QSM-hyperintense CLs mirrored the intense microglia activation found close by the pial surface in most subpial CLs observed in postmortem SPMS cases. Indeed, the intense band of microglia activation frequently found at the depth of cerebral sulci of active CLs (Fig 3*A*, *B*, -*E*, blue arrowheads), with a characteristic gradient of increased microglia density in the external cortical layers (I-III), decreasing toward the most inner cortical layers (Fig 3*E*), resembled the hyperintense QSM signal seen in Fig 3*J* (blue arrowheads). Similar intense MHC-II immunostaining was also observed along the surface of the cerebral sulci (Fig 3*A*, -*C* yellow arrowheads), especially in regions of active demyelinating subpial GM, comparable with the QSM hyperintensity edge found in proximity to the pial surface within cerebral sulci (Fig 3*J*, yellow arrowheads). Also, the QSM hyperintensity edge found at the WM/GM border seems to resemble the microglia/macrophage activation detected at the WM/GM interface in leukocortical lesions (Fig 3*H*). Most interesting, a marked difference in MHC-II+ density and morphology has been observed in WM and GM (Fig 3*H*) portions of type I CLs, suggesting functional differences in the resident microglia cells in these areas and a different ratio of microglia/monocyte-derived macrophages in the presence of a higher myelin density.

DISCUSSION

In this preliminary study, we combined neuropathologic analysis of GM lesion activity and a new imaging approach with 3D DIR and QSM, with the aim of better characterizing CLs in patients with RRMS and SPMS. Our results suggest that combined 3D DIR and QSM may reveal the area of intense microglia/macrophage activity and density in CLs as also detected by neuropathologic assessment. Furthermore, our data show that CLs are highly heterogeneous as revealed by their susceptibility maps. This heterogeneity was present across, and in some cases within, the lesions. These data are partially in contrast to a recent MR imaging study performed at 7T showing negative relative susceptibility values in 25 of the 27 CLs.[22] However, the low number of patients and CLs analyzed might account for this discordance. Moreover, it is likely that the

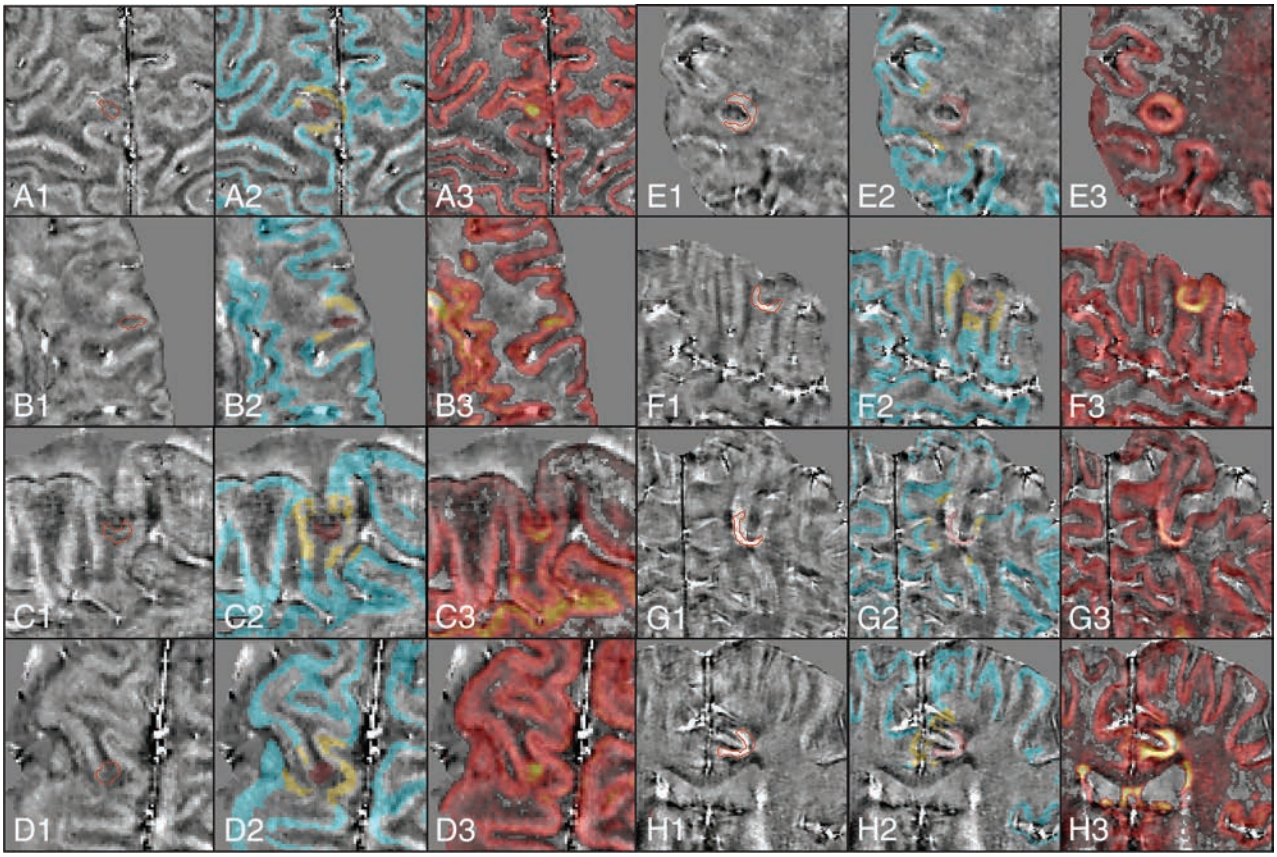

FIG 2. Illustration of examples of cortical lesion appearance on the quantitative susceptibility map obtained with the total generalized variation algorithm from the 3D EPI susceptibility-weighted scan. Each panel denoted by a letter is divided in 3 subpanels: 1) QSM with contoured CL (*red line*); 2) QSM with a superimposed CL (red), the NAGM reference tissue used in the CL classification (yellow), and NAGM obtained from the segmentation of the 3D T1 MPRAGE (cyan); 3) QSM with superimposed the 3D double inversion recovery sequence, where the CL detection and segmentation was performed. *A–D*, Hypointense lesions. *E–H*, Hyperintense lesions. The classification of CLs was performed with a 2-sided *t* test between QSM estimates in the lesion (with subtracted the median value of the reference QSM value in the NAGM) and a zero mean Gaussian distribution. When the *t* test was significant and the mean of nQSM was greater (lesser) than zero, the lesion was classified as hyperintense (hypointense).

susceptibility of CLs changes with time in relation to their activity as previously shown for WM lesions. Therefore, the low activity of the patients with MS and of the number of CLs detected at the time of the MR imaging might also help explain this contradiction.[31-33]

The high variability of CLs in inflammatory activity in patients with MS has been already described by several neuropathologic studies mainly based on SPMS patients with a relatively long disease duration[3,8,12,34] or on material from biopsies of patients with early MS with tumefactive lesions.[9] Despite these neuropathologic observations, there are no available data in vivo that characterize the inflammatory activity of CLs in the early phase of the disease. In a previous MR imaging study, we observed that a small subgroup of CLs was significantly hyperperfused; this finding suggested the presence of an active inflammatory process within cortical GM.[35]

Although the number of patients with SPMS was quite low for drawing definitive conclusions, QSM-hyperintense CLs appeared to be more frequent in the RRMS group, while QSM-hypointense lesions were more frequent in SPMS. This result, along with the moderate inverse correlation between the number of QSM-hyperintense CLs and disease duration, might suggest that QSM-hyperintense lesions characterize the more inflammatory and acute phases of the disease, while QSM-hypointense CLs characterize the chronic (less inflammatory) disease stage. Nevertheless, the presence of each type of QSM-visible CL in both RRMS and SPMS suggests that the heterogeneity of GM lesion types persists during the entire disease course. Of course, we are aware that the DIR sequence detects only a reduced portion of CLs[36] and that the use of other sequences such as phase-sensitive inversion recovery might help improve their detection.[37] However, recent comparative histologic/MR imaging studies have demonstrated that the "tip of the iceberg" detected by MR imaging and its "bulk" differ only in size and that the number of detectable CLs correlates with their overall number and with the overall percentage of cortical demyelination.[36] The ability of QSM in detecting CLs itself has not been tested; however, we do not advise acquiring only the SWI sequence. Using the DIR or even the phase-sensitive inversion recovery sequence is recommended as a guide for detecting CLs.

Although the factors contributing to the susceptibility in the cortex are not fully established,[38] initial studies of healthy brains both in vivo and postmortem have suggested that myelin and both heme and nonheme iron have dominant effects in conditioning the susceptibility map.[39,40] In contrast to R2*, which increases proportionally to the concentration of both iron[41] and myelin,[42] the 2 substances have opposing effects on the magnetic

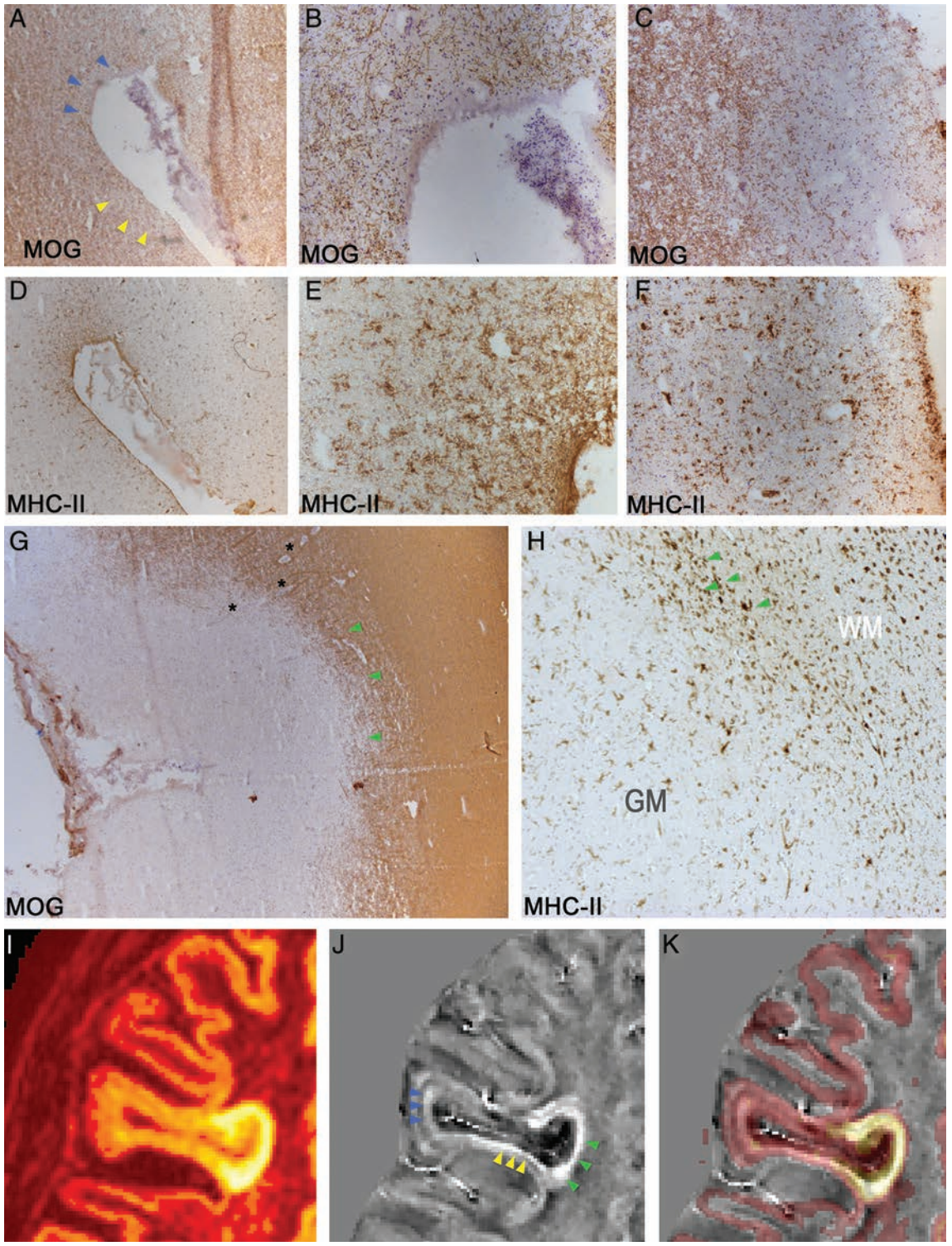

FIG 3. Combined neuropathologic and MR imaging characterization of lesion activity in CLs. *A–H*, Immunohistochemistry staining of MOG (*A–C* and *G*) and MHC class II (*D–F* and *H*) in subpial (*A–F*) and leukocortical (*G* and *H*) CLs in postmortem MS brains. *I–K*, MR images of heterogeneous CLs in patients with MS in vivo; *I*, 3D double inversion recovery. *J*, Quantitative susceptibility mapping calculated with the total generalized variation algorithm. *K*, DIR superimposed on the QSM map. MOG and MHC-II immunostaining on serial sections show ongoing subpial demyelination (*blue arrowheads* in *A*, higher magnification in *B*) and intense pick of MHC-II+ glia activation (*D*, higher magnification in *E*) at the depth of a cerebral sulcus, resembling the QSM hyperintense signal (*blue arrowheads* in *J*) in similar regions. Concurrent complete subpial demyelination (*yellow arrowheads* in *A*, higher magnification in *C*) and intense peak of MHC-II+ glia activation (*F*) were also detected along the pial surface of the same cerebral sulcus (*yellow arrowheads* in *A*), respectively, resembling similar QSM hyperintense signal (*yellow arrowheads* in *J*). In type I leukocortical lesions, shown by MOG immunostaining (*G*), high occurrence and density of MHC-II+ activated microglia and macrophages (*H*) were observed at the GM/WM interface (*green arrowheads* in *G* and *H*). Higher magnification of the GM/WM interface (*green arrowheads* in *H*) reveals higher density of MHC-II+ cells mainly in proximity to inflammatory infiltrates (*asterisks* in *G*) within the WM border of the lesions, possibly corresponding to the frequent QSM hyperintense signal shown by *green arrowheads* in *J*. Original magnifications ×100 (*A*, *D*, and *G*), ×200 (*B*, *C*, *E*, *F*, and *H*).

susceptibility maps,[43,44] because the proteins and lipids associated with myelin render its susceptibility diamagnetic.[45,46]

Our neuropathologic data, in line with previous studies,[3,8,47] confirmed that a significant proportion of type III and type I chronic active CLs are associated with a gradient of increased microglia activation in the most external cortical layer, close to the pial surface (in subpial type III CLs; Fig 3, yellow arrows) or to the WM interface (in leukocortical type I CLs; Fig 3, blue arrows). This finding was also observed in a recent neuropathologic study[12] showing that in a subset of patients with MS with CLs, part of the CLs were characterized by a rim of activated microglia at their border. The examined postmortem SPMS cohort included MS cases that, at the time of death, had differences in both disease duration and clinical disability compared with the in vivo SPMS cases. These differences may explain the increased activity of the CLs detected in the postmortem SPMS cases.

Although our pathologic and MR imaging analyses are derived from 2 different cohorts of patients and therefore a direct comparison is only theoretic, on the basis of the similarity of the neuropathlogic and MR images, we hypothesize that the QSM-hyperintensity could be due to activated microglia/macrophages that phagocytose nonheme iron–rich cellular debris. As suggested by previous pathologic and imaging studies,[3,10,48,49] the presence of a hyperintense rim in part of the detected CLs could indicate the presence of iron accumulation in microglia/macrophages at the subpial edge (in type III CLs) or at the WM/GM interface. If this is the case, the sensitivity of QSM in detecting activated microglia might explain some of the subpial hyperintensities observed with this sequence and not with the DIR sequence, which is usually not sensitive enough for subpial lesions (Fig 2). A recent study[50] on a limited number of patients showed the capability of QSM to better discriminate intracortical and leukocortical lesions, thus suggesting that QSM could be useful in predicting and detecting early modifications of normal-appearing tissues.[51] Nevertheless, further studies that combine postmortem MR imaging and neuropathologic analysis on the same cohort are currently in progress.

The QSM hyperintense signal frequently observed in proximity to, or within, the WM portion of the detected leukocortical lesions might resemble the similar increased density of MHC-II+ microglia found in the WM portion of the type I CLs. This resemblance might indicate the expanding inflammatory rim involved in the neuropathogenesis of type I CLs.

At least 2 alternative hypotheses might explain the presence of a hyperintense QSM signal: The hyperintense QSM signal could be generated by the increased iron release from intracellular deposits to extracellular spaces or by the iron leakage following blood-brain barrier damage in the acute phases of the disease. However, it is not usual within the cortical GM to have a BBB breakdown.[52] The second hypothesis suggests that oligodendrocytes constitute an important source of iron, and changes in iron signal could be associated with a loss of oligodendrocytes and reduction of nonheme iron within oligodendrocytes and myelin in MS plaques and periplaque areas.[52] Therefore, the detected QSM-hypointensity could be due to a decrease of nonheme tissue iron, which characterizes those inactive GM lesions without activated microglia and is more frequent in patients with a long disease duration.[53]

Several observations have suggested that an abnormal deposition of iron might also play a significant role in the pathophysiology of GM damage in patients with MS[54] as also is shown for many age-related degenerative disorders.[55] While confirming the well-known relationship between CLs and disability,[56] our data have extended these results, showing a significant correlation between QSM-hyperintense CLs (more than the hypointense CLs) and EDSS within the RRMS group. The reason for the lack of correlation in the SPMS group may be likely found in the low number of patients included in the study and in the lower number of QSM-hyperintense CLs; this possibility is in line with the neuropathologic observation of the higher frequency of chronic active lesions in the examined postmortem SPMS brains. Nevertheless, the correlation with disability has not been found with hypointense or isointense CLs because of the possible detrimental role of chronic activated microglia.[57] Further longitudinal studies on larger sample sizes may clarify this interesting clinical point.

CONCLUSIONS

Our study revealed that CLs in MS are heterogeneous during the entire course of the disease, not only among patients but also within the same patient and, sometimes, within the same lesion. These results corroborate the hypothesis of substantial clinical and immunopathologic heterogeneous patterns of MS inflammation/demyelination during the disease course. Moreover, the highest frequency of QSM-hyperintense CLs in RRMS and their correlation with EDSS in this group of patients seem to suggest a key role of activated microglia/macrophages in the early and acute phases of the disease. The combined use of QSM and DIR could be a useful tool to monitor the disease evolution and to identify those patients with higher rates of inflammatory cortical demyelination and associated neurodegeneration.

Disclosures: Roberta Magliozzi—*RELATED*: *Grant*: Italian Ministry of Health, *Comments*: Young Investigator Grant GR-2010-2313255*. Richard Reynolds—*RELATED*: *Grant*: UK Multiple Sclerosis Society, *Comments*: funded the work performed in the UK at Imperial College.* Massimiliano Calabrese—*UNRELATED*: *Board Membership*: Biogen Idec, Teva Pharmaceutical Industries; *Consultancy*: Genzyme; *Travel/Accommodations/Meeting Expenses Unrelated to Activities Listed*: Biogen Idec, Genzyme, Teva Pharmaceutical Industries, Novartis. *Money paid to the institution.

REFERENCES

1. Calabrese M, Magliozzi R, Ciccarelli O, et al. **Exploring the origins of grey matter damage in multiple sclerosis.** *Nat Rev Neurosci* 2015;16:147–58 CrossRef Medline
2. Lassmann H. **Multiple sclerosis: lessons from molecular neuropathology.** *Exp Neurol* 2014;262(pt A):2–7 CrossRef Medline
3. Magliozzi R, Howell O, Vora A, et al. **Meningeal B-cell follicles in secondary progressive multiple sclerosis associate with early onset of disease and severe cortical pathology.** *Brain* 2007;130:1089–104 Medline
4. Calabrese M, Atzori M, Bernardi V, et al. **Cortical atrophy is relevant in multiple sclerosis at clinical onset.** *J Neurol* 2007;254:1212–20 Medline
5. Calabrese M, Poretto V, Favaretto A, et al. **Cortical lesion load associates with progression of disability in multiple sclerosis.** *Brain* 2012;135:2952–61 CrossRef Medline
6. Brink BP, Veerhuis R, Breij EC, et al. **The pathology of multiple sclerosis is location-dependent: no significant complement activation is detected in purely cortical lesions.** *J Neuropathol Exp Neurol* 2005;64:147–55 CrossRef Medline
7. van Horssen J, Brink BP, de Vries HE, et al. **The blood-brain barrier**

in cortical multiple sclerosis lesions. *J Neuropathol Exp Neurol* 2007; 66:321–28 CrossRef Medline
8. Peterson JW, Bö L, Mörk S, et al. **Transected neurites, apoptotic neurons, and reduced inflammation in cortical multiple sclerosis lesions.** *Ann Neurol* 2001;50:389–400 CrossRef Medline
9. Lucchinetti CF, Popescu BFG, Bunyan RF, et al. **Inflammatory cortical demyelination in early multiple sclerosis.** *N Engl J Med* 2011; 365:2188–97 CrossRef Medline
10. Pitt D, Boster A, Pei W, et al. **Imaging cortical lesions in multiple sclerosis with ultra-high-field magnetic resonance imaging.** *Arch Neurol* 2010;67:812–18 CrossRef Medline
11. Li X, Harrison DM, Liu H, et al. **Magnetic susceptibility contrast variations in multiple sclerosis lesions.** *J Magn Reson Imaging* 2016; 43:463–73 CrossRef Medline
12. Kooi EJ, Strijbis EM, van der Valk P, et al. **Heterogeneity of cortical lesions in multiple sclerosis: clinical and pathologic implications.** *Neurology* 2012;79:1369–76 CrossRef Medline
13. Yao B, Hametner S, van Gelderen P, et al. **7 Tesla magnetic resonance imaging to detect cortical pathology in multiple sclerosis.** *PLoS One* 2014;9:e108863 CrossRef Medline
14. Deistung A, Rauscher A, Sedlacik J, et al. **Susceptibility weighted imaging at ultra high magnetic field strengths: theoretical considerations and experimental results.** *Magn Reson Med* 2008;60: 1155–68 CrossRef Medline
15. Haacke EM, Xu Y, Cheng YC, et al. **Susceptibility weighted imaging (SWI).** *Magn Reson Med* 2004;52:612–18 CrossRef Medline
16. Li TQ, van Gelderen P, Merkle H, et al. **Extensive heterogeneity in white matter intensity in high-resolution T2*-weighted MRI of the human brain at 7.0 T.** *Neuroimage* 2006;32:1032–40 CrossRef Medline
17. Hammond KE, Metcalf M, Carvajal L, et al. **Quantitative in vivo magnetic resonance imaging of multiple sclerosis at 7 Tesla with sensitivity to iron.** *Ann Neurol* 2008;64:707–13 CrossRef Medline
18. Hagemeier J, Weinstock-Guttman B, Bergsland N, et al. **Iron deposition on SWI-filtered phase in the subcortical deep gray matter of patients with clinically isolated syndrome may precede structure-specific atrophy.** *AJNR Am J Neuroradiol* 2012;33:1596–601 CrossRef Medline
19. de Rochefort L, Liu T, Kressler B, et al. **Quantitative susceptibility map reconstruction from MR phase data using Bayesian regularization: validation and application to brain imaging.** *Magn Reson Med* 2010;63:194–206 CrossRef Medline
20. Langkammer C, Liu T, Khalil M, et al. **Quantitative susceptibility mapping in multiple sclerosis.** *Radiology* 2013;267:551–59 CrossRef Medline
21. Chen W, Gauthier SA, Gupta A, et al. **Quantitative susceptibility mapping of multiple sclerosis lesions at various ages.** *Radiology* 2014;271:183–92 CrossRef Medline
22. Bian W, Tranvinh E, Tourdias T, et al. **In vivo 7T MR quantitative susceptibility mapping reveals opposite susceptibility contrast between cortical and white matter lesions in multiple sclerosis.** *AJNR Am J Neuroradiol* 2016 Jun 9. [Epub ahead of print] CrossRef Medline
23. Howell OW, Reeves CA, Nicholas R, et al. **Meningeal inflammation is widespread and linked to cortical pathology in multiple sclerosis.** *Brain* 2011;134:2755–71 CrossRef Medline
24. Reynolds R, Roncaroli F, Nicholas R, et al. **The neuropathological basis of clinical progression in multiple sclerosis.** *Acta Neuropathol* 2011;122:155–70 CrossRef Medline
25. Polman CH, Reingold SC, Banwell B, et al. **Diagnostic criteria for multiple sclerosis: 2010 revisions to the McDonald criteria.** *Ann Neurol* 2011;69:292–302 CrossRef Medline
26. Kurtzke JF. **Rating neurologic impairment in multiple sclerosis: an Expanded Disability Status Scale (EDSS).** *Neurology* 1983;33: 1444–52 CrossRef Medline
27. Langkammer C, Bredies K, Poser BA, et al. **Fast quantitative susceptibility mapping using 3D EPI and total generalized variation.** *Neuroimage* 2015;111:622–30 CrossRef Medline
28. Geurts JJ, Roosendaal SD, Calabrese M, et al; MAGNIMS Study Group. **Consensus recommendations for MS cortical lesion scoring using double inversion recovery MRI.** *Neurology* 2011;76:418–24 CrossRef Medline
29. Avants BB, Tustison NJ, Wu J, et al. **An open source multivariate framework for n-tissue segmentation with evaluation on public data.** *Neuroinformatics* 2011;9:381–400 CrossRef Medline
30. Calabrese M, Castellaro M, Bertoldo A, et al. **Epilepsy in multiple sclerosis: the role of temporal lobe damage.** *Mult Scler* 2016 Jun 3. [Epub ahead of print] CrossRef Medline
31. Zhang Y, Gauthier SA, Gupta A, et al. **Longitudinal change in magnetic susceptibility of new enhanced multiple sclerosis (MS) lesions measured on serial quantitative susceptibility mapping (QSM).** *J Magn Reson Imaging* 2016;44:426–32 CrossRef Medline
32. Zhang Y, Gauthier SA, Gupta A, et al. **Quantitative susceptibility mapping and R2* measured changes during white matter lesion development in multiple sclerosis: myelin breakdown, myelin debris degradation and removal, and iron accumulation.** *AJNR Am J Neuroradiol* 2016;37:1629–35 CrossRef Medline
33. Zhang Y, Gauthier SA, Gupta A, et al. **Magnetic susceptibility from quantitative susceptibility mapping can differentiate new enhancing from nonenhancing multiple sclerosis lesions without gadolinium injection.** *AJNR Am J Neuroradiol* 2016 Jun 30. [Epub ahead of print] CrossRef Medline
34. Kidd D, Barkhof F, McConnell R, et al. **Cortical lesions in multiple sclerosis.** *Brain* 1999;122 (pt 1):17–26 CrossRef Medline
35. Peruzzo D, Castellaro M, Calabrese M, et al. **Heterogeneity of cortical lesions in multiple sclerosis: an MRI perfusion study.** *J Cereb Blood Flow Metab* 2013;33:457–63 CrossRef Medline
36. Seewann A, Vrenken H, Kooi E-J, et al. **Imaging the tip of the iceberg: visualization of cortical lesions in multiple sclerosis.** *Mult Scler J* 2011;17:1202–10 CrossRef Medline
37. Sethi V, Yousry TA, Muhlert N, et al. **Improved detection of cortical MS lesions with phase-sensitive inversion recovery MRI.** *J Neurol Neurosurg Psychiatry* 2012;83:877–82 CrossRef Medline
38. Wharton S, Bowtell R. **Fiber orientation-dependent white matter contrast in gradient echo MRI.** *Proc Natl Acad Sci U S A* 2012;109: 18559–64 CrossRef Medline
39. Bagnato F, Hametner S, Yao B, et al. **Tracking iron in multiple sclerosis: a combined imaging and histopathological study at 7 Tesla.** *Brain* 2011;134(pt 12):3602–15 CrossRef Medline
40. Yao B, Bagnato F, Matsuura E, et al. **Chronic multiple sclerosis lesions: characterization with high-field-strength MR imaging.** *Radiology* 2012;262:206–15 CrossRef Medline
41. Langkammer C, Krebs N, Goessler W, et al. **Quantitative MR imaging of brain iron: a postmortem validation study.** *Radiology* 2010; 257:455–62 CrossRef Medline
42. Lee J, Shmueli K, Kang BT, et al. **The contribution of myelin to magnetic susceptibility-weighted contrasts in high-field MRI of the brain.** *Neuroimage* 2012;59:3967–75 CrossRef Medline
43. Li W, Wu B, Liu C. **Quantitative susceptibility mapping of human brain reflects spatial variation in tissue composition.** *Neuroimage* 2011;55:1645–56 CrossRef Medline
44. Schweser F, Deistung A, Lehr BW, et al. **Quantitative imaging of intrinsic magnetic tissue properties using MRI signal phase: an approach to in vivo brain iron metabolism?** *Neuroimage* 2011;54: 2789–807 CrossRef Medline
45. Langkammer C, Schweser F, Krebs N, et al. **Quantitative susceptibility mapping (QSM) as a means to measure brain iron? A post mortem validation study.** *Neuroimage* 2012;62:1593–99 CrossRef Medline
46. Li W, Wu B, Avram AV, et al. **Magnetic susceptibility anisotropy of human brain in vivo and its molecular underpinnings.** *Neuroimage* 2012;59:2088–97 CrossRef Medline
47. Kutzelnigg A, Lucchinetti CF, Stadelmann C, et al. **Cortical demyelination and diffuse white matter injury in multiple sclerosis.** *Brain* 2005;128:2705–12 CrossRef Medline
48. Craelius W, Migdal MW, Luessenhop CP, et al. **Iron deposits sur-**

rounding multiple sclerosis plaques. *Arch Pathol Lab Med* 1982;106:397–99 Medline
49. Bagnato F, Ikonomidou VN, van Gelderen P, et al. **Lesions by tissue specific imaging characterize multiple sclerosis patients with more advanced disease.** *Mult Scler* 2011;17:1424–31 CrossRef Medline
50. Kakeda S, Futatsuya K, Ide S, et al. **Improved detection of cortical gray matter involvement in multiple sclerosis with quantitative susceptibility mapping.** *Acad Radiol* 2015;22:1427–32 CrossRef Medline
51. Stüber C, Pitt D, Wang Y. **Iron in multiple sclerosis and its noninvasive imaging with quantitative susceptibility mapping.** *Int J Mol Sci* 2016;17(1) CrossRef Medline
52. Hametner S, Wimmer I, Haider L, et al. **Iron and neurodegeneration in the multiple sclerosis brain.** *Ann Neurol* 2013;74:848–61 CrossRef Medline
53. Paling D, Tozer D, Wheeler-Kingshott C, et al. **Reduced R2′ in multiple sclerosis normal appearing white matter and lesions may reflect decreased myelin and iron content.** *J Neurol Neurosurg Psychiatry* 2012;83:785–92 CrossRef Medline
54. Khalil M, Langkammer C, Pichler A, et al. **Dynamics of brain iron levels in multiple sclerosis: a longitudinal 3T MRI study.** *Neurology* 2015;84:2396–402 CrossRef Medline
55. Schenck JF, Zimmerman EA. **High-field magnetic resonance imaging of brain iron: birth of a biomarker?** *NMR Biomed* 2004;17:433–45 CrossRef Medline
56. Calabrese M, Reynolds R, Magliozzi R, et al. **Regional distribution and evolution of gray matter damage in different populations of multiple sclerosis patients.** *PLoS One* 2015;10:e0135428 CrossRef Medline
57. Trapp BD, Wujek JR, Criste GA, et al. **Evidence for synaptic stripping by cortical microglia.** *Glia* 2007;55:360–68 CrossRef Medline

Myelin Detection Using Rapid Quantitative MR Imaging Correlated to Macroscopically Registered Luxol Fast Blue–Stained Brain Specimens

J.B.M. Warntjes, A. Persson, J. Berge, and W. Zech

ABSTRACT

BACKGROUND AND PURPOSE: Myelin detection is of great value in monitoring diseases such as multiple sclerosis and dementia. However, most MR imaging methods to measure myelin are challenging for routine clinical use. Recently, a novel method was published, in which the presence of myelin is inferred by using its effect on the intra- and extracellular water relaxation rates and proton density, observable by rapid quantitative MR imaging. The purpose of this work was to validate this method further on the brains of 12 fresh, intact cadavers.

MATERIALS AND METHODS: The 12 brains were scanned with a quantification sequence to determine the longitudinal and transverse relaxation rates and proton density as input for the myelin estimations. Subsequently, the brains were excised at postmortem examination, and brain slices were stained with Luxol fast blue to verify the presence of myelin. The optical density values of photographs of the stained brain slices were registered with the MR images and correlated with the myelin estimation performed by quantitative MR imaging.

RESULTS: A correlation was found between the 2 methods with a mean Spearman ρ for all subjects of 0.74 $\pm$ 0.11. Linear regression showed a mean intercept of 1.50% $\pm$ 2.84% and a mean slope of 4.37% $\pm$ 1.73%/%. A lower correlation was found for the separate longitudinal relaxation rates and proton density (ρ = 0.63 $\pm$ 0.12 and -0.73 ± 0.09, respectively). For transverse relaxation rates, the ρ was very low (0.11 $\pm$ 0.28).

CONCLUSIONS: The observed correlation supports the validity of myelin measurement by using the MR imaging quantification method.

ABBREVIATIONS: LFB = Luxol fast blue; OD = optical density; PD = proton density; qMRI = quantitative MRI; R_1 = longitudinal relaxation rate; R_2 = transverse relaxation rate

The measurement of myelin content in the brain is important for neurodegenerative diseases such as multiple sclerosis or dementia, in which increasing cerebral demyelination can be observed in the course of the disease.[1-3] Also, for brain development, monitoring increasing myelination has clinical value.[4,5] With MR imaging, there are a number of indirect measures for the detection of myelin, most of them based on multicomponent analysis of the T2 relaxation. In this approach, the observation of a short T2 relaxation component is attributed to the presence of thin layers of water trapped inside the myelin sheaths.[6-10]

Recently, a model has been published that infers the presence of myelin partial volume based on its effect on intra- and extracellular water due to magnetization exchange.[11] The vicinity of myelin reduces the local longitudinal relaxation rate (R_1), the transverse relaxation rate (R_2), and proton density (PD). By rapid quantitative MR imaging (qMRI) of the relaxation rates and proton density, a multiparametric space is measured, forming the basis for an estimation of myelin partial volume in each acquisition voxel. Because the quantification sequence requires only 5–7 minutes for full coverage of the brain, it may be suitable for routine clinical use.

The aim of this study was to validate the model further by correlating the estimated myelin content by qMRI with myelin estimations from photographs of brain slices that were stained with myelin-sensitive Luxol fast blue (LFB) in a postmortem application.

MATERIALS AND METHODS

Study Group

Twelve fresh, intact cadavers were prospectively investigated in the study, 9 men and 3 women, with a mean age 62 $\pm$ 10 years (range, 46–74 years). The study cases were routine forensic cases

Received October 27, 2016; accepted after revision February 3, 2017.

From the Center for Medical Image Science and Visualization (J.B.M.W., A.P., W.Z.) and Division of Cardiovascular Medicine, Department of Medical and Health Sciences (J.B.M.W.), Linköping University, Linköping, Sweden; SyntheticMR AB (J.B.M.W.), Linköping, Sweden; Institute of Forensic Medicine (J.B., W.Z.), Linköping, Sweden; and Institute of Forensic Medicine (W.Z.), University of Bern, Bern, Switzerland.

Please address correspondence to J.B.M. Warntjes, MD, Center for Medical Image Science and Visualization, Linköping University, 58185 Sweden; e-mail: marcel.warntjes@cmiv.liu.se

http://dx.doi.org/10.3174/ajnr.A5168

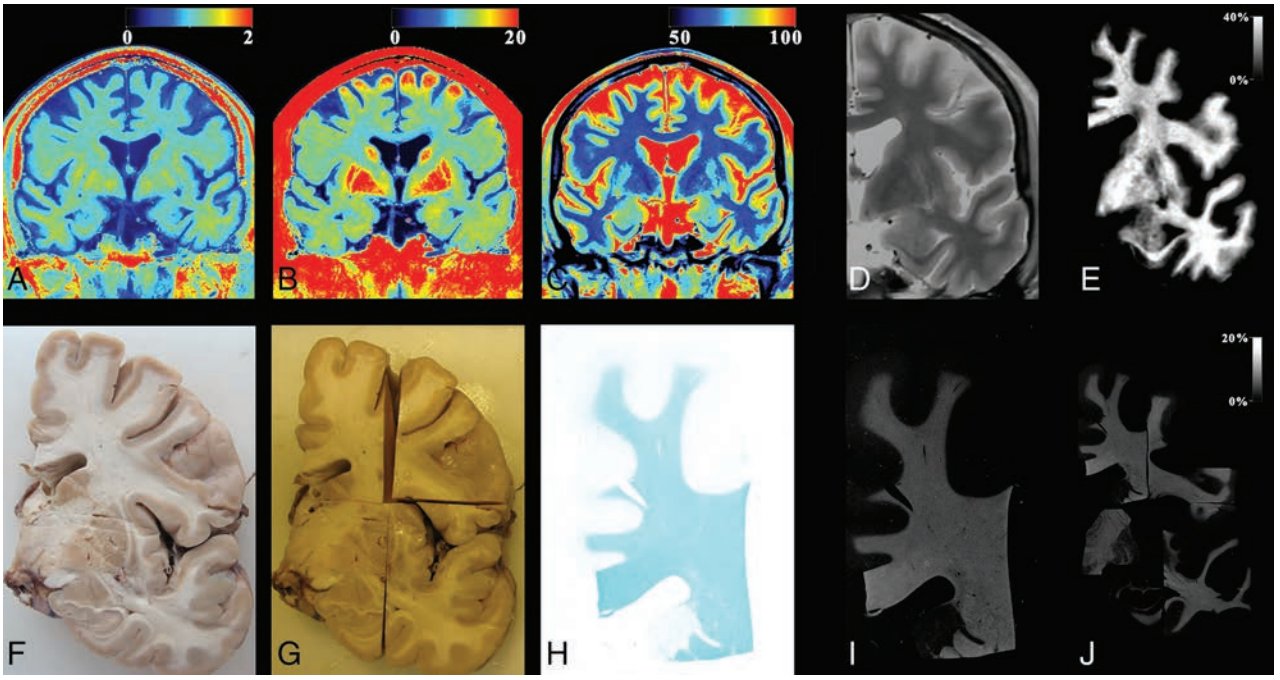

FIG 1. The process used for myelin evaluation on a male subject, 69 years of age, acquired at a temperature of 10°C. The MR imaging quantification sequence provided the R_1, R_2, and PD maps of coronal slices of the cadaver (*A–C*). A synthetic proton density–weighted image was created for registration purposes using the R_1, R_2, and PD maps as input, resampled to 0.1 mm/pixel (*D*, zoomed in). The R_1 map was corrected for temperature and then used, with the original R_2 and PD maps, to generate the myelin partial volume map with the same algorithm as used for living subjects (*E*). For the histologic images, the brain was extracted and cut into coronal slices (*F*). Slices were fixated by using formaldehyde and cut into smaller pieces after fixation (*G*). The separate pieces of brain slices were stained with Luxol fast blue and photographed (*H*). The optical density of the photographs was converted to an intensity scale. These images were also resampled to 0.1 mm/pixel (*I*). All pieces were registered to the synthetic proton density–weighted image (*J*), so that each pixel from the slice photographs was at the same place as the corresponding MR imaging pixel. Finally, the resolution of both MR images and photographs was down-sampled to the original MR imaging resolution of 0.7 mm/pixel.

from the local forensic institution, in which forensic postmortem examinations were ordered by the local authorities. Cadavers were refrigerated in cooling chambers before imaging to avoid progressing putrefaction. Trauma cases and cases with known brain diseases in their medical history were excluded. Pre-MR imaging and prepostmortem information about cases was received from paramedic reports, police, relatives of the deceased, or the bureau of the district attorney. Due to the forensic nature of the cases, no further clinical data were available. MR imaging examinations and the use of the imaging data were approved by the local ethics committee. Postmortem interval (the time between death and the postmortem MRI examination) ranged from 20 hours to 3 days. During MR imaging, the cadaver core body temperatures were assessed in real-time with MR imaging–compatible temperature probes that were placed in the esophagus before the MR imaging examination. The mean core body temperature of the cadavers during acquisition was 7.8° ± 3.1°C. Board-certified forensic pathologists performed postmortem examinations immediately after the MR imaging examinations. The causes of death were myocardial infarction ($n = 5$), acute cardiac arrest ($n = 3$), pulmonary embolism ($n = 2$), and internal exsanguination ($n = 2$).

MR Imaging Acquisition Method

An overview of the entire process is provided in Fig 1. The study subjects underwent a qMRI acquisition[12] to measure T1 and T2 relaxation times and proton-density values. Relaxation rate R_1 corresponds to 1/T1; and R_2, to 1/T2. The sequence was a saturation recovery turbo-spin-echo with a multiecho readout. Four different saturation delay times (at 170, 660, 2290, and 4740 ms) and 2 different TEs (at 23 and 105 ms) were acquired, resulting in a matrix of $4 \times 2 = 8$ images per section with different signal intensities depending on the delay time and TE. The TR was 4.9 seconds. In total, 30 sections of 4-mm thickness were acquired in the coronal plane, with an FOV of 230 × 190 mm, with an in-plane acquisition resolution of 0.7 mm/pixel, reconstructed at 0.45 mm/pixel. The scan time was 7 minutes. The MR imaging scanner was a 3T Ingenia (Philips Healthcare, Best, the Netherlands) using 16-channel head/base combination. Postprocessing was performed with SyMRI 8.0 (SyntheticMR, Linköping Sweden).

Temperature Correction

Four ROIs were placed in the frontal white matter; 4, in the anterior cingulate cortex; and 4, in the lateral ventricles of all subjects to obtain an estimate of the mean T1 and T2 relaxation times for white matter, gray matter, and CSF as a function of temperature. These data were used to derive a correction function to compensate for relaxation time differences due to the lower temperature of the subjects than 37°C. A linear change per degree Celsius was assumed.[13,14] Differences due to age, illness, or any other subject-specific changes were ignored.

MR Imaging Myelin Estimation

The temperature-corrected R_1, R_2, and PD maps were used as input into the myelin model as previously described.[11] In summary, this model consists of 4 partial volumes per acquisition voxel: myelin partial volume, cellular partial volume, free water partial volume, and excess parenchymal partial volume, in which each partial volume has its own R_1, R_2, and PD properties. The properties of free water partial volume and excess parenchymal partial volume were fixed to the properties of CSF (R_1 = 0.24 seconds^{-1}, R_2 = 0.87 seconds^{-1}, and PD = 100%). The myelin partial volume R_2 was fixed to a literature value of 77 seconds^{-1}. The remaining parameters of the model were then set by the observable R_1, R_2, and PD properties for each voxel in the brains of a group of healthy subjects. Subsequently, potential pathologic changes were modeled as 2 factors: a decrease of myelin partial volume and an increase of excess parenchymal partial volume, in comparison with the healthy brain. All distributions of the 4 partial volumes, ranging from 0% to 100% of the acquisition volume, generated a grid in R_1, R_2, and PD space. The observed R_1, R_2, and PD combinations from the qMRI acquisition were projected onto this grid, to estimate the myelin partial volume for each voxel.

Photographs of LFB-Stained Brain Slices and Histologic Examinations

The subjects' brains were extracted at forensic postmortem and cut into 2-cm-thick coronal slices. In each case, 1 anterior slice through the head of the caudate nucleus and 1 posterior slice through the thalamus were taken for further examinations. Only the left hemisphere was included. The brain specimens were soaked in formalin for 5 days. After formalin fixation, the brain slices were further cut into 6 smaller pieces to fit the 4 × 6 cm glass plates and sliced to 4-μm thickness. A Luxol fast blue staining was applied on brain slices. Photographs of LFB-stained brain slices were taken in a fixed setup with a light bench for uniform backlighting of the specimens and a stative. The glass plates covered about half of the final image so that most of the photograph was exposed to the background light, keeping the white filter of the camera similar for all photographs. Zoom and focus were set to manual and kept constant. The acquired JPG image resolution was 0.02 mm/pixel. The photographs were decomposed into red (R), green (G) and blue (B) channels with values in the range of 0–255 with a custom-built IDL program (ITT Visual Information Solutions, Boulder, Colorado). Optical density (OD) was defined as the sum of the RGB channels for the background light minus the sum of the RGB channels of each pixel. The values were normalized by dividing by 3 × 255. With this scale, OD varied between 0 (no color) and 1 (fully colored). Histologic evaluation of the investigated brain slices was conducted by a board-certified forensic pathologist who was blinded to the MR imaging findings.

Image Registration

A synthetic proton density–weighted image was generated from the R_1, R_2, and PD maps to show an image with good contrast between WM and GM. The histologic photographs were manually registered to the proton density–weighted image by using rotation, translation, and scaling. For this process, both quantification maps and photographs were resampled by interpolation to a resolution of 0.1 mm/pixel. The final registered maps and photographs were down-sampled again to the original MR image resolution of 0.7 mm/pixel to prevent an excessive number of data points for the correlation. In the down-sampling procedure, zeroes were excluded—that is, each pixel in the 0.7-mm/pixel image was mapped to an area of 7 × 7 pixels of the 0.1-mm/pixel image, where the value was calculated by the sum of the 7 × 7 pixels, divided by the number of pixels with a value larger than zero. By excluding zeroes, we avoided smoothing effects at the edges and cracks of the histologic specimen.

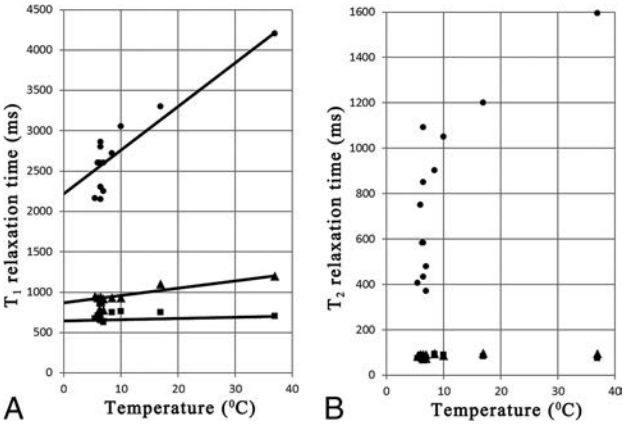

FIG 2. *A*, The observed mean T1 relaxation time in frontal white matter (*squares*), cortical gray matter (*triangles*), and ventricular CSF (*dots*) as a function of the core body temperature of all subjects. Added are the estimated slopes of T1 change per temperature. *B*, The observed mean T2 relaxation time in frontal WM (*squares*), cortical GM (*triangles*), and ventricular CSF (*dots*) as a function of core body temperature of all subjects.

Statistics

Linear regression was performed on the LFB-OD as a function of R_1, R_2, PD, and MR imaging myelin partial volume estimation for all registered pixels, excluding the value zero. The slope and intercept together with Spearman ranked correlation coefficient (Spearman ρ) were recorded for each subject and then averaged for the entire group. To visualize these >100,000 data points, we plotted them as 2D histograms of 40 × 40 bins, similar to plots in Engström et al.[15] The intensity of the 2D histograms corresponds to the number of times a value occurs within each value interval. For each 2D histogram, 2 positions of highest density were determined to provide an estimate of the positions of GM and WM. These positions were averaged for the entire group. The line through the 2 positions was used as a second estimate of slope and intercept.

RESULTS

Temperature Correction

The mean T1 values for frontal WM, cortical GM, and ventricular CSF for the different temperatures are plotted in Fig 2*A*. Slopes were estimated at 1.5 ms/°C for WM, 9.0 ms/°C for GM, and 54 ms/°C for CSF. The intersection point for all 3 slopes was determined at T1 = 600 ms and temperature (T) = −30°C. With this point as an origin, all observed T1 values at lower temperatures ($T_{1,obs}$) in the entire acquisition volume were corrected for temperature (obtaining $T_{1,cor}$) by using

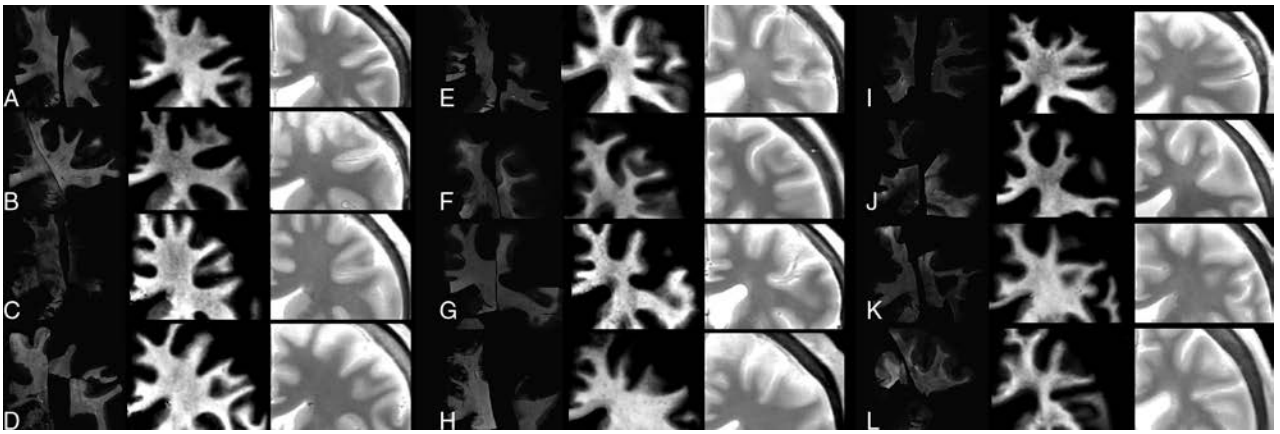

FIG 3. Zoomed-in images of all subjects, ordered according to increasing age (*A*, 46; *B*, 47; *C*, 52; *D*, 55; *E*, 59; *F*, 61; *G*, 69; *H*, 70; *I*, 70; *J*, 71; *K*, 72; and *L*, 74 years of age). On the left, the registered LFB stains are shown as optical density, in the center is the MR imaging–detected myelin partial volume, and on the right is the synthetic PD-weighted images.

Table 1: The mean and SD for all subjects of the intercept and slope[a]

	Intercept	Slope	Spearman ρ
R_1	$1.19 \pm 0.10\ s^{-1}$	$0.065 \pm 0.009\ s^{-1}/\%$	0.63 ± 0.12
R_2	$12.31 \pm 1.17\ s^{-1}$	$0.044 \pm 0.131\ s^{-1}/\%$	0.11 ± 0.28
PD	$71.96 \pm 4.22\%$	$-2.45 \pm 0.53\ \%/\%$	-0.73 ± 0.09
Myelin	$1.50\% \pm 2.84\%$	$4.37\% \pm 1.73\ \%/\%$	$0.74\% \pm 0.11$

[a] Estimated by linear regression and the Spearman ρ of the LFB optical density as a function of (uncorrected) R_1 and R_2 relaxation, proton density, and (temperature-corrected) MRI-estimated myelin partial volume.

$$T_{1,\mathrm{cor}} = 600 + \frac{T_{1,\mathrm{obs}} - 600}{0.015 \times (T + 30)}.$$

For the lowest temperature at T = 5.5°C, the temperature correction corresponds to a 7.2% increase for WM T1 values, a 30.8% increase for GM T1 values, and a 67.6% increase for CSF T1 values.

The mean T2 values are plotted in Fig 2*B*. No clear trends were observed for changes of T2 as a function of temperature for WM or GM. The mean T2 for WM for all subjects was 80.5 ± 8.0 ms; the mean T2 for GM for all subjects was 87.2 ± 8.3 ms. The T2 values for CSF decrease with decreasing temperatures, but these exhibit a large variation. For this study, no T2 correction for temperature was made. Hence, the input values for the myelin model were $R_{1,\mathrm{cor}} = 1/T_{1,\mathrm{cor}}$, $R_2 = 1/T2$ and PD.

Correlation of Estimated Myelin Partial Volume with LFB Optical Density

In Fig 3, a zoomed-in image is shown of all the subjects, including the registered myelin estimation with histology staining (left column) and the myelin estimation with the qMRI method (center column). Visual inspection showed a good correspondence between the 2, though in some cases, the variability of the LFB method is evident. For example, in Fig 3*B*, 2 histologic specimens are positioned close together, showing an obviously different overall intensity. Also, peripheral areas (in eg, Fig 3*D*, -*K*, and -*L*) show an enhancing LFB-OD gradient.

In Table 1, the mean and SD of the intercept, slope, and Spearman ρ of R_1 and R_2 relaxation, proton density, and MR imaging–estimated myelin partial volume are given as a function of the LFB-OD. The Spearman ρ shows a correlation for all parameters; weakest for R_2 and stronger for R_1, PD, and myelin. The observed slope of myelin partial volume and LFB-OD was 4.37% ± 1.73%/%; the intercept was 1.50% ± 2.84%.

All pixels (>0) were plotted with 2D histograms, as shown in Fig 4, where LFB-OD is taken as the x-axis, and R_1, R_2, PD, and qMRI-based myelin, as the y-axis. In Table 2, the mean and SD of the 2 positions of highest density in the 2D histograms are listed, attributed to WM and GM. The line through these 2 positions provides another way of estimating the slope and intercept, as listed in Table 2. The estimated slopes and intercepts in Table 2 are very similar to the values observed in Table 1.

Histologic Examinations

In each of the 12 cases, histologic signs of slight cerebral edema (slight distension of perivascular and pericellular spaces, slight rarefaction of subpial spaces, and slight vacuolar appearance of gray matter neuropil) were present. Apart from that, no remarkable findings were seen.

DISCUSSION

In this work, a postmortem comparison was made between brain specimens dyed with myelin-sensitive Luxol fast blue and a qMRI method for estimating myelin. A challenging issue for postmortem MR imaging is to limit the influence of postmortem changes on the brain tissue, due to, for example, cause of death, the duration of the dying process, temperature, lack of blood flow, decay processes, and so forth. In our case, the cadavers were fresh and quickly refrigerated after death to limit changes due to decay processes. The brains were intact, and hence no effects of brain extraction or preservation played a role. However, all investigated brains showed histologic signs of slight cerebral edema, even though the brains appeared unremarkable at gross examination during the following postmortem examination. The reason for the appearance of slight cerebral edema may have been hypoxia during agony, despite all cases having causes of death that did not primarily affect the brain. Agony can last at least several minutes, which may be enough time to cause hypoxia in the brain due to deprived circulation and blood oxygenation.[16-18]

The presence of various degrees of edema most likely caused the near-zero slope in R_2 values (Table 1), which is much lower in

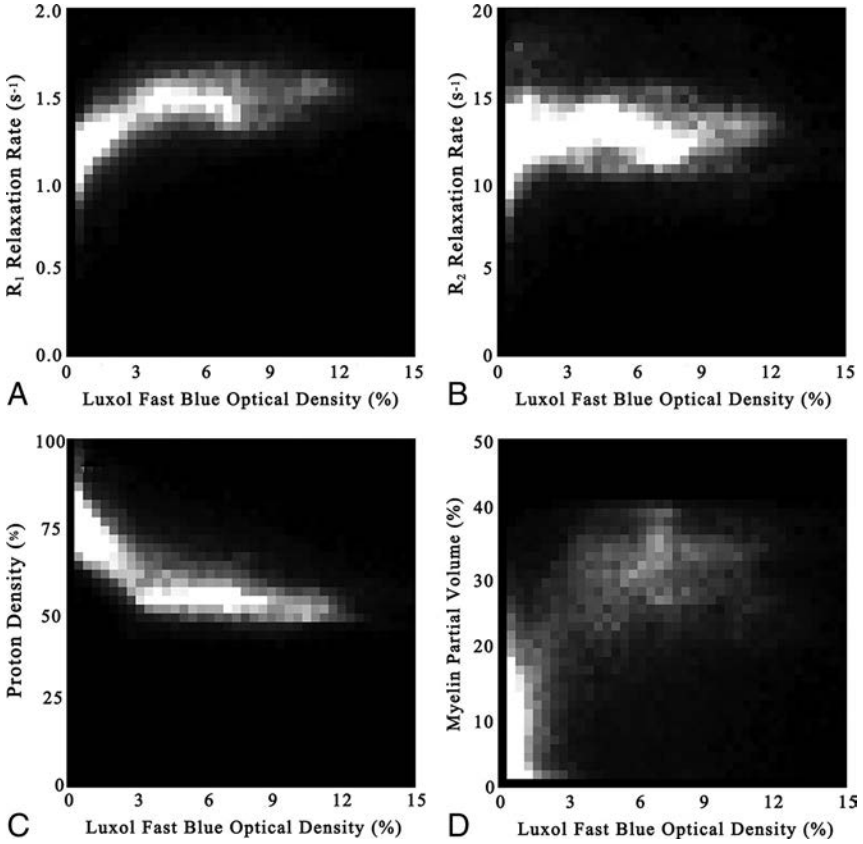

FIG 4. 2D histograms of all subjects of the Luxol fast blue optical density values, plotted as a function of the observed R_1 relaxation rate (*A*), R_2 relaxation rate (*B*), and proton density (*C*). Also, the estimated myelin partial volume, based on temperature-corrected R_1, R_2, and PD is plotted (*D*). The intensity of the 2D histograms corresponds to the number of times a value occurs within each value interval. Intervals were divided into 40 × 40 bins.

Table 2: The mean and SD for all subjects of the position of highest value density for white matter and gray matter observed in the 2D histograms[a]

	WM	GM	Intercept	Slope
R_1	1.47 ± 0.08 s^{-1}	1.27 ± 0.09 s^{-1}	1.24 s^{-1}	0.030 s^{-1}/%
R_2	12.55 ± 1.25 s^{-1}	12.11 ± 1.08 s^{-1}	12.06 s^{-1}	0.066 s^{-1}/%
PD	52.01% ± 2.98%	71.36% ± 3.95%	73.46%	−2.85 %/%
Myelin	30.98% ± 3.77%	4.84% ± 2.30%	2.01%	3.84 %/%
LFB	7.54% ± 2.06%	0.74% ± 0.65%	–	–

[a] Added are the derived slopes and intercepts when using the positions of R_1, R_2, PD, and myelin as a function of the position of LFB.

comparison with the slope observed in the living.[19,20] Also, the relatively large SD of the R_2 slope indicates the sensitivity of R_2 values to changes in the brain. Peculiar is the observation of lower PD values than in living subjects (intercept of 71.96%), but this may be a scaling issue in postprocessing. An important aspect of our data is the temperature of the cadaver. The mean core body temperature of the 12 subjects was 7.8°C, which reduces the T1 and T2 relaxation times. The largest reduction was seen for CSF, whereas this occurred to a lesser extent for brain tissue. To get reasonable input data for the myelin model, we made a temperature correction only on the T1 relaxation times. The observed changes in T1 as a function of temperature were in line with those in previous reports, in which a linear behavior in T1 was shown for brain tissue.[13,14,20] The observed slopes, however, were about half of the reported values from Birkl et al[20] (1.5 versus 3 ms/°C for WM and 9 versus 17 ms/°C for GM). With the temperature correction, the input data to the myelin model were similar to those for living patients, in as much as possible for the deceased.

Concerning the LFB stains, the LFB-OD is not a quantitative measure, and the final OD values depend on the details of the staining procedure. Care was taken to keep all conditions as similar as possible, but color differences can occur due to small dye concentration differences, timing differences, or variation in sample thickness. The OD values of GM and WM in all subjects were within a reasonable interval for natural variation, but as shown in Fig 3, the staining method does not always show a uniform performance. The relatively large SD of the myelin slope (1.73%/%; corresponding to 40% of the mean value of 4.37%/%) indicates the variability between subjects, and it is likely that issues with staining uniformity also affected the within-subject correlation and Spearman ρ.

Registration of LFB-stained brain slice photographs to MR images is a challenging ordeal. The orientation of the cuts is generally not identical to the MR images, and the fixation process of brain slices leads to shrinkage, cracks, and different kinds of distortions of the samples.[21,22] Moreover, there is a tremendous difference in the resolution of MR imaging and photographs of LFB-stained tissue specimens. Each pixel in an MR image corresponds (in our case) to 0.7 × 0.7 × 4.0 mm, whereas each pixel in a photograph corresponds to 0.02 × 0.02 × 0.004 mm. The difference in sharpness, in combination with imperfect registration, will cause substantial issues with partial volume at tissue interfaces, randomly spreading the data points in the correlation plots. The resolution mismatch will affect the regression analysis and probably lower the values of the Spearman ρ. The 2 approaches to retrieve the slopes (Tables 1 and 2), however, provided similar results. It can be speculated that the correlation values would improve by the application of ROIs to avoid tissue interfaces. This would, however, introduce a user dependency in the method, which we wanted to avoid.

A correlation was observed between LFB myelin staining and the qMRI-derived myelin estimation. The qMRI sequence is not sufficiently fast to resolve the short relaxation of myelin water directly, but the presence of myelin partial volume is inferred by its magnetization exchange effect on the (slower) cellular R_1 and R_2 relaxation rate components, as well as the decrease in observable proton density. The correlation of LFB-OD with the qMRI-derived myelin detection shows a higher value ($\rho = 0.74 \pm 0.11$) than separate correlations with R_1, R_2, and PD ($\rho = 0.63 \pm 0.12$, 0.11 ± 0.28, and 0.73 ± 0.09, respectively, Table 1). This finding supports the notion that the model can extract information from

all 3 parameters to determine a myelin estimate. Most intriguing though are the substantially higher values for R_1 and PD than for R_2, but these may be due to the mentioned postmortem edema effect. An indirect measurement such as this may have its limitations in comparison with a more direct multicomponent approach, but for clinical use, the robustness of the measurement may be more important. The qMRI method used is, for example, insensitive for B_1 field inhomogeneity and radiofrequency pulse profile imperfections,[9] and repeatability studies have shown a very low error in measured volume, for example 0.14% in brain size.[23] The clinical usefulness of the method is further supported by initial observations by Hagiwara et al,[24] in which significant differences were found among normal-appearing white matter, MS plaque, and periplaque white matter in a group of patients with MS.

Our results show that myelin exhibits a nonsignificant but positive intercept with LFB-OD, suggesting that the myelin model may indicate values for GM that are higher in comparison with the LFB-OD. This finding is surprising because the expected limitations of both methods would rather lead to a negative intercept, in which qMRI-derived myelin in GM is measured at lower values than the LFB-OD. The MR imaging method is sensitive to the changes in the relaxation of intra- and extracellular water due to the proximity of fast relaxing, thin layers of myelin water, which are trapped between the myelin sheaths. Hence, it is not a direct measurement of myelin but rather a detection method of the thin-layered structure of the heavily myelinated nerve fibers. If axons or dendrites in GM are insulated with a single sheath, no water can be trapped in thin layers and the MR imaging method will cease to measure the presence of myelin. An issue for the LFB staining, on the other hand, is that the dye targets lipoproteins; hence, it may also stain substances other than myelin, such as neuropil, the cell membranes, and nuclei of nerve cells. This staining may create a small, positive offset in optical density, for example, as observed by Laule et al.[25,26] Possibly, the explanation lies in the noise of the MR imaging measurements: Detection of a higher myelin value due to noise is allowed, whereas there can be no values lower than zero. Low myelin values may therefore exhibit a small rectification offset.

A limitation of the study is the low number of cases included. Also, no specific brain pathology such as multiple sclerosis or dementia was investigated. Full clinical medical records of the subjects were not made available to the study due to the forensic nature of cases. However, the available preliminary information did not reveal the existence of relevant neurologic illnesses. Moreover, gross brain examinations at postmortem examination and histologic examinations of investigated brain slices did not present relevant pathology. For future work, it would be very interesting to repeat the study for specific patient groups with relevant demyelination pathologies, microangiopathy, or lacunar infarcts, provided it is practically possible to retrieve full medical history in the short time between death and investigation.

In the histologic investigation, evidence of edema was found. Edema can alter relaxation times[27,28] and hence will have an effect on the myelin detection. The quantification of edema is included in the qMRI model used, but there is no straightforward method of histologically mapping edema, precluding a possible correlation analysis for this study.

CONCLUSIONS

A correlation was shown between a myelin-detection method based on qMRI and myelin staining of brain slice by using Luxol fast blue in a postmortem setting, supporting the validity of myelin measurement with the qMRI method.

Disclosures: Marcel Warntjes—*UNRELATED*: *Employment*: SyntheticMR AB, *Comments*: part-time employment; *Stock/Stock Options:* SyntheticMR AB.

REFERENCES

1. Miller DH, Barkhof F, Frank JA, et al. **Measurement of atrophy in multiple sclerosis: pathological basis, methodological aspects and clinical relevance.** *Brain* 2002;125:1676–95 CrossRef Medline
2. Bakshi R, Thompson AJ, Rocca MA, et al. **MRI in multiple sclerosis: current status and future prospects.** *Lancet Neurol* 2008;7:615–25 CrossRef Medline
3. Ihara M, Polvikoski TM, Hall R, et al. **Quantification of myelin loss in frontal lobe white matter in vascular dementia, Alzheimer's disease, and dementia with Lewy bodies.** *Acta Neuropathol* 2010;119:579–89 CrossRef Medline
4. Back SA, Riddle A, McClure MM. **Maturation-dependent vulnerability of perinatal white matter in premature birth.** *Stroke* 2007;38:724–30 CrossRef Medline
5. Croteau-Chonka EC, Dean DC 3rd, Remer J, et al. **Examining the relationships between cortical maturation and white matter myelination throughout early childhood.** *Neuroimage* 2016;125:413–21 CrossRef Medline
6. MacKay A, Laule C, Vavasour I., et al. **Insights into brain microstructure from the T2 distribution.** *Magn Reson Imag* 2006;24:515–25 CrossRef Medline
7. Oh J, Han ET, Lee MC, et al. **Multislice brain myelin water fractions at 3T in multiple sclerosis.** *J Neuroimaging* 2007;17:156–63 CrossRef Medline
8. Deoni SC, Rutt BK, Arun T, et al. **Gleaning multicomponent T1 and T2 information from steady-state imaging data.** *Magn Reson Med* 2008;60:1372–87 CrossRef Medline
9. Levesque IR, Pike GB. **Characterizing healthy and diseased white matter using quantitative magnetization transfer and multicomponent T(2) relaxometry: A unified view via a four-pool model.** *Magn Reson Med* 2009;62:1487–96 CrossRef Medline
10. Alonso-Ortiz E, Levesque IR, Pike GB. **MRI-based myelin water imaging: a technical review.** *Magn Reson Med* 2015;73:70–81 CrossRef Medline
11. Warntjes M, Engström M, Tisell A, et al. **Modelling the presence of myelin and edema in the brain based on multi-parametric quantitative MRI.** *Front Neurol* 2016;7:16 CrossRef Medline
12. Warntjes JBM, Dahlqvist O, West J, et al. **Rapid magnetic resonance quantification on the brain: optimization for clinical usage.** *Magn Reson Med* 2008;60:320–29 CrossRef Medline
13. Tashiro K, Shiotani S, Kobayashi T, et al. **Cerebral relaxation times from postmortem MR imaging of adults.** *Magn Reson Med Sci* 2015;14:51–56 CrossRef Medline
14. Zech WD, Hottinger AL, Schwendener N, et al. **Post-mortem 1.5T MR quantification of regular anatomical brain structures.** *Int J Legal Med* 2016;130:1071–80 CrossRef Medline
15. Engström M, Warntjes JB, Tisell A, et al. **Multi-parametric representation of voxel-based quantitative magnetic resonance imaging.** *PLoS One* 2014;9:e111688 CrossRef Medline
16. Hausmann R, Vogel C, Seidl S, et al. **Value of morphological parameters for grading of brain swelling.** *Int J Legal Med* 2006;120:219–25 CrossRef Medline
17. Dettmeyer RB. *Forensic Neuropathology: Forensic Histopathology.* Berlin: Springer; 2011:413–438

18. Oehmichen M, Auer RN, König HG. **Cell and tissue reactions.** In: Oehmichen M, Auer RN, König HG. *Forensic Neuropathology and Associated Neurology.* Berlin: Springer; 2006:42–76
19. Warntjes JB, Engström M, Tisell A, et al. **Brain characterization using normalized quantitative magnetic resonance imaging.** *PLoS One* 2013;8:e70864 CrossRef Medline
20. Birkl C, Langkammer C, Haybaeck J, et al. **Temperature dependency of T1 relaxation time in unfixed and fixed human brain tissue.** *NMR Biomed* 2016;29:458–65
21. Moore GR, Leung E, MacKay AL, et al. **A pathology-MRI study of the short-T2 component in formalin-fixed multiple sclerosis brain.** *Neurology* 2000;55:1506–10 CrossRef Medline
22. Bronge L, Bogdanovic N, Wahlund LO. **Postmortem MRI and histopathology of white matter changes in Alzheimer brains: a quantitative, comparative study.** *Dement Geriatr Cogn Disord* 2002;13:205–12 CrossRef Medline
23. Granberg T, Uppman M, Hashim F, et al. **Clinical feasibility of synthetic MRI in multiple sclerosis: a diagnostic and volumetric validation study.** *AJNR Am J Neuroradiol* 2016;37:1023–29 CrossRef Medline
24. Hagiwara A, Hori M, Yokoyama K, et al. **Utility of a multiparametric quantitative MRI model that assesses myelin and edema for evaluating plaques, periplaque white matter, and normal-appearing white matter in patients with multiple sclerosis: a feasibility study.** *AJNR Am J Neuroradiol* 2017;38:237–42 CrossRef Medline
25. Laule C, Leung E, Lis DK, et al. **Myelin water imaging in multiple sclerosis: quantitative correlations with histopathology.** *Mult Scler* 2006;12:747–53 CrossRef Medline
26. Laule C, Vavasour IM, Leung E, et al. **Pathological basis of diffusely abnormal white matter: insights from magnetic resonance imaging and histology.** *Mult Scler* 2011;17:144–50 CrossRef Medline
27. Neema M, Stankiewicz J, Arora A, et al. **T1- and T2-based MRI measures of diffuse gray matter and white matter damage in patients with multiple sclerosis.** *J Neuroimaging* 2007;17:16S–21S CrossRef Medline
28. Larsson HB, Frederiksen J, Petersen J, et al. **Assessment of demyelination, edema and gliosis by in-vivo determination of T1 and T2 in the brain of patients with acute attack of multiple sclerosis.** *Magn Reson Med* 1989;11:337–48 Medline

Synthetic MRI for Clinical Neuroimaging: Results of the Magnetic Resonance Image Compilation (MAGiC) Prospective, Multicenter, Multireader Trial

L.N. Tanenbaum, A.J. Tsiouris, A.N. Johnson, T.P. Naidich, M.C. DeLano, E.R. Melhem, P. Quarterman, S.X. Parameswaran, A. Shankaranarayanan, M. Goyen, and A.S. Field

ABSTRACT

BACKGROUND AND PURPOSE: Synthetic MR imaging enables reconstruction of various image contrasts from 1 scan, reducing scan times and potentially providing novel information. This study is the first large, prospective comparison of synthetic-versus-conventional MR imaging for routine neuroimaging.

MATERIALS AND METHODS: A prospective multireader, multicase noninferiority trial of 1526 images read by 7 blinded neuroradiologists was performed with prospectively acquired synthetic and conventional brain MR imaging case-control pairs from 109 subjects (mean, 53.0 ± 18.5 years of age; range, 19–89 years of age) with neuroimaging indications. Each case included conventional T1- and T2-weighted, T1 and T2 FLAIR, and STIR and/or proton density and synthetic reconstructions from multiple-dynamic multiple-echo imaging. Images were randomized and independently assessed for diagnostic quality, morphologic legibility, radiologic findings indicative of diagnosis, and artifacts.

RESULTS: Clinical MR imaging studies revealed 46 healthy and 63 pathologic cases. Overall diagnostic quality of synthetic MR images was noninferior to conventional imaging on a 5-level Likert scale ($P < .001$; mean synthetic-conventional, -0.335 ± 0.352; $\Delta = 0.5$; lower limit of the 95% CI, -0.402). Legibility of synthetic and conventional morphology agreed in >95%, except in the posterior limb of the internal capsule for T1, T1 FLAIR, and proton-density views (all, >80%). Synthetic T2 FLAIR had more pronounced artifacts, including +24.1% of cases with flow artifacts and +17.6% cases with white noise artifacts.

CONCLUSIONS: Overall synthetic MR imaging quality was similar to that of conventional proton-density, STIR, and T1- and T2-weighted contrast views across neurologic conditions. While artifacts were more common in synthetic T2 FLAIR, these were readily recognizable and did not mimic pathology but could necessitate additional conventional T2 FLAIR to confirm the diagnosis.

ABBREVIATIONS: κ = Kappa statistic; MAGiC = MAGnetic resonance image Compilation; MDME = multiple-dynamic multiple-echo; PD = proton density

Synthetic MR imaging uses quantitative probing of multiple physical properties to reconstruct multiple contrasts from 1 scan. Parameters like TR, TE, and TI can be modified with mathematic inferences rather than being predetermined.[1-3] The speed of diagnostic brain studies can thus be reduced to only about 5 minutes with synthetic MR imaging.[4] This advancement may help improve throughput and reduce rescanning, while also providing quantitative information of research interest.[4-6]

Clinical studies of synthetic MR imaging are highly heterogeneous in that they examine a variety of conditions with widely varying scan parameters, with a paucity of large, randomized trials to inform clinical usage.[3,6] Blystad et al[5] (2012) reported that synthetic images had diagnostic utility similar to that of conventional imaging series, though with some quality issues like granulation and contrast particularly apparent in FLAIR views. Other studies reported good quality and contrast

Received December 2, 2016; accepted after revision February 2, 2017.

From Lenox Hill Radiology (L.N.T.), RadNet Inc, New York, New York; Department of Radiology (A.J.T.), Weill Cornell Medical Center, New York, New York; Department of Technical Communication (A.N.J.), Science and Healthcare, Texas Tech University, Lubbock, Texas; Technology and Medical Innovation Organization (A.N.J., S.X.P.), Healthcare Imaging-MRI (P.Q.), Healthcare Imaging-MRI Neuro Applications (A.S.), and Medical Affairs (M.G.), GE Healthcare, Milwaukee, Wisconsin; Department of Neuroradiology (T.P.N.), The Mount Sinai Hospital, New York, New York; Division of Radiology and Biomedical Imaging (M.C.D.), Michigan State University, Advanced Radiology Services, PC, and Spectrum Health, Grand Rapids, Michigan; Department of Diagnostic Radiology and Nuclear Medicine (E.R.M.), University of Maryland School of Medicine, Baltimore, Maryland; and Department of Radiology (A.S.F.), University of Wisconsin School of Medicine and Public Health, Madison, Wisconsin.

This work was supported by GE Healthcare to participating institutions.

Please address correspondence to Lawrence Tanenbaum, MD, 400 E 66th St, NY, NY 10065; e-mail: Nuromri@radnet.com; @nuromri

Indicates open access to non-subscribers at www.ajnr.org

Indicates article with supplemental on-line tables.

Indicates article with supplemental on-line photos.

http://dx.doi.org/10.3174/ajnr.A5227

for synthetic images among certain indications, such as multiple sclerosis, brain metastasis,[6,7] and myelination patterns.[8] Because image quality endpoints are reliant on reader judgment (reported to have up to 41% variability and only fair-to-moderate interrater agreement[9,10]) and scanning conditions, drawing clinically relevant inferences from diverse small trials is challenging. Furthermore, the broad diversity of both healthy and pathologic morphologic variants encountered in routine neuroimaging necessitates more robust clinical studies of synthetic MR imaging for clinical neuroimaging.

This study was designed to compare the overall image quality of synthetic MR imaging with conventional MR imaging in a general neuroimaging population. Secondary aims included legibility of anatomic and morphologic features, artifact prevalence, and diagnostic performance across a range of cases helpful in informing clinical usage and adoption of synthetic MR imaging.

MATERIALS AND METHODS

Participants and Clinical Assessments

Subjects ($n = 117$) were enrolled prospectively into a multireader multicenter case-control study across 6 hospitals from November 2015 to January 2016 (ClinicalTrials.gov Identifier NCT02596854). Of these, all complete cases ($n = 109$; 45 men, 64 women; mean, 53.0 ± 18.5 years of age; range, 19–89 years) with synthetic and conventional (control) acquisitions were read. Subjects were 18 years of age or older with clinical indications for neuroimaging and without contraindications to MR imaging or previously diagnosed congenital conditions or extensive trauma prohibiting scanning. Governing ethics committees at each site approved this study, and subjects provided written informed consent.

Image Acquisition

Images were prospectively acquired by using a fixed set of scanning parameters closely approximating current standard of care brain MR imaging (as detailed for 1.5T and 3T scanners in Online Table 1). First, conventional images were acquired by using conventional 2D axial plane T1- and T2-weighted, T1 and T2 fluid-attenuated inversion recovery, short tau inversion recovery, and proton density (PD) sequences. Then, a multiple-dynamic multiple-echo (MDME) sequence was performed for synthetic reconstruction, for a complete conventional and synthetic case-control series. MDME uses a repeat version of the same gradient-reversal process used to create a single gradient-echo to produce additional gradient-echoes after a single radiofrequency pulse. This is known as multiple (or dual) echo gradient-echo, which is possible when complete loss of the transverse magnetization by T2* relaxation has not yet occurred. Because MDME is a quantitative sequence, it enables absolute quantification of tissue physical properties, like longitudinal R_1 relaxation rate, transverse R_2 relaxation rate, and PD independent of the scanner settings. MDME parameters acquired in 1 scan are used in synthetic imaging to calculate pixel intensity, producing an appearance similar to that of conventional MR images with modifiable TE, TR, and TI.[5,11] Thus, synthetic (based on MDME) and conventional T1, T2, T1 FLAIR, T2 FLAIR, PD, and STIR contrast views were collected. MDME data were reconstructed outside the clinical care environment by using MAGnetic resonance image Compilation (MAGiC) software on a 64-bit Advantage Workstation (GE Healthcare, Milwaukee, Wisconsin). No errors were logged during processing, and the average processing time was approximately 2 minutes per case. Scan duration, subject disposition, and imaging results were recorded for each case.

The site-determined diagnosis was recorded on the basis of the results of MR imaging studies and work-up performed according to the standard of care by clinical neuroradiologists. The sites reported the reference (site-determined diagnosis) by using the same scale as the study readers, which reports normal or ≥1 pathologic subtype adapted from Osborn et al (2010)[12]: 1) traumatic, complex, indeterminate, or other condition or injury; 2) congenital malformation; 3) ischemic or hemorrhagic stroke; subarachnoid hemorrhage/aneurysm; 4) vascular malformation; 5) neoplasm/primary neoplastic cysts; 6) infectious/demyelinating disease; or 7) metabolic/degenerative disorders.

Radiologic Assessments

Synthetic and conventional images sets were randomized and assessed by 7 blinded independent neuroradiologists (>10 years' experience) on standard imaging workstations. Case-control pairs from the same subject were separated and read across 2 sessions, separated by a 4-week memory-washout period. Each read included either all synthetic or all conventional contrast views from a case. Overall diagnostic image quality was rated (considering all available contrast views) on a 5-point Likert-type scale: 5 = excellent (acceptable for diagnostic use), 4 = good (acceptable for diagnostic use), 3 = acceptable (acceptable for diagnostic use but with minor issues), 2 = poor (not acceptable for diagnostic use), or 1 = unacceptable (not acceptable for diagnostic use). Ratings of ≥3 were considered acceptable overall. For image sets rated as unacceptable (1 or 2), the rationale was recorded as "open text." Readers also recorded radiologic findings indicative of a diagnosis with corresponding Osborn classifications.

For each contrast view, readers rated the legibility (or visibility of margins and structures associated with key anatomic/morphologic features) of anatomies defined a priori. Legibility ratings supplemented overall image-quality data, which consider all regions of the brain, as a means of providing specific information about anatomic regions in brain imaging. Each anatomy was rated on a binary scale (legible/illegible), including the following: central sulcus, head of the caudate nucleus, posterior limb of the internal capsule, cerebral peduncle, middle cerebellar peduncle, and cervicomedullary junction. Readers recorded whether any of the following artifacts were present:[13] low signal-to-noise, motion and section issues, infolding or wrap-around, white pixel or spike noise, phase encoding, flow, contrast-to-noise, low image resolution, or blurring. Readers could provide free text comments on any other observations.

Statistical Analysis

Statistical analysis was performed in SAS 9.2 (SAS Institute, Cary, North Carolina), and sample size was calculated in PASS12

Diagnostic image-quality ratings by static field strength of scanner and overall[a]

Diagnostic Quality[b]	1.5T Scanner		3T Scanner		Overall (1.5T + 3T)	
	Syn (*N* = 392)	Con (*N* = 392)	Syn (*N* = 371)	Con (*N* = 371)	Syn (*N* = 763)	Con (*N* = 763)
Acceptable for diagnostic use (3,4,5)	380 (97%)	387 (99%)	354 (95%)	358 (96%)	734 (96%)	745 (98%)
Excellent (rated 5)	64 (16%)	183 (47%)	37 (10%)	103 (28%)	101 (13%)	286 (37%)
Good (rated 4)	266 (68%)	170 (43%)	230 (62%)	199 (54%)	496 (65%)	369 (48%)
Acceptable (rated 3)	50 (13%)	34 (9%)	87 (23%)	56 (15%)	137 (18%)	90 (12%)
Unacceptable for diagnostic use (1,2)	12 (3%)	5 (1%)	17 (5%)	13 (4%)	29 (4%)	18 (2%)
Poor (rated 2)	10 (3%)	5 (1%)	16 (4%)	12 (3%)	26 (3%)	17 (2%)
Unacceptable (rated 1)	2 (1%)	0	1 (0.3%)	1 (0.3%)	3 (0.4%)	1 (0.1%)

Note:—Syn indicates synthetic MR imaging; Con = conventional MR imaging (control).

[a] All data are shown as *n* (*n*/N%), where *n* is the count and *N* is the total reads per category (defined in the upper row of this table).

[b] Five-point scale.

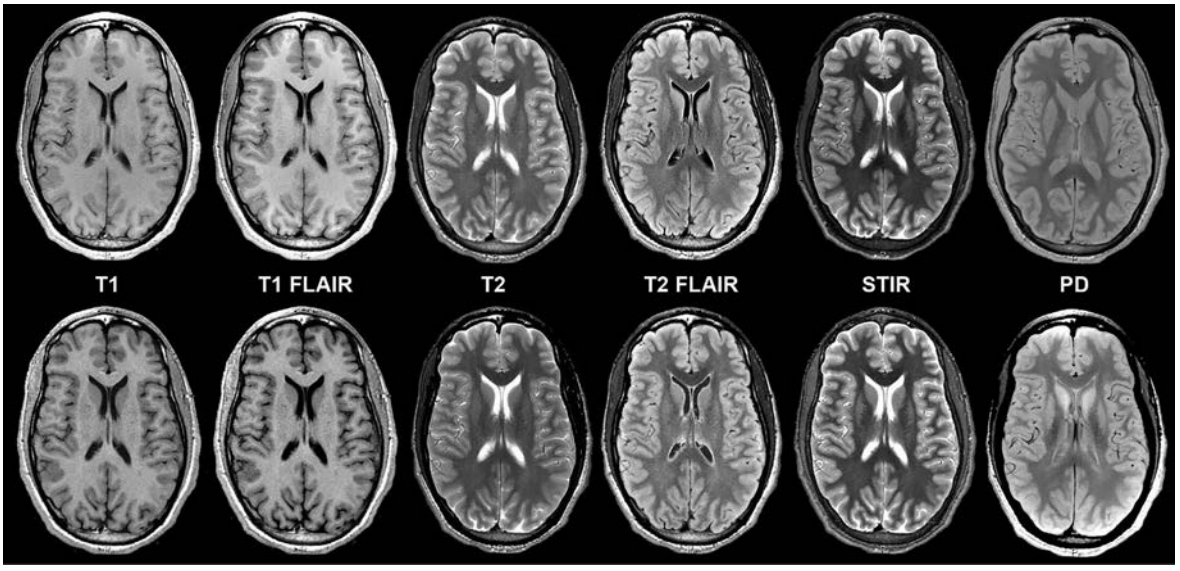

FIG 1. Axial synthetic and conventional 3T MR imaging of a normal brain. Conventional (*upper row*) and synthetic (*lower row*) image sets exhibit similar legibility and quality. Slight differences in contrast levels are apparent, which do not adversely impact the diagnostic utility of images, particularly between T1 FLAIR and T2 FLAIR views.

(NCSS Statistical Software, Kaysville, Utah). Per the prospective statistical plan to determine noninferiority, a Wilcoxon signed rank test was used to determine noninferiority of synthetic-to-conventional MR imaging in terms of the overall diagnostic image quality score, by using a 1-sided $\alpha = .025$ test with a noninferiority margin of $\Delta = .5$ with a 5-level Likert scale. The primary hypothesis is 1-sided and can be stated as H_0:$S \leq -\Delta$ and H_A:$S > -\Delta$, where the S is the median difference of overall diagnostic image quality across readers for synthetic-versus-conventional MR imaging, in which noninferiority is established by rejecting the null hypothesis. The margin (Δ) of .5 was determined statistically on the basis of the population and was confirmed by clinical estimates from prior research[5] and institutional pilot data, in accordance with recommendations for determination of noninferiority margins described in the US Food and Drug Administration *Guidance for Industry: Non-Inferiority Clinical Trials to Establish Effectiveness* (2016) (https://www.fda.gov/downloads/Drugs/GuidanceComplianceRegulatoryInformation/Guidances/UCM202140.pdf) and trial designs for noninferiority testing in radiology reviewed by Ahn et al (2012).[14] Descriptive statistics were used to summarize secondary endpoints of anatomic/morphology legibility by anatomic region, artifact prevalence, and diagnostic performance (sensitivity/specificity) by the Osborn classification. Interrater reliability between readers was assessed by kappa (κ) statistic.

RESULTS

Overall Diagnostic Quality

Each of 7 blinded neuroradiologists read all 109 clinically acquired case-control image sets (109 synthetic and 109 conventional) for a total of 1526 reads (763 synthetic and 763 conventional reads). Of these, 56/109 were acquired on 1.5T static field strength scanners and 53/109 were acquired on 3T scanners. Because no significant differences for 5-level image quality scores (acceptable = 3, 4, or 5 versus unacceptable = 1 or 2) were observed on the basis of scanner static field strength (1.5T or T) or acquisition site ($P > .05$ with a 2-tailed t test), results were pooled for analysis. The duration of scanning was recorded, with a single-acquisition sequence for synthetic reconstruction requiring 5 minutes 36 seconds on 1.5T scanners and 5 minutes 4 seconds on 3T scanners (On-line Table 1).

Considering all contrast views, 734 (96%) synthetic cases and 745 (98%) conventional cases were rated as acceptable (≥3 on a 5-point scale) (Table). Figure 1 shows comparable synthetic and conventional case-control images from a normal (no pathology present) brain by contrast view. Figures 2–5 show case-control

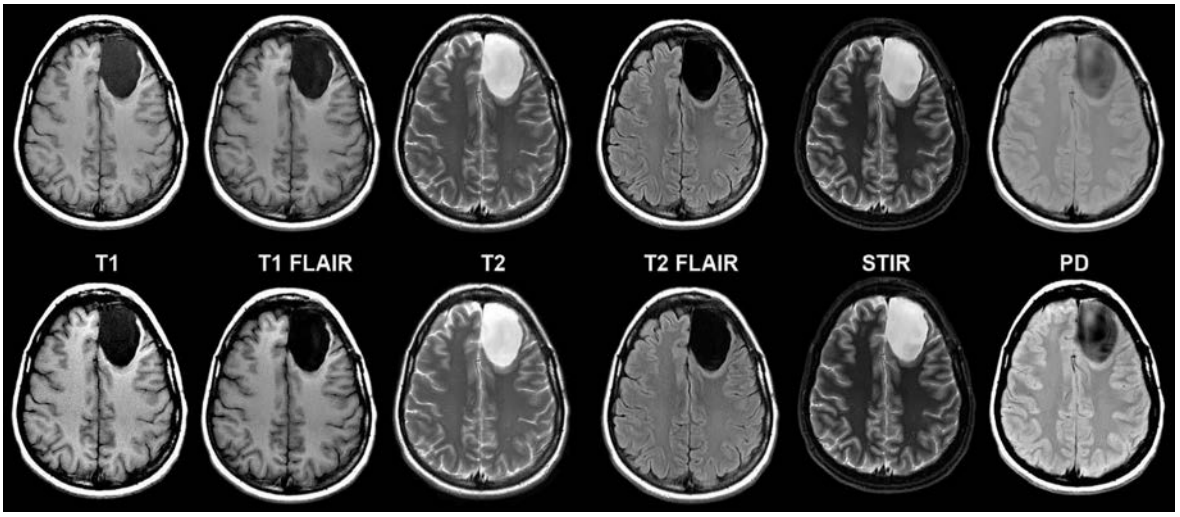

FIG 2. Left frontal lobe cystic tumor on axial synthetic and conventional 3T MR imaging in a 31-year-old woman. Conventional (*upper row*) and synthetic (*lower row*) image sets exhibit similar legibility and quality.

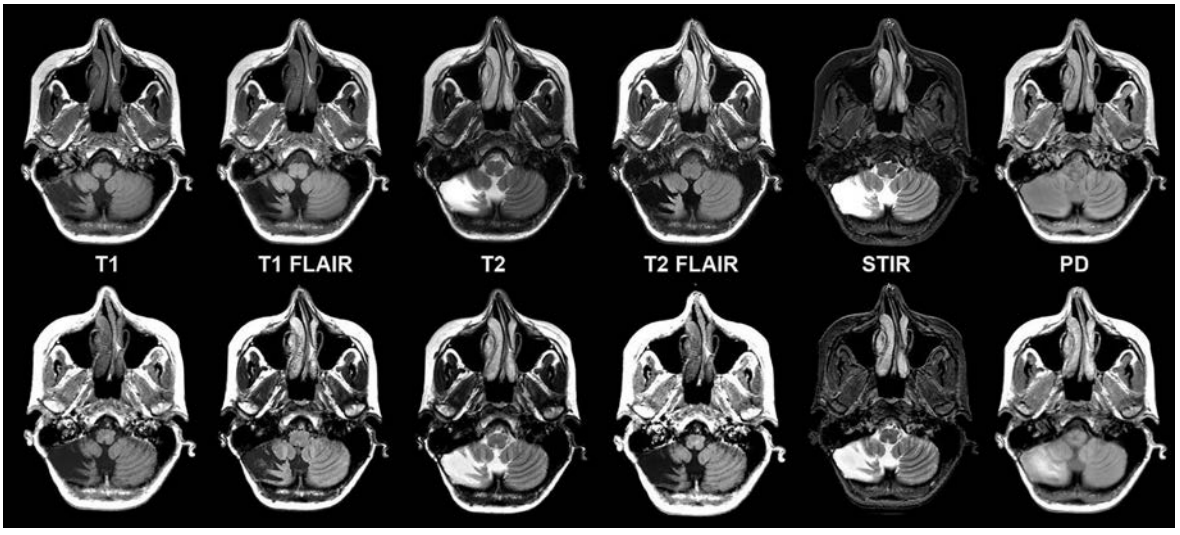

FIG 3. Chronic right cerebellar infarction in a 37-year-old woman on axial synthetic and conventional 3T MR imaging. Conventional (*upper row*) and synthetic (*lower row*) image sets exhibit similar legibility and quality.

images across a range of brain pathologies (continued in On-line Figs 1–3). Overall diagnostic image quality of synthetic images was statistically noninferior to conventional images, with a mean difference (synthetic-conventional) across readers of -0.335 ± 0.352 with a lower limit of the (1-sided) 95% CI of -0.402 (median, -0.428; minimum, -1.286; and maximum, 0.714; $P < .001$). Among synthetic images rated as poor or unacceptable (1 or 2 on a 5-point scale), the most common quality issue was patient motion in synthetic image sets owing to generating from a single acquisition (where a single motion event propagates across all reconstructed contrast views).

Legibility of Anatomic/Morphologic Features

Anatomic/morphologic features were visualized and rated as legible in synthetic and conventional imaging for ≥98% of regions across contrast views, except in the cervicomedullary junction rated at 96% on both synthetic and conventional imaging (On-line Table 2). For synthetic and conventional pairs from the same subject, readers agreed for ≥95% of anatomic/morphologic regions across contrast views, except in the posterior limb of the internal capsule for T1, T1 FLAIR, and PD views (>80% agreement). Notably, 6 of 7 readers had agreement of 99%–100% for T1 FLAIR, with 1 reader as an outlier at 89%, possibly related to experience. Further study will be needed to investigate the influence of experience on reading synthetic images and possible training solutions.

Artifacts Occurrence and Characterization

Fewer artifacts (all characterizations) were identified in synthetic than in conventional imaging for T1-weighted (9.2%), STIR (24.8%), and PD (1.1%) contrast views (On-line Table 3). Synthetic images had more artifacts overall on the T2-weighted (5.0%), T1 FLAIR (17.9%), and T2 FLAIR (49.3%) contrast views (On-line Table 3). Phase-encoding artifacts were less frequent in synthetic STIR images (27.2%) and synthetic T1 contrast views (13.0%). Synthetic contrast views were more likely to contain

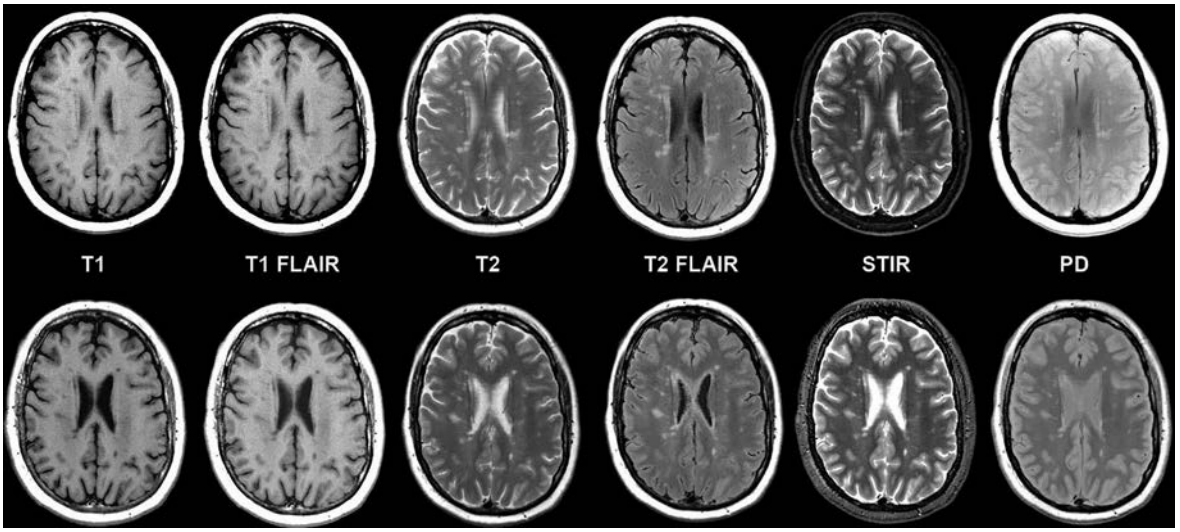

FIG 4. Multiple sclerosis in axial synthetic and conventional 3T MR imaging in a 58-year-old woman. Multifocal demyelinating lesions are apparent within the cerebral white matter; these lesions appear similar on conventional (*upper row*) and synthetic (*lower row*) image sets. A slight misregistration is apparent due to patient motion between the MDME scan (used for synthetic reconstruction, lower row) and the comparable conventional scan acquired in the study (*upper row*). While misregistration due to motion can pose challenges in conventional serial acquisitions due to partial section differences in images across contrast views, synthetic reconstruction inherently prevents misregistration across synthetic contrast views.

white pixels/spike noise artifacts across contrast views (except PD), and flow artifacts were more common in synthetic views, most notably in the synthetic T1-weighted (13.0%), T1 FLAIR (22.1%), and T2 FLAIR (24.1%) contrast views.

Readers identified relatively more artifacts among synthetic T2 FLAIR contrast views compared with other synthetic and conventional contrast views. Synthetic T2 FLAIR showed 24.1% more flow artifacts, 17.6% more white noise artifacts, and 59.2% more artifacts marked as "other" compared with conventional views. Examination of reader free text comments revealed that artifacts marked as "other" primarily described localized, granulated hyperintensities apparent in the margins only in synthetic T2 FLAIR contrast views (Fig 6). These artifacts were recognizable by a distinct pixelated appearance and a tendency to occur along tissue-CSF boundaries only in T2 FLAIR views in otherwise unremarkable image sets. Readers reported that synthetic T2 FLAIR may have some diagnostic limitations in practice, which could necessitate a conventional T2 FLAIR scan. However, owing to the nature of synthetic imaging (which results in a full range of possible contrast views for cross-comparison), neuroradiologists were readily able to distinguish T2 FLAIR artifacts from pathology, without impacting diagnostic utility.

Diagnostic Performance

Overall interrater agreement (κ correlation coefficient) for pathology detection was 0.502 for synthetic images and slightly higher at 0.605 for conventional images. Across the 7 readers (1526 total reads, including 763 synthetic and 763 conventional pairs), overall sensitivity for correct identification of pathology ranged from 60.32 (95% CI, 47.20–72.43) to 95.24 (95% CI, 86.71–99.01) among readers for conventional versus 55.56 (95% CI, 42.49–68.08) to 96.83 (95% CI, 89.00–99.61) among readers for synthetic imaging, with the site-determined diagnosis as the criterion standard. On the basis of clinically confirmed diagnoses reported by the site (based on clinical MR imaging studies and, when necessary, additional follow-up or laboratory testing), the study included 46 healthy and 63 pathologic cases (of which 2 cases contained 2 pathology types and 1 case contained 3 pathology types), including 7 traumatic or complex injuries, 2 congenital malformations, 12 strokes/hemorrhages, 2 vascular malformations, 32 neoplasms/primary neoplastic cysts, 10 infectious/demyelinating conditions, and 2 metabolic/degenerative disorders. Readers of synthetic MR imaging showed equal or higher ability to diagnose all pathologies, except for neoplasms/primary neoplastic cysts ($n = 2$, difference in detection of $\pm 6.3\%$ sensitivity and $\pm 1.3\%$ specificity among readers) subgroup and infectious diseases ($n = 10$, difference in detection of $\pm 10.0\%$ sensitivity and $\pm 3.0\%$ specificity).

DISCUSSION

To our knowledge, this is the first large, prospective, randomized study of synthetic MR imaging technology to enroll a cross-section of the neuroimaging population, including a variety of brain pathologies encountered in clinical practice. On the basis of blinded assessments from 7 neuroradiologists, the overall diagnostic quality of synthetic MR imaging was statistically noninferior to conventional MR imaging series for T1- and T2-weighted, T1 and T2 FLAIR, STIR, and PD contrast views. Furthermore, neuroradiologists reported similar anatomic/morphologic feature legibility in both synthetic and conventional images. Both synthetic and conventional sequences exhibited similar quality issues and artifact trends for T1- and T2-weighted, STIR, and PD contrast views, while synthetic imaging had more FLAIR artifacts. Synthetic FLAIR artifacts were readily recognizable by cross-comparison within contrast views and thus did not significantly impact the diagnostic use of synthetic MR imaging. Overall, study results demonstrated that both synthetic and conventional imaging have similar diagnostic utility.

Anatomic and morphologic characteristics were visible in

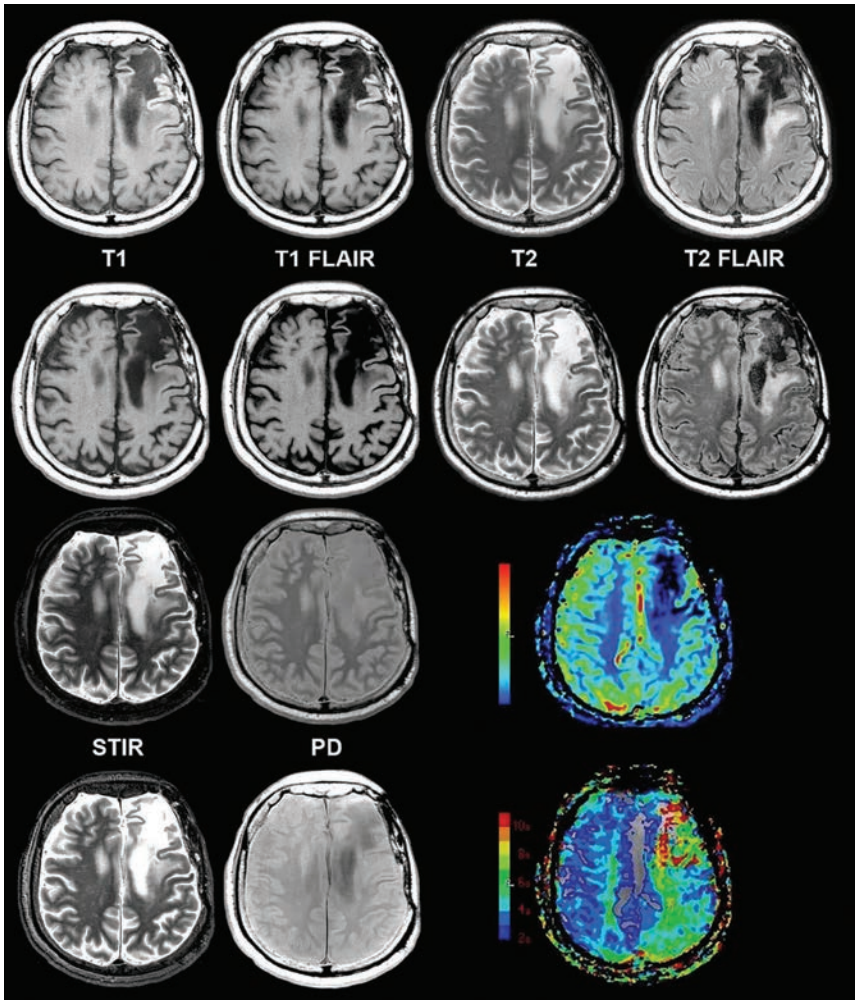

FIG 5. Chronic infarction in synthetic and conventional 3T MR imaging shown alongside color functional perfusion maps in a 62-year-old man. Conventional (*rows 1 and 3*) and synthetic (*rows 2 and 4*) views show similar legibility and quality. T1 FLAIR and T2 FLAIR views have some granulated white noise in the margins. Color quantitative perfusion maps (*lower right*) demonstrate decreased flow and prolonged transit time in this region of chronic infarction.

both synthetic and conventional views, though both exhibited issues pertaining to visualizing the craniocervical junction, CSF suppression, and pulsation artifacts that are well-documented in MR imaging.[5,15-18] Synthetic imaging exhibited characteristic hyperintense artifacts in FLAIR views, corroborating previous reports that further work will be necessary before synthetically generated FLAIR views can fully replace conventional FLAIR in practice.[5,6] While FLAIR artifacts contributed to lower overall image quality scores (because all views were considered in this composite primary end point), the overall impact of FLAIR artifacts on diagnosis was inherently limited by the nature of the synthetic views, in which immediate cross-comparison with other contrast views is possible. On rare occasions, encoding artifacts in FLAIR views could necessitate clinical workflow changes such as the addition of a single conventional scan; however, the impact on the patient's overall scan experience is offset by the time savings of the synthetic acquisition. Furthermore, motion and signal-encoding artifacts were observed to affect all reconstructed synthetic views if present in the original acquisition. As few as 7.5% of single MR images exhibited motion artifacts, while up to 19.8% of long scans of multiple contrasts may be affected.[19] Because synthetic imaging reduces the overall scan time, the impact of acquisition issues is expected to be limited in practice.

Diagnostic performance of synthetic imaging was similar to that of conventional MR imaging, as indicated by statistical noninferiority of synthetic images. While the noninferiority model is decisive for effectiveness in therapeutic studies, which directly assess ultimate patient outcomes, elucidating the clinical implications of noninferiority findings in radiology is less straightforward because the negative effects of image quality may have variable effects on ultimate patient outcomes.[14] Thus, from a clinical perspective, we observed that in both synthetic and conventional MR imaging, some neoplasms/primary neoplastic cysts and infectious or demyelinating conditions were challenging for readers to identify without additional clinical or laboratory work-up, possibly due to overlapping appearances of neoplastic and inflammatory conditions on MR images.[20,21]

The sensitivity and specificity of MR imaging in neuroradiology have been reported to range from 39% to 98% and 33% to 100%, respectively, with wide variations based on reader experience and the pathologic condition studied.[22-25] Across study readers, synthetic MR imaging sensitivity and specificity had values within typical clinically observed ranges for blinded MR imaging reads (without clinical context).[22-25] Statistical variations in diagnostic classifications may be centrally attributable to small samples of certain pathologies in the present study, meriting further study of these pathologic subgroups. Synthetic scanning is performed in the axial view only, and some clinical cases may be limited by spatial resolution in this section direction. Owing to the relatively shorter synthetic acquisition time, however, additional sequences can also be combined with the synthetic acquisition in a single examination session with minimal burden on the patient.

The strengths of this study include the use of a prospective acquisition protocol with matched scanning parameters (On-line Table 1). Because scans were acquired in a fixed order with MDME (synthetic reconstruction) acquired last, a relative propensity toward motion artifacts in synthetic images may not be representative of actual occurrence. Reports have, however, shown that single scans of short duration have lower incidences of motion than longer scans.[13,26] The trial results support the use of synthetic MR imaging in brain imaging to reduce scan time and

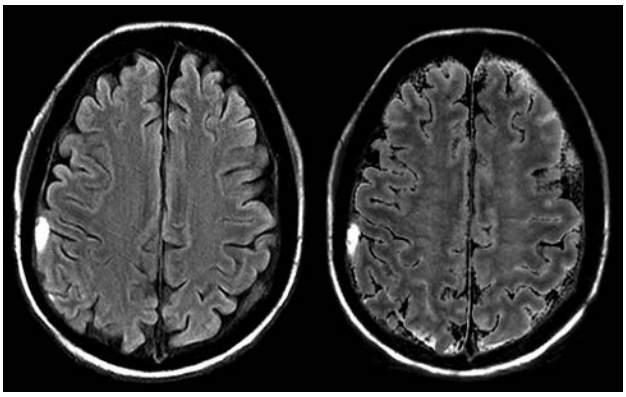

FIG 6. Subdural hematoma on T2 FLAIR in synthetic and conventional 3T MR imaging demonstrating pronounced artifacts. Conventional (*left*) and synthetic (*right*) T2 FLAIR images are shown for a patient with subdural hematoma, in which synthetic T2 FLAIR has notable granulated hyperintensities and lacks contrast between the lesion and surrounding tissues. Artifacts of this severity level were rare among synthetically reconstructed images, possibly due to issues in the MDME acquisition that are typically resolved on rescanning. For cases demonstrating these granulated hyperintensities on the synthetic T2 FLAIR, artifacts were readily recognizable by characteristic distortion and correlation with other contrast views without apparent artifacts. While these could necessitate rescanning with conventional T2 FLAIR in some cases, when coupled with other contrast views, these artifacts did not interfere with the diagnostic accuracy of synthetic MR imaging.

the associated discomfort for patients undergoing brain MR imaging, with diagnostic performance similar to that of conventional imaging.

CONCLUSIONS

The current study demonstrated that synthetic images were statistically noninferior in terms of overall diagnostic image quality compared with conventional MR images, with similar diagnostic utility for detecting a range of brain pathologies. Both synthetic and conventional MR imaging could visualize anatomic and morphologic features of the brain, with similar trends in artifacts and diagnostic utility. Because synthetic reconstructions rely on the quality of a single scan, care should be taken to minimize motion and acquisition artifacts. While more artifacts were observed in synthetic T2 FLAIR reconstructions, cross-comparison with other contrast views enabled neuroradiologists to readily detect these artifacts without interfering with the diagnostic ability of synthetic images. The trial results support the use of synthetic MR imaging in brain imaging to reduce scan time and discomfort for patients undergoing brain MR imaging, while acquiring high-quality diagnostic MR images. We expect that further research may reveal additional applications for synthetic MR imaging.

ACKNOWLEDGMENTS

We thank the participants of the study, the study coordinators across multiple sites, and the study readers. We also acknowledge the contributions of Dr Michael Starc (Department of Radiology, Weill Cornell Medical College, New York, NY) in study conduct and of Dr Keyi Wang (GE Healthcare, Technology and Medical Innovation) for assistance with the statistical design of the trial.

Disclosures: Lawrence N. Tanenbaum—*RELATED*: *Grant*: GE Healthcare, *Comments*: sponsored trial payments for patient scanning*; *UNRELATED*: *Consulting Fee or Honorarium*: GE Healthcare; *Consultancy:* GE Healthcare. Angela N. Johnson—*RELATED*: *Support for Travel to Meetings for the Study or Other Purposes*: GE Healthcare, *Comments*: Funding for travel was provided by GE Healthcare for US FDA agency and investigator meetings associated with study conduct. No additional funding was provided for the publication activities; *UNRELATED*: *Employment*: GE Healthcare, *Comments*: Angela N. Johnson is an employee of the Technology and Medical Innovation Organization of GE Healthcare. Providing publication assistance is not a requirement of employment or incentivized by GE Healthcare; *Payment for Lectures Including Service on Speakers Bureaus*: Regulatory Affairs Professional Society, *Comments*: conference faculty for the annual conference, receiving honorarium; *Stock/Stock Options*: GE Healthcare, *Comments*: I hold employee stock options in GE Healthcare; *OTHER RELATIONSHIPS*: I am a doctoral student at Texas Tech University receiving employee-sponsored tuition benefits for doctoral research. Ajit Shankaranarayanan—*UNRELATED*: *Employment*: GE Healthcare. Mathias Goyen—*UNRELATED*: *Employment*: GE Healthcare, *Comments*: full-time employment, Chief Medical Officer Oncology; *Stock/Stock Options*: GE Healthcare. Aaron S. Field—*RELATED*: *Grant*: GE Healthcare, *Comments*: grant from study sponsor to cover institutional costs associated with participation in the trial. This did not include any salary or other support paid to me*. *Money paid to the institution.

REFERENCES

1. Riederer S, Suddarth S, Bobman S. **Automated MR image synthesis: feasibility studies.** *Radiology* 1984;153:203–06 CrossRef Medline
2. Warntjes J, Dahlqvist O, Lundberg P. **Novel method for rapid, simultaneous T1, T2*, and proton density quantification.** *Magn Reson Med* 2007;57:528–37 CrossRef Medline
3. Krauss W, Gunnarsson M, Andersson T, et al. **Accuracy and reproducibility of a quantitative magnetic resonance imaging method for concurrent measurements of tissue relaxation times and proton density.** *Magn Reson Imaging* 2015;33:584–91 CrossRef Medline
4. Warntjes J, Leinhard O, West J, et al. **Rapid magnetic resonance quantification on the brain: optimization for clinical usage.** *Magn Reson Med* 2008;60:320–29 CrossRef Medline
5. Blystad I, Warntjes J, Smedby O, et al. **Synthetic MRI of the brain in a clinical setting.** *Acta Radiol* 2012;53:1158–63 CrossRef Medline
6. Granberg T, Uppman M, Hashim, et al. **Clinical feasibility of synthetic MRI in multiple sclerosis: a diagnostic and volumetric validation study.** *AJNR Am J Neuroradiol* 2016;37:1023–29 CrossRef Medline
7. Hagiwara A, Hori M, Suzuki M, et al. **Contrast-enhanced synthetic MRI for the detection of brain metastases.** *Acta Radiol Open* 2016;5: 2058460115626757 CrossRef Medline
8. Betts M, Leach J, Jones B, et al. **Brain imaging with synthetic MR in children: clinical quality assessment.** *Neuroradiology* 2016;58: 1017–26 CrossRef Medline
9. Struck A, Westover M. **Variability in clinical assessment of neuroimaging in temporal lobe epilepsy.** *Seizure* 2015;30:132–35 CrossRef Medline
10. Wattjes M, Wijburg M, Vennegoor A, et al. **Diagnostic performance of brain MRI in pharmacovigilance of natalizumab-treated MS patients.** *Mult Scler* 2016;22:1174–83 CrossRef Medline
11. Gulani V, Schmitt P, Griswold M. **Towards a single-sequence neurologic magnetic resonance imaging examination: multiple-contrast images from an IR TrueFISP experiment.** *Invest Radiol* 2004; 39:767–74 CrossRef Medline
12. Osborn AG, Salzman KL, Barkovich AJ. *Diagnostic Imaging: Brain.* 2nd ed. Friesens: Amirsys; 2010
13. Krupa K, Bekiesińska-Figatowska M. **Artifacts in magnetic resonance imaging.** *Pol J Radiol* 2015;80:93–106 CrossRef Medline
14. Ahn S, Park SH, Lee KH. **How to demonstrate similarity by using noninferiority and equivalence statistical testing in radiology research.** *Radiology* 2013;267:328–38 CrossRef Medline
15. Tha K, Terae S, Kudo K, et al. **Differential diagnosis of hyperintense cerebrospinal fluid on fluid-attenuated inversion recovery images of the brain, Part II: non-pathological conditions.** *Br J Radiol* 2009; 82:610–14 CrossRef Medline
16. Tha K, Terae S, Kudo K, et al. **Differential diagnosis of hyperintense cerebrospinal fluid on fluid-attenuated inversion recovery images of the brain, Part I: pathological conditions.** *Br J Radiol* 2009;82: 426–34 Medline

17. Ogbole G, Soneye M, Okorie C, et al. **Intraventricular cerebrospinal fluid pulsation artifacts on low-field magnetic resonance imaging: potential pitfall in diagnosis?** *Niger Med J* 2016;57:59–63 CrossRef Medline
18. Hakky M, Pandey S, Kwak E, et al. **Application of basic physics principles to clinical neuroradiology: differentiating artifacts from true pathology on MRI.** *Am J Roentgenol* 2013;201:369–77 CrossRef Medline
19. Andre J, Bresnahan B, Mossa-Basha M, et al. **Toward quantifying the prevalence, severity, and cost associated with patient motion during clinical MR examinations.** *J Am Coll Radiol* 2015;12:689–95 CrossRef Medline
20. Dagher AP, Smirniotopoulos J. **Tumefactive demyelinating lesions.** *Neuroradiology* 1996;38:560–65 CrossRef Medline
21. Mabray M, Cohen B, Villanueva-Meyer J, et al. **Performance of apparent diffusion coefficient values and conventional MRI features in differentiating tumefactive demyelinating lesions from primary brain neoplasms.** *AJR Am J Roentgenol* 2015;205:1075–85 CrossRef Medline
22. Atighechi S, Zolfaghari A, Baradaranfar M, et al. **Estimation of sensitivity and specificity of brain magnetic resonance imaging and single photon emission computed tomography in the diagnosis of olfactory dysfunction after head traumas.** *Am J Rhinol Allergy* 2013;27:403–06 CrossRef Medline
23. Wollman D. **Sensitivity and specificity of neuroimaging for the diagnosis of Alzheimer's disease.** *Dialogues Clin Neurosci* 2003;5:89–99 Medline
24. Sabol Z, Resić B, Juraski R, et al. **Clinical sensitivity and specificity of multiple T2-hyperintensities on brain magnetic resonance imaging in diagnosis of neurofibromatosis type 1 in children: diagnostic accuracy study.** *Croat Med J* 2011;52:488–96 CrossRef Medline
25. Polman C, Reingold S, Banwell B, et al. **Diagnostic criteria for multiple sclerosis: 2010 revisions to the McDonald criteria.** *Ann Neurol* 2011;69:292–302 CrossRef Medline
26. Zaitsev M, Maclaren J, Herbst M. **Motion artifacts in MRI: a complex problem with many partial solutions.** *J Magn Reson Imaging* 2015;42:887–901 CrossRef Medline

Determining the Orientation of Directional Deep Brain Stimulation Electrodes Using 3D Rotational Fluoroscopy

P.C. Reinacher, M.T. Krüger, V.A. Coenen, M. Shah, R. Roelz, C. Jenkner, and K. Egger

ABSTRACT

BACKGROUND AND PURPOSE: New deep brain stimulation leads with electrode contacts that are split along their circumference allow steering of the electrical field in a predefined direction. However, imaging-assisted directional stimulation requires detailed knowledge of the exact orientation of the electrode array. The purpose of this study was to evaluate whether this information can be obtained by rotational 3D fluoroscopy.

MATERIALS AND METHODS: Two directional leads were inserted into a 3D-printed plaster skull filled with gelatin. The torsion of the lead tip versus the lead at the burr-hole level was investigated. Then, 3 blinded raters evaluated 12 3D fluoroscopies with random lead orientations. They determined the lead orientation considering the x-ray marker only and considering the overlap of the gaps between the contact segments. Intraclass correlation coefficients and an extended version of the Bland-Altman plot were used to determine interrater reliability and agreement of the measurements of the different raters.

RESULTS: Electrode torsion of up to 35° could be demonstrated. Evaluation of the lead rotation considering the x-ray marker only revealed limits of agreement of ±9.37° and an intraclass correlation coefficient of 0.9975. In addition, taking into account the lines resulting from overlapping of the gaps between the electrode segments, the limits of agreement to the mean were ±2.44° and an intraclass correlation coefficient of 0.9998.

CONCLUSIONS: In directional deep brain stimulation systems, rotational 3D fluoroscopy combined with the described evaluation method allows for determining the exact orientation of the leads, enabling the full potential of imaging-assisted personalized programming.

ABBREVIATION: DBS = deep brain stimulation

Deep brain stimulation (DBS) is an established treatment for movement disorders (eg, Parkinson disease, tremor, and dystonia), drug-resistant epilepsy, and obsessive-compulsive disorder (for which DBS is still regarded experimental).[1-4] The spectrum of indications is currently increasing: Several psychiatric indications are under investigation, including major depression, addiction, Alzheimer disease and dementias, eating disorders, Gilles de la Tourette syndrome, and schizophrenia. Although the stimulation technology stems from the 1970s and has seen little development, the therapeutic window of DBS can be limited by side effects that are caused by inadvertent co-stimulation of structures in the proximity of the targeted regions. Typically, DBS electrodes contained cylindrical contacts. Their activation resulted in roughly spherical stimulation fields around the surface of the contacts, which represent the volume of activated tissue. The potential advantages of current steering between contacts or in defined directions have been anticipated for many years.[5] Recently, DBS electrode leads with electrode contacts that are split into 3 parts along the circumference of the electrode became available.[6,7] Distributing the stimulation among these electrode segments allows steering of the electrical field in a predefined direction. In the subthalamic nucleus, DBS by this approach theoretically allows one to steer the field away from the internal capsule while at the same time allowing a better coverage of the nucleus and relevant pathways (eg, hyperdirect pathway), with a possibly better therapeutic window. Advanced imaging with individualized visualization of target structures is increasingly being used for personalized

Received November 14, 2016; accepted after revision January 23, 2017.

From the Departments of Stereotactic and Functional Neurosurgery (P.C.R., V.A.C.), Neurosurgery (M.T.K., M.S., R.R.), and Neuroradiology (K.E.), and Clinical Trial Unit (C.J.), Freiburg University Medical Center, Freiburg, Germany.

Please address correspondence to Peter C. Reinacher, MD, Department of Stereotactic and Functional Neurosurgery, Freiburg University Medical Center, Freiburg (i.Br.), Germany; e-mail: peter.reinacher@uniklinik-freiburg.de; @p_reinacher

Indicates open access to non-subscribers at www.ajnr.org

http://dx.doi.org/10.3174/ajnr.A5153

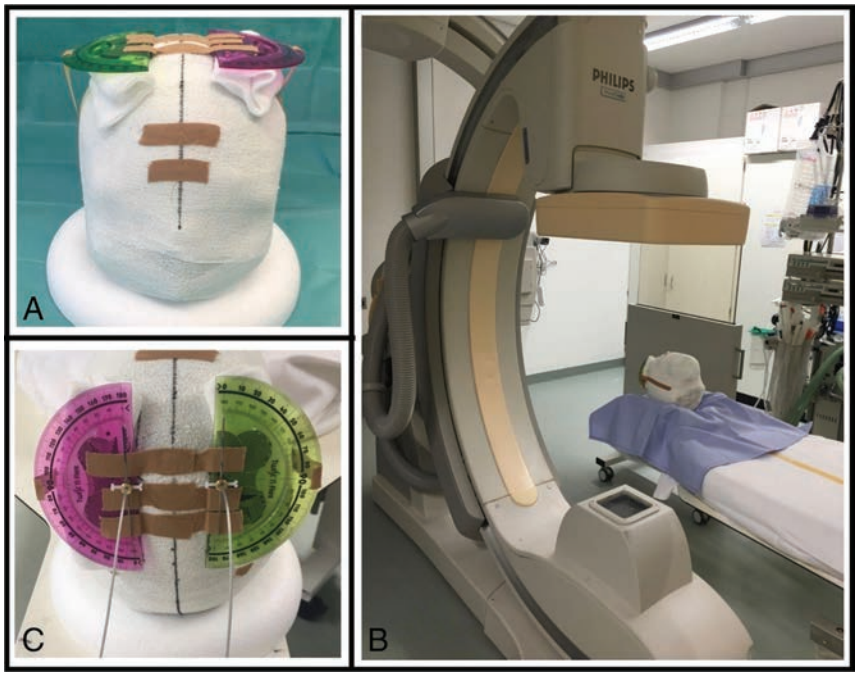

FIG 1. Two directional leads inserted in a 3D-printed plaster head filled with gelatin. At the entry site of the electrodes, a marker was attached in the same orientation as the x-ray marker at the electrode tip. The electrodes were guided through protractors (*A*,*C*), which allows for determining the rotation of each electrode between 0° and 360°(*C*, both oriented at 0°). Figure 1*B* shows the setup in the 3D rotational fluoroscopy.

and direct stimulation planning.[8-11] However, imaging-assisted directional stimulation requires detailed knowledge of the exact orientation of the electrode array with respect to its functional environment. The exact orientation of the segmented leads has to be determined by postoperative imaging because the degree of rotation varies during implantation and fixation of the electrode. Therefore, directional electrodes contain an x-ray marker. However, presently, no imaging technique has been described that sufficiently allows the exact determination of the degree of a possible lead rotation:

- Anteroposterior and lateral x-rays allow only a rough estimation of the lead orientation depending on the angle between the marker and the image plane.
- In a CT scan, the marker generates a large artifact. Under defined, but, however, unrealistic conditions in clinical practice (ie, leads parallel to scanner axis), this artifact could be used to estimate the lead orientation.
- MR imaging is no option because, for now, the available directional DBS systems are not MR-imaging compatible.

We here investigated whether 3D fluoroscopy could serve as the imaging technique of choice to determine the exact degree of lead rotation and orientation of an implanted electrode array.

MATERIALS AND METHODS

Experimental Setup

A 3D-printed plaster skull was filled with gelatin. Two burr-holes were drilled at the typical location for DBS electrode implantation and 2 directional electrodes (Model DB-2202-30; Boston Scientific, Natick, Massachusetts) were inserted. At the entry site of the electrodes, a marker was attached in the same orientation as the fluoroscopy marker at the electrode tip, and the electrodes were guided through protractors (Fig 1*A*, -*C*), which allow for determining the rotation of each electrode between 0° and 360°. (Fig 1*B* shows the setup in the 3D rotational fluoroscopy). We defined the lead orientation with the marker oriented exactly anteriorly as 0°, counting up to 360° with clockwise lead rotation when looking at the lead from above the skull.

Test for Electrode Torsion

To evaluate whether torsion of the electrodes that leads to a difference between orientation of the marker at the burr-hole and the marker at the electrode tip occurs, 1 3D fluoroscopy was obtained after electrode implantation, 1 after rotation of the electrodes 360° clockwise, and 1 after rotation of the electrodes counterclockwise. The orientation of the electrode markers was determined on the 3D fluoroscopy images.

Image Acquisition

In total, 12 3D fluoroscopy rotation scans were obtained via a flat panel detector C-arm system (Allura Xper FD20; Philips Healthcare, Best, the Netherlands). During a −120° to +120° rotation of the C-arm around the phantom, 120 frames were acquired. The rotation time was 4 seconds, and a standard "3D cerebral" protocol was used. The registered dose-area product was 2.327 mGy × cm^2. The flat panel detector system provided a spatial resolution of 0.37 mm.

Determining the Electrode Rotation

A list of 24 random numbers between 1 and 360 was generated (Excel; Microsoft, Redmond, Washington), and the 2 electrodes were rotated for each 3D fluoroscopy according to this list.

Three blinded raters (1 neuroradiologist and 2 neurosurgeons) evaluated the lead rotation on a DICOM Viewer (Philips DICOM Viewer, Version R3.0 SP3; Philips Healthcare). First, they were asked to identify the image in the 3D rotational fluoroscopy where the plaster model with 1 metal marker attached to the inion and 1 to the nasion was depicted exactly in anteroposterior orientation. Then, they used 2 different methods to determine the lead rotation.

Method Using the Marker at the Electrode Tip

The first evaluation was based exclusively on the rotation of the marker at the electrode tip. Each rater evaluated the orientation of the 2 electrodes in the phantom for each of the 12 rotational angiography series. The raters were asked to determine the image with the marker exactly facing to the left side of the screen, facing the rater, and facing to the right side of the screen. The lead orientations were calculated accordingly, and the median values were compared. The agreement of the measurements of the raters was determined by using an extended version of the Bland-Alt-

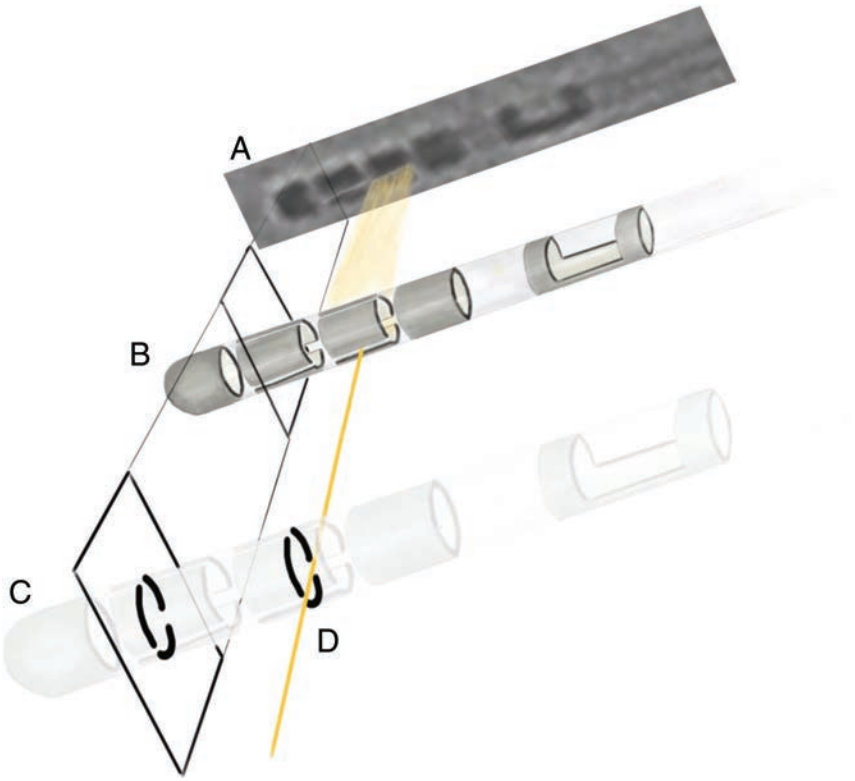

FIG 2. The gaps between the electrode segments can be considered as "iron sights." They overlap when looking at the electrode from defined perspectives, resulting in a visible line (*A*). This line is seen only when the fluoroscopy beam (*D*) hits the electrode from exactly 1 these perspectives (*B*, *C*) and allows a precise definition of the electrode orientation.

man plot[12] to accommodate multiple observers proposed by Jones et al.[13]

The "Iron Sights" Method

Two of the 4 contacts at the tip of the directional leads are split into 3 parts along the circumference of the electrode. When rotating the fluoroscopy around the head model with implanted electrodes, the gaps between these segments overlap in defined angles of view, resulting in a visible line. At lead orientations of exactly 30°, 90°, 150°, 210°, 270°, and 330°, these overlapping gaps can be detected because, at these angles, they align like iron sights in a weapon when aiming at a target (Figs 2 and 3).

The raters were asked to determine the 2 lateral angles of view (looking at the lead from 90° and 270°) and 2 more oblique angles of view (30°, 150°, 210°, or 330°). The lead orientations were calculated accordingly, and the median values were compared. The agreement of the measurements of the raters was determined by using an extended version of the Bland-Altman plot[12] to accommodate multiple observers proposed by Jones et al.[13]

Sample Size

Sample size estimation for the comparison of 2 rater reliabilities or agreement has hardly been investigated to date. A rule of thumb was proposed by Fleiss[14] by using 15–20 samples in reliability studies. Julious[15] found that a sample size of 12 in pilot studies seems reasonable for the generation of pilot data. Given a continuous outcome, increasing the sample size beyond 12 samples per group did not have a profound influence on the confidence interval. Because there was no prior knowledge about the range of reliability, 12 samples with 2 electrodes each, and thus, 24 in total, were investigated.

Statistical Analysis

A random sample of 3 raters was chosen. Every rater measured each of the 24 orientations independently by using 2 different procedures of measurement (marker measurement and "iron sights" measurement). To assess the interrater reliability of the continuous measurements, intraclass correlation coefficients based on 2-way random-effects models were calculated.[16] The 95% confidence intervals of the 2 intraclass correlation coefficients were compared. In addition, an extended version of the Bland-Altman plot[12] to accommodate multiple observers, as proposed by Jones et al,[13] was used to determine agreement of the measurements of different raters. Limits of agreement to the mean of the 3 measurements were calculated for each of the measurements. The limits of agreement were compared descriptively. All analyses were performed by using STATA/IC 12.1 (StataCorp, College Station, Texas).

RESULTS

Electrode Torsion

The orientation of the electrode tip after straight implantation of the lead was +3.8° for the right electrode and +5.4° for the left electrode evaluated when applying the iron sights method. After 360° rotation clockwise, the right electrode tip was oriented at −5.5° and the left at +5.4°. After the rotation of −360° the electrode tips were oriented at +35.0° (right electrode) and +16.0° (left electrode).

Determining the Electrode Rotation

Each rater determined the degree of rotation of the electrode tip for the 2 electrodes in each of the 12 rotational angiography series. The first evaluation was based exclusively on the rotation of the marker. The results and the agreement of the measurements of the raters are shown in Fig 4.

The second evaluation, using the iron sights method, was based on determining the perspectives in which the gaps between the directional electrode segments overlap. Lead orientations were calculated for these perspectives, and the median values were compared. The results and the agreement of the measurements of the raters are shown in Fig 5.

Statistical Analysis

Both procedures of measurement showed a very high interrater reliability. The marker measurement had an intraclass correlation coefficient of 0.9975 (CI, 0.9951–0.9988). The iron sights measurement resulted in an intraclass correlation coefficient of 0.9998

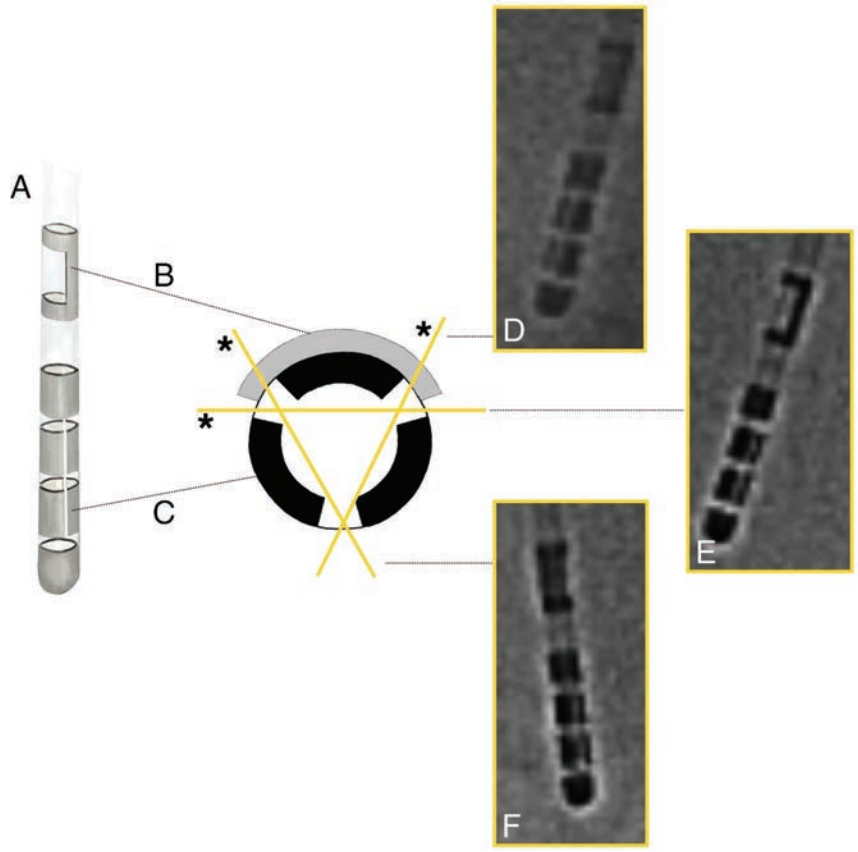

FIG 3. The directional lead (*A*) contains an x-ray marker (*B*) and segmented electrodes. The marker alone does not allow determining the exact lateral or anteroposter perspective. The gaps between the electrode segments overlap only when looking at the electrode from defined perspectives (*D**, 30°, *E*, 90°, *F*, 150°, *D*, 210°, *E**, 270°, and *F**, 330°), resulting in a visible line.

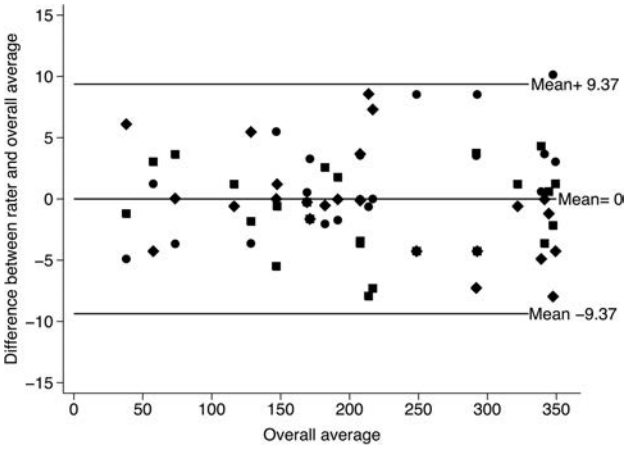

FIG 4. The 3 raters determined the lead orientations for each of the 12 rotational angiography series and 2 electrodes, considering only the x-ray marker. The extended version of the Bland-Altman plot[12] to accommodate multiple observers proposed by Jones et al[13] shows the mean difference between the raters and the overall average versus the overall average. The rotation could be defined between limits of agreement of ±9.37°.

(CI, 0.9997–0.9999). These high values might be the result of the wide range of observational values. Still, the confidence intervals for the 2 intraclass correlation coefficients are not overlapping, indicating a considerable difference between the 2 procedures of measurement.

To additionally assess the agreement of the raters, adjusted Bland-Altman plots were produced. The limits of agreement to the mean (of the 3 raters) for the marker measurement are ±9.37° (ie, 95% of the measurements are in the range of ±9.37° deviation of the mean of the 3 measurements). For the iron sights method, the limits of agreement are ±2.44°. The agreement for the iron sights methods is thus higher because the range of deviation is ±7° smaller than for the marker method.

DISCUSSION

The availability of directional leads offers new possibilities for DBS therapy. Instead of the previous limitation (to apply only spherical stimulation fields around the surface of cylindrical contacts), the configuration of segmented electrodes now allows one to steer the electrical field in a predefined direction. If anatomic structures in the proximity of the lead limit the stimulation of the target region, the possibility to steer the field away from this structure can increase the therapeutic window. The full potential of this new technology includes visualization of anatomic structures responsible for effects and side effects and imaging-assisted personalized programming of the DBS system. DBS programming software integrating this feature is becoming available (eg, the GUIDE System [Boston Scientific]). This new technology requires the knowledge of the exact degree of rotation for each individual electrode to fully exploit these possibilities. One solution would be an exact orientation in a defined direction for all implanted electrodes (eg, 0°). Unfortunately, during the operation, the rotation of the lead cannot be exactly predicted because of several factors. The lead can turn during fixation and when securing the cable under the skin. Correction of the lead rotation by marking the direction of the contact segments at the level of the burr-hole and turning the electrode there does not lead to reliable results, as demonstrated by our test for electrode torsion: electrode rotation (+360° and −360°) resulted in a deviation of −5.5°, +5.4, +35.0°, and +16.0° from the expected orientation (0°) in the rotational 3D fluoroscopies. Therefore, an imaging technique that reliably allows for determining the lead orientation is needed, but has not been described so far. Anteroposterior and lateral x-rays depict the marker only from 2 perspectives, allowing only a rough estimation of the electrode rotation. In CT, the marker generates a large artifact. Bokil et al[17] have investigated in vitro whether the CT signature of the electrode could be used to determine the orientation of the lead. They scanned with 0.6-mm section thickness and 50% overlap. When orienting the lead parallel to the scanner axis, they could determine the rotation with a mean ac-

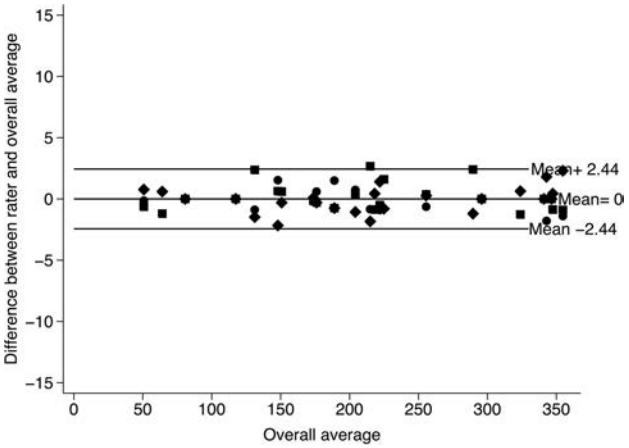

FIG 5. Mean difference between the raters and the overall average versus the overall average of the results applying the "iron sights" method. The rotation could be defined between limits of agreement of ±2.44°.

curacy of less than 3°. However, this setting is not realistic in clinical practice. With the leads oriented in physiologically plausible orientations relative to the scanner axis, the mean accuracy was described as less then 10°. They do not describe the dose of this CT.

Rotational 3D fluoroscopy is typically used to depict aneurysms. Delavallée et al[18] described the application of 3D fluoroscopy for intraoperative control of the positioning of nondirectional DBS leads (Lead 3389; Medtronic, Minneapolis, Minnesota) in 10 patients by image fusion with the preoperative MR imaging scans. This imaging method can also display the marker of directional leads from multiple perspectives. We assumed that determining the best anteroposterior and lateral images of the marker should allow for defining the exact lead orientation. However, during evaluation of the different perspectives of the marker, configured as a C, we found that it is difficult to determine the exact lateral or anteroposterior perspective. The ideal markers should have features like iron sights in a gun, overlapping only when aiming exactly at the target. The gaps between the electrode segments have exactly this feature. They overlap when looking at the electrode from defined perspectives (30°, 90°, 150°, 210°, 270°, and 330°), resulting in a visible line. This line is seen only when the fluoroscopy beam hits the electrode from exactly 1 of the mentioned perspectives and allows a clearer definition of the electrode orientation than looking at the surface of the contacts. In combination with the torsion of the electrodes demonstrated in our first test, this iron sight method gives us a better ground truth than the electrode orientation defined at the protractor at the burr-hole. We hypothesized that if this method is as exact as we assume, there should be a very high interrater reliability. This is supported by the results of our investigation. The limits of agreement were ±2.44°. When using the marker alone to determine the lead orientation, the mean difference between the raters and the overall mean was ±9.37°. The interrater reliability was very high in both methods (the iron sights measurement resulted in an intraclass correlation coefficient of 0.9998 [CI, 0.9997–0.9999]). The marker measurement had an intraclass correlation coefficient of 0.9975 (CI, 0.9951–0.9988). But still, a significant difference was observed.

The limits of agreement only describe the agreement between the raters and do not provide information on the agreement to the true orientation of the electrode. Because the true orientation is unknown and no criterion standard measurement is available, a comparison of the agreement of the 2 measurements would not provide information on the accuracy of the measurements, either. Analyzing the properties of the 2 measurements by using rater reliability and agreement therefore provides helpful information to compare the quality and reproducibility of the measurements. For these criteria, significant differences could be found.

The only disadvantage is the radiation dose to the patient. The dose-area product of the 3D 240° rotational fluoroscopy used in our setup was 2.327 mGy × cm^2, which is comparable with 4 standard skull x-rays with 600 mGy × cm^2 per x-ray (reference values according to Bundesamt für Strahlenschutz). Regarding the effective dose of a head CT, which is approximately 2.3 mSv, the effective dose of a 3D 210° rotational scan with only 0.2 mSv is comparatively low.[19] Because a head CT is an accepted standard diagnostic procedure, the usage of a 3D 210° rotational fluoroscopy scan for providing the required information on each individual DBS electrode rotation, and producing approximately one-tenth of the effective head CT radiation dose, is more than acceptable. Nevertheless, by optimizing the scan parameters, this already low effective radiation dose of the 3D rotational fluoroscopy scan may be decreased even further.

CONCLUSIONS

We could demonstrate that rotational 3D fluoroscopy can obtain the information needed to determine the orientation of the directional leads. However, the built-in marker, configured as a C (Fig 3*B*), does not allow for defining the exact lateral or anteroposterior perspective. Using this marker, the rotation could be defined between limits of agreement of ±9.37°. When using the overlapping gaps between the contacts at defined angles of view like iron sights, the degree of electrode rotation could be determined between limits of agreement of ±2.44°. No other available imaging technique after DBS surgery with directional electrodes (eg, CT and plain x-ray) can determine the electrode orientation in such accuracy. Therefore, rotational 3D fluoroscopy combined with the described (iron sights) evaluation is, in our opinion, the postoperative imaging of choice to enable the full potential of imaging-assisted personalized programming of the directional DBS system.

ACKNOWLEDGMENTS

The scientific work of this study has received no industry funding or other third-party support.

Disclosures: Peter C. Reinacher—*UNRELATED*: *Grants/Grants Pending*: German Ministry for Economic Affairs and Energy*; *Travel/Accommodations/Meeting Expenses Unrelated to Activities Listed:* Boston Scientific, BrainLab.* Volker A. Coenen—*UNRELATED*: *Grants/Grants Pending*: Investigator-initiated trial support, *Comments*: Ongoing IITs with Boston Scientific and Medtronic (limited funding)*; *OTHER*: Clinical collaborative project with BrainLab AG, *Comments*, clinical collaborative project on the Elements software package for evaluation purposes; postdoc position is funded over 3 years. *Money paid to the institution.

REFERENCES

1. Deep-Brain Stimulation for Parkinson's Disease Study Group. **Deep-brain stimulation of the subthalamic nucleus or the pars interna of the globus pallidus in Parkinson's disease.** *N Engl J Med* 2001;345:956–63 CrossRef Medline
2. Deuschl G, Schade-Brittinger C, Krack P, et al. **A randomized trial of deep-brain stimulation for Parkinson's disease.** *N Engl J Med* 2006;355:896–908 CrossRef Medline
3. Benabid AL, Pollak P, Gao D, et al. **Chronic electrical stimulation of the ventralis intermedius nucleus of the thalamus as a treatment of movement disorders.** *J Neurosurg* 1996;84:203–14 CrossRef Medline
4. Vidailhet M, Vercueil L, Houeto JL, et al. **Bilateral deep-brain stimulation of the globus pallidus in primary generalized dystonia.** *N Engl J Med* 2005;352:459–67 CrossRef Medline
5. Butson CR, McIntyre CC. **Current steering to control the volume of tissue activated during deep brain stimulation.** *Brain Stimulat* 2008;1:7–15 CrossRef Medline
6. Pollo C, Kaelin-Lang A, Oertel MF, et al. **Directional deep brain stimulation: an intraoperative double-blind pilot study.** *Brain J Neurol* 2014;137:2015–26 CrossRef Medline
7. Steigerwald F, Müller L, Johannes S, et al. **Directional deep brain stimulation of the subthalamic nucleus: a pilot study using a novel neurostimulation device.** *Mov Disord Off J Mov Disord Soc* 2016;31:1240–43 CrossRef Medline
8. Coenen VA, Rijntjes M, Prokop T, et al. **One-pass deep brain stimulation of dentato-rubro-thalamic tract and subthalamic nucleus for tremor-dominant or equivalent type Parkinson's disease.** *Acta Neurochir (Wien)* 2016;158:773–81 CrossRef Medline
9. Schlaepfer TE, Bewernick BH, Kayser S, et al. **Rapid effects of deep brain stimulation for treatment-resistant major depression.** *Biol Psychiatry* 2013;73:1204–12 CrossRef Medline
10. Coenen VA, Allert N, Mädler B. **A role of diffusion tensor imaging fiber tracking in deep brain stimulation surgery: DBS of the dentato-rubro-thalamic tract (drt) for the treatment of therapy-refractory tremor.** *Acta Neurochir (Wien)* 2011;153:1579–85, discussion 1585 Medline
11. Coenen VA, Allert N, Paus S, et al. **Modulation of the cerebello-thalamo-cortical network in thalamic deep brain stimulation for tremor: a diffusion tensor imaging study.** *Neurosurgery* 2014;75:657–69, discussion 669–70 Medline
12. Bland JM, Altman DG. **Statistical methods for assessing agreement between two methods of clinical measurement.** *Lancet* 1986;1:307–10 CrossRef Medline
13. Jones M, Dobson A, O'Brian S. **A graphical method for assessing agreement with the mean between multiple observers using continuous measures.** *Int J Epidemiol* 2011;40:1308–13 CrossRef Medline
14. Fleiss JL. *The Design and Analysis of Clinical Experiments*. New York: Wiley; 1986
15. Julious SA. **Sample size of 12 per group rule of thumb for a pilot study.** *Pharm Stat* 2005;4:287–91 CrossRef
16. Shrout PE, Fleiss JL. **Intraclass correlations: uses in assessing rater reliability.** *Psychol Bull* 1979;86:420–28 CrossRef Medline
17. Bokil H, Dorman D, Velasco R. Determining the orientation of directional deep brain stimulation leads from computed tomography data. Poster presented at: WSSFN Interim meeting, Mumbai, India. September 3–6, 2015. http://www.epostersonline.com/wssfn2015/node/126. Accessed March 6, 2017
18. Delavallée M, Delaunois J, Ruwet J, et al. **STN DBS for Parkinson's disease: results from a series of ten consecutive patients implanted under general anaesthesia with intraoperative use of 3D fluoroscopy to control lead placement.** *Acta Neurochir (Wien)* 2016;158:1783–88 CrossRef Medline
19. Bridcut RR, Murphy E, Workman A, et al. **Patient dose from 3D rotational neurovascular studies.** *Br J Radiol* 2007;80:362–66 CrossRef Medline

Role of High-Resolution Dynamic Contrast-Enhanced MRI with Golden-Angle Radial Sparse Parallel Reconstruction to Identify the Normal Pituitary Gland in Patients with Macroadenomas

R. Sen, C. Sen, J. Pack, K.T. Block, J.G. Golfinos, V. Prabhu, F. Boada, O. Gonen, D. Kondziolka, and G. Fatterpekar

ABSTRACT

BACKGROUND AND PURPOSE: Preoperative localization of the pituitary gland with imaging in patients with macroadenomas has been inadequately explored. The pituitary gland enhancing more avidly than a macroadenoma has been described in the literature. Taking advantage of this differential enhancement pattern, our aim was to evaluate the role of high-resolution dynamic MR imaging with golden-angle radial sparse parallel reconstruction in localizing the pituitary gland in patients undergoing trans-sphenoidal resection of a macroadenoma.

MATERIALS AND METHODS: A retrospective study was performed in 17 patients who underwent trans-sphenoidal surgery for pituitary macroadenoma. Radial volumetric interpolated brain examination sequences with golden-angle radial sparse parallel technique were obtained. Using an ROI-based method to obtain signal-time curves and permeability measures, 3 separate readers identified the normal pituitary gland distinct from the macroadenoma. The readers' localizations were then compared with the intraoperative location of the gland. Statistical analyses were performed to assess the interobserver agreement and correlation with operative findings.

RESULTS: The normal pituitary gland was found to have steeper enhancement-time curves as well as higher peak enhancement values compared with the macroadenoma ($P < .001$). Interobserver agreement was almost perfect in all 3 planes ($\kappa = 0.89$). In the 14 cases in which the gland was clearly identified intraoperatively, the correlation between the readers' localization and the true location derived from surgery was also nearly perfect ($\kappa = 0.95$).

CONCLUSIONS: This study confirms our ability to consistently and accurately identify the normal pituitary gland in patients with macroadenomas with the golden-angle radial sparse parallel technique with quantitative permeability measurements and enhancement-time curves.

ABBREVIATIONS: ETC = enhancement-time curve; GRASP = golden-angle radial sparse parallel

Hormonal deficiency is a major complication of trans-sphenoidal surgery for pituitary adenomas.[1-3] While the trans-sphenoidal approach offers optimal access to the sellar and suprasellar regions,[4-8] approximately 5% of patients experience new hypopituitarism due to excision of or damage to the normal pituitary gland.[9] In the case of large macroadenomas, this complication is often due to poor visualization of the gland, which is markedly attenuated and displaced by the tumor.

Given the importance of preserving the gland, localization with preoperative imaging will be of use to surgeons. Although dynamic MR imaging is the criterion standard for radiographic evaluation of pituitary adenomas,[10] its role in preoperative localization of the pituitary gland in patients with macroadenomas has not been adequately explored.

Golden-angle radial sparse parallel (GRASP) MR imaging is a new volumetric dynamic technique based on a 3D gradient-echo sequence with radial "stack-of-stars" *k*-space sampling[11,12] and golden-angle ordering.[13,14] The GRASP technique acquires all dynamic information in a single, continuous scan after contrast is introduced. Images are reconstructed iteratively by combining signals from all coils and using compressed sensing,[12,15] which enables reconstructing images from largely undersampled data. These unique characteristics allow GRASP to obtain images with both high spatial and temporal resolution. While GRASP-acquired permeability measurements, including signal-enhancement patterns of the normal pituitary gland, have been demonstrated,[16] its role in the evaluation of macroadenomas has yet to be elucidated.

Received November 11, 2016; accepted after revision January 25, 2017.

From the New York University School of Medicine, NYU Langone Medical Center, New York, New York.

Paper previously presented at: American Society of Neuroradiology Annual Meeting and the Foundation of the ASNR Symposium, April 25–30, 2015; Chicago, Illinois.

Please address correspondence to Girish Fatterpekar, MD, 660 1st Ave, New York, NY 10016; e-mail: girish.fatterpekar@nyumc.org

http://dx.doi.org/10.3174/ajnr.A5244

The purpose of our study, therefore, was to evaluate the role of GRASP MR imaging in localizing the pituitary gland in patients with macroadenomas with 3 readers with vastly varying levels of expertise and to correlate such localization with intraoperative findings.

MATERIALS AND METHODS

Patients

An institutional review board–approved Health Insurance Portability and Accountability Act–compliant study was performed. We retrospectively identified patients with macroadenomas who underwent trans-sphenoidal surgery from November 2014 through November 2015. Of these, only those patients who had undergone preoperative dynamic MR imaging evaluation at our institution with GRASP were considered. Patients who had prior partial or subtotal resection of the macroadenoma were excluded from the study. Seventeen patients were included.

MR Imaging

All patients underwent MR imaging at 3T (Magnetom Skyra; Siemens, Erlangen, Germany) with a 20-channel head/neck coil. Imaging protocol included a coronal radial volumetric interpolated brain examination with a GRASP acquisition (TR/TE, 6.4/2.4 ms; 800 spokes at a 9.5° flip angle; 180 × 180 mm^2 in-plane FOV with a 256 × 256 matrix for a 0.7 × 0.7 mm^2 in-plane resolution at 391-Hz/pixel bandwidth; 32 sections, 0.8-mm-thick each, for a 180-second total acquisition time). This was followed by precontrast sagittal T1 (TR/TE, 440/2.66 ms; 160-mm^2 in-plane FOV; 320^2 matrix; 380-Hz/pixel bandwidth; 90° flip angle; 25 sections 3-mm-thick each), coronal T2 (TR/TE, 4000/97 ms; 15 sections, 2-mm-thick each; 140-mm^2 FOV; 320^2 matrix, at 260-Hz/pixel bandwidth; 150° flip angle), and axial FLAIR sequences (TR/TE/TI, 9000/90/2500 ms; 220-mm^2 FOV; 320^2 matrix; 290-Hz/pixel bandwidth; 150° flip angle; 15 sections, 5-mm-thick each). Gadopentetate dimeglumine (Magnevist; Bayer HealthCare Pharmaceuticals, Wayne, New) contrast material at 0.01 mmol per kilogram of body weight was administered at 4 mL/s on initiation of the GRASP acquisition.

Image Data Analysis and Processing

The acquired data from GRASP scans were exported and reconstructed off-line by using a C++ implementation of the GRASP algorithm, creating 9 dynamic image frames with a temporal resolution of 20 seconds each. Reconstructed images were sent to the PACS and were analyzed by using the software Olea Sphere, Version 2.3 (Olea Medical, La Ciotat, France). Permeability measurements were performed, including enhancement-time curves (ETCs) and peak enhancement.

To ascertain how robust the GRASP image interpretation was to readers' experience, 3 independent readers with vastly varying levels of neuroradiology experience evaluated the images: a medical student, a radiology resident (postgraduate year 4), and an attending neuroradiologist (with 15 years of neuroradiology experience). We evaluated the pituitary gland and macroadenoma by placing 2 ROIs, 1 within each of these 2 locations, and obtained permeability measurements (peak) and ETCs for each. Sagittal reconstructions confirmed the placement of the ROIs within their respective locations. We then compared the location of the gland in 3D between observers and correlated our measurements with the intraoperative location as per the surgeon's operative report.

Statistical Analysis

All statistics were performed in SPSS, Version 23.0 (IBM, Armonk, New York). The analysis was divided into 2 parts. First, the Fleiss κ test was performed on all 17 cases to determine the level of agreement among the 3 readers in rating the gland position in each plane (superior versus inferior, anterior versus posterior, right versus left) and the exact 3D position (eg, right anterosuperior, left posteroinferior, and so forth), irrespective of the operative findings. Subsequently, after we excluded cases in which operative findings of adenoma localization were ambiguous or indeterminate ($n = 4$), we repeated the same Fleiss κ calculation on the remaining 13 cases, comparing our readers' performance with definitive operative findings, both as a group and individually.

RESULTS

During our study period, 17 patients were included. Of these, 7 were women and 10 were men, with an age range of 22–69 years. The macroadenoma size ranged from 3.3 to 37.7 cm^3, with a median of 7.8 cm^3. Only 6 macroadenomas were homogeneous, 10 demonstrated necrosis, and 6 contained hemorrhage. Four of the operative reports did not contain complete localization data and were excluded from the calculation of observer agreement with intraoperative findings. Localization was determined in all 3 planes.

The interobserver agreement in our study was excellent, with a total characterization of $\kappa = 0.89$. The agreement in the transverse and coronal planes was slightly better than that in the sagittal plane: $\kappa = 0.85$, $\kappa = 0.86$, and $\kappa = 0.63$, respectively.

When we compared the readers' preoperative localizations with the operative reports, the overall characterization in all 3 planes was excellent ($\kappa = 0.95$). There was perfect agreement in the coronal and transverse planes, $\kappa = 1.0$, while agreement in the anteroposterior dimension was slightly less at $\kappa = 0.78$.

Evaluation of the ETCs derived from the pituitary gland and the macroadenoma showed greater peak enhancement in the normal gland (1014 versus 635.5, $P < .001$). Also, the ETC was noted to be steeper in the gland compared with the adenoma (Fig 1).

DISCUSSION

Our study demonstrates the role of preoperative, contrast-enhanced dynamic MR imaging to accurately and consistently differentiate the pituitary gland from the macroadenoma. Using GRASP reconstruction, we were able to confirm our localization with quantitative measures such as ETCs and peak enhancement values.

Dynamic contrast-enhanced MR imaging is the criterion standard for evaluating sellar-based lesions.[7-9] In contrast to cases of microadenomas in which identifying the tumor itself is the primary objective, cases of macroadenomas require evaluation of tumor extension into adjacent structures, including supra- and parasellar regions. For the surgeon, in addition to assessing such tumoral extension, localizing the pituitary gland becomes impor-

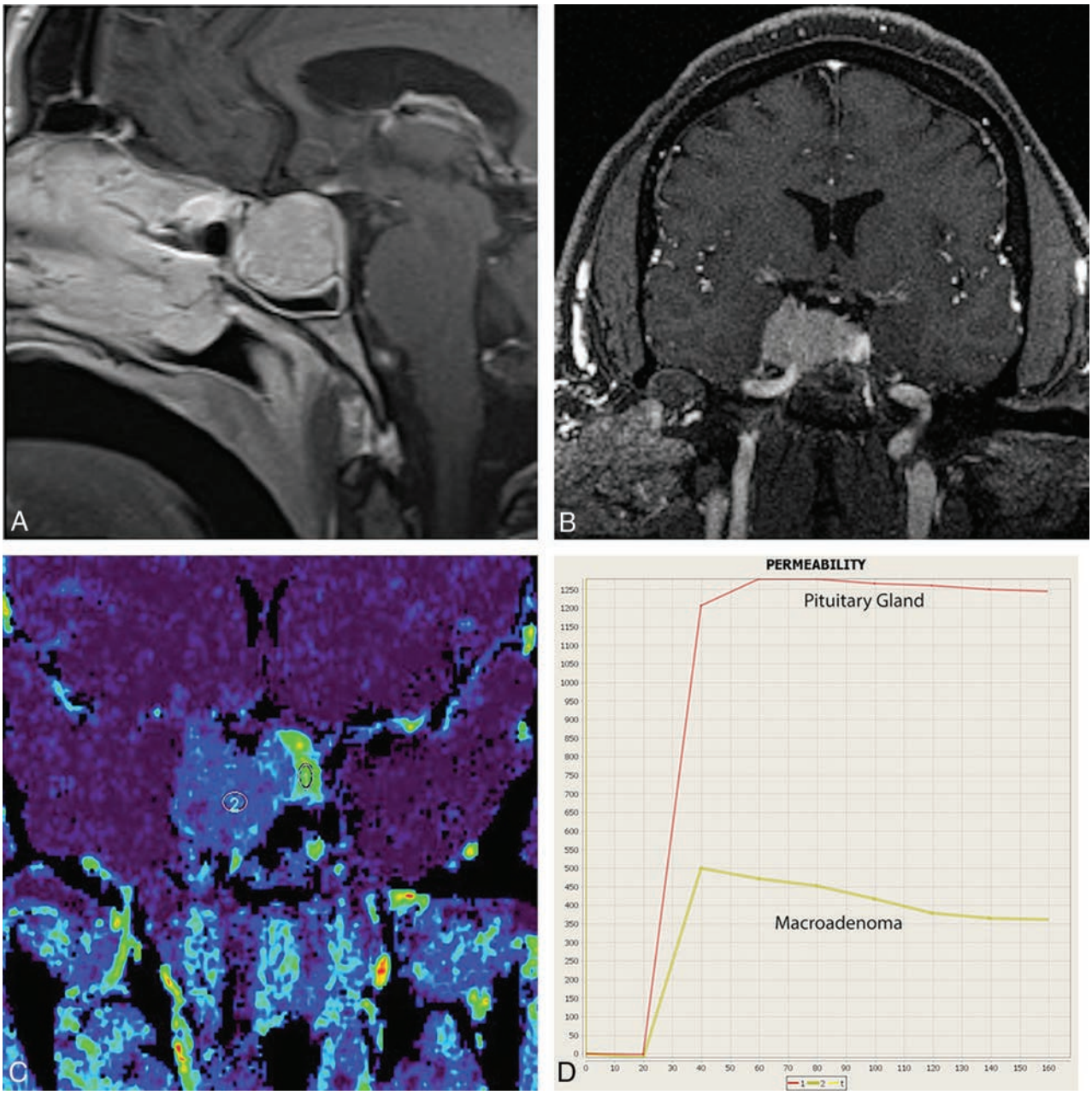

FIG 1. *A*, Contrast-enhanced sagittal T1WI demonstrates a macroadenoma. *B*, GRASP dynamic MR imaging through the sella demonstrates the macroadenoma extending into the right cavernous sinus. A focal area of increased enhancement is seen along the left lateral aspect of the lesions. *C*, Postprocessed MR permeability peak scan demonstrates a focal area of increased contrast uptake (ROI 1) from the left lateral aspect of the sella compared with the macroadenoma (ROI 2). *D*, The enhancement-time curve confirms that the normal pituitary gland, localized along the left lateral aspect of the sella, enhances earlier and more robustly than the macroadenoma.

tant to minimize hormonal deficiency postoperatively. Such preoperative localization of the pituitary gland can be challenging.

The GRASP 3D gradient-echo MR imaging sequence for dynamic imaging provides the reader with markedly enhanced spatial and temporal resolution compared with conventional dynamic MR imaging sequences. This study aimed to take advantage of these improved features to preoperatively localize the pituitary gland distinct from macroadenomas and to confirm such localization with intraoperative findings.

Using permeability measures, we found minimal interobserver variability in identifying the gland within the macroadenoma in both the coronal and sagittal planes. The κ score in the anteroposterior dimension was slightly lower at $\kappa = 0.63$, which we believe is due to our limitations in viewing the most appropriate section in the sagittal plane. Overall, these results highlight the reliability of this tool in identifying the pituitary gland. Furthermore, the range of training levels among the 3 readers emphasizes the ease of use of the software.

An additional benefit to this study was in its use of ETCs to validate the ROI placement. It is well-known that the pituitary gland is more avidly contrast-enhancing than the macroadenoma.[17-19] This feature is likely due to the differences in the vasculature of the normal and adenomatous pituitary tissue. Several previous studies have shown histologically that the normal

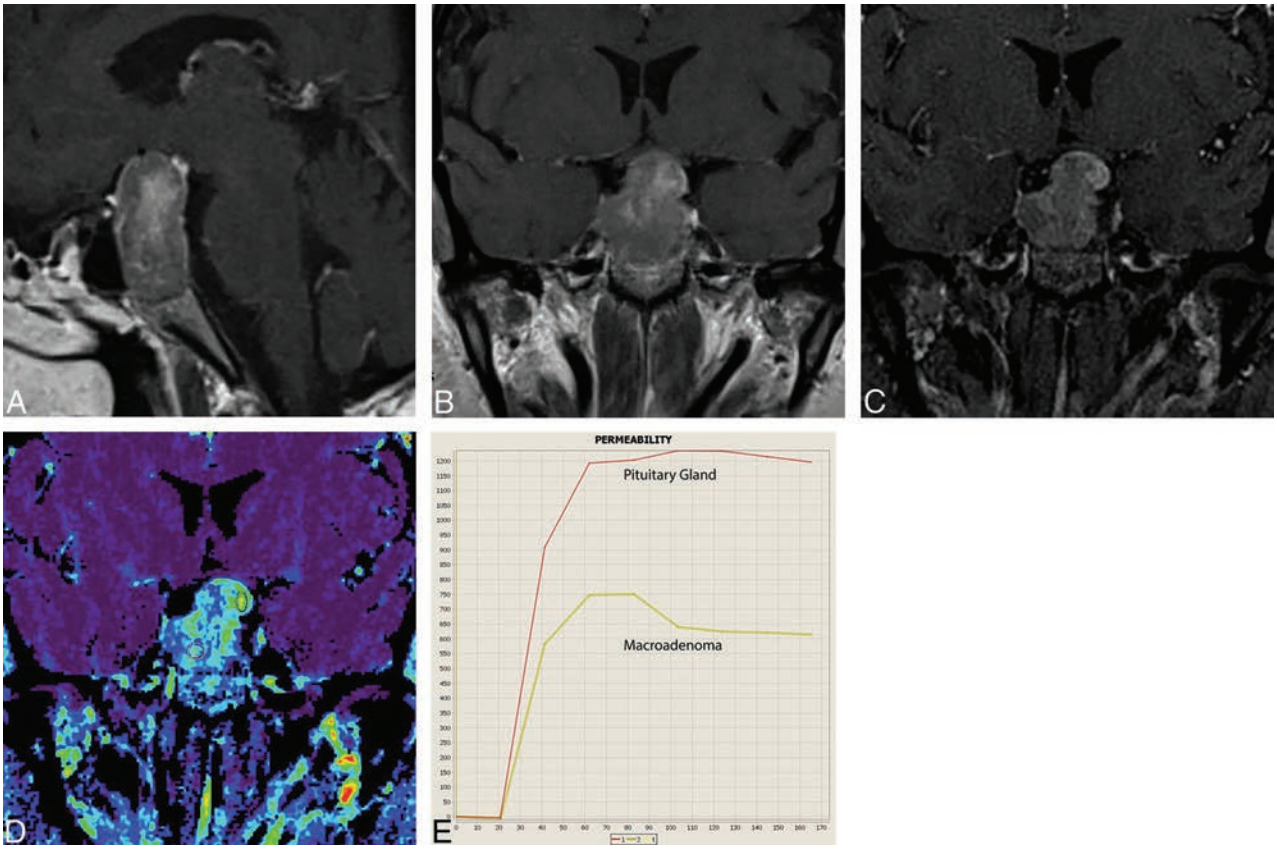

FIG 2. *A*, Contrast-enhanced sagittal T1WI through the sella demonstrates a heterogeneously enhancing lesion expanding the sella and extending into the suprasellar compartment, suggestive of a macroadenoma. *B*, Contrast-enhanced coronal T1WI demonstrates the macroadenoma. The heterogeneous enhancement within the lesion makes it difficult to localize the pituitary gland. *C*, GRASP dynamic study at 90 seconds (early dynamic phase) demonstrates more prominent enhancement along the left superolateral aspect of the lesion. *D*, Wash-in permeability study with ROIs placed within the central, heterogeneous portion of the lesion (ROI 2) and the more avidly enhancing region seen along its left superolateral aspect (ROI 1). *E*, Enhancement-time curves demonstrate a difference in rate and peak contrast uptake for each ROI. The ROI from the more avidly enhancing component seen along the left superolateral aspect of the lesion demonstrates a more pronounced peak enhancement than the more central, heterogeneously enhancing component. These curves validate that the pituitary gland is localized along the left superolateral aspect of this lesion, which was also confirmed at the operation.

pituitary gland is more highly vascularized than a pituitary adenoma.[20,21] Furthermore, more recent studies have used objective mathematic models to prove that the vascular supply to the normal pituitary gland is a more complex and well-organized microvascular network than that of a pituitary adenoma.[22,23] This feature subsequently leads to more robust blood flow to the normal pituitary gland and presumably more avid contrast enhancement. We were able to use this inherent difference between the 2 tissues to support our ROI placement because the ETC for the pituitary gland had a significantly greater peak enhancement and a relatively steeper slope than that of the macroadenoma. The use of ETCs can be particularly useful when confronted with heterogeneously enhancing macroadenomas, in which the normal gland is difficult to visualize with the naked eye (Fig 2).

After establishing reader agreement, we assessed our accuracy using intraoperative findings as a representation of the true gland location within the tumor. When we compared the readers' localizations with the intraoperative locations, 4 of the 17 cases were excluded, given the uncertainty in the operating room regarding the pituitary gland location. Analysis of the remaining 13 cases led to $\kappa = 0.95$ between readers and intraoperative findings. In fact, all 3 readers were perfect in identifying the pituitary gland in the coronal and transverse planes with variability occurring only in the sagittal plane. These results validate the ability of readers with various degrees of experience to use the GRASP MR imaging sequence and ETCs to accurately identify the pituitary gland in patients with macroadenomas.

To further validate this largely qualitative method of gland localization, we compared the quantitative measurement of peak enhancement between the pituitary gland and a macroadenoma. As predicted, the pituitary gland had a statistically higher mean peak contrast value compared with the tumor (1014 versus 635.5).

To our knowledge, only 1 previous study using dynamic MR imaging has tried to localize the pituitary gland in patients with macroadenomas.[24] Using dynamic MR imaging and multidetector-row CT imaging, this group found that they were able to correctly identify the gland in 28 of 33 cases. However, the authors relied solely on subjective visualization of the preoperative scan. There was no quantitative measure confirmation. In addition, the authors did not mention the mean size of the macroadenomas in their patient population. This is an important consideration because normal pituitary gland localization can be difficult in larger macroadenomas; hence, submillimeter voxel thickness is of great

importance when acquiring the data. In the aforementioned study, 3-mm-thick sections were used for performing dynamic studies.

The implications of our results cover a range of areas, which include facilitating surgical planning, influencing better endocrine outcomes, and minimizing operative time, which can lead to an overall reduction of costs. Furthermore, this work has value for alternative therapeutic approaches, including pituitary tumor stereotactic radiosurgery.

Limitations to this study include its retrospective nature and the small sample size of 17 patients. Also, for particularly large macroadenomas of >4 cm in the craniocaudal dimension, evaluation of the gland was more challenging. Another limitation is the potential for the normal pituitary gland to shift intraoperatively, leading to a false preoperative localization. Last, the software used limited our ability to view the normal gland in the sagittal plane, making anteroposterior localization more variable. We plan to continue the work with a prospective study of a larger cohort along with exploring the role of this MR sequence in intraoperative navigation.

CONCLUSIONS

To our knowledge, clear identification of the pituitary gland in patients with macroadenoma has not been thoroughly studied, most likely due to the limitations in the resolution of current MR imaging sequences. Given that endocrine insufficiency is the most common complication of trans-sphenoidal surgery for macroadenomas, accurate localization of the gland preoperatively may provide surgeons with valuable information to preserve endocrine function. We have demonstrated the utility of dynamic GRASP MR imaging in successfully localizing the pituitary gland in patients with macroadenomas, and we supported our findings with quantitative permeability measurements.

Disclosures: Kai Tobias Block—*UNRELATED*: *Patents (Planned, Pending or Issued)*: New York University GRASP patent, *Comments*: New York University holds a patent on the GRASP technique, which was used in this study. This patent has not generated financial income.* John G. Golfinos—*UNRELATED*: *Consultancy*: Major League Baseball Players' Association, *Comments*: head injury consultant; *Stock/Stock Options*: ViewRay and Surgical Theater, *Comments*: ViewRay is a MRI-guided linear accelerator; Surgical Theater is a 3D display of surgical anatomy; neither conflict is relevant in any way to this article. Oded Gonen—*UNRELATED*: *Employment*: New York University School of Medicine. Douglas Kondziolka—*OTHER*: I receive research support from Brainlab for an unrelated project that evaluates brain tumor neuroimaging after radiosurgery. *Money paid to the institution.

REFERENCES

1. Ciric I, Ragin A, Baumgartner C, et al. **Complications of transsphenoidal surgery: results of a national survey, review of the literature, and personal experience.** *Neurosurgery* 1997;40:225–36; discussion 236–37 CrossRef Medline
2. Ciric I, Mikhael M, Stafford T, et al. **Transsphenoidal microsurgery of pituitary macroadenomas with long-term follow-up results.** *J Neurosurg* 1983;59:395–401 CrossRef Medline
3. Chabot JD, Chakraborty S, Imbarrato G, et al. **Evaluation of outcomes after endoscopic endonasal surgery for large and giant pituitary macroadenoma: a retrospective review of 39 consecutive patients.** *World Neurosurg* 2015;84:978–88 CrossRef Medline
4. Zhao B, Wei YK, Li GL, et al. **Extended transsphenoidal approach for pituitary adenomas invading the anterior cranial base, cavernous sinus, and clivus: a single-center experience with 126 consecutive cases.** *J Neurosurg* 2010;112:108–17 CrossRef Medline
5. Pinar E, Yuceer N, Imre A, et al. **Endoscopic endonasal transsphenoidal surgery for pituitary adenomas.** *J Craniofac Surg* 2015;26:201–05 CrossRef Medline
6. Juraschka K, Khan OH, Godoy BL, et al. **Endoscopic endonasal transsphenoidal approach to large and giant pituitary adenomas: institutional experience and predictors of extent of resection.** *J Neurosurg* 2014;121:75–83 CrossRef Medline
7. Hofstetter CP, Shin BJ, Mubita L, et al. **Endoscopic endonasal transsphenoidal surgery for functional pituitary adenomas.** *Neurosurg Focus* 2011;30:E10 CrossRef Medline
8. Ceylan S, Koc K, Anik I. **Endoscopic endonasal transsphenoidal approach for pituitary adenomas invading the cavernous sinus.** *J Neurosurg* 2010;112:99–107 CrossRef Medline
9. Fatemi N, Dusick JR, Mattozo C, et al. **Pituitary hormonal loss and recovery after transsphenoidal adenoma removal.** *Neurosurgery* 2008;63:709–18; discussion 718–19 CrossRef Medline
10. Lee HB, Kim ST, Kim HJ, et al. **Usefulness of the dynamic gadolinium-enhanced magnetic resonance imaging with simultaneous acquisition of coronal and sagittal planes for detection of pituitary microadenomas.** *Eur Radiol* 2012;22:514–18 CrossRef Medline
11. Chandarana H, Block TK, Rosenkrantz AB, et al. **Free-breathing radial 3D fat-suppressed T1-weighted gradient echo sequence: a viable alternative for contrast-enhanced liver imaging in patients unable to suspend respiration.** *Invest Radiol* 2011;46:648–53 CrossRef Medline
12. Chandarana H, Feng L, Block TK, et al. **Free-breathing contrast-enhanced multiphase MRI of the liver using a combination of compressed sensing, parallel imaging, and golden-angle radial sampling.** *Invest Radiol* 2013;48:10–16 CrossRef Medline
13. Winkelmann S, Schaeffter T, Koehler T, et al. **An optimal radial profile order based on the Golden Ratio for time-resolved MRI.** *IEEE Trans Med Imaging* 2007;26:68–76 CrossRef Medline
14. Feng L, Grimm R, Block KT, et al. **Golden-angle radial sparse parallel MRI: combination of compressed sensing, parallel imaging, and golden-angle radial sampling for fast and flexible dynamic volumetric MRI.** *Magn Reson Med* 2014;72:707–17 CrossRef Medline
15. Usman M, Atkinson D, Odille F, et al. **Motion corrected compressed sensing for free-breathing dynamic cardiac MRI.** *Magn Reson Med* 2013;70:504–16 CrossRef Medline
16. Rossi Espagnet MC, Bangiyev L. **High-resolution DCE-MRI of the pituitary gland using radial k-space acquisition with compressed sensing reconstruction.** *AJNR Am J Neuroradiol* 2015;36:1444–49 CrossRef Medline
17. Miki Y, Matsuo M, Nishizawa S, et al. **Pituitary adenomas and normal pituitary tissue: enhancement patterns on gadopentetate-enhanced MR imaging.** *Radiology* 1990;177:35–38 CrossRef Medline
18. Yuh WT, Fisher DJ, Nguyen HD, et al. **Sequential MR enhancement pattern in normal pituitary gland and in pituitary adenoma.** *AJNR Am J Neuroradiol* 1994;15:101–08 Medline
19. Lundin P, Bergström K. **Gd-DTPA-enhanced MR imaging of pituitary macroadenomas.** *Acta Radiol* 1992;33:323–32 Medline
20. Schechter J. **Ultrastructural changes in the capillary bed of human pituitary tumors.** *Am J Pathol* 1972;67:109–26 Medline
21. Gorczyca W, Hardy J. **Microadenomas of the human pituitary and their vascularization.** *Neurosurgery* 1988;22:1–6 Medline
22. Di Ieva A, Weckman A, Di Michele J, et al. **Microvascular morphometrics of the hypophysis and pituitary tumors: from bench to operating theatre.** *Microvasc Res* 2013;89:7–14 CrossRef Medline
23. Di Ieva A, Grizzi F, Ceva-Grimaldi G, et al. **Fractal dimension as a quantitator of the microvasculature of normal and adenomatous pituitary tissue.** *J Anat* 2007;211:673–80 CrossRef Medline
24. Miki Y, Kanagaki M, Takahashi JA, et al. **Evaluation of pituitary macroadenomas with multidetector-row CT (MDCT): comparison with MR imaging.** *Neuroradiology* 2007;49:327–33 CrossRef Medline

Proton Chemical Shift Imaging Study of the Combined Antiretroviral Therapy Impact on Neurometabolic Parameters in Chronic HIV Infection

J. Boban, D. Kozic, V. Turkulov, D. Lendak, M. Bjelan, M. Semnic, and S. Brkic

ABSTRACT

BACKGROUND AND PURPOSE: The introduction of combination antiretroviral therapy has failed to reduce the high prevalence of mild forms of HIV-associated neurocognitive disorders. The aim of this study was to test the effect of combined antiretroviral therapy on brain metabolite ratios in chronic HIV infection by using proton chemical shift imaging.

MATERIALS AND METHODS: We performed 2D chemical shift imaging in 91 subjects (31 HIV+ patients with chronic infection on combination antiretroviral therapy, 19 combination antiretroviral therapy–naïve HIV+ subjects with chronic infection, and 41 healthy controls), covering frontal and parietal subcortical white and cingulate gyrus gray matter, analyzing ratios of NAA/Cr and Cho/Cr on long-TE and mIns/Cr on short-TE MR spectroscopy. We correlated neurometabolic parameters with immunologic, clinical, data and combined antiretroviral therapy efficacy scores.

RESULTS: There was a significant decrease in NAA/Cr ($P < .05$) in HIV-positive patients on and without combined antiretroviral therapy, compared with healthy controls in all locations. There were significant differences in Cho/Cr ($P < .05$) and mIns/Cr ($P < .05$) ratios between HIV+ patients on and without therapy, compared with healthy controls, but these differed in distribution. There were no significant differences in brain metabolite ratios between the 2 groups of chronically HIV-infected patients. The CNS penetration efficacy score showed weak positive correlations only with Cho/Cr ratios in some locations.

CONCLUSIONS: The impact of combined antiretroviral therapy on the process of neuronal loss and dysfunction in chronic HIV infection appears to be suboptimal in successful peripheral suppression of viral replication. Spectroscopic imaging might be a useful tool for monitoring the effects of different combined antiretroviral therapy regimens on brain metabolite ratios.

ABBREVIATIONS: ACG = anterior cingulate gyrus; ANI = asymptomatic neurocognitive impairment; cART = combined antiretroviral therapy; CPE = CNS penetration efficacy index; FDWM = frontal deep white matter; FSWM = frontal subcortical white matter; HAND = HIV-associated neurocognitive disorders; PCG = posterior cingulate gyrus; PSWM = parietal subcortical white matter

Combined antiretroviral therapy (cART) has substantially altered the clinical course and epidemiology of HIV infection during the past decade.[1] cART has been revolutionary in the control of peripheral viral replication and has reduced the high prevalence of HIV-associated neurocognitive disorders (HAND). HAND includes a variety of neurologic disorders ranging from asymptomatic neurocognitive impairment (ANI) and mild neurocognitive disorders to HIV-associated dementia.[2] Nevertheless, recent studies suggest that in stable, chronic HIV infection, neurologic and cognitive symptoms persist or even progress despite cART introduction.[3,4]

cART is thought to improve the clinical course of HAND by suppressing peripheral and CNS viral replication and by normalizing the level of CD4+ T-cells.[5-7] Although cART has greatly reduced the prevalence of HIV-associated dementia, the prevalence of 2 milder forms remains practically unaltered.[8] Current theories on the pathogenesis of HAND suggest that early HIV invasion of the brain initiates a cascade of inflammation and neuronal injury, through toxic viral factors and/or activation of the host immune system, which even amplifies neuronal damage. Also, it is hypothesized that the process of neurodegeneration and inflammation can be attenuated to a degree after initiation of cART.[7,9]

Proton MR spectroscopy is a useful tool in the detection of

Received October 3, 2016; accepted after revision January 27, 2017.

From the Faculty of Medicine (J.B., D.K., M.B.), University of Novi Sad, Vojvodina Institute of Oncology, Diagnostic Imaging Center, Novi Sad, Serbia; Faculty of Medicine (V.T., D.L., S.B.), University of Novi Sad, Clinical Center of Vojvodina, Clinic for Infectious Diseases, Novi Sad, Serbia; and Faculty of Medicine (M.S.), University of Novi Sad, Clinical Center of Vojvodina, Clinic for Neurology, Novi Sad, Serbia.

Please address correspondence to Jasmina Boban, MD, Put dr Goldmana 4, 21204 Sremska Kamenica, Serbia; e-mail: jasmina.boban@mf.uns.ac.rs

Indicates article with supplemental on-line tables.

http://dx.doi.org/10.3174/ajnr.A5160

Demographic, clinical, and lifestyle data on the observed groups of patients

Variables	HIV+ Patients on cART	HIV+ Therapy-Naïve Patients	Healthy Controls	*P* Value
No.	31	19	41	
Men (No.) (%)	28 (90.32)	17 (89.47)	37 (90.24)	.98
Women (No.) (%)	3 (9.68)	2 (10.53)	4 (9.76)	.98
Age (yr)	41.35 ± 9.66, 25–56	36.53 ± 8.15, 25–52	38.57 ± 6.97, 27–53	.09
Nicotine smoking (No.) (%)	11 (39.28)	8 (42.11)	17 (46.41)	.43
Marijuana smoking (No.) (%)	2 (7.14)	1 (5.3)	–	–
Years of education[a]	10.84 ± 2.91, 4–16	11.79 ± 2.82, 4–17	12.72 ± 3.32, 4–18	.22
Self-reported infection duration[a]	6.44 ± 4.36, 1–16	6.26 ± 4.36, 1–15	–	.89
Duration of cART (yr)[a]	5.1 ± 3.81, 1–16	–	–	–
Nadir CD4+ count (cells/μL)[a]	199.28 ± 140.134, 1–487	228.26 ± 145.29, 11–420	–	.48
Current CD4+ count (cells/μL)[a]	620.28 ± 254.36, 147–1119	205.53 ± 192.91, 11–580	–	<.001
CPE[a]	8.26 ± 0.89, 6–10	–	–	–

Note:— – indicates not applicable.

[a] All values are expressed as mean or minimum–maximum.

longitudinal subtle cerebral metabolite changes in cognitively impaired HIV+ patients.[10] A classic pattern of changes in the chronic HIV infection pattern consists of decreased *N*-acetylaspartate (NAA, a neuronal density marker), increased choline-containing metabolites (Cho, a marker of cell membrane metabolism and inflammation), and increased myo-inositol (mIns, a marker of glial proliferation and inflammation).[11-13]

The aim of this study was to test the potential benefit of cART in the control of neurodegenerative processes reflected in changes in chronic HIV-positive (HIV+) patients on and without cART. For the purpose of detailed and region-specific analysis, we used 2D chemical shift spectroscopic imaging, targeting subcortical frontal and parietal white matter and cingular gray matter.

MATERIALS AND METHODS

Subject Selection

The study was conducted on 91 subjects, divided into 3 groups: 31 chronic HIV+ patients receiving cART (28 men and 3 women; mean age, 41.35 ± 9.66 years; range, 25–56 years) and 19 chronically HIV-infected, therapy-naïve subjects (17 men and 2 women; mean age, 36.53 ± 8.15 years; range, 25–52 years). The control group consisted of 41 age-, sex- and education level–matched subjects (37 men and 4 women; mean age, 38.57 ± 6.97 years; range, 27–53 years). Both groups of HIV+ patients were chronically infected (>1 year after transmission). The second group of patients were without cART due to former CD4+ count criteria (11 patients) and the presence of active opportunistic infection that needed to be treated before the introduction of cART (8 patients). However, the current European AIDS Clinical Society guidelines recommend that all HIV+ subjects commence cART independent of CD4+ counts.[14] Patients who have been continuously on cART had undetectable plasma viral loads (<40 copies/mL).

The study was approved by the ethics committee of the Faculty of Medicine, University of Novi Sad, and all the subjects signed a fully informed written consent.

Inclusion criteria for HIV+ subjects were the following: the presence of HIV infection verified by polymerase chain reaction testing and conventional MR imaging showing no focal or diffuse white matter lesions. Exclusion criteria included the following: active opportunistic infection, active neurologic illness, active usage of drugs of abuse, hepatitis B or C coinfection, the presence of white matter lesions, and contraindications for MR imaging. No subjects were excluded from the study.

Basic clinical data on the HIV+ subjects were obtained from laboratory testing (current CD4+ counts). Additionally, we collected the data on nadir CD4+ counts for all the HIV+ patients. The duration of infection was self-reported by every HIV+ patient.

Anamnestic data on the use of recreational drugs (cannabinoids, marijuana), psychostimulants (methamphetamine), alcohol, and nicotine smoking were obtained for all participants. Clinical data on CD4+ counts, nadir CD4+ counts, infection duration, and CNS penetration efficacy index (CPE) of cART are shown in the Table.

Multivoxel MR Spectroscopy

Conventional MR imaging was performed on a 3T MR imaging scanner (Tim Trio; Siemens, Erlangen, Germany) with a matrix head coil. The imaging protocol consisted of sagittal, T1-weighted, spin-echo (TR/TE, 440/3.8 ms; section thickness, 5 mm; duration time, 2 minutes); axial, T2-weighted, turbo spin-echo (TR/TE, 5150/105 ms; section thickness, 5 mm; duration time, 2 minutes 57 seconds); axial fluid-attenuated inversion recovery (TR/TE, 8000/101 ms; section thickness, 5 mm; duration time, 3 minutes 30 seconds); diffusion-weighted imaging (TR/TE, 4100/91 ms; section thickness, 5 mm; duration time, 2 minutes 7 seconds); coronal, T2-weighted TSE (TR/TE, 7150/111 ms; section thickness, 5 mm; duration time, 2 minutes 17 seconds); and 3D T1-weighted multiplanar reconstruction sequences (TR/TE, 1530/2.97 ms; section thickness, 1 mm; duration time, 5 minutes 12 seconds).

We performed 2D chemical shift imaging for each participant, placing the voxel network in the supraventricular white and gray matter of the frontal and parietal lobes. Imaging datasets were acquired with point-resolved spectroscopy by using long (TR/TE, 1700/135 ms) and short (TR/TE, 1700/30 ms) TEs. Chemical shift imaging slab size features were the following: FOV, 160 × 160 × 10 mm; VOI, 80 × 80 × 10 mm; thickness, 10 mm. Chemical shift imaging slab was positioned parallel to the axial images. There were 16 phase-encoding steps (scan resolution) in all directions (right-left, anteroposterior, foot-head), resulting in a VOI of 10 × 10 × 10 mm and a scan time of 8 minutes 17 seconds (we applied a weighted phase-encoding scheme). Six saturation regions were manually positioned along the margin of the VOI. The automatic,

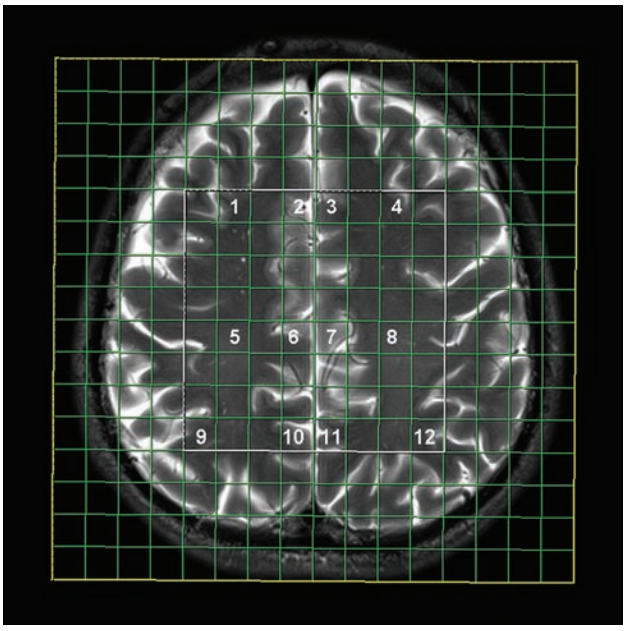

FIG 1. Multivoxel MR spectroscopy voxel network with labeled observed locations: 1) FSWM on the right, 2) ventral ACG on the right, 3) ventral ACG on the left, 4) FSWM on the left, 5) FDWM on the right, 6) dorsal ACG on the right, 7) dorsal ACG on the left, 8) FDWM on the left, 9) PSWM on the right, 10) PCG on the right, 11) PCG on the left, and 12) PSWM on the left).

volume-selective shimming method was used to optimize homogeneity of the magnetic field. The ROI was positioned identically in every subject to achieve the reproducibility (placement was performed by a single experienced radiologist), while analyzed voxel positions were chosen manually.

The spectra were imported to a Leonardo workstation (Siemens), where dedicated manufacturer software for spectroscopy was applied for baseline corrections, peak identification, and calculation of the ratios throughout the voxels.

Data Analysis

We analyzed spectra obtained on long- and short-TE MR spectroscopy from 12 different voxels in the brain: 1) the frontal subcortical white matter (FSWM) of the right hemisphere, 2) the gray matter of the ventral anterior cingulate gyrus (ACG) of the right hemisphere, 3) the gray matter of the ventral ACG of the left hemisphere, 4) the FSWM of the left hemisphere, 5) the frontal deep white matter (FDWM) of the right hemisphere, 6) the dorsal ACG of the right hemisphere, 7) the dorsal ACG of the left hemisphere, 8) the FDWM of the left hemisphere, 9) the parietal subcortical white matter (PSWM) of the right hemisphere, 10) the gray matter of the posterior cingulate gyrus (PCG) of the right hemisphere, 11) the PCG gray matter of the left hemisphere, and 12) the PSWM of the left hemisphere (Fig 1). We analyzed >6500 spectra.

Characteristic signals included in the analysis were NAA at 2.02 ppm, Cho at 3.2 ppm, and mIns at 3.5 ppm. Ratios of NAA/Cr, Cho/Cr, and mIns/Cr were calculated.

Statistical Analysis

Statistical calculations were performed by using SPSS software (Version 21.0; IBM, Armonk, New York). Because all variables followed normal distribution, we determined mean values, SD, and range. Intergroup differences (HIV+ subjects on cART, cART-naive HIV+ subjects, and healthy controls) in acquired metabolite ratios were evaluated by using analysis of variance with the post hoc Tukey honest significant difference test to determine the differences among the groups. We used *t* tests to analyze the differences in current CD4+ counts, infection duration, and nadir CD4+ counts between HIV+ subjects on and without therapy. Correlations between MR spectroscopy ratios and CPE, as well as with current CD4+ counts, were performed by using the Pearson linear correlation. Statistical significance was set at $P < .05$. Because all subjects in our study were scanned with a single scanner, there were no potential scanner-dependent differences.

RESULTS

Subject Features

The age of subjects did not differ significantly among groups ($P = .098$). Considering level of education expressed in years, no significant difference among the subgroups was observed ($P = .22$). HIV+ subjects had been receiving antiretroviral therapy for a mean of 5.1 years (range, 1–16 years), with a mean CPE index of 8.26 ± 0.89. The mean self-reported duration of infection for this group of patients was 6.44 years (range, 1–16 years). HIV+ therapy-naïve subjects were all chronically infected (>1 year after transmission), with a mean self-reported duration of infection of 6.26 years (range, 1–15 years). The 2 groups of HIV+ subjects were similar with respect to infection duration ($P = .89$). In addition, the groups did not differ significantly regarding the nadir CD4+ counts either ($P = .48$). The current CD4+ count for the treated group was 620.28 ± 254.36 cells/μL; and for the therapy-naïve group, 205.53 ± 192.91 cells/μL ($P < .001$). We divided HIV+ patients in 3 groups according to current CD4+ counts: <200 cells/mL, 201–400 cells/mL, and >401 cells/mL. Nicotine smoking was self-reported by 11 (39.28%) HIV+ subjects on cART, 8 HIV+ patients without cART (42.11%), and 17 (41.46%) healthy controls. There were no significant correlations of nicotine use or any metabolite ratios in any of the observed locations. Three HIV+ subjects reported occasional use of marijuana, while no subjects reported active alcohol or drug abuse (no history of drug or alcohol abuse was obtained either). Demographic and clinical characteristics of the subjects are shown in the Table.

Metabolite Ratios

NAA/Cr Ratios. We observed significantly lower NAA/Cr ratios in HIV+ patients compared with healthy subjects in all observed locations (On-line Table 1). Separate analyses among groups revealed that chronically infected HIV+ patients both on and without cART showed significantly lower NAA/Cr levels in all observed locations compared with controls. However, there were no differences between HIV+ patients on and without therapy in NAA/Cr ratios (On-line Table 2). Figures 2 and 3 show long-TE spectra in HIV+ patients on cART (Fig 2) and therapy-naïve HIV+ patients (Fig 3), with a significant reduction in NAA/Cr levels.

There were no significant correlations between NAA/Cr levels

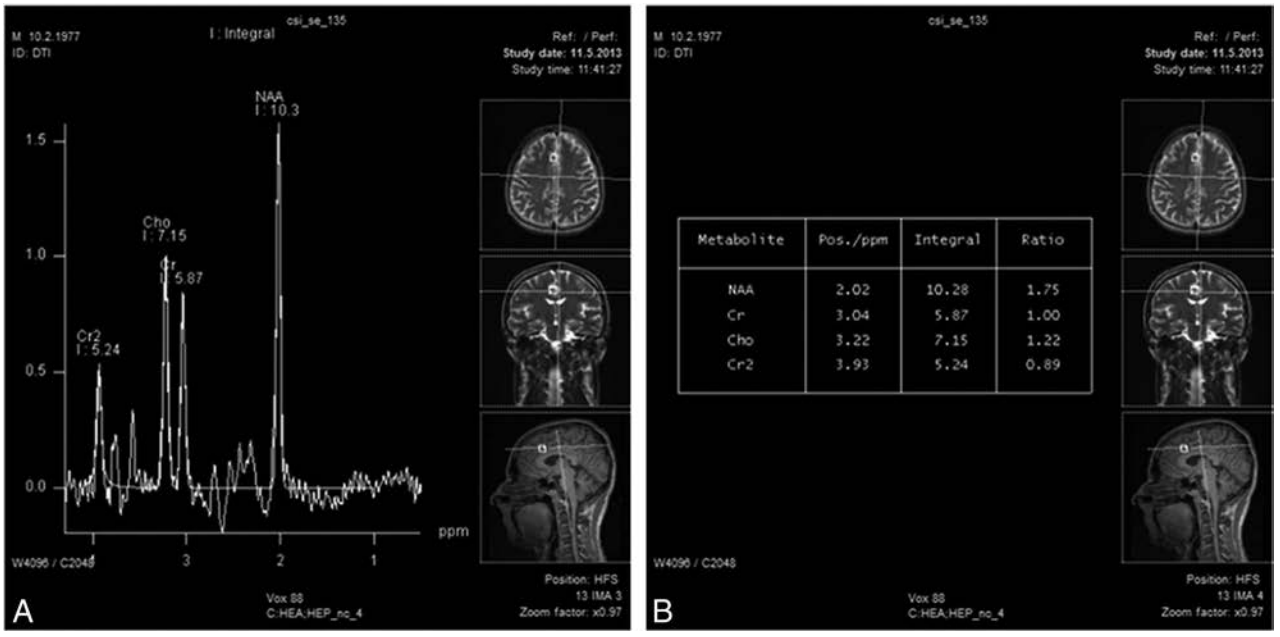

FIG 2. Long-TE multivoxel MR spectroscopy (*A*) (in a patient on cART) in the gray matter of the ventral ACG on the right shows a significant reduction in NAA/Cr (1.75) (*B*).

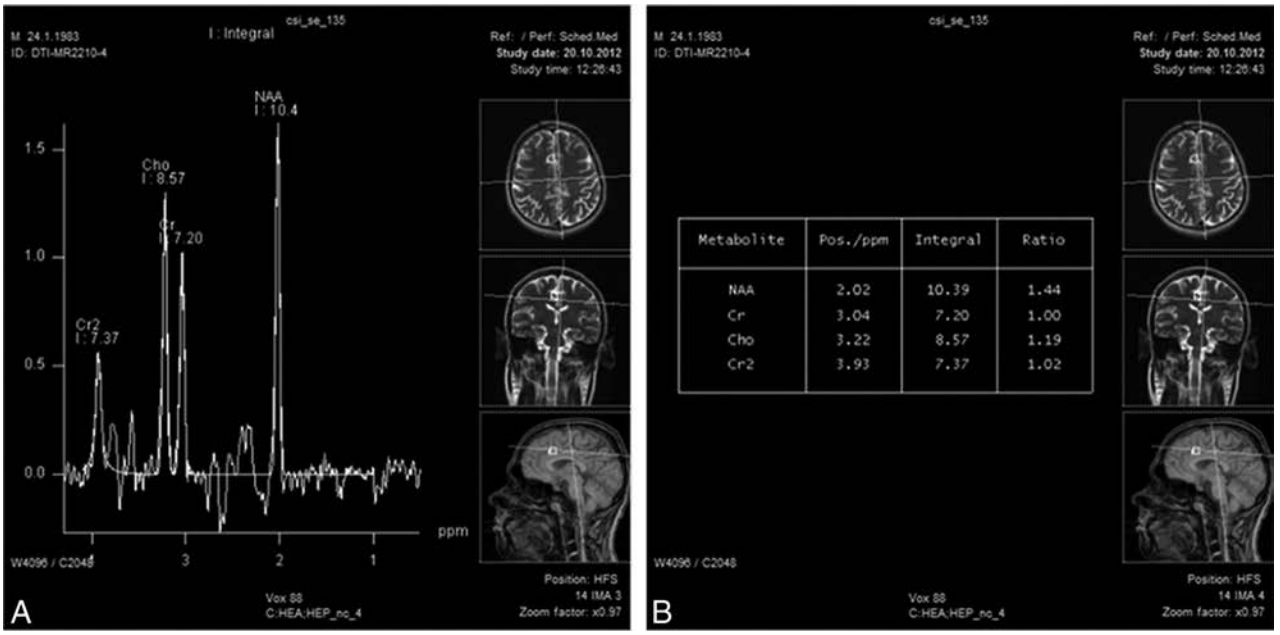

FIG 3. Long-TE multivoxel MR spectroscopy (*A*) (in a therapy-naïve patient) in the gray matter of the ventral ACG on the left shows a significant reduction in NAA/Cr (1.44) and a slight increase in Cho/Cr (1.19) (*B*).

and CPE scores in any of the observed locations (On-line Table 1). We observed positive correlations with current CD4+ scores in the FDWM on the right ($P = .016$) and in the PSWM on the left ($P = .004$) (On-line Table 1).

Cho/Cr Ratios. We observed a significant decrease in the Cho/Cr ratios in HIV+ patients compared with controls in several locations, namely the FSWM on the left, the dorsal ACG on the right, the PCG on both sides, and the PSWM on the left (On-line Table 3). On post hoc separate analysis, we noted a significant decrease in Cho/Cr ratios in HIV+ patients with chronic infection without cART in 5 locations (the FSWM on the left [$P < .001$], the dorsal ACG on the right [$P = .03$], the PCG on the right [$P < .001$], the PCG on the left [$P = .02$], and the PSWM on the left [$P = .02$], On-line Table 2). Levels of Cho/Cr were significantly decreased in HIV+ patients with chronic infection on cART in the FSWM on the left ($P = .03$) and the PSWM on the left ($P = .02$), both compared with controls. Again, no significant difference was observed in Cho/Cr levels between the 2 groups of chronically infected HIV+ patients (On-line Table 2).

Among the 3 observed metabolite ratios, the Cho/Cr ratio was the only one that showed some significant correlations with the

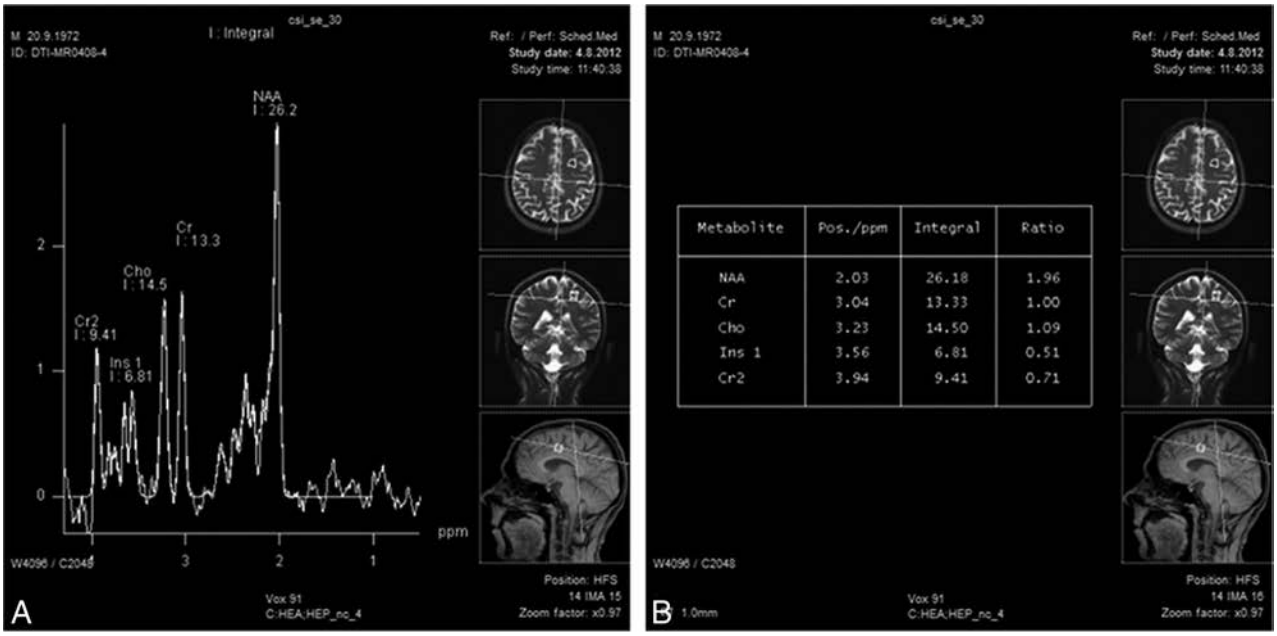

FIG 4. Short-TE multivoxel MR spectroscopy (*A*) (in an HIV+ patient on cART) in the frontal subcortical white matter on the left shows a reduction in NAA/Cr (1.96) and an increase in mIns/Cr (0.51) (*B*).

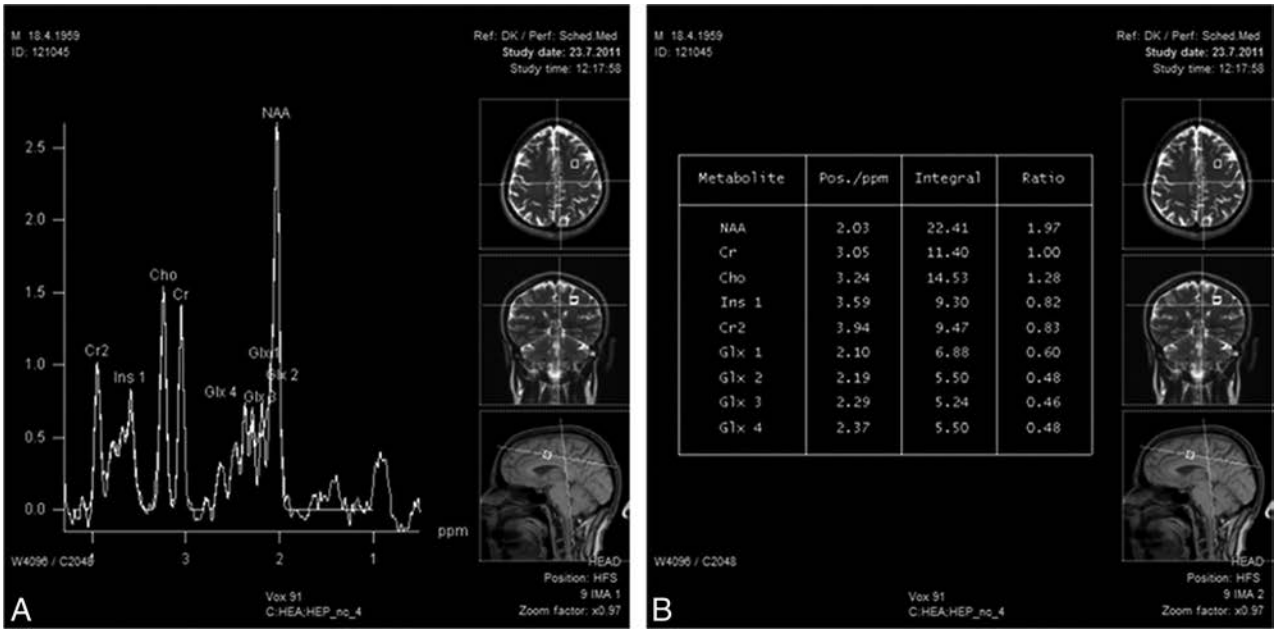

FIG 5. Short-TE multivoxel MR spectroscopy (*A*) in an HIV+ therapy-naïve patient shows a reduction in NAA/Cr (1.98) and an increase in mIns/Cr (0.82) and Cho/Cr (1.28) (*B*).

CPE score. Cho/Cr ratios showed positive correlations with the CPE score in the ventral ACG on the right ($P = .005$), the dorsal ACG on the right ($P = .001$), and in the FDWM of the left lobe ($P = .03$, On-line Table 3). A weak negative correlation with current CD4+ counts was observed in the ventral ACG on the right ($P = .04$) (On-line Table 3).

mIns/Cr Ratios. There was a significant increase in mIns/Cr ratios in HIV+ patients compared with healthy controls in the ventral ACG on right side, the FSWM on the left, the dorsal ACG on the left, the FDWM on the left, and the PSWM on the right (On-line Table 4). Post hoc analysis revealed an increase in mIns/Cr ratios in HIV+ therapy-naïve patients compared with controls in 3 locations, 2 in the ACG (right ventral, $P = .002$, and left dorsal, $P < .001$) and 1 in the FDWM on the left ($P = .001$). Finally, we observed an increase in mIns/Cr levels in HIV+ patients on cART compared with controls in only 1 location (the dorsal ACG on the left, $P = .01$). No significant difference was observed between chronically infected HIV+ patients on and without cART (On-line Table 4). Short-TE MR spectroscopy in a patient on cART and a therapy-naïve patient are shown in Figs 4 and 5.

There were no significant correlations of mIns/Cr ratios with CPE scores in any of the observed locations. Some positive corre-

lations with the current CD4+ count were shown in the dorsal ACG on the left ($P = .03$, On-line Table 4).

Power calculations showed satisfactory sample sizes for analysis of NAA/Cr (0.839–0.999). However, the results for Cho/Cr and mIns/Cr show a lack of power in certain voxels (the lowest value for Cho/Cr was 0.107; and for mIns/Cr, 0.066). Nevertheless, there were several voxels in which power was >0.8 (the FSWM on the left, the PCG on the right, and the PSWM on the left for Cho/Cr and the ventral ACG on the right, the dorsal ACG on the left, and the FDWM on the left).

DISCUSSION

Several recent studies have shown evidence that timely initiation of cART reduces the neuroinflammatory process in acute HIV infection, reflected in normalization of increased levels of mIns/Cr and Cho/Cr soon after therapy introduction.[11,15,16] However, levels of NAA/Cr are not significantly reduced immediately after seroconversion, so no relevant change in this neuronal marker was observed.[15]

In this study, we confirmed a significant decrease in the levels of NAA/Cr throughout the observed volume of the brain (comprising gray matter of the cingulate gyrus, subcortical frontal and parietal white matter, and frontal deep white matter on both sides) in chronically infected HIV+ subjects (with similar mean durations of known HIV infection), irrespective of cART administration. This result leads to 2 important conclusions: first, the process of neurodegeneration is diffuse; and second, administration of antiretroviral drugs cannot attenuate the changes in brain metabolite ratios observed in therapy-naïve HIV+ subjects.

Low NAA/Cr levels in chronically infected HIV+ patients are concordant with findings in the most recent MR spectroscopy studies,[15,17] resembling the progressive neurodegeneration that is thought to be the framework of HIV-associated neurocognitive disorders.[4]

The locations of the observed declines in NAA/Cr ratios were in the cingulate gyrus and subcortical frontal and parietal and deep frontal white matter. The posterior cingulate cortex was affected by the process of neuronal injury in both groups of HIV+ subjects. It is a highly connected and metabolically active brain region, with a suggested (not yet proved) important cognitive role. Recent data suggest that it has a central role in supporting internally directed cognition. However, other evidence suggests that it may play a direct role in regulating the focus of attention. In addition, its interactions with other brain networks may be important for conscious awareness.[18] It is functionally connected to the region of dorsal ACG and the prefrontal cortex (regions also affected by neuronal loss and dysfunction, according to our results). The anterior cingulate gyrus is divided into 2 functionally separate parts (ventral and dorsal). The ventral part has been proved to have connections to the emotional limbic system, while the dorsal part (also called the middle cingulate gyrus) has connections to the cognitive prefrontal cortex.[19] Some of the main symptoms of mild HAND forms, concerning mood disorders, depression, and anxiety could be due to these specific regions being affected by the extensive process of neurodegeneration.

In this study, we present a decline in Cho/Cr levels in some observed locations in both HIV+ therapy-naïve and HIV+ treated subjects. In HIV+ therapy-naïve subjects, this decrease was observed in the dorsal ACG, PCG, and subcortical white matter of the frontal and parietal lobes on the left. In treated HIV+ patients, the decrease in Cho/Cr levels was found to be significant in only 2 locations: subcortical frontal and parietal white matter (in this group, Cho/Cr levels were more likely to resemble those in healthy controls). Again, no significant differences between these 2 groups were reported. A recent study by Harezlak et al[20] presented the decrease in Cho/Cr in aging individuals with HIV infection. These changes have not been explained to date but may, in part, reflect attenuated immune-mediated responses in aging individuals or represent the effects of brain atrophy in chronic HIV-induced neuronal injury.

Finally, mIns/Cr was increased in both untreated and treated HIV+ subjects. mIns/Cr was increased in 3 locations in untreated patients, covering the ventral and dorsal ACG and the FDWM on the left. The dorsal ACG in treated HIV+ patients was the only region in which we observed a decline in these ratios, compared with healthy controls. This finding could indicate that in this region, inflammation and glial proliferation persist for the longest time despite therapy administration. No significant differences were shown between HIV+ patients on and without therapy in mIns/Cr ratios in the observed locations. The reason for this result is not clear because one of the primary roles of cART in the CNS is the restriction of inflammatory processes in the brain (measured by increases of mIns levels). One of the possible reasons for the absent diffuse increase in markers of glial proliferation in our study can be the uneven distribution of glial cells in the brain, not concordant with the locations we observed.[21] However, additional explanation is needed in the light of concomitant normal or slightly reduced Cho/Cr levels in the same regions. Progressive brain atrophy could explain the decrease in Cho/Cr and the concurrent absence of an mIns/Cr increase in the observed regions.

There were some more interesting conclusions regarding regional diversity of obtained results. First, in the subcortical white matter in the frontal and parietal lobes, there was a simultaneous drop in NAA/Cr and Cho/Cr levels in HIV+ patients on cART. This could be due to the quantitative loss of neurons and could reflect brain atrophy in subcortical regions. However, as we indicated, there was no intersection between disturbed mIns/Cr and Cho/Cr levels in these patients. This finding could suggest that there are different processes that accompany neuronal injury. One of them is certainly the proliferation of glial cells (indicated by increased mIns/Cr levels), while the other may be the loss of cell aggregation in the volume unit or some other (yet not clearly understood) mechanism. In cART-naïve patients, however, there were no voxels in which a significant decrease in Cho/Cr followed a significant decrease in NAA/Cr. On the contrary, in all locations where mIns/Cr was significantly increased, NAA/Cr levels decreased (with a significance of $P < .001$, compared with controls). This finding could support a relatively new concept of neurodegeneration in treated HIV+ subjects, with some indications that HAND is a (potentially reversible) metabolic encephalopathy rather than pure subcortical dementia.[1]

In addition, a recent study by Hidalgo et al[22] systematically addressed the question of the relationship between HIV infection and some personal habits, such as nicotine smoking, abuse or use

of alcohol and some recreational drugs (cannabis, marijuana), and psychostimulants. All of these substances are claimed to have a certain, most often synergistic, effect on the neurodegenerative process and neurocognitive impairment in HIV-infected individuals, though through different mechanisms and pathways.[22] There are some controversial findings regarding the effect of tobacco smoke extract on neurons in HIV. On the one hand, there are some data on neurotoxicity, expressed as depletion of memory formation and synaptic plasticity, while on the other hand, some beneficial outcomes were shown in HIV-infected individuals with neurologic deficits.[23] Nicotine use was the most widespread habit in our study population, equally distributed in healthy and HIV+ subjects. However, we failed to find correlations of MR spectroscopy parameters with nicotine smoking in our study population. The use of cannabinoids has a negative effect on the CD4+ count and on the memory processes.[24] The consumption of marijuana has some controversial effects on cognition. Cristiani et al[25] have shown some synergistic effects of marijuana and HIV infection in individuals with advanced HIV disease, while the effects are minimal in those at the early stages of HIV. In our study, only a few subjects (3 HIV-infected subjects, 2 on cART, and 1 cART-naïve subject) reported recreational use of marijuana. However, this number was not significant enough for any valid statistical analysis of the impact of this substance on brain metabolite ratios. The abuse of alcohol is connected with oxidative stress, impairment of the blood-brain barrier, and glutamate-associated neurotoxicity.[22] However, the effects of alcohol are classically more pronounced in the peripheral nervous system (painful peripheral neuropathy). Nevertheless, Green et al[26] have shown a synergistic effect of HIV infection and alcohol on the CNS, observed as a negative effect on reaction time, auditory processing, and verbal reasoning. No subjects with a history of active alcohol or opioid drug abuse were enrolled in our study.

Finally, HIV+ patients on and without cART were similar in aspects of duration of known HIV infection and nadir CD4+ count. A lower nadir CD4+ count reflects a longer duration of HIV infection and a longer exposure of neuronal cells to the negative effects of HIV.[20,27] The expected consequence of cART administration is a decline of inflammation and glial proliferation parameters (mIns/Cr first) and some beneficial effects on NAA/Cr ratios (optimally stagnation). However, we were not able to demonstrate a significant positive impact of cART on the neurobiochemical profile in the observed regions. One possible explanation might be the lack of power observed in several voxels for mIns/Cr and Cho/Cr, meaning that our sample was inadequate to show potential differences. Nevertheless, the locations where we observed significant differences had a satisfactory power sample (>0.8). Additionally, there is a scant possibility that the group of untreated patients had lower inflammatory responses (the presence of so-called slow responders). The CNS HIV Antiretroviral Therapy Effects Research (CHARTER) Group was also not able to demonstrate positive effects of cART in CNS in their large observational study, while they clearly stated undoubtedly positive effects on immune function and peripheral viral load reduction.[28] A positive effect on the immune system was also confirmed in our study, with the current CD4+ count being significantly higher in the treated group ($P < .001$) than in drug-naïve patients. In other words, even though (peripheral) viral replication is adequately suppressed with cART, progressive changes in the neurobiochemical profile are not. However, nonreplicating-but-viable viruses might still affect the function of neuronal cells through release of their toxins or by stimulating the constant activity of the host immune system.

The efficacy of cART in the CNS compartment is classically evaluated with the CPE score.[29] In our study, only weak positive correlations of the Cho/Cr ratio with the CPE score were observed (in the cingulate gyrus and deep frontal white matter). Presumably, the decline of Cho/Cr reflected the process of atrophy, so this correlation could be attributed to a positive effect of cART on preventing chronic CNS injury in HIV infection (because most of our subjects had high CPE scores). This finding is concordant with recent studies showing that CPE fails to predict neuronal damage measured by MR spectroscopy (the CPE score shows the lowest predictive value of all the observed parameters).[19]

Finally, we tested the impact of current CD4+ counts (reflecting the immune status at the moment of scanning) on metabolite ratios. In general, correlations of brain metabolite ratios with current CD4+ counts were poor. We observed positive correlations of NAA/Cr with current CD4+ counts, significant only in the white matter (deep frontal and subcortical parietal). This observation supports the theory that immune restitution has a positive effect on NAA/Cr levels as the means of preventing further neuronal injury.[15,16] Cho/Cr showed poor (negative) correlations with CD4+ counts, trending toward significance only in the ventral ACG. mIns/Cr showed a positive correlation with the CD4+ count only in the dorsal ACG, probably reflecting immune activation persistent in this region.

CONCLUSIONS

According to the results of proton chemical shift imaging covering some locations in subcortical and deep white matter of frontal and parietal lobes, as well as some locations in the cingulate gray matter, the positive impact of cART on the process of neuronal loss and dysfunction in chronic HIV infection is suboptimal. Our findings show that regional differences in glial proliferation and neurometabolic profile induced by HIV viral and reactive host factors exist and persist in era of cART. This finding raises the question of change in the neuronal damage mechanism in the light of treated chronic HIV infection (metabolic encephalopathy as the pathologic substrate). MR spectroscopy might be a useful tool in monitoring the effect of different cART regimens in affecting the alternative viral pathways of neuronal injury (with successful peripheral viral suppression). Finally, the effect of some lifestyle habits (consumption of alcohol, marijuana, nicotine, and opioid drugs) on neuronal dysfunction in chronic HIV infection is yet to be defined.

REFERENCES

1. Bryant AK, Ellis RJ, Umlauf A, et al. **Antiretroviral therapy reduces neurodegeneration in human immunodeficiency virus infection.** *AIDS* 2015;29:323–30 CrossRef Medline
2. Antinori A, Arendt G, Becker JT, et al. **Updated research nosology for HIV-associated neurocognitive disorders.** *Neurology* 2007;69:1789–99 CrossRef Medline
3. Tate DF, Sampat M, Harezlak J, et al; HIV Neuroimaging Consor-

tium. **Regional areas and widths of the midsagittal corpus callosum among HIV-infected patients on stable antiretroviral therapies.** *J Neurovirol* 2011;17:368–79 CrossRef Medline
4. Cohen RA, Harezlak J, Schifitto G, et al. **Effects of nadir CD4 count and duration of human immunodeficiency virus infection on brain volumes in the highly active antiretroviral therapy era.** *J Neurovirol* 2010;16:25–32 CrossRef Medline
5. Cysique LA, Vaida F, Letendre S, et al. **Dynamics of cognitive change in impaired HIV-positive patients initiating antiretroviral therapy.** *Neurology* 2009;73:342–48 CrossRef Medline
6. Joska JA, Gouse H, Paul RH, et al. **Does highly active antiretroviral therapy improve neurocognitive function? A systematic review.** *J Neurovirol* 2010;16:101–14 CrossRef Medline
7. Vassallo M, Durant J, Biscay V, et al. **Can high central nervous system penetrating antiretroviral regimens protect against the onset of HIV-associated neurocognitive disorders?** *AIDS* 2014;28:493–501 CrossRef Medline
8. Heaton RK, Clifford DB, Franklin DR, et al; CHARTER Group. **HIV-associated neurocognitive disorders persist in the era of potent antiretroviral therapy: CHARTER Study.** *Neurology* 2010;75:2087–96 CrossRef Medline
9. Moore DJ, Masliah E, Rippeth JD, et al; HNRC Group. **Cortical and subcortical neurodegeneration is associated with HIV neurocognitive impairment.** *AIDS* 2006;20:879–87 CrossRef Medline
10. Ances BM, Hammoud DA. **Neuroimaging of HIV associated neurocognitive disorders (HAND).** *Curr Opin HIV AIDS* 2014;9:545–51 CrossRef Medline
11. Sailasuta N, Ross W, Ananworanich J, et al; RV254/SEARCH 010 protocol teams. **Change in brain magnetic resonance spectroscopy after treatment during acute HIV infection.** *PLoS One* 2012;7:e49272 CrossRef Medline
12. Valcour V, Chalermchai T, Sailasuta N, et al; RV254/SEARCH 010 Study Group. **Central nervous system viral invasion and inflammation during acute HIV infection.** *J Infect Dis* 2012;206:275–82 CrossRef Medline
13. Harezlak J, Buchtal S, Taylor M, et al; HIV Neuroimaging Consortium. **Persistence of HIV-associated cognitive impairment, inflammation and neuronal injury in era of highly active antiretroviral treatment.** *AIDS* 2011;25:625–33 CrossRef Medline
14. Europen AIDS Clinical Society. EACS Guidelines. Version 8.0: http://www.eacsociety.org/files/guidelines_8_0-english_web.pdf. Accessed November 13, 2016
15. Young AC, Yiannoutsos CT, Hegde M, et al. **Cerebral metabolite changes prior to and after antiretroviral therapy in primary HIV infection.** *Neurology* 2014;83:1592–600 CrossRef Medline
16. Sailasuta N, Ananworanich J, Lerdlum S, et al; SEARCH 011 Study Group. **Neuronal-glia markers by magnetic resonance spectroscopy in HIV before and after combination antiretroviral therapy.** *J Acquir Immune Defic Syndr* 2016;71:24–30 CrossRef Medline
17. Bladowska J, Zimny A, Koltowska A, et al. **Evaluation of metabolic changes within the normal appearing gray and white matters in neurologically asymptomatic HIV-1-positive and HCV-positive patients: magnetic resonance spectroscopy and immunologic correlation.** *Eur J Radiol* 2013;82:686–92 CrossRef Medline
18. Leech R, Sharp DJ. **The role of posterior cingulate cortex in cognition and disease.** *Brain* 2014;137:12–32 CrossRef Medline
19. Stevens FL, Hurley RA, Taber KH. **Anterior cingulate cortex: unique role in cognition and emotion.** *J Neuropsychiatry Clin Neurosci* 2011;23:121–25 CrossRef Medline
20. Harezlak J, Cohen R, Gongvatana A, et al.; HIV Neuroimaging Consortium. **Predictors of CNS injury as measured by proton magnetic resonance spectroscopy in the setting of chronic HIV infection and CART.** *J Neurovirol* 2014;20:294–303 CrossRef Medline
21. Mittelbronn M, Dietz K, Schluesener HJ, et al. **Local distribution of microglia in the normal adult human central nervous system differs by up to one order of magnitude.** *Acta Neuropathol* 2001;101:249–55 Medline
22. Hidalgo M, Atluri VS, Nair M. **Drugs of abuse in HIV infection and neurotoxicity.** *Front Microbiol* 2015;6:217 CrossRef Medline
23. Cao J, Wang S, Wang J, et al. **RNA deep sequencing analysis reveals that nicotine restores impaired gene expression by viral proteins in the brains of HIV-1 transgenic mice.** *PLoS One* 2013;8:e68517 CrossRef Medline
24. Byrd DA, Fellows RP, Morgello S, et al; CHARTER Group. **Neurocognitive impact of substance use in HIV infection.** *J Acquir Immune Defic Syndr* 2011;58:154–62 CrossRef Medline
25. Cristiani SA, Pukay-Martin ND, Bornstein RA. **Marijuana use and cognitive function in HIV-infected people.** *J Neuropsychiatry Clin Neurosci* 2004;16:330–35 CrossRef Medline
26. Green JE, Saveanu RV, Bornstein RA. **The effect of previous alcohol abuse on cognitive function in HIV infection.** *Am J Psychiatry* 2004;161:249–54 CrossRef Medline
27. Ellis RJ, Badiee J, Vaida F, et al; CHARTER Group. **CD4 nadir is a predictor of HIV neurocognitive impairment in the era of combination antiretroviral therapy.** *AIDS* 2011;25:1747–51 CrossRef Medline
28. Heaton RK, Franklin DR Jr, Deutsch R, et al; CHARTER group. **Neurocognitive change in the era of HIV combination antiretroviral therapy: the longitudinal CHARTER study.** *Clin Infect Dis* 2015;60:473–80 CrossRef Medline
29. Shikuma CM, Nakamoto B, Shiramizu B, et al. **Antiretroviral monocyte efficacy score linked to cognitive impairment in HIV.** *Antivir Ther* 2012;17:1233–42 CrossRef Medline

Relationships among Cortical Glutathione Levels, Brain Amyloidosis, and Memory in Healthy Older Adults Investigated In Vivo with ^{1}H-MRS and Pittsburgh Compound-B PET

G.C. Chiang, X. Mao, G. Kang, E. Chang, S. Pandya, S. Vallabhajosula, R. Isaacson, L.D. Ravdin, for the Alzheimer's Disease Neuroimaging Initiative, and D.C. Shungu

ABSTRACT

BACKGROUND AND PURPOSE: Oxidative stress has been implicated as an important pathologic mechanism in the development of Alzheimer disease. The purpose of this study was to assess whether glutathione levels, detected noninvasively with proton MR spectroscopy, are associated with brain amyloidosis and memory in a community-dwelling cohort of healthy older adults.

MATERIALS AND METHODS: Fifteen cognitively healthy subjects were prospectively enrolled in this study. All subjects underwent ^{1}H-MR spectroscopy of glutathione, a positron-emission tomography scan with an amyloid tracer, and neuropsychological testing by using the Repeatable Battery for the Assessment of Neuropsychological Status. Associations among glutathione levels, brain amyloidosis, and memory were assessed by using multivariate regression models.

RESULTS: Lower glutathione levels were associated with greater brain amyloidosis in the temporal ($P = .03$) and parietal ($P = .05$) regions, adjusted for *apolipoprotein E* ε4 carrier status. There were no significant associations between glutathione levels and cognitive scores.

CONCLUSIONS: This study found an association between cortical glutathione levels and brain amyloidosis in healthy older adults, suggesting a potential role for ^{1}H-MR spectroscopy measures of glutathione as a noninvasive biomarker of early Alzheimer disease pathogenesis.

ABBREVIATIONS: AD = Alzheimer disease; ADNI = Alzheimer's Disease Neuroimaging Initiative; *APOE* = *apolipoprotein E*; GSH = glutathione; PiB = Pittsburgh compound-B; RBANS = Repeatable Battery for the Assessment of Neuropsychological Status

Alzheimer disease (AD), a devastating neurodegenerative disorder afflicting >11% of individuals older than 65 years of age,[1] is currently the sixth leading cause of death in the United States. Various forms of therapy have failed to show clinical benefit in individuals with AD.[2] In the absence of disease-modifying pharmacotherapy for AD, identifying and potentially targeting early pathologic processes that may lead to the development of AD are essential in developing prevention strategies.

Oxidative stress, defined as excessive production of free radicals relative to total tissue antioxidant reserves, has emerged from in vitro and preclinical studies as a key pathologic process in the development of AD.[3-8] In transgenic mouse models, depletion of the reduced form of the tripeptide thiol glutathione (GSH)—the most abundant intracellular antioxidant and free radical scavenger and a reliable marker of oxidative stress[9]—has been reported to precede amyloid oligomerization and plaque formation,[10,11] both pathologic hallmarks of AD. A self-propagating cycle of free radical formation, oxidative stress, and amyloid plaque formation has also been shown in vitro.[12] Furthermore, it has been suggested that amyloid may have antioxidant properties, thereby serving as a compensatory mechanism in the presence of oxidative stress.[13] However, the relationship between oxidative stress and amyloidosis in humans remains poorly understood, particularly early in the disease course when oxidative stress may serve as a potential target for disease-modifying interventions.

The primary aim of this study was therefore to assess the relationship between proton MR spectroscopy measures of GSH levels and brain amyloidosis, as assessed by positron-emission tomography with the amyloid tracer Pittsburgh compound-B (PiB),[14] in a prospective cognitively healthy community cohort of elderly subjects. Secondarily, we aimed to assess the relationship between GSH levels and memory. Last, we investigated whether GSH levels were associated with potentially modifiable AD risk factors.

Received October 17, 2016; accepted after revision January 19, 2017.

From the Departments of Radiology (G.C.C., X.M., G.K., E.C., S.P., S.V., D.C.S.) and Neurology (R.I., L.D.R.), Weill Cornell Medical College, NewYork-Presbyterian Hospital, New York, New York.

This work was supported by a National Institutes of Health National Center for Advancing Translational Sciences/CTSC grant (UL1 TR000457-06) and by NIH grant S10 OD021782.

Please address correspondence to Gloria C. Chiang, MD, Department of Radiology, Division of Neuroradiology, Weill Cornell Medical College, NewYork-Presbyterian Hospital, 525 East 68th St, Starr Pavilion, Box 141, New York, NY 10065; e-mail: gcc9004@med.cornell.edu

http://dx.doi.org/10.3174/ajnr.A5143

MATERIALS AND METHODS

Subjects

Fifteen cognitively healthy subjects, recruited through flyers posted in the community, newspaper advertisements, and ambulatory care clinics, were prospectively enrolled. All subjects gave written informed consent to participate in this study, which was approved by the institutional review board of our institution.

Inclusion criteria consisted of individuals between 55 and 75 years of age with intact ability to perform all routine activities of daily living, including living independently in the community. None of the subjects met the criteria for mild cognitive impairment or AD. Subjects were also excluded if they had comorbid medical conditions that could impact brain function, including major psychiatric disorders (ie, major depression, bipolar disorder, psychosis), brain tumors, prior strokes, significant traumatic brain injury (defined as requiring a visit to the emergency department or a hospital admission), seizure disorders, recent illicit drug use, alcohol abuse, and other major medical conditions, such as heart failure, recent myocardial infarction, renal failure, liver disease, chronic obstructive pulmonary disease, and malignancy.

Clinical Data

All subjects completed detailed questionnaires about their medical history and medical records were also examined. Clinical data collected included recent weight and height, cholesterol levels, blood pressure measurements, and the number of hours of exercise per week, because these factors have been reported to be associated with the risk for AD.[15,16] Exercise was defined as physical activity more strenuous than daily routine activity. We also elicited a family history of dementia, because genetics could explain increased brain amyloidosis in otherwise cognitively healthy subjects.[17]

Cognitive Battery

Cognitive testing was performed by a board-certified neuropsychologist (L.D.R.). Patients were first screened for depression and anxiety by using the Beck Depression Inventory-II[18] and the Beck Anxiety Inventory.[19] Immediate and delayed memory were assessed by using subscores of the Repeatable Battery for the Assessment of Neuropsychological Status (RBANS) based on tasks that involved recalling a list of words and a short story.[20] Additional cognitive domains assessed included visuospatial and constructional function, assessed with figure copying and line orientation tasks; attention, assessed with digit span and coding tasks; and language, assessed with picture naming and semantic fluency tasks. The RBANS has been previously reported to have 90% accuracy for discriminating between cognitively healthy individuals and those with mild cognitive impairment.[21]

Apolipoprotein E ε4 Genotyping

Blood samples were obtained from all subjects to isolate DNA for *Apolipoprotein E* (*APOE*) genotyping, which was performed by using polymerase chain reaction amplification, allele-specific primers, and identification of fragments on an agarose gel.[22]

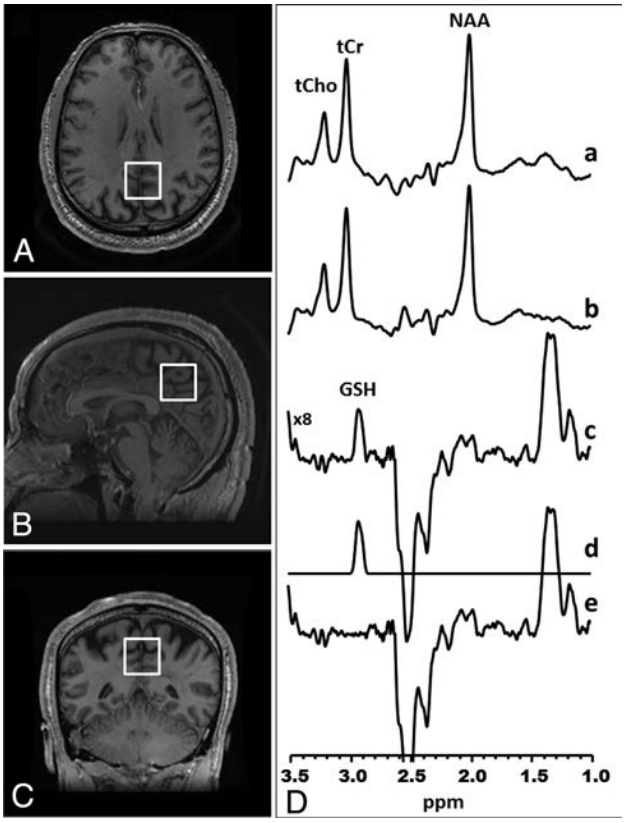

FIG 1. Glutathione detection in the medial parietal lobe with J-edited ^{1}H-MR spectroscopy. Axial (*A*), sagittal (*B*), and coronal (*C*) MR images of a human brain, with depiction of the size, location, and angulation of the voxel of interest in the medial parietal lobe. *D*, Demonstration of in vivo human brain glutathione detection by ^{1}H-MR spectroscopy: spectra *a* and *b*, single-voxel subspectra acquired in 15 minutes with the editing pulse on and off and 290 (580 total) interleaved averages; spectrum *c*, difference between spectra *a* and *b*, showing the edited brain GSH resonance at 2.98 ppm; spectrum *d*, model fitting of spectrum *c* to obtain the GSH peak area; spectrum *e*, residual of the difference between spectra *c* and *d*. tCho indicates total choline; tCr, total creatine.

MR Imaging and Spectroscopy Data Acquisition and Analysis

All subjects underwent standardized structural MR imaging of the brain and single-voxel ^{1}H-MR spectroscopy on a research-dedicated 3T MR imaging system (Excite HD; GE Healthcare, Milwaukee, Wisconsin) with an 8-channel phased array head coil. The MR imaging protocol consisted of a structural T1-weighted spoiled gradient-recalled echo volumetric scan for tissue segmentation and an axial fast fluid-attenuated inversion recovery scan to exclude focal pathology.

In vivo ^{1}H-MR spectroscopy data were obtained from a 2.5 × 2.5 × 2.5 cm^{3} voxel prescribed in the medial parietal lobe to include the posterior cingulate gyrus and precuneus—a region chosen because multiple prior studies reported early involvement of these regions by AD due to their inclusion in the memory network.[23-26] The standard J-edited spin-echo difference method with TE/TR = 68/1500 ms was used to measure the levels of reduced GSH, as previously described[27-30] and illustrated in Fig 1. Although it has been suggested that a TE of 120 ms is optimal for GSH detection by J-editing,[31] we opted to use a TE of 68 ms because it yields a difference spectrum in which the coedited as-

partyl (CH2) resonances of NAA around 2.5 ppm are inverted and clearly separated from the noninverted GSH resonance, facilitating spectral fitting (Fig 1).[27,28]

Briefly, a pair of frequency-selective inversion pulses was inserted into the standard point-resolved spectroscopy sequence method and was applied on alternate scans at the frequency of the GSH α-cysteinyl resonance at 4.56 ppm while avoiding excitation of oxidized GSH α-cysteinyl at 3.28 ppm.[32] This process resulted in 2 subspectra in which reduced GSH, but not oxidized GSH, was alternately inverted or not inverted. Subtracting these 2 subspectra yielded a ^{1}H-MR spectrum consisting of only the edited GSH β-cysteinyl resonance at 2.98 ppm. A high test-retest reliability has been reported for detection of γ-aminobutyric acid with this MR spectroscopy technique on the same 3T GE Healthcare Excite HD instrument.[33] Spectral data for this study were acquired in 15 minutes by using 290 interleaved excitations (580 total) with the editing pulses on or off. The area under the GSH resonance, which is proportional to the concentration of GSH in the voxel of interest, was obtained by frequency-domain spectral fitting as previously described.[28] The derived GSH peak areas were then expressed semiquantitatively as ratios relative to the unsuppressed intravoxel water signal for normalization across subjects before being used in group analyses. To estimate the proportions of gray matter, white matter, and CSF contained in the voxel of interest, the volumetric spoiled gradient-recalled echo MR imaging data were segmented by using Statistical Parametric Mapping software (SPM8; http://www.fil.ion.ucl.ac.uk/spm/software/spm8).

Pittsburgh Compound-B PET Image Acquisition and Analysis

All subjects underwent an amyloid PET scanning on a Biograph PET-CT scanner (Siemens, Erlangen, Germany; 1-mm full width at half maximum, 25-cm FOV) by using a standardized research protocol.[17] All subjects received an intravenous catheter for injection of 15 mCi of PiB. Sixty minutes after injection, subjects were scanned for 30 minutes with their eyes open in a quiet, dimly lit room. A low-dose CT scan was acquired for attenuation correction, and all images were reconstructed into a 512 $\times$ 512 matrix.

Summed PET images corresponding to the 60–90 minutes of PiB data were generated and nonlinearly normalized to a PiB template. The PiB template was generated by averaging the summed images of 48 cognitively healthy individuals in the same age range, which were downloaded from the Alzheimer's Disease Neuroimaging Initiative (ADNI) on-line data repository (adni.loni.usc.edu). The ADNI was launched in 2003 as a public-private partnership, led by Principal Investigator Michael W. Weiner, MD, with the primary goal of testing whether serial MR imaging, positron-emission tomography, other biologic markers, and clinical and neuropsychological assessment may be combined to measure the progression of mild cognitive impairment and early Alzheimer disease. More information may be obtained at www.adni-info.org.

Orientation and origin for all the PiB PET images were automatically fixed to the anterior commissure to match the templates used in Statistical Parametric Mapping (SPM; Wellcome Department of Imaging Neuroscience, London, UK), because the "normalize" function of SPM uses the origin as a starting estimate. These reoriented PiB PET images and the mean PiB template were skull-stripped with the FSL Brain Extraction Tool (http://fsl.fmrib.ox.ac.uk/fsl/fslwiki/BET)[34] to avoid any bias induced by skull staining. All the skull-stripped PiB PET images were then nonlinearly warped to the skull-stripped mean PiB template. Gray matter regions were parcellated by using the Automated Anatomical Labeling atlas of SPM to obtain 116 automated ROIs.[35] Regional PiB uptake values were then normalized by the subject's cerebellar reference uptake.

Prior ADNI publications determined that the 4 large regions of the brain that are most useful in measuring the degree of brain amyloidosis are the frontal, anterior/posterior cingulate, lateral parietal, and lateral temporal regions, with the cerebellum as a reference region.[36-39] Using ROIs from the Automated Anatomical Labeling atlas, we determined amyloid deposition in the frontal region by averaging the uptake values from the bilateral superior frontal, bilateral superior orbital frontal, bilateral middle frontal, bilateral inferior frontal opercular, bilateral inferior frontal triangularis, bilateral supplemental motor, bilateral medial superior frontal, and bilateral middle orbital frontal regions of the brain. The cingulate region included the bilateral anterior, middle, and posterior cingulum regions. The lateral parietal region included the bilateral superior and inferior parietal regions, as well as the precuneus. The lateral temporal region included the bilateral and superior middle temporal regions.

Statistical Analysis

All statistical analyses were performed in STATA, Version 13 (StataCorp, College Station, Texas).

The potential influence of voxel tissue heterogeneity and brain matter content in the analyses was examined by testing for associations between brain matter proportions in the voxel of interest and both MR spectroscopy measures of GSH levels and PiB PET measures of amyloid levels. We also examined the distribution of brain tissue proportions within our subject cohort to identify outliers.

To assess whether there was an association between GSH and brain amyloidosis, based on uptake on PiB PET, we used ordinary least-squares regression analysis with amyloid levels in each of the 4 brain regions as the outcome variable and GSH as the predictor variable. Because *APOE* ε4 carrier status has been shown to be associated with increased brain amyloidosis in the literature,[40-43] carrier status was included as a covariate to adjust for this confounding factor.

The robustness of any association between GSH and amyloidosis was examined by bootstrapping the original cohort of subjects 1000 times to obtain 95% confidence intervals.[44] The effect of a clear outlier (high parietal amyloidosis and low GSH) on the association was examined by performing the analyses both with and without this data point. To assess the effect sizes of our associations, we estimated the correlation coefficients between GSH and amyloidosis, with $<$0.1 indicating a small effect, 0.1–0.5 indicating a medium effect, and $>$0.5 indicating a large effect.[45] We also calculated the partial eta-squared for GSH on the basis of the regression models,[46] with $<$0.06 indicating a small effect, 0.06–0.14 indicating a medium effect, and $>$0.14 indicating a large effect.[47]

Table 1: Results of the regression analyses showing associations between glutathione and regional brain amyloidosis

	Regression Coefficients			
	Frontal Amyloidosis	Cingulate Amyloidosis	Parietal Amyloidosis	Temporal Amyloidosis
Glutathione levels (±SE)	−39 ± 90	−27 ± 174	−308 ± 143	−209 ± 85
P value	.67	.88	.05	.03

Note:—SE indicates standard error.

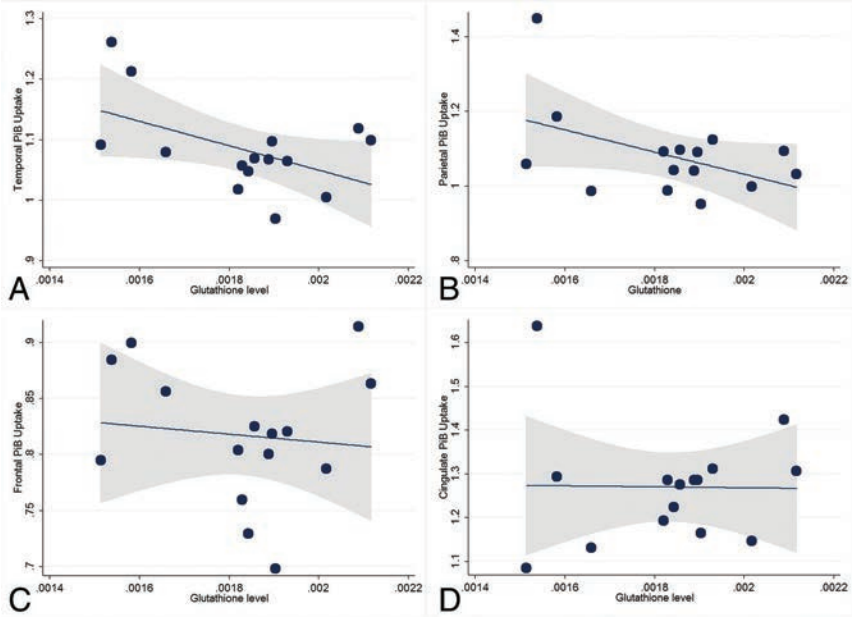

FIG 2. Scatterplots showing the relationship between glutathione levels and brain amyloidosis by region. After we adjusted for *APOE4* carrier status, lower glutathione levels were associated with higher levels of amyloidosis in the temporal (*A*) ($P = .03$) and in the parietal (*B*) ($P = .05$) regions, but not in the frontal (*C*) ($P = .67$) or cingulate (*D*) ($P = .88$) regions. Fitted lines and 95% confidence intervals (*shaded area*) are also shown.

Table 2: Results of the regression analyses showing associations between glutathione and age-adjusted cognitive scores on the Repeatable Battery for the Assessment of Neuropsychological Status

	Regression Coefficients (×10²)				
	Immediate Memory Subscore	Delayed Memory Subscore	Visuospatial/ Construction Subscore	Language Subscore	Attention Subscore
Glutathione levels (±SE)	317 ± 198	232 ± 171	113 ± 183	−24 ± 242	361 ± 247
P value	.14	.20	.55	.92	.17

Note:—SE indicates standard error.

To assess whether there was an association between GSH levels and memory, we again used ordinary least-squares regression analysis with GSH as the predictor and the age-adjusted subscores from the RBANS as the outcome variable. Because *APOE ε4* carrier status is known to be a risk factor for AD,[48,49] it was again included as a covariate.

Finally, we explored the associations between GSH and potential mediators of oxidative stress, including obesity, hypercholesterolemia, hypertension, and exercise, again by using ordinary least-squares regression analyses.

RESULTS

Subjects ranged in age from 55 to 72 years (mean, 63 ± 5 years), and 5 (33%) of the subjects were women. All subjects completed at least a year of college, with a mean of 16 ± 3 years of education. Five (33%) subjects had a family history of dementia. Ten (67%) subjects had the *APOE ε3/ε3* genotype, 2 (13%) subjects carried the *APOE ε2/ε3* genotype, and 3 (20%) subjects had the *APOE ε3/ε4* genotype. Eight (53%) subjects had comorbid hypercholesterolemia, and 7 (47%) subjects had comorbid hypertension. Body mass index ranged from 22 to 37, with a mean of 29 ± 4. Subjects reported exercising 0–14 hours per week, with a mean of 3 ± 4 hours.

The results of the regression analyses evaluating the association between ^{1}H-MR spectroscopy GSH and amyloidosis as assessed by PiB PET are provided in Table 1 and shown in Fig 2. There were no significant associations between tissue proportions and GSH levels or amyloidosis. After we adjusted for *APOE ε4* status, GSH levels were inversely associated with levels of amyloidosis in both the temporal region ($P = .03$, coefficient = −209; 95% confidence interval, −395 to −23) and parietal region ($P = .05$, coefficient = −308; 95% confidence interval, −621 to 3). Post hoc bootstrapping yielded a *P* value of .08 (95% confidence interval, −441 to 23) for the temporal region and 0.1 (95% confidence interval, −705 to 88) for the parietal region. In addition, the association between parietal region amyloidosis and GSH appears to have been primarily driven by 1 subject with high amyloidosis and low GSH. The association was no longer significant when this outlier was excluded (coefficient = −62, $P = .60$). There was no significant association between GSH levels and either frontal ($P = .67$) or cingulate ($P = .88$) region amyloidosis.

The correlation coefficient between GSH and temporal region amyloidosis was −0.51, indicating a large effect size. The correlation coefficient between GSH and parietal region amyloidosis was −0.47, indicating a medium effect size. In the regression models, the effect sizes for GSH were large, explaining a greater proportion of the variance in amyloidosis than in *APOE ε4* status. The partial eta-squared for GSH and *APOE ε4* was 0.33 and 0.25, respectively, for the temporal region. The partial eta-squared for GSH and *APOE ε4* was 0.28 and 0.23, respectively, for the parietal region.

The results of the regression analyses evaluating the association between GSH and cognition are provided in Table 2 and shown in Fig 3. None of the associations were statistically significant.

The results of the exploratory regression analyses evaluating

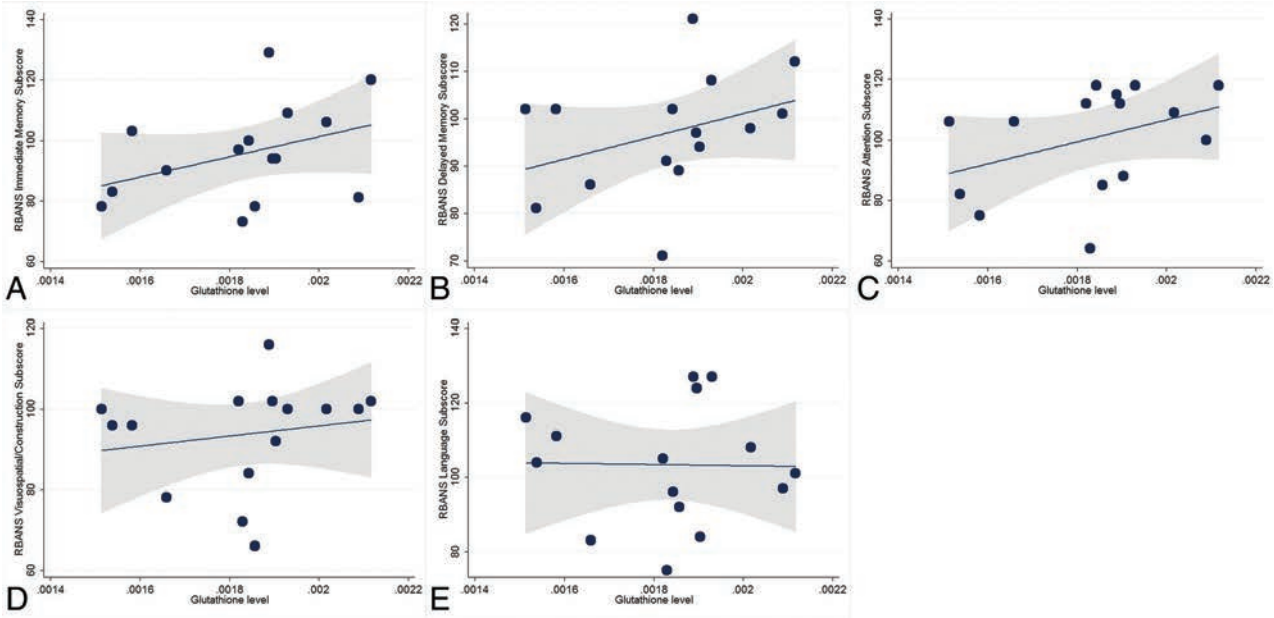

FIG 3. Scatterplots showing the relationship between glutathione levels and scores on the Repeatable Battery for the Assessment of Neuropsychological Status. There were no significant associations between higher glutathione levels and higher age-adjusted immediate (*A*) ($P = .14$) and delayed (*B*) ($P = .20$) memory subscores. Higher glutathione levels were not associated with attention (*C*) ($P = .17$), visuospatial/construction (*D*) ($P = .55$), or language (*E*) ($P = .92$) subscores. Fitted lines and 95% confidence intervals (*shaded area*) are also shown.

Table 3: Association between Alzheimer risk factors and glutathione levels

	Regression Coefficients ($\times 10^{-5}$)			
	Body Mass Index	Exercise (hr per wk)	Comorbid Hypertension	Comorbid Hypercholesterolemia
Glutathione levels ($\pm$SE)	-2.2 ± 1.23	-1.3 ± 1.4	-5.5 ± 9.9	-8.4 ± 11.0
P value	.08	.36	.59	.46

Note:—SE indicates standard error.

the association between GSH levels and risk factors for AD are shown in Table 3. There was a trend-level inverse association between body mass index and GSH levels ($P = .08$). Exercise, hypercholesterolemia, and hypertension were not significantly associated with GSH levels ($P > .05$).

DISCUSSION

The value of noninvasive measurement of GSH by ^{1}H-MR spectroscopy lies in its potential to directly implicate and support a role for oxidative stress in the early stages of AD development. Using this technique, the present study sought to identify a role for oxidative stress in a prospective cohort of healthy older subjects, assessing potential associations between cortical GSH levels and brain amyloidosis and between GSH and memory. The major finding was that GSH levels, measured with ^{1}H-MR spectroscopy, are negatively associated with brain amyloidosis, as assessed with PiB PET, in the temporal and parietal regions. In this cognitively healthy cohort, there were no associations between GSH levels and immediate and delayed memory.

The inverse association between levels of GSH and temporal and parietal amyloid levels supports a role for oxidative stress in amyloid plaque formation—a finding that is consistent with prior laboratory and preclinical studies.[5,6-8,46-49] An association between oxidative stress and amyloidosis has also been suggested by clinical studies on AD. Mandal et al[50] found that GSH levels measured by ^{1}H-MR spectroscopy could accurately discriminate among healthy subjects, individuals with mild cognitive impairment, and patients with AD, with decreased GSH levels being associated with increased levels of cognitive impairment. In postmortem AD brains,[51] depleted GSH levels accompanied the diagnosis of AD. There have also been reports associating GSH depletion with mitochondrial dysfunction[52,53] and neuronal degeneration.[54,55] On the other hand, increased GSH levels have been reported in those with mild cognitive impairment compared with healthy subjects, suggesting that there may be a compensatory up-regulation of GSH in the early stages of AD.[56] However, no direct relationship between oxidative stress and amyloidosis was established in any of the prior clinical studies because subject groups were defined clinically without quantifying the degree of underlying amyloidosis. In the present study, with an advanced ^{1}H-MR spectroscopy editing technique that enables reliable in vivo measurements of GSH, we have obtained strong preliminary evidence of an inverse relationship between GSH levels and amyloidosis in older adults, even before the onset of mild cognitive impairment. Replication in larger cohorts would both solidify this result and support measurement of brain GSH levels with ^{1}H-MR spectroscopy as a noninvasive biomarker of AD risk early in disease development.

This study also investigated whether GSH levels are associated with memory because memory deficits are known to be the earliest clinical manifestation of AD[57] and predict time-to-progression from cognitively healthy to mild cognitive impairment.[58] Because oxidative stress can exert deleterious effects on mitochondrial function and neuronal integrity, we surmised that GSH depletion could also lead to memory dysfunction. Two prior studies that included subjects with mild cognitive impairment and AD

reported conflicting results, with one reporting GSH deficits in mild cognitive impairment and AD[50] and the other reporting a potential compensatory increase of GSH in mild cognitive impairment.[56] Our study found no associations between GSH levels and cognitive scores in our cognitively healthy cohort, necessitating further studies in larger cohorts.

In exploring associations between GSH and AD risk factors, we found a trend-level inverse association between GSH levels and body mass index. Barnes and Yaffe[15] previously reported that up to 54% of AD cases may be attributable to modifiable risk factors, with 21% attributable to physical inactivity and 7% attributable to obesity. In the present cohort, we explored the association between these risk factors and GSH levels and found a trend-level negative association with body mass index, which could be consistent with a prior large cohort study of >2000 subjects, which found increased markers of oxidative stress, which would deplete GSH, with increased body mass index.[59] If this finding is validated, monitoring GSH levels by ^{1}H-MR spectroscopy could also serve as a biomarker of the potential benefits of various lifestyle-modification regimens, without the radiation risk and cost of PET imaging.

Finally, this study has a number of limitations. First, the sample size was relatively small, potentially limiting both statistical power and generalizability of the findings. Replication of these findings in larger cohorts will be necessary. Second, our cohort consisted of cognitively healthy individuals. As a result, subjects did not have significant memory deficits, possibly limiting our ability to detect statistically significant associations between GSH and memory, particularly in a small cohort. Third, we targeted the precuneus for GSH measurement with MR spectroscopy because this region is affected early in AD pathology. However, there may be abnormalities in other brain regions, which would need to be investigated to obtain a more complete understanding of oxidative stress–associated brain damage in AD and its prodromal stages. Furthermore, although we found associations between GSH and amyloidosis, longitudinal studies are necessary to determine whether decreased GSH levels increase subsequent risk of developing AD. Finally, we did not enroll a control group for comparison with our cognitively healthy cohort. As a result, it is not known whether the GSH levels detected in our cohort are significantly abnormal.

CONCLUSIONS

This is the first study, to our knowledge, to explore in vivo associations between GSH and brain amyloidosis, as well as GSH and memory in a cognitively healthy cohort. This supports a role for ^{1}H-MR spectroscopy measures of cortical glutathione as a potential early biomarker of AD pathology and therapeutic response monitoring of existing or future disease-modifying interventions targeting oxidative stress.

ACKNOWLEDGMENTS

We are grateful to Dr Amy Kuceyeski for assistance with the imaging atlas creation and analysis.

Data collection and sharing for this project were funded by the Alzheimer's Disease Neuroimaging Initiative (National Institutes of Health Grant U01 AG024904) and Department of Defense ADNI (Department of Defense award number W81XWH-12-2-0012). ADNI is funded by the National Institute on Aging, the National Institute of Biomedical Imaging and Bioengineering, and through generous contributions from the following: AbbVie; Alzheimer's Association; Alzheimer's Drug Discovery Foundation; Araclon Biotech; BioClinica; Biogen; Bristol-Myers Squibb Company; CereSpir; Cogstate; Eisai; Elan Pharmaceuticals; Eli Lilly and Company; Euroimmun; F. Hoffmann-La Roche Ltd and its affiliated company Genentech; Fujirebio; GE Healthcare; IXICO Ltd; Janssen Alzheimer Immunotherapy Research & Development, LLC; Johnson & Johnson Pharmaceutical Research & Development LLC; Lumosity; Lundbeck; Merck & Co; Meso Scale Diagnostics LLC; NeuroRx Research; Neurotrack Technologies; Novartis Pharmaceuticals Corporation; Pfizer; Piramal Imaging; Servier; Takeda Pharmaceutical Company; and Transition Therapeutics. The Canadian Institutes of Health Research is providing funds to support ADNI clinical sites in Canada. Private sector contributions are facilitated by the Foundation for the National Institutes of Health (www.fnih.org). The grantee organization is the Northern California Institute for Research and Education, and the study is coordinated by the Alzheimer's Therapeutic Research Institute at the University of Southern California. ADNI data are disseminated by the Laboratory for Neuro Imaging at the University of Southern California.

Data used in preparation of this article were obtained from the Alzheimer's Disease Neuroimaging Initiative database (adni.loni.usc.edu). Thus, the investigators within the ADNI contributed to the design and implementation of ADNI and/or provided data but did not participate in analysis or writing of this report. A complete listing of ADNI investigators can be found at http://adni.loni.usc.edu/wp-content/uploads/how_to_apply/ADNI_Acknowledgement_List.pdf.

Disclosures: Eileen Chang—*RELATED*: *Grant*: Clinical and Translational Science Center, *Comments*: Clinical and Translational Science Center/National Center for Advancing Translational Sciences UL1 RR024996.* Lisa D. Ravdin—*UNRELATED*: *Board Membership*: Biomedical Research Alliance of New York, *Comments*: institutional review board work. Dikoma C. Shungu—*UNRELATED*: *Grants/Grants Pending*: National Institutes of Health, Department of Defense, *Comments*: I had a number of regular/standard R-type grants funded by the federal government.* *Money paid to the institution.

REFERENCES

1. Alzheimer's Association. 2016 Alzheimer's disease facts and figures. http://www.alz.org/facts/. Accessed May 29, 2016
2. Mangialasche F, Solomon A, Winblad B, et al. **Alzheimer's disease: clinical trials and drug development.** *Lancet Neurol* 2010;9:702–16 CrossRef Medline
3. Apelt J, Bigl M, Wunderlich P, et al. **Aging-related increase in oxidative stress correlates with developmental pattern of beta-secretase activity and beta-amyloid plaque formation in transgenic Tg2576 mice with Alzheimer-like pathology.** *Int J Dev Neurosci* 2004;22:475–84 CrossRef Medline
4. Nunomura A, Perry G, Aliev G, et al. **Oxidative damage is the earliest event in Alzheimer disease.** *J Neuropathol Exp Neurol* 2001;60:759–67 CrossRef Medline
5. Praticò D, Uryu K, Leight S, et al. **Increased lipid peroxidation precedes amyloid plaque formation in an animal model of Alzheimer amyloidosis.** *J Neurosci* 2001;21:4183–87 Medline
6. Komatsu H, Liu L, Murray IV, et al. **A mechanistic link between oxidative stress and membrane mediated amyloidogenesis revealed**

by infrared spectroscopy. *Biochim Biophys Acta* 2007;1768:1913–22 CrossRef Medline
7. Nunomura A, Castellani RJ, Zhu X, et al. **Involvement of oxidative stress in Alzheimer disease.** *J Neuropathol Exp Neurol* 2006;65: 631–41 CrossRef Medline
8. Bonda DJ, Wang X, Lee HG, et al. **Neuronal failure in Alzheimer's disease: a view through the oxidative stress looking-glass.** *Neurosci Bull* 2014;30:243–52 CrossRef Medline
9. Pocernich CB, Butterfield DA. **Elevation of glutathione as a therapeutic strategy in Alzheimer disease.** *Biochim Biophys Acta* 2012; 1822:625–30 CrossRef Medline
10. Resende R, Moreira PI, Proença T, et al. **Brain oxidative stress in a triple-transgenic mouse model of Alzheimer disease.** *Free Radic Biol Med* 2008;44:2051–57 CrossRef Medline
11. Zhang C, Rodriguez C, Spaulding J, et al. **Age-dependent and tissue-related glutathione redox status in a mouse model of Alzheimer's disease.** *J Alzheimers Dis* 2012;28:655–66 CrossRef Medline
12. Hensley K, Carney JM, Mattson MP, et al. **A model for beta-amyloid aggregation and neurotoxicity based on free radical generation by the peptide: relevance to Alzheimer disease.** *Proc Natl Acad Sci U S A* 1994;91:3270–74 CrossRef Medline
13. Smith MA, Casadesus G, Joseph JA, et al. **Amyloid-beta and tau serve antioxidant functions in the aging and Alzheimer brain.** *Free Radic Biol Med* 2002;33:1194–99 CrossRef Medline
14. Rowe CC, Villemagne VL. **Brain amyloid imaging.** *J Nucl Med* 2011; 52:1733–40 CrossRef Medline
15. Barnes DE, Yaffe K. **The projected effect of risk factor reduction on Alzheimer's disease prevalence.** *Lancet Neurol* 2011;10:819–28 CrossRef Medline
16. Sato N, Morishita R. **The roles of lipid and glucose metabolism in modulation of β-amyloid, tau, and neurodegeneration in the pathogenesis of Alzheimer disease.** *Front Aging Neurosci* 2015;7:199 CrossRef Medline
17. Mosconi L, Rinne JO, Tsui WH, et al. **Increased fibrillar amyloid-β burden in normal individuals with a family history of late-onset Alzheimer's.** *Proc Natl Acad Sci U S A* 2010;107:5949–54 CrossRef Medline
18. Lasa L, Ayuso-Mateos JL, Vázquez-Barquero JL, et al. **The use of the Beck Depression Inventory to screen for depression in the general population: a preliminary analysis.** *J Affect Disord* 2000;57:261–65 CrossRef Medline
19. Beck AT, Epstein N, Brown G, et al. **An inventory for measuring clinical anxiety: psychometric properties.** *J Consult Clin Psychol* 1988;56:893–97 CrossRef Medline
20. Randolph C, Tierney MC, Mohr E, et al. **The Repeatable Battery for the Assessment of Neuropsychological Status (RBANS): preliminary clinical validity.** *J Clin Exp Neuropsychol* 1998;20:310–19 CrossRef Medline
21. Karantzoulis S, Novitski J, Gold M, et al. **The Repeatable Battery for the Assessment of Neuropsychological Status (RBANS): utility in detection and characterization of mild cognitive impairment due to Alzheimer's disease.** *Arch Clin Neuropsychol* 2013;28:837–44 CrossRef Medline
22. Saykin AJ, Shen L, Foroud TM, et al; Alzheimer's Disease Neuroimaging Initiative. **Alzheimer's Disease Neuroimaging Initiative biomarkers as quantitative phenotypes: genetics core aims, progress, and plans.** *Alzheimers Dement* 2010;6:265–73 CrossRef Medline
23. Herholz K, Salmon E, Perani D, et al. **Discrimination between Alzheimer dementia and controls by automated analysis of multicenter FDG PET.** *Neuroimage* 2002;17:302–16 CrossRef Medline
24. Vogt BA, Vogt LJ, Vrana KE, et al. **Multivariate analysis of laminar patterns of neurodegeneration in posterior cingulate cortex in Alzheimer's disease.** *Exp Neurol* 1998;153:8–22 CrossRef Medline
25. Murray ME, Przybelski SA, Lesnick TG, et al. **Early Alzheimer's disease neuropathology detected by proton MR spectroscopy.** *J Neurosci* 2014;34:16247–55 CrossRef Medline
26. Kantarci K. **1H magnetic resonance spectroscopy in dementia.** *Br J Radiol* 2007;80:S146–52 CrossRef Medline
27. Shungu DC, Weiduschat N, Murrough JW, et al. **Increased ventricular lactate in chronic fatigue syndrome, III: relationships to cortical glutathione and clinical symptoms implicate oxidative stress in disorder pathophysiology.** *NMR Biomed* 2012;25:1073–87 CrossRef Medline
28. Weiduschat N, Mao X, Hupf J, et al. **Motor cortex glutathione deficit in ALS measured in vivo with the J-editing technique.** *Neurosci Lett* 2014;570:102–07 CrossRef Medline
29. Geramita M, van der Veen JW, Barnett AS, et al. **Reproducibility of prefrontal γ-aminobutyric acid measurements with J-edited spectroscopy.** *NMR Biomed* 2011;24:1089–98 CrossRef Medline
30. Mullins PG, McGonigle DJ, O'Gorman RL, et al. **Current practice in the use of MEGA-PRESS spectroscopy for the detection of GABA.** *Neuroimage* 2014;86:43–52 CrossRef Medline
31. An L, Zhang Y, Thomasson DM, et al. **Measurement of glutathione in normal volunteers and stroke patients at 3T using J-difference spectroscopy with minimized subtraction errors.** *J Magn Reson Imaging* 2009;30:263–70 CrossRef Medline
32. Nepravishta R, Sabelli R, Iorio E, et al. **Oxidative species and S-glutathionyl conjugates in the apoptosis induction by allyl thiosulfate.** *FEBS J* 2012;279:154–67 CrossRef Medline
33. Shungu DC, Mao X, Gonzales R, et al. **Brain γ-aminobutyric acid (GABA) detection in vivo with the J-editing (1) H MRS technique: a comprehensive methodological evaluation of sensitivity enhancement, macromolecule contamination and test-retest reliability.** *NMR Biomed* 2016;29:932–42 CrossRef Medline
34. Smith SM. **Fast robust automated brain extraction.** *Hum Brain Mapp* 2002;17:143–55 CrossRef Medline
35. Tzourio-Mazoyer N, Landeau B, Papathanassiou D, et al. **Automated anatomical labeling of activations in SPM using a macroscopic anatomical parcellation of the MNI MRI single-subject brain.** *Neuroimage* 2002;15:273–89 CrossRef Medline
36. Mormino EC, Kluth JT, Madison CM, et al; Alzheimer's Disease Neuroimaging Initiative. **Episodic memory loss is related to hippocampal-mediated beta-amyloid deposition in elderly subjects.** *Brain* 2009;132(pt 5):1310–23 CrossRef Medline
37. Jagust WJ, Landau SM, Shaw LM, et al; Alzheimer's Disease Neuroimaging Initiative. **Relationships between biomarkers in aging and dementia.** *Neurology* 2009;73:1193–99 CrossRef Medline
38. Landau SM, Breault C, Joshi AD, et al; Alzheimer's Disease Neuroimaging Initiative. **Amyloid-β imaging with Pittsburgh compound B and florbetapir: comparing radiotracers and quantification methods.** *J Nucl Med* 2013;54:70–77 CrossRef Medline
39. Jagust WJ, Landau SM, Koeppe RA, et al. **The Alzheimer's Disease Neuroimaging Initiative 2 PET Core: 2015.** *Alzheimers Dement* 2015; 11:757–71 CrossRef Medline
40. Schmechel DE, Saunders AM, Strittmatter WJ, et al. **Increased amyloid beta-peptide deposition in cerebral cortex as a consequence of apolipoprotein E genotype in late-onset Alzheimer disease.** *Proc Natl Acad Sci U S A* 1993;90:9649–53 CrossRef Medline
41. Reiman EM, Chen K, Liu X, et al. **Fibrillar amyloid-beta burden in cognitively normal people at 3 levels of genetic risk for Alzheimer's disease.** *Proc Natl Acad Sci U S A* 2009;106:6820–25 CrossRef Medline
42. Bu G. **Apolipoprotein E and its receptors in Alzheimer's disease: pathways, pathogenesis and therapy.** *Nat Rev Neurosci* 2009;10: 333–44 CrossRef Medline
43. Small GW, Siddarth P, Burggren AC, et al. **Influence of cognitive status, age, and APOE-4 genetic risk on brain FDDNP positron-emission tomography imaging in persons without dementia.** *Arch Gen Psychiatry* 2009;66:81–87 CrossRef Medline
44. Vittinghoff E, Shiboski S, Glidden D, et al. *Regression Methods in Biostatistics: Linear, Logistic, Survival, and Repeated Measures Models.* New York: Springer-Science and Business Media; 2005;62:138–39
45. Cohen J. **A power primer.** *Psychol Bull* 1992;112:155–59 Medline
46. How can I compute effect size in Stata for regression? UCLA: Institute for Digital Research and Education. http://www.ats.ucla.edu/stat/stata/faq/regeffectsize.htm. Accessed December 15, 2016

47. Cohen JW. *Statistical Power Analysis for the Behavioral Sciences*. 2nd ed. Hillsdale: Lawrence Erlbaum Associates; 1988
48. Corder EH, Saunders AM, Strittmatter WJ, et al. **Gene dose of apolipoprotein E type 4 allele and the risk of Alzheimer's disease in late onset families.** *Science* 1993;261:921–23 CrossRef Medline
49. Seshadri S, Drachman DA, Lippa CF. **Apolipoprotein E epsilon 4 allele and the lifetime risk of Alzheimer's disease: what physicians know, and what they should know.** *Arch Neurol* 1995;52:1074–79 CrossRef Medline
50. Mandal PK, Saharan S, Tripathi M, et al. **Brain glutathione levels–a novel biomarker for mild cognitive impairment and Alzheimer's disease.** *Biol Psychiatry* 2015;78:702–10 CrossRef Medline
51. Gu M, Owen AD, Toffa SE, et al. **Mitochondrial function, GSH and iron in neurodegeneration and Lewy body diseases.** *J Neurol Sci* 1998;158:24–29 CrossRef Medline
52. Jain A, Mårtensson J, Stole E, et al. **Glutathione deficiency leads to mitochondrial damage in brain.** *Proc Natl Acad Sci U S A* 1991;88:1913–17 CrossRef Medline
53. Venkateshappa C, Harish G, Mahadevan A, et al. **Elevated oxidative stress and decreased antioxidant function in the human hippocampus and frontal cortex with increasing age: implications for neurodegeneration in Alzheimer's disease.** *Neurochem Res* 2012;37:1601–14 CrossRef Medline
54. Gibson GE, Starkov A, Blass JP, et al. **Cause and consequence: mitochondrial dysfunction initiates and propagates neuronal dysfunction, neuronal death and behavioral abnormalities in age-associated neurodegenerative diseases.** *Biochim Biophys Acta* 2010;1802:122–34 CrossRef Medline
55. Lin MT, Beal MF. **Mitochondrial dysfunction and oxidative stress in neurodegenerative diseases.** *Nature* 2006;443:787–95 CrossRef Medline
56. Duffy SL, Lagopoulos J, Hickie IB, et al. **Glutathione relates to neuropsychological functioning in mild cognitive impairment.** *Alzheimers Dement* 2014;10:67–75 CrossRef Medline
57. Lezak MD, Howieson D, Loring D. *Neuropsychological Assessment*, 4th ed. Oxford: Oxford University Press; 2004:207–15
58. Blacker D, Lee H, Muzikansky A, et al. **Neuropsychological measures in normal individuals that predict subsequent cognitive decline.** *Arch Neurol* 2007;64:862–71 CrossRef Medline
59. Wonisch W, Falk A, Sundl I, et al. **Oxidative stress increases continuously with BMI and age with unfavourable profiles in males.** *Aging Male* 2012;15:159–65 CrossRef Medline

Noninvasive Assessment of *IDH* Mutational Status in World Health Organization Grade II and III Astrocytomas Using DWI and DSC-PWI Combined with Conventional MR Imaging

Z. Xing, X. Yang, D. She, Y. Lin, Y. Zhang, and D. Cao

ABSTRACT

BACKGROUND AND PURPOSE: *Isocitrate dehydrogenase* (*IDH*) has been shown to have both diagnostic and prognostic implications in gliomas. The purpose of this study was to examine whether DWI and DSC-PWI combined with conventional MR imaging could noninvasively predict *IDH* mutational status in World Health Organization grade II and III astrocytomas.

MATERIALS AND METHODS: We retrospectively reviewed DWI, DSC-PWI, and conventional MR imaging in 42 patients with World Health Organization grade II and III astrocytomas. Minimum ADC, relative ADC, and relative maximum CBV values were compared between *IDH*-mutant and wild-type tumors by using the Mann-Whitney *U* test. Receiver operating characteristic curve and logistic regression were used to assess their diagnostic performances.

RESULTS: Minimum ADC and relative ADC were significantly higher in *IDH*-mutated grade II and III astrocytomas than in *IDH* wild-type tumors ($P < .05$). Minimum ADC with the cutoff value of $\geq 1.01 \times 10^{-3}$ mm^2/s could differentiate the mutational status with a sensitivity, specificity, positive predictive value, and negative predictive value of 76.9%, 82.6%, 91.2%, and 60.5%, respectively. The threshold value of <2.35 for relative maximum CBV in the prediction of *IDH* mutation provided a sensitivity, specificity, positive predictive value, and negative predictive value of 100.0%, 60.9%, 85.6%, and 100.0%, respectively. A combination of DWI, DSC-PWI, and conventional MR imaging for the identification of *IDH* mutations resulted in a sensitivity, specificity, positive predictive value, and negative predictive value of 92.3%, 91.3%, 96.1%, and 83.6%.

CONCLUSIONS: A combination of conventional MR imaging, DWI, and DSC-PWI techniques produces a high sensitivity, specificity, positive predictive value, and negative predictive value for predicting *IDH* mutations in grade II and III astrocytomas. The strategy of using advanced, semiquantitative MR imaging techniques may provide an important, noninvasive, surrogate marker that should be studied further in larger, prospective trials.

ABBREVIATIONS: ADC_{min} = minimum ADC; cMRI = conventional MR imaging; *IDH* = *isocitrate dehydrogenase*; rADC = relative ADC; rCBV = relative CBV; $rCBV_{max}$ = relative maximum CBV; WHO = World Health Organization

Infiltrating astrocytomas are the most common primary central nervous system tumors, ranging variably from grade II to IV according to the 2007 World Health Organization classification system.[1,2] Glioma grading is based on histopathologic analysis of tumor differentiation, mitotic activity, cellularity, nuclear atypia, and the extent of microvascular proliferation and may result in a great deal of interobserver variability.[1-3] Therefore, quantitative molecular analyses have the potential to reduce subjectivity and improve diagnosis, prognostication, risk stratification, and management plans. Notably, in the 2016 World Health Organization (WHO) classification, grade II and III astrocytomas are molecularly divided into *isocitrate dehydrogenase* (*IDH*) mutant, *IDH* wild type, and not otherwise specified categories, emphasizing the value of *IDH* mutation status in astrocytomas.[4]

IDH gene mutations, originally discovered in high-grade gliomas in 2008, exist in 60%–90% of grade II and III astrocytomas.[5,6] The *IDH* gene (including *IDH1* and *IDH2* genes) plays prominent roles in the metabolism, pathogenesis, and progression of astrocytomas.[7-9] In addition, stratification of grade II and III gliomas

Received October 22, 2016; accepted after revision February 6, 2017.

From the Department of Radiology, First Affiliated Hospital of Fujian Medical University, Fuzhou, P.R. China.

Zhen Xing and Xiefeng Yang contributed equally to this work.

This work was supported by the Leading Project of the Department of Science and Technology of Fujian Province (No. 2016Y0101) to Dairong Cao, Special Funds of the Provincial Finance of Fujian Province (No. BPB-CDR2013) to Dairong Cao, and the Research Foundation for Young Scholars of the Health Department of Fujian Province (No. 2013–1-34) to Zhen Xing.

Please address correspondence to Dairong Cao, MD, Department of Radiology, First Affiliated Hospital of Fujian Medical University, 20 Cha-Zhong Rd, Fuzhou 350005, Fujian, P.R. China; e-mail: dairongcao@163.com

http://dx.doi.org/10.3174/ajnr.A5171

into subsets defined by *IDH* mutation would help identify subgroups with distinct prognostic characteristics, therapeutic response, and clinical management.[10-16] In a study with a cohort of 475 patients, comparison of overall survival between those with WHO grade II and III *IDH*-mutated astrocytomas showed no remarkable difference, whereas the patients with *IDH*-mutated tumors survived much longer than those with *IDH* wild-type tumors.[10] Patients with grade II astrocytomas without *IDH* mutation were shown to have a poorer prognosis with a 5-year progression-free survival and overall survival rate of 14% and 51%, respectively, compared with 42% and 93% for those with *IDH*-mutant tumors ($P < .001$).[17] Moreover, patients with gliomas whose lesions had *IDH* mutations were more sensitive to chemoradiation therapy and survived longer than those with wild-type *IDH*.[10,15]

Currently, immunohistochemical staining and DNA sequencing are the most common methods for determining the *IDH* mutational status in gliomas. *IDH* gene mutations may reflect alterations in metabolism, cellularity, and angiogenesis, which may manifest characteristic features on DWI and DSC-PWI.[8,18] DWI can noninvasively provide direct insight into the microscopic physical properties of tissues through observing the Brownian movement of water and reflecting cellularity within the lesions by ADC values.[19-21] In vivo measurement of relative CBV (rCBV) has been demonstrated to correlate with tumor vascularity.[22-24] ADC values derived from DWI and DSC-PWI have been used to detect *IDH* gene status in gliomas in recent research.[24-26] Meanwhile, conventional MR imaging (cMRI) was also used to assess other characteristics of gliomas (eg, location, distinctness of borders, enhancement, and edema).[17,27,28]

To our knowledge, there is no study in the literature combining cMRI with diffusion and perfusion techniques to distinguish *IDH* genotypes. The purpose of this study was to explore whether a novel approach, in which DWI and DSC-PWI were combined with cMRI, was able to noninvasively predict *IDH* mutational status in WHO grade II and III astrocytomas.

MATERIALS AND METHODS

Patients

The ethics committee of our hospital approved this retrospective study, and the requirement for patient informed consent was waived due to the nature of the retrospective study. Ninety-six patients who underwent surgical resection or stereotactic biopsy at our institution from July 2014 through June 2016 were selected. The inclusion criteria were as follows: 1) definite histopathologic diagnosis of grade II and III astrocytomas based on the WHO 2016 classification criteria, 2) cMRI, DWI, and DSC-PWI performed before treatment, and 3) all data available in 3T MR imaging. As a result, 42 patients (26 males and 16 females; mean age, 41.83 ± 15.98 years; age range, 8–72 years) were included in the study.

MR Imaging Techniques

Images were acquired in the routine clinical work-up on a 3T MR imaging system (Magnetom Verio Tim; Siemens, Erlangen, Germany) with an 8-channel head matrix coil. The conventional MR imaging protocols consisted of the following sequences: axial T1-weighted gradient-echo imaging (TR = 250 ms; TE = 2.48 ms), axial T2-weighted turbo spin-echo imaging (TR = 4000 ms; TE = 96 ms), axial fluid-attenuated inversion recovery imaging (TR/TE = 9000/94 ms; TI= 2500 ms), and 3 orthogonal plane contrast-enhanced gradient-echo T1-weighted imaging scans (TR/TE, 250/2.48 ms) acquired following the acquisition of DSC-PWI sequences. The section thickness (5 mm), intersection gap (1 mm), and FOV (220 × 220 mm) were uniform in all sequences.

DWI was performed in the axial plane with a spin-echo echo-planar sequence before injection of contrast material. The imaging parameters used were as follows: TR/TE = 8200/102 ms, NEX = 2.0, section thickness = 5 mm, intersection gap = 1 mm, FOV = 220 × 220 mm. The b-values were 0 and 1000 s/mm^2 with diffusion gradients encoded in the 3 orthogonal directions to generate 3 sets of diffusion-weighted images. Processing of the ADC map was generated automatically by the MR imaging system.

DSC-PWI was performed with a gradient-recalled T2*-weighted echo-planar imaging sequence. The imaging parameters were as follows: TR/TE = 1000–1250/54 ms, flip angle = 35°, section thickness = 5 mm, intersection gap = 1 mm, NEX = 1.0, FOV = 220 × 220 mm. During the first 3 phases, images were acquired before injecting the contrast material to establish a precontrast baseline. When the scan was to the fourth phase of DSC-PWI, a bolus of gadobenate dimeglumine at a dose of 0.1 mmol/kg of body weight and 5 mL/s was injected intravenously with an MR imaging–compatible power injector. After we injected a bolus of the contrast material, a 20.0-mL bolus of saline was administered at the same injection rate. The series of 20 sections, 60 phases, and 1200 images was obtained in 1 minute 36 seconds.

Table 1: The main clinical and cMRI features of *IDH* mutational status in grade II and III astrocytomas[a]

	IDH Mutation (*n* = 17)	*IDH* Wild Type (*n* = 25)	*P* Value
Sex (male/female)	9/8	17/8	.157
Age (yr)	35.76 ± 9.13	45.96 ± 18.36	.041
Location			.006
Frontal lobe	9 (52.9%)	4 (16.0%)	
Parietal lobe	1 (5.9%)	3 (12.0%)	
Temporal lobe	6 (35.3%)	4 (16.0%)	
Occipital lobe	0	0	
Insular lobe	1 (5.9%)	3 (12.0%)	
Others	0	11 (44.0%)	
Homogeneity			.439
Homogeneous	4 (23.5%)	7 (28.0%)	
Heterogeneous	13 (76.5%)	18 (72.0%)	
Edema			.746
Presence	3 (17.6%)	7 (28.0%)	
Absence	14 (82.4%)	18 (72.0%)	
Borders			.037
Sharp	11 (64.7%)	8 (32.0%)	
Indistinct	6 (35.3%)	17 (68.0%)	
Contrast enhancement			.286
No	11 (64.7%)	12 (48.0%)	
Yes	6 (35.3%)	13 (54.0%)	
Histology			.051
Grade II astrocytomas	12 (70.6%)	12 (48.0%)	
Grade III astrocytomas	5 (29.4%)	13 (54.0%)	

[a] Data are number (%) unless otherwise indicated.

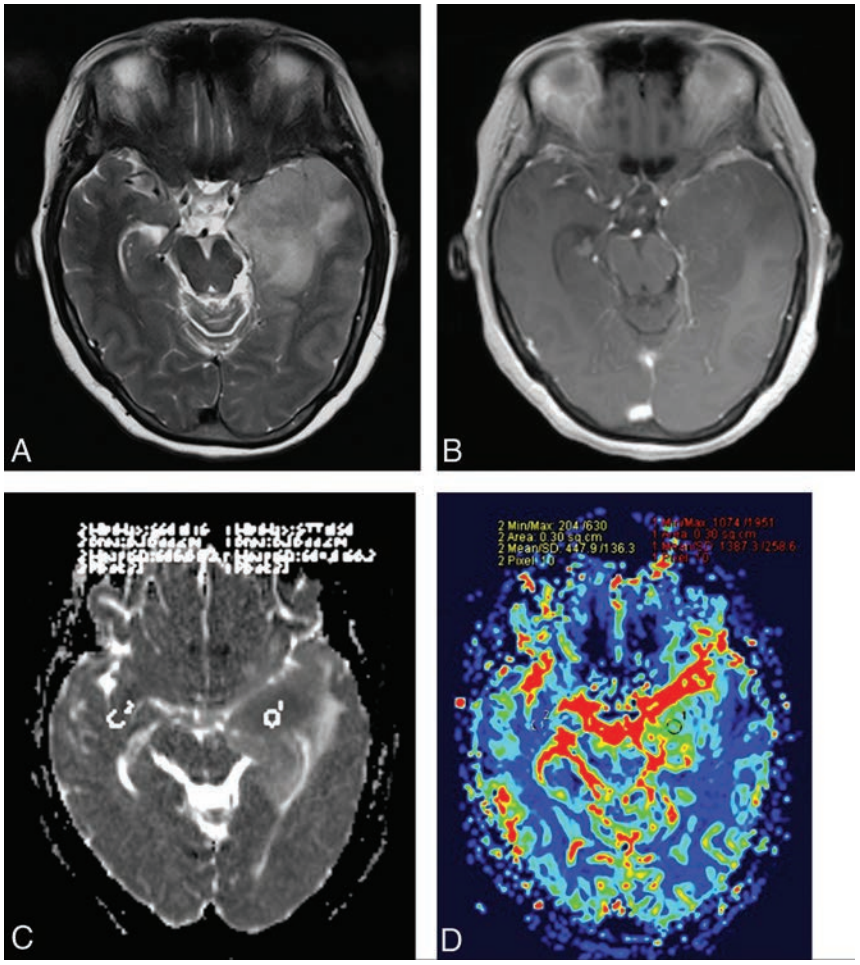

FIG 1. A 52-year-old woman with a diffuse astrocytoma without *IDH* mutation. *A*, Axial T2WI demonstrates heterogeneous high signal intensity with indistinct borders on the left temporal lobe. *B*, Contrast-enhanced axial T1-weighted image demonstrates a lesion enhancement with blurred borders. *C*, A corresponding ADC map shows the tumor with a decreased ADC value ($ADC_{min} = 0.684 \times 10^{-3}$ mm^2/s, rADC = 1.08). *D*, Correlative color CBV image shows elevated perfusion with the calculated $rCBV_{max}$ of 3.10.

Data Processing

Image postprocessing of perfusion data and perfusion measurements was performed on an off-line syngo B19 workstation (Siemens) with standard software. All cMRI data with respect to tumor locations, heterogeneity, borders, peritumoral edema, and contrast-enhancement pattern were assessed by 2 neuroradiologists who were blinded to tumor histology and molecular characteristics. Tumor location, considered to be the lobe within which the bulk of the tumor resided, was divided into 6 groups: frontal lobe, temporal lobe, parietal lobe, insular lobe, occipital lobe, and others (basal ganglia, thalamus, brain stem, and cerebellum). Edema was defined as a nonenhanced area on contrast-enhanced T1WI and higher signal outside the tumoral solid area on T2WI and FLAIR. Tumor borders were classified as sharp or indistinct on the basis of T2WI and FLAIR sequences (relatively decreased signal intensity on T2WI or FLAIR should be regarded as tumor area rather than edema in gliomas). A senior neuroradiologist made the final decision when 2 observers disagreed.

For evaluation of DWI data, ADC values were measured by manually selecting ROIs inside the tumor regions on the ADC maps. All continuous sections including tumors were observed. At least 5 small round ROIs (30–40 mm^2) were placed inside the tumors on the ADC maps without overlap. The bigger the tumor was, the more ROIs were selected. Finally, the ROI with the lowest ADC value was chosen to calculate minimum ADC (ADC_{min}). We made the ROI placement from the solid portion of the lesion (defined on T2WI and contrast-enhanced T1WI), avoiding hemorrhagic, cystic, necrotic, or apparent blood vessel regions that might influence the ADC values. The minimum ADC is calculated as the mean value of the ROI of the lowest ADC value. The same method was applied to a corresponding area in the contralateral normal-appearing white matter judged on both T2WI and contrast-enhanced T1WI. Relative ADC (rADC) of the tumors was determined as the ratio of the minimum ADC divided by the mean ADC of the contralateral unaffected white matter. ADC_{min} values were expressed as $\times 10^{-3}$ square millimeters per second.

For assessment of DSC-PWI data, whole-brain CBV maps were generated by applying a single-compartment model and an automated arterial input function. The relative maximum CBV ($rCBV_{max}$) was calculated by dividing the tumor CBV voxel value by the mean CBV value of the contralateral unaffected white matter to minimize variances in $rCBV_{max}$ values in each individual patient. Measurements of $rCBV_{max}$ values were performed with the same ROIs as those used for ADC measurements. The ROIs for the ADC and rCBV measurements were not identical and were not from the same region of the tumor in each patient. The signal intensities on DWI, rADC, ADC_{min}, and $rCBV_{max}$ parameters were determined by another senior neuroradiologist who was experienced in diffusion and perfusion data acquisition and blinded to the tumor histology and molecular data. This method has been shown to provide the highest interobserver and intraobserver reproducibility.[29]

Immunohistochemistry Staining

Immunohistochemistry was performed on 5-μm-thick sections from paraffin-embedded tumor specimens of all evaluated patients. Sections were incubated overnight at 4°C with the monoclonal anti-mIDH1 antibody (DIA-H09; Dianova, Hamburg, Germany) that specifically reacts with the mutant IDH1-R132, the most common glioma-derived mutation,[30] but not with the wild-type *IDH1*. Following incubation with horseradish peroxidase–conjugated secondary antibody, the slides were then stained with the Cytomation EnVision + System horseradish peroxidase (diaminobenzidine) detection

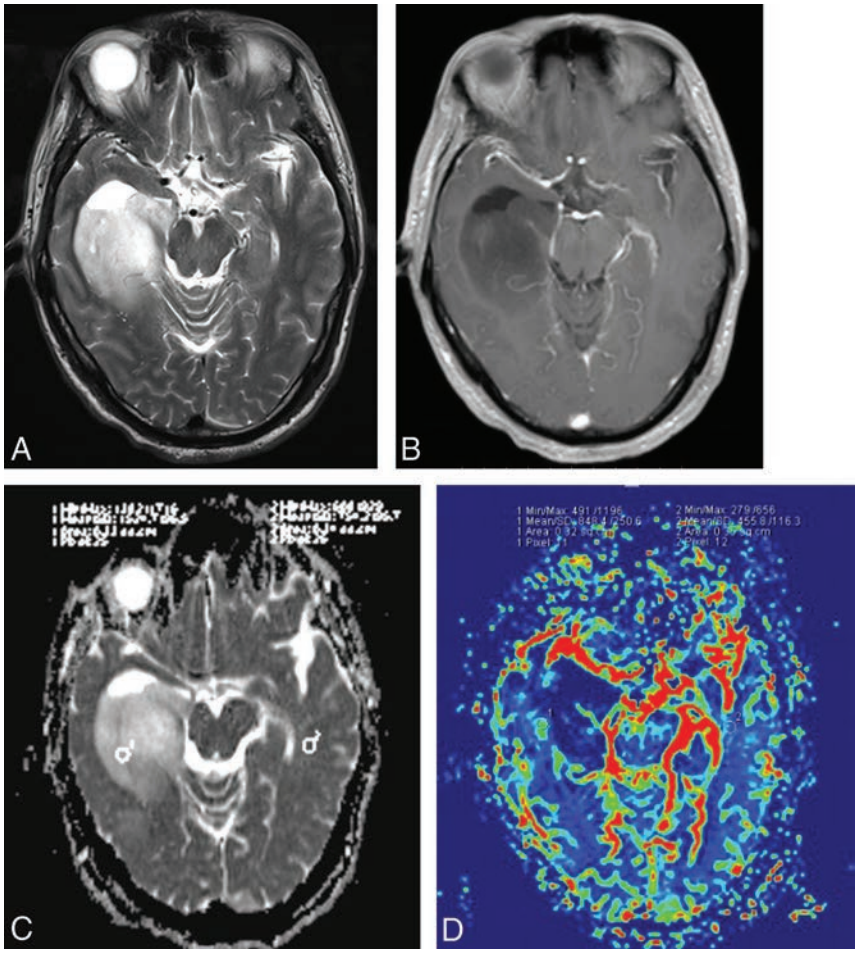

FIG 2. A 50-year-old man with an anaplastic astrocytoma with an *IDH* mutation. *A*, Axial T2WI demonstrates heterogeneous high signal intensity with sharp borders on the right temporal lobe. *B*, Contrast-enhanced axial TI-weighted image demonstrates a nonenhancing lesion in the right temporal region. *C*, A corresponding ADC map shows the tumor with an increased ADC value ($ADC_{min} = 1.456 \times 10^{-3} mm^2/s$, rADC = 2.51). *D*, Correlative color CBV image shows relatively low perfusion with the calculated $rCBV_{max}$ of 1.86.

Table 2: Comparison of DWI and DSC-PWI variables between *IDH* mutation and wild-type grade II and III astrocytomas

	IDH Mutation	*IDH* Wild Type	*P* Value
ADC_{min} ($\times 10^{-3}$ mm^2/s)	1.21 ± 0.27	0.87 ± 0.18	<.001
rADC	1.88 ± 0.41	1.37 ± 0.31	<.001
$rCBV_{max}$	1.41 ± 0.50	3.47 ± 2.34	.004

[a] Data are means.

kit (Dako, Carpenteria, California) and counterstained with hematoxylin. Staining was interpreted as positive when ≥10% of tumor cells showed a strong cytoplasmic staining for mIDH1, whereas staining of <10% of tumor cells was counted as negative findings.[31]

DNA Sequencing

Genomic DNA was extracted from formalin-fixed, paraffin-embedded tissue sections by using MyghtyAmp for FFPE (Takara Bio, Shiga, Japan), according to the manufacturer's instructions. Mutational alterations of *IDH1* and *IDH2* at hotspot codons R132 and R172 were assessed by a bidirectional cycle sequencing of polymerase chain reaction–amplified fragments with the following primers: IDH1f (5′-TGCCACCAACGACCAAGTCA-3′) and IDH1r (5′-CATGCAAAA TCACATATTTGCC-3′); IDH2f (5′-TGAAAGATGGCGGCTGCAGT-3′) and IDH2r (5′-GGGGTGAAGACCATTTTGAA-3′).

Data Analysis

All quantitative parameters are presented as mean ± SD. Comparisons of ADC_{min}, rADC, and $rCBV_{max}$ values between *IDH*-mutant and wild type of grade II and III astrocytomas were made with the Mann-Whitney *U* test. The receiver operating characteristic and logistic regression analysis were performed to determine the best cutoff value in discriminating *IDH*-mutant from wild-type tumors. The sensitivity, specificity, positive predictive value, negative predictive value, Youden index, and area under the curve based on optimum thresholds for variable parameters were calculated. We chose the cutoff value for each quantitative parameter that provided optimal sensitivity and specificity. In addition, comparisons of the areas under the curve for different variables were made with the *Z*-test. Statistical analysis was calculated in SPSS, Version 19.0 (IBM, Armonk, New York). $P < .05$ was considered significant.

RESULTS

Forty-two histologically confirmed grade II and III astrocytoma cases including 17 cases with *IDH* mutation and 25 cases without such mutation were enrolled in this study. The clinical, histologic, and cMRI characteristics are summarized in Table 1. Twenty-five patients with no *IDH1* or *IDH2* mutations were older (*IDH* mutation = 35.76 ± 9.13 years, *IDH* wild type = 45.96 ± 18.36 years, $P = .041$) and demonstrated more indistinct margins than those with *IDH* mutations (*IDH* mutation, 6/17; *IDH* wild type, 17/25; $P = .037$). Tumors with *IDH* mutations were more likely to occur in the frontal lobes (Figs 1*A*, -*B*, and 2*A*, -*B*). No differences in heterogeneous appearance were observed among the groups.

The ADC_{min} values, rADC ratios, and $rCBV_{max}$ calculated for *IDH*-mutant and wild-type grade II and III astrocytomas are summarized in Table 2. Both the ADC_{min} (*IDH* mutation = 1.21 ± 0.27, *IDH* wild type = 0.87 ± 0.18; $P < .001$) and rADC (*IDH* mutation = 1.88 ± 0.41; *IDH* wild type = 1.37 ± 0.31; $P < .001$) were significantly higher in *IDH*-mutant tumors than in wild types (Figs 1*C* and 2*C*). The $rCBV_{max}$ (*IDH* mutation = 1.41 ± 0.50; *IDH* wild type = 3.47 ± 2.34; $P = .004$) in patients with *IDH*-mutant tumors was significantly lower than in those with *IDH* wild-type tumors (Table 2 and Figs 1*D* and 2*D*).

The results of the receiver operating characteristic curve analysis are shown in Table 3 and Fig 3. Logistic regression analysis

Table 3: Measurement of TV, sensitivity, specificity, PPV, NPV, YI, and AUC of ADC_{min} values, rADC, $rCBV_{max}$, cMRI, DWI + DSC-PWI, and cMRI+ DWI + DSC-PWI for assessing the *IDH* status of grade II and III astrocytomas

	TV	Sensitivity (%)	Specificity (%)	PPV (%)	NPV (%)	YI	AUC (95% CI)
ADC_{min}	1.01	76.92	82.61	91.20	60.50	0.60	0.87 (0.71–0.96)
rADC	1.60	84.62	73.91	88.30	67.30	0.59	0.84 (0.68–0.94)
$rCBV_{max}$	2.35	100.00	60.87	85.60	100.00	0.61	0.82 (0.66–0.93)
cMRI		88.24	52.00	88.50	44.30	0.40	0.78 (0.63–0.89)
DWI + DSC-PWI		100.00	65.22	87.00	100.00	0.65	0.88 (0.54–0.84)
cMRI+ DWI + DWI-PWI		92.31	91.30	96.10	83.60	0.84	0.92 (0.78–0.98)

Note:—TV indicates threshold values; PPV, positive predictive value; NPV, negative predictive value; YI, Youden Index; AUC, area under the curve.

was used to test these cMRI parameters among groups; then, a combination of cMRI, DWI, and DSC-PWI for the diagnosis of *IDH* mutation yielded a sensitivity, specificity, positive predictive value, negative predictive value, and Youden index of 92.31%, 91.30%, 96.10%, 83.60%, and 0.84, respectively. A significant difference was found in the areas under the curve between cMRI and cMRI + DWI + DSC-PWI ($Z = 2.8$, $P = .005$).

DISCUSSION

The present study demonstrates that cMRI, DWI, and DSC-PWI can be used to evaluate the *IDH* mutational status in gliomas and that a combination of DWI, DSC-PWI, and cMRI further improves the diagnostic accuracy. We found that patients with *IDH* wild-type tumors were significantly older than those with *IDH*-mutated tumors. This correlation between age and *IDH* mutation status in grade II gliomas has also been reported by Metellus et al.[17] Our finding that *IDH*-mutated tumors tend to reside in the frontal lobes is consistent with previous studies reporting that *IDH*-mutation tumors are strongly associated with frontal locations.[9,28] In this study, all 11 tumors that did not involve the cerebral cortex were *IDH* wild type, which confirmed a previous finding in anaplastic gliomas that tumors not located in the cerebral cortex were *IDH*-intact tumors.[27] While the radiologic appearance of infiltrating lesions in anaplastic gliomas was associated with *IDH* mutation status,[17] these cMRI characteristics lack the ability to quantify the findings. Indeed, it is challenging to determine molecular alterations of such tumors by using cMRI only.

ADC_{min} values have been extensively used to investigate brain tumors and their prognosis.[21,32-34] Tan et al[25] reported that ADC_{min} and rADC could be used to identify gliomas with and without *IDH* mutation. Similarly, Lee et al[35] found that the mean ADC value was a useful parameter for differentiating *IDH1* gene mutation–positive high-grade gliomas from the mutation-negative subtypes with histogram analysis. Our study demonstrated that the ADC_{min} and rADC values of *IDH*-mutant grade II and III astrocytomas were higher than those of wild types. ADC_{min} has been shown to depict the sites of highest cellularity within heterogeneous tumors.[21,33] Therefore, we chose this simple-but-efficient method for the tumor analysis and differentiation. Accumulating evidence has indicated that mutation in the *IDH* gene family could reduce catalytic generation of α-ketoglutarate and, in turn, lead to the production of the oncometabolite (R)-2-hydroxyglutarate [(R)-2HG], ultimately giving rise to increased cell proliferation or cellularity.[36-38] Therefore, it is conceivable that differences in ADC_{min} and rADC values as presented in the current study might be useful for predicting the molecular profile in astrocytomas with respect to *IDH* mutational status.

DSC-PWI has the potential to noninvasively provide morphologic and functional information about gliomas.[22,23] Law et al[39] reported that DSC-PWI could be used to predict the median time to progression in gliomas and that a lower rCBV corresponds to significantly prolonged progression-free survival. However, these authors did not investigate the rCBV-related molecular mechanisms such as *IDH* mutation. Our data suggest that $rCBV_{max}$ values are significantly associated with the *IDH* mutational status. Recent research showed that *IDH* mutation leads to 2HG (an activator of Egl-9 prolyl-4-hydroxylases) accumulation, resulting in decreased hypoxia-inducible-factor 1-α activation and downstream inhibition of angiogenesis-related signaling.[38,40] As demonstrated by Kickingereder et al[18] that *IDH*-mutant and wild-type tumors were both associated with distinct imaging phenotypes and were predictable with rCBV imaging in a clinical setting, rCBV maps were used to evaluate *IDH* mutational status of high-grade gliomas with similar results (ie, *IDH* mutant tumors represented considerably lower rCBV).[35] Similarly, the $rCBV_{max}$ values in our cases with *IDH* mutation were significantly lower than wild types. Therefore, our findings are in good agreement with prior results and theories. In this study, *IDH*-mutated grade II and III astrocytomas were found to correlate with higher ADC_{min} and rADC and lower rCBV; this correlation corresponds to low levels of cellular density and angiogenesis. These relationships may explain why *IDH* mutation is an independent favorable prognostic marker in patients with gliomas.[14-19] Glioblastoma is the most common malignant and fatal type of brain tumor, with a poor prognosis.[5,10] Although the presence of an *IDH* mutation is a strong, independent prognostic factor in gliomas, it had been shown that even *IDH*-mutated glioblastomas exhibited clinical outcomes similar to those of grade III astrocytomas without *IDH* mutation.[6] The *IDH* mutation is relatively rare in glioblastomas because it is associated with secondary but not primary tumors.[5] Thus, glioblastomas were excluded from our study.

IDH mutation in diffuse gliomas has been considered the most robust prognostic implication in previous studies.[10-17] *IDH* mutation was associated with a significantly better clinical outcome with 5-year overall survival (93% compared with 51% for wild type).[17] Although our results demonstrated that MR imaging parameters could noninvasively predict *IDH* mutational status in WHO grade II and III astrocytomas, the correlation between imaging parameters and clinical outcomes has not been studied because of the retrospective nature of this study and a short-term follow-up. Nevertheless, a few studies have demonstrated that low ADC values related directly to poor survival in high-grade astrocytomas and that rCBV values

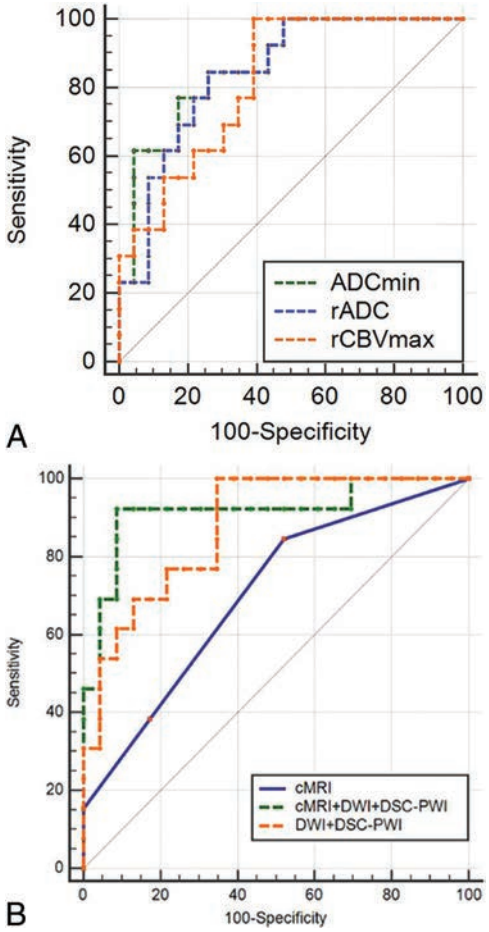

FIG 3. Comparison of receiver operating characteristic curves of ADC_{min}, rADC, $rCBV_{max}$ (*A*) and cMRI, DWI + DSC-PWI, and cMRI + DWI + DSC-PWI (*B*) in differentiating *IDH*-mutant grade II and III astrocytomas from wild types.

were positively correlated with median time to progression in patients with gliomas.[32,39,41,42]

There are a few limitations to this study. It has inherent biases associated with retrospective analyses and a relatively small sample size. A multicentered prospective investigation with a larger sample size is warranted to verify these results and ensure the reproducibility. Second, owing to the short-term follow-up, the clinical outcomes are not available. Imaging parameters as predictors of clinical outcomes should be further studied in larger, prospective trials. Third, the classic biomarker of the human p53 tumor suppressor gene (*TP53*) mutation and O6-methylguanine-DNA methyltransferase (*MGMT*) promoter methylation status was not used in this study for case grouping due to lack of relevant molecular pathologic data in our research. Finally, tumor borders were defined with reference to high signal intensity on T2WI and FLAIR, but it is difficult to differentiate tumor infiltration and peritumoral edema merely on the basis of their radiologic appearance.

CONCLUSIONS

Compared with *IDH* wild-type tumors, *IDH*-mutant tumors tend to have a higher ADC_{min} and rADC and a lower $rCBV_{max}$. Application of cMRI with advanced imaging modalities such as DWI and DSC-PWI is useful to predict *IDH* mutational status in grade II and III astrocytomas and may provide an important, noninvasive, surrogate marker that should be studied further and clinically correlated in larger, prospective trials.

REFERENCES

1. Daumas-Duport C, Scheithauer B, O'Fallon J, et al. **Grading of astrocytomas: a simple and reproducible method.** *Cancer* 1988;62:2152–65 Medline
2. Fuller GN, Scheithauer BW. **The 2007 Revised World Health Organization (WHO) Classification of Tumours of the Central Nervous System: newly codified entities.** *Brain Pathol* 2007;17:304–07 CrossRef Medline
3. van den Bent MJ. **Interobserver variation of the histopathological diagnosis in clinical trials on glioma: a clinician's perspective.** *Acta Neuropathol* 2010;120:297–304 CrossRef Medline
4. Louis DN, Perry A, Reifenberger G, et al. **The 2016 World Health Organization Classification of Tumors of the Central Nervous System: a summary.** *Acta Neuropathol* 2016;131:803–20 CrossRef Medline
5. Parsons DW, Jones S, Zhang X, et al. **An integrated genomic analysis of human glioblastoma multiforme.** *Science* 2008;321:1807–12 CrossRef Medline
6. Hartmann C, Meyer J, Balss J, et al. **Type and frequency of IDH1 and IDH2 mutations are related to astrocytic and oligodendroglial differentiation and age: a study of 1,010 diffuse gliomas.** *Acta Neuropathol* 2009;118:469–74 CrossRef Medline
7. Yan H, Parsons DW, Jin G, et al. **IDH1 and IDH2 mutations in gliomas.** *N Engl J Med* 2009;360:765–73 CrossRef Medline
8. Balss J, Meyer J, Mueller W, et al. **Analysis of the IDH1 codon 132 mutation in brain tumors.** *Acta Neuropathol* 2008;116:597–602 CrossRef Medline
9. Watanabe T, Nobusawa S, Kleihues P, et al. **IDH1 mutations are early events in the development of astrocytomas and oligodendrogliomas.** *Am J Pathol* 2009;174:1149–53 CrossRef Medline
10. Olar A, Wani KM, Alfaro-Munoz KD, et al. **IDH mutation status and role of WHO grade and mitotic index in overall survival in grade II–III diffuse gliomas.** *Acta Neuropathol* 2015;129:585–96 CrossRef Medline
11. Nikiforova MN, Hamilton RL. **Molecular diagnostics of gliomas.** *Arch Pathol Lab Med* 2011;135:558–68 CrossRef Medline
12. Reuss DE, Mamatjan Y, Schrimpf D, et al. **IDH mutant diffuse and anaplastic astrocytomas have similar age at presentation and little difference in survival: a grading problem for WHO.** *Acta Neuropathol* 2015;129:867–73 CrossRef Medline
13. Sanson M, Marie Y, Paris S, et al. **Isocitrate dehydrogenase 1 codon 132 mutation is an important prognostic biomarker in gliomas.** *J Clin Oncol* 2009;27:4150–54 CrossRef Medline
14. Bleeker FE, Atai NA, Lamba S, et al. **The prognostic IDH1 (R132) mutation is associated with reduced NADP+-dependent IDH activity in glioblastoma.** *Acta Neuropathol* 2010;119:487–94 CrossRef Medline
15. Krell D, Mulholland P, Frampton AE, et al. **IDH mutations in tumorigenesis and their potential role as novel therapeutic targets.** *Future Oncol* 2013;9:1923–35 CrossRef Medline
16. Rohle D, Popovici-Muller J, Palaskas N, et al. **An inhibitor of mutant IDH1 delays growth and promotes differentiation of glioma cells.** *Science* 2013;340:626–30 CrossRef Medline
17. Metellus P, Coulibaly B, Colin C, et al. **Absence of IDH mutation identifies a novel radiologic and molecular subtype of WHO grade II gliomas with dismal prognosis.** *Acta Neuropathol* 2010;120:719–29 CrossRef Medline
18. Kickingereder P, Sahm F, Radbruch A, et al. **IDH mutation status is associated with a distinct hypoxia/angiogenesis transcriptome signature which is non-invasively predictable with rCBV imaging in human glioma.** *Sci Rep* 2015;5:16238 CrossRef Medline

19. Schaefer PW, Grant PE, Gonzalez RG. **Diffusion-weighted MR imaging of the brain.** *Radiology* 2000;217:331–45 CrossRef Medline
20. Le Bihan D. **Looking into the functional architecture of the brain with diffusion MRI.** *Nat Rev Neurosci* 2003;4:469–80 CrossRef Medline
21. Humphries PD, Sebire NJ, Siegel MJ, et al. **Tumors in pediatric patients at diffusion-weighted MR imaging: apparent diffusion coefficient and tumor cellularity.** *Radiology* 2007;245:848–54 CrossRef Medline
22. Guzmán-De-Villoria JA, Mateos-Pérez JM, Fernández-García P, et al. **Added value of advanced over conventional magnetic resonance imaging in grading gliomas and other primary brain tumors.** *Cancer Imaging* 2014;14:1–10 CrossRef Medline
23. Cuccarini V, Erbetta A, Farinotti M, et al. **Advanced MRI may complement histological diagnosis of lower grade gliomas and help in predicting survival.** *J Neurooncol* 2016;126:279–88 CrossRef Medline
24. Jain R, Gutierrez J, Narang J, et al. **In vivo correlation of tumor blood volume and permeability with histologic and molecular angiogenic markers in gliomas.** *AJNR Am J Neuroradiol* 2011;32:388–94 CrossRef Medline
25. Tan WL, Huang WY, Yin B, et al. **Can diffusion tensor imaging noninvasively detect IDH1 gene mutations in astrogliomas? A retrospective study of 112 cases.** *AJNR Am J Neuroradiol* 2014;35:920–27 CrossRef Medline
26. Khayal IS, Vandenberg SR, Smith KJ, et al. **MRI apparent diffusion coefficient reflects histopathologic subtype, axonal disruption, and tumor fraction in diffuse-type grade II gliomas.** *Neuro Oncol* 2011;13:1192–201 CrossRef Medline
27. Sonoda Y, Shibahara I, Kawaguchi T, et al. **Association between molecular alterations and tumor location and MRI characteristics in anaplastic gliomas.** *Brain Tumor Pathol* 2015;32:99–104 CrossRef Medline
28. Carrillo JA, Lai A, Nghiemphu PL, et al. **Relationship between tumor enhancement, edema, IDH1 mutational status, MGMT promoter methylation, and survival in glioblastoma.** *AJNR Am J Neuroradiol* 2012;33:1349–55 CrossRef Medline
29. Wetzel SG, Cha S, Johnson G, et al. **Relative cerebral blood volume measurements in intracranial mass lesions: interobserver and intraobserver reproducibility study.** *Radiology* 2002;224:797–803 CrossRef Medline
30. Kato Y, Jin G, Kuan CT, et al. **A monoclonal antibody IMab-1 specifically recognizes IDH1R132H, the most common glioma-derived mutation.** *Biochem Biophys Res Commun* 2009;390:547–51 CrossRef Medline
31. Takano S, Tian W, Matsuda M, et al. **Detection of IDH1 mutation in human gliomas: comparison of immunohistochemistry and sequencing.** *Brain Tumor Pathol* 2011;28:115–23 CrossRef Medline
32. Higano S, Yun X, Kumabe T, et al. **Malignant astrocytic tumors: clinical importance of apparent diffusion coefficient in prediction of grade and prognosis.** *Radiology* 2006;241:839–46 CrossRef Medline
33. Murakami R, Hirai T, Sugahara T, et al. **Grading astrocytic tumors by using apparent diffusion coefficient parameters: superiority of a one- versus two-parameter pilot method.** *Radiology* 2009;251:838–45 CrossRef Medline
34. Lee EJ, Lee SK, Agid R, et al. **Preoperative grading of presumptive low-grade astrocytomas on MR imaging: diagnostic value of minimum apparent diffusion coefficient.** *AJNR Am J Neuroradiol* 2008;29:1872–77 CrossRef Medline
35. Lee S, Choi SH, Ryoo I, et al. **Evaluation of the microenvironmental heterogeneity in high-grade gliomas with IDH1/2 gene mutation using histogram analysis of diffusion-weighted imaging and dynamic-susceptibility contrast perfusion imaging.** *J Neurooncol* 2015;121:141–50 CrossRef Medline
36. Dang L, White DW, Gross S, et al. **Cancer-associated IDH1 mutations produce 2-hydroxyglutarate.** *Nature* 2009;462:739–44 CrossRef Medline
37. Xiong J, Tan W, Wen J, et al. **Combination of diffusion tensor imaging and conventional MRI correlates with isocitrate dehydrogenase 1/2 mutations but not 1p/19q genotyping in oligodendroglial tumours.** *Eur Radiol* 2016;26:1705–15 CrossRef Medline
38. Losman JA, Looper R, Koivunen P, et al. **(R)-2-hydroxyglutarate is sufficient to promote leukemogenesis and its effects are reversible.** *Science* 2013;339:1621–25 CrossRef Medline
39. Law M, Young RJ, Babb JS, et al. **Gliomas: predicting time to progression or survival with cerebral blood volume measurements at dynamic susceptibility-weighted contrast-enhanced perfusion MR imaging.** *Radiology* 2008;247:490–98 CrossRef Medline
40. Koivunen P, Lee S, Duncan CG, et al. **Transformation by the (R)-enantiomer of 2-hydroxyglutarate linked to EGLN activation.** *Nature* 2012;483:484–88 CrossRef Medline
41. Mangla R, Ginat DT, Kamalian S, et al. **Correlation between progression free survival and dynamic susceptibility contrast MRI perfusion in WHO grade III glioma subtypes.** *J Neurooncol* 2014;116:325–31 CrossRef Medline
42. Zulfiqar M, Yousem DM, Lai H. **ADC values and prognosis of malignant astrocytomas: does lower ADC predict a worse prognosis independent of grade of tumor? A meta-analysis.** *AJR Am J Roentgenol* 2013;200:624–29 CrossRef Medline

Differentiation of Enhancing Glioma and Primary Central Nervous System Lymphoma by Texture-Based Machine Learning

P. Alcaide-Leon, P. Dufort, A.F. Geraldo, L. Alshafai, P.J. Maralani, J. Spears, and A. Bharatha

ABSTRACT

BACKGROUND AND PURPOSE: Accurate preoperative differentiation of primary central nervous system lymphoma and enhancing glioma is essential to avoid unnecessary neurosurgical resection in patients with primary central nervous system lymphoma. The purpose of the study was to evaluate the diagnostic performance of a machine-learning algorithm by using texture analysis of contrast-enhanced T1-weighted images for differentiation of primary central nervous system lymphoma and enhancing glioma.

MATERIALS AND METHODS: Seventy-one adult patients with enhancing gliomas and 35 adult patients with primary central nervous system lymphomas were included. The tumors were manually contoured on contrast-enhanced T1WI, and the resulting volumes of interest were mined for textural features and subjected to a support vector machine–based machine-learning protocol. Three readers classified the tumors independently on contrast-enhanced T1WI. Areas under the receiver operating characteristic curves were estimated for each reader and for the support vector machine classifier. A noninferiority test for diagnostic accuracy based on paired areas under the receiver operating characteristic curve was performed with a noninferiority margin of 0.15.

RESULTS: The mean areas under the receiver operating characteristic curve were 0.877 (95% CI, 0.798–0.955) for the support vector machine classifier; 0.878 (95% CI, 0.807–0.949) for reader 1; 0.899 (95% CI, 0.833–0.966) for reader 2; and 0.845 (95% CI, 0.757–0.933) for reader 3. The mean area under the receiver operating characteristic curve of the support vector machine classifier was significantly noninferior to the mean area under the curve of reader 1 ($P = .021$), reader 2 ($P = .035$), and reader 3 ($P = .007$).

CONCLUSIONS: Support vector machine classification based on textural features of contrast-enhanced T1WI is noninferior to expert human evaluation in the differentiation of primary central nervous system lymphoma and enhancing glioma.

ABBREVIATIONS: AUC = area under the receiver operating characteristic curve; PCNSL= primary central nervous system lymphoma; SVM = support vector machine

Gliomas and primary central nervous system lymphoma (PCNSL) represent the 2 most common primary malignant brain tumors.[1] Treatment of PCNSL consists of chemotherapy and/or radiation.[2] Because resection of PCNSL confers no survival benefit for patients,[3] stereotactic brain biopsy sampling is the standard procedure for obtaining a pathologic diagnosis.[4] In high-grade gliomas, on the contrary, extensive resections have been shown to improve survival.[5,6] Accurate preoperative diagnosis is also important to avoid administration of steroids before biopsy in PCNSL because this medication can cause false-negative results of histologic examinations.[7]

Differentiation between enhancing glial tumors and PCNSL by conventional MR imaging can be challenging. Multiple imaging techniques have been used to solve this problem, including different types of MR perfusion,[8-10] ADC quantification,[10,11] SWI,[12] DTI,[13] and [^{18}F]-fluorodeoxyglucose positron-emission tomography.[14] Texture analysis has also been used to differentiate high-grade gliomas and PCNSL,[15,16] and only 1 study[15] has combined this approach with machine learning to improve the diagnostic accuracy of textural features on conventional MR images. To our knowledge, no prior studies on the differentiation between glioma and lymphoma have adequately compared the accuracy of a machine-learning algorithm and neuroradiologists.

PCNSL typically demonstrates intense homogeneous en-

Received November 21, 2016; accepted after revision February 1, 2017.

From the Departments of Medical Imaging (P.A.-L., A.B.) and Neurosurgery (J.S.), St. Michael's Hospital, University of Toronto, Toronto, Ontario, Canada; Department of Medical Imaging (P.D., A.F.G.) Toronto Western Hospital, University Health Network, University of Toronto, Toronto, Ontario, Canada; Department of Medical Imaging (L.A.), Mount Sinai Hospital, University Health Network, University of Toronto, Toronto, Ontario, Canada; and Department of Medical Imaging (P.J.M.), Sunnybrook Research Institute, University of Toronto, Toronto, Ontario, Canada.

This project was funded by the Term Chair Cerebrovascular and Brain Tumour Research Fund (St Michael's Hospital).

Please address correspondence to Paula Alcaide-Leon, MD, St. Michael's Hospital. Department of Medical Imaging, University of Toronto, 30 Bond St, Toronto, ON M5B 1W8, Canada; e-mail: paulaalcaideleon@hotmail.com

http://dx.doi.org/10.3174/ajnr.A5173

hancement as opposed to more heterogeneous enhancement of glial tumors. We hypothesized that the extraction of textural features of tumors and posterior input of these features in a machine-learning algorithm could provide a model for accurate and robust tumor classification. In machine learning, support vector machines (SVMs) are supervised learning algorithms that analyze data used for classification. From a set of training examples, each of them belonging to one of the categories, the SVM can build a model that classifies new data in the different categories. The purpose of this study was 3-fold: 1) to develop a classification model by using texture analysis and a machine-learning algorithm to differentiate PCNSL and enhancing glial tumors; 2) to compare the diagnostic accuracy of the SVM classifier with that of neuroradiologists; and 3) to examine whether the SVM classifier and the radiologists tend to misclassify the same cases.

MATERIALS AND METHODS

Study Design

A noninferiority statistical design with a noninferiority margin of 0.15 was adopted for this study. The study entailed comparisons of diagnostic accuracy between the radiologists and the SVM classifier in the differentiation of enhancing glioma and PCNSL. The area under the receiver operating characteristic curve (AUC) was the primary outcome measure. The sample size for the comparison of diagnostic accuracies between the radiologists and the SVM classifier was estimated by using 1-sided calculations with an α of .05 and a power of 80% based on a noninferiority margin[17] of −15%. The selection of this noninferiority margin was based on the goal of this technique not substituting for the radiologist's judgment but assisting in the diagnosis; therefore a noninferiority margin of −15% seems clinically acceptable. A priori sample size calculation was based on prior reported accuracies of 99.1% for texture analysis in a machine-learning algorithm[16] and 88.9% for radiologists.[16] The total sample size required was 22 (11 gliomas and 11 PCNSLs) according to the formula described by Blackwelder[18]: $n = f(\alpha, \beta) \times (\pi s \times [100 - \pi s] + \pi e \times [100 - \pi e]) / (\pi s - \pi e - d)^2$, where πs and πe are the true percentage "success" in the standard and experimental treatment group, respectively, and $f(\alpha, \beta) = [\Phi\text{-}1(\alpha) + \Phi - 1(\beta)]^2$, with Φ-1 being the cumulative distribution function of a standardized normal deviate. We opted for a more conservative approach with a larger sample size because our sample of tumors was more heterogeneous compared with other studies and accuracies may differ substantially.

Subjects

Institutional review board approval was obtained and informed consent was waived for this Health Insurance Portability and Accountability Act–compliant retrospective study. Inclusion criteria consisted of consecutive adult patients (older than 18 years of age) with a pathologic diagnosis of PCNSL or enhancing glial tumor and preoperative MR imaging performed at St. Michael's Hospital, including contrast-enhanced T1WI, between January 2005 and December 2015. An exclusion criterion was poor image quality due to motion or other artifacts. A random sample of 10% of patients with enhancing gliomas and 20% of patients with PCNSLs was selected. Two patients with enhancing glial tumors were excluded due to motion artifacts degrading the images. One hundred six patients were included (71 patients with enhancing glial tumors and 35 patients with PCNSLs). Surgery and histologic evaluation were performed within a month interval after imaging.

Image Acquisition

Thirty-two patients (20 with gliomas and 12 with PCNSLs) were scanned in a 3T magnet (Magnetom Skyra; Siemens, Erlangen, Germany) equipped with a 20-channel head-neck coil. A T1WI FLASH sequence (TR/TE, 250/2.49 ms; flip angle, 70°; section thickness, 5 mm; in-plane voxel size, 0.6 × 0.6 mm; FOV, 200 mm; gap, 0.5 mm; NEX, 1) was performed after administration of 10 mL of gadobenate dimeglumine. The total duration of the sequence was 1:1 minutes. Seventy-four patients (51 with gliomas and 23 with PCNSLs) were scanned in a 1.5T magnet (Intera; Philips Healthcare, Best, the Netherlands) equipped with a 6-channel head coil. A T1WI spin-echo sequence was acquired in the axial plane after administration of 10 mL of gadobenate dimeglumine (TR/TE, 400/8 ms; flip angle, 90°; section thickness, 5 mm; in-plane voxel size, 0.83 × 0.83 mm; FOV, 200 mm; gap, 1 mm; NEX, 2). The total duration of the sequence was 4:19 minutes.

Reading of Radiologists

Three neuroradiologists (L.A., A.F.G., and P.J.M. with 3, 2, and 4 years of experience in neuroradiology after residency) classified 106 tumors as gliomas or PCNSLs independently and blinded to clinical information and pathology reports. The 3 readers evaluated the contrast-enhanced T1WI of 106 patients and recorded their diagnoses and degrees of confidence by using a 4-point scale: 1, definite glioma; 2, likely glioma; 3, likely PCNSL; and 4, definite PCNSL. The readers were selected from other hospitals to ensure lack of prior exposure to the cases, and they were not informed of the number of cases in each category. The readers spent between 1 and 2 hours reviewing the images.

Texture Metrics

A neuroradiologist (P.A.-L.) with 6 years of experience in neuroradiology created tumor volumes of interest by contouring the outer margin of the enhancing component of the tumors in all sections on the contrast-enhanced T1WI sequence. In cases of multiple enhancing lesions, only the 2 largest lesions were contoured. The process of manual VOI generation took around 10 hours.

The generation of the texture features was accomplished by using a customized code written by one of the authors (P.D.) and took on the order of a few seconds for each study. The calculation of most texture features involves 2 steps: The first is the accumulation of histograms, and the second is the evaluation of nonlinear functions that take the histograms as input. The first-order texture metrics require 1D histograms that count the number of times image voxels of each possible value occur in the VOI. The functions that take these histograms as input can evaluate percentiles of the distribution or other measures of its shape such as means, variances, skewness, and kurtosis. The second-order metrics are based on 2D histograms that count the number of times voxels of one value are found spatially adjacent to voxels of another value over the entire VOI. Many nonlinear functions take

these histograms as input to produce second-order texture metrics such as entropy, correlation, contrast, and the angular second moment.

A set of 11 first-order and 142 second-order texture metrics was generated from each VOI. The first-order metrics consisted of the 11 image-intensity percentiles from each VOI, ranging from 0% (minimum value) to 100% (the maximum value) with 9 steps of 10% between them. These metrics provide a characterization of the 1D image-intensity histogram shape.

Before we computed the 142 second-order texture metrics, the intensities within each VOI were binned into 32 equal-sized bins spanning the range of image intensities between the first percentile at the bottom and the 99th percentile at the top. The binning is a standard technique for minimizing histogram noise when computing second-order texture metrics, while the use of image intensities between the first and 99th percentiles serves to minimize the effect of outliers on the bin layout. The second-order texture features consisted of metrics from 4 classes computed from multidimensional histograms: 1) the mean and range of the 13 Haralick features computed from the gray-scale co-occurrence matrix[19] taken over all 13 neighbor orientations[20]; 2) 5 features based on the neighborhood gray tone difference matrix[21]; 3) 10 features from the gray-level run-length matrix[22]; and 4) the same 10 features from the gray-level size zone matrix.[23] A detailed, illustrated description of these metrics has been previously published.[20] The result of this computation is a set of 153 texture features that are then fed into the machine-learning algorithm as predictors.

Machine Learning

The goal of the machine learning was to train a classifier to predict whether each tumor was a glioma or lymphoma based on the texture features extracted from the VOIs. All machine learning was performed by using the SVM algorithm with a radial basis function kernel. The Matlab (MathWorks, Natick, Massachusetts) interface to the LibSVM software library (http://www.csie.ntu.edu.tw/~cjlin/libsvm/)[24] was used to apply the SVM training algorithm to the data. The SVM[25] was selected over other machine-learning methods such as deep learning (eg, convolutional neural networks) for 2 reasons: first, because deep learning in general and convolutional neural networks in particular requires very large datasets for training; second, because the tumors investigated in this study have very predictable internal structures and whatever exploitable regularity may be present in tumors has so far been shown to be primarily statistical in nature, a category of pattern that is much better quantified by using texture metrics than convolutional kernels. For each SVM training run, it was necessary to tune 3 hyperparameters governing the behavior of the classifier. The first hyperparameter pertained to feature selection. An *F*-statistic approach[26] was used to rank the 153 input texture features in the order of their association with the response classification. A tunable hyperparameter representing the fraction of the most highly associated features to keep was then applied to select the features that were used. The second hyperparameter was the standard cost parameter common to all types of SVM, while the third was the width of the Gaussian that makes up the radial basis function kernel.

A nested cross-validation scheme was used to tune the 3 hyperparameters while keeping the assessment of accuracy completely independent. In each of 100 iterations of the outer loop, 10-fold cross-validation was used to hold out 10% of the data for testing, while the remaining 90% was passed to the inner loop. Within the inner loop, a further 10-fold cross-validation protocol was used for each point in a 3D grid covering a range of fractions of the best features to retain, values of the SVM cost parameter, and values of the radial basis function width. The inner loop cross-validation result was recorded for each grid point searched, and at the conclusion of the inner loop, the best performing triple of the hyperparameters was used to train a classifier by using all of the inner loop data. This classifier was then applied to classify the held-out data from the outer loop. A SVM classifier does not produce a dichotomous binary classification as its output, but rather a single, continuous number on the real line. Only when a threshold is applied, is it transformed into a classification. Repeating the outer loop of the nested cross-validation protocol 100 times yields 100 such numbers for each tumor. Each of the 100 numbers for a particular tumor represents an instance in which it was held out during cross-validation with a different 10% of the data. The percentage of trials in which each case was classified as a PCNSL was recorded.

The training of the classifier took a few days of computer time to complete, and the estimation of the accuracy of the classifier took 3 weeks. After the classifier has been produced, its application to each new case in a production environment would take only a small fraction of a second.

Statistical Analysis

Receiver operating characteristic curves were constructed for each reader and for the SVM classifier by using SPSS, Version 21 (IBM, Armonk, New York). For the receiver operating characteristic curve and AUC calculation, glioma was considered "negative" and PCNSL was considered "positive." The AUCs were estimated in each case by nonparametric methods. The noninferiority test for diagnostic accuracy based on the paired AUCs described in Zhou et al[27] was performed to compare each radiologist with the SVM classifier. The standard error of the difference between AUCs was calculated by taking into account the correlation derived from the paired nature of the data as described by Hanley and McNeil.[28]

To assess whether the radiologists and the SVM classifier tended to misclassify the same cases, we estimated interrater agreement among the 3 readers, and the SVM classifier was estimated by a linearly weighted κ.[29] The results from the SVM classifier were simplified to 4 categories so that they could be compared with the radiologists' readings. These categories were defined by the percentage of trials in which each case classified as PCNSL: 0%–25%, definite glioma; 26%–50%, likely glioma; 51%–75%, likely PCNSL; and 76%–100%, definite PCNSL.

RESULTS

In the glioma group ($n = 71$), there were 23 women (mean age, 59.5 years; range, 33–88 years) and 48 men (mean age, 54.5 years; range, 19–84 years). Two gliomas were grade III, and 69 were grade IV. In the PCNSL group ($n = 35$), there were 14 women

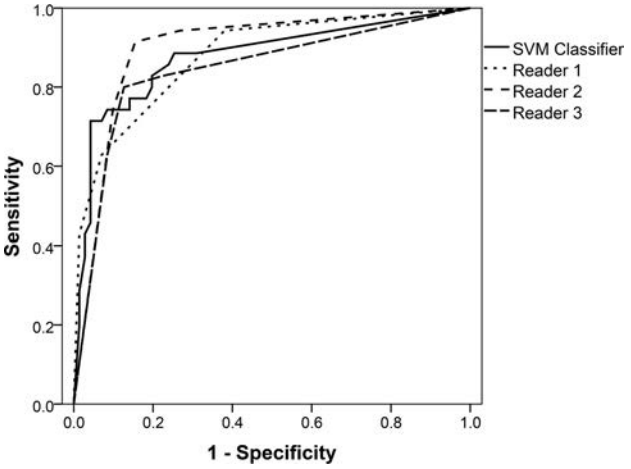

FIG 1. Receiver operating characteristic curves for discrimination of primary central nervous system lymphoma (positive) and glioblastoma (negative) of the support vector machine classifier (*continuous line*) and the 3 readers (*dashed lines*). The mean areas under the curve estimated under the nonparametric assumption were 0.877 (95% confidence interval, 0.798–0.955) for the SVM classifier; 0.878 (95% confidence interval, 0.807–0.949) for reader 1; 0.899 (95% confidence interval, 0.833–0.966) for reader 2; and 0.845 (95% confidence interval, 0.757–0.933) for reader 3.

Table 1: Differences in mean AUC between the SVM classifier and the neuroradiologists

Comparison	Difference	95% CI for Difference	*P* Value[a]
SVM classifier vs reader 1	−0.001	−0.096, 0.094	.021
SVM classifier vs reader 2	−0.022	−0.106, 0.062	.035
SVM classifier vs reader 3	0.032	−0.074, 0.138	.007

[a] *P* value for the test of noninferiority.

(mean age, 55.7 years; range, 41–71 years) and 21 men (mean age, 58.9 years; range, 39–83 years). Thirty-four cases of PCNSL corresponded to diffuse large B-cell lymphomas, and 1 was a T-cell lymphoma. Thirty-three cases of PCNSL occurred in immunocompetent patients, 1 in a patient with HIV, and 1 corresponded to an Epstein-Barr virus–driven lymphoma in a patient with a kidney transplant.

Diagnostic Accuracy

The mean AUCs were 0.877 (95% CI, 0.798–0.955) for the SVM classifier; 0.878 (95% CI, 0.807–0.949) for reader 1; 0.899 (95% CI, 0.833–0.966) for reader 2; and 0.845 (95% CI, 0.757–0.933) for reader 3. Receiver operating characteristic curves are shown in Fig 1. The mean AUC of the SVM classifier was significantly noninferior to the radiologists' mean AUCs. Differences in the AUCs between the SVM classifier and each of the readers are detailed in Table 1 and featured in Fig 2.

Agreement

Table 2 shows the linearly weighted Cohen κ coefficients for each pair of readers or reader-SVM classifier. Agreement was slightly higher among radiologists than between the SVM classifier and the radiologists.

Figure 3 shows the percentage of correctly classified trials by the SVM classifier in the order of decreasing accuracy on a case-by-case basis. The number of radiologists who classified each tumor correctly is also represented.

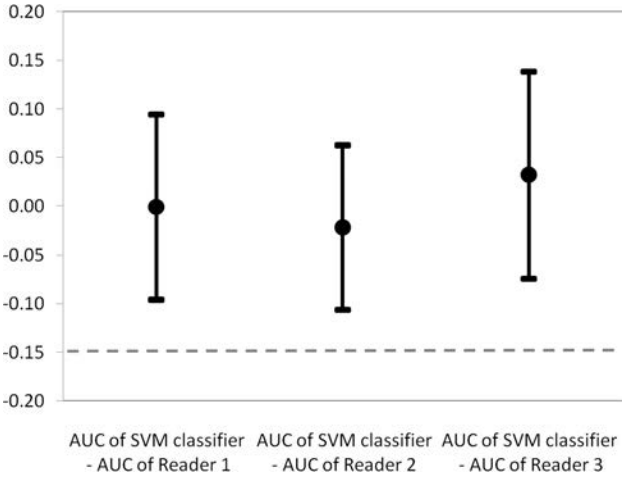

FIG 2. The chart shows the mean differences in area under the curve (95% confidence interval between the support vector machine classifier and reader 1 = −0.001 (95% CI, −0.096–0.094); between the SVM classifier and reader 2 = −0.022 (95% CI, −0.106–0.062); and between SVM classifier and reader 3 = 0.032 (95% CI, −0.074–0.138). All the confidence intervals sit wholly above the −0.15 limit (*dashed line*) representing the noninferiority margin.

Table 2: Linearly weighted κ coefficients representing the agreement between the neuroradiologists and the SVM classifier

	Reader 1	Reader 2	Reader 3	SVM Classifier
Reader 1	–	0.58	0.56	0.40
Reader 2		–	0.63	0.55
Reader 3			–	0.46

Figure 4 shows images from 2 cases in which there was agreement between the radiologists but a mismatch between the SVM classifier and the radiologists.

DISCUSSION

This article presents an SVM classification scheme for differentiating enhancing glioma and PCNSL noninferior to human evaluation. Prior studies with smaller samples have used texture analysis for differentiation of PCNSL and glioblastoma with[16] and without [15] machine learning. Yamasaki et al,[15] in a study including 40 patients, reported an accuracy of 91%. Their higher accuracy can be explained by lack of grade III glial tumors in their sample, which was limited to grade IV glial tumors. Grade III tumors typically lack necrosis, making the differential diagnosis with PCNSL more challenging. This study also lacks details regarding enrollment and a comparison with the accuracy of radiologists. The work by Liu et al,[16] also based on texture analysis, incorporates machine learning. They included only 18 patients and excluded not only non-grade IV glial tumors but also immunocompromised patients with PCNSLs. PCNSLs in immunocompromised patients commonly show atypical features (necrosis and hemorrhage), mimicking high-grade glial tumors and metastases. These exclusion criteria may explain the high accuracy of the machine learning algorithm (99.1%) in the work by Liu et al,[16] which was reported to be higher than that of the radiologists (88.9%) despite lack of statistical analysis for this comparison. In summary, prior studies on the topic lack representative samples and direct comparison with the diagnostic performance of radiologists. Our study on a random sample of

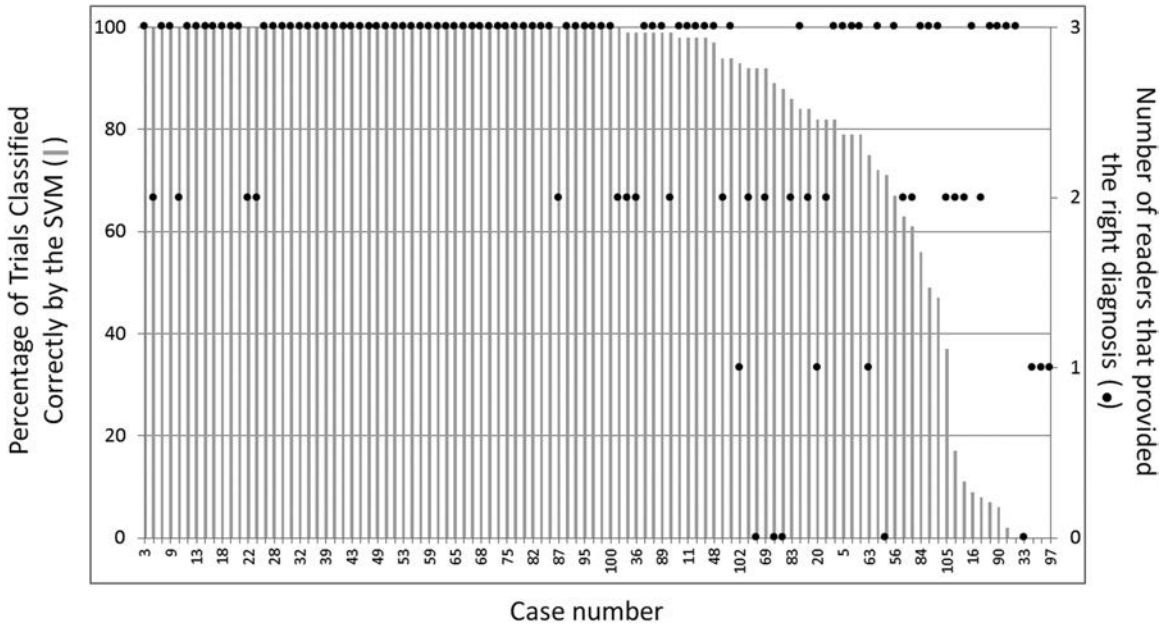

FIG 3. Comparison between the accuracy of the radiologists and the support vector machine classifier for each of the 106 cases. The horizontal axis shows the different cases sorted in order of decreasing SVM classifier accuracy. The left vertical axis shows the percentage of correctly classified trials by the SVM across 100 nested cross-validation trials. The right vertical axis shows the number of radiologists that classified the tumor correctly. For this graph, the results of the radiologists were simplified to 2 categories "glioma" and "lymphoma" without taking into account the degree of certainty. Although agreement is slightly better among radiologists than between radiologists and the SVM classifier, the cases in which the SVM provides different results for different trials (midright area of the graph) correspond to cases with more disagreements among the radiologists.

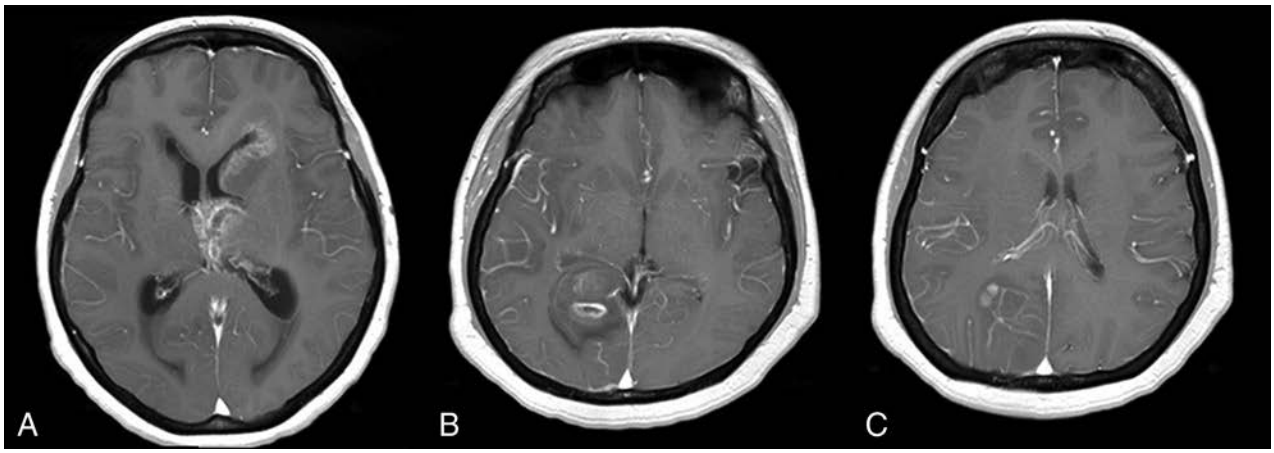

FIG 4. *A*, Axial contrast-enhanced T1-weighted image of a 51-year-old woman with a grade IV glioma. All 3 radiologists incorrectly classified the tumor as PCNSL, whereas the SVM classified it correctly in 92% of the trials. *B* and *C*, Axial contrast-enhanced T1WI of a 47-year-old woman with a grade IV glioma. All 3 radiologists incorrectly classified the tumor as PCNSL, whereas the SVM classifier provided the right diagnosis in 88% of the trials.

consecutive patients including 106 subjects is more likely to encompass the whole imaging spectrum of enhancing gliomas and PCNSLs, providing more realistic estimates of diagnostic accuracy than prior work.

The radiologists tended to agree slightly more among themselves than with the SVM classifier. It is interesting to analyze the disagreements, particularly those cases in which the SVM provided the right diagnosis and the radiologists failed. Figure 4 shows 2 such cases. In the case illustrated in Fig 4*A*, the tumor has a very heterogeneous appearance, more typical of gliomas; however, the radiologists classified it as a lymphoma, likely due to the periventricular location. The SVM classifier, on the contrary, only uses textural information and classified the case correctly as a glioma. One of the sources of disagreements between radiologists and the SVM classifier may be that radiologists take other tumor features into account such as the location and the presence of nonenhancing infiltrative components. Another possible source of disagreement is that the SVM classifier had only textural information from the 2 largest enhancing lesions, whereas the radiologists analyzed the whole brain. In the future, SVM and other types of machine-learning algorithms will be able to analyze the full dataset of images, combine it with the clinical information, and provide more reliable results. Adequately trained SVMs may support preoperative tumor diagnosis, especially in centers with-

out experienced neuroradiologists. This support will help avoid unnecessary neurosurgical resections in patients with PCNSL.

Our study has a number of limitations. First, the evaluation of contrast-enhanced T1WI in isolation from other valuable sequences such as ADC, perfusion, and T2 gradient-echo is not representative of the real clinical scenario. Second, the requirement of VOI tracing from an expert makes our approach semiautomatic and therefore subject to intra- and interobserver variability. Third, only the 2 largest enhancing lesions were segmented and analyzed by the SVM in cases of multiple lesions.

CONCLUSIONS

Our results show that SVMs can be trained to distinguish PCNSL and enhancing gliomas on the basis of textural features of contrast-enhanced T1WI with an accuracy significantly noninferior to that of neuroradiologists. The testing of larger datasets including other MR images will not only provide better accuracy estimations but also further improve the performance of the classifier, because SVM classification systems benefit from more extensive training.

Disclosures: Paul Dufort—*RELATED*: *Consulting Fee or Honorarium*: St. Michael's Hospital, Toronto, Canada. Pejman Jabehdar Maralani—*UNRELATED*: *Grants/Grants Pending*: grants from the Radiological Society of North America and the Brain Tumour Foundation of Canada.* *Money paid to the institution.

REFERENCES

1. Dolecek TA, Propp JM, Stroup NE, et al. **CBTRUS statistical report: primary brain and central nervous system tumors diagnosed in the United States in 2005–2009.** *Neuro Oncol* 2012;14(suppl 5):v1–49 CrossRef Medline
2. DeAngelis L. **Primary CNS lymphoma: treatment with combined chemotherapy and radiotherapy.** *J Neurooncol* 1999;43:249–57 CrossRef Medline
3. Bataille B, Delwail V, Menet E, et al. **Primary intracerebral malignant lymphoma: report of 248 cases.** *J Neurosurg* 2000;92:261–66 CrossRef Medline
4. Sherman ME, Erozan YS, Mann RB, et al. **Stereotactic brain biopsy in the diagnosis of malignant lymphoma.** *Am J Clin Pathol* 1991;95:878–83 CrossRef Medline
5. Sanai N, Polley MY, McDermott MW, et al. **An extent of resection threshold for newly diagnosed glioblastomas.** *J Neurosurg* 2011;115:3–8 CrossRef Medline
6. Li YM, Suki D, Hess K, et al. **The influence of maximum safe resection of glioblastoma on survival in 1229 patients: can we do better than gross-total resection?** *J Neurosurg* 2016;124:977–88 CrossRef Medline
7. Weller M. **Glucocorticoid treatment of primary CNS lymphoma.** *Neurooncol* 1999;43:237–39 CrossRef Medline
8. Kickingereder P, Sahm F, Wiestler B, et al. **Evaluation of microvascular permeability with dynamic contrast-enhanced MRI for the differentiation of primary CNS lymphoma and glioblastoma: radiologic-pathologic correlation.** *AJNR Am J Neuroradiol* 2014;35:1503–08 CrossRef Medline
9. Furtner J, Schöpf V, Preusser M, et al. **Non-invasive assessment of intratumoral vascularity using arterial spin labeling: a comparison to susceptibility-weighted imaging for the differentiation of primary cerebral lymphoma and glioblastoma.** *Eur J Radiol* 2014;83:806–10 CrossRef Medline
10. Shim WH, Kim HS, Choi CG, et al. **Comparison of apparent diffusion coefficient and intravoxel incoherent motion for differentiating among glioblastoma, metastasis, and lymphoma focusing on diffusion-related parameter.** *PLoS One* 2015;10:e0134761 CrossRef Medline
11. Ahn SJ, Shin HJ, Chang JH, et al. **Differentiation between primary cerebral lymphoma and glioblastoma using the apparent diffusion coefficient: comparison of three different ROI methods.** *PLoS One* 2014;9:e112948 CrossRef Medline
12. Radbruch A, Wiestler B, Kramp L, et al. **Differentiation of glioblastoma and primary CNS lymphomas using susceptibility weighted imaging.** *Eur J Radiol* 2013;82:552–56 CrossRef Medline
13. Toh CH, Castillo M, Wong AM, et al. **Primary cerebral lymphoma and glioblastoma multiforme: differences in diffusion characteristics evaluated with diffusion tensor imaging.** *AJNR Am J Neuroradiol* 2008;29:471–75 CrossRef Medline
14. Zhou W, Wen J, Hua F, et al. **FDG-PET in immunocompetent patients with primary central nervous system lymphoma: differentiation from GBM and correlation with DWI.** *J Nucl Med* 2016;57(suppl 2):1613
15. Yamasaki T, Chen T, Hirai T, et al. **Classification of cerebral lymphomas and glioblastomas featuring luminance distribution analysis.** *Comput Math Methods Med* 2013;2013:619658 CrossRef Medline
16. Liu Y, Muftah M, Das T, et al. **Classification of MR tumor images based on Gabor wavelet analysis.** *J Med Biol Eng* 2012;32:22–28 CrossRef
17. Ahn S, Park SH, Lee KH. **How to demonstrate similarity by using noninferiority and equivalence statistical testing in radiology research.** *Radiology* 2013;267:328–38 CrossRef Medline
18. Blackwelder WC. **"Proving the null hypothesis" in clinical trials.** *Control Clin Trials* 1982;3:345–53 CrossRef Medline
19. Haralick RM, Shanmugam K, Dinstein I. **Textural features for image classification.** *IEEE Trans Syst Man Cybern* 1973;3:610–21 CrossRef
20. Tixier F, Le Rest CC, Hatt M, et al. **Intratumor heterogeneity characterized by textural features on baseline 18F-FDG PET images predicts response to concomitant radiochemotherapy in esophageal cancer.** *J Nucl Med* 2011;52:369–78 CrossRef Medline
21. Amadasun M, King R. **Textural features corresponding to textural properties.** *IEEE Trans Syst Man Cybern* 1989;19:1264–74 CrossRef
22. Loh HH, Leu JG, Luo RC. **The analysis of natural textures using run length features.** *IEEE Trans Ind Electron* 1988;35:323–28 CrossRef
23. Thibault G, Fertil B, Navarro C, et al. **Shape and texture indexes application to cell nuclei classification.** *Intern J Pattern Recognit Artif Intell* 2013;27:1357002
24. Chang CC, Lin CJ. **LIBSVM: a library for support vector machines.** *ACM Trans Intell Syst Technol* 2011;2:1–27
25. Orrù G, Pettersson-Yeo W, Marquand AF, et al. **Using support vector machine to identify imaging biomarkers of neurological and psychiatric disease: a critical review.** *Neurosci Biobehav Rev* 2012;36:1140–52 CrossRef Medline
26. Chen YW, Lin CJ. **Combining SVMs with various feature selection strategies.** In: Guyon I, Nikravesh M, Gunn S, et al, eds. *Feature Extraction: Foundations and Applications.* Berlin, Heidelberg: Springer; 2006:315–324
27. Zhou XH, Obuchowski NA, McClish DK. **Comparing the accuracy of two diagnostic tests.** In: *Statistical Methods in Diagnostic Medicine.* Hoboken: John Wiley & Sons; 2011:165–92
28. Hanley JA, McNeil BJ. **A method of comparing the areas under receiver operating characteristic curves derived from the same cases.** *Radiology* 1983;148:839–43 CrossRef Medline
29. Fleiss JL, Cohen J. **The equivalence of weighted kappa and the intraclass correlation coefficient as measures of reliability.** *Educ Psychol Meas* 1973;33:613–19

Safety and Efficacy of Aneurysm Treatment with the WEB: Results of the WEBCAST 2 Study

L. Pierot, I. Gubucz, J.H. Buhk, M. Holtmannspötter, D. Herbreteau, L. Stockx, L. Spelle, J. Berkefeld, A.-C. Januel, A. Molyneux, J.V. Byrne, J. Fiehler, I. Szikora, and X. Barreau

ABSTRACT

BACKGROUND AND PURPOSE: Flow disruption with the Woven EndoBridge (WEB) device is an innovative technique for the endovascular treatment of wide-neck bifurcation aneurysms. The initial version of the device (WEB Double-Layer) was evaluated in the WEB Clinical Assessment of IntraSaccular Aneurysm Therapy (WEBCAST) study, whereas the French Observatory study evaluated both WEB Double-Layer and Single-Layer versions of the device. WEBCAST 2 was designed to evaluate the WEB Single-Layer with Enhanced Visualization.

MATERIALS AND METHODS: Patients with wide-neck bifurcation aneurysms for which WEB treatment was possible were included. Clinical data including adverse events and clinical status at 1 month and 1 year were collected and analyzed. A core laboratory evaluated anatomic results at 1 year following the procedure.

RESULTS: Ten European neurointerventional centers included 55 patients (38 women; 27–77 years of age; mean, 54.4 ± 10.0 years) with 55 aneurysms. Aneurysm locations were the middle cerebral artery in 25 aneurysms (45.5%), the anterior communicating artery in 16 (29.1%), the basilar artery in 9 (16.4%), and the internal carotid artery terminus in 5 (9.1%). Procedural morbidity and mortality at 1 month were, respectively, 1.8% (1/55 patients) and 0.0% (0/55 patients). Morbidity and mortality at 1 year were, respectively, 3.9% (2/51 patients) and 2.0% (1/51 patients). At 1 year, complete occlusion was observed in 27/50 aneurysms (54.0%); neck remnant, in 13/50 (26.0%); and aneurysm remnant, in 10/50 (20.0%) (adequate occlusion in 40/50, 80.0%).

CONCLUSIONS: WEBCAST 2 confirms the high safety and efficacy of WEB aneurysm treatment demonstrated in the WEBCAST and French Observatory studies.

ABBREVIATIONS: EV = Enhanced Visualization; WEB = Woven EndoBridge; WEBCAST = WEB Clinical Assessment of IntraSaccular Aneurysm Therapy; WEB-DL = WEB Double-Layer; WEB-SL = WEB Single-Layer; WEB-SLS = Single-Layer Spherical

Endovascular treatment is now the first-line treatment for ruptured aneurysms.[1] For unruptured aneurysms, no randomized trial has been completed that permits the direct comparison of clipping with endovascular treatment. However, at least in Europe, the tendency is to give priority to endovascular treatment.[2] Some aneurysms, especially those with a wide-neck, are difficult to treat due to the challenges of stabilizing coils inside the aneurysm sac and avoiding their protrusion into the parent artery. Thus, more complex endovascular techniques have been developed, such as balloon-assisted coiling, stent-assisted coiling, and flow diversion.[3-8]

Flow disruption is now a well-established procedure for the treatment of wide-neck bifurcation aneurysms.[9-13] Today, it is also used in narrow-neck aneurysms and sidewall aneurysms.[14] The therapy involves the placement of an intrasaccular device that alters the flow inside the aneurysm, inducing intrasaccular thrombosis. Introduced in 2010 in Europe, the Woven EndoBridge (WEB; Sequent Medical, Aliso Viejo, California) is the only intrasaccular device that has been extensively evaluated in

Received November 15, 2016; accepted after revision February 7, 2017.

From the Department of Neuroradiology (L.P.), Hôpital Maison-Blanche, Université Reims-Champagne-Ardenne, Reims, France; National Institute of Clinical Neurosciences (I.G., I.S.), Budapest, Hungary; Department of Neuroradiology (J.H.B., J.F.), University Medical Center Hamburg-Eppendorf, Hamburg, Germany; Rigshospitalet (M.H.), Copenhagen, Denmark; Centre Hospitalier Universitaire Tours (D.H.), Tours, France; Ziekenhuis Oost-Limburg Genk (L. Stockx), Genk, Belgium; Hôpital Bicêtre (L. Spelle), Assistance Publique-Hôpitaux de Paris, Le Kremlin Bicêtre, France; Institut für Neuroradiologie (J.B.), Klinikum der Johann Wolfgang Goethe-Universitaet, Frankfurt, Germany; Centre Hospitalier Universitaire Toulouse (A.-C.J.), Toulouse, France; Oxford Neurovascular and Neuroradiology Research Unit (J.V.B., A.M.), John Radcliffe Hospital, Oxford, UK; and Centre Hospitalier Universitaire Bordeaux (X.B.), Bordeaux, France.

The WEBCAST 2 trial was supported by Sequent Medical.

Clinical Trial Registration is provided at http://www.clinicaltrials.gov. The unique identifier is NCT01778322.

Please address correspondence to Laurent Pierot, MD, PhD, Department of Neuroradiology, Hôpital Maison-Blanche, 45 Rue Cognacq-Jay, 51092 Reims Cedex, France; e-mail: lpierot@gmail.com

http://dx.doi.org/10.3174/ajnr.A5178

the literature with several single- and multicenter, retrospective, and prospective series.[9-21] Good Clinical Practice studies, including the WEB Clinical Assessment of IntraSaccular Aneurysm Therapy (WEBCAST) and the French Observatory studies, have shown a high level of safety with the device.[15-18] Efficacy has to be further evaluated, but 1-year anatomic results in both the WEBCAST and French Observatory studies are encouraging. However, important changes in the device have been introduced across the time, moving from a dual-layer, larger profile version (WEB-DL) to single-layer, lower profile versions (WEB-SL and WEB Single-Layer Spherical [SLS]) and more recently Single-Layer with Enhanced Visualization (EV) obtained by introducing composite wires of nitinol and platinum in the braid itself.

The WEBCAST study evaluated the WEB-DL, whereas the French Observatory evaluated the WEB-DL, WEB-SL, and the WEB-SLS.[15-18] In the continuing effort to assess the clinical and anatomic performance of these new devices, it was logical to further evaluate this technique with a series of patients treated exclusively with single-layer (SL, SLS) and Enhanced Visualization devices.

MATERIALS AND METHODS

WEBCAST 2 is a prospective, consecutive, multicenter, European registry dedicated to the evaluation of WEB-SL EV and WEB-SLS EV treatment for bifurcation aneurysms.

The study received national regulatory authorization (Advisory Committee on Information Processing in Material Research in the Field of Health), Reims Institutional Review Board approval, and National Commission for Data Processing and Freedom approval. Written informed consent was obtained for all patients.

Trial Design and Procedural Modalities

WEBCAST 2 protocol was similar to that in WEBCAST with some amendments.[17] Inclusion criteria were ruptured (Hunt and Hess 1, 2, or 3) and unruptured bifurcation aneurysms located in the basilar artery, middle cerebral artery, anterior communicating artery, posterior communicating artery, and internal carotid artery terminus. The indication for endovascular treatment was determined in each center by a local multidisciplinary team that included neurosurgeons and neuroradiologists. The selection of aneurysms treated with the WEB device was performed autonomously in each center by the interventional neuroradiologists according to aneurysm characteristics (aneurysm status, aneurysm location and size, and neck size).

The treatment of aneurysms with the WEB was performed by using techniques similar to those used in the treatment of aneurysms with coils. The study protocol did not specify the antiplatelet regimen to be followed, and it was managed in each center as indicated for typical endovascular treatment with coils or stents and coils. Triaxial access was recommended. A very careful sizing of the aneurysm was recommended because previous evaluation showed that oversizing of the device plays an important role in the quality of anatomic results. On the basis of the size of the WEB device to be used, VIA-21 (WEB SL/SLS 4–7 mm), VIA-27 (WEB SL/SLS 8–9 mm), and VIA-33 (WEB SL/SLS 1011 mm) microcatheters (Sequent Medical) were used to catheterize the aneurysm. If the treatment plan included use of ancillary implant devices, the patient was not enrolled in the study. Treatment with ancillary devices (coils, stent, flow diverters) was allowed during the procedure if deemed necessary by the physician and was not considered a treatment failure.

Data Collection

The following data were collected for each patient: age and sex; aneurysm rupture status; aneurysm characteristics including location, size, and neck size; date of the procedure; perioperative antiplatelet medications; occurrence of complications during or after the procedure; and use of additional devices during the procedure (coils, remodeling balloons, stents, or flow diverters). The preoperative Hunt and Hess grade was collected in case of ruptured aneurysms. The modified Rankin Scale score was collected before treatment (unruptured aneurysms) and at 30 ± 7 days and 12 ± 3 months for all patients. Vascular imaging at 12 ± 3 months was collected.

Data Analysis

Clinical data were independently monitored and analyzed, including all adverse events. Morbidity was defined as mRS > 2 if preoperative mRS was ≤2 (or in case of ruptured aneurysm), or an increase of 1 point when the preoperative mRS was >2.

An expert interventional neuroradiologist (J.B.) independently evaluated aneurysm measurements and occlusion by using a 3-grade scale: complete occlusion, neck remnant, and aneurysm remnant. According to a previous publication, opacification of the proximal recess of the WEB device was considered complete occlusion.[15]

Statistical Analysis

Continuous variables were described as mean ± SD. Categoric data were described numerically as a categoric total and as a percentage of the population analyzed. Binomial data were described as a ratio of the true value and the population analyzed. Confidence intervals for binomial data were calculated by the Clopper-Pearson method, and *P* values were calculated by the Fisher exact test. Analyses were conducted by using SPSS statistical software (IBM, Armonk, New York) for confidence intervals and *P* values.

RESULTS

Patient and Aneurysm Population

Between August 2014 and May 2015, 10 European centers included 55 patients (38 women, 69.1%; 27–77 years of age; mean, 54.4 ± 10.0 years) with 55 aneurysms.

Four (7.3%) aneurysms were ruptured, and 51 (92.7%), unruptured. In patients with ruptured aneurysms, the Hunt and Hess grade was 1 in 1 patient and 3 in 3 patients. For patients treated for unruptured aneurysms, the preoperative mRS was 0 in 39/51 patients (76.5%), 1 in 10/51 patients (19.6%), 2 in 1/51 patients (2.0%), and 4 in 1/51 patients (2.0%). Aneurysm locations were the MCA in 25 aneurysms (45.5%), the anterior communicating artery in 16 (29.1%), the basilar artery in 9 (16.4%), and the ICA terminus in 5 (9.1%). The aneurysm neck was between 2.5 and 8.0 mm (mean, 4.6 ± 1.1 mm). The aneurysm neck was ≥4 mm in 41/55 aneurysms (74.5%). Aneurysm size was

between 2.8 and 17.0 mm (mean, 6.7 ± 2.3 mm). The aneurysm was ≥10 mm in 3/55 aneurysms (5.5%).

Modalities of antiplatelet treatment before, during, and after the procedure are described in Table 1.

Treatment Feasibility, Adjunctive Treatments, and Adverse Events

Treatment was successfully performed in all except 2 patients (96.4%), with the WEB-SL in 47/53 patients and the WEB-SLS in 6/53 patients.

An adjunctive device (flow diverter and stent) was used in 1/53 aneurysms (1.9%).

Intraoperative thromboembolic events were reported in 8 patients (8/55, 14.5%). Four of these 8 patients had 1 antiplatelet agent, and 4 had 2 antiplatelet agents before the complication. There was no clinical worsening in 2 patients (3.6%), a transient deficit in 3 patients (5.4%), and a permanent deficit in 3 patients (5.4%). These 3 patients had a 1-month mRS of, respectively, 1, 2, and 3.

Another thromboembolic event was reported 5 months postprocedure, related to a concurrent condition (history of stroke). The patient had dual antiplatelet treatment before and after the procedure. The patient had a small cerebral infarct, which was not associated with a permanent deficit.

Intraoperative rupture was reported in 1/55 patients (1.8%) and was not symptomatic.

Mortality/Morbidity at 1 Month

At 30 days, all patients enrolled in the study had a clinical evaluation with mRS scoring. There was no mortality at 1 month. Procedural morbidity was observed in 1/55 patients (1.8%) related to a thromboembolic event (mRS 3). One patient (1.8%) with a ruptured aneurysm was mRS 4 at 1 month due to the initial bleeding. Global morbidity at 1 month was 3.6% (2/55).

Mortality/Morbidity at 1 Year

At 12 months, 51 of the 55 patients enrolled in the study were clinically evaluated with mRS scoring. Four patients were not included in the 1 year mortality/morbidity analysis (2 patients not treated with the WEB, 1 patient lost for follow-up, and 1 patient withdrawing his consent before 12-month follow-up).

One patient died between 1 month and 1 year follow-up: This patient had a huge retroperitoneal hematoma after the WEB procedure, further associated with intensive care complications (cardiac and respiratory). Mortality at 1 year was 1/51 (2.0%). Among the 2 patients who had mRS > 2 at 1 month, the patient with the initial ruptured aneurysm improved at 1 year (mRS 2). The patient with a TE event due to the procedure was still mRS 3 at 1 year. Another patient retreated at 14 months with a flow diverter had a thromboembolic complication with mRS 3 at discharge. Global morbidity at 1 year was 2/51 (3.9%).

Retreatment

Of the 53 aneurysms treated with the WEB, aneurysm occlusion and retreatment were not evaluated in 3 patients at 1 year: One patient died, 1 patient withdrew consent, and follow-up was missing for 1 patient. During the 12 ± 3 months' follow-up period, 4/50 aneurysms (8.0%) were retreated or had an attempted retreatment (Table 2). In all 4 cases, aneurysm remnants were detected at 6 months. In 1 patient, additional treatment by clipping was attempted 8 months after the initial procedure. Clipping was unsuccessful, and the patient had hemiplegia immediately after the procedure. Neurologic improvement was rapid, and the patient was mRS 2 at 1 year. This aneurysm was successfully retreated with the WEB SLS at 14 months. In another case, retreatment with Y-stent placement and coiling took place 10 months after the initial treatment.

In the 2 other cases, aneurysm retreatment took place after the 1-year DSA showed that the aneurysm remnant remained. Retreatment was performed in these 2 patients at 14 months. One was successfully retreated with Y-stent placement and coiling, and 1 patient was treated with a flow diverter. For this last patient, an intrastent thrombosis occurred during the procedure and the flow diverter was removed. The patient had clinical worsening with mRS 3 at discharge.

Anatomic Results at 1 Year

The vascular imaging technique was digital subtraction angiography in 39/50 patients (78.0%), MRA in 10 patients (20.0%), and CTA in 1 patient (2.0%).

Complete occlusion was observed in 27/50 aneurysms (54.0%); neck remnant, in 13/50 aneurysms (26.0%); and aneurysm remnant, in 10/50 aneurysms (20.0%). Adequate occlusion (complete occlusion or neck remnant) was observed in 40/50 aneurysms (80.0%).

Table 1: Antiplatelet treatment before, during, and after WEB procedure

	Before	During	After (1-Mo FU)
No antiplatelet (No.)	16/55 (29.1%)	10/55 (18.2%)	11/55 (20.0%)
Single antiplatelet (No.)	15/55 (27.3%)	16/55 (29.1%)	31/55 (56.4%)
Dual antiplatelet (No.)	24/55 (43.6%)	29/55 (51.7%)	13/55 (23.6%)

Note:—FU indicates follow-up.

DISCUSSION

The rapid technologic evolution of the WEB device (Single-Layer, Enhanced Visualization) makes it necessary to have a proper evaluation of the latest generation of devices. In continuity with previ-

Table 2: Retreatment completed 12 ± 3 months

Patient Sex, Age (yr)	Aneurysm Location	Aneurysm Transverse Diameter (mm)	WEB Size (mm)	Retreatment Delay (mo)	Retreatment Type
M, 65	AcomA	6.3	SL 6 × 3	14	Y-stenting/coils
F, 41	MCA	5.9	SL 6 × 3	8, 14	Operation (failed)/WEB SLS
F, 27	BA	7.9	SL 10 × 5	10	Y-stenting/coils
F, 50	BA	9.6[a]	SLS 11	14	Flow diverter (failed)

Note:—AcomA indicates anterior communicating artery; BA, basilar artery.

[a] Giant partially thrombosed aneurysm. Transverse diameter of the circulating part.

ously published WEB Good Clinical Practice studies (WEBCAST, French Observatory) and in parallel with ongoing Good Clinical Practice studies (WEB- Intrasaccular Therapy Study under FDA investigational device exemption in the United States, and CLinical Assessment of WEB Device in Ruptured aneurYSms [CLARITY] in Europe), WEBCAST 2 was designed according to the same protocol as WEBCAST to evaluate the WEB-SL with Enhanced Visualization in wide-neck bifurcation aneurysms.[17] However, recent reports have outlined the possibility of using the WEB in other indications, including sidewall and narrow-neck aneurysms not included in WEBCAST 2.[14]

The results of WEBCAST 2 confirm that WEB treatment, with lower profile devices and smaller inner diameter microcatheters, is highly feasible, with a technical success rate of 96.4%, similar to that observed in the WEBCAST (94.1%) and the French Observatory (98.4%) studies.[16,17] All patients in WEBCAST were treated with the WEB-DL, and in the French Observatory, 31/63 aneurysms were treated with the WEB-DL, with the remaining aneurysms treated with the WEB-SL or -SLS (most without the EV materials). Of note, the feasibility rate is not higher in WEBCAST 2 than in WEBCAST, given that the WEB-SL and SLS were thought to be easier to navigate and deploy. In fact, the selection of patients and aneurysms for WEB treatment was different in WEBCAST and WEBCAST 2 as illustrated by the higher percentage of anterior communicating artery aneurysms treated in WEBCAST 2 (29.1%) compared with WEBCAST (7.8%). A similar difference in patient/aneurysm selection when treating with the WEB-DL and WEB-SL and SLS was also observed in the French Observatory study.[15,16]

WEBCAST 2 confirms the high safety of aneurysm treatment with the WEB observed in the WEBCAST study. Morbidity and mortality at 1 month were very similar at 2.0% and 0.0%, respectively.[17] Similar results were also reported in the French Observatory with 1-month morbidity at 3.2% and mortality at 0.0%.[15,16] Moreover, morbidity and mortality at 1 month were not different in the DL and SL/SLS groups.

Efficacy as evaluated with anatomic results at 1-year is as good in WEBCAST 2 as in the WEBCAST (at 6 months) and French Observatory studies. Adequate occlusion was observed in 80.0% in WEBCAST 2, 85.4% in WEBCAST, and 79.3% in French Observatory.[16,17] This result is quite important because it means that the new braiding of the single-layer devices provides a low-porosity equivalent, at least in term of anatomic results, to the previous braiding placed in 2 layers at the level of the neck. The new braiding decreases the porosity and provides a single-layer device that is less rigid than a dual-layer one, and easier to navigate, without worsening its efficacy. Also, the single-layer device has permitted a reduction in the size of the microcatheter used for delivery and deployment.

Finally, the retreatment rate is similar to that reported in the cumulative population of the WEBCAST and French Observatory studies, in which the retreatment rate was 6.4%, including retreatment effectively performed (3.6%), failed retreatment (0.9%), and planned retreatment (1.8%). In WEBCAST 2, retreatment was performed in 2 patients when the WEB device was not oversized (as currently recommended) and in 1 patient with a giant partially thrombosed aneurysm. A recent, single-center series showed that adequate occlusion was more frequent (but not significantly so) when the WEB device was appropriately sized (92.9%) than undersized (70.0%).[22] In WEBCAST 2, two patients were retreated as a consequence of WEB undersizing; this scenario must be avoided.

Compared with alternative therapeutics, the safety of aneurysms treatment with the WEB-SL is similar to that of coiling. In CLARITY (ruptured aneurysms) and Analysis of Treatment by Endovascular Approach of Nonruptured Aneurysms (ATENA) (unruptured aneurysms), intraoperative rupture occurred in 3.7% and 2.6%, respectively, and thromboembolic events, in 13.3% and 7.1%, respectively.[1,2] In ATENA, morbidity and mortality rates at 1 month were 1.7% and 1.4%, respectively, whereas in CLARITY, treatment morbidity and mortality were 3.7% and 1.5%, respectively. Comparison with surgical series is more difficult because the rate of thromboembolic events and intraoperative rupture is rarely reported, possibly because it is less frequent or underestimated.[23] When we looked at the morbidity/mortality, in the largest meta-analysis dealing with unruptured aneurysms treated by clipping, the rate of death (1.7%) was higher compared with that in WEBCAST 2 (0.0%) and the rate of unfavorable outcome at 1 year was 6.7% compared with 5.9% in WEBCAST 2.[23] The same meta-analysis showed interesting results regarding the efficacy of clipping. In 82.2% of all clipped aneurysms, the postoperative aneurysm occlusion rate was not reported. When it was reported, it was not independently evaluated (unlike the entire series of Good Clinical Practice WEB studies). When reported, complete occlusion was 91.8% (neck remnant in 3.9% and aneurysm remnant in 4.3%). There are no data on long-term follow-up.

This study has several limitations. First, the population was relatively small (55 patients). However, it is the first prospective, multicenter study evaluating the safety and efficacy of aneurysm treatment with WEB-SL and WEB-SLS devices with independent assessment of adverse events and anatomic results. Second, it is not a randomized study, and comparison with other techniques is not easy. However, safety data are excellent and quite comparable with those observed in large coiling series. Efficacy data are more difficult to compare with historical series because most are mixed sidewall and bifurcation locations, with both narrow- and wide-neck aneurysms. Third, the potential WEB "compression" phenomenon has not been evaluated in this study, and further work is being conducted on this topic.[24,25] Finally, anatomic results were evaluated with heterogeneous imaging techniques (DSA, MRA, and CTA), and MRA has a relatively low sensitivity for aneurysm remnant detection.[26]

CONCLUSIONS

WEBCAST 2 results are in line with WEBCAST and French Observatory results, showing high safety and great efficacy of aneurysm treatment with WEB-SL devices.

Disclosures: Laurent Pierot—*RELATED*: *Consulting Fee or Honorarium*: Sequent Medical; *UNRELATED*: *Consultancy*: Blockade Medical, Medtronic, MicroVention, Neuravi, Penumbra. Jan Hendrik Buhk—*UNRELATED*: *Consultancy*: Acandis, Codman Neurovascular, MicroVention, Sequent Medical. Markus Holtmannspötter—*UNRELATED*: *Consultancy*: MicroVention, Covidien, Sequent Medical, Mentice, Stryker, *Comments*: consultancy and proctoring fees; *Payment for Lectures Including Service on Speakers Bureaus*: MicroVention, Covidien, Sequent Medical; *Travel/Ac-*

commodations/Meeting Expenses Unrelated to Activities Listed: MicroVention, Covidien, Sequent Medical, Mentice, Stryker. Denis Herbreteau—*RELATED*: *Support for Travel to Meetings for the Study or Other Purposes*: Sequent Medical; *Other*: Sequent, *Comments*: proctoring; *UNRELATED*: *Payment for Manuscript Preparation*: Sequent Medical; *Travel/Accommodations/Meeting Expenses Unrelated to Activities Listed*: Sequent Medical. Laurent Spelle—*UNRELATED*: *Consultancy:* Sequent, Medtronic, Stryker. Joachim Berkefeld—*RELATED*: *Consulting Fee or Honorarium*: Sequent Medical; *Support for Travel to Meetings for the Study or Other Purposes*: Sequent Medical, *Comments*: invited speaker for user meetings and sponsored symposium; *UNRELATED*: *Board Membership*: Acandis, Pforzheim, Germany, *Comments*: member of the scientific advisory board; *Consultancy*: Siemens, Erlangen, Germany, *Comments*: scientific cooperation.* Anne-Christine Januel—*UNRELATED*: *Grant*: Association pour le développement de la Neuroradiologie, *Comments*: for data monitoring*; *Travel/Accommodations/Meeting Expenses Unrelated to Activities Listed*: Sequent, *Comments*: fees and accommodation paid for participation in meetings. Andrew Molyneux—*RELATED*: *Grant*: Sequent; *Consulting Fee or Honorarium*: Sequent Medical, *Comments*: time for consulting to review adverse events*; *Fees for Participation in Review Activities such as Data-Monitoring Boards, Statistical Analysis, Endpoint Committees, and the Like*: attended the Society of NeuroInterventional Surgery investigator meeting. James V. Byrne—*UNRELATED*: *Employment*: Oxford University Hospital National Health Service Trust, *Comments*: salary as consultant interventional neuroradiologist; *Fees for Participation in Review Activities such as Data-Monitoring Boards, Statistical Analysis, Endpoint Committees, and the Like*: Nuffield Department of Surgical Sciences, Oxford University, *Comments*: contracted core laboratory services.* Jens Fiehler—*RELATED*: *Consulting Fee or Honorarium*: Sequent Medical; *Support for Travel to Meetings for the Study or Other Purposes*: Sequent Medical; *UNRELATED*: *Consultancy*: MicroVention, Covidien, Stryker, Codman, Medina, Penumbra; *Payment for Lectures Including Service on Speakers Bureaus*: MicroVention, Covidien, Stryker, Codman, Medina, Penumbra. Istvan Szikora—*RELATED*: *Consulting Fee or Honorarium*: Sequent Medical, *Comments*: clinical trial fee; *Support for Travel to Meetings for the Study or Other Purposes*: Sequent Medical*; *Other*: Sequent Medical, *Comments*: clinical trial fee*; *UNRELATED*: *Consultancy*: Stryker, Codman, Medtronic. Xavier Barreau—*RELATED*: *Consulting Fee or Honorarium*: *Sequent*; *Support for Travel to Meetings for the Study or Other Purposes*: Sequent; *UNRELATED*: *Consultancy*: Stryker. *Money paid to the institution.

REFERENCES

1. Cognard C, Pierot L, Anxionnat R, et al; Clarity Study Group. **Results of embolization used as the first treatment choice in a consecutive nonselected population of ruptured aneurysms: clinical results of the Clarity GDC study.** *Neurosurgery* 2011;69:837–41; discussion 842 CrossRef Medline
2. Pierot L, Spelle L, Vitry F. **ATENA: the first prospective, multicentric evaluation of the endovascular treatment of unruptured intracranial aneurysms.** *J Neuroradiol* 2008;35:67–70. Erratum in *J Neuroradiol* 2008;35:252 CrossRef Medline
3. Pierot L, Cognard C, Spelle L, et al. **Safety and efficacy of balloon remodeling technique during endovascular treatment of intracranial aneurysms: critical review of the literature.** *AJNR Am J Neuroradiol* 2012;33:12–15 CrossRef Medline
4. Pierot L, Spelle L, Leclerc X, et al. **Endovascular treatment of unruptured intracranial aneurysms: comparison of safety of remodeling technique and standard treatment with coils.** *Radiology* 2009;251:846–55 CrossRef Medline
5. Pierot L, Cognard C, Anxionnat R, et al; CLARITY Investigators. **Remodeling technique for endovascular treatment of ruptured intracranial aneurysms had a higher rate of adequate postoperative occlusion than did conventional coil embolization with comparable safety.** *Radiology* 2011;258:546–53 CrossRef Medline
6. Shapiro M, Becske T, Sahlein, et al. **Stent-supported aneurysm coiling: a literature survey of treatment and follow-up.** *AJNR Am J Neuroradiol* 2012;33: 159–63 CrossRef Medline
7. Berge J, Biondi A, Machi P, et al. **Flow-diverter Silk stent for the treatment of intracranial aneurysms: 1-year follow-up in a multicenter study.** *AJNR Am J Neuroradiol* 2012;33:1150–55 CrossRef Medline
8. Pierot L, Wakhloo AK. **Endovascular treatment of intracranial aneurysms: current status.** *Stroke* 2013;44:2046–54 CrossRef Medline
9. Pierot L, Liebig T, Sychra V, et al. **Intrasaccular flow-disruption treatment of intracranial aneurysms: preliminary results of a multicenter clinical study.** *AJNR Am J Neuroradiol* 2012;33:1232–38 CrossRef Medline
10. Pierot L, Klisch J, Cognard C, et al. **Endovascular WEB flow disruption in middle cerebral artery aneurysms: preliminary feasibility, clinical, and anatomical results in a multicenter study.** *Neurosurgery* 2013;73:27–34; discussion 34–35 CrossRef Medline
11. Papagiannaki C, Spelle L, Januel AC, et al. **WEB intrasaccular flow disruptor—prospective, multicenter experience in 83 patients with 85 aneurysms.** *AJNR Am J Neuroradiol* 2014;35:2006–11 CrossRef Medline
12. Lubicz B, Klisch J, Gauvrit JY, et al **WEB-DL endovascular treatment of wide-neck bifurcation aneurysms: short- and midterm results in a European study.** *AJNR Am J Neuroradiol* 2014;35:432–38 CrossRef Medline
13. Pierot L, Klisch J, Liebig T, et al. **WEB-DL endovascular treatment of wide-neck bifurcation aneurysms: long-term results in a European series.** *AJNR Am J Neuroradiol* 2015;36:2314–19 CrossRef Medline
14. Pierot L, Biondi A, Narata AP, et al. **Should indications for WEB aneurysm treatment be enlarged? Report of a series of 20 patients with aneurysms in "atypical" locations for WEB treatment.** *J Neuroradiol* 2017 Mar 2. [Epub ahead of print] CrossRef Medline
15. Pierot L, Moret J, Turjman F, et al. **WEB treatment of intracranial aneurysms: feasibility, complications, and 1-month safety results with WEB-DL and WEB-SL/SLS in the French Observatory.** *AJNR Am J Neuroradiol* 2015;36:922–27 CrossRef Medline
16. Pierot L, Moret J, Turjman F, et al. **WEB treatment of intracranial aneurysms: clinical and anatomical results in the French Observatory.** *AJNR Am J Neuroradiol* 2016;37:655–59 CrossRef Medline
17. Pierot L, Costalat V, Moret J, et al. **Safety and efficacy of aneurysm treatment with WEB: results of WEBCAST study.** *J Neurosurg* 2016; 124:1250–56 CrossRef Medline
18. Pierot L, Spelle L, Molyneux A, et al. **Clinical and anatomical follow-up in patients with aneurysms treated with WEB device: 1-year follow-up report in the cumulated population of 2 prospective, multicenter series (WEBCAST, French Observatory).** *Neurosurgery* 2016;78:133–41 CrossRef Medline
19. Muskens IS, Senders JT, Dasenbrock HH, et al. **The Woven Endobridge device for treatment of intracranial aneurysms: a systematic review.** *World Neurosurg* 2017;98:809–817.e1 CrossRef Medline
20. Asnafi S, Rouchaud A, Pierot L, et al. **Efficacy and safety of the Woven EndoBridge (WEB) device for the treatment of intracranial aneurysms: a systematic review and meta-analysis.** *AJNR Am J Neuroradiol* 2016;37:2287–92 CrossRef Medline
21. Van Rooij W, Peluso JP, Bechan RS, et al. **WEB treatment of ruptured intracranial aneurysms.** *AJNR Am J Neuroradiol* 2016;37: 1679–83 CrossRef Medline
22. Herbreteau D, Bibi R, Narata AP, et al. **Are anatomical results influenced by WEB shape modification? Analysis in a prospective, single-center series of 39 patients with aneurysms treated with WEB.** *AJNR Am J Neuroradiol* 2016;37:2280–2286 CrossRef Medline
23. Kotowski M, Naggara O, Darsaut TE, et al. **Safety and occlusion rates of surgical treatment of unruptured intracranial aneurysms: a systematic review and meta-analysis of the literature from 1990 to 2011.** *J Neurol Neurosurg Psychiatry* 2013;84:42–48 CrossRef Medline
24. Cognard C, Januel AC. **Remnants and recurrences after the use of the WEB intrasaccular device in large-neck bifurcation aneurysms.** *Neurosurgery* 2015;76:522–30; discussion 530 CrossRef Medline
25. Pierot L. **Letter: WEB aneurysm treatment: stability and "compression."** *Neurosurgery* 2015;77:E666–67 CrossRef Medline
26. Timsit C, Soize S, Benaissa A, et al. **Contrast-enhanced and time-of-flight MRA at 3T compared with DSA for the follow-up of intracranial aneurysms treated with the WEB device.** *AJNR Am J Neuroradiol* 2016;37:1684–89 CrossRef Medline

Large Basilar Apex Aneurysms Treated with Flow-Diverter Stents

V. Da Ros, J. Caroff, A. Rouchaud, C. Mihalea, L. Ikka, J. Moret, and L. Spelle

ABSTRACT

BACKGROUND AND PURPOSE: The treatment of wide-neck, large basilar apex aneurysms is challenging with either an endovascular or a surgical approach. The aim of the present study was to report our experience treating basilar apex aneurysms with flow-diverter stents and to evaluate their efficacy and safety profile in this specific anatomic condition.

MATERIALS AND METHODS: We retrospectively analyzed data from all consecutive patients treated with flow-diverter stents at our institution between January 2011 and January 2015. Patients with large basilar apex aneurysms treated with a flow-diverter stent were included in the study. Clinical presentations, technical details, intra- and perioperative complications, and clinical and angiographic outcomes were recorded, with a midterm follow-up.

RESULTS: Of the 175 aneurysms treated with flow-diverter stents at our institution, 5 patients (2 women and 3 men; age range, 44–58 years) received flow-diverter stent for basilar apex aneurysms. The mean follow-up after stent deployment was 21 months (range, 15–24 months). One patient died on day 31 from an early postprocedural midbrain hemorrhage. One patient had a right cerebellar hemispheric ischemic lesion with a transient cerebellar syndrome resolved within 24 hours without neurologic sequelae at the latest follow-up. The mRS was 0 in 4 patients and 6 in 1 patient at last follow-up.

CONCLUSIONS: Flow diversion is a feasible technique with an efficacy demonstrated at a midterm follow-up, especially in the case of basilar apex aneurysm recurrences after previous endovascular treatments. Concern about its safety profile still exists.

ABBREVIATIONS: BAA = basilar apex aneurysm; mRR = modified Raymond-Roy; PCA = posterior cerebral artery

Wide-neck, large basilar apex aneurysms (BAA) are rare lesions that account for approximately 7%–8% of all intracranial aneurysms.[1,2] Their treatment is challenging when using either endovascular or surgical approaches.[3,4]

The endovascular approach is considered the "gold standard" for posterior circulation intracranial aneurysms because of a lower rate of procedural complications compared with surgery.[5] However, long-term angiographic studies of large posterior circulation aneurysms after coiling show high recurrence rates.[6]

The advent of flow-diverter stents has allowed for the treatment of wide-neck, large aneurysms with promising clinical and angiographic outcomes.[7-9] Only a few articles have reported the results of the use of flow-diverter stents in posterior circulation aneurysms,[7,10,11] and concerns remain regarding their use.

Large BAAs are characterized by specific issues when a flow-diverter stent is the treatment of choice. These issues are mostly related to their anatomic location and include the risk of occlusion of the posterior cerebral (PCA) and superior cerebellar arteries,[12] brain stem ischemic lesions caused by coverage of the perforator arteries,[13] and delayed rupture of the treated aneurysm.[14]

The aim of this study was to report midterm follow-up results after the treatment of wide-neck, large BAAs with flow-diverter stents. We describe our experience in terms of the feasibility, safety, and efficacy of the procedure in this specific anatomic condition.

MATERIALS AND METHODS

From a prospective data base that collected data from all patients treated with a flow-diverter stent for intracranial aneurysms at our institution between January 2011 and January 2015, we searched for complex large BAAs. These were defined as aneu-

Received December 6, 2016; accepted after revision January 31, 2017.

From the Department of Diagnostic Imaging and Interventional Radiology, Molecular Imaging and Radiotherapy (V.D.R.), Policlinico Tor Vergata, Rome, Italy; Interventional Neuroradiology NEURI Center (V.D.R., J.C., A.R., C.M., L.I., J.M., L.S.), Hôpital Bicêtre, Le Kremlin Bicêtre, France; Department of Neurosurgery (C.M.), University of Medicine and Pharmacy "Victor Babes," Timisoara, Romania; and Université Paris-Sud XI (L.S.), Le Kremlin-Bicêtre, France.

Please address correspondence to Valerio Da Ros, Hôpital Bicêtre - Interventional Neuroradiology NEURI Center, 78 rue du Général Leclerc, 94270 Le Kremlin Bicêtre, France; e-mail: daros.valerio@gmail.com

Indicates article with supplemental on-line table.

http://dx.doi.org/10.3174/ajnr.A5167

rysms with a large diameter (>10 mm) and a wide neck treated with a flow-diverter stent either as the first-line treatment or after a recurrence after previous coiling.

As part of a multidisciplinary team, neurosurgeons and neuroradiologists discussed all the cases to determine the optimum aneurysm management. The individual risk-benefit analysis of different treatment modalities was taken into account, and a flow-diverter stent was chosen as the best treatment of choice after the exclusion of other endovascular (coiling, stent, or balloon-assisted coiling) or microsurgical (clip reconstruction or vessel sacrifice with or without bypass) approaches. Each decision was made in consensus with the patients and/or their relatives. Informed consent was obtained from all patients.

The periprocedural pharmacologic protocol for patients undergoing flow-diverter stent implantation was uniform throughout the study period. All patients were premedicated with a dual-antiplatelet regimen (75 mg of clopidogrel with 160 mg of aspirin per day) for at least 7 days before the procedure. Thrombocyte inhibition levels were confirmed by using the VerifyNow P2Y12 assay (Accumetrics, San Diego, California) and 4 hematologic laboratory tests. P2Y12 percent inhibition of 30%–40% was generally used as a minimum degree of preprocedure P2Y12 receptor inhibition required. All procedures were performed under heparinization, with a bolus of 2000–5000 IU of heparin administered once the femoral sheath was in place.

In all cases, the flow-diverter stent was delivered to cover the whole length of the aneurysm neck or remnant. The correct deployment was assessed with a VasoCT (Phillips Healthcare, Best, the Netherlands) scan,[15] used to evaluate the necessity of further maneuver after stent deployment (ie, ballooning).

All patients underwent radiologic follow-up with conventional angiography, scheduled at 3–6, 12, and 24 months after treatment. MR imaging and MR angiography imaging were performed during the follow-up only where clinical symptoms changed.

For each patient, the following outcomes were evaluated: 1) the feasibility of the procedure, defined as the technical possibility of delivering the flow-diverter stent to the desired position; 2) the safety of the procedure, including early complications (defined as those occurring within 24–48 hours of the procedure) and late events (defined as events occurring during the follow-up period); 3) the efficacy in achieving target aneurysm occlusion, categorized by using the modified Raymond-Roy (mRR) classification[16]; adequate aneurysm occlusion (complete occlusion + neck remnant) considered as stable results during the subsequent follow-up was also assessed[17]; 4) major recurrence rates after flow-diverter stent deployment, defined as any increase in the size of the aneurysmal remnant that required retreatment during the follow-up period; and, 5) clinical outcome assessed by the mRS during midterm follow-up.

RESULTS

Between January 2011 and January 2015, 175 aneurysms were treated with flow-diverter stents at our institution. We identified 5 patients (3 men and 2 women) with wide-neck, large BAAs. Patient demographics and aneurysm characteristics are summarized in the On-line Table. Patient ages varied from 44–58 years, with a mean age of 50 years.

Aneurysm size ranged from 10–23 mm, with a median value of 20 mm. Of the 3 patients presenting with a ruptured aneurysm, 2 were treated with conventional coiling in the first instance, and 1 was treated with stent-assisted coiling (Patient 3).

The indications for flow-diverter stent implantation included: aneurysm recurrence after previous endovascular treatment with coils alone (Patients 4 and 5) or with stent and coils (Patient 3), intention-to-cure treatment with a single staged session of flow-diverter stent implantation after conventional coiling (Patient 2), or 2-step treatment with coils and a scheduled flow-diverter stent implantation within 6 weeks (Patient 1). Moreover, chiasmal compression syndrome was an additional indication for treatment in 1 patient (Patient 4).

The flow-diverter stents used were the Pipeline Embolization Device (Covidien, Irvine, California) in Patients 1 and 3, the Silk flow diverter (Balt Extrusion, Montmorency, France) in Patient 2, and the Flow-Redirection Endoluminal Device (FRED; MicroVention, Tustin, California) in Patients 4 and 5. The choice of the flow-diverter stent type was based on the operator's confidence with the device. Stent deployment was feasible without intraprocedural complications in all cases.

In all 5 cases, adequate occlusion of the BAAs was achieved at last follow-up (mean delay, 6 months) without any major recurrence after flow-diverter stent implantation.

PCAs and superior cerebellar arteries covered by the flow diverter were patent during the follow-up for Patients 1, 2, 3, and 4. In Patient 5, both covered superior cerebellar arteries were not visualized at the subsequent DSA follow-up (Fig 1). This patient presented with a postprocedural transient cerebellar syndrome caused by a small infarction of the right cerebellar hemisphere that resolved within 24 hours, without associated neurologic sequelae during the follow-up; in Patient 2, a fatal postprocedural hemorrhage occurred 12 hours after flow-diverter stent deployment. The 3 remaining patients did not present with changes to their clinical symptoms during the follow-up period. Patient 4, who presented with an amputation of the visual field, with "tunnel vision" caused by chiasmal compression, completely recovered visual acuity within 6 months of flow-diverter stent implantation.

Here, we report a brief description of each case.

Illustrative Cases

Patient 1. A 44-year-old man underwent an MR imaging evaluation for acute severe headache, which identified an incidental, large, wide-neck, nonthrombosed BAA.

On 3D-DSA, the BAA measured 20 × 18 × 12 mm (Fig 2).

The aneurysm was first treated with a simple coiling with loose packing attenuation; the treatment was completed 6 weeks later, with the deployment of a 3.5 × 20 mm Pipeline flow-diverter stent. The latest DSA follow-up (24 months) revealed complete aneurysmal occlusion (mRR class I; mRS, 0).

Patient 2. A 58-year-old woman presented with a progressive midbrain compression syndrome caused by a large BAA discovered on MR imaging.

The 3D-DSA showed a 23 × 21 mm wide-neck, large BAA

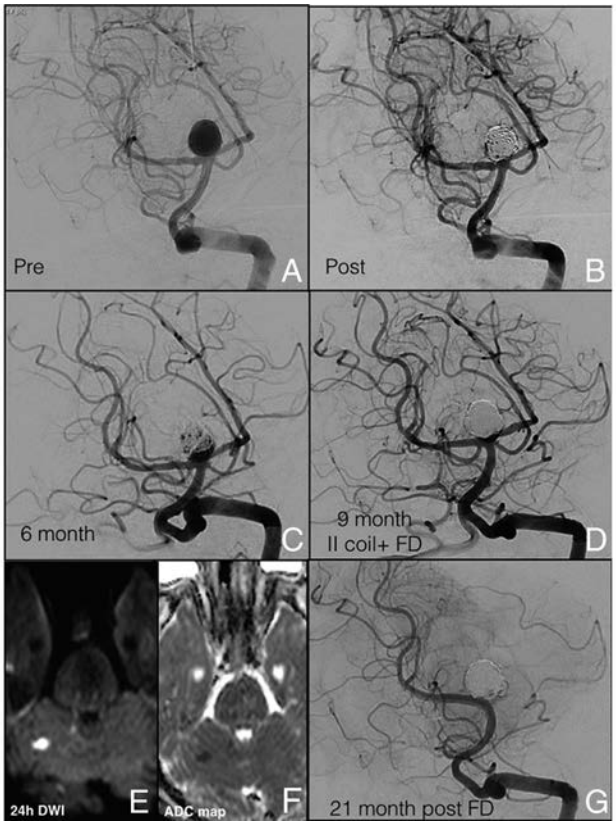

FIG 1. *A*, DSA shows a ruptured large BAA (10 × 10 mm; neck, 4.4 mm). *B*, Aneurysmal embolization was performed with the balloon-remodeling technique. *C*, Six-month DSA follow-up shows a significant neck recanalization (5 mm × 6 mm). *D*, At the 9-month follow-up, a second coiling remodeling technique associated with the deployment of a FRED flow-diverter stent across the right PCA was performed. *E* and *F*, The 24-hour postprocedural MR imaging, with DWI and ADC map, shows the presence of a small ischemic right cerebellar lesion. *G*, At 21-month DSA follow-up, both covered superior cerebellar arteries were not visualized, and the persistence of complete BAA occlusion was confirmed (mRR class I; mRS, 0).

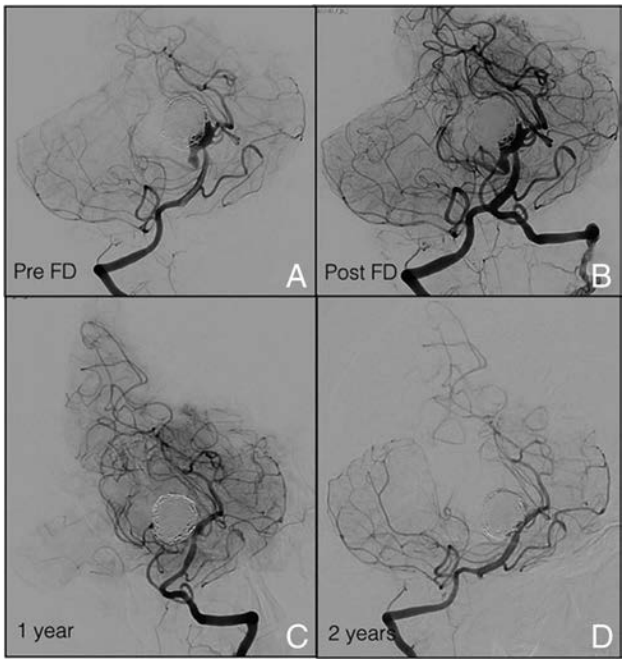

FIG 2. *A*, DSA shows the remnant of a wide-neck, large BAA aneurysm that involved both superior cerebellar arteries and the left P1 segment, with a 5-mm right superior cerebellar artery fusiform aneurysm, and a fetal origin of the right PCA, treated with a simple coiling. *B*, Six weeks later, the remnant was treated with a Pipeline stent. *C*, Twelve-month and *D*, 24-month follow-up DSA reveal complete aneurysmal occlusion (mRR class I).

treated in a single session with coiling and a Silk flow-diverter stent (Fig 3).

Twelve hours after the treatment, the patient experienced an acute loss of consciousness. The MR imaging showed a midbrain hematoma associated with an intraventricular hemorrhage and an acute hydrocephalus. Steroids were administered to reduce the midbrain posthemorrhagic edema, and a second flow-diverter stent was deployed; then, an external ventricular shunt was inserted.

After 5 days, the patient, already under mechanical ventilation, experienced fever and severe pneumonia. The 2-week DSA and MR imaging follow-up demonstrated aneurysmal sac occlusion (mRR class I) and mild increase of the initial hydrocephalus.

After the recurrence of a second episode of hypoxic pneumonia, the patient died on day 31 of hospitalization (mRS, 6).

Patient 3. A 45-year-old man presented with an acute SAH and a Glasgow Coma Scale score of 13. The initial DSA showed a wide-neck BAA (8 × 10 mm), which was embolized with a stent-assisted (Neuroform; Stryker Neurovascular, Kalamazoo, Michigan [3.5 mm × 20 mm]) coiling technique (Fig 4). At 15-month follow-up, DSA revealed a residual aneurysmal neck, which appeared enlarged on the subsequent DSA follow-up 4 months later (8 mm × 5 mm × 2 mm). A Pipeline flow-diverter stent was used to treat the neck remnant. The 15-month DSA showed adequate sac occlusion (mRR class IIIa; mRS, 0).

Patient 4. A 53-year-old man had a recent history of a large (20 mm), wide-neck, ruptured BAA that had been partially coiled at another institution. Four months later, an increased aneurysmal mass effect on the chiasma was seen on MR imaging. At that time, the patient presented with an amputation of the visual field with "tunnel vision," and a second partial coiling embolization was performed (Fig 5). After a 3-month early aneurysmal recurrence (10 mm × 9 mm), an additional coiling of the sac remnant and flow-diverter stent deployment (FRED 3.5 mm × 16–22 mm) was performed.

The 24-month DSA follow-up showed adequate BAA occlusion (mRR class IIIa), along with complete recovery of the visual field (mRS, 0).

Patient 5. A 46-year-old woman was referred to the emergency department with an acute SAH (classified as Fisher 4 with hydrocephalus; Glasgow Coma Scale, 12) caused by a ruptured BAA (10 × 10 mm; neck, 4.4 mm). The aneurysm was coiled, and at the 6-month DSA follow-up, a neck recanalization (5 mm × 6 mm) was observed (Fig 1).

At 9-month follow-up, a second coiling was performed, along with a FRED flow-diverter stent deployment.

Upon waking from anesthesia, the patient presented with a

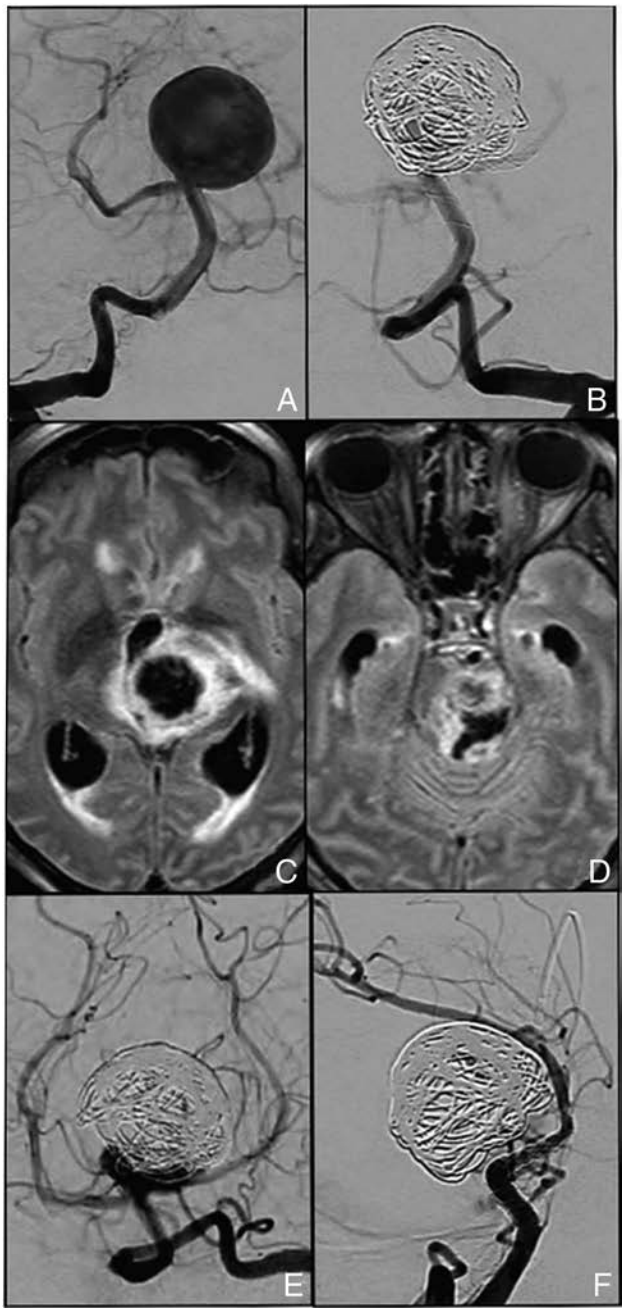

FIG 3. *A*, DSA shows a wide-neck, large BAA aneurysm (*B*) treated in a single session with coiling and a Silk flow-diverter stent across the left PCA. *C* and *D*, MR imaging shows the presence of a midbrain hematoma 12 hours after the treatment. *E*, Anteroposterior view DSA shows residual filling at the level of the aneurysmal neck. A second Pipeline flow diverter was then deployed. *F*, The 2-week DSA follow-up shows complete aneurysmal sac occlusion (mRR class I).

cerebellar kinetic syndrome with diplopia, confirmed by the presence of a small ischemic right cerebellar lesion on the postprocedural MR imaging; the neurologic symptoms completely resolved within 24 hours.

The patient was maintained on a full dose of heparin and an elevated arterial pressure (mean, 140 mm Hg) for 1 week.

At 21-month DSA follow-up, both covered superior cerebellar arteries were not visualized, and the persistence of complete BAA occlusion was confirmed (mRR class I; mRS, 0).

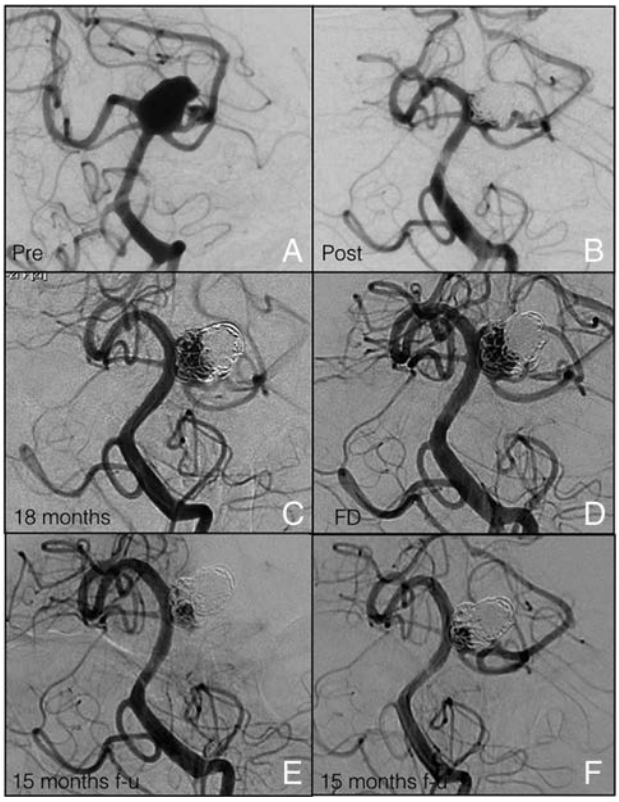

FIG 4. *A*, The initial DSA demonstrates a wide-neck, large BAA involving the origin of both PCAs and superior cerebellar arteries (*B*) treated with a stent-assisted coiling technique (Neuroform 3.5 mm × 20 mm). *C*, The 18-month DSA follow-up reveals an aneurysmal recurrence at the level of the neck. *D*, A Pipeline stent was used to treat the neck remnant with (*E*) adequate aneurysm occlusion at 15-month DSA follow-up (mRR class IIIa) demonstrated in the working projection. *F*, The compression test performed confirms the result.

DISCUSSION

Of the few articles reporting the treatment of posterior circulation aneurysms with flow-diverter stents,[7,10,11] to the best of our knowledge, none have focused on the use of flow-diverter stents for the treatment of wide-neck, large BAAs. In this clinical report, we describe the remarkable midterm follow-up results we obtained with the use of flow-diverter stents in this infrequent location. We detailed the feasibility and efficacy of the technique, including its ability to determine aneurysmal growth arrest in all the cases of aneurysmal recurrence after previous endovascular treatments.

Use of flow diverters in the posterior circulation carries higher complication rates compared with use in the anterior circulation. However, in the literature, flow diverters in the posterior circulation were mostly used for the treatment of dissecting, fusiform, and/or partially thrombosed aneurysms[18]; this makes the comparison of our findings with previous series difficult.

In this study, flow-diverter stent deployment was feasible in all patients, and compared with surgical clipping, the flow-diverter stent deployment presented a less technical challenge.[19] The fact that all treated patients in this series except 1 (Patient 2) had wide-neck, large BAA recurrences after previous endovascular treatments (ie, coiling or stent + coiling) was the determinant for us to adopt a different strategy concept: flow diversion. In all cases

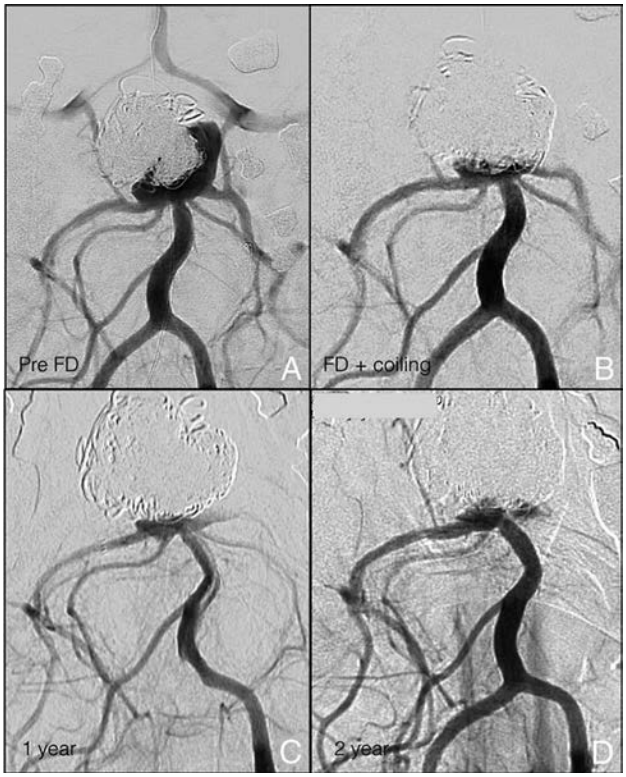

FIG 5. *A*, The preoperative DSA shows a large, wide-neck BAA, twice partially coiled in an emergency setting, responsible for a chiasmal compression syndrome. *B*, Additional coiling of the sac remnant occurred and a subsequent flow-diverter stent (FRED 3.5 mm × 22–16 mm) was deployed across the right P1 segment. *C*, Twelve-month and *D*, 24-month DSA follow-up demonstrate adequate BAA occlusion (mRR class IIIa), and the visual field was completely recovered.

of BAA recurrence (Patients 1, 3, 4, and 5), the flow-diverter stent was intended as a "rescue" strategy where a coiling procedure had failed. The flow-diverter deployment determined progressive sac exclusion, with no need for further treatments during follow-up.

Although other treatment options were available, the use of a flow-diverter stent offered a more effective scaffolding to the diseased target artery compared with a conventional stent; moreover, other techniques such as Y-stent placement have demonstrated efficacy in previous studies. However, according to Bartolini et al,[20] Y-stent placement carries the risk of up to 10% procedure-related permanent neurologic deficits. Finally, the flow-diverter stent deployment was a less technically demanding procedure than the Y-stent placement technique.

Patient 2 was treated for an unruptured BAA with coiling and flow-diverter stent in a single session, with a "first intention-to-cure" strategy, and the patient experienced an early postprocedural hemorrhage.

The delayed aneurysm rupture risk after flow-diverter stent deployment has been previously described.[14] The small population of this study determines the impossibility of relating the only hemorrhagic complication observed to a specific type of device rather than to the flow-diversion effect. However, the rapid intraaneurysmal thrombus formation is a source of various proteases with high proteolytic activity, which could participate in the degradation of the arterial wall and lead to aneurysm rupture. Moreover, the larger aneurysms, like those presented in this series, are generally more likely to have intraluminal thrombus.[21-23] Thus, this mechanism probably was the most involved in the delayed aneurysm rupture observed in Patient 2. In this case, the steroids were administered only after aneurysmal rupture, mainly to reduce the midbrain posthemorrhagic edema because, to the best of our knowledge, the efficiency of steroids to prevent the lytic activity has not been demonstrated yet.[24] Unfortunately, how to prevent this dramatic complication is still a matter of debate.

To protect against delayed aneurysm rupture,[25] our choice was the use of loose-packing coiling before flow-diverter stent. Retrospectively, we assume that the loose-packing coiling was not sufficient to act as a scaffold to organize thrombi into stable fibrous tissue[26] and that the time between the procedures was not long enough to allow a progressive thrombus formation after coiling. Our experience confirms that the optimum packing attenuation of coils and the timing between coiling and flow-diverter stent placement is still to be determined.

Posterior circulation flow-diverter stents carry a risk of ischemic lesions caused by the occlusion of covered branches (ie, superior cerebellar arteries and PCAs),[27] including a higher rate of injury to posterior perforators relative to their anterior counterparts.[3,28,29]

In this series, we observed 1 case (Patient 5) of early ischemic lesion after flow-diverter stent coverage. In this case, the placement of a flow diverter in front of the superior cerebellar arteries led to their early occlusion, with a unilateral transient cerebellar syndrome observed after the procedure. At the subsequent follow-up, the superior cerebellar artery occlusion remained clinically silent. To the best of our knowledge, there is no previous literature specifically analyzing superior cerebellar artery occlusion after flow-diverter coverage. However, in the anterior circulation, slow flow of the side branches covered by the flow-diverter stent is observed in up to 19.1% of cases[30] and vessel occlusion is observed in up to 21%.[31] In most of these cases, neither permanent deficit or death nor neurologic deficit were described within covered branches, perhaps because of the good collateral circulation.[11,27,30] As described by Alqadri et al,[32] several collateral anastomoses also exist in the posterior circulation. These findings suggest that in Patient 5, the occlusion of the superior cerebellar arteries after flow-diverter stent deployment was responsible for an initial vascular and hemodynamic regional unbalance, which determined an early initial clinical manifestation. The subsequent early activation of the posterior collateral circulation allowed for the patient's rapid clinical improvement without neurologic manifestation during the follow-up. In case of uncertainty regarding the collateral circulation, it could be valuable to perform a balloon occlusion test to assess the vascular territory supply of the covered branches.

Finally, deploying flow-diverter stents in the basilar bifurcation determines flow modification at the level of the covered PCA.

In accordance with the anatomic knowledge of Brassier et al,[33] to protect as many perforators as possible, the flow diverter should reasonably be deployed in the most caudal PCA, where the number of perforators is less common. However, it also should be taken into account that most of the flow diverters are composed of microfilaments of 30–35 μm, and the pore size varies between 110–250 μm (much depending on the final FD mor-

phology and selection of the proper size adapted to the vessel diameter).[34] These anatomic characteristics suggest that in the worst case, when 2 filaments cross in front of a 100 μm perforator vessel, this small artery will lose no more than 55% of its orifice area. This still provides sufficient blood flow to the distribution territory.[35]

Thus, to choose which PCA to put the stent in, we mostly focused our attention on hemodynamic criteria. In particular, we simply decided to cover the smallest P1 segment with the largest posterior communicating artery with the stent. This approach was based on several reasons. First, in case of subsequent occlusion of the covered P1 segment, this would be supplied by a larger posterior communicating artery. Second, in this configuration, the larger uncovered posterior communicating artery is preferentially used to supply the distal P2 segment in an anterograde fashion (rather than the P1 segment in a retrograde fashion). As a consequence, the filling flow into the aneurysmal sac from the covered P1 is potentially reduced. Finally, a flow diverter deployed in the P1 segment with the smaller or absent posterior communicating artery determines a higher gradient pressure at that level because of the reduced flow competition between the P1 segment and posterior communicating artery. This theoretically favors the perforators' patency maintenance.

In line with these considerations, in Patients 1, 2, and 3, this approach induced flow changes in the smaller covered posterior communicating artery, with posterior communicating arteries still patent, but no more visible except after performing an occlusion test (Patient 3); in Patient 4, we decided to put the flow-diverter stent in the right PCA because the right posterior communicating artery was smaller compared with the left one; finally, in Patient 5, we decided to deploy the stent in the right PCA only because it was technically easier because neither anatomic nor hemodynamic differences were observed between the right and left side (with a symmetry of both PCAs and posterior communicating arteries and the aneurysmal neck centered between the 2 PCAs). This approach has proved to be efficient in preserving covered PCA patency without significant aneurysm sac supply at midterm follow-up and with no perforator infarction observed.

Limitations

This clinical report has several limitations, including the small number of patients and the retrospective collection of the cases. However, all the wide-neck, large BAAs treated with flow-diverter stents in our department have been included in this series without any selection. In addition, the follow-up period is quite short; longer follow-up is essential to assess the long-term stability of adequate occlusion. Because of the small size of this study, we did not perform between-case analysis.

CONCLUSIONS

A wide-neck, large BAA is a complex, multifactorial problem, for which the use of flow-diverter stents plus coiling appears to be a promising approach. However, the exact staging of the treatments and the packing density of coiling require further evaluation to minimize the risk of its application.

Disclosures: Jacques Moret—*UNRELATED*: *Consultancy*: Microvention-Stryker-Medtronic. Laurent Spelle—*UNRELATED*: *Consultancy*: Stryker, Medtronic, Sequent.

REFERENCES

1. Brisman JL, Song JK, Newell DW. **Cerebral aneurysms.** *N Engl J Med* 2006;355:928–39 CrossRef Medline
2. Vallee JN, Aymard A, Vicaut E, et al. **Endovascular treatment of basilar tip aneurysms with Guglielmi detachable coils: predictors of immediate and long-term results with multivariate analysis 6-year experience.** *Radiology* 2003;226:867–79 CrossRef Medline
3. Wong GK, Kwan MC, Ng RY, et al. **Flow diverters for treatment of intracranial aneurysms: current status and ongoing clinical trials.** *J Clin Neurosci* 2011;18:737–40 CrossRef Medline
4. Taki W, Sakai N, Nakahara I, et al. **Circulatory arrest with profound hypothermia during the surgical treatment of large internal carotid artery aneurysm–case report.** *Neurol Med Chir (Tokyo)* 1998;38:725–29 CrossRef Medline
5. Sekhar LN, Tariq F, Morton RP, et al. **Basilar tip aneurysms: a microsurgical and endovascular contemporary series of 100 patients.** *Neurosurgery* 2013;72:284–98; discussion 298–99 CrossRef Medline
6. Jin SC, Ahn JS, Kwun BD, et al. **Analysis of clinical and radiological outcomes in microsurgical and endovascular treatment of basilar apex aneurysms.** *J Korean Neurosurg Soc* 2009;45:224–30 CrossRef Medline
7. Lylyk P, Miranda C, Ceratto R, et al. **Curative endovascular reconstruction of cerebral aneurysms with the Pipeline embolization device: the Buenos Aires experience.** *Neurosurgery* 2009;64:632–42; discussion 642–43; quiz N6 CrossRef Medline
8. Lubicz B, Collignon L, Raphaeli G, et al. **Flow-diverter stent for the endovascular treatment of intracranial aneurysms: a prospective study in 29 patients with 34 aneurysms.** *Stroke* 2010;41:2247–53 CrossRef Medline
9. Becske T, Kallmes DF, Saatci I, et al. **Pipeline for uncoilable or failed aneurysms: results from a multicenter clinical trial.** *Radiology* 2013;267:858–68 CrossRef Medline
10. Fiorella D, Kelly ME, Albuquerque FC, et al. **Curative reconstruction of a giant midbasilar trunk aneurysm with the Pipeline embolization device.** *Neurosurgery* 2009;64:212–17; discussion 217 CrossRef Medline
11. Szikora I, Berentei Z, Kulcsar Z, et al. **Treatment of intracranial aneurysms by functional reconstruction of the parent artery: the Budapest experience with the Pipeline embolization device.** *AJNR Am J Neuroradiol* 2010;31:1139–47 CrossRef Medline
12. Kan P, Duckworth E, Puri A, et al. **Treatment failure of fetal posterior communicating artery aneurysms with the Pipeline embolization device.** *J Neurointerv Surg* 2016;8:945–48 CrossRef Medline
13. Kulcsár Z, Ernemann U, Wetzel SG, et al. **High-profile flow diverter (Silk) implantation in the basilar artery: efficacy in the treatment of aneurysms and the role of the perforators.** *Stroke* 2010;41:1690–96 CrossRef Medline
14. Rouchaud A, Brinjikji W, Lanzino G, et al. **Delayed hemorrhagic complications after flow diversion for intracranial aneurysms: a literature overview.** *Neuroradiology* 2016;58:171–77 CrossRef Medline
15. Caroff J, Mihalea C, Neki H, et al. **Role of C-arm VasoCT in the use of endovascular WEB flow disruption in intracranial aneurysm treatment.** *AJNR Am J Neuroradiol* 2014;35:1353–57 CrossRef Medline
16. Mascitelli JR, Moyle H, Oermann EK, et al. **An update to the Raymond-Roy Occlusion Classification of intracranial aneurysms treated with coil embolization.** *J Neurointerv Surg* 2015;7:496–502 CrossRef Medline
17. Lubicz B, Van der Elst O, Collignon L, et al. **Silk flow-diverter stent for the treatment of intracranial aneurysms: a series of 58 patients with emphasis on long-term results.** *AJNR Am J Neuroradiol* 2015;36:542–46 CrossRef Medline
18. Wang CB, Shi WW, Zhang GX, et al. **Flow diverter treatment of posterior circulation aneurysms. A meta-analysis.** *Neuroradiology* 2016;58:391–400 CrossRef Medline

19. Spetzler RF, Hadley MN, Rigamonti D, et al. **Aneurysms of the basilar artery treated with circulatory arrest, hypothermia, and barbiturate cerebral protection.** *J Neurosurg* 1988;68:868–79 CrossRef Medline
20. Bartolini B, Blanc R, Pistocchi S, et al. **"Y" and "X" stent-assisted coiling of complex and wide-neck intracranial bifurcation aneurysms.** *AJNR Am J Neuroradiol* 2014;35:2153–58 CrossRef Medline
21. Turowski B, Macht S, Kulcsár Z, et al. **Early fatal hemorrhage after endovascular cerebral aneurysm treatment with a flow diverter (SILK-stent): do we need to rethink our concepts?** *Neuroradiology* 2011;53:37–41 CrossRef Medline
22. Berge J, Biondi A, Machi P, et al. **Flow-diverter Silk stent for the treatment of intracranial aneurysms: 1-year follow-up in a multicenter study.** *AJNR Am J Neuroradiol* 2012;33:1150–55 CrossRef Medline
23. Velioglu M, Kizilkilic O, Selcuk H, et al. **Early and midterm results of complex cerebral aneurysms treated with Silk stent.** *Neuroradiology* 2012;54:1355–65 CrossRef Medline
24. Thielen E, McClure M, Rouchaud A, et al. **Concomitant coiling reduces metalloproteinase levels in flow diverter-treated aneurysms but anti-inflammatory treatment has no effect.** *J Neurointerv Surg* 2017;9:307–10 CrossRef Medline
25. Cebral JR, Mut F, Raschi M, et al. **Aneurysm rupture following treatment with flow-diverting stents: computational hemodynamics analysis of treatment.** *AJNR Am J Neuroradiol* 2011;32:27–33 CrossRef Medline
26. Natarajan SK, Lin N, Sonig A, et al. **The safety of Pipeline flow diversion in fusiform vertebrobasilar aneurysms: a consecutive case series with longer-term follow-up from a single US center.** *J Neurosurg* 2016;125:111–19 CrossRef Medline
27. Brinjikji W, Lanzino G, Cloft HJ, et al. **Patency of the posterior communicating artery after flow diversion treatment of internal carotid artery aneurysms.** *Clin Neurol Neurosurg* 2014;120:84–88 CrossRef Medline
28. Marinković SV, Gibo H. **The surgical anatomy of the perforating branches of the basilar artery.** *Neurosurgery* 1993;33:80–87 CrossRef Medline
29. Marinković S, Milisavljević M, Kovacević M. **Interpeduncular perforating branches of the posterior cerebral artery. Microsurgical anatomy of their extracerebral and intracerebral segments.** *Surg Neurol* 1986;26:349–59 CrossRef Medline
30. Gascou G, Lobotesis K, Brunel H, et al. **Extra-aneurysmal flow modification following Pipeline embolization device implantation: focus on regional branches, perforators, and the parent vessel.** *AJNR Am J Neuroradiol* 2015;36:725–31 CrossRef Medline
31. Puffer RC, Kallmes DF, Cloft HJ, et al. **Patency of the ophthalmic artery after flow diversion treatment of paraclinoid aneurysms.** *J Neurosurg* 2012;116:892–96 CrossRef Medline
32. Alqadri S, Adil MM, Watanabe M, et al. **Patterns of collateral formation in basilar artery steno-occlusive diseases.** *J Vasc Interv Neurol* 2013;6:9–13 Medline
33. Brassier G, Morandi X, Fournier D, et al. **Origin of the perforating arteries of the interpeduncular fossa in relation to the termination of the basilar artery.** *Interv Neuroradiol* 1998;4:109–20 CrossRef Medline
34. Shapiro M, Raz E, Becske T, et al. **Variable porosity of the Pipeline embolization device in straight and curved vessels: a guide for optimal deployment strategy.** *AJNR Am J Neuroradiol* 2014;35:727–33 CrossRef Medline
35. Seong J, Wakhloo AK, Lieber BB. **In vitro evaluation of flow diverters in an elastase-induced saccular aneurysm model in rabbit.** *J Biomech Eng* 2007;129:863–72 CrossRef Medline

Preliminary Experience with Stent-Assisted Coiling of Aneurysms Arising from Small (<2.5 mm) Cerebral Vessels Using The Low-Profile Visualized Intraluminal Support Device

C.-C. Wang, W. Li, Z.-Z. Feng, B. Hong, Y. Xu, J.-M. Liu, and Q.-H. Huang

ABSTRACT

BACKGROUND AND PURPOSE: The Low-Profile Visualized Intraluminal Support (LVIS) stent is a new device recently introduced for the treatment of wide-neck intracranial aneurysms. This single-center study presents the authors' preliminary experience using the LVIS stent to treat saccular aneurysms with parent arteries smaller than 2.5 mm.

MATERIALS AND METHODS: Aneurysms with a LVIS stent used in a small parent vessel (<2.5 mm in diameter) between October 2014 and April 2016 were included. Procedure-related complications, angiographic results, clinical outcomes, and midterm follow-up data were analyzed retrospectively.

RESULTS: A total of 22 patients was studied, including 5 ruptured and 17 unruptured aneurysms. Most of the aneurysms were located in the anterior circulation (90.9%). Stent placement in the parent arteries measuring 1.7–2.4 mm in diameter (mean, 2.1 mm) was successful in 100% of cases. Procedure-related complication developed in 1 patient (4.5%) who presented with aneurysm rupture. No permanent morbidity and mortality occurred. Immediate angiographic outcome showed complete occlusion in 8 aneurysms (36.4%), neck residual in 8 (36.4%), and residual aneurysm in 6 (27.3%). All patients underwent angiographic follow-up at a mean of 8.3 months, which revealed complete occlusion in 18 (81.8%) patients, neck remnant in 3 (13.6%), and residual sac in 1 (4.5%). No recanalization of the target aneurysm was observed. There was 1 case with asymptomatic in-stent stenosis.

CONCLUSIONS: Our preliminary results show that the deployment of LVIS stents in small vessels is feasible, safe, and effective in the midterm. Larger studies with long-term follow-up are needed to validate our promising results.

ABBREVIATION: LVIS = Low-Profile Visualized Intraluminal Support

The introduction of stent devices has greatly advanced the endovascular treatment options of intracranial aneurysms. Many aneurysms that had been previously considered untreatable because of their morphology, including those with unfavorable dome-to-neck ratios and/or location, are now amenable to coiling with the use of stents.[1,2] However, the use of stents for treating wide-neck distal intracranial aneurysms with small parent vessels remains challenging. Several previous studies reported relatively high rates of periprocedural thromboembolic events and in-stent stenosis.[3-11]

The Low-Profile Visualized Intraluminal Support (LVIS) device (MicroVention, Tustin, California), a new device offering an option between conventional stents and flow diverters, is designed for the stent-assisted coil embolization of wide-neck intracranial aneurysms. There is an increasing number of publications on the use of the LVIS device.[12-16] However, to our knowledge, no studies to date have specifically investigated the placement of the LVIS device in small vessels. Hence, we conducted this retrospective study to examine the LVIS device in terms of its safety, deployment feasibility, and treatment effectiveness in intracranial aneurysms with parent vessels measuring <2.5 mm in diameter.

MATERIALS AND METHODS

This retrospective study was approved by our hospital's institutional review board.

Received October 25, 2016; accepted after revision January 23, 2017.

From the Department of Neurosurgery, Changhai Hospital, Second Military Medical University, Shanghai, China.

Chuan-Chuan Wang and Wei Li have contributed equally to the manuscript and are listed as co-first authors.

This work was supported in part by the National Key Research and Development Program of China during the 13th Five-Year Plan Period (grant 2016YFC1300700), Key Program of Shanghai Science and Technology Commission Foundation (grant 13411950300), and Scientific Research and Innovation Project of Shanghai Municipal Education Commission (grant 14ZZ081).

Please address correspondence to Qing-Hai Huang or Jian-Min Liu, Department of Neurosurgery, Changhai Hospital, Second Military Medical University, Shanghai, China 200433; e-mail: ocinhqh@163.com or chstroke@163.com

Indicates open access to non-subscribers at www.ajnr.org

http://dx.doi.org/10.3174/ajnr.A5145

Table 1: Clinical data of all patients

Patient No.	Age (yr), Sex	Risk Factors	Presentation	HHG	Aneurysm Location	Aneurysm Size	Aneurysm Neck	PA Size	Initial Angiogram Results	Complications	FU Angiogram Results	FU Time
1	42, F	NS	Chronic headaches	0	BT	8.5	8.2	1.9	RA	N/A	NR	13
2	57, M	HP	Lt hemiparesis, unconsciousness	3	MCA	8.8	5.1	1.8	NR	N/A	CO	8
3	65, M	HP	Acute onset of headaches	2	ACA	5.6	4.6	1.7	NR	N/A	NR	14
4	63, M	HP, DM	Lt UE weakness, slurred speech	0	AComA	2.1	1.4	2.1	CO	Rupture	CO	11
5	44, F	NS	Incidental	0	AComA	10.8	5.2	2.1	CO	N/A	CO	8
6	61, M	HP	Acute onset of headaches	2	MCA	4.4	3.2	2.0	CO	N/A	CO	10
7	53, M	NS	Incidental	0	AComA	3.6	3.1	2.1	NR	N/A	CO	6
8	40, M	HP, S	Recanalized	0	MCA	3.0	2.9	2.3	NR	N/A	CO	8
9	49, M	NS	Headaches, seizure	1	MCA	5.0	4.7	2.4	NR	N/A	NR	6
10	52, M	NS	Incidental	0	BT	4.4	3.6	1.8	CO	N/A	CO	6
11	61, M	HP, DM	Incidental	0	MCA	6.5	6.0	2.3	RA	N/A	CO	9
12	35, M	NS	Chronic headaches	0	AComA	6.7	3.3	2.3	CO	N/A	CO	6
13	51, F	HP	Chronic headaches and dizziness	0	MCA	4.8	2.7	1.8	RA	N/A	CO	11
14	55, F	HP, DL	Incidental	0	MCA	3.5	1.8	2.2	NR	N/A	CO	6
15	46, F	HP	Incidental	0	MCA	1.8	1.5	2.1	RA	N/A	CO	10
16	33, M	S	Recanalized	0	AComA	3.0	2.3	2.1	NR	N/A	CO and PA stenosis	8
17	54, M	HP	Acute onset of headaches	2	MCA	3.6	2.5	2.0	CO	N/A	CO	8
18	54, F	NS	Incidental	0	MCA	3.2	2.0	2.3	CO	N/A	CO	8
19	59, M	S, DL	Incidental	0	MCA	1.7	1.5	1.9	RA	N/A	RA	6
20	60, F	HP	Dizziness, nausea, vomiting	0	MCA	7.9	5.0	1.9	NR	N/A	CO	7
21	49, F	NS	Chronic headaches	0	MCA	3.6	2.6	2.3	CO	N/A	CO	8
22	53, F	HP	Chronic headaches	0	MCA	3.7	3.2	2.2	RA	N/A	CO	6

Note:—ACA indicates anterior cerebral artery; AComA, anterior communicating artery; BT, basilar tip; CO, complete occlusion; DL, dyslipidemia; DM, diabetes mellitus; FU, follow-up; HP, hypertension; Lt, left; N/A, not available; NR, neck residual; NS, not significant; PA, parent artery; RA, residual aneurysm; S, smoking; UE, upper extremity; HHG, Hunt and Hess grade.

Patients

All patients who underwent stent-assisted coiling treatment with the LVIS device at our institution from October 2014 to April 2016 were retrospectively reviewed. We identified 30 patients with 30 saccular aneurysms arising from parent arteries that were <2.5 mm in diameter with no atherosclerotic stenosis. Eight patients without angiographic follow-up were excluded. For the remaining 22 patients, clinical data, aneurysm characteristics, indication for stent use, periprocedural complications, initial angiographic results, and follow-up angiography data were carefully reviewed. Particular attention was given to vessel patency, aneurysm occlusion, and the incidence of thromboembolic events, and they were reviewed after intervention and on follow-up imaging by 2 experienced interventional neurosurgeons (Q.-H.H. and J.-M.L.). Before treatment, informed written consent was obtained from all patients after careful evaluation of risks, benefits, and treatment alternatives, including but not limited to observation, surgical clipping, and various endovascular options. Therapeutic decision-making entailed a multidisciplinary deliberation by both surgical and nonsurgical neurointervention teams.

Endovascular Treatment

All procedures were performed with patients under general anesthesia. DSA was performed on a biplane angiographic system (Artis zee Biplane; Siemens, Erlangen, Germany). A 6F guiding catheter was introduced through a femoral sheath into the internal carotid artery for anterior circulation aneurysms or into the vertebral artery for posterior circulation aneurysms. A 0.021-in internal diameter Headway microcatheter (Microvention) was used to deliver the LVIS stent in each case. The smallest 3.5-mm LVIS stent (which is different from the LVIS Jr stent) in various lengths was used for all cases because the diameter of the parent artery was smaller than 2.5 mm. After the deployment, DynaCT (Siemens) or multiprojection fluoroscopy were performed to identify wall apposition.

Periprocedure Anticoagulation and Antiplatelet Management

Heparin was titrated during the procedure to achieve an activated clotting time of 2–2.5 times that of baseline. If stent placement was proposed for a patient with an unruptured aneurysm, dual antiplatelet drugs (aspirin, 100 mg/d plus clopidogrel, 75 mg/d) were given for at least 3 days before the procedure. However, for patients with acutely ruptured aneurysms, a loading dose of clopidogrel and aspirin (300 mg of each) was administered orally by gastrointestinal tube or per rectum 2 hours before stent placement. Regardless of whether their aneurysm was ruptured, all patients were administrated a daily dose of aspirin (100 mg) and clopidogrel (75 mg) postoperatively for 6 weeks, followed by aspirin alone, which was maintained indefinitely. During the procedure, 0.1 μg/kg/min of glycoprotein IIb/IIIa antagonist (tirofiban) was injected intravenously when acute intrastent thrombosis occurred.

Clinical and Angiographic Follow-Up

The efficacy of aneurysm coiling was assessed by using the Raymond scale. MR angiography was recommended 3 months after embolization. Postprocedural DSA follow-up was performed at 6-month intervals. Hemodynamical in-stent stenosis and branch vessel stenosis were defined as equal to or greater than 50% diameter loss. Clinical outcome was assessed with the mRS based on the latest follow-up record retrieved from an outpatient department. Evidence of stroke in the treated territory identi-

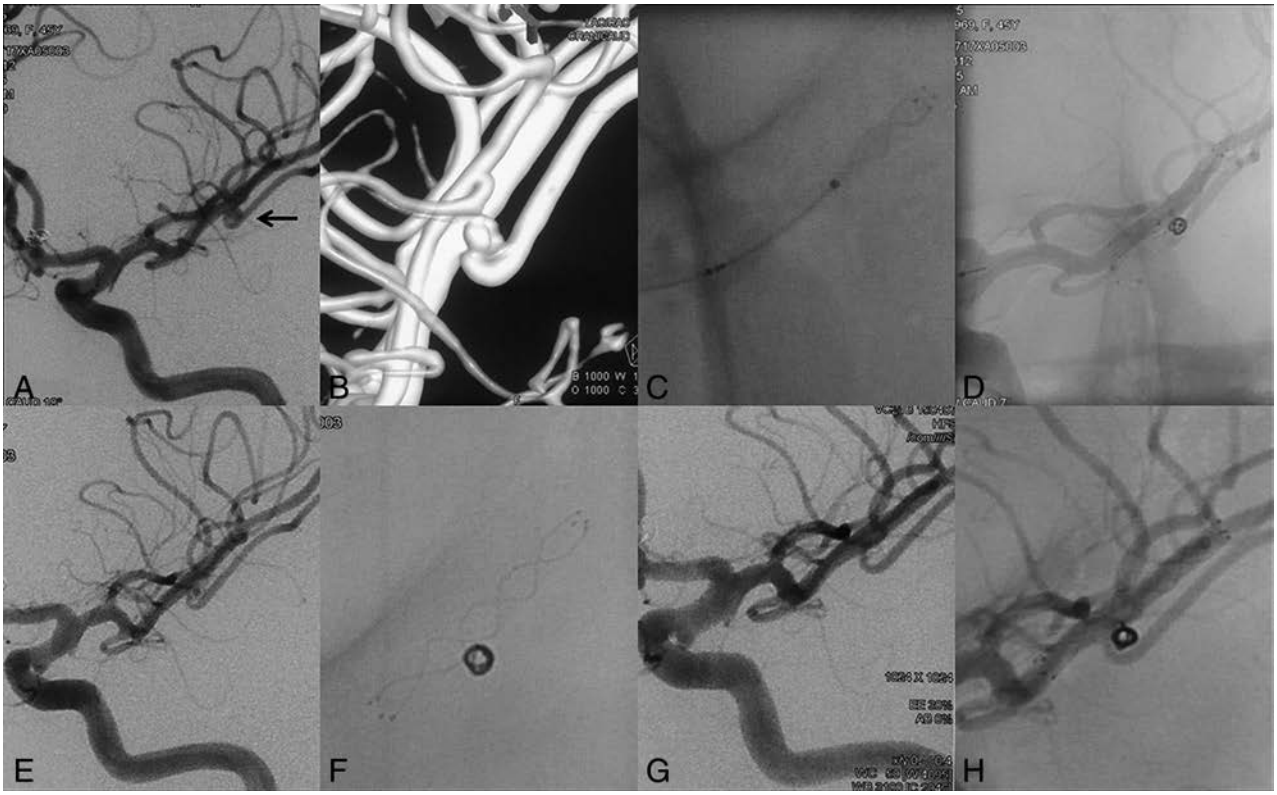

FIG 1. (Patient #15) This 46-year-old woman has a history of SAH 6 months ago, with multiple aneurysms (a ruptured anterior communicating artery aneurysm [previously coiled] and bilateral unruptured MCA aneurysms). *A*, Left ICA DSA showed a tiny saccular aneurysm at left MCA M2 bifurcation (*black arrow*). *B*, 3D DSA demonstrated the branch artery arising from the proximal aspect of the aneurysm sac. *C*, An LVIS stent was deployed in the MCA M2 trunk initially. *D*, A coil delivery microcatheter was navigated close to the stent interstices, but not through the interstice. Only 1 coil was introduced into the aneurysm sac. *E*, Initial angiogram after treatment showed the sac residual with patency of the parent vessels. *F*, The final fluoroscopy demonstrated that the stent was completely opened and totally covered the aneurysm neck. *G* and *H*, Follow-up angiography at 10 months demonstrated complete obliteration of the aneurysm with preserved patency of the parent and branch arteries.

fied via MR imaging, perfusion status, and stent patency was documented.

RESULTS

Clinical and demographic data of all patients are detailed in Table 1.

Study Population

A total of 22 patients (9 women and 13 men) with 22 intracranial aneurysms were included. Their mean age was 51.6 years (range, 33–65 years). Patient risk factors included hypertension (54.5%), smoking (18.2%), diabetes (13.6%), and dyslipidemia (9.1%). Five patients presented with SAH. According to Hunt-Hess grading, 1 case was classified as Hunt and Hess grade 1, 3 as grade 2, and 1 as grade 3.

Aneurysm Characteristics

Most of the aneurysms were located in the anterior circulation (90.9%), with 14 MCA aneurysms (63.6%), 5 anterior communicating artery aneurysms (22.7%), and 1 anterior cerebral artery aneurysm (4.5%). Two aneurysms were located at the basilar artery tip. Two aneurysms had been previously coiled, but recanalized, and were thus retreated with an LVIS stent. The parent vessel sizes varied from 1.7–2.4 mm (mean, 2.1 mm). The maximum sizes of aneurysms (or the circulating portion in recanalized aneurysms) varied from 1.7–10.8 mm (mean, 4.8 mm).

Immediate Outcome and Periprocedural Complications

The technical success rate of stent placement was 100%, and there was no failure in navigating or deploying the LVIS stent. Immediate postprocedural angiograms showed complete occlusion in 8 aneurysms (36.4%), neck residual in 8 (36.4%), and residual aneurysm in 6 (27.3%).

Procedure-related complications occurred in 1 patient (4.5%). This patient developed aneurysm perforation during the treatment of an anterior communicating artery aneurysm. A mild contrast extravasation from the aneurysm developed during coiling. Complete aneurysm occlusion was achieved within a few minutes, and the patient awoke with a mild headache. The postprocedural CT image revealed the contrast extravasation and SAH. This patient did not develop any neurologic deficits. No thromboembolic event was observed in our series, and there was no permanent morbidity or mortality. All patients were independent with a mRS score of 0–2 at discharge.

Follow-Up Results

All 22 patients underwent DSA follow-up at intervals ranging from 6–14 months (mean, 8.3 months). According to follow-up images, complete occlusion was achieved in 18 (81.8%) patients, neck remnant in 3 (13.6%), and residual sac in 1 (4.5%). None of the patients had any target aneurysm recurrence (Fig 1). One

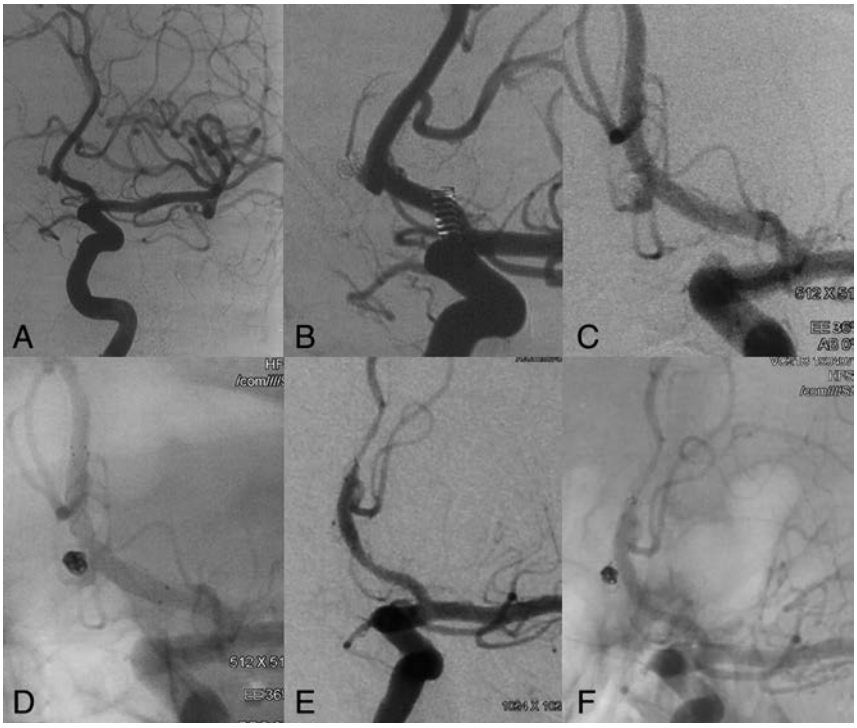

FIG 2. (Patient #16) *A*, Angiogram showed a ruptured anterior communicating artery aneurysm. *B*, The aneurysm underwent conventional coiling initially. *C* and *D*, Follow-up at 1 month revealed the residual sac filling, and an LVIS stent was then deployed in the ipsilateral anterior cerebral artery. *E* and *F*, Total aneurysm occlusion was achieved at 8-month follow-up. In-stent stenosis occurred at the distal stent marker for approximately 55%.

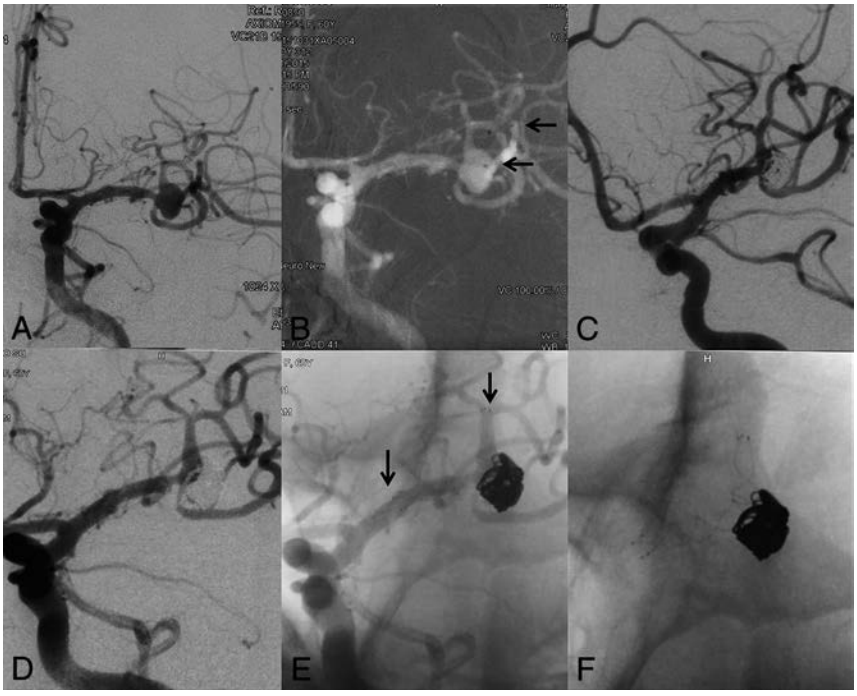

FIG 3. (Patient #21) *A*, Oblique left ICA angiogram showed an MCA M1 bifurcation aneurysm. *B*, Roadmap image revealed the coiling microcatheter and stent placement microcatheter in place (*black arrows*). *C*, Native image after stent-assisted coil embolization. *D*, Seven-month follow-up demonstrated complete occlusion of the aneurysm with the patency of the parent vessel. Insignificant stenosis was found in the inferior branch covered by stent. *E* and *F*, The fluoroscopy demonstrated that the stent was fully deployed, with the midsegment expanded across the aneurysm neck and good stent apposition to parent vessel wall.

asymptomatic in-stent stenosis occurred in 1 follow-up case (4.5%). The stenosis was located at the distal stent marker, and distal cerebral perfusion was normal (Fig 2). In addition, mild stenosis of branch arteries covered by the stents occurred in 1 case, and the patient did not present any neurologic deficit (Fig 3). Clinical follow-up at 6–23 months (mean, 16.1 months) was achieved in all patients, and no new neurologic deterioration or death was observed.

DISCUSSION

In our study, we describe our preliminary experience of using the LVIS stent to treat saccular aneurysms with parent arteries smaller than 2.5 mm. Overall, the results of this single-center cohort demonstrated high rates of complete occlusion at midterm follow-up for aneurysms treated with the LVIS device. Initial in-stent thrombus and in-stent stenosis at follow-up are uncommon. We also demonstrated that procedure-related complications are acceptable, with a rate of 4.5%. No procedure-related morbidity or mortality occurred in our case series. These findings suggest that LVIS deployment in small intracranial vessels is a safe and effective means for treating intracranial aneurysms amenable to this endovascular approach. To our knowledge, this is the first reported series of patients with LVIS device placement in small vessels.

Stent-assisted coiling of wide-neck aneurysms in small parent vessels measuring <2.5 mm in diameter is a technically challenging procedure. Several studies had detailed the use of different stents, including Neuroform (Stryker Neurovascular, Kalamazoo, Michigan), Wingspan (Stryker), LEO (Balt Extrusion, Montmorency, France), and Enterprise (Codman & Shurtleff, Raynham, Massachusetts) for the treatment of wide-neck intracranial aneurysms with small vessels.[4-9] According to the previous literature, thromboembolic events or vascular occlusions are major complications of stent-assisted coiling of these aneurysms (Table 2). Puri et al[3] published a case series on the use of small flow diverters (Pipeline Embolization Device; Covidien, Irvine, California) in 7 patients, showing good safety and effectiveness. Among them, 1 patient suffered in-stent stenosis

Table 2: Clinical and anatomic results of the stent deployment in small intracranial vessels in previous studies

Series, yr	Sample Size (no.)	Vessel Diameter (mm)	Stent	Technical Success Rate (%)	Complication (%)		Near or Complete Occlusion Rate (%)	Follow-Up (%)	
					Thromboembolic	Hemorrhagic		Recurrence Rate	In-Stent Stenosis
Turk et al, 2007[9]	8	1.5	NF	100	25	0	100	0	N/A
Siddiqui et al, 2009[8]	8	1.58	EP	100	12.5	0	100	25	12.5
Yun and Cho, 2010[7]	11	1.6	NF	100	0	0	100	0	9.1
Zhang et al, 2010[6]	12	1.8	NF, LEO, WP	100	8.3	0	91.6	NA	N/A
Chung et al, 2015[5]	31	1.6	EP	100	9.7	0	96.3	0	11.1
Kühn et al, 2016[4]	44	1.7	NF, EP	93.2	13.6	2.3	88.6	9.1	6.1
Aydin et al, 2015[11]	80	2.35	LEO Baby	97.5	7.5	1.3	96.3	6.5	15.6
Alghamdi et al, 2016[10]	43	2.2	LVIS Jr	100	10	5	95.3	5	17.5
Puri et al, 2016[3]	7	1.9	PED	100	0	0	N/A	0	28

Note:—N/A indicates not available; NF, Neuroform stent; EP, Enterprise stent; WP, Wingspan stent; PED, Pipeline Embolization Device.

at follow-up. Recently, 2 low-profile self-expandable microstents, LEO Baby and LVIS Jr, were introduced. These stents can be delivered and deployed in small distal arteries via a 0.017-in microcatheter and are dedicated for the endovascular treatment of aneurysms with small parent arteries from 2–3.5 mm. Thus, surgeons have recently been using the Leo Baby and LVIS Jr stents in small cerebral arteries. However, according to 2 case series reported by Aydin et al[11] and Alghamdi et al,[10] thromboembolic events and in-stent stenosis are also not negligible in the deployment of the LEO Baby and LVIS Jr stents in small cerebral arteries. In addition, the LEO Baby and LVIS Jr stents have not been approved for aneurysm treatment in our country. Similar to the design of LEO Baby and LVIS Jr, a higher-profile LVIS stent is a self-expandable braided stent that provides higher metal coverage rate and higher radial force. The safety and efficacy of the LVIS device deployment in small vessels is worthy of attention.

Incomplete stent expansion and poor wall apposition are common causes for the thromboembolic events.[17,18] Increased metal surface coverage might also increase the risk of thromboembolism when stents are deployed in small arteries. The LVIS stent, with braided morphology and full-length visualization design, allows greater flexibility and visibility to provide operators more control for stent deployment. The higher radial force of LVIS stents could facilitate better apposition to vessel wall. Moreover, the minimum size of the LVIS device is 3.5 mm in diameter; therefore, when an LVIS stent is deployed in a vessel smaller than 2.5 mm, it may be elongated, and the stent cells may become larger. Decreased metal surface coverage might lower the vascular stimulation and, hence, decrease the risk of thromboembolism. In our study, no periprocedural thromboembolic complications occurred. One asymptomatic in-stent stenosis occurred in 1 follow-up case (4.5%). The stenosis was located at the distal stent marker, which might result from vascular injury by the distal flares during stent manipulation and then neointimal hyperplasia at the distal stent marker segment.

Endovascular treatment of wide-neck bifurcation cerebral aneurysms is challenging, especially with small arteries involved. The special design of the LVIS device provides more bulging capability at bifurcation. Therefore, we use the so-called "barrel technique" to expand a segment of the stent into the aneurysm neck, providing greater neck coverage and changing a wide-neck aneurysm into a narrow-neck one, which consequently protects the parent vessel and the bifurcation (Fig 3).[19] In addition, the stent was pushed at the aneurysm neck to make a denser metal surface coverage and improve flow diversion effect, which may facilitate aneurysm thrombosis and enable more complete rate of occlusion during the long-term follow-up. Our results showed only 1 aneurysm that demonstrated residual sac filling and no case of recanalization on follow-up angiography examinations. However, pushing the stent microcatheter may change the tension of the coil microcatheter and then increase the related risk of perforation, so caution must be used in the manipulation of microcatheters when pushing the stent. In our study, 1 intraprocedural aneurysm rupture developed during the stent deployment in an anterior communicating artery aneurysm.

Limitations of this study include its retrospective design, limited number of cases from a single institution, the nonblinded authors' interpretation of the radiographic results, and the relatively short angiographic follow-up.

CONCLUSIONS

This study shows that the LVIS stent is a safe and effective device for endovascular treatment of intracranial aneurysms with small parent vessels. Periprocedural thromboembolic complications and in-stent stenosis are uncommon. Larger studies with long-term follow-up are needed to validate our promising results.

REFERENCES

1. Zheng Y, Song Y, Liu Y, et al. **Stent-assisted coiling of 501 wide-necked intracranial aneurysms: a single-center 8-year experience.** *World Neurosurg* 2016;94:285–95 CrossRef Medline
2. Piotin M, Blanc R, Spelle L, et al. **Stent-assisted coiling of intracranial aneurysms: clinical and angiographic results in 216 consecutive aneurysms.** *Stroke* 2010;41:110–15 CrossRef Medline
3. Puri AS, Massari F, Asai T, et al. **Safety, efficacy, and short-term follow-up of the use of Pipeline embolization device in small (<2.5 mm) cerebral vessels for aneurysm treatment: single institution experience.** *Neuroradiology* 2016;58:267–75 CrossRef Medline
4. Kühn AL, Hou SY, Puri AS, et al. **Stent-assisted coil embolization of aneurysms with small parent vessels: safety and efficacy analysis.** *J Neurointerv Surg* 2016;8:581–85 CrossRef Medline
5. Chung J, Suh SH, Hong CK, et al. **Preliminary experience with self-expanding closed-cell stent placement in small arteries less than 2 mm in diameter for the treatment of intracranial aneurysms.** *J Neurosurg* 2015;122:1503–10 CrossRef Medline
6. Zhang J, Lv X, Jiang C, et al. **Endovascular treatment of cerebral aneurysms with the use of stents in small cerebral vessels.** *Neurol Res* 2010;32:119–22 CrossRef Medline
7. Yun JH, Cho CS. **Experiences of Neuroform stent applications for rup-**

tured anterior communicating artery aneurysms with small parent vessel. *J Korean Neurosurg Soc* 2010;48:53–58 CrossRef Medline
8. Siddiqui MA, J Bhattacharya J, Lindsay KW, et al. **Horizontal stent-assisted coil embolisation of wide-necked intracranial aneurysms with the Enterprise stent–a case series with early angiographic follow-up.** *Neuroradiology* 2009;51:411–18 CrossRef Medline
9. Turk AS, Niemann DB, Ahmed A, et al. **Use of self-expanding stents in distal small cerebral vessels.** *AJNR Am J Neuroradiol* 2007;28:533–36 Medline
10. Alghamdi F, Mine B, Morais R, et al. **Stent-assisted coiling of intracranial aneurysms located on small vessels: midterm results with the LVIS Junior stent in 40 patients with 43 aneurysms.** *Neuroradiology* 2016;58:665–71 CrossRef Medline
11. Aydin K, Arat A, Sencer S, et al. **Stent-assisted coiling of wide-neck intracranial aneurysms using low-profile LEO baby stents: initial and midterm results.** *AJNR Am J Neuroradiol* 2015;36:1934–41 CrossRef Medline
12. Zhang X, Zhong J, Gao H, et al. **Endovascular treatment of intracranial aneurysms with the LVIS device: a systematic review.** *J Neurointerv Surg* 2016 May 20. [Epub ahead of print] CrossRef Medline
13. Cho YD, Sohn CH, Kang HS, et al. **Coil embolization of intracranial saccular aneurysms using the low-profile visualized intraluminal support (LVIS™) device.** *Neuroradiology* 2014;56:543–51 CrossRef Medline
14. Feng Z, Fang Y, Xu Y, et al. **The safety and efficacy of low profile visualized intraluminal support (LVIS) stents in assisting coil embolization of intracranial saccular aneurysms: a single center experience.** *J Neurointerv Surg* 2016;8:1192–96 CrossRef Medline
15. Fiorella D, Arthur A, Boulos A, et al. **Final results of the US humanitarian device exemption study of the low-profile visualized intraluminal support (LVIS) device.** *J Neurointerv Surg* 2016;8:894–97 CrossRef Medline
16. Ge H, Lv X, Yang X, et al. **LVIS stent versus Enterprise stent for the treatment of unruptured intracranial aneurysms.** *World Neurosurg* 2016;91:365–70 CrossRef Medline
17. Seo DH, Yoon SM. **Thromboembolic event detected by diffusion weighted magnetic resonance imaging after coil embolization of cerebral aneurysms.** *J Cerebrovasc Endovasc Neurosurg* 2014;16:175–83 CrossRef Medline
18. Song J, Yeon JY, Kim JS, et al. **Delayed thromboembolic events more than 30 days after self expandable intracranial stent-assisted embolization of unruptured intracranial aneurysms.** *Clin Neurol Neurosurg* 2015;135:73–78 CrossRef Medline
19. Darflinger RJ, Chao K. **Using the barrel technique with the LVIS Jr (low-profile visualized intraluminal support) stent to treat a wide neck MCA bifurcation aneurysm.** *J Vasc Interv Neurol* 2015;8:25–27 Medline

4D DSA for Dynamic Visualization of Cerebral Vasculature: A Single-Center Experience in 26 Cases

S. Lang, P. Gölitz, T. Struffert, J. Rösch, K. Rössler, M. Kowarschik, C. Strother, and A. Doerfler

ABSTRACT

BACKGROUND AND PURPOSE: 4D DSA allows acquisition of time-resolved 3D reconstructions of cerebral vessels by using C-arm conebeam CT systems. The aim of our study was to evaluate this new method by qualitative and quantitative means.

MATERIALS AND METHODS: 2D and 4D DSA datasets were acquired in patients presenting with AVMs, dural arteriovenous fistulas, and cerebral aneurysms. 4D DSA was compared with 2D DSA in a consensus reading of qualitative and quantitative parameters of AVMs (eg, location, feeder, associated aneurysms, nidus size, drainage, Martin-Spetzler Score), dural arteriovenous fistulas (eg, fistulous point, main feeder, diameter of the main feeder, drainage), and cerebral aneurysms (location, neck configuration, aneurysmal size). Identifiability of perforators and diameters of the injection vessel (ICA, vertebral artery) were analyzed in 2D and 4D DSA. Correlation coefficients and a paired *t* test were calculated for quantitative parameters. The effective patient dose of the 4D DSA protocol was evaluated with an anthropomorphic phantom.

RESULTS: In 26 patients, datasets were acquired successfully (AVM = 10, cerebral aneurysm = 10, dural arteriovenous fistula = 6). Qualitative and quantitative evaluations of 4D DSA in AVMs (nidus size: $r = 0.99$, $P = .001$), dural arteriovenous fistulas (diameter of the main feeder: $r = 0.954$, $P = .03$), and cerebral aneurysms (aneurysmal size: $r = 1$, $P = .001$) revealed nearly complete accordance with 2D DSA. Perforators were comparably visualized with 4D DSA. Measurement of the diameter of the injection vessel in 4D DSA was equivalent to that in 2D DSA ($P = .039$). The effective patient dose of 4D DSA was 1.2 mSv.

CONCLUSIONS: 4D DSA is feasible for imaging of AVMs, dural arteriovenous fistulas, and cerebral aneurysms. 4D DSA offers reliable visualization of the cerebral vasculature and may improve the understanding and treatment of AVMs and dural arteriovenous fistulas. The number of 2D DSA acquisitions required for an examination may be reduced through 4D DSA.

ABBREVIATIONS: dAVF = dural arteriovenous fistula; IQ = image quality; MS-S = Martin-Spetzler Score; VA = vertebral artery

The current criterion standard for visualization of the cerebral vasculature is DSA by acquisition of dynamic 2D series (2D DSA). Additional 3D rotational angiography is used for the diagnostic work-up of arteriovenous malformations, dural arteriovenous fistulas (dAVFs), and cerebral aneurysms.[1-3] Despite the high image quality of 2D DSA and the opportunity to visualize vessels at any angle by 3D DSA, this method is limited due to overlap of arterial and venous structures.[4,5] This may impair recognition of anatomic details, especially in complex pathologies. Despite the use of 3D DSA images for improved spatial understanding, 2D DSA series are still necessary to better understand the dynamics of blood flow. The more complex the pathology, the more 2D projections might be necessary. It would be obligatory to limit the number of 2D series to reduce the effective patient dose and contrast volumes. Therefore, a technique that combines flow information with 3D imaging would be desirable in the visualization of the cerebral vasculature.

A novel method has been described recently, which is based on the rotational acquisitions of mask and fill projection images and generates a static 3D DSA dataset and a series of time-resolved 3D vascular volumes (4D DSA), that illustrates the contrast in- and outflow with time. In 2013, Davis et al[6] demonstrated the technical feasibility of this new technique. Meanwhile, Sandoval-Garcia et al[7,8]

Received September 2, 2016; accepted after revision January 23, 2017.

From the Departments of Neuroradiology (S.L., P.G., T.S., J.R., A.D.) and Neurosurgery (K.R.), University of Erlangen-Nuremberg, Erlangen, Germany; Angiography & Interventional X-Ray Systems (M.K.), Siemens Healthcare GmbH, Forchheim, Germany; and Department of Radiology (C.S.), University of Wisconsin School of Medicine and Public Health, Madison, Wisconsin.

The Department of Neuroradiology, University of Erlangen-Nuremberg has a research agreement with Siemens Healthcare GmbH, Forchheim, Germany.

Please address correspondence to Stefan Lang, MD, Department of Neuroradiology, University of Erlangen-Nuremberg, Schwabachanlage 6, 91054 Erlangen, Germany; e-mail: Stefan.Lang3@uk-erlangen.de

http://dx.doi.org/10.3174/ajnr.A5161

have shown the clinical feasibility of 4D DSA both in a canine model and in patients, with promising results. Recently, the detailed analysis of dAVFs and AVMs with 4D DSA of Lescher et al[9] demonstrated a significantly improved visualization of a fistulous point of the dAVF or a nidus of the AVM by using 4D DSA; in many cases, 4D DSA even came close to superselective angiography.

In this article, we present our initial clinical experience with 4D DSA in the diagnostic work-up of vascular malformations by comparing 4D with 2D DSA. Furthermore, we provide information about the effective radiation dose for this new technique.

MATERIALS AND METHODS

Patients

Patients presenting with AVMs, dural fistulas, or cerebral aneurysms were included in this study. Ethics committee approval was obtained before this study, and informed consent was obtained from all patients enrolled.

4D DSA

4D DSA refers to a novel acquisition method to create time-resolved datasets of vascular volumes by using C-arm conebeam CT systems.[6,10] This is accomplished with a 3D DSA acquisition protocol that comprises 2 rotational runs: mask and fill. Proper timing of the contrast injection allows visualization of the inflow of contrast in any projection. The enlarged rotational angle in comparison with established 3D DSA programs (5s DSA program; Siemens, Erlangen, Germany) generates a sufficiently large number of projections for an adequate time duration that is sufficient to follow the contrast bolus throughout the vasculature.

We used an acquisition protocol (12s 4D DSA program, Siemens) that applies 2 runs (native and fill run) of 12 seconds each. Each run yields a total of 304 projection images over a rotational angle of 260°. The detector dose per projection image is selected as 0.36 μGy (70 kV, 1240 × 960 detector elements with 2-by-2 binning of pixels, projection on a 30 × 40 cm flat panel size, increment of 0.85°/frame, frame rate of 30 frames/s).

Postprocessing generates a conventional 3D DSA reconstruction before the reconstruction of the time-resolved series of volumes (4D DSA). The subsequent reconstruction of 4D DSA volumes is based on embedding the temporal flow information extracted from the rotational projections of the fill run to the preliminary reconstructed conventional 3D DSA dataset. Technically, this computational step is referred to a "constrained reconstruction."[10] With the 4D DSA prototype software, each projection of the rotational fill run leads to a temporal volume of the 4D DSA image series. Hence, the time-resolved series of vascular volumes covers 304 time-steps, providing a temporal solution of 12 seconds in total. On the basis of the combination of a conventional 3D DSA dataset with flow information from these 304 projection images, 4D DSA can provide "any view at any time."[6]

Data Acquisition and Postprocessing

Cerebral angiography (including 2D DSA and 4D DSA) was performed by using a biplane flat panel detector angiographic system (Artis zee biplane; Siemens). By standard angiographic methods (via the transfemoral route), a diagnostic catheter (5F) was positioned in the proximal internal carotid artery or in the vertebral artery (VA) to obtain standard posteroanterior and lateral projections (2D DSA). After we adjusted the C-arm (as known from other flat-detector acquisition protocols), we obtained the rotational scan by using the identical 4D DSA acquisition protocol provided by the manufacturer in all patients. An initial rotational scan (native "mask run") is followed by a second rotational scan (contrast-enhanced "fill run"). According to our examination protocol, manual injection of the contrast medium was started after initiation of the fill run for illustration of the contrast material inflow into the cerebral vasculature. The injection was maintained for 8 seconds. Then, the injection was stopped to display venous outflow as well. The total contrast volume was 15 mL (iopamidol, Imeron 300; Bracco, Milan, Italy). The angiographic data were transferred to a dedicated workstation (syngo X Workplace; Siemens) running prototype software for postprocessing of 4D DSA images. According to standardization and previous experience, we used reconstruction parameters identical to those used in conventional 3D DSA (kernel type: "edge enhanced"; image characteristics: "smooth"; mode of reconstruction: "subtracted"; 512 × 512 image matrix). Before image interpretation, postprocessing of 4D DSA datasets requires, depending on selected voxel size, between 3 minutes 30 seconds for aneurysms and 6 minutes 45 seconds for AVMs or dAVFs. On the basis of static and time-resolved reconstructions of 4D DSA, we determined the best projections for subsequent enlarged oblique 2D series ("target projections").

Data Evaluation

Any 2D and 4D data were anonymized and stored in random order. 2D DSA series as the criterion standard were analyzed with regular viewing software. The range of 2D DSA series considered for evaluation was confined to the injection vessel of the corresponding 4D DSA. Image evaluation of 4D DSA was performed with volume-rendered, multiplanar, and MIP reconstructions by using the syngo InSpace plug-in of the prototype software (Siemens).

Analysis of 2D and 4D DSA datasets was performed by 2 experienced neuroradiologists in a consensus reading, blinded to clinical information.

Image Quality

All 2D and 4D DSA datasets were evaluated by the 2 neuroradiologists for parameters that compromise image and diagnostic quality (eg, movement). The quality of the acquired 2D and 4D DSA datasets was assessed in a consensus reading by using a 5-fold scaled grading system: 4 = excellent (high contrast, no artifacts); 3 = good (high contrast; minimal artifacts, eg, due to movement or metallic implants); 2 = compromised (eg, noticeable movement artifacts and/or reduced homogeneity of the vessel contrast); 1 = heavily compromised (low contrast and/or strong movement artifacts); 0 = not diagnostic (vasculature is not differentiable due to heavy artifacts and/or missing contrast).

Qualitative and Quantitative Evaluation of the 2D and 4D DSA Datasets

AVM. For qualitative assessment of AVM involvement of an eloquent brain area, origin of the main feeders, venous drainage

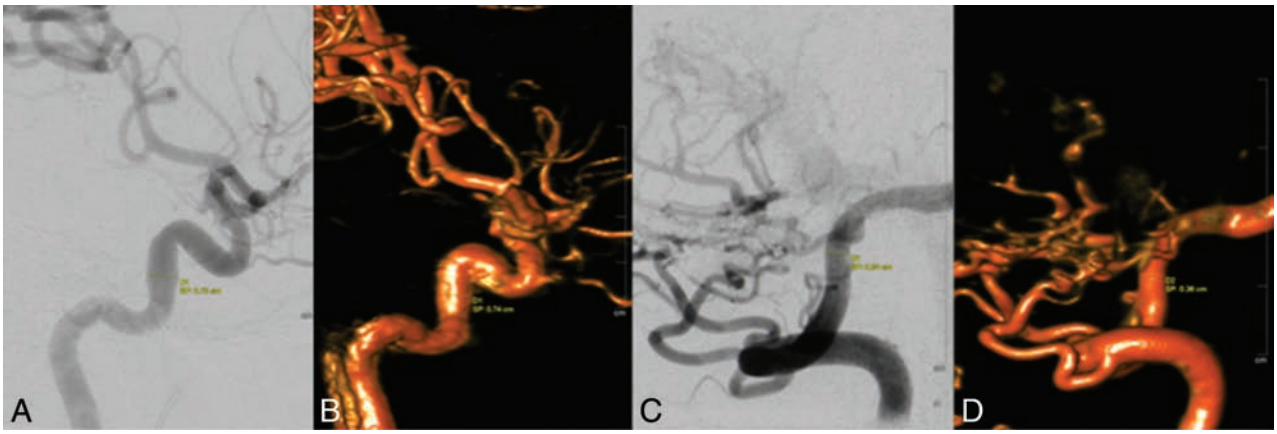

FIG 1. Images show measurements in 2D (*A* and *C*) and 4D DSA (*B* and *D*) of the vessel diameters of the ICA and VA in lateral projections of the anterior left-sided circulation and the posterior circulation, respectively. Comparable vessel diameters can be evaluated for the ICA (2D DSA = 0.72 cm, 4D DSA = 0.74 cm) and the VA (2D DSA = 0.34 cm, 4D DSA = 0.36 cm).

(superficial, deep), and pathologies of venous vessels (stenosis, pouch) were evaluated in both 2D and 4D DSA datasets with standard and working projections. As quantitative parameters, the number of feeders (with standard and working projections), the number of associated flow-related/intranidal aneurysms (with standard and working projections), and the maximum diameter of the nidus (with a strict lateral projection) were analyzed in both modalities. On the basis of the collected data, the Martin-Spetzler Scores (MS-S) for the 2D and 4D DSA datasets were calculated.

dAVF. For qualitative assessment of the origin of the main feeders of the dAVFs (eg, internal carotid artery, ophthalmic artery, posterior meningeal artery), the primary vessel of venous drainage (vein or sinus), the localization of the fistulous point (anterior/middle/posterior cranial fossa), and drainage of the fistula (transverse-sigmoid, petrous, superior sagittal, and straight sinuses) were evaluated in both 2D and 4D DSA datasets by using standard and working projections. As a quantitative parameter, the maximum diameter of the main feeder was measured in both modalities by using a strict lateral projection.

Cerebral Aneurysms. For qualitative assessment of cerebral aneurysms, location (parent vessel, eg, internal carotid artery, middle cerebral artery, basilar artery), neck configuration (small, <5 mm; medium, >5 mm/<10 mm; large, >10 mm; not definable), and aneurysmal configuration (sacciform, fusiform) were evaluated in both 2D and 4D DSA datasets by using standard and working projections. As a quantitative parameter, the maximal aneurysmal size was measured in both modalities by using a working projection.

Qualitative Evaluation of Perforators

4D DSA was compared with 2D DSA concerning visualization of the smallest vessels (perforators): exemplarily and due to standardization, the identifiability of lenticulostriate and thalamoperforating arteries (in datasets of the anterior and posterior circulation, respectively) was assessed by both readers with standard projections.

Quantitative Assessment of the Injection Vessel

To compare 4D DSA with 2D DSA in terms of accuracy, both readers measured the maximum-diameter vessel with standard tools of the prototype workstation in strict lateral projections. Measurement for datasets of the anterior circulation was performed via the ICA at the C4 segment according to the Bouthillier classification, as exemplarily demonstrated in Fig 1. Measurement for datasets of the posterior circulation was performed via the VA at the V4 segment.

Statistical Analysis

Qualitative parameters (eg, location of the pathology, origin of the main feeder, drainage, and so forth) were analyzed by using descriptive statistics only. Quantitative parameters (measurements of the nidus size, aneurysmal size, diameters of the main feeder of the dural fistula, and injection vessels) were tested for normal distribution by using the D'Agostino-Pearson test (if $P > .05$ normality was accepted). The Pearson correlation coefficient (r) was used to evaluate correlations for linear scaled variables (the number of AVM feeders, the number of intranidal aneurysms, nidus size, the main feeder of the fistula, aneurysm size); the Kendall $\tau\,\beta$ was used for ordinal scaled variables (image quality [IQ], number of flow-associated aneurysms). A paired t test was performed for statistical analysis of the diameter of the injection vessels.

Dose Measurement

We used an anthropomorphic phantom (Alderson RANDO; Radiology Support Devices, Long Beach, California), as previously described, and thermoluminescent dosimeters (Thermo Fisher Scientific, Waltham, Massachusetts) to measure the effective dose to the patient of the new 12s 4D DSA protocol.[11-13]

RESULTS

Patients

Twenty-six patients (mean age, 55.04 ± 15 years; 8 women and 18 men) with 10 AVMs, 10 cerebral aneurysms, and 6 dAVFs were enrolled in our study. Six patients (23%) had intracranial hemorrhage; 20 patients (77%) had an incidental finding. In all cases, a 4D DSA dataset was acquired in addition to conventional 2D DSA. Contrast medium was applied in 21 patients via the ICA (81%) and in 5 patients via the VA (19%).

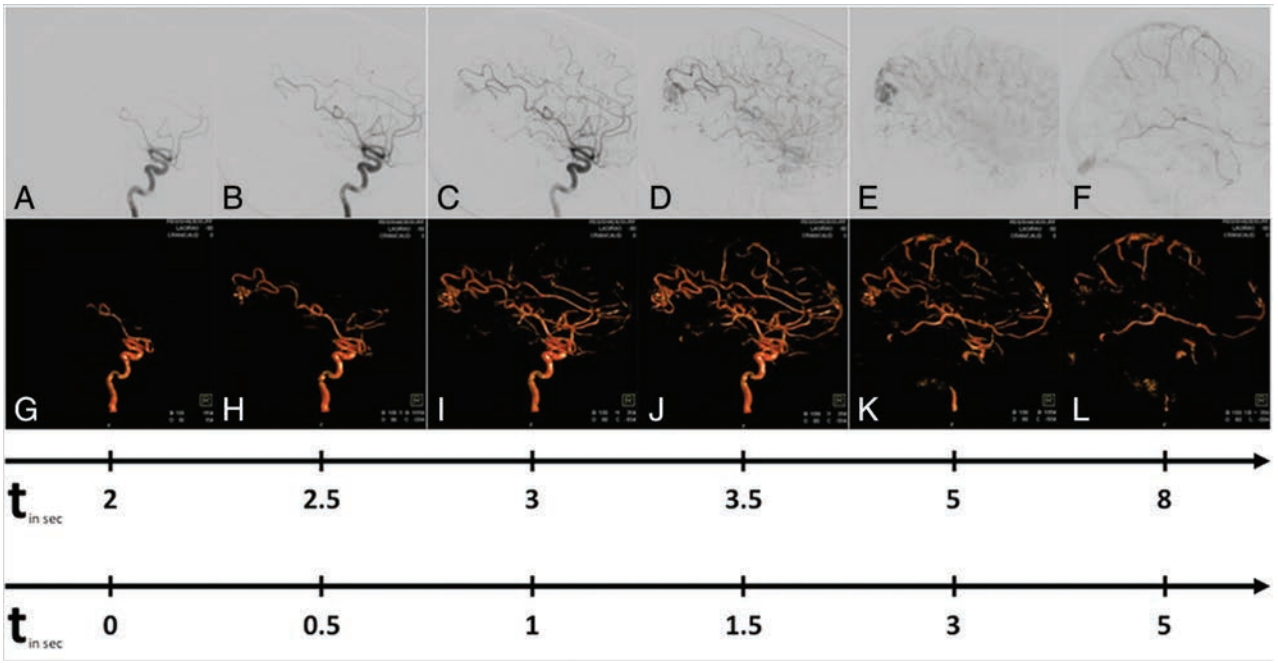

FIG 2. Illustrative case 1. MR imaging reveals an incidental AVM of the right occipital lobe in a 47-year-old man with persistent headache. This case demonstrates the potential of 4D DSA (*G–L*, *lower row*) to illustrate sequential filling of cerebral vessels concordant with 2D DSA (*A–F*, *upper row*). Early 4D volumes show both feeders originating from the posterior parietal artery and the initial enhancement of the nidus. Later volumes of 4D DSA display the compact nidus. Flow-associated/intranidal aneurysms and a direct AVF can be excluded. Late volumes illustrate exclusive venous outflow via superficial veins and the superior sagittal sinus (Martin-Spetzler Score 2). The upper timeline shows the real-time of the filling phases; the lower timeline shows the temporal differences between each image.

Image Quality

In all cases ($n = 26$), 4D DSA yielded diagnostic quality (average$_{2D} = 3.88 \pm 0.43$; average$_{4D} = 3.85 \pm 0.46$; $\tau_{IQ} = 0.78$, $P = .001$). The IQ of three 2D and three 4D datasets was limited because of motion artifacts.

Qualitative and Quantitative Evaluation of Vascular Pathologies

AVM. Ten 4D datasets were successfully acquired by injection via the ICA ($n_{left} = 8$, $n_{right} = 2$). Analysis of 4D datasets revealed identical results concerning qualitative parameters: effect on eloquent brain areas ($n_{2D} = 5$, $n_{4D} = 5$), main feeder of the AVM (MCA: $n_{2D} = 10$, $n_{4D} = 10$), venous drainage (superficial: $n_{2D} = 7$, $n_{4D} = 7$; deep: $n_{2D} = 3$, $n_{4D} = 3$), and pathologies of venous vessels (stenosis: $n_{2D} = 1$, $n_{4D} = 1$; pouch: $n_{2D} = 2$, $n_{4D} = 2$). The number of arterial feeders ($n_{2D} = 26$, $n_{4D} = 26$; $r = 1$, $P = .001$) was rated identically; the number of associated aneurysms (flow-related: $n_{2D} = 2$, $n_{4D} = 2$; $\tau = 1$, $P = .001$; intranidal: $n_{2D} = 7$, $n_{4D} = 8$; $r = 0.9$, $P = .001$) was rated nearly identically (compare with Fig 2). Measurement of the nidus size in the acquired 4D datasets (2.78 ± 1.4 cm) showed a strong correlation ($r = 0.99$, $P = .001$) to the 2D datasets (2.79 ± 1.4 cm). Martin-Spetzler Scores were identical for AVMs in 2D and 4D DSA ($n_{MS\text{-}S1} = 2$; $n_{MS\text{-}S2} = 4$; $n_{MS\text{-}S3} = 3$; $n_{MS\text{-}S4} = 1$).

dAVF. In total, six 4D datasets were successfully acquired by selective injection via the ICA ($n = 4$) and the VA ($n = 2$). Analysis of 4D datasets revealed identical results with regard to qualitative parameters (compare with Fig 3): the origin of the main feeders (ICA: $n_{2D} = 2$, $n_{4D} = 2$; ophthalmic artery: $n_{2D} = 2$, $n_{4D} = 2$; posterior meningeal artery: $n_{2D} = 2$, $n_{4D} = 2$), localization of the fistulous point (anterior cranial fossa: $n_{2D} = 2$, $n_{4D} = 2$; middle cranial fossa: $n_{2D} = 2$, $n_{4D} = 2$; posterior cranial fossa: $n_{2D} = 2$, $n_{4D} = 2$), primary vessel of venous drainage (vein: $n_{2D} = 5$, $n_{4D} = 5$; sinus: $n_{2D} = 1$, $n_{4D} = 1$), and drainage of the fistula (transverse sigmoid sinus: $n_{2D} = 2$, $n_{4D} = 2$; petrous sinus: $n_{2D} = 1$, $n_{4D} = 1$; straight sinus: $n_{2D} = 1$, $n_{4D} = 1$; superior sagittal sinus: $n_{2D} = 2$, $n_{4D} = 2$). Measurement of the main feeder of the fistula in the acquired 4D datasets (0.12 ± 0.04 cm) showed a strong correlation ($r = 0.954$, $P = .003$) to the 2D datasets (0.11 ± 0.03 cm).

Cerebral Aneurysms. In total, 10 4D datasets were successfully acquired by selective injection via the ICA ($n = 7$) and the VA ($n = 3$). Analysis of 4D datasets revealed identical results for qualitative parameters (compare with Fig 4): location (basilar artery: $n_{2D} = 3$, $n_{4D} = 3$; right ICA: $n_{2D} = 5$, $n_{4D} = 5$; left ICA: $n_{2D} = 2$, $n_{4D} = 2$), aneurysmal configuration (sacciform: $n_{2D} = 9$, $n_{4D} = 9$; fusiform: $n_{2D} = 1$, $n_{4D} = 1$), and aneurysmal neck (small: $n_{2D} = 4$, $n_{4D} = 4$; medium: $n_{2D} = 3$, $n_{4D} = 3$; large: $n_{2D} = 2$, $n_{4D} = 2$; not definable: $n_{2D} = 1$, $n_{4D} = 1$). Measurement of the aneurysm size in the acquired 4D datasets (1.33 ± 0.9 cm) showed a strong correlation ($r = 1$, $P = .001$) to the 2D datasets (1.34 ± 0.98 cm).

Qualitative Evaluation of Perforators

Analysis of 4D datasets revealed nearly identical results compared with 2D DSA with regard to visualization of perforators ($n_{\text{lenticulostriate arteries 2D}} = 19$, $n_{\text{lenticulostriate arteries 4D}} = 18$; $n_{\text{thalamoperforating arteries 2D}} = 5$, $n_{\text{thalamoperforating arteries 4D}} = 5$; examples are shown in Figs 5 and 6). In 2 cases, lenticulostriate

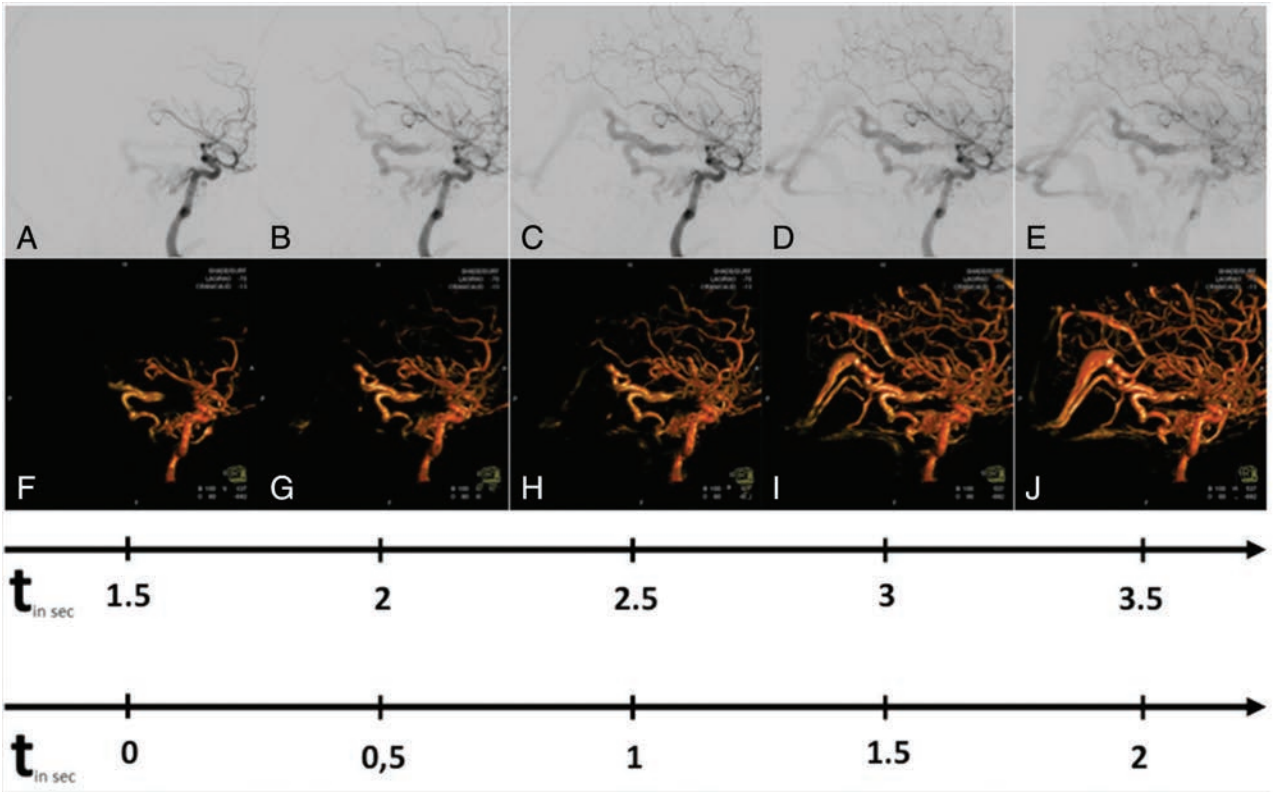

FIG 3. Illustrative case 2. This 39-year-old male patient has left-sided pulsatile tinnitus. Comparable with 2D DSA (*A–E*, *upper row*), 4D DSA (*F–J*) illustrates the early enhancement of a fistulous network on the left-sided skull base originating from the distal ICA. Later volumes show the early filling of the straight sinus via the ectatic basal vein. The upper timeline shows, in real-time, the filling phases; the lower timeline shows the temporal differences between each image.

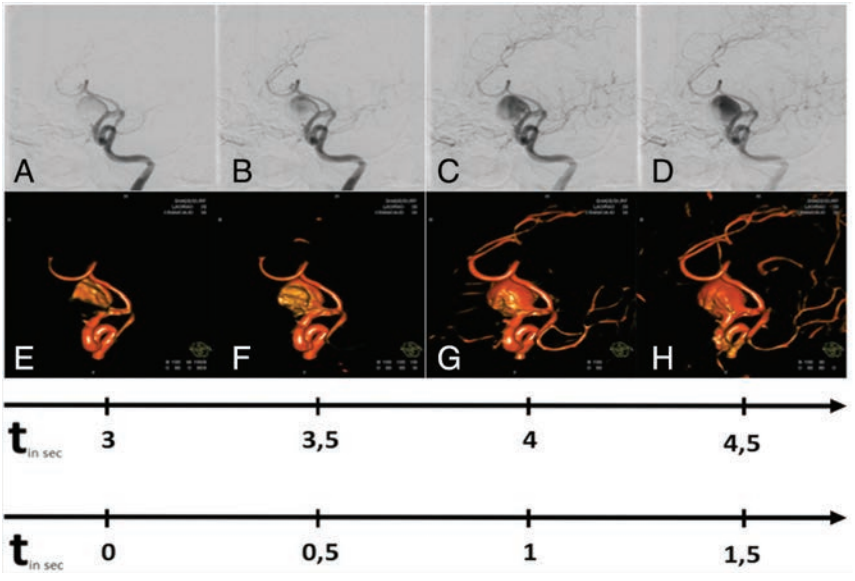

FIG 4. Illustrative case 3. This 73-year-old male patient has visual loss on the left side due to a giant sacciform aneurysm of the left carotid-T. Comparable with 2D DSA (*A–D*, *upper row*), 4D DSA (*E–H*, *lower row*) shows successive intra-aneurysmal filling with contrast medium. The best time for evaluation of the aneurysmal neck was a late arterial volume that shows a fully enhanced aneurysm. Later volumes offer only residual contrast of the aneurysmal sac due to the washout of contrast agent. The upper timeline shows, in real-time, the filling phases; the lower timeline shows the temporal differences between each image.

arteries were not detected in either 2D or 4D DSA datasets due to heavy steal effects caused by high-flow AVMs (MS-S 3; MS-S 4). In 1 dAVF case, lenticulostriate arteries were not clearly identified due to reduced IQ (IQ = 2) caused by movement artifacts during 4D DSA acquisition.

Quantitative Assessment of the Injection Vessel

In all 2D and 4D datasets ($n = 26$), measurement of the diameter of the injection vessel was successfully performed (ICA = 21, VA = 5). Acquired values did not differ significantly ($mean_{2D}$ = 0.45 ± 0.08 cm; $mean_{4D}$ = 0.46 ± 0.09 cm; $P = .039$).

Dose Measurement

The calculated effective dose for the 12s 4D DSA was 1.2 mSv. The rotation angle differed by 60° between 3D and 4D DSA (200° versus 260°) DSA, whereas tube potential and dose per frame were chosen equally.

DISCUSSION

Currently, 2D DSA (in combination with 3D DSA) is regarded as the criterion standard in the diagnostic work-up of cerebrovascular disease.[2,13] However, existing 2D and 3D techniques are limited in different ways. Although 2D DSA offers high spatial and temporal resolution, it is limited by the C-arm system

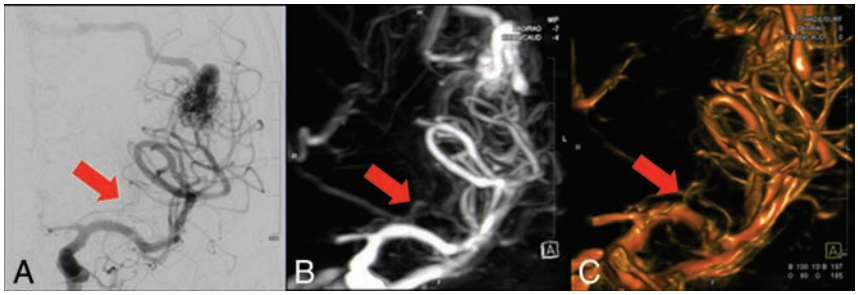

FIG 5. This 52-year-old female patient has an AVM in the left hemisphere with feeders from the MCA territory and superficial drainage. The magnified 2D DSA image (*A*) and the MIP and volume rendered images of 4D DSA (*B* and *C*) of the left-sided anterior circulation demonstrate comparable visualization of lenticulostriate arteries in 2D and 4D DSA (*red arrows*), respectively. Especially, MIP images (*B*) are a helpful tool for identification of perforators.

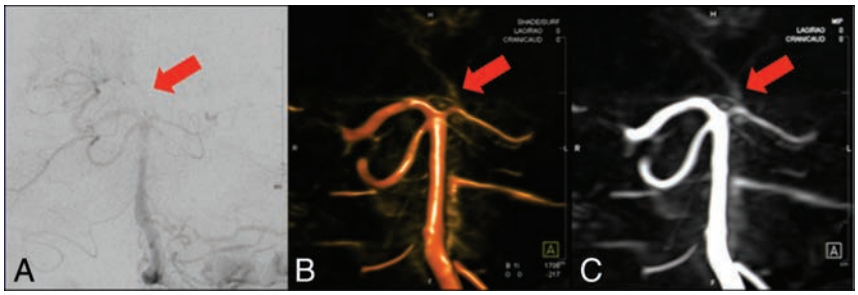

FIG 6. This 59-year-old male patient has pulsatile tinnitus caused by a dAVF (Cognard I) with feeders originating from the posterior meningeal artery and antegrade drainage via the transverse sigmoid sinus. The magnified 2D DSA image (*A*) and the MIP and volume rendered images of 4D DSA (*B* and *C*) of the basilar tip demonstrate comparable visualization of thalamoperforating arteries in both modalities (*red arrows*).

in special projections (eg, with extreme angulation). Despite 3D DSA offering no limitation concerning the choice of projections, this method is limited because of lack of temporal information and consecutive vascular overlap. This limitation is especially true in the case of AVMs and AVFs. Therefore, 4D DSA might be helpful in such tasks as evaluation of the AVM angioarchitecture and details of dAVF filling and drainage because it combines advantages of both techniques.

In our case series, 4D DSA, as a novel imaging technique, was performed successfully in all patients and was suitable for imaging of vascular malformations such as AVMs, cerebral aneurysms, and dAVFs. We describe a possible postprocessing method that offers conventional and time-resolved 3D DSA images with high resolution.

In line with recent literature, qualitative parameters obtained from 4D DSA also demonstrated excellent agreement with 2D DSA in our series regarding image quality and arteriovenous visualization of the angioarchitecture of the pathology. Sandoval-Garcia et al[8] and Lescher et al[9] observed a superior visualization of intranidal structures and the fistulous point of a dAVF, respectively, with 4D DSA because time-resolved 3D imaging enables easy differentiation of arterial and venous structures. We fully agree with the hypothesis of Sandoval-Garcia et al that 4D DSA might simplify the understanding of complex vascular malformations and provides valuable support in risk assessment and therapeutic strategies.[8] Especially after publication of A Randomized Trial of Unruptured Brain Arteriovenous Malformations (ARUBA),[14] an individual assessment of the risk factors regarding hemorrhage has become even more important for generating individual therapeutic strategies.

Previous publications have exclusively analyzed 4D DSA in regard to qualitative parameters.[6-8] To evaluate the accuracy of 4D DSA compared with the current criterion standard (2D DSA), we measured, on the one hand, the maximum diameter of the injection vessel and, on the other hand, specific architectural features of vascular pathologies (eg, nidus size in AVMs, aneurysm size, diameter of the main feeder of a dAVF). Our quantitative evaluation of 4D DSA shows excellent agreement with 2D DSA and demonstrates the reliability of this new technique. However, due to the wide range of possible windowing and missing standardization of the postprocessing, over- and undersizing of vascular structures might be a potential source of error. Moreover, due to the maximum 12-second scan time, 4D DSA could be limited in the visualization of very slow vascular malformations, (eg, low-flow dAVFs, with a bolus passage of >12 seconds). Therefore, 4D DSA might not be considered a substitution for the conventional 2D DSA series, but it has the potential to replace 3D DSA in complex vascular malformations and can help decrease the amount of 2D projections in many cases. Hence, a significant reduction of radiation dose and contrast medium, especially in patients with complex vascular pathologies,[6] is possible. Consequently, this new technique might offer obvious advantages, in particular for young patients or those with renal dysfunction, and might lead to a reduction of the procedural time, which is seen as a protective factor in periprocedural complications.[15]

In contrast to Lescher et al,[9] who observed a limited visualization of small meningeal dAVF feeders, our readers did not feel restricted in identifying even the smallest vessels (eg, lenticulostriate or thalamoperforating arteries). Especially, the use of MIP images can be helpful in differentiating the smallest vessels. Only in cases of heavy steal phenomena ($n = 2$) or movement artifacts ($n = 1$), was visualization of the smallest vessels limited in our series. In our experience, these different findings might refer to different injection protocols (8 seconds in our series versus 7 seconds in the series of Lescher et al) because the duration of arterial contrast could have a significant influence on the IQ and visualization of vessels. Because prolonged injection potentially generates, as also observed by other authors,[8,9] overlapping angiographic phases, further investigation of contrast application to establish optimized injection protocols seems obligatory.

The effective patient dose was measured as 1.2 mSv, which is slightly higher than that of a conventional 3D rotational angiography (0.9 mSv, 5s DSA) and a standard 2D angiographic series

(1 mSv).[11] Similar to 3D rotational angiography, the effective patient dose can be additionally decreased by using collimation, which has not been performed during the dose measurements with the anthropomorphic phantom.[11]

Several noninvasive approaches have tried to generate time-resolved 3D images of the cerebral vasculature. Several authors applied time-resolved MR angiography (4D MRA) with spin-labeling or contrast-enhanced sequences on typical cerebrovascular pathologies and demonstrated high agreement with DSA in hemodynamic information[16] in the assessment of AVMs[17-19] and fistulas.[20-22] 4D MRA seems to be a promising alternative for DSA. In fact, 4D MRA avoids the use of radiation and, in using arterial spin-labeling techniques, contrast agents. However, these techniques are limited in various ways. Compared with DSA, 4D MRA provides reduced spatial resolution[18,22,23] with resulting difficulty in differentiating small arterial vessels[18,21,22] or draining veins.[19,20] Furthermore, ferromagnetic artifacts (eg, retainers, dental implants)[18] and a long acquisition time[20] might contribute to reduced diagnostic quality. Still, recent literature advises performing DSA for definite evaluation of the preferred therapy strategy[17] or the posttherapeutic follow-up of AVMs.[24]

Another encouraging approach is time-resolved CT angiography (4D CTA), which has already found multifunctional applications in cerebrovascular diagnostics (eg, in the evaluation of dAVFs, AVMs, and cerebral collaterals in cases of vessel occlusion).[25] Several publications demonstrated the clinical feasibility[26] and a high agreement between 4D CTA and DSA.[27-29] Although the spatial resolution of 4D CTA is rated higher than that of 4D MRA,[30] both modalities are struggling with the same limitations. Small vessels (eg, tiny feeders of an AVM[27]) and specific angioarchitectural details of dAVFs[29] do not have the same visual quality as in DSA. Willems et al[31] analyzed the value of 4D CTA in the diagnostic work-up of dAVFs in 11 cases. Although both readers fully agreed in 11 cases on an established classification system, there was 1 low-flow fistula that was not detected on 4D CTA at all. Therefore, relying on 4D CTA alone might lead to loss of detailed information (eg, on the exact number of feeders or the exact angioarchitecture of the nidus).

Although data acquisition was successful in all 26 cases, our analysis has several limitations. First, it was limited by the small amount of any pathology. Moreover, any dataset in our series was acquired by selective injections either via the ICA or VA. Therefore, our series does not cover datasets acquired by injection from the subclavian, external, or common carotid artery. Missing standardization for contrast application and postprocessing is the most important limitation of our analysis.

CONCLUSIONS

4D DSA is a promising new method for time-resolved 3D imaging of cerebral vessels that allows visualization of the vascular anatomy comparable with that of 2D DSA with an effective dose within the range of a standard angiographic series. Therefore, 4D DSA might simplify the understanding and improve treatment planning of complex malformations. Furthermore, because the diagnostic information from a 4D DSA was equivalent to that in the 2D acquisitions, we believe that the number of 2D acquisitions required for an examination may be reduced through the use of 4D DSA.

Disclosures: Markus Kowarschik—*UNRELATED: Employment*: Siemens, *Comments*: full-time employee. Charles Strother—*UNRELATED: Grant*: National Institutes of Health.* *Money paid to the institution.

REFERENCES

1. Ogilvy CS, Stieg PE, Awad I, et al; Special Writing Group of the Stroke Council, American Stroke Association. **AHA Scientific Statement: recommendations for the management of intracranial arteriovenous malformations—a statement for healthcare professionals from a special writing group of the Stroke Council, American Stroke Association.** *Stroke* 2001;32:1458–71 CrossRef Medline
2. Oppenheim C, Meder JF, Trystram D, et al. **Radiosurgery of cerebral arteriovenous malformations: is an early angiogram needed?** *AJNR Am J Neuroradiol* 1999;20:475–81 Medline
3. Gandhi D, Chen J, Pearl M, et al. **Intracranial dural arteriovenous fistulas: classification, imaging findings, and treatment.** *AJNR Am J Neuroradiol* 2012;33:1007–13 CrossRef Medline
4. Lauriola W, Nardella M, Strizzi V, et al. **3D angiography in the evaluation of intracranial aneurysms before and after treatment: initial experience** [Article in English, Italian]. *Radiol Med* 2005;109:98–107 Medline
5. Tanoue S, Kiyosue H, Kenai H, et al. **Three-dimensional reconstructed images after rotational angiography in the evaluation of intracranial aneurysms: surgical correlation.** *Neurosurgery* 2000;47:866–71 CrossRef Medline
6. Davis B, Royalty K, Kowarschik M, et al. **4D digital subtraction angiography: implementation and demonstration of feasibility.** *AJNR Am J Neuroradiol* 2013;34:1914–21 CrossRef Medline
7. Sandoval-Garcia C, Royalty K, Aagaard-Kienitz B, et al. **A comparison of 4D DSA with 2D and 3D DSA in the analysis of normal vascular structures in a canine model.** *AJNR Am J Neuroradiol* 2015;36:1959–63 CrossRef Medline
8. Sandoval-Garcia C, Royalty K, Yang P, et al. **4D DSA a new technique for arteriovenous malformation evaluation: a feasibility study.** *J Neurointerv Surg* 2016;8:300–04 CrossRef Medline
9. Lescher S, Gehrisch S, Klein S, et al. **Time-resolved 3D rotational angiography: display of detailed neurovascular anatomy in patients with intracranial vascular malformations.** *J Neurointerv Surg* 2016 Aug 4. [Epub ahead of print] CrossRef Medline
10. Mistretta CA. **Sub-Nyquist acquisition and constrained reconstruction in time resolved angiography.** *Med Phys* 2011;38:2975–85 CrossRef Medline
11. Struffert T, Hauer M, Banckwitz R, et al. **Effective dose to patient measurements in flat-detector and multislice computed tomography: a comparison of applications in neuroradiology.** *Eur Radiol* 2014;24:1257–65 CrossRef Medline
12. **The 2007 Recommendations of the International Commission on Radiological Protection. ICRP publication 103.** *Ann ICRP* 2007;37:1–332 CrossRef Medline
13. Struffert T, Lang S, Scholz R, et al. **Radiation dose in cerebral angiography and flat detector CT applications in neuroradiology** [in German]. *Radiologe* 2015;55:654–62 CrossRef Medline
14. Mohr JP, Parides MK, Stapf C, et al; international ARUBA investigators. **Medical management with or without interventional therapy for unruptured brain arteriovenous malformations (ARUBA): a multicentre, non-blinded, randomised trial.** *Lancet* 2014;383:614–21 CrossRef Medline
15. Bendszus M, Koltzenburg M, Burger R, et al. **Silent embolism in diagnostic cerebral angiography and neurointerventional procedures: a prospective study.** *Lancet* 1999;354:1594–97 CrossRef Medline
16. Robson PM, Dai W, Shankaranarayanan A, et al. **Time-resolved vessel-selective digital subtraction MR angiography of the cerebral vasculature with arterial spin labeling.** *Radiology* 2010;257:507–15 CrossRef Medline
17. Kukuk GM, Hadizadeh DR, Boström A, et al. **Cerebral arteriovenous malformations at 3.0 T: intraindividual comparative study of 4D-MRA in combination with selective arterial spin labeling and digital**

subtraction angiography. *Invest Radiol* 2010;45:126–32 CrossRef Medline
18. Eddleman CS, Jeong HJ, Hurley MC, et al. **4D radial acquisition contrast-enhanced MR angiography and intracranial arteriovenous malformations: quickly approaching digital subtraction angiography.** *Stroke* 2009;40:2749–53 CrossRef Medline
19. Xu J, Shi D, Chen C, et al. **Noncontrast-enhanced four-dimensional MR angiography for the evaluation of cerebral arteriovenous malformation: a preliminary trial.** *J Magn Reson Imaging* 2011;34:1199–205 CrossRef Medline
20. Hori M, Aoki S, Oishi H, et al. **Utility of time-resolved three-dimensional magnetic resonance digital subtraction angiography without contrast material for assessment of intracranial dural arterio-venous fistula.** *Acta Radiol* 2011;52:808–12 CrossRef Medline
21. Iryo Y, Hirai T, Kai Y, et al. **Intracranial dural arteriovenous fistulas: evaluation with 3-T four-dimensional MR angiography using arterial spin labeling.** *Radiology* 2014;271:1939–39 CrossRef Medline
22. Nishimura S, Hirai T, Sasao A, et al. **Evaluation of dural arteriovenous fistulas with 4D contrast-enhanced MR angiography at 3T.** *AJNR Am J Neuroradiol* 2010;31:80–85 CrossRef Medline
23. Raoult H, Bannier E, Robert B, et al. **Time-resolved spin-labeled MR angiography for the depiction of cerebral arteriovenous malformations: a comparison of techniques.** *Radiology* 2014;271:524–33 CrossRef Medline
24. Soize S, Bouquigny F, Kadziolka K, et al. **Value of 4D MR angiography at 3T compared with DSA for the follow-up of treated brain arteriovenous malformation.** *AJNR Am J Neuroradiol* 2014;35:1903–09 CrossRef Medline
25. Frölich AM, Wolff SL, Psychogios MN. **Time-resolved assessment of collateral flow using 4D CT angiography in large-vessel occlusion stroke.** *Eur Radiol* 2014;24:390–96 CrossRef Medline
26. Ono Y, Abe K, Suzuki K, et al. **Usefulness of 4D-CTA in the detection of cerebral dural sinus occlusion or stenosis with collateral pathways.** *Neuroradiol J* 2013;26:428–38 CrossRef Medline
27. Wang H, Ye X, Gao X, et al. **The diagnosis of arteriovenous malformations by 4D-CTA: a clinical study.** *J Neuroradiol* 2014;41:117–23 CrossRef Medline
28. Beijer TR, van Dijk EJ, de Vries J. **4D-CT angiography differentiating arteriovenous fistula subtypes.** *Clin Neurol Neurosurg* 2013;115:1313–16 CrossRef Medline
29. Willems PW, Brouwer PA, Barfett JJ, et al. **Detection and classification of cranial dural arteriovenous fistulas using 4D-CT angiography: initial experience.** *AJNR Am J Neuroradiol* 2011;32:49–53 CrossRef Medline
30. Brouwer PA, Bosman T, van Walderveen MA, et al. **Dynamic 320-section CT angiography in cranial arteriovenous shunting lesions.** *AJNR Am J Neuroradiol* 2010;31:767–70 CrossRef Medline
31. Willems PW, Taeshineetanakul P, Schenk B, et al. **The use of 4D-CTA in the diagnostic work-up of brain arteriovenous malformations.** *Neuroradiology* 2012;54:123–31 CrossRef Medline

Minor Stroke Syndromes in Large-Vessel Occlusions: Mechanical Thrombectomy or Thrombolysis Only?

M.P. Messer, S. Schönenberger, M.A. Möhlenbruch, J. Pfaff, C. Herweh, P.A. Ringleb, and S. Nagel

ABSTRACT

SUMMARY: While mechanical thrombectomy for large-vessel occlusions is now an evidence-based treatment, its efficacy and safety in minor stroke syndromes (NIHSS ≤ 5) is not proved. We identified, in our prospective data base, 378 patients with minor strokes in the anterior circulation; 54 (14.2%) of these had proved large-vessel occlusions. Eight of 54 (14.8%) were immediately treated with mechanical thrombectomy, 6/54 (11.1%) after early neurologic deterioration, and the rest were treated with standard thrombolysis only. Rates of successful recanalization were similar between the 2 mechanical thrombectomy groups (75% versus 100%). Rates of excellent outcome (modified Rankin Scale 0–1) were higher in patients with immediate thrombectomy (75%) compared with patients with delayed thrombectomy (33.3%) and thrombolysis only (55%). No symptomatic intracranial hemorrhage occurred in either group. These descriptive data are encouraging, and further analysis of large registries or even randomized controlled trials in this patient subgroup should be performed.

ABBREVIATIONS: IV = intravenous thrombolysis only; MSS = minor stroke syndrome; MT = mechanical thrombectomy; END = early neurologic deterioration; MT-I = mechanical thrombectomy immediately; sICH = symptomatic intracranial hemorrhage

In addition to thrombolysis, mechanical thrombectomy has become the standard of care for patients presenting with ischemic strokes due to large-vessel occlusions in the anterior circulation.[1] In general, large-vessel occlusions are associated with severe stroke symptoms indicated by high National Institutes of Health Stroke Scale scores. However, large-vessel occlusions may also present as a minor stroke syndrome (MSS).

Three of the 5 seminal thrombectomy studies enrolled patients with a baseline NIHSS ≥ 6 (Endovascular Treatment for Small Core and Proximal Occlusion Ischemic Stroke [ESCAPE], Endovascular Revascularization With Solitaire Device Versus Best Medical Therapy in Anterior Circulation Stroke Within 8 Hours [REVASCAT]) or ≥8 (Solitaire With the Intention for Thrombectomy as Primary Endovascular Treatment [SWIFT-PRIME]), therefore excluding MSS.[1-4] The Multicenter Randomized Clinical Trial of Endovascular Treatment for Acute Ischemic Stroke in the Netherlands (MR CLEAN) and Extending the Time for Thrombolysis in Emergency Neurological Deficits–Intra-Arterial (EXTEND-IA) trials did not set a lower NIHSS cutoff but included only a small number of patients with MSS, resulting in a mean baseline NIHSS of 17.[1,5,6] Hence, it is unclear whether patients presenting with MSS due to large-vessel occlusions may benefit from thrombectomy. Here we present a retrospective and descriptive analysis of a case series derived from a large prospective stroke data base, with particular focus on mechanical thrombectomy performed immediately after presentation with MSS or as rescue therapy after clinical deterioration.

Case Series

We searched our prospective data base between 1998 and 2015 for patients with ischemic strokes due to large-vessel occlusions in the anterior circulation who received an acute recanalization therapy and presented with MSS. All patients were treated according to current in-house standard operating procedures in either our stroke unit or neurointensive care unit. Clinical baseline, radiologic data, and outcome data were obtained from the data base. Recanalization was assessed with the TICI scale by 2 blinded investigators on a consensus basis, and successful recanalization was defined as ≥TICI 2b. The outcome was measured with the modified Rankin Scale after 3 months and was obtained through rehabilitation reports, outpatient assessments, or a standardized interview by an unblinded investigator. Symptomatic intracranial hemorrhage (sICH) was defined according to the European Cooperative Acute Stroke Study-II (blood at any site in the brain and

Received November 2, 2016; accepted after revision January 31, 2017.

From the Departments of Neurology (M.P.M., S.S., P.A.R., S.N.) and Neuroradiology (M.A.M., J.P., C.H.), University of Heidelberg, Heidelberg, Germany.

Please address correspondence to Simon Nagel, MD, Department of Neurology, University Hospital Heidelberg, INF 400, 69120 Heidelberg, Germany; e-mail: simon.nagel@med.uni-heidelberg.de

Indicates article with supplemental on-line table.

http://dx.doi.org/10.3174/ajnr.A5164

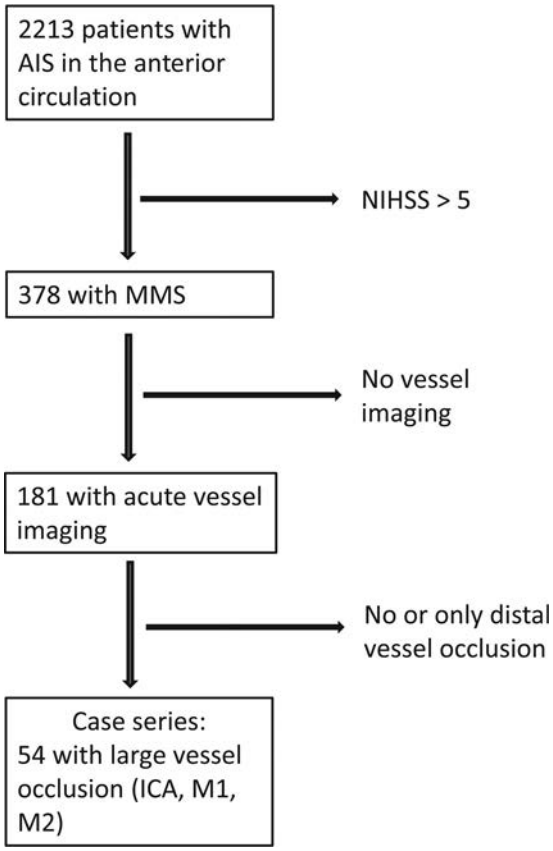

FIG 1. Flow chart of the patient inclusion criteria, indicating how patients were selected for the case series.

clinical deterioration with an increase in the NIHSS score of at least 4 points compared with the lowest value within the first 7 days or any intracranial hemorrhage leading to death).[7] Early neurologic deterioration (END) was defined as an increase of the NIHSS of ≥4 points within the first 24 hours. Patients with MSS with occlusions of the internal carotid artery and the M1 and M2 segments of the middle cerebral artery were divided into 3 groups: patients who received mechanical thrombectomy immediately (MT-I) or mechanical thrombectomy after early neurologic deterioration (MT-END) or intravenous thrombolysis only (IV). Due to the small sample size and the explorative and descriptive nature of the data, no statistical analysis was performed and data were presented either as frequencies, mean ± SD for continuous data, or median with range for ordinal data.

Of 2213 patients in our recanalization data base with ischemic strokes in the anterior circulation, we identified 378 (17.1%) with MSS (Fig 1). Of those, 250 (66%) had an excellent outcome (mRS 0–1) and sICH occurred in 9 (2.4%). One-hundred eighty-one of the patients with MSS (47.9%) underwent either CT or MR angiography. Of those, 54 (29.8%) patients had a large-vessel occlusion (ICA, M1, or M2) and 14 (7.7%) had an occlusion of the distal ICA or combined ICA/M1 occlusions and 18 (9.9%) had an M1 occlusion. Eight of 54 (14.8%) were initially treated with thrombectomy (MT-I); 6/54 (11.1%), after deterioration (MT-END); and 40/54 (74%), with thrombolysis only (IV). Of these IV patients, another 3 experienced END and no thrombectomy was performed. Clinical baseline characteristics were similar in all groups. The On-line Table shows all relevant parameters. Neither onset-to-earliest treatment nor door-to-needle time was considerably different among the groups, but mean door-to-vessel time was much shorter in MT-I compared with MT-END (207 ± 144 versus 663 ± 534 minutes) for obvious reasons. The median NIHSS was lower in MT-I at baseline and before thrombectomy (2 versus 4 and 4 versus 14). All (22/57) M2 occlusions were in the IV group. Three patients in the MT-I group did not receive thrombolysis, whereas all patients in the MT-END group were initially treated with thrombolysis. Acute carotid artery stent placement was performed in 50% of patients in each MT group. Rates of successful recanalization were very similar between the MT-I and the MT-END groups (75% versus 100%). In only 22.5% (9/40) of patients receiving IV thrombolysis was follow-up MR vessel imaging performed. Of those, only 44.4 (4/9) showed signs of recanalization on MRA. MRA, however, is not comparable with a cerebral angiography.

No changes regarding the site and extent of occlusion were seen between the initial imaging and the endovascular treatment. Rates of excellent outcome (modified Rankin Scale 0–1) were highest in patients with MT-I (75%) compared with the other groups (MT-END, 33.3%; IV, 55%). Excluding the M2 occlusions, thrombolysis accounted for an excellent functional outcome of merely 39%, similar to MT-END with 33%, but again in contrast to MT-I with 75%. No sICH occurred in any group. In total, only 2 treated patients with MSS died within 3 months.

DISCUSSION

Patients presenting with MSS usually have a high chance of excellent outcome.[8] However, patients with MSS and large-vessel occlusions have a less favorable outcome than patients presenting with MSS without these major vessel occlusions.[8,9] In our case series, we found that patients with MSS and large-vessel occlusions had, if immediately treated with MT, slightly better outcomes compared with patients with MSS who were only thrombolyzed (75% [MT-I] versus 66% for all our patients with MSS or 55% for those with MSS with large-vessel occlusions). Delaying mechanical thrombectomy until neurologic deterioration seemed to lower the beneficial effect, with a rate of excellent outcome of only 33.3%. The functional outcome of patients in the MT-I group was also very similar to that described in a previous report of patients with MSS presenting without large vessel occlusion who had been treated with IV only.[9] In contrast, a meta-analysis of the 5 seminal thrombectomy studies did not show a significant effect in patients with NIHSS ≤ 10.[1] However, few patients with NIHSS ≤ 10 were analyzed. Considering that there was a high fraction (55%, 22/40) of M2 occlusions in the IV group whereas all occlusions in the MT groups were located in the ICA or M1, the efficacy of thrombectomy may be even higher. According to our data, the rates of excellent outcomes were then the following: 75% (MT-I), 33% (MT-END), and 39% (IV). Clearly, in this series, the more recent use of (immediate) thrombectomy compared with thrombolysis alone was dependent on the increased availability and performance of thrombectomy since the introduction of modern stent retrievers (all our patients undergoing MT

were treated with these) and our clinical experience with time. Also, the overall standard of care might have improved during that time.

The median NIHSS score at baseline, and expectedly before thrombectomy, in the MT-END group was considerably higher than in the MT-I group; this might have contributed to the reduced chance of an excellent outcome. Because there was no thrombus dislodgement observed between the initial imaging and the endovascular treatment, we presume that hemodynamic disturbances over time caused END.[10] Fifty percent of all MT patients required carotid artery stenting, which is an interesting finding, also indicating that patients with MSS with combined ICA/MCA occlusions might benefit from immediate treatment. MT led to a similar recanalization rate in both groups; most important, no sICH occurred in either group, which is in line with the published data on recanalization and safety of the recent thrombectomy trials.[2-6] Another interesting finding of this analysis is that of 181 patients with MSS who received acute vessel imaging, large vessel occlusion (ICA, M1, and M2) was detected in almost 30%, indicating that this is not a rare finding.

Due to the small sample size, the retrospective and exploratory nature of our data must be interpreted with caution. Owing to these circumstances, no statistical analysis was performed and the data should be regarded as hypothesis-generating and descriptive. Our results do not support previous findings that suggested that patients with MSS due to large vessel occlusion being treated with MT have an increased rate of sICH and that only thrombolysis and not MT was associated with significantly greater chances of full recovery.[11] In our opinion, patients with large vessel occlusion and MSS do represent a subgroup of patients in whom considerable uncertainty remains with regard to the optimal acute recanalization therapy (ie, thrombolysis only or MT only after deterioration or MT immediately). Our data indicate that further analysis of larger registries or maybe even randomized trials in these patients should be performed. Our data also suggest that every patient with acute ischemic stroke should receive immediate vessel imaging because in this cohort, approximately 30% of patients with MMS in the anterior circulation did have large-vessel occlusion (ICA, M1, and M2).

Disclosures: Markus M. Möhlenbruch—*UNRELATED*: *Board Membership*: Codman; *Payment for Lectures Including Service on Speakers Bureaus*: MicroVention, Phenox, Stryker Neurovascular. Johannes Pfaff—*UNRELATED*: *Payment for Lectures Including Service on Speakers Bureaus*: Siemens Healthineers; *Travel/Accommodations/Meeting Expenses Unrelated to Activities Listed*: Stryker Neurovascular. Christian Herweh—*UNRELATED*: *Payment for Lectures Including Service on Speakers Bureaus*: Bristol-Myers Squibb; *Travel/Accommodations/Meeting Expenses Unrelated to Activities Listed*: travel and registration fees paid by Stryker Neurovascular. Peter A. Ringleb—*UNRELATED*: *Consultancy*: Advisory Board for Boehringer Ingelheim, Covidien, Daichii Sankyo; *Payment for Lectures Including Service on Speakers Bureaus*: lecture fees from Bayer, Boehringer Ingelheim, Pfizer, and Daiichi Sankyo. Simon Nagel—*UNRELATED*: *Consultancy*: Brainomix; *Grants/Grants Pending*: Brainomix*; *Payment for Lectures Including Service on Speakers Bureaus*: Bayer Healthcare, Pfizer, Medtronic; *Travel/Accommodations/Meeting Expenses Unrelated to Activities Listed*: Brainomix, Böhringer Ingelheim, Bayer Healthcare, Medtronic. *Money paid to the institution.

REFERENCES

1. Goyal M, Menon BK, van Zwam WH, et al; HERMES collaborators. **Endovascular thrombectomy after large-vessel ischaemic stroke: a meta-analysis of individual patient data from five randomised trials.** *Lancet* 2016;387:1723–31 CrossRef Medline
2. Goyal M, Demchuk AM, Menon BK, et al; ESCAPE Trial Investigators. **Randomized assessment of rapid endovascular treatment of ischemic stroke.** *N Engl J Med* 2015;372:1019–30 CrossRef Medline
3. Jovin TG, Chamorro A, Cobo E, et al; REVASCAT Trial Investigators. **Thrombectomy within 8 hours after symptom onset in ischemic stroke.** *N Engl J Med* 2015;372:2296–306 CrossRef Medline
4. Saver JL, Goyal M, Bonafe A, et al; SWIFT PRIME Investigators. **Stent-retriever thrombectomy after intravenous t-PA vs. t-PA alone in stroke.** *N Engl J Med* 2015;372:2285–95 CrossRef Medline
5. Berkhemer OA, Fransen PS, Beumer D, et al. **A randomized trial of intraarterial treatment for acute ischemic stroke.** *N Engl J Med* 2015; 372:11–20 CrossRef Medline
6. Campbell BCV, Mitchell PJ, Kleinig TJ, et al; EXTEND-IA Investigators. **Endovascular therapy for ischemic stroke with perfusion-imaging selection.** *N Engl J Med* 2015;372:1009–18 CrossRef Medline
7. Hacke W, Kaste M, Fieschi C, et al; Second European-Australasian Acute Stroke Study Investigators. **Randomised double-blind placebo-controlled trial of thrombolytic therapy with intravenous alteplase in acute ischaemic stroke (ECASS II).** *Lancet* 1998;352:1245–51 CrossRef Medline
8. Nedeltchev K, Schwegler B, Haefeli T, et al. **Outcome of stroke with mild or rapidly improving symptoms.** *Stroke* 2007;38: 2531–35 CrossRef Medline
9. Zhu W, Churilov L, Campbell BCV, et al. **Does large vessel occlusion affect clinical outcome in stroke with mild neurologic deficits after intravenous thrombolysis?** *J Stroke Cerebrovasc Dis* 2014;23:2888–93 CrossRef Medline
10. Tisserand M, Seners P, Turc G, et al. **Mechanisms of unexplained neurological deterioration after intravenous thrombolysis.** *Stroke* 2014;45:3527–34 CrossRef Medline
11. Urra X, San Román L, Gil F, et al; Catalan Stroke Code and Reperfusion Consortium (Cat-SCR). **Medical and endovascular treatment of patients with large-vessel occlusion presenting with mild symptoms: an observational multicenter study.** *Cerebrovasc Dis* 2014;38:418–24 CrossRef Medline

Understanding Angiography-Based Aneurysm Flow Fields through Comparison with Computational Fluid Dynamics

J.R. Cebral, F. Mut, B.J. Chung, L. Spelle, J. Moret, F. van Nijnatten, and D. Ruijters

ABSTRACT

BACKGROUND AND PURPOSE: Hemodynamics is thought to be an important factor for aneurysm progression and rupture. Our aim was to evaluate whether flow fields reconstructed from dynamic angiography data can be used to realistically represent the main flow structures in intracranial aneurysms.

MATERIALS AND METHODS: DSA-based flow reconstructions, obtained during interventional treatment, were compared qualitatively with flow fields obtained from patient-specific computational fluid dynamics models and quantitatively with projections of the computational fluid dynamics fields (by computing a directional similarity of the vector fields) in 15 cerebral aneurysms.

RESULTS: The average similarity between the DSA and the projected computational fluid dynamics flow fields was 78% in the parent artery, while it was only 30% in the aneurysm region. Qualitatively, both the DSA and projected computational fluid dynamics flow fields captured the location of the inflow jet, the main vortex structure, the intrasaccular flow split, and the main rotation direction in approximately 60% of the cases.

CONCLUSIONS: Several factors affect the reconstruction of 2D flow fields from dynamic angiography sequences. The most important factors are the 3-dimensionality of the intrasaccular flow patterns and inflow jets, the alignment of the main vortex structure with the line of sight, the overlapping of surrounding vessels, and possibly frame rate undersampling. Flow visualization with DSA from >1 projection is required for understanding of the 3D intrasaccular flow patterns. Although these DSA-based flow quantification techniques do not capture swirling or secondary flows in the parent artery, they still provide a good representation of the mean axial flow and the corresponding flow rate.

ABBREVIATIONS: CFD = computational fluid dynamics; MAFA = mean aneurysm flow amplitude (determined from DSA); MEAN = projection average; VEL = mean aneurysm velocity (determined from CFD)

Visualization of in vivo aneurysmal flow structures and quantification of aneurysm hemodynamic characteristics is important in understanding the role of hemodynamics in the mechanisms responsible for wall degeneration and progression toward rupture or stabilization[1] as well as for evaluating endovascular procedures such as flow diversion.[2,3]

Previous studies have used computational fluid dynamics (CFD) to characterize the hemodynamic environment of the aneurysm to study aneurysm evolution[4,5] and rupture.[6-8] Other studies have used CFD to evaluate flow-diverting devices and procedures.[9,10] On the other hand, imaging researchers have investigated using phase-contrast MR imaging to depict the in vivo flow fields within cerebral aneurysms,[11] while others have developed flow-quantification methods from dynamic angiography.[12,13] Visualization and quantification of flow fields directly from angiography data are attractive because they can be performed directly in the angiography suite while imaging the aneurysm for diagnosis or treatment. Previous studies along this line have shown the potential clinical value of these techniques and have compared the results with those of Doppler sonography and synthetic angiography generated from CFD simulations.[14]

The purpose of our study was to analyze the flow fields reconstructed from dynamic angiography data by comparing them with patient-specific CFD models; in particular, we investigated

Received October 18, 2016; accepted after revision January 25, 2017.

From the Bioengineering Department (J.R.C., F.M., B.J.C.), Volgenau School of Engineering, George Mason University, Fairfax, Virginia; Faculté de Médecine Paris-Sud (L.S.), Le Kremlin-Bicetre, France; Interventional Neuroradiology (J.M.), Beaujon University Hospital, Clichy, France; and Image Guided Therapy Innovation (F.v.N., D.R.), Philips Healthcare, Best, the Netherlands.

This work was supported by Philips Healthcare.

Please address correspondence to Juan R. Cebral, PhD, Bioengineering Department, Volgenau School of Engineering, George Mason University, 4400 University Dr, MSN 2A1, Fairfax, VA 22030; e-mail: jcebral@gmu.edu

Indicates article with supplemental on-line table.

Indicates article with supplemental on-line photo.

http://dx.doi.org/10.3174/ajnr.A5158

whether these fields can be used to realistically represent the main intra-aneurysmal flow structures and identify limitations and factors that affect the flow field reconstruction.

MATERIALS AND METHODS

Angiography-Based Flow Quantification

Fifteen cerebral aneurysms with diameters of >5 mm, imaged with 3D rotational angiography and 2D digital subtraction angiography at 60 frames per second and a typical in-plane resolution of 0.29 mm, were studied. Because the dose per frame is relatively low, the dose-area product level is comparable with a standard 3-frames per second DSA acquisition (dose-area product = 716 mGy · cm^2/s for the 60-frames per second protocol versus 786 mGy · cm^2/s for the 3-frames per second protocol). We acquired the 2D DSA sequences from 2 different viewpoints, trying to minimize the overlap between the aneurysm and the surrounding vessels. These sequences spanned approximately 7–12 cardiac cycles. In 2 patients, DSA sequences were acquired from a single projection, making a total of 28 sequences for all 15 patients.

2D flow fields in the aneurysms and surrounding vessels were reconstructed from the DSA sequences by using a previously developed technique based on an optical flow approach.[12] Visualizations of these DSA flow fields were created by using virtual particle tracing (ie, a visualization technique based on integration of the equation of motion of massless particles to visualize velocity vector fields). Measurements of the instantaneous flow rate in the parent artery were obtained by integration of the velocity profile in ROIs placed on the proximal parent artery. The mean aneurysm flow amplitude (MAFA) was calculated by averaging the velocity magnitude over an ROI delineating the aneurysm contour.[13]

Computational Fluid Dynamics Modeling

Computational fluid dynamics models with patient-specific geometries were constructed from the 3D rotational angiography images by using previously described methods.[15] We performed pulsatile flow simulations by numerically solving the 3D incompressible Navier-Stokes equations, assuming rigid walls and Newtonian fluid.[16] These assumptions seem reasonable because aneurysm walls in general do not undergo large displacements, and shear thinning effects do not have enough time to develop in aneurysm flows.[16] The maximum element size was set to 0.02 cm, and a minimum of 10 points across any vessel cross-section was specified. The resulting number of elements ranged from 3 to 4 million tetrahedra. The time-dependent flow rate measurements obtained in the parent artery from the DSA sequences were used to prescribe patient-specific inflow boundary conditions. The simulations were performed for all cardiac cycles covered by the dynamic DSA sequences, by using 120 time-steps per cycle. To avoid possible imprecisions due to the initialization of the flow calculations, we discarded data from the first cardiac cycle. The resulting CFD fields were saved at 60 frames per cycle, coinciding with the time instants of the DSA sequences. The mean aneurysm velocity (VEL) was calculated as the average of the 3D velocity magnitude over the aneurysm region and over the cardiac cycles and compared with the MAFA.

Similarity of DSA and MEAN CFD projected flow fields in the region of the vessel, aneurysm, and both regions combined

Patient	View	Vessel	Aneurysm	Combined
1	1	80.3%	66.0%	76.2%
2	1	93.9%	52.7%	76.7%
3	1	80.5%	46.4%	76.3%
	2	91.3%	39.4%	86.0%
4	1	59.6%	55.9%	57.9%
	2	73.4%	50.2%	67.9%
5	1	91.4%	−23.0%	48.0%
	2	81.9%	−64.6%	20.3%
6	1	71.4%	66.8%	70.7%
	2	71.3%	41.8%	66.8%
7	1	57.6%	−1.0%	46.8%
	2	74.3%	9.8%	64.7%
8	1	78.9%	12.5%	71.2%
	2	77.3%	−2.0%	66.9%
9	1	80.0%	32.8%	69.5%
	2	85.2%	65.0%	79.6%
10	1	66.8%	67.9%	67.3%
	2	83.0%	84.9%	83.7%
11	1	88.5%	25.7%	73.3%
	2	81.5%	11.5%	68.7%
12	1	71.4%	46.1%	66.4%
	2	82.9%	44.2%	76.8%
13	1	77.5%	63.1%	72.6%
	2	93.6%	9.8%	72.5%
14	1	74.2%	15.3%	62.8%
	2	58.3%	25.5%	52.1%
15	1	73.2%	−0.6%	43.2%
	2	80.5%	26.8%	56.2%
Mean		78.4% ± 10.1%	30.4% ± 32.0%	66.0% ± 13.7%

For comparison, the CFD flow fields were projected to the same views used for the DSA acquisitions. This projection results in a 2D vector field on the imaging plane normal to the line of sight. Because the 3D rotational angiography images used to reconstruct the CFD models and the 2D DSA sequences were acquired relative to the same reference frame, this projection was straightforward (ie, it did not require any image coregistration). During the projection, the CFD velocity components along the line of sight were discarded. The remaining in-plane components were averaged along the line of sight. All CFD mesh points mapped to the same DSA pixels were averaged (for a MEAN or average projection), or the vector with the maximum magnitude was taken (for an MIP projection). The projected 2D CFD flow fields were visualized in a manner similar to the DSA fields by using virtual particle tracing.

Data Analysis

The 2D DSA and CFD flow fields were quantitatively compared by using a directional similarity measure s defined as

$$s = \frac{1}{N}\sum_{i \in ROI} \frac{v_i \cdot u_i}{|v_i||u_i|} = 100,$$

where v_i is the DSA velocity vector; u_i, the projected CFD velocity vector; *ROI*, the region of interest (aneurysm or parent vessel); N, the number of pixels in the *ROI*; and the dot operator denotes the dot product. This quantity measures the similarity of the directions of the 2 vector fields over the ROI. A similarity of 100% means a perfect match, random input would yield a 0%, and op-

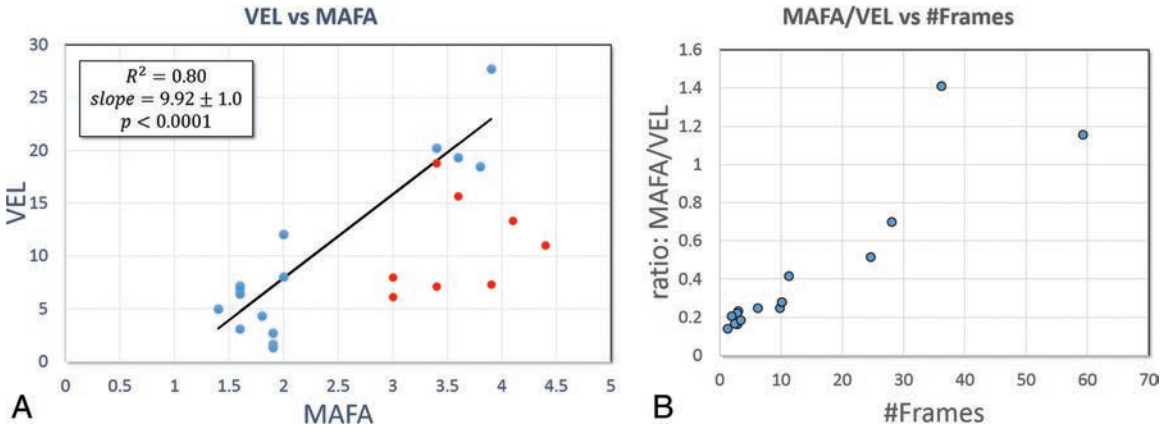

FIG 1. *A*, Linear correlation between the MAFA and VEL. *Red dots* represent cases discarded from the regression analysis due to substantial overlap between the aneurysm and surrounding vessels in the selected DSA view. *B*, Ratio of MAFA/VEL as a function of the number of frames needed for a particle to traverse the aneurysm diameter (mean aneurysm transit time).

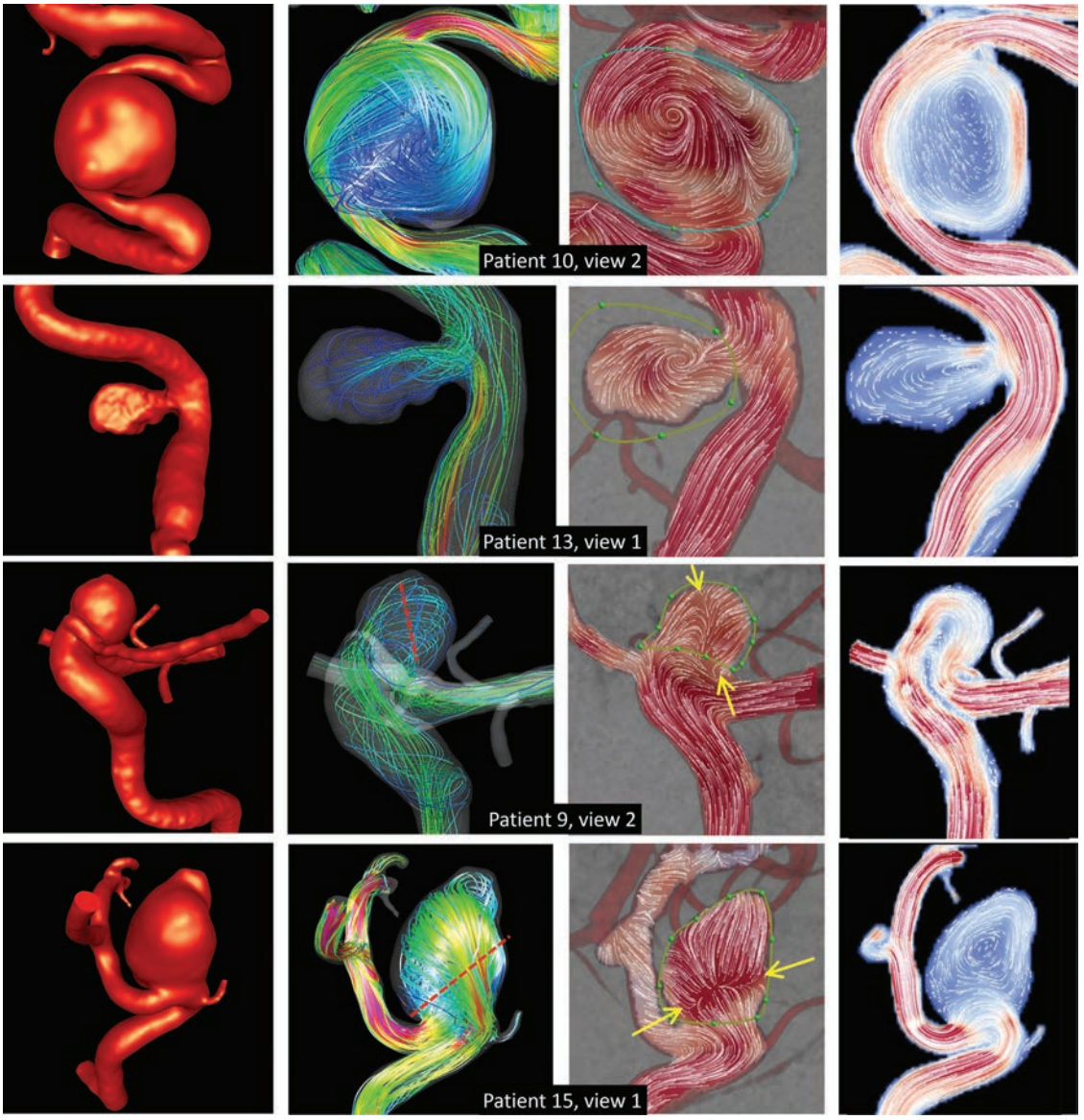

FIG 2. Examples of 4 aneurysms (rows) with vortex structures with varying alignment with the line of sight of DSA sequences. From left to right, columns show the following: reconstructed CFD model, visualization of 3D flow field by using streamlines, 2D DSA flow field, and 2D projected MEAN CFD flow field. *Dotted red lines* indicate the location of the vortex in the 3D flow. *Yellow arrows* indicate flow artifacts (divergence of particle paths) in the DSA flow reconstruction aligned with the vortex centers.

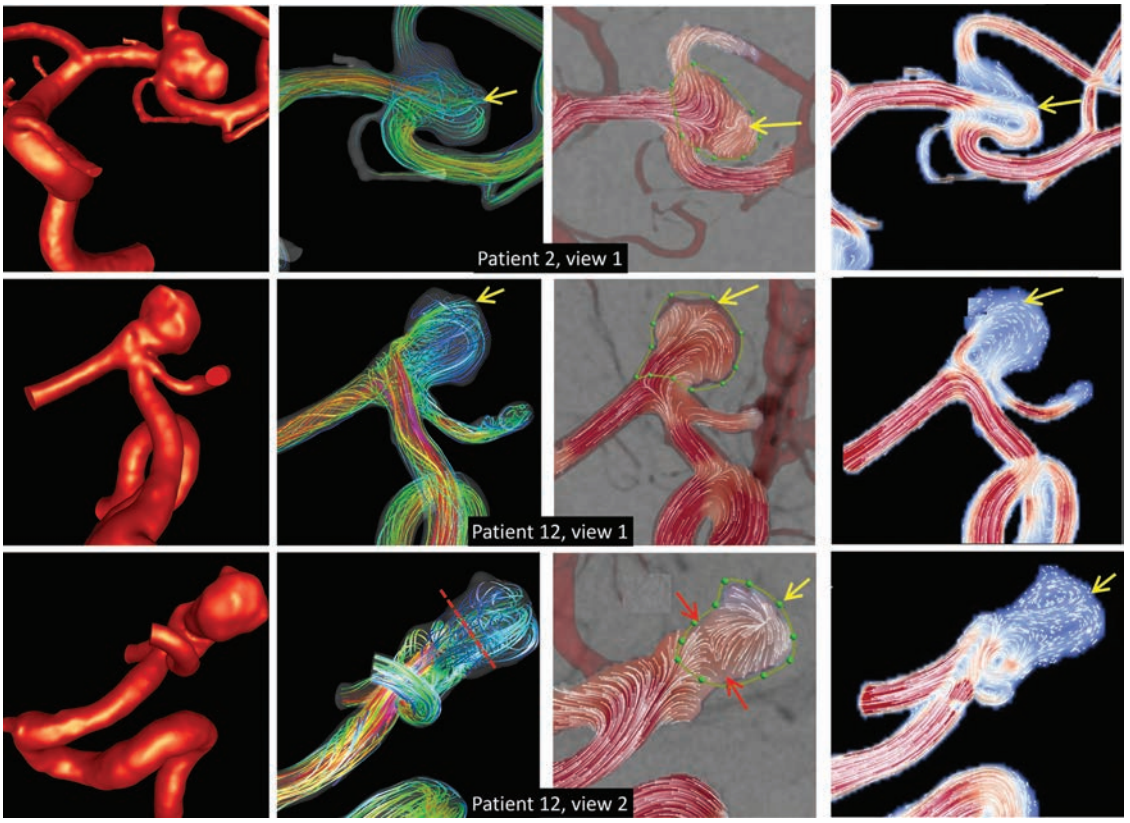

FIG 3. Top row: an example of when the DSA flow visualization does not depict the intrasaccular flow split. Center and bottom rows: an example of when the DSA flow visualizations from 2 roughly normal projections depict the intrasaccular flow split and allow understanding of the 3D flow structure. From left to right, columns show the reconstructed CFD model, visualization of 3D flow field by using streamlines, 2D DSA flow field, and the 2D projected MEAN CFD flow field. *Yellow arrows* point to the region of flow split. *Red dotted line* indicates center of rotation, and *red arrows*, the "convergent vectors" effect.

posing fields would give a −100%. Similarities of the 2D DSA and CFD fields were calculated for the aneurysm and parent artery regions separately and for both regions combined.

The DSA flow fields and the 2D projected CFD fields were qualitatively compared with visualizations of the 3D flow fields obtained from the CFD models by using streamlines. These comparisons were performed to evaluate whether the DSA or the projected CFD fields were able to depict the location of the inflow jet, the main vortex structure within the aneurysm, the flow split within the aneurysm (if any), the direction of flow rotation within the aneurysm, and the swirling or secondary flows in the parent artery.

RESULTS

The directional similarity measures between the DSA and the projected CFD flow fields are presented in the Table for the aneurysm and vessel regions and for both regions combined. In the parent artery, the DSA and projected CFD flow fields are in good agreement with an average similarity of 78%. In contrast, the average agreement within the aneurysm region alone is quite poor with a mean similarity of only 30%.

To understand this discrepancy in the agreement of the DSA and CFD fields between the aneurysm and parent artery regions, we visually compared the 2D fields with visualizations of the 3D field. The results are presented in the On-line Table. This table indicates whether the DSA or projected CFD fields capture different flow characteristics observed in the streamline visualizations of the 3D fields. As explained previously, the in-plane components of the projected CFD velocity were averaged along the line of sight. We denoted this field as MEAN. A second field was computed by keeping the in-plane vector with the largest magnitude, similar to a maximum intensity projection used for visualization of 3D images. We denoted this second field as MIP. The MIP field was introduced to highlight the effects of vessel overlaps and to better understand the effects of projection of 3D vector fields onto a 2D plane. The On-line Table includes results for both the MEAN and MIP fields. The results indicate that the DSA and MEAN CFD flow fields often fail to capture many of the flow features of interest (ie, they only provide reasonable representations in <60% of the cases). Furthermore, in many cases, certain features are captured by the DSA field but not by the MEAN CFD field or vice versa. Qualitatively, the MIP CFD fields give a better depiction of the intrasaccular flow structure and provide a direct visualization of vessel overlaps but cannot be used directly to quantify the similarity with the DSA fields because the MIP projection loses any depth information and vessel overlaps tend to distort the aneurysm fields as discussed below.

Linear regression analysis (Fig 1*A*) indicates that the mean aneurysm flow amplitude determined from 2D DSA is linearly correlated to the mean aneurysm velocity estimated from the CFD models after discarding views with noticeable overlaps of the an-

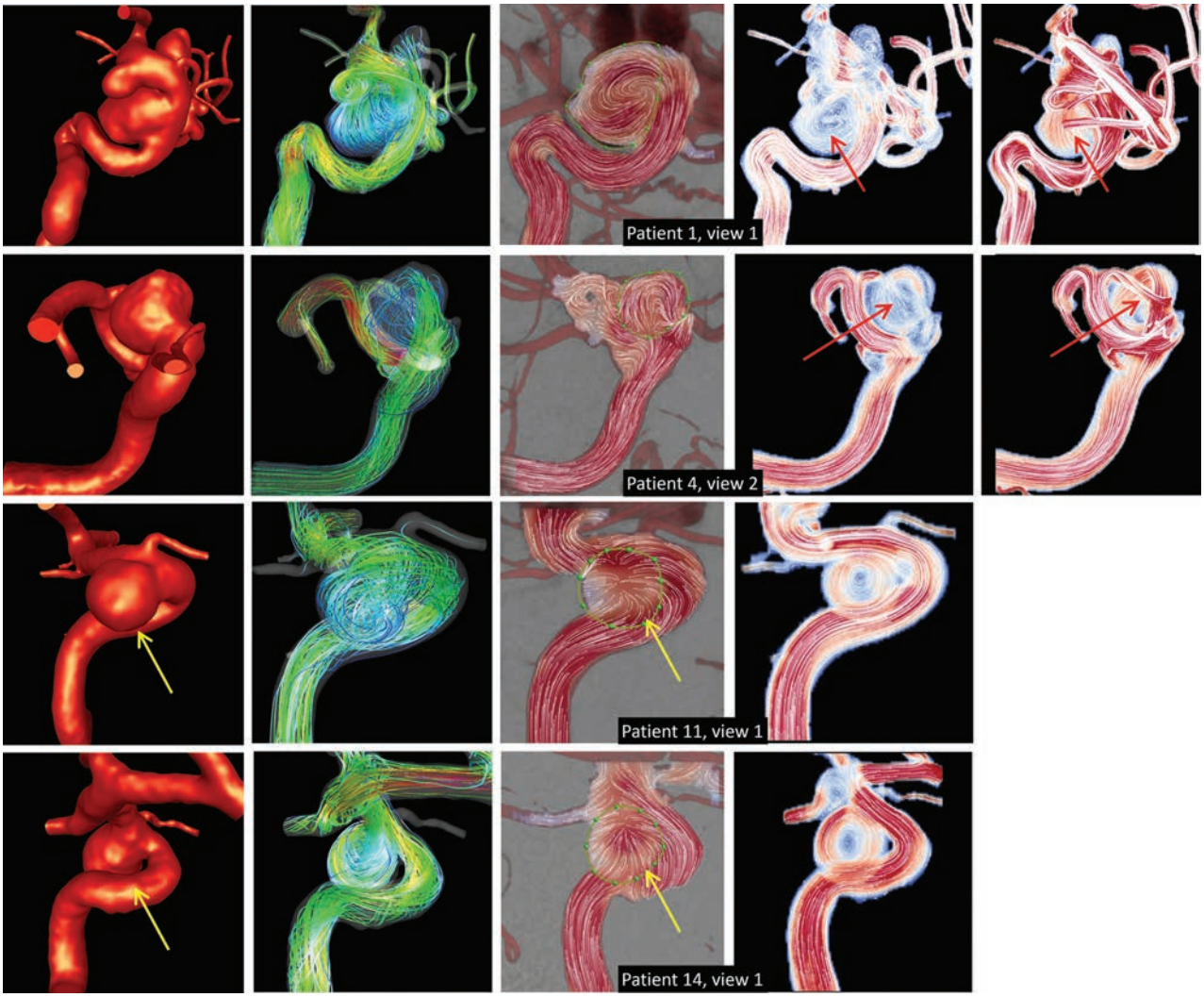

FIG 4. Examples of the effects of vessel overlaps on 4 aneurysms (rows). From left to right, columns show the following: the reconstructed CFD model, visualization of the 3D flow field by using streamlines, 2D DSA flow field, 2D projected MEAN CFD flow field, and 2D projected MIP CFD flow field. *Red arrows* show false vortex structures in projected CFD fields, while *yellow arrows* indicate false aneurysm inflow regions.

eurysm and surrounding vessels (slope = 7.92 ± 1.00, $R^2 = 0.80$, $P < .001$). Vessel overlap was determined by inspection of the DSA and the projected CFD model and flow fields. Eight of the 25 DSA views were discarded (32%). This correlation is in agreement with earlier work comparing the MAFA ratios generated by DSA and CFD simulations.[17] This suggests that the MAFA is a good surrogate measure for VEL but needs to be interpreted carefully because it provides an underestimation of the aneurysm mean velocity because it discards velocity components along the line of sight.

DISCUSSION

Several factors can affect the flow field quantification from DSA data and the projection of 3D CFD flow fields. CFD is not a criterion standard for representing intra-aneurysmal flow fields; however, the comparison of DSA and CFD fields allows us to understand and interpret the flow structures observed in vivo with the DSA-based technique and to identify artifacts and limitations.

First, the alignment of the main intrasaccular vortex structure relative to the line of sight of the DSA projections can have an important effect on the reconstructed flow fields and the CFD projections. Four examples are presented in Fig 2 to illustrate this effect. In the first 2 examples (top two rows), the vortex core is roughly aligned with the line of sight and both the DSA and projected CFD field can depict the main vortex structure. In contrast, in the third and fourth examples (bottom 2 rows), the vortex core is roughly perpendicular to the line of sight. In these cases, the DSA flow field shows interesting artifacts along a line roughly aligned with the vortex core. Along this line, the flow fields seem to converge. To explain this effect, see the example on the bottom row. Below the vortex line, the traces point upward toward the line and are aligned with the inflow velocity near the anterior wall of the aneurysm. However, above this line, the traces point downward toward the line and are aligned with the velocity of the recirculating blood near the posterior wall of the aneurysm. Thus, this feature gives the impression of converging flow toward the vortex core line. The projected CFD fields provide a misleading representation of the flow field because in these cases, they give the impression that there is a vortex roughly aligned with the line

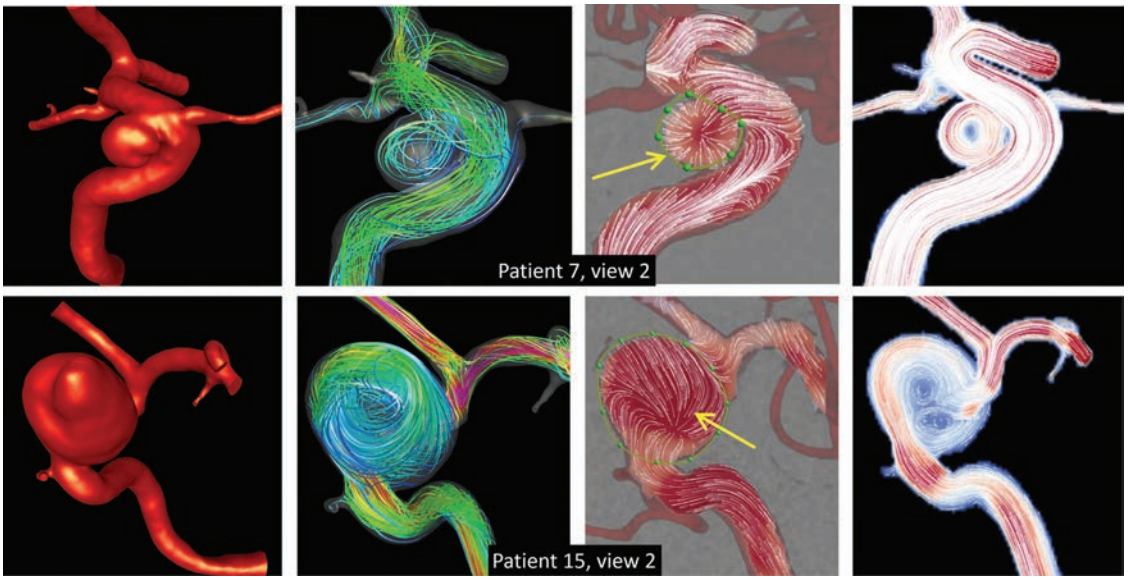

FIG 5. Examples of undersampling DSA flow fields in 2 aneurysms (rows). From left to right, columns show the following: the reconstructed CFD model, visualization of the 3D flow field by using streamlines, 2D DSA flow field, and 2D projected MEAN CFD flow field. *Arrows* point to the regions where fluid particles are observed to move across streamlines.

of sight when in reality, it is perpendicular to it. See the On-line Figure for further details.

Second, in cases in which the flow splits within the aneurysm cavity, the correct representation of the flow split by the DSA and projected CFD flow fields depends on the location of the inflow stream in 3D as well as the 3D structure of the recirculation regions. Two examples are presented in Fig 3. In the first example (top row), the inflow stream is located near the posterior wall of the vessel and the flow recirculates toward the anterior wall before flowing into the daughter branches. In this case, the flow split is properly visualized by the MEAN CFD field but not by the DSA field. In the second case (center row), the inflow stream is located near the anterior wall of the aneurysm and both the DSA and projected CFD fields provide adequate visualizations of the flow split. Furthermore, it is important to visualize the flow from >1 projection to understand the 3D flow structures. The bottom row of Fig 3 shows a second projection of the second example of this figure. In this second projection, the flow split is still visible in the DSA field, as well as the effect of the converging vectors when the main vortex is perpendicular to the line of sight described previously. Taken together, the DSA flow visualizations from the 2 roughly normal projections (Fig 3, center and bottom rows) provide a picture that allows us to understand the main structures of the 3D flow field.

Third, overlapping of the aneurysm with surrounding vessels for a given view point can affect the projected MEAN CFD flow fields by, for instance, generating false vortex structures. Examples of these kinds of distortions are presented in Fig 4 and are indicated by the red arrows. The MIP CFD fields shown in this figure clearly illustrate the effect of overlapping vessels on the field averaged along the line of sight and also illustrate why the MIP fields are also not appropriate for evaluating the DSA fields. On the other hand, vessel overlaps can affect the reconstruction of flow fields from DSA sequences by, for instance, generating false inflow or outflow regions, as illustrated in Fig 4 and indicated by the yellow arrows. Thus, vessel overlaps can affect the DSA and projected CFD fields differently; these different results can lead to poor similarity between these fields.

Finally, in cases in which the displacements of fluid particles in 1 timeframe are comparable with the dimensions of the aneurysm, an interesting effect can be observed in which particle traces seem to jump across streamlines instead of following them. This undersampling effect is illustrated in Fig 5. The arrows point to regions where this effect is thought to take place. Note that this affects the DSA flow reconstruction but not the CFD projections; therefore, it can lead to poor similarity between the DSA and projected CFD fields. Because this can also affect the MAFA quantification, the difference (ratio) between MAFA and VEL is plotted in Fig 1*B* as a function of mean aneurysm transit time or the number of frames required for fluid particles to traverse the aneurysm, estimated as Frames = 60 × Aneurysm Diameter / Mean Aneurysm Velocity. The difference decreases (the ratio becomes closer to 1) as the number of frames increases (the flow within the aneurysm is better resolved in time).

Most interesting, both the DSA and projected MEAN CFD flow fields neglect swirling or secondary flows in the parent artery but provide reasonable representations of the mean axial flow profile (which explains why the similarities are good in the vessel region). In the first example of Fig 2 (top row), the flow in the proximal parent artery has strong secondary flows shown by the streamline visualization and the MIP CFD projection, but not by the DSA or MEAN CFD fields. Similarly, in the first example of Fig 3 (top row), a strong swirling can be observed proximal to the internal carotid artery bifurcation in the streamline visualization, but the DSA or MEAN CFD fields give the impression of a perfect laminar parallel flow in this region.

CONCLUSIONS

Linear regression analysis suggests that the mean aneurysm flow amplitude determined from DSA is linearly correlated to the

mean aneurysm velocity determined from CFD after discarding views with substantial vessel overlap.

While a good correspondence between the arterial flow fields detected in DSA and CFD reconstructions has been observed (directional similarity of 78% on average), the similarity fluctuated considerably for the aneurysm flow fields. Several factors affect the reconstruction of 2D aneurysm flow fields from angiography sequences. The most important factors are the 3-dimensionality of the intrasaccular flow patterns and inflow jets; the alignment of the main vortex structure with the line of sight; the overlapping of surrounding vessels, which many times is unavoidable; and possible frame-rate undersampling. Flow visualization with DSA from >1 projection is required for understanding the 3D intrasaccular flow patterns.

Although these DSA-based flow quantification techniques do not capture swirling or secondary flows in the parent artery, they still provide a good representation of the mean axial flow and the corresponding flow rate. This information is valuable for prescribing patient-specific flow conditions in CFD models of cerebral aneurysms used to understand mechanisms of aneurysm evolution and rupture and to evaluate endovascular procedures and devices.

Disclosures: Juan R. Cebral—*UNRELATED*: *Grants/Grants Pending*: National Institutes of Health, Philips Healthcare.* Fernando Mut—*UNRELATED*: *Grant*: National Institutes of Health.* Laurent Spelle—*UNRELATED*: *Consultancy*: Medtronic, Stryker. Jacques Moret—*UNRELATED*: *Consultancy*: MicroVention, Stryker, Medtronic. Fred van Nijnatten—*UNRELATED*: *Employment*: Philips Healthcare. Daniel Ruijters—*UNRELATED*: *Employment*: Philips Healthcare. *Money paid to the institution.

REFERENCES

1. Sforza D, Putman CM, Cebral JR. **Hemodynamics of cerebral aneurysms.** *Annu Rev Fluid Mech* 2009;41:91–107 Medline
2. Chong W, Zhang Y, Qian Y, et al. **Computational hemodynamics analysis of intracranial aneurysms treated with flow diverters: correlation with clinical outcomes.** *AJNR Am J Neuroradiol* 2014;35:136–42 CrossRef Medline
3. Sadasivan C, Cesar L, Seong J, et al. **Treatment of rabbit elastase-induced aneurysm models by flow diverters: development of quantifiable indexes of device performance using digital subtraction angiography.** *IEEE Trans Med Imaging* 2009;28:1117–25 CrossRef Medline
4. Watton PN, Raberger NB, Holzapfel GA, et al. **Coupling the hemodynamic environment to the evolution of cerebral aneurysms: computational framework and numerical examples.** *J Biomech Eng* 2009;131:101003 CrossRef Medline
5. Sforza DM, Kono K, Tateshima S, et al. **Hemodynamics in growing and stable cerebral aneurysms.** *J Neurointerv Surg* 2016;8:407–12 CrossRef Medline
6. Shojima M, Oshima M, Takagi K, et al. **Magnitude and role of wall shear stress on cerebral aneurysm: computational fluid dynamic study of 20 middle cerebral artery aneurysms.** *Stroke* 2004;35:2500–05 CrossRef Medline
7. Xiang J, Natarajan SK, Tremmel M, et al. **Hemodynamic-morphologic discriminants for intracranial aneurysm rupture.** *Stroke* 2011;42:144–52 CrossRef Medline
8. Cebral JR, Mut F, Weir J, et al. **Association of hemodynamic characteristics and cerebral aneurysm rupture.** *AJNR Am J Neuroradiol* 2011;32:264–70 CrossRef Medline
9. Mut F, Raschi M, Scrivano E,, et al. **Association between hemodynamic conditions and occlusion times after flow diversion in cerebral aneurysms.** *J Neurointerv Surg* 2015;7:286–90 CrossRef Medline
10. Huang Q, Xu J, Cheng J, et al. **Hemodynamic changes by flow diverters in rabbit aneurysm models: a computational fluid dynamic study based on micro-computed tomography reconstruction.** *Stroke* 2013;44:1936–41 CrossRef Medline
11. Wetzel S, Meckel S, Frydrychowicz A, et al. **In vivo assessment and visualization of intracranial arterial hemodynamics with flow-sensitized 4D MR imaging at 3T.** *AJNR Am J Neuroradiol* 2007;28:433–38 Medline
12. Bonnefous O, Pereira VM, Ouared R, et al. **Quantification of arterial flow using digital subtraction angiography.** *Med Phys* 2012;39:6264–75 CrossRef Medline
13. Pereira VM, Bonnefous O, Ouared R, et al. **A DSA-based method using contrast-motion estimation for the assessment of the intra-aneurysmal flow changes induced by flow-diverter stents.** *AJNR Am J Neuroradiol* 2013;34:805–15 CrossRef Medline
14. Brina O, Ouared R, Bonnefous O, et al. **Intra-aneurysmal flow patterns: illustrative comparison among digital subtraction angiography, optical flow, and computational fluid dynamics.** *AJNR Am J Neuroradiol* 2014;35:2348–53 CrossRef Medline
15. Cebral JR, Castro MA, Appanaboyina S,, et al. **Efficient pipeline for image-based patient-specific analysis of cerebral aneurysm hemodynamics: technique and sensitivity.** *IEEE Trans Med Imaging* 2005;24:457–67 CrossRef Medline
16. Cebral JR, Duan X, Gade PS, et al. **Regional mapping of hemodynamics and wall characteristics of intracranial aneurysms.** *Ann Biomed Eng* 2016;44:3553–67 CrossRef Medline
17. Van Nijnatten F, Bonnefuus O, Morales HG. **Mean aneurysm flow amplitude ratio comparison between DSA and CFD.** In: Navab N, Hornegger J, Wells W, Frangi A, eds. *Medical Image Computing and Computer-Assisted Intervention – MICCAI 2015*. Lecture Notes in Computer Science, vol 9350. Switzerland: Springer; 2015:485–92 CrossRef

Resting-State Seed-Based Analysis: An Alternative to Task-Based Language fMRI and Its Laterality Index

K.A. Smitha, K.M. Arun, P.G. Rajesh, B. Thomas, and C. Kesavadas

ABSTRACT

BACKGROUND AND PURPOSE: Language is a cardinal function that makes human unique. Preservation of language function poses a great challenge for surgeons during resection. The aim of the study was to assess the efficacy of resting-state fMRI in the lateralization of language function in healthy subjects to permit its further testing in patients who are unable to perform task-based fMRI.

MATERIALS AND METHODS: Eighteen healthy right-handed volunteers were prospectively evaluated with resting-state fMRI and task-based fMRI to assess language networks. The laterality indices of Broca and Wernicke areas were calculated by using task-based fMRI via a voxel-value approach. We adopted seed-based resting-state fMRI connectivity analysis together with parameters such as amplitude of low-frequency fluctuation and fractional amplitude of low-frequency fluctuation (fALFF). Resting-state fMRI connectivity maps for language networks were obtained from Broca and Wernicke areas in both hemispheres. We performed correlation analysis between the laterality index and the *z* scores of functional connectivity, amplitude of low-frequency fluctuation, and fALFF.

RESULTS: Pearson correlation analysis between signals obtained from the *z* score of fALFF and the laterality index yielded a correlation coefficient of 0.849 ($P < .05$). Regression analysis of the fALFF with the laterality index yielded an R^2 value of 0.721, indicating that 72.1% of the variance in the laterality index of task-based fMRI could be predicted from the fALFF of resting-state fMRI.

CONCLUSIONS: The present study demonstrates that fALFF can be used as an alternative to task-based fMRI for assessing language laterality. There was a strong positive correlation between the fALFF of the Broca area of resting-state fMRI with the laterality index of task-based fMRI. Furthermore, we demonstrated the efficacy of fALFF for predicting the laterality of task-based fMRI.

ABBREVIATIONS: ALFF = amplitude of low-frequency fluctuation; BOLD = blood oxygen level–dependent; fALFF = fractional amplitude of low-frequency fluctuation; FC = functional connectivity; LI = laterality index; rsfMRI = resting-state fMRI

Brain surgery demands preservation of eloquent areas, including the language functional areas. Many studies have illustrated that fMRI is a noninvasive imaging technique that facilitates the lateralization of language function in individual patients.[1-3] The hemispheric language laterality index (LI) is estimated by evaluating the asymmetry in the activation of language areas in the right and left hemispheres of the human brain during a particular task.[4] The ease of integrating fMRI with other MR imaging techniques allows the correct identification of pathology and its landmark with respect to language areas.[5-7]

During the acquisition of language fMRI, the subject is instructed to perform particular tasks designed to elicit a response from language functional areas. However, not all subjects, such as those with low intelligence quotients and pediatric patients, will be able to cooperate with the task-based fMRI. Resting-state fMRI (rsfMRI) is gradually evolving as an alternative to task-based fMRI. The rsfMRI technique extracts the low-frequency fluctuations in the blood oxygen level–dependent (BOLD) signal when subjects are instructed to lie relaxed inside the scanner.[7,8]

Tie et al[9] extracted language networks from rsfMRI and evaluated the effectiveness of the automatic identification of language components by using independent component analysis. The study separated the activation patterns corresponding to the language network components from individual rsfMRI data. Another study adopted rsfMRI connectivity analysis to examine the degree of hemispheric dominance for language processing in healthy controls and patients with temporal lobe epilepsy.[10]

Received June 25, 2016; accepted after revision February 2, 2017.

From the Departments of Imaging Sciences and Interventional Radiology (K.A.S., K.M.A., B.T., C.K.) and Neurology (P.G.R.), Sree Chitra Tirunal Institute for Medical Sciences and Technology, Trivandrum, Kerala, India.

This work was supported by the Department of Biotechnology, Ministry of Science and Technology, Government of India.

Please address correspondence to K.A. Smitha, PhD, Department of Imaging Sciences and Interventional Radiology, Sree Chitra Tirunal Institute for Medical Sciences and Technology, Trivandrum, Kerala, India, Pin code: 695011; e-mail: mithamahesh@gmail.com

http://dx.doi.org/10.3174/ajnr.A5169

Functional connectivity (FC) analysis of the frontal cortex in the control group revealed a strong correlation with the LI. The authors found a good correlation between the LI and the epileptogenic mesial temporal lobe. Similarly, Pravatà et al[11] studied the correlation between the strength of FC between language networks and language performance in healthy controls and patients with epilepsy. They demonstrated an overall reorganization and reduction of the connectivity pattern within the language network of patients with intractable epilepsy. These studies evaluated the FC of language networks rather than regional abnormalities in the low-frequency fluctuations.

In rsfMRI, the parameters FC, amplitude of low-frequency fluctuation (ALFF), and fractional amplitude of low-frequency fluctuation (fALFF) are used to examine the network-related and regional characteristics of low-frequency oscillations. FC analysis evaluates the correlation between the time courses of voxels in a seed region with every other region within the brain. The regions with strong correlations will be shown as an FC map.[7,12] ALFF and fALFF are rsfMRI metrics that help in identifying regional BOLD signal changes of rsfMRI fluctuations. ALFF quantifies the amplitude of the low-frequency fluctuations of rsfMRI BOLD signals. fALFF corresponds to the power spectrum of the low-frequency band with respect to all frequencies detectable with the applied time of repetition of the study.[13,14] Different studies reported the clinical application of these metrics.[13,15,16] However, none of the studies considered the accuracy of these metrics in determining the LI.[9-11]

The objective of our study was to determine the potential of rsfMRI to evaluate language lateralization in comparison with task-based fMRI. In the current study, we evaluated the *z* scores of FC, ALFF, and fALFF obtained via rsfMRI and assessed the correlations of each of these metrics with the LI of task-based fMRI from individual seed regions. We hypothesized that the metrics of seed-based rsfMRI analysis are strongly correlated with the LI obtained by using task-based fMRI. If this hypothesis is proved, then rsfMRI can be used instead of task-fMRI in patients who cannot perform the task.

MATERIALS AND METHODS

In this prospective observational study, MR imaging was performed in 18 healthy right-handed volunteers (12 men and 6 women). The Edinburgh Handedness Inventory was used to evaluate the handedness of the subjects. The mean age of the cohort was 30 ± 7.8 years. Subject scanning was conducted by using a 1.5T MR imaging scanner (Magnetom Avanto, Tim; Siemens, Erlangen, Germany). Informed consent was obtained from all participating subjects. The study received clearance from the institutional ethics committee. The imaging sequence included structural imaging, rsfMRI, and task-based fMRI. Structural imaging was performed by using the MPRAGE sequence with the following imaging protocol: TR = 2400 ms, TE = 3.72 ms, TI = 1000 ms, NEX = 2, flip angle = 8°, section thickness = 1 mm, imaging matrix = 256 × 256 with an isotropic voxel of 1 × 1 mm. Resting-state fMRI was acquired with a gradient-echo EPI sequence with the following imaging protocol: TR = 2000 ms, TE = 20 ms, flip angle = 90°, section thickness = 5 mm, number of sections = 25 acquired in the interleaved bottom up order, imaging matrix = 320 × 320 with an isotropic voxel of 3.75 × 3.75. During rsfMRI, subjects were instructed to concentrate on the white crosshair on the black background displayed on the screen.

Subsequently, task-based fMRI was performed with the same imaging protocol. Language fMRI was conducted with the visual-verb paradigm.[17] During the active block, subjects were instructed to think about the verb associated with the pictures presented on the screen. During the rest block, subjects were instructed to concentrate on the white crosshair on the black background displayed on the screen. The stimulus presentation paradigm was designed as blocks of tasks and rest with 5 cycles (5 rest and 5 active blocks).

Image Analysis

The reconstructed DICOM images were converted to the NIfTI format for further processing. We used SPM8 (http://www.fil.ion.ucl.ac.uk/spm/software/spm12) to process task-based fMRI. The rsfMRI processing was performed by using the Data Processing Assistant for Resting State fMRI (http://restfmri.net/forum/DPARSF), the Resting-State fMRI Data Analysis Toolkit (REST; http://www.restfmri.net), and RESTplus software (http://restfmri.net/forum/RESTplusV1.2).[18,19]

The NIfTI images were preprocessed in the SPM pipeline. The images were realigned, section time-corrected, and normalized. The normalized images were smoothed with a Gaussian kernel at a full width at half maximum of 8 mm. The general linear model design matrix was defined with a canonical hemodynamic response function as the basis function, and it was estimated to obtain β values. Furthermore, we performed family-wise error correction for individual subjects ($P < .05$). Six ROIs from both the left and right hemispheres of the Broca area, Brodmann area 6, and Wernicke area were identified. Using MarsBaR software (https://sourceforge.net/projects/marsbar/files/), we created spheric masks with Montreal Neurological Institute coordinates to obtain these ROIs.[20] These masks were used to derive the LI by using the LI Toolbox (http://www.medizin.uni-tuebingen.de/kinder/en/research/neuroimaging/software/) implemented in SPM8. We used a method called "voxel value of LI" to calculate the activated voxels, in which the value of the voxel represents the strength of its correlation with the task.[21] The LI varies from −1 to +1. An individual with a positive LI is said to be left-lateralized, and a person with a negative LI is right-lateralized. The equation for LI is as follows[4,17,22,23]:

$$LI = \Sigma Li - \Sigma Ri/\Sigma Li + \Sigma Ri,$$

where ΣLi is the number of voxels activated at a particular threshold in the left hemisphere of the ROI and ΣRi is that of the right hemisphere.

For rsfMRI, the same pipeline of preprocessing used for task-based fMRI was followed. Nuisance covariate regression and temporal bandpass filtering in the range of 0.01–0.08 Hz were performed for FC analysis. The Brodmann areas 47, 45, 44, 6, 21, and 22 of both hemispheres were taken as seed regions for rsfMRI analysis. After performing seed-based FC analysis, ALFF and fALFF were calculated by using RESTplus software.

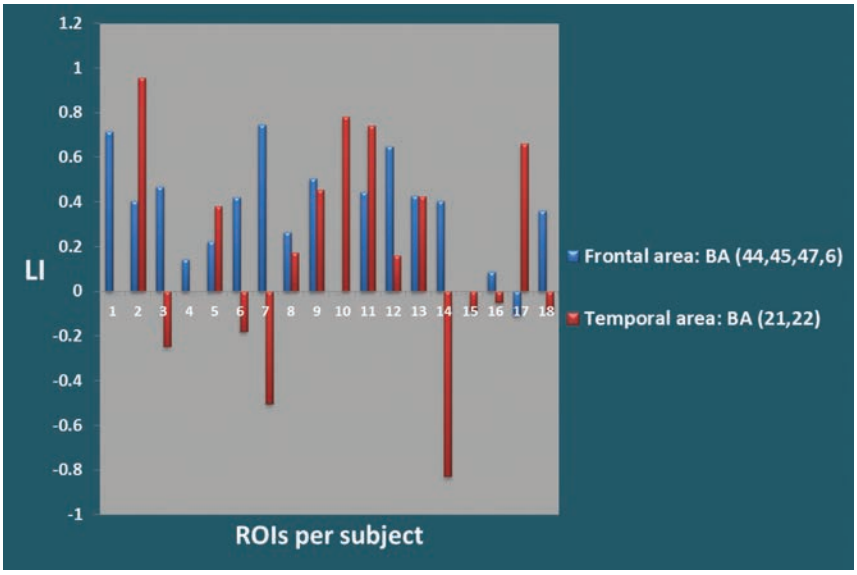

FIG 1. The bar chart presents the average value of the laterality indices obtained by using task-based fMRI for all the subjects in the Broca area, Brodmann area 6 (frontal area), and Wernicke area (temporal area).

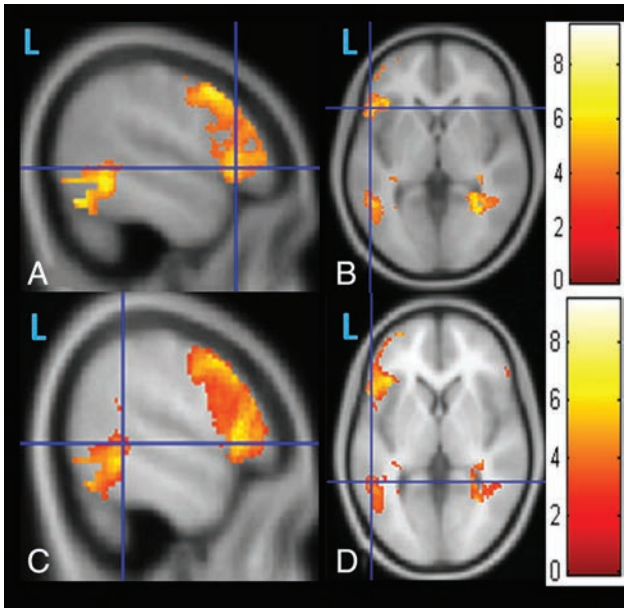

FIG 2. *A* and *B*, Sagittal and axial images obtained after the 1-sample *t* test of the task-fMRI for the Broca area and Brodmann area 6. *C* and *D*, Wernicke area of 18 healthy controls.

Statistical Analysis

Statistical analysis was performed by using Excel (Microsoft, Redmond, Washington) and SPSS, Version 17 for Windows (IBM, Armonk, New York). The FC, ALFF, and fALFF scores were converted into *z* scores by using the Fisher transformation. A 1-sample *t* test on *Z*-maps of FC, ALFF, and fALFF on all subjects yielded a *T*-map. This was performed by using RESTplus software. Thereafter, the FC, ALFF, and fALFF values of the corresponding ROIs were extracted from the *T*-map and correlated with the LI.

Pearson correlation analysis was conducted to find the associations between rsfMRI metrics and the LI. Linear regression analysis and R^2 values were obtained only for the specific rsfMRI metrics that showed a significant correlation with LI.

RESULTS

LI values were computed from all individual ROIs. Figure 1 presents the bar diagram of LI for each of the ROIs from all subjects. Figure 2 indicates the task-based fMRI BOLD signal activations obtained from the Broca area, Brodmann area 6, and Wernicke area.

The seed-based rsfMRI connectivity analysis was performed in the language regions of both hemispheres, such as the Broca area, Brodmann area 6, and Wernicke area. The *Z*-maps corresponding to FC, ALFF, and fALFF for the Broca area are depicted in Fig 3. Table 1 shows the mean value of the LI obtained for all subjects for the respective ROIs. Table 2 presents the Pearson correlation coefficient obtained between the rsfMRI seed-based metrics for the respective ROIs with the LI obtained from task-based fMRI. When *z* scores extracted from the Broca area were analyzed, only fALFF displayed a statistically significant correlation with the LI with a correlation coefficient of 0.849 ($P < .032$). Regression analysis of the *z* score obtained from fALFF analysis and the LI yielded an R^2 value of 0.721, as shown in Fig 4. Similarly, a positive correlation coefficient of 0.531 was observed between the *z* score of FC and the LI, and a negative correlation coefficient of −0.153 was obtained between the *z* score of ALFF and LI. When *z* scores extracted from the Wernicke area and Brodmann area 6 were analyzed, we observed a weak positive correlation between the *z* scores of ALFF and fALFF with the LI, whereas a negative correlation was observed between FC and the LI, as shown in Table 2.

DISCUSSION

The current study evaluated the effectiveness of rsfMRI in predicting the language dominance of hemispheres in healthy controls by correlating the rsfMRI metrics FC, ALFF, and fALFF with the LI of task-based fMRI. We studied task-based fMRI activation in the Broca area, Wernicke area, and Brodmann area 6 and compared the findings with those of rsfMRI connectivity analysis in the same areas as the seed regions. We evaluated the *z* scores of FC, ALFF, and fALFF of the respective areas for all subjects and correlated the values with the LI of task-based fMRI. These connectivity metrics have been analyzed to focus on the frequency-specific characteristics of rsfMRI networks.[24] ALFF is the average amplitude of the low-frequency band (0.08–0.1 Hz) because it measures the magnitude of spontaneous neuronal activity.[14,25] fALFF is the ratio between the power spectrum of the low-frequency signal and the entire frequency range that is dependent on the TR of the imaging protocol. Consequently, the peculiarity of fALFF with respect to ALFF is that it markedly reduces the noises in the high-frequency band in cisternal regions of the brain.[13-15,26-29]

Numerous studies have investigated the clinical applications of ALFF and fALFF metrics.[13-16,27-29] Turner et al[13] examined ALFF and fALFF to clarify differences between patients with

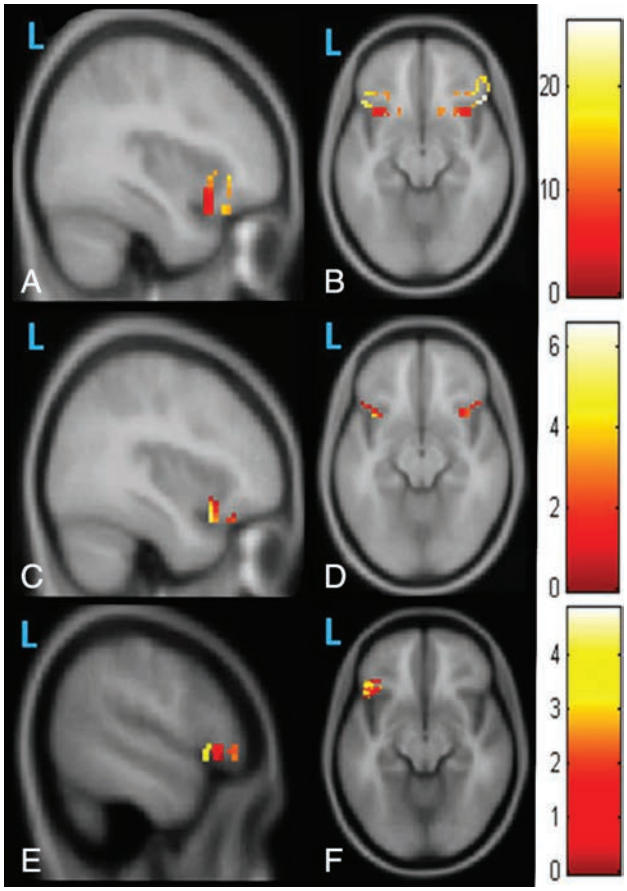

FIG 3. The first row shows the sagittal and axial images obtained after a 1-sample *t* test of the *Z*-maps of 18 functional connectivity images obtained with the Broca area as the seed area. The second row shows sagittal and axial images obtained after a 1-sample *t* test of the *Z*-maps of the amplitude of low-frequency fluctuations in 18 healthy controls. We observed limited correlated activity for functional connectivity (*A* and *B*) and ALFF (*C* and *D*); it seems to be fragmented and potentially less clinically reliable at the individual level. The third row shows the sagittal and axial images obtained after a 1-sample *t* test of the *Z*-maps of fractional amplitude of low-frequency fluctuations in 18 healthy controls. By contrast, the map of fALFF (*E* and *F*) appears more robust and potentially more reliable.

Table 1: The mean value of the laterality index obtained from Brodmann areas 44, 45, 47, 6, 21, and 22 using task-based fMRI for all subjects

Language Areas	Mean LI of 18 Subjects
Brodmann Area 44	0.375
Brodmann Area 45	0.238
Brodmann Area 47	0.430
Brodmann Area 6	0.377
Brodmann Area 21	0.166
Brodmann Area 22	0.218

schizophrenia and healthy controls. The study analyzed these metrics from different sites and found that patients with schizophrenia had a lower fALFF than healthy controls across the cortex. Another group found variations in ALFF and fALFF associated with the right precuneus and left medial prefrontal gyrus and suggested that the changes in these measures can be used as surrogate markers of minimal hepatic encephalopathy.[16]

In our study, the *z* scores of FC, ALFF, and fALFF were extracted from Broca and Wernicke areas separately. The *Z*-map of

Table 2: Correlation of the seed-based analysis metrics FC, ALFF, and fALFF of rsfMRI with the LI of task-based fMRI

Region	Correlation between the *Z* Score of FC and LI	Correlation between the *Z* Score of ALFF and LI	Correlation between the *Z* Score of fALFF and LI
Broca area	0.531 ($P = .277$)	−0.153 ($P = .771$)	0.849 ($P = .032$)
Wernicke area and Brodmann area 6	−0.752 ($P = .085$)	0.182 ($P = .729$)	0.372 ($P = .467$)

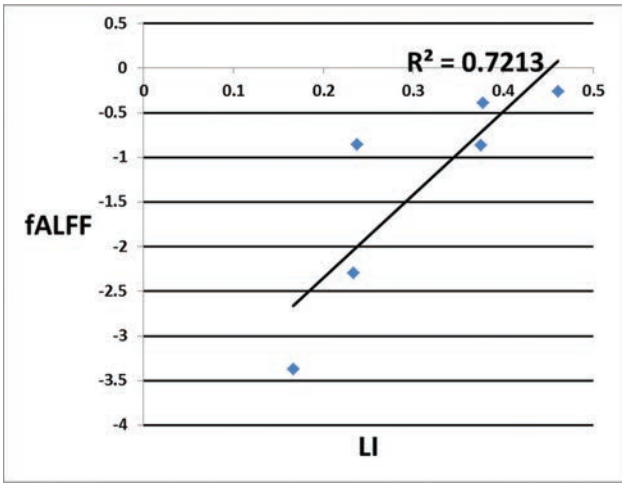

FIG 4. The regression line plotted with signals extracted from the *T*-map of the *z* scores of the fractional amplitude of low-frequency fluctuations from the Broca area of resting-state fMRI with the laterality index obtained from all ROIs of task-based fMRI.

fALFF obtained from rsfMRI seed-based analysis revealed that the Broca area is mainly left hemisphere–lateralized. In addition, we observed a strong correlation between the *z* score of fALFF obtained from the Broca area on rsfMRI and the LI obtained from task-based fMRI. Regression analysis of the *z* score of fALFF and LI showed a noticeable R^2 value, indicating the usefulness of rsfMRI connectivity analysis in predicting the LI of language areas. Meanwhile, a weak positive correlation coefficient of 0.372 was observed when the *z* score of fALFF in Brodmann area 6 and the Wernicke area was correlated with the LI of task-based fMRI.

To the best of our knowledge, including a review of the literature, no previous study evaluated rsfMRI FC analysis and task-based fMRI to correlate resting-state connectivity metrics with LIs associated with task-based fMRI. From the individual cases of task-based fMRI, we observed that BOLD activations in the Broca area in most subjects were left-lateralized; conversely, for the Wernicke area, half of the subjects were right-lateralized or they had an LI close to zero, as shown in Fig 1. We therefore consider this finding is a reason for the negative correlation between the *z* score of FC of the Wernicke area and the LIs of the respective ROIs. Thus, the task-based fMRI analysis demonstrated more consistency in Broca activation and more variability in Wernicke activation. Our findings reveal that frontal lateralization is more robust than temporal activation. This result may be because frontal activity is more easily detected than temporal activity, which can be masked by susceptibility artifacts.[17] Zhu et al[30] examined rsfMRI seed-based FC with Broca and Wernicke regions as seed regions. It is evident from their observations that the activations in the Broca

area were left-lateralized, and those in the Wernicke area remained right-lateralized. The outcome of their analysis is in line with our results from task-based fMRI. Their study did not estimate the seed-based rsfMRI metrics; instead, they assessed the consistency of rsfMRI language networks and found that language networks are highly reproducible.

Doucet et al[10] provided evidence that resting-state FC can be used to predict the strength of hemispheric language laterality in patients with temporal lobe epilepsy and controls. The ability of regional resting-state FCs to predict the LI was determined and compared. Although the results of the present study are in line with those of Doucet et al, additional metrics for predicting LI such as ALFF and fALFF were investigated.[10] We hypothesized that FC analysis alone may not be sufficient to uncover subtle abnormalities in low-frequency fluctuations of BOLD signals and that the use of ALFF and fALFF can disclose more meaningful information. Although ALFF simply measures the power of the low-frequency fluctuation of a specific ROI, the negative correlation between ALFF in the Broca area and the LI may be due to the lower power of filtered frequency signals within the low-frequency band (0.01–0.08 Hz) in the Broca area in healthy subjects during the resting-state than during a task.[13,14,16,31] Zou et al[14] observed that fALFF exhibits greater sensitivity and specificity than ALFF.

Pravatà et al[11] investigated the correlation between FC and neuropsychological evaluations of language. The study observed an overall decrease in FC within the language network of patients with intractable epilepsy compared with that in controls.[11] The study did not consider the efficacy of FC to calculate language lateralization, but it emphasized that FC analysis provides a more illustrative assessment of functional modification. Tie et al[9] investigated the feasibility of rsfMRI in right-handed healthy controls by using the group independent component analysis method. A new semiautomated method was used to identify the language components and compare rsfMRI and task-based fMRI activations in the language area. Rather than the LI, they adopted the Dice coefficient to determine the overlap between the language network areas from rsfMRI and task-based fMRI. The group-level analysis of task-based fMRI and rsfMRI uncovered markedly similar language regions in right-handed subjects. Resting-state fMRI identified more left lateralization and suggested that the semiautomatic language component identification procedure provides the best strategy for rsfMRI with the independent component analysis technique.

A study with a larger number of subjects, including more right-language-lateralized subjects, and thinner sections and a higher Tesla MR imaging device is required to confirm our findings. In addition, we need to investigate whether we can reproduce these results in a patient cohort by validating the results with neuropsychology analysis and the Wada test for language lateralization. Methodologic improvements such as automatic parcellation of language regions may strengthen the reliability of the analysis in the future. This method of analysis can provide better results than the Montreal Neurological Institute–based spheric ROI method. A cross-validation with other rsfMRI analysis techniques would also be useful.

CONCLUSIONS

The current study highlighted a strong correlation between the seed-based rsfMRI metric fALFF of the Broca area and the LI of task-based fMRI. The study demonstrated that rsfMRI connectivity analysis can be used for assessing language networks and fALFF can be used as an effective predictor for evaluating language laterality. The outcome of the study might be useful in testing the efficacy of rsfMRI in patients who are unable to perform task-based fMRI in preoperative language lateralization.

ACKNOWLEDGMENTS

We acknowledge Professor Sankara Sarma for his valuable advice regarding the statistical analysis methods.

Disclosures: K.A. Smitha—*RELATED*: *Grant*: Research Associateship, Department of Biotechnology, Ministry of Science and Technology, Government of India. Bejoy Thomas—*UNRELATED*: *Grants/Grants Pending*: GE Healthcare, *Comments*: research project grant*; *Patents (Planned, Pending or Issued)*: Sree Chitra Tirunal Institute for Medical Sciences and Technology (employer), *Comments*: Indian patent applied, unrelated to the current publication*. Chandrasekharan Kesavadas—*RELATED*: *Grant*: research funded by Department of Biotechnology, Ministry of Science and Technology, Government of India*; *UNRELATED: Grants/Grants Pending*: GE Healthcare*. *Money paid to the institution.

REFERENCES

1. Ruff IM, Petrovich Brennan NM, Peck KK, et al. **Assessment of the language laterality index in patients with brain tumor using functional MR imaging: effects of thresholding, task selection, and prior surgery.** *AJNR Am J Neuroradiol* 2008;29:528–35 CrossRef Medline
2. Zaca D, Jarso S, Pillai JJ. **Role of semantic paradigms for optimization of language mapping in clinical fMRI studies.** *AJNR Am J Neuroradiol* 2013;34:1966–71 CrossRef Medline
3. James JS, Kumari SR, Sreedharan RM, et al. **Analyzing functional, structural, and anatomical correlation of hemispheric language lateralization in healthy subjects using functional MRI, diffusion tensor imaging, and voxel-based morphometry.** *Neurol India* 2015;63:49–57 CrossRef Medline
4. Seghier ML. **Laterality index in functional MRI: methodological issues.** *Magn Reson Imaging* 2008;26:594–601 CrossRef Medline
5. Garrett MC, Pouratian N, Liau LM. **Use of language mapping to aid in resection of gliomas in eloquent brain regions.** *Neurosurg Clin N Am* 2012;23:497–506 CrossRef Medline
6. Gupta S. **fMRI for mapping language networks in neurosurgical cases.** *Indian J Radiol Imaging* 2014;24:37–43 CrossRef Medline
7. Biswal BB. **Resting state fMRI: a personal history.** *Neuroimage* 2012;62:938–44 CrossRef Medline
8. Lee MH, Smyser CD, Shimony JS. **Resting-state fMRI: a review of methods and clinical applications.** *AJNR Am J Neuroradiol* 2013;34:1866–72 CrossRef Medline
9. Tie Y, Rigolo L, Norton IH, et al. **Defining language networks from resting-state fMRI for surgical planning: feasibility study.** *Hum Brain Mapp* 2014;35:1018–30 CrossRef Medline
10. Doucet GE, Pustina D, Skidmore C, et al. **Resting-state functional connectivity predicts the strength of hemispheric lateralization for language processing in temporal lobe epilepsy and normals.** *Hum Brain Mapp* 2015;36:288–303 CrossRef Medline
11. Pravatà E, Sestieri C, Mantini D, et al. **Functional connectivity MR imaging of the language network in patients with drug-resistant epilepsy.** *AJNR Am J Neuroradiol* 2011;32:532–40 CrossRef Medline
12. Biswal B, Yetkin FZ, Haughton VM, et al. **Functional connectivity in the motor cortex of resting human brain using echo-planar MRI.** *Magn Reson Med* 1995;34:537–41 CrossRef Medline
13. Turner JA, Damaraju E, van Erp TG, et al. **A multi-site resting state fMRI study on the amplitude of low frequency fluctuations in schizophrenia.** *Front Neurosci* 2013;7:137 CrossRef Medline
14. Zou QH, Zhu CZ, Yang Y, et al. **An improved approach to detection**

of amplitude of low-frequency fluctuation (ALFF) for resting-state fMRI: fractional ALFF. *J Neurosci Methods* 2008;172:137–41 CrossRef Medline
15. Tadayonnejad R, Yang S, Kumar A, et al. **Clinical, cognitive, and functional connectivity correlations of resting-state intrinsic brain activity alterations in unmedicated depression.** *J Affect Disord* 2015; 172:241–50 CrossRef Medline
16. Zhong WJ, Zhou ZM, Zhao JN, et al. **Abnormal spontaneous brain activity in minimal hepatic encephalopathy: resting-state fMRI study.** *Diagn Interv Radiol* 2016;22:196–200 CrossRef Medline
17. Rosazza C, Ghielmetti F, Minati L, et al. **Preoperative language lateralization in temporal lobe epilepsy (TLE) predicts peri-ictal, pre- and post-operative language performance: an fMRI study.** *Neuroimage Clin* 2013;3:73–83 CrossRef Medline
18. Chao-Gan Y, Yu-Feng Z. **DPARSF: A MATLAB toolbox for "pipeline" data analysis of resting-state fMRI.** *Front Syst Neurosci* 2010; 4:13 CrossRef Medline
19. Song XW, Dong ZY, Long XY, et al. **REST: a toolkit for resting-state functional magnetic resonance imaging data processing.** *PLoS One* 2011;6:e25031 CrossRef Medline
20. Wang L, Chen D, Yang X, et al. **Group independent component analysis and functional MRI examination of changes in language areas associated with brain tumors at different locations.** *PLoS One* 2013;8:e59657 CrossRef Medline
21. Wilke M, Lidzba K. **LI-tool: a new toolbox to assess lateralization in functional MR-data.** *J Neurosci Methods* 2007;163:128–36 CrossRef Medline
22. Binder JR, Swanson SJ, Hammeke TA, et al. **Determination of language dominance using functional MRI: a comparison with the Wada test.** *Neurology* 1996;46:978–84 CrossRef Medline
23. Desmond JE, Sum JM, Wagner AD, et al. **Functional MRI measurement of language lateralization in Wada-tested patients.** *Brain* 1995;118(pt 6):1411–19 CrossRef Medline
24. Zuo XN, Di Martino A, Kelly C, et al. **The oscillating brain: complex and reliable.** *Neuroimage* 2010;49:1432–45 CrossRef Medline
25. Shimony JS, Zhang D, Johnston JM, et al. **Resting-state spontaneous fluctuations in brain activity: a new paradigm for presurgical planning using fMRI.** *Acad Radiol* 2009;16:578–83 CrossRef Medline
26. Tomasi D, Wang R, Wang GJ, et al. **Functional connectivity and brain activation: a synergistic approach.** *Cereb Cortex* 2014;24: 2619–29 CrossRef Medline
27. McHugo M, Rogers BP, Talati P, et al. **Increased amplitude of low frequency fluctuations but normal hippocampal-default mode network connectivity in schizophrenia.** *Front Psychiatry* 2015;6:92 CrossRef Medline
28. Fryer SL, Roach BJ, Ford JM, et al. **Relating intrinsic low-frequency BOLD cortical oscillations to cognition in schizophrenia.** *Neuropsychopharmacology* 2015;40:2705–14 CrossRef Medline
29. Yang M, Li J, Li Y, et al. **Altered intrinsic regional activity and interregional functional connectivity in post-stroke aphasia.** *Sci Rep* 2016;6:24803 CrossRef Medline
30. Zhu L, Fan Y, Zou Q, et al. **Temporal reliability and lateralization of the resting-state language network.** *PLoS One* 2014;9:e85880 CrossRef Medline
31. Yuan R, Di X, Kim EH, et al. **Regional homogeneity of resting-state fMRI contributes to both neurovascular and task activation variations.** *Magn Reson Imaging* 2013;31:1492–500 CrossRef Medline

Initial Performance of NI-RADS to Predict Residual or Recurrent Head and Neck Squamous Cell Carcinoma

D.A. Krieger, P.A. Hudgins, G.K. Nayak, K.L. Baugnon, A.S. Corey, M.R. Patel, J.J. Beitler, N.F. Saba, Y. Liu, and A.H. Aiken

ABSTRACT

BACKGROUND AND PURPOSE: The Head and Neck Imaging Reporting and Data System (NI-RADS) surveillance template for head and neck cancer includes a numeric assessment of suspicion for recurrence (1–4) for the primary site and neck. Category 1 indicates no evidence of recurrence; category 2, low suspicion of recurrence; category 3, high suspicion of recurrence; and category 4, known recurrence. Our purpose was to evaluate the performance of the NI-RADS scoring system to predict local and regional disease recurrence or persistence.

MATERIALS AND METHODS: This study was classified as a quality-improvement project by the institutional review board. A retrospective database search yielded 500 consecutive cases interpreted using the NI-RADS template. Cases without a numeric score, non-squamous cell carcinoma primary tumors, and primary squamous cell carcinoma outside the head and neck were excluded. The electronic medical record was reviewed to determine the subsequent management, pathology results, and outcome of clinical and radiologic follow-up.

RESULTS: A total of 318 scans and 618 targets (314 primary targets and 304 nodal targets) met the inclusion criteria. Among the 618 targets, 85.4% were scored NI-RADS 1; 9.4% were scored NI-RADS 2; and 5.2% were scored NI-RADS 3. The rates of positive disease were 3.79%, 17.2%, and 59.4% for each NI-RADS category, respectively. Univariate association analysis demonstrated a strong association between the NI-RADS score and ultimate disease recurrence, with $P < .001$ for primary and regional sites.

CONCLUSIONS: The baseline performance of NI-RADS was good, demonstrating significant discrimination among the categories 1–3 for predicting disease.

ABBREVIATIONS: AUC = area under the curve; CECT = contrast-enhanced CT; H&N = head and neck; NI-RADS = Head and Neck Imaging Reporting and Data System; ROC = receiver operating characteristic

Radiologists are major stake-holders in the shift toward value-based performance. The American College of Radiology is leading the effort to re-engineer the radiology enterprise to be "patient centric, data-driven, and outcomes-based." Standardized reporting systems, dictation templates, and linked management recommendations have been identified as key contributions to value.[1] Much of this shift toward data-driven and outcomes-based reporting stems from the success of the BI-RADS system for standardizing mammography reports. Similar templates have been developed for hepatocellular carcinoma,[2] prostate cancer,[3] and thyroid nodules.[4]

The Head and Neck Imaging Reporting and Data System (NI-RADS) was recently developed for surveillance contrast-enhanced CT (CECT) with and without positron-emission tomography in patients with treated head and neck (H&N) cancer.[5] Both the primary tumor site and neck are assessed for recurrence and assigned a category of 1–4 based on imaging suspicion with linked management recommendations:

- Category 1: No evidence of recurrence
  Imaging: Expected posttreatment change (tissue distortion, scar, radiation change)

Received November 22, 2016; accepted after revision January 22, 2017.

From the Department of Radiology, Hackensack University Medical Center (D.A.K.), Hackensack, New Jersey; Departments of Radiology and Imaging Sciences (P.A.H., A.H.A., K.L.B., A.S.C.) and Otolaryngology Head and Neck Surgery (M.R.P., J.J.B.), Emory University School of Medicine, Atlanta, Georgia; Departments of Radiation Oncology (J.J.B.), Hematology and Medical Oncology (J.J.B., N.F.S.), and Biostatistics (Y.L.), Winship Cancer Institute, Emory University School of Medicine, Atlanta, Georgia; and Department of Radiology (G.K.N.), New York University School of Medicine, New York, New York.

Paper previously presented as an oral presentation at: Annual Meeting of the American Society of Neuroradiology and the Foundation of the ASNR Symposium, May 21–26, 2016; Washington, DC.

Please address correspondence to Ashley Aiken, MD, Emory University Hospital, 1364 Clifton Rd NE, Atlanta, GA 30322; e-mail: Ashley.aiken@emoryhealthcare.org; @phudge54

http://dx.doi.org/10.3174/ajnr.A5157

Management: Routine surveillance (6 months typically, see "Materials and Methods")

- Category 2: Low suspicion of recurrence
  Imaging: Ill-defined abnormality with only mild enhancement and/or FDG uptake
  Management: Direct inspection for mucosal findings or short (3-month) follow-up with CECT or PET for deep findings
- Category 3: High suspicion of recurrence
  Imaging: Discrete, new, or enlarging lesions with intense enhancement and/or focal FDG uptake
  Management: Biopsy
- Category 4: Known recurrence, pathologically proved or definite radiologic or clinical progression.

NI-RADS categories 1–4 are the same for CECT or CECT/PET, but the linked management recommendations and lexicon are slightly different (because FDG avidity is included in the latter). Furthermore, the first version of NI-RADS category 2 contains subcategories that also address lesion size and location (superficial or deep): 2a, superficial/mucosal surface; 2b, deep abnormality of <1 cm; and 2c, deep abnormality of >1 cm.[5] These subcategories are useful to direct management, for example superficial mucosal abnormalities are amenable to direct inspection. Size criteria were not added to predict disease but rather to avoid biopsy in this indeterminate category unless immediate management depended on the biopsy.[5] This template-driven approach reflects common language to promote collaboration between radiologists and referring providers, data-driven optimization of H&N cancer imaging, and greater direct engagement with patients.

An obstacle to improvement in value-based performance and direct patient reporting is lack of a data-driven standard surveillance imaging algorithm. PET/CECT at 12 weeks is often the first posttreatment study, though a recent study suggests that it can be performed at 8 weeks.[6] At our institution, patients with advanced H&N cancer are scanned with CECT/PET at 12 weeks as a baseline. If the findings are negative, they undergo CECT alone 6 months later, and if these findings are negative, they undergo CECT alone 12 months later. Although studies have investigated PET/CT for surveillance,[7-9] ordering practices among treating physicians remain variable. The 2015 National Comprehensive Cancer Network recommendations advocate imaging within 6 months for T3/4 primary tumors or N2/3 nodal disease and then additional imaging only for new signs/symptoms, smoking, or areas inaccessible to clinical inspection (the latter being arbitrary and difficult to apply).[10] Yet, 79% of H&N cancer surgeons self-reported using PET/CT for asymptomatic patients.[11] Given this variation in practice, it is critical to have measurable categories to correlate with outcomes to develop a data-driven universal surveillance algorithm.

NI-RADS allows H&N radiologists to perform structured radiologic-pathologic correlation and to determine accuracy, prognostic value, and interobserver agreement in contrast to subjective interpretations that provide no data for retrospective analysis. Our objective was to determine the initial performance of the NI-RADS scoring system to predict tumor recurrence or persistence in patients treated for squamous cell carcinoma of the H&N undergoing imaging surveillance.

MATERIALS AND METHODS

This study was designated a Quality Improvement project by our institutional review board at the Emory University School of Medicine. An electronic medical record search from June 12, 2014 to January 28, 2015 yielded 500 consecutive neck CECT examinations interpreted with the NI-RADS template, including patients with a variety of tumor types and primary locations. The following was gathered from a review of the electronic medical record:

1) Age and sex
2) Date and site of original diagnosis
3) Human papillomavirus status
4) Initial tumor stage (Tumor, Node, Metastasis)
5) Treatment (ie, surgery, chemotherapy, radiation)
6) Date of the index scan
7) Type of index scan (CECT alone versus CECT with PET scan)
8) First posttreatment scan versus subsequent surveillance scan
9) Length of imaging and clinical follow-up

Inclusion Criteria

1) Treated primary H&N squamous cell carcinoma.
2) CECT and/or CECT/PET for surveillance.
3) NI-RADS template used for interpretation.

A total of 402 scans met the inclusion criteria.

Criteria for tumor recurrence or persistence included the following: 1) Biopsy positive for squamous cell carcinoma, 2) evidence of disease progression on subsequent imaging (per Response Evaluation Criteria In Solid Tumors criteria; http://www.radiologytutor.com/index.php/cases/oncol/139-recist), or 3) obvious tumor on physical examination. To confirm the lack of tumor recurrence, we assessed the following: 1) follow-up imaging at least 90 days after the index scan, 2) clinical follow-up for at least 6 months without evidence of recurrence, or 3) biopsy of an abnormality detected on the index scan with pathology results negative for tumor.

Exclusion Criteria

1) Insufficient outcomes data to determine positive or negative disease.

2) Score of "4, known recurrence" because recurrence had already been proved before the scan. However, it is possible to have a score of 4 for the primary site and 1, 2, or 3 for lymph nodes (or vice versa). Thus, an outcome could still be determined for nodes so that each scan had 2 possible sites for target abnormalities (primary and neck).

3) Multiple scans in the same patient if there were back-to-back scores of 1 for both primary and neck. In this case, subsequent index scans were excluded because the final outcome of "recurrence or not" for the primary or neck would be the same for these 2 data points.

These criteria yielded 287 patients, 318 scans, and 618 total targets (314 primary targets and 304 nodal targets) for which outcomes could be determined.

Surveillance Algorithm and Image Interpretation

At our institution, all patients with advanced H&N cancer (almost all patients except those with T1 N0 disease) are scanned with CECT/PET at 12-week baseline, and if the findings are negative, they undergo a CECT alone 6 months later. If these findings are negative, they undergo a CECT 12 months later. All NI-RADS surveillance scans were interpreted prospectively using the template by 1 of 4 dedicated H&N neuroradiologists (30, 15, 10, and 9

years of experience). Both the primary site and neck were assigned a NI-RADS category of 1–4. For this study, all category 2 subcategories were recorded as general category 2. For scores of 2–4, the target abnormality was described briefly in the impression after the numeric score. The NI-RADS template, created by a multidisciplinary team and implemented in 2014, has been subject to ongoing peer review through weekly tumor boards and the American College of Radiology RADPEER. Interpreting radiologists reviewed prior clinical history and endoscopic notes. Comparison with baseline imaging, including pretreatment FDG avidity when available, was made. The subjective interpretation of the PET/CECT included evaluation of disease on both fused PET and CECT. As noted in the NI-RADS template, factors incorporated into lesion assessment included the following: size, FDG avidity, morphology, and enhancement pattern. Because previous studies have established that the standard uptake value data do not improve diagnostic accuracy for disease after treatment for H&N cancer, a strict threshold for standard uptake value was not used.[6,12,13] Instead, a subjective dichotomous analysis of intense FDG uptake was determined.

Image Acquisition

All PET/CT imaging followed standard protocol, and was performed on GE Discover 600 and 690 PET/CT scanners (GE Healthcare, Milwaukee, Wisconsin). Patients fasted for 6 hours before the scan, and serum glucose concentration was obtained immediately before FDG administration. The examination was deferred if glucose was >200 mg/dL. Combined PET/CT from the skull vertex through the midthigh was obtained 1 hour after intravenous administration of 10–14 mCi of FDG. Helical noncontrast CT from the vertex through midthigh was performed before PET for attenuation correction and anatomic localization. A CECT of the neck with the arms down was performed following PET. Our split-bolus technique used 110 mL of intravenous iopamidol (Isovue-370; Bracco, Princeton, New Jersey), with 55 mL injected first at 2.5 mL/s, a 40-second delay, then another 55 mL at the same rate, with a total scan delay of 90 seconds. We acquired axial images from the frontal sinuses through the mediastinum at 1.25-mm section thickness; pitch, 0.984:1; gantry rotation, 0.7 seconds; FOV, 25 cm; 120 kV(peak); and Smart milliampere with a noise index of 13.78. Reformatted images at 2.5-mm thickness in the axial planes and 3-mm sagittal and coronal reformations were sent to the PACS.

Statistical Methods

Univariate association between recurrence and scan score (1–3) was estimated by the χ^2 test and the nonparametric Fisher exact test. The same analysis was repeated for primary site, lymph node, and their combination separately. The overall performance of discrimination of the scan score on recurrence status (yes versus no) is measured as the area under curve (AUC) by receiver operating characteristic (ROC) analysis with 95% confidence intervals. The sensitivity and specificity at each cut-point of the scan score were presented accordingly for score 1 versus 2–3 and for scores 1–2 versus 3. Additionally, the same ROC analyses for subgroup performed for CECT alone versus CECT + PET and for the first posttreatment examination versus the subsequent surveillance examination were explored. The interobserver agreement was measured by κ statistics among 40 scans for primary and neck sites by 2 graders. The statistical significance level was set at $P < .05$, and analyses were conducted in SAS 9.4 (SAS Institute, Cary, North Carolina).

Table 1: Tumor site and initial stage (patient level)

Site/Stage	% (No.)
Primary site	
Oropharynx	43.2% (124)
Larynx	22.3% (64)
Oral cavity	25.4% (73)
Hypopharynx	4.2% (12)
Skin	2.1% (6)
Unknown	2.8% (8)
Primary stage	
Tx	7.7% (22)
Tis	0.3% (1)
T1	16.4% (47)
T2	25.4% (73)
T3	12.2% (35)
T4a	32.8% (94)
T4b	4.2% (12)
T4	0.8% (3)
Nodal stage	
Nx	4.5% (13)
N0	28.9% (83)
N1	11.8% (34)
N2a	3.1% (9)
N2b	33.8% (97)
N2c	16.4% (47)
N3	1.4% (4)
Distant stage	
M0	97.9% (281)
M1	2.1% (6)

RESULTS

Of the 318 examinations, there were 221 CECTs alone (69.5%) and 97 CECT/PETs (30.5%). Sixty studies (16.4%) were initial baseline posttreatment examinations (performed at 12 weeks); the remainder were follow-up examinations during routine surveillance per protocol.

Median imaging follow-up after the index scan was 51 weeks; median clinical follow-up was 54 weeks. The distribution of tumor site and initial stage (when known) is outlined in Table 1. Primary tumors of the oropharynx were the largest group (43.2%), followed by tumors of the oral cavity (25.4%) and larynx (22.3%). At the primary site, almost one-third had moderately advanced (T4a) disease (32.8%). More than half had at least N2 nodal disease (54.7%). Distant metastatic disease at initial staging was rare (2.1%).

Interobserver Agreement

The interobserver agreement determined by κ statistics after review of 40 scans (80 targets) by 2 graders was very good, 0.821 (95% CI, 0.657–0.986) with $P < .001$.

Incidence of Disease Recurrence/Persistence Based on NI-RADS Score

The incidence of recurrence for each NI-RADS category is detailed in Table 2. Overall, the incidence of tumor persistence/recurrence was 7.9%, with an 8.9% (28/314) recurrence rate at the primary site and a 6.9% (21/304) regional nodal recurrence rate.

Table 2: Recurrence rates among the NI-RADS categories

NI-RADS Categories	Total	Recurrence Rate (No.)
Primary site		
NI-RADS 1	254	3.5% (9)
NI-RADS 2	38	18.4% (7)
NI-RADS 3	22	54.6% (12)
All primary site categories	314	8.9% (28)
Lymph nodes		
NI-RADS 1	274	4.0% (11)
NI-RADS 2	20	15.0% (3)
NI-RADS 3	10	70.0% (7)
All nodal categories	304	6.9% (21)
Combined primary and nodes		
NI-RADS 1	528	3.8% (20)
NI-RADS 2	58	17.2% (10)
NI-RADS 3	32	59.4% (19)
Combined, all categories	618	7.9% (49)

NI-RADS 1. Five hundred twenty-eight of 618 targets (85.4%) were scored "NI-RADS 1, no evidence of recurrence" with only 3.8% having recurrent disease during the follow-up. When considered separately, the recurrence rate for primary and nodal NI-RADS 1 scores was similar (3.5% and 4.0%, respectively).

NI-RADS 2. Fifty-eight of 618 targets (9.4%) were scored "NI-RADS 2, questionable recurrence" and had a higher overall rate of recurrence of 17.2%, with similar rates for primary and nodes separately (18.4% versus 15.0%). Of 58/618 category 2 lesions, there were 38 primary site category 2 lesions (27/38 "2a," 7/38 "2b," and 4/38 "2c"). Seven of 38 underwent biopsy with 5/7 positive, and 2 patients had imaging progression, for a total recurrence of 7/38 (18.4%). There were 20 neck category 2 lesions (15 "2a" and 5 "2b") with 2/20 having pathology-proven recurrence and 1/20 with clinical disease progression, for a total recurrence rate of 3/20 (15.0%) for the neck. There was no difference in the rate of positive disease based on lesion size within the confines of this small sample size.

NI-RADS 3. Thirty-two of 618 targets (5.2%) were "NI-RADS 3, highly suspicious for recurrence" and had the highest overall recurrence rate of 59.4%, with a 54.6% recurrence at the primary site and a 70.0% rate at nodes. Of the 32/618 category 3 lesions, there were 22 primary site lesions and 10 neck lesions. Twenty-two of 32 category 3 targets had pathologic confirmation of disease presence or absence. The remaining 10/32 did not have pathologic confirmation because it would not affect management ($n = 7$) or the ultrasound or CT correlate of the suspected lesion could not be found when biopsy was attempted ($n = 3$). Eight of these 10 (80.0%) had clinical or radiologic evidence for recurrence (7 primary site lesions and 1 nodal site), defined as progression at the target site on imaging or clinically obvious tumor.

NI-RADS Performance

Univariate association analysis demonstrated a strong association between the NI-RADS score and ultimate disease persistence/recurrence, with $P < .001$ for primary site, lymph node scores, and combined scores. ROC curves for NI-RADS performance at the primary site (Fig 1), lymph nodes (Fig 2), and combined (Fig 3) were obtained and reflect an overall good performance. For the primary site ROC curve (Fig 1) (AUC = 0.787; 95% CI, 0.691–0.881), $P < .001$ indicated a good performance of the NI-RADS score to discriminate primary site recurrence versus no recurrence (an AUC value of 1 indicates a perfect discrimination, and an AUC value of 0.5 indicates no use). For lymph nodes, the AUC of 0.712 and an AUC of 0.756 for combined primary and nodal sites indicated good overall performance of this rating scale.

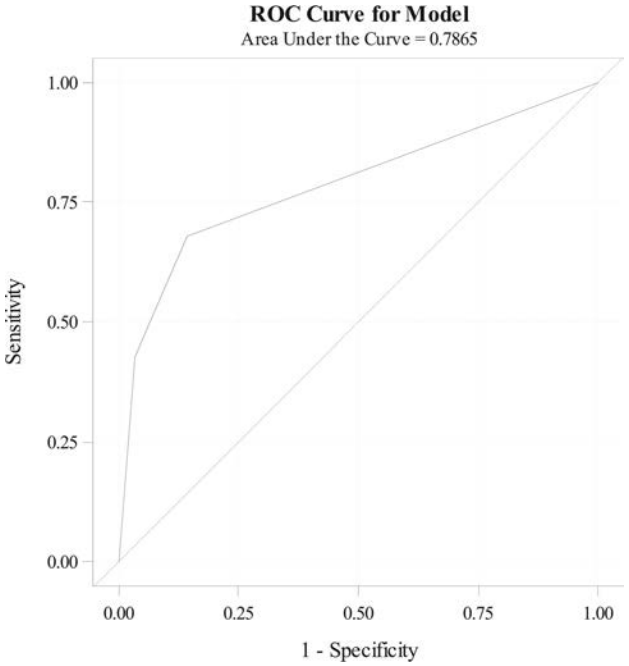

FIG 1. ROC curve for NI-RADS at the primary site with AUC = 0.786 (95% CI, 0.691–0.881).

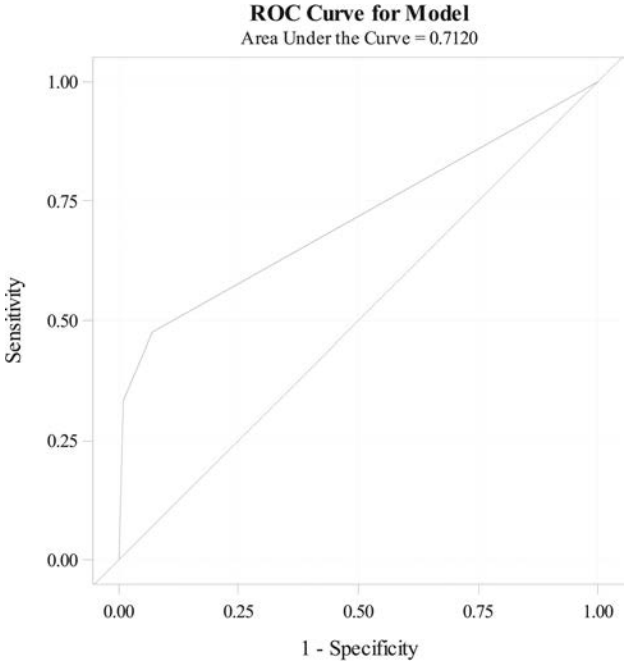

FIG 2. ROC curve for NI-RADS at the lymph nodes with AUC = 0.71 (95% CI, 0.597–0.826).

Subgroup Analysis of CECT Alone versus PET/CECT

A subgroup analysis was undertaken comparing the performance of CECT alone versus CECT + PET/CT (Table 3). The overall

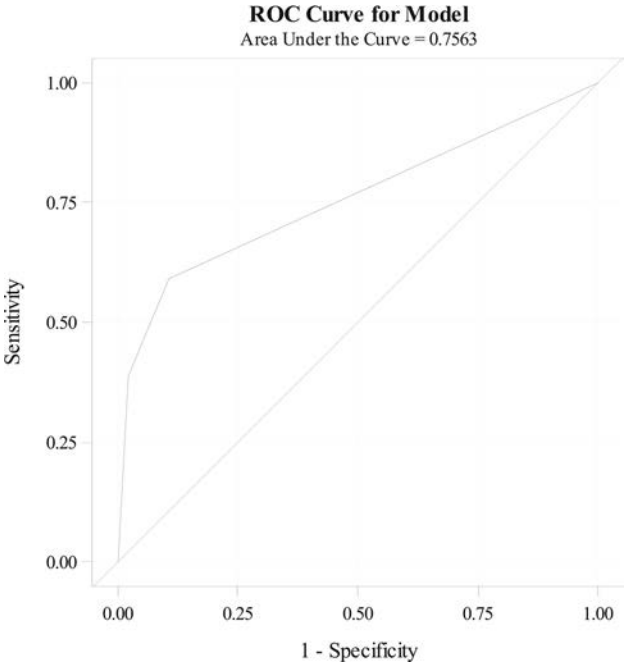

FIG 3. ROC curve for NI-RADS for primary site and lymph nodes combined, with AUC = 0.756 (95% CI, 0.682–0.8).

Table 3: CECT alone versus CECT with PET/CT

	CECT	CECT + PET/CT
Combined primary and nodes		
NI-RADS 1	3.1% (12/385)	5.6% (8/143)
NI-RADS 2	21.9% (7/32)	11.5% (3/26)
NI-RADS 3	91.7% (11/12)	40.0% (8/20)
Combined, all categories	7.0% (30/429)	10.1% (19/189)

Table 4: Initial posttreatment versus subsequent follow-up

Combined Primary and Nodes	Posttreatment	Follow-Up
NI-RADS 1	5.7% (5/88)	3.4% (15/440)
NI-RADS 2	20.0% (4/20)	15.8% (6/38)
NI-RADS 3	50.0% (4/8)	62.5% (15/24)
Combined, all categories	11.2% (13/116)	7.2% (36/502)

recurrence rate in these 2 groups was similar (7.0% versus 10.1%). Although there was no statistical difference in overall performance of NI-RADS for CECT (AUC = 0.779) versus CECT/PET (AUC = 0.709), a NI-RADS 3 on CECT alone was more likely to correctly identify recurrence (primary or nodal) compared with a NI-RADS 3 on CECT + PET (91.7% versus 40.0%).

Subgroup Analysis of Initial Posttreatment Study versus Subsequent Studies

An additional subgroup analysis compared the performance on initial posttreatment studies with performance on subsequent follow-up (Table 4). While there was no statistical difference in the overall performance of NI-RADS in initial posttreatment surveillance (AUC = 0.729) versus subsequent scans (AUC = 0.760), the recurrence rate for NI-RADS 1 was greater for the initial baseline scan group (5.7%, 5/88) compared with the subsequent follow-up examination group (3.4%, 15/440). This difference was even more pronounced when looking at the primary site alone (9.3% versus 2.4%). As expected, the incidence of positive disease was also greater in the initial posttreatment group versus surveillance studies (11.2% versus 7.2%).

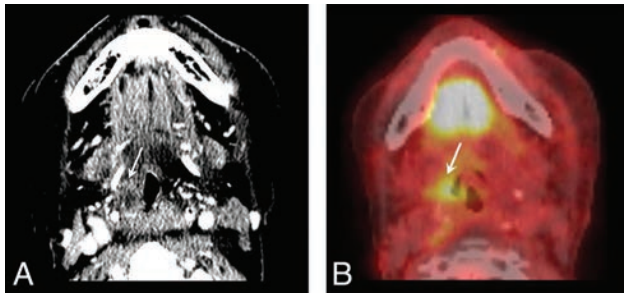

FIG 4. NI-RADS primary site category 2a: superficial mucosal abnormality. Primary T4a N2c base of tongue squamous cell carcinoma, status post chemoradiotherapy. *A*, CECT showed only subtle/questionable asymmetric enhancement in the right vallecula (*arrow*) retrospectively after review of PET. *B*, Fused PET image shows asymmetric uptake in the right vallecula (*arrow*). Direct visualization did show ulcerated mucosa, but the biopsy was negative for tumor. Clinically, this was deemed a radiation-related injury.

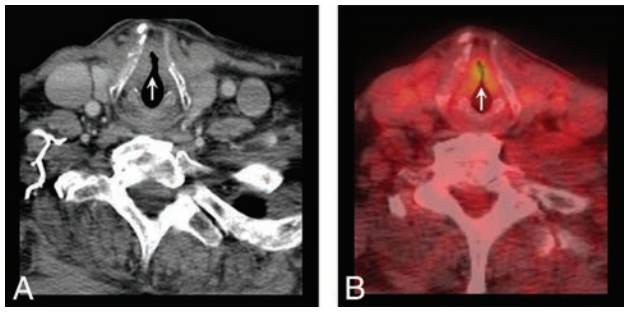

FIG 5. NI-RADS primary site category 2a: superficial mucosal abnormality. Primary T2 larynx squamous cell carcinoma status post chemoradiotherapy. *A*, CECT showed subtle irregularity of the anterior commissure and anterior true vocal cords bilaterally (*arrow*). *B*, Corresponding fused PET image shows focal mucosal uptake (*arrow*). After direct visualization revealed suspicious mucosal findings, the biopsy showed persistent disease. Although this lesion does demonstrate focal avid FDG uptake, it is in a special category of mucosal abnormality. In the published NI-RADS 1.0 by Aiken et al,[5] these are scored as 2a because the linked management recommendation is direct visualization.

DISCUSSION

The baseline performance of NI-RADS demonstrated significant discrimination between groups, with disease recurrence/persistence rates of 3.8% for NI-RADS 1, 17.2% for NI-RADS 2, and 59.4% for NI-RADS 3. A strong association between score and positive disease was found for primary site, lymph nodes, and all targets combined, and ROC analysis also demonstrated clinically significant and accurate performance in these categories. While adding additional NI-RADS categories may improve ROC performance, the simplicity of the current scale is appropriate for the limited management options: routine surveillance, shorter interval follow-up, additional PET/CT imaging, mucosal inspection, or biopsy.

Because all these patients are part of our institutional surveillance program, with routine follow-up, it is reasonable for the specificity to be high and sensitivity lower. In fact, size cutoffs were set for the "ill-defined" or "questionable" NI-RADS 2 lesions to avoid low-yield, difficult, dangerous, or likely nondiagnostic

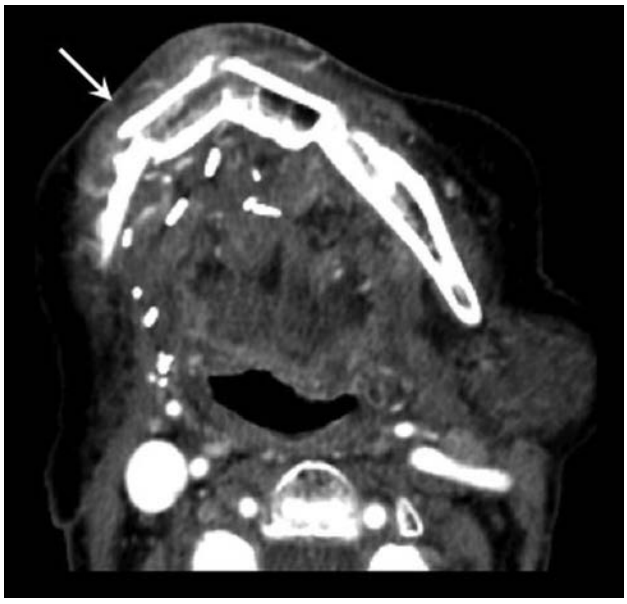

FIG 6. NI-RADS primary site category 2b: ill-defined asymmetric soft tissue. T4N0 oral cavity squamous cell carcinoma. CECT shows asymmetric full soft tissue around fibular reconstruction of the mandible (*arrow*). The linked management recommendation is shorter interval surveillance. Repeat CECT at 3 months showed no interval change (not shown). Subsequent clinical follow-up also demonstrated improvement and no disease recurrence.

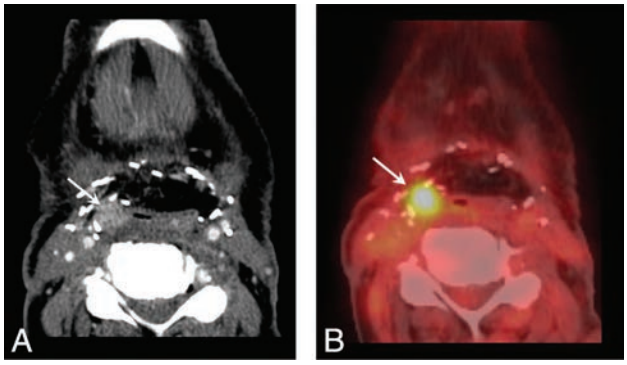

FIG 7. NI-RADS primary site category 3: discrete enhancing lesion. T4a larynx squamous cell carcinoma, status post total laryngectomy, bilateral neck dissection, and chemoradiotherapy. *A*, CECT shows a 1-cm discrete rounded hyperenhancing nodule along the lateral border of neopharynx, deep to the flap (*arrow*). *B*, Fused PET images show focal high FDG uptake (*arrow*). This was given a category 3 score, and endoscopic biopsy demonstrated recurrence.

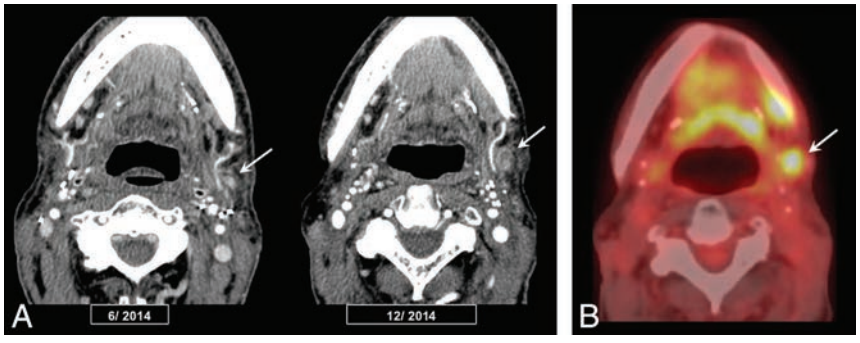

FIG 8. NI-RADS neck category 3: new or enlarged lymph node. T2N0 oral cavity squamous cell carcinoma status post resection, neck dissection, and adjuvant radiation therapy. *A*, CECT at 6-month intervals shows enlarging left level 1B lymph node with necrosis (*arrows*). *B*, Fused PET images show marked focal FDG uptake (*arrow*). Revision neck dissection was positive for disease recurrence.

biopsies for an intermediate suspicion lesion in a complex posttreatment neck if short-interval follow-up or PET would be a viable option. Because size was not helpful in predicting recurrence or for practical management decisions, our revised NI-RADS category 2 does not have size criteria and management consists of earlier follow-up or PET. Biopsy recommendations are reserved for category 3 lesions only. In our experience with highly suspicious lesions, size rarely determines recurrence, compared with enhancement characteristics, morphology, interval change, and FDG uptake, which have been incorporated into the NI-RADS lexicon.

Our NI-RADS template has been useful in daily clinical practice. For the primary site, the 2a category is used for low-suspicion superficial mucosal lesions with a linked recommendation of direct inspection. Focal asymmetric enhancement and FDG uptake are not an uncommon finding in posttreatment imaging and could represent benign mucositis or early recurrence/persistence. Although many mucosal abnormalities are false-positives (Fig 4), we are able to identify mucosal recurrences, especially in the post-radiated larynx where abnormalities may be subtle on CECT (Fig 5*A*). In this clinical scenario, the fused PET images (Fig 5*B*) help direct inspection and biopsy. For the primary site, the 2b category is used for deep, ill-defined, nondiscrete, low-suspicion lesions with only mild FDG uptake (if combined with PET) (Fig 6). In practice, most category 2 lesions are managed with short-term follow-up rather than biopsy because clinicians and patients were comfortable waiting. Short-term follow-up has become our official recommendation in this category because size criteria were removed.

Finally, NI-RADS 3 is reserved for a discrete, nodular, robustly enhancing lesion (Fig 7*A*) with marked FDG uptake if PET was also performed (Fig 7*B*), and the recommendation is for biopsy. In the neck, NI-RADS 3 is a new or enlarging lymph node (Fig 8*A*) with marked FDG uptake if PET is combined (Fig 8*B*). The positive predictive value for NI-RADS 3 primary site lesions was lower (54.6%) than for the neck (70%); this finding likely reflects the more complex posttreatment imaging appearance at the primary site. Overall, we believe that the NI-RADS template yielded a reasonable rate of recommending biopsy. Only 32 of 618 possible targets (5.2%) were scored category 3 with biopsy recommendation, balanced against a relatively high positive predictive value (54.6% for the primary site, 70% for the neck).

Our subgroup analyses highlight areas for future study. Although the numbers are small, our data suggest that CECT alone may be more specific because the rate of true persistence/recurrence was much higher for a NI-RADS 3 for CECT (91.7%) alone versus CECT/PET (40%). We also separated our scans into the first posttreatment baseline at 3 months and subsequent surveillance studies to understand the variation of NI-RADS performance at different time points. As expected, a NI-RADS 1 on a subsequent follow-up examination had a higher negative predictive value than on the initial posttreatment examination. This is valu-

able in providing guidance to patients regarding their risk of disease at different time points.

Finally, NI-RADS provides a meaningful framework for discussion of results with patients. For example, a patient with a NI-RADS 2 on surveillance imaging has a chance of recurrence of roughly 17.2%. We can also reassure patients with NI-RADS 1 that their overall recurrence rate is low (3.8%). There is an opportunity to understand the negative and positive predictive values of NI-RAD scores at different time points in further subpopulation studies. For example, our subgroup analysis and comparison of NI-RADS 1 score primary site recurrence rates for the initial posttreatment examinations versus subsequent examinations found a difference (9.3% versus 2.4%, $P = .047$), but the overall numbers were small because the incidence of recurrence in this group was so low. This analysis suggests that a NI-RADS 1 on the initial baseline posttreatment examination is not as reassuring as a NI-RADS 1 on subsequent surveillance examinations.

CONCLUSIONS

The performance of NI-RADS was good, demonstrating significant discrimination between groups, with positive disease rates of 3.8% for NI-RADS 1, 17.2% for NI-RADS 2, and 59.4% for NI-RADS 3. Standardization of linked management recommendations and correlation with patient outcomes should validate performance and highlight the added value of radiologists in patient care.

REFERENCES

1. Dodd GD 3rd, Allen B Jr, Birzniek D, et al. **Reengineering the radiology enterprise: a summary of the 2014 Intersociety Committee Summer Conference.** *J Am Coll Radiol* 2015;12:228–34 CrossRef Medline
2. Mitchell DG, Bruix J, Sherman M, et al. **LI-RADS (Liver Imaging Reporting and Data System): summary, discussion, and consensus of the LI-RADS Management Working Group and future directions.** *Hepatology* 2015;61:1056–65 CrossRef Medline
3. Weinreb JC, Barentsz JO, Choyke PL, et al. **PI-RADS Prostate Imaging-Reporting and Data System: 2015, Version 2.** *Eur Urol* 2016;69:16–40 CrossRef Medline
4. Cheng SP, Lee JJ, Lin JL, et al. **Characterization of thyroid nodules using the proposed thyroid imaging reporting and data system (TI-RADS).** *Head Neck* 2013;35:541–47 CrossRef Medline
5. Aiken AH, Farley A, Baugnon KL, et al. **Implementation of a novel surveillance template for head and neck cancer: Neck Imaging Reporting and Data System (NI-RADS).** *J Am Coll Radiol* 2016;13:743–46.e1 CrossRef Medline
6. Leung AS, Rath TJ, Hughes MA, et al. **Optimal timing of first posttreatment FDG PET/CT in head and neck squamous cell carcinoma.** *Head Neck* 2016;38(suppl 1):E853–58 CrossRef Medline
7. Gilbert MR, Branstetter BF 4th, Kim S. **Utility of positron-emission tomography/computed tomography imaging in the management of the neck in recurrent laryngeal cancer.** *Laryngoscope* 2012;122:821–25 CrossRef Medline
8. Koshkareva Y, Branstetter BF 4th, Gaughan JP, et al. **Predictive accuracy of first post-treatment PET/CT in HPV-related oropharyngeal squamous cell carcinoma.** *Laryngoscope* 2014;124:1843–47 CrossRef Medline
9. McDermott M, Hughes M, Rath T, et al. **Negative predictive value of surveillance PET/CT in head and neck squamous cell cancer.** *AJNR Am J Neuroradiol* 2013;34:1632–36 CrossRef Medline
10. Pfister DG, Spencer S, Brizel DM, et al; National Comprehensive Cancer Network. **Head and neck cancers, Version 2.2014: clinical practice guidelines in oncology.** *J Natl Compr Canc Netw* 2014;12:1454–87 Medline
11. Roman BR, Patel SG, Wang MB, et al. **Guideline familiarity predicts variation in self-reported use of routine surveillance PET/CT by physicians who treat head and neck cancer.** *J Natl Compr Canc Netw* 2015;13:69–77 Medline
12. Ho AS, Tsao GJ, Chen FW, et al. **Impact of positron emission tomography/computed tomography surveillance at 12 and 24 months for detecting head and neck cancer recurrence.** *Cancer* 2013;119:1349–56 CrossRef Medline
13. Ong SC, Schöde H, Lee NY, et al. **Clinical utility of 18F-FDG PET/CT in assessing the neck after concurrent chemoradiotherapy for locoregional advanced head and neck cancer.** *J Nucl Med* 2008;49:532–40 CrossRef Medline

Pretreatment ADC Values Predict Response to Radiosurgery in Vestibular Schwannomas

A. Camargo, T. Schneider, L. Liu, J. Pakpoor, L. Kleinberg, and D.M. Yousem

ABSTRACT

BACKGROUND AND PURPOSE: The response rate of vestibular schwannomas to radiation therapy is variable, and there are surgical options available in the event of treatment failure. The aim of this study was to determine whether pre- and posttreatment ADC values can predict the tumor response to radiation therapy.

MATERIALS AND METHODS: From a data base of 162 patients with vestibular schwannomas who underwent radiation therapy with gamma knife, CyberKnife, or fractionated stereotactic radiation therapy as the first-line therapy between January 2003 and December 2013, we found 20 patients who had pretreatment ADC values. There were 108 patients (including these 20) had serial MR images that included DWI allowing calculated ADC values from 2–132 months after radiation therapy. Two reviewers measured the mean, minimum, and maximum ADC values from elliptical ROIs that included tumor tissue only. Treatment responders were defined as those with a tumor total volume shrinkage of 20% or more after radiation therapy.

RESULTS: The pretreatment mean minimum ADC for nonresponders was 986.7×10^{-6} mm^2/s (range, 844–1230 $\times 10^{-6}$ mm^2/s) and it was 669.2×10^{-6} mm^2/s (range, 345–883 $\times 10^{-6}$ mm^2/s) for responders. This difference was statistically significant ($P < .001$). Using a minimum ADC value of 800×10^{-6} mm^2/s led to the correct classification of 18/20 patients based on pretreatment ADC values. The intraclass correlation between reviewers was 0.61. No posttreatment ADC values predicted response.

CONCLUSIONS: Pretreatment ADC values of vestibular schwannomas are lower in responders than nonresponders. Using a minimum ADC value of 800×10^{-6} mm^2/s correctly classified 90% of cases.

ABBREVIATIONS: TTV = total tumor volume; VS = vestibular schwannoma

Tumors localized in the cerebellopontine angle comprise 5%–10% of all intracranial tumors.[1] Vestibular schwannomas (VSs) are the most common tumors in the cerebellopontine angle, accounting for 80% of all tumors there.[2,3] Epidemiologic data of VSs suggest the most common patients to be white and aged 50–60 years, with equal distribution between the sexes.[4]

The diagnosis of VS is suggested by symptoms that may include tinnitus, hearing loss, trigeminal neuropathy, facial nerve palsy, unstable gait, or increased intracranial pressure.[5,6] High-resolution MR imaging has led to a greater number of smaller VSs being diagnosed in recent decades.[7]

Few studies have evaluated the appearance of vestibular schwannomas on DWI. Chuang and colleagues[8] have proposed that high ADCs of VSs may correlate with Antoni type B, which is associated with a cystic tumor pattern. However, this correlation is still controversial because the reviewed literature has not proved the correlation between Antoni type dominance and cystic composition.[9] Tumors with sparse cellularity (Antoni B type) are associated with higher ADC values compared with tumors with an attenuated cellularity.[10]

The options for managing VS include observation, surgery, and radiation therapy.[11-14] Usually, newly diagnosed and small VSs are managed expectantly with serial imaging follow-up and observation because many tumors remain stable over long periods of time. However, up to half of the tumors grow within 5 years of follow-up.[15] Studies also state, however, that a wait-and-see policy is not recommended for patients with cystic tumors[16,17] because they tend to be larger and usually have a more rapid clinical evolution.[6,18] Specifically, for cystic VS, surgical treat-

Received October 27, 2016; accepted after revision January 22, 2017.

From the Division of Neuroradiology and Russell H. Morgan Department of Radiology and Radiological Science (A.C., L.L., J.P., D.M.Y.) and Department of Radiation Oncology (L.K.), Johns Hopkins Medical Institutions, Baltimore, Maryland; and the Department of Diagnostic and Interventional Neuroradiology (T.S.), University Medical Center Hamburg-Eppendorf, Hamburg Germany.

Please address correspondence to David M. Yousem, MD, MBA, Johns Hopkins Medical Institutions, 600 North Wolfe St, Phipps B100F, Baltimore, MD 21287; e-mail: dyousem1@jhu.edu

http://dx.doi.org/10.3174/ajnr.A5144

ment is the best option, and it is associated with better results than radiosurgery.[1] Other than in this cystic VS scenario, where the recommendation is firm, patient preference becomes paramount in the selection between surgery and radiosurgery for treatment. Both are considered appropriate, with similarly acceptable side effects and long-term success. The decision may be guided by multiple variables, such as the size at initial diagnosis, tumor growth rate on serial imaging, or patient symptoms.[7,19] More reliable patient-specific predictors of outcome with therapy are needed to guide patients and physicians in this important decision.

ADC is a measure of the random motion of water molecules within a tissue, and it is calculated by using data from DWI or DTI.[20,21] ADC values have been shown to be correlated with astrocytoma tumor grading and tumor cellularity.[19,20] ADC measurements may serve as diagnostic and prognostic biomarkers as well as predictors of tumor response to treatment in glial tumors.[22,23] Thus, ADC values are often used in treatment planning.[24]

The aim of this study was to determine whether the pre- and posttreatment ADC values may be associated with the response of VS to radiosurgery and to provide guidance for further study.

MATERIALS AND METHODS

This single-center retrospective study was approved by the institutional review board and was compliant with the U.S. Health Insurance Portability and Accountability Act. The study took place at the Johns Hopkins Medical Institution. Patient consent requirements were waived for this retrospective study.

We selected patients with VS who underwent radiation therapy with gamma knife, CyberKnife (Accuray, Sunnyvale, California), or fractionated stereotactic radiation therapy as the first-line therapy at our institution between January 2003 and December 2013. Based on our initial list of 162 patients, 142 patients had MR imaging scans that either did not include pretreatment DWI scans or had artifacts that precluded measurement of ADC values. Twenty patients had pretreatment studies with diffusion-weighted sequences that allowed ADC calculations and ROI analysis. These scans took place 1–24 months before radiation therapy. The ADC values were derived by putting elliptical ROIs on the tumor from the postprocessed ADC maps derived from the DWI sequences. We used a single ROI encompassing the entire tumor on the single section that had the least amount of artifact from the adjacent (aerated) petrous/mastoid temporal bone. The ROI provided mean, maximum, and minimum ADC values from the Carestream PACS (Carestream Health, Rochester, New York) (Figs 1 and 2). Maximum, minimum, and mean ADC values were derived from DWI pulse sequences. The person performing the ADC ROI analysis was blinded to the tumor response. A second reviewer performed the ADC analyses independently and was blinded to the radiation therapy results. Based on the presence or absence of bright T2WI signal intensity and peripheral enhancement, the tumors were labeled as cystic or solid.

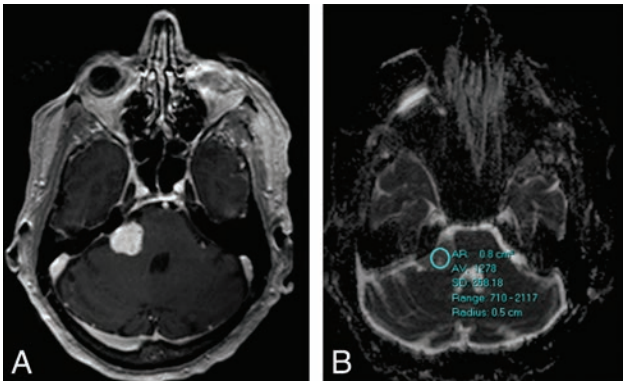

FIG 1. *A*, Postcontrast T1-weighted axial scan through the posterior fossa shows a right cerebellopontine angle vestibular schwannoma. *B*, The ADC values were calculated from an elliptical region of interest.

Standard DWI pulse sequences with 3 tensors were performed on Siemens (1.5T and 3T; Erlangen, Germany), GE Healthcare (1.5T; Milwaukee, Wisconsin), and Philips Healthcare (1.5T and 3T; Best, the Netherlands) magnets. DWI was performed with an EPI sequence with a TR/TE range of 4900–10000 ms/80–133 ms; 5-mm thin contiguous sections; FOV, 220 × 220 mm to 240 × 240 mm; and a matrix size of 96 × 96 to 192 × 192. Diffusion was measured in the 6 orthogonal directions with 2 b-values (0 and 1000 seconds/mm^2) with automated postprocessed ADC maps. MR imaging studies were obtained on 1.5T (84%; GE Healthcare, Siemens, or Philips Healthcare) or 3T scanners (16%; Siemens or Philips Healthcare).

Single-session radiosurgery was performed with Leksell Gamma Knife Perfexion (Elekta Instruments, Stockholm, Sweden). Fractionated stereotactic radiation therapy was linear accelerator-based, using either the BrainLAB (BrainLAB, Feldkirchen, Germany) or Pinnacle (Philips Healthcare) treatment planning system.

To further evaluate the role of ADC values as a predictor of therapy response, we sought to collect the ADC values during the follow-up period after radiation therapy. Of the 162 patients evaluated, 54 patients were excluded due to absent or nondiagnostic ADC maps. The ADC values of 108 patients were collected during the follow-up period, from 2–132 months after the date of radiation therapy.

Tumor response was defined as a tumor total volume (TTV) shrinkage of 20% or more after radiation therapy. The tumor total volume was derived by subtracting the follow-up volume from the initial tumor volume and dividing by the initial tumor volume. This value was chosen based on previous work by Plotkin et al,[25] who proposed a tumor volumetric reduction of 20% to define treatment response, based on pre- and posttreatment tumor volumes. The TTV for each patient was obtained from a previous research project that evaluated the VS volumetrically.[26] The volumetric

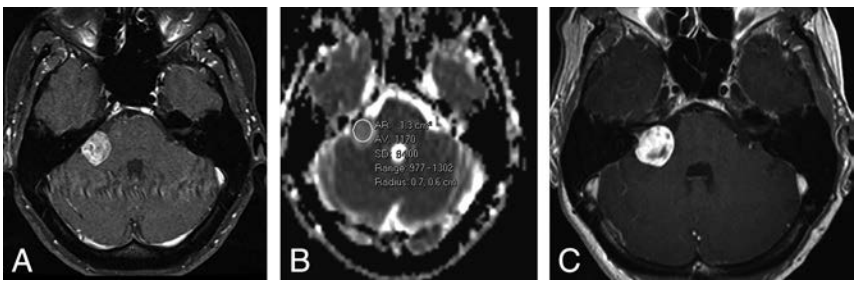

FIG 2. *A*, Right vestibular schwannoma at baseline on postcontrast axial T1-weighted scan. *B*, ADC calculation showing minimum value of 977 × 10^{-6} mm^2/s. This would predict treatment failure. *C*, Four-year follow-up shows tumor growth on the postcontrast axial T1-weighted scan.

Characteristics of nonresponders versus responders[a]

Characteristics	Nonresponders (n = 11)	Responders (n = 9)	P Value
Sex (F/M)	8/3	5/4	.64
Age (yr)	62.2 (54–86)	61.8 (41–84)	.71
Pretreatment measures			
Initial TTV (cc^3)	0.87 (0.35–2.78)	2.34 (0.39–13.39)	.15
Linear size (cm)	1.7 (1.0–2.0)	1.6 (1.1–3.4)	.28
Mean minimum ADC ($\times 10^{-6}$ mm^2/s)	986.7 (844–1230)	669.2 (345–884)	<.01
Mean of mean ADC ($\times 10^{-6}$ mm^2/s)	1444.4 (1259.6–1629.1)	1182.1 (988.8–1375.4)	.04
Posttreatment measures			
Posttreatment TTV (cc^3)	2.10 (0.30–5.68)	0.43 (0.29–6.84)	.08
Percent of TTV reduction (%)	−26.05 (−333.33–18.92)	48.92 (20.37–88.32)	<.01

[a] Data presented as median (range).

analysis was performed by a 3D semiautomated quantitative assessment of TTV, and the follow-up was defined as the time from the last radiation therapy session to the date of the most recent MR imaging study obtained in our institution.[26]

We also measured the longest dimension of the tumor in axial, craniocaudal, or anteroposterior dimension. We used electronic calipers to measure the largest diameter of the lesion from axial and coronal images.

Statistical Analysis

Statistical analyses were performed by using Stata 12 (StataCorp, College Station, Texas). The Student t test was used to test the difference in mean ADC value between responders and nonresponders. The association between ADC values and tumor size measures was evaluated by using the Spearman correlation. Logistic regression was used to assess the pretreatment ADC values in predicting the treatment response (responders versus nonresponders), adjusting for initial tumor size. Robust option was used for variance estimates. ROC curve analyses were performed on the serial cutoff values of minimum ADC. Sensitivity and specificity and area under the curve, with 95% CI, were used to evaluate the overall classification accuracy. Intraclass correlation coefficient and κ values were calculated for the reliability test on ADC values reported by the 2 observers. For the wide range of tumor volume data, log-transformed TTV values were used for the statistical significance test and modeling. A P value of .05 or less was considered statistically significant.

RESULTS

Pretreatment ADC Values

For the 20 patients who had pretreatment ADC values, the median follow-up was 3.54 years. Based on a TTV reduction of 20% or more as response criterion, 11 did not respond (55%) and 9 responded (45%) to treatment. The initial TTV was higher for responders than nonresponders (Table). Responders received fractionated stereotactic radiation therapy (n = 3), CyberKnife (n = 1), and gamma knife (n = 5); nonresponders received fractionated stereotactic radiation therapy (n = 2), CyberKnife (n = 2), and gamma knife (n = 7).

The mean of the minimum ADC values for nonresponders was 986.7 × 10^{-6} mm^2/s (range, 844–1230 × 10^{-6} mm^2/s; median, 944 × 10^{-6} mm^2/s; SD, 261 × 10^{-6} mm^2/s) and for responders, the mean was 669.2 × 10^{-6} mm^2/s (range, 345–884 × 10^{-6} mm^2/s; median, 747 × 10^{-6} mm^2/s; SD, 184.0 × 10^{-6} mm^2/s). Nonresponse status was associated with statistically significant higher minimum ADC values (P < .001). If one used a minimum ADC value of 800 × 10^{-6} mm^2/s as the cut-point, one could distinguish nonresponders from responders in 18/20 (90.0%) patients, with the 2 outliers being responders with a minimum ADC value of 877 × 10^{-6} mm^2/s and 884 × 10^{-6} mm^2/s based on pretreatment ADC values. The resulting sensitivity and specificity were 77.8% and 100%, respectively. The ROC area was 0.89 (95% CI, 0.74–1.00). The minimum ADC value had a statistically significant correlation with percent of tumor size reduction (Spearman ρ = 0.71; P < .001). The logistic regression analysis showed that the pretreatment ADC values were predictive of response. The odds ratio of being a nonresponder for each 10 × 10^{-6} mm^2/s increase of minimum ADC value was 1.32 (95% CI, 1.14–1.52) and was 1.04 (95% CI, 1.01–1.08) for the same increase in mean ADC value. When controlling for pretreatment tumor volume and the largest 2D linear measurement of the tumor, each 10 × 10^{-6} mm^2/s increase in the mean ADC value predicted an 8% increase in the likelihood of being a nonresponder (odds ratio, 1.08; 95% CI, 1.02–1.14).

Based on the 20 patients who had baseline data, nonresponders had a smaller initial volume than responders (0.87 mL versus 2.34 mL) and similar maximum linear measurements (1.7 cm versus 1.6 cm), but the differences were not statistically significant. The correlation between pretreatment TTV and percent of tumor size reduction was not significant (correlation coefficient, 0.39; P = .09).

There was no association between mean and maximum ADC values, initial and posttreatment TTV, or linear size and response.

Reliability tests on ADC values were performed on 20 images by 2 observers. For the quantitative minimum ADC values, the intraclass correlation coefficient is 0.61. Using the cutoff of 800 × 10^{-6} mm^2/s and making the minimum ADC values as 2 categorical scales, the actual agreement is 89.4% and κ is 0.77 (95% CI, 0.34–0.94). Based on Landis and Koch's[27] seminal work (with κ values graded as follows: <0 as no agreement, 0–0.20 as slight, 0.21–0.40 as fair, 0.41–0.60 as moderate, 0.61–0.80 as substantial, and 0.81–1 as almost perfect), the level of agreement was substantial.

Posttreatment ADC Values

Posttreatment ADC values were available for 108 patients. There were 197 posttreatment ADC values obtained from the 108 patients. Of the 108 patients, 48 had only 1 posttreatment ADC value available. The median follow-up to assess TTV among all 108 patients was 4.96 years. Eighty-one (75%) patients received fractionated stereotactic radiation therapy, 21 (19.5%) received gamma knife, and 6 (5.5%) received CyberKnife. Based on the same response criteria, there were 56 nonresponders and 52 responders. We calculated the mean ADC values of all patients at each year, from year 1 to year 10. Repeated measure analysis on multiple ADC values observed over the years after radiation therapy did not result in any significant findings in the change/pattern of any ADC values (mean, minimum, and maximum).

Imaging Features Besides ADC Values

Of the 20 patients evaluated before treatment, 18 had solid tumors (based on homogeneous enhancement) and 2 had mixed cystic and solid tumors (predominantly solid). The T2-weighted signal intensity was graded based on comparison with cortical gray matter. Fourteen VSs were darker on T2WI than the gray matter, 2 were brighter, 2 were isointense, and 2 had mixed darker and brighter portions (the cystic and solid cases described above). None of these factors were predictive of radiation response. One mixed lesion was a responder, and the other was not.

DISCUSSION

Small to medium-sized VSs have proved to be, in general, the best candidates for radiation therapy because of better hearing preservation, less facial nerve palsy, good tumor control, and favorable mortality and morbidity rates in patients.[28,29] Ninety-two percent of patients treated with gamma knife radiosurgery have shown tumor control in a follow-up of 7 years, associated with high rates of quality of life.[30] It also has been stated that fractionated stereotactic radiation therapy is associated with a tumor control rate of 97.5% and excellent quality of life (improvement of tinnitus and vertigo and low rates of hearing impairment and trigeminal and facial nerve damage).[31,32] Very long-term outcome data are not available.

Studies have tried to correlate the initial imaging findings and the clinical presentation of VS with tumor natural course and/or treatment response. It has been reported, however, that clinical worsening and original VS volume and size are not able to predict tumor growth.[15,33,34] Our study has shown that minimum ADC values for VS tumors, using a cutoff of 800×10^{-6} mm^2/s, predict tumor response with 90% accuracy, 77.8% sensitivity, and 100% specificity. All nonresponders showed ADC values greater than 800×10^{-6} mm^2/s.

As in this study, Plotkin et al[25] defined a treatment response based on tumor volumetric reduction of 20% when comparing pre- and posttreatment tumor volumes. Studies based on this 20% threshold reported that 17% of tumors have pseudoprogression (see explanation below), 52% regress, and 10.6% progress.[25,35] In this study, we report a 20% reduction in tumor volume in 9 (45%) of 20 patients with preoperative ADC values and 52 (48.1%) of the 108 patients. Please note that by Plotkin et al's[25] definition, a stable tumor volume (no growth) would be considered absence of response, a definition to which most radiation oncologists may object.

After radiation therapy, the well-known phenomenon of transient tumor enlargement must be considered before classifying the response as treatment failure.[36,37] This pseudoprogression phenomenon is often transient and tends to start 6–9 months after radiosurgery peaking in the year that follows radiosurgery[35-38] Five percent to 10% of patients show tumor volume increase, followed by stabilization.[35-37,39]

Failure of radiation therapy, defined as sustained tumor growth, is rare, accounting for less than 5% of cases, and has been (in the literature, but not our study) more frequently associated with large tumor volume at the time of treatment, inadequate radiation therapy dose coverage, and cystic VS.[29] However, it is important to report that no guideline or consensus is available to standardize the definition of responders and nonresponders for VS management. This explains the different rates of treatment failure versus success in the literature, given the variable criteria adopted.

Microsurgery and/or additional radiosurgery are the options for treatment failure; the choice is based on the tumor size and clinical tolerance.[29] Patients who have undergone salvage microsurgery after radiation therapy have experienced poorer outcomes compared with those who never received irradiation,[40] and salvage microsurgery is associated with a high risk of facial nerve injury, likely resulting from the challenge of postradiosurgery fibrosis.[41] It is better to get the choice of treatment at the outset rather than after a failed therapy. Hence, the goal of this study was to find parameters that will predict radiosurgery treatment response.

Because sustained tumor growth must be confirmed with sequential follow-up images after radiation therapy before determining response,[29] the recommended time for tumor response assessment should be at or after 36 months.[35] This is particularly important if the clinical symptoms do not correlate with the treatment response.[37] It also has been proposed that VSs that enlarge beginning after 24 months usually correspond to treatment failure.[35] To ensure a reliable final TTV and, thus, response classification, we selected cases from before 2013 to obtain accurate treatment response volumes (median, 3.54 years for pretreatment ADC assessment and 4.96 years for posttreatment ADC evaluation).

ADC values have been correlated with the tumor cell attenuation, with high values usually indicating low cellularity, necrosis, or cystic features.[42-44] We found that the minimum ADC values were more reflective of tumor response than mean or maximum ADC values, which might be useful in characterizing cystic schwannomas. Our study observed that patients classified as nonresponders had higher ADC values, whereas responders showed the opposite trend, with lower ADC values. We did not find studies in the literature based on pretreatment ADC values in VS as therapeutic predictors. Thus, we believe that our findings should lead to prospective studies regarding the use of ADC before therapy to guide treatment planning and management.

Chuang and colleagues[8] have stated that ADC may be used during follow-up to assess tumor response in VS after gamma knife radiosurgery. In our study, however, the evaluation of posttreatment ADC values did not show statistically significant correlation with tumor response. After radiation therapy, the tumor tissue architecture is affected, cytotoxicity may occur, and vasogenic edema arises, leading to changes in the water diffusion within the tumor and, therefore, in ADC values.[8,9,45] We believe that these phenomena may occur in the tumor architecture after radiation therapy and can lead to changes in ADC values, making them unable to predict a reliable response/nonresponse status.

This study has some limitations. Being a retrospective study, we could not control the heterogeneity of MR imaging quality, artifacts regarding ADC, the heterogeneity of DWI/DTI pulse sequences performed, and the timing of the MR imaging before the institution of radiation therapy. In addition, imaging was performed on different scanner types. In a similar fashion, there was lack of uniformity in the type of radiation therapy used (gamma knife, CyberKnife, and fractionated stereotactic radiation therapy were the modalities used). In this study, we adopted only radiologic response criteria; no quality of life assessment was used.

Nonetheless, the difference in minimum pretreatment ADC values between responders and nonresponders was striking and statistically significant. Using a minimum ADC value of 800×10^{-6} mm^2/s correctly classified tumor response in 90% of cases, with high ($\kappa = 0.77$) interobserver agreement.

CONCLUSIONS

It would be useful, a priori, to predict a vestibular schwannoma's likely response to radiosurgery techniques. Our study suggests that high ADC values before treatment (above 800×10^{-6} mm^2/s) predict less benefit for radiosurgery. This statistically significant correlation should lead to prospective studies, using homogeneous pulse sequences and scanning techniques, confirming the value of pretreatment ADC as an important predictor for the planning and management of vestibular schwannomas.

REFERENCES

1. Sinha S, Sharma BS. **Cystic acoustic neuromas: surgical outcome in a series of 58 patients.** *J Clin Neurosci* 2008;15:511–15 CrossRef Medline
2. Wandong S, Meng L, Xingang L, et al. **Cystic acoustic neuroma.** *J Clin Neurosci* 2005;12:253–55 CrossRef Medline
3. Benech F, Perez R, Fontanella MM, et al. **Cystic versus solid vestibular schwannomas: a series of 80 grade III-IV patients.** *Neurosurg Rev* 2005;28:209–13 CrossRef Medline
4. Berkowitz O, Iyer AK, Kano H, et al. **Epidemiology and environmental risk factors associated with vestibular schwannoma.** *World Neurosurg* 2015;84:1674–80 CrossRef Medline
5. Asano K, Ebina K, Sekiya T, et al. **Acoustic neurinomas with large cystic components: a clinical and pathological study of 3 cases. [Article in Japanese]** *No Shinkei Geka* 1995;23:1075–82
6. Kameyama S, Tanaka R, Kawaguchi T, et al. **Cystic acoustic neurinomas: studies of 14 cases.** *Acta Neurochir (Wien)* 1996;138:695–99 CrossRef Medline
7. Stangerup SE, Caye-Thomasen P. **Epidemiology and natural history of vestibular schwannomas.** *Otolaryngol Clin North Am* 2012;45:257–68, vii CrossRef Medline
8. Chuang CC, Chang CS, Tyan YS, et al. **Use of apparent diffusion coefficients in evaluating the response of vestibular schwannomas to Gamma Knife surgery.** *J Neurosurg* 2012;117:63–68 CrossRef
9. Park CK, Kim DC, Park SH, et al. **Microhemorrhage, a possible mechanism for cyst formation in vestibular schwannomas.** *J Neurosurg* 2006;105:576–80 CrossRef Medline
10. Chenevert TL, McKeever PE, Ross BD. **Monitoring early response of experimental brain tumors to therapy using diffusion magnetic resonance imaging.** *Clin Cancer Res* 1997;3:1457–66 Medline
11. Sawamura Y, Shirato H, Sakamoto T, et al. **Management of vestibular schwannoma by fractionated stereotactic radiotherapy and associated cerebrospinal fluid malabsorption.** *J Neurosurg* 2003;99:685–92 CrossRef Medline
12. Godefroy WP, van der Mey AG, de Bruine FT, et al. **Surgery for large vestibular schwannoma: residual tumor and outcome.** *Otol Neurotol* 2009;30:629–34 CrossRef Medline
13. Link MJ, Driscoll CL, Foote RL, et al. **Radiation therapy and radiosurgery for vestibular schwannomas: indications, techniques, and results.** *Otolaryngol Clin North Am* 2012;45:353–66, viii-ix CrossRef Medline
14. Gerganov VM, Samii M. **Giant vestibular schwannomas.** *World Neurosurg* 2012;77:627–28 CrossRef Medline
15. Paldor I, Chen AS, Kaye AH. **Growth rate of vestibular schwannoma.** *J Clin Neurosci* 2016;32:1–8 CrossRef Medline
16. Charabi S, Tos M, Børgesen SE, et al. **Cystic acoustic neuromas. Results of translabyrinthine surgery.** *Arch Otolaryngol Head Neck Surg* 1994;120:1333–38 CrossRef Medline
17. Charabi S, Thomsen J, Mantoni M, et al. **Acoustic neuroma (vestibular schwannoma): growth and surgical and nonsurgical consequences of the wait-and-see policy.** *Otolaryngol Head Neck Surg* 1995;113:5–14 CrossRef Medline
18. Kameyama S, Tanaka R, Honda Y, et al. **The long-term growth rate of residual acoustic neurinomas.** *Acta Neurochir (Wien)* 1994;129:127–30 CrossRef Medline
19. Bakkouri WE, Kania RE, Guichard JP, et al. **Conservative management of 386 cases of unilateral vestibular schwannoma: tumor growth and consequences for treatment.** *J Neurosurg* 2009;110:662–69 CrossRef Medline
20. Le Bihan D, Breton E, Lallemand D, et al. **Separation of diffusion and perfusion in intravoxel incoherent motion MR imaging.** *Radiology* 1988;168:497–505 CrossRef Medline
21. Lu S, Ahn D, Johnson G, et al. **Peritumoral diffusion tensor imaging of high-grade gliomas and metastatic brain tumors.** *AJNR Am J Neuroradiol* 2003;24:937–41 Medline
22. Baehring JM, Bi WL, Bannykh S, et al. **Diffusion MRI in the early diagnosis of malignant glioma.** *J Neurooncol* 2007;82:221–25 CrossRef Medline
23. Hwang EJ, Cha Y, Lee AL, et al. **Early response evaluation for recurrent high grade gliomas treated with bevacizumab: a volumetric analysis using diffusion-weighted imaging.** *J Neurooncol* 2013;112:427–35 CrossRef Medline
24. Ignjatović J, Stojanov D, Zivković V, et al. **Apparent diffusion coefficient in the evaluation of cerebral gliomas malignancy.** *Vojnosanit Pregl* 2015;72:870–75 CrossRef Medline
25. Plotkin SR, Halpin C, Blakeley JO, et al. **Suggested response criteria for phase II antitumor drug studies for neurofibromatosis type 2 related vestibular schwannoma.** *J Neurooncol* 2009;93:61–77 CrossRef Medline
26. Schneider T, Chapiro J, Lin M, et al. **3D quantitative assessment of response to fractionated stereotactic radiotherapy and single-session stereotactic radiosurgery of vestibular schwannoma.** *Eur Radiol* 2016;26:849–57 CrossRef Medline
27. Landis JR, Koch GG. **The measurement of observer agreement for categorical data.** *Biometrics* 1977;33:159–74 CrossRef Medline
28. Myrseth E, Møller P, Pedersen PH, et al. **Vestibular schwannoma: surgery or gamma knife radiosurgery? A prospective, nonrandomized study.** *Neurosurgery* 2009;64:654–63; discussion 661–63 CrossRef Medline
29. Roche PH, Noudel R, Régis J. **Management of radiation/radiosurgical complications and failures.** *Otolaryngol Clin North Am* 2012;45:367–74, ix CrossRef Medline
30. Wangerid T, Bartek J Jr, Svensson M, et al. **Long-term quality of life and tumour control following gamma knife radiosurgery for vestibular schwannoma.** *Acta Neurochir* 2014;156:389–96 CrossRef Medline
31. Fuss M, Debus J, Lohr F, et al. **Conventionally fractionated stereotactic radiotherapy (FSRT) for acoustic neuromas.** *Int J Radiat Oncol Biol Phys* 2000;48:1381–87 CrossRef Medline
32. Litre F, Rousseaux P, Jovenin N, et al. **Fractionated stereotactic radiotherapy for acoustic neuromas: a prospective monocenter study of about 158 cases.** *Radiat Oncol* 2013;106:169–74 CrossRef Medline
33. Mohyuddin A, Vokurka EA, Evans DG, et al. **Is clinical growth index a reliable predictor of tumour growth in vestibular schwannomas?** *Clin Otolaryngol Allied Sci* 2003;28:85–90 CrossRef Medline
34. Herwadker A, Vokurka EA, Evans DGR, et al. **Size and growth rate of sporadic vestibular schwannoma: predictive value of information available at presentation.** *Otol Neurotol* 2005;26:86–92 CrossRef Medline
35. Hayhurst C, Zadeh G. **Tumor pseudoprogression following radiosurgery for vestibular schwannoma.** *Neuro Oncol* 2012;14:87–92 CrossRef Medline
36. Pollock BE, Lunsford LD, Kondziolka D, et al. **Vestibular schwannoma management. Part II. Failed radiosurgery and the role of delayed microsurgery.** *J Neurosurg* 1998;89:949–55 CrossRef Medline
37. Pollock BE. **Management of vestibular schwannomas that enlarge after stereotactic radiosurgery: treatment recommendations based on a 15 year experience.** *Neurosurgery* 2006;58:241–47 discussion 241–48 CrossRef Medline

38. Yu CP, Cheung JY, Leung S, et al. **Sequential volume mapping for confirmation of negative growth in vestibular schwannomas treated by gamma knife radiosurgery.** *J Neurosurg* 2000;93(Suppl 3):82–89 CrossRef Medline
39. Nagano O, Higuchi Y, Serizawa T, et al. **Transient expansion of vestibular schwannoma following stereotactic radiosurgery.** *J Neurosurg* 2008;109:811–16 CrossRef Medline
40. Friedman RA, Brackmann DE, Hitselberger WE, et al. **Surgical salvage after failed irradiation for vestibular schwannoma.** *Laryngoscope* 2005;115:1827–32 CrossRef Medline
41. Limb CJ, Long DM, Niparko JK. **Acoustic neuromas after failed radiation therapy: challenges of surgical salvage.** *Laryngoscope* 2005; 115:93–98 CrossRef Medline
42. Yang D, Korogi Y, Sugahara T, et al. **Cerebral gliomas: prospective comparison of multivoxel 2D chemical-shift imaging proton MR spectroscopy, echoplanar perfusion and diffusion-weighted MRI.** *Neuroradiol* 2002;44:656–66 CrossRef Medline
43. Ellingson BM, Timothy F, Cloughesy TF, et al. **Cell invasion, motility, and proliferation level estimate (CIMPLE) maps derived from serial diffusion MR images in recurrent glioblastoma treated with bevacizumab.** *J Neurooncol* 2011;105:91–101 CrossRef Medline
44. Nakamura H, Murakami R, Hirai T, et al. **Can MRI-derived factors predict the survival in glioblastoma patients treated with postoperative chemoradiation therapy?** *Acta Radiol* 2013;54:214–20 CrossRef Medline
45. Kauppinen RA. **Monitoring cytotoxic tumour treatment response by diffusion magnetic resonance imaging and proton spectroscopy.** *NMR Biomed* 2002;15:6–17 CrossRef Medline

MR Imaging Grading System for Skull Base Chordoma

K. Tian, L. Wang, J. Ma, K. Wang, D. Li, J. Du, G. Jia, Z. Wu, and J. Zhang

ABSTRACT

BACKGROUND AND PURPOSE: Skull base chordoma has been widely studied in recent years, however, imaging characteristics of this tumor have not been well elaborated. The purpose of this study was to establish an MR imaging grading system for skull base chordoma.

MATERIALS AND METHODS: In this study, 156 patients with skull base chordomas were retrospectively assessed. Tumor-to-pons signal intensity ratios were calculated from pretreatment MR images R_{T1} (ratio of tumor to pons signal intensity in T1 FLAIR sequence), R_{T2} (ratio of tumor to pons signal intensity in T2 sequence) and R_{EN} (ratio of tumor to pons signal intensity in enhanced T1 FLAIR sequence), and significant ratios for overall survival and progression-free survival were selected to establish a grading system. Clinical variables among different MR imaging grades were then analyzed to evaluate the usefulness of the grading system.

RESULTS: R_{T2} ($P < .001$) and R_{EN} ($P = .04$) were identified as significant variables affecting progression-free survival. After analysis, the classification criteria were set as follows: MR grade I, $R_{T2} > 2.49$ and $R_{EN} \leq 0.77$; MR grade II, $R_{T2} > 2.49$ and $R_{EN} > 0.77$, or $R_{T2} \leq 2.49$ and $R_{EN} \leq 0.77$; and MR grade III, $R_{T2} \leq 2.49$ and $R_{EN} > 0.77$. MR grade III tumors had a more abundant tumor blood supply than MR grade I tumors ($P < .001$), and the intraoperative blood loss of MR grade III tumors was higher than that of MR grade I tumors ($P = .002$). Additionally, skull base chordoma progression risk increased by 2.071 times for every single MR grade increase ($P < .001$).

CONCLUSIONS: A higher R_{T2} value was a negative indicator of tumor progression, whereas a higher R_{EN} value was a positive risk factor of tumor progression. MR grade III tumors showed a more abundant blood supply than MR grade I tumors, and the risk of skull base chordoma progression increased with every single MR grade increase.

ABBREVIATIONS: OS = overall survival; PFS = progression-free survival; SBC = skull base chordoma; SI = signal intensity

Chordoma is a malignant tumor that originates from notochord remnants, and this tumor often exhibits mild-to-moderate enhancement. It comprises 1.8%–4.3% of bone tumors and 3.9%–6.1% of malignant bone tumors,[1-3] and it shows a marked predilection for the axial skeleton. Chordoma primarily occurs in the skull base (32%–42%) and sacrococcygeal region (29.2%).[4,5] The prevalence of chordomas is 0.08–0.089 per 100,000, and males (0.01–0.016 per 100,000) have a higher incidence than females (0.06–0.066 per 100,000).[4-6] Chordoma is locally aggressive and may destroy surrounding bone. Skull base chordoma (SBC) often involves vital blood vessels, cranial nerves, and other important structures. Extensive resection of a skull base chordoma is difficult and may result in severe complications.[7] Chemotherapy usually has a minimal effect on chordomas, and the current best treatment is radical resection plus postoperative radiation therapy.[8,9] The median survival for patients with SBC is 151 months.[10] In recent years, new technologies such as endoscopy, intraoperative navigation, and electrophysiologic monitoring have facilitated more radical resections.[11] Although the proton beam, carbon ion, modulated and stereotactic techniques were applied in radiation therapy, the progression and mortality rates of skull base chordoma are still very high.[11-14]

The diagnosis and classification of chordoma primarily de-

Received October 14, 2016; accepted after revision January 22, 2017.

From the Department of Neurosurgery (K.T., L.W., J.M., K.W., D.L., G.J., Z.W., J.Z.), Beijing Tiantan Hospital, Capital Medical University, Beijing, China; China National Clinical Research Center for Neurological Diseases (K.T., L.W., J.M., K.W., D.L., G.J., Z.W., J.Z.), Beijing, China; Center of Brain Tumor (K.T., L.W., J.M., K.W., D.L., G.J., Z.W., J.Z.), Beijing Institute for Brain Disorders, Beijing, China; Beijing Key Laboratory of Brian Tumor (K.T., L.W., J.M., K.W., D.L., G.J., Z.W., J.Z.), Beijing, China; Department of Neuropathology (J.D), Beijing Neurosurgical Institute, Capital Medical University, Beijing, China; China National Clinical Research Center for Neurological Diseases (J.D.), Center of Brain Tumor, Beijing, China; and Institute for Brain Disorders (J.D.), Beijing Key Laboratory of Brain Tumor, Beijing, China.

This work was supported in part by the National Natural Science Foundation of China (grant no. 81472370 and 81541146), the Natural Science Foundation of Beijing Municipality, China (grant No. 7142052 and 7163212), and the National High Technology Research and Development Program 863 (grant no. 2014AA020610).

Please address correspondence to Junting Zhang, MD, and Liang Wang, MD, Department of Neurosurgery, Beijing Tiantan Hospital, Capital Medical University, Tiantan Xili 6, Dongcheng District, Beijing, 100050, China; e-mail: zhangjunting2003@aliyun.com and saintage7@126.com

http://dx.doi.org/10.3174/ajnr.A5152

pend on histopathologic evaluation and preoperative imaging data. Chordoma has 3 histologic types: conventional, chondroid, and dedifferentiated.[15] Conventional chordoma is the most common type, and patients with chondroid chordoma are reported to have the best prognoses.[8] Chordoma often shows low density and bone destruction on CT.[16] MR imaging is superior in detecting the tumor and delineating its extent.[17] Chordomas have a highly heterogeneous appearance on MR imaging, demonstrating hypo- to isointensity on T1 sequences and moderate-to-very-high intensity on T2 sequences. The tumor may exhibit minimal-to-moderate enhancement on enhanced T1 sequences (Fig 1). The clinical significance of this MR imaging heterogeneity has not been discussed in the literature, to our knowledge.

We thought that the clinical features and prognosis of SBCs were associated with the characteristics on MR imaging (Figs 1 and 2). The purpose of this study was to explore the value of MR signal intensity (SI) in establishing a grading system for SBC.

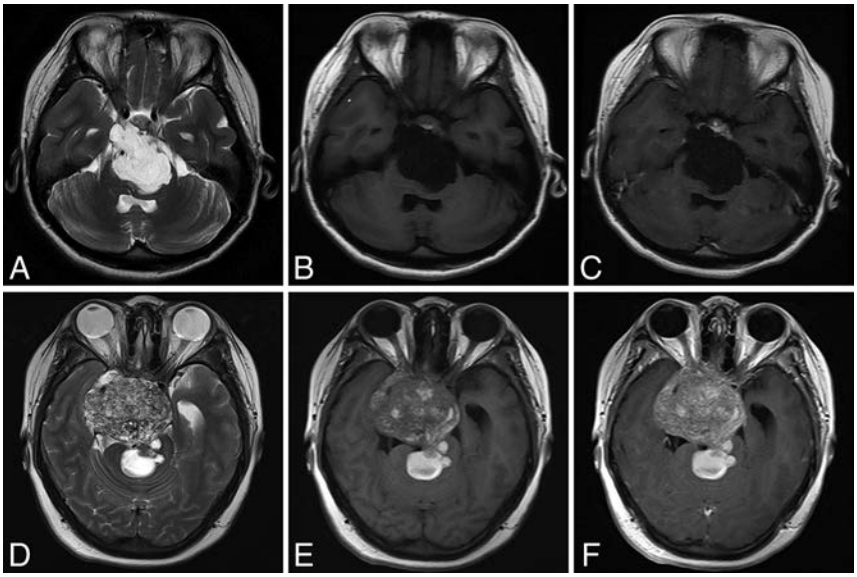

FIG 1. MR imaging of 2 patients with SBC. Patient 1 (*A–C*), 21-years of age. Pathologic findings were conventional chordoma. The patient underwent subtotal tumor resection with no progression at 48 months. *A*, Axial T2-weighted MR imaging. Tumor demonstrates homogeneous high signal intensity. *B*, Axial T1 FLAIR-weighted MR imaging. Tumor has relatively homogeneous hypointense signal compared with the pons. *C*, Enhanced T1 FLAIR MR imaging shows no enhancement of the lesion. Patient 2 (*D–F*), 25 years of age. Pathologic findings revealed conventional chordoma with necrosis and nuclear division. This patient underwent subtotal tumor resection with tumor progression at 8 months. *D*, Axial T2-weighted MR imaging demonstrates tumor heterogeneity. The signal intensity is relatively lower than that in patient 1. *E*, Axial T1 FLAIR MR imaging. The tumor is heterogeneous and hyperintense compared with the pons. *F*, Enhanced T1 FLAIR MR imaging. Tumor exhibits moderate enhancement.

MATERIALS AND METHODS

Overview

This study was approved by the ethics committee of Beijing Tiantan Hospital, Capital Medical University, and informed consent was acquired from all patients. There were no financial conflicts of interest associated with this project. The method used in this study was similar to that in the study of Tian et al.[14] All MR imaging data used in this study were acquired before any treatment, and all the enrolled patients underwent an operation in our hospital.

Patients

In this study, 242 patients underwent an operation for SBC from February 2005 to December 2014 in the skull base ward of our hospital. We developed inclusion and exclusion criteria as follows: The inclusion criteria were the following: 1) All patients had their primary operation at our institute, 2) no prior treatment (eg, biopsy, radiation therapy, and chemother-

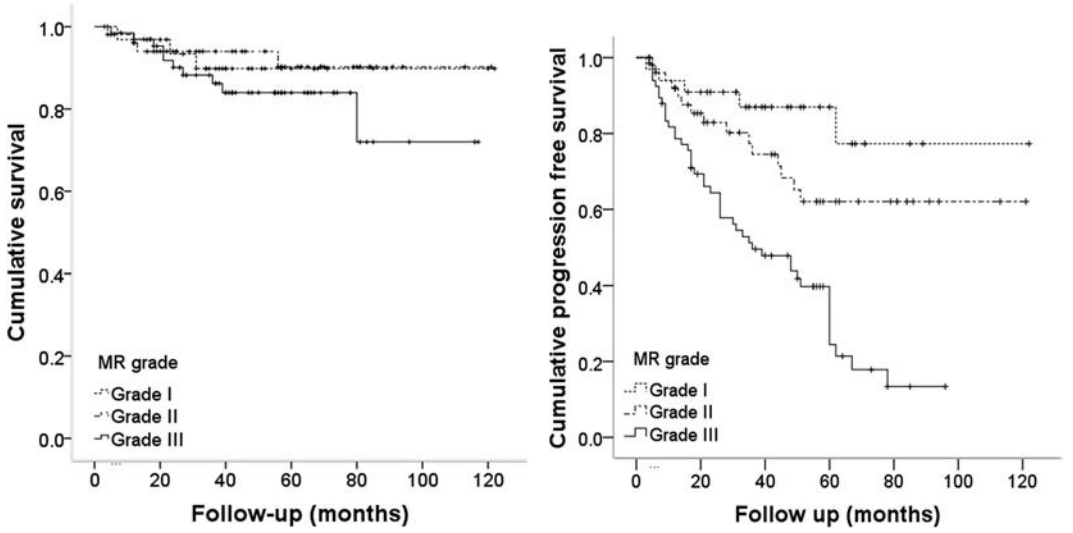

FIG 2. Kaplan-Meier analysis illustrating survival (left) and progression-free survival (right) for different MR imaging grades. There were no differences in overall survival among the 3 MR grade groups (log-rank = 1.669, $P = .43$). Progression-free survival was different among the 3 MR grades (log-rank = 25.889, $P < .001$), with grade III tumors being associated with shorter progression-free survival than grade I (log-rank = 18.561, $P < .001$) and grade II (log-rank = 12.668, $P < .001$) tumors.

apy) had been attempted, and 3) there was availability of MR images before the operation (including T1 FLAIR, T2, and enhanced T1 FLAIR sequences). The exclusion criteria were lack of a complete MR imaging examination before treatment and the presence of other significant diseases that might affect survival.

Clinical Analysis

Demographic information for patients was obtained from medical records. The data included surgical approaches, tumor blood supply, tumor consistency, intraoperative blood loss, and postoperative radiation therapy. The tumor blood supply was classified as either abundant or poor. Tumor consistency was recorded as either soft or hard (the latter included heterogeneous tumors with both soft and hard components). We followed patients in clinics or by telephone. Patients who were lost to follow-up were not included in the subsequent regression analyses. Tumor progression stands for tumor growth after operation.

Histopathologic Analysis

All histologic specimens were examined by 2 experienced pathologists with >10 years' experience in chordoma analysis. According to the International Agency for Research on Cancer, the lesions include conventional, chondroid, and dedifferentiated types.[15] No dedifferentiated chordomas were found; thus, the group included only conventional and chondroid chordomas.

MR Imaging Protocol

MR imaging examinations were performed by using a 3T Magnetom Tim Trio scanner (Siemens, Erlangen, Germany). T1 FLAIR, T2, and enhanced T1 FLAIR sequences were included in each patient's images. The TR/TE range was 1850–2500/9.4–19.8 ms for the T1 FLAIR sequence and 4500–6000/84–97 ms for the T2 sequence. Gadopentetate dimeglumine was injected at a concentration of 0.2 mL/kg (0.5 mol/L). Scanning was performed 2 minutes after the injection. The TR/TE ranges for the enhanced T1 FLAIR sequence were 1850–2500/9.4–19.8 ms. All MR imaging data were analyzed in the PACS.

MR Imaging Analysis

All MR imaging data were evaluated by 2 radiologists. MR image quality was evaluated first. For diagnosis, all tumor images were free of significant artifacts. The maximum diameters of the tumors in 3 perpendicular dimensions were measured, and the largest value was recorded as the "largest diameter." Categories were defined as follows: morphology, with and without lobulation; location, occipitocervical and other types; and resection degree, aggressive (>90%) and nonaggressive (≤90%) resection.

Finally, tumor SI was measured in the PACS. Because image noise and other conditions might affect the SI in MR images, normalization was performed by selecting an area as a control. The pons was selected as our control. The SI of a small region in the pons was measured in each patient, and SI values of T1 FLAIR, T2, and enhanced T1 FLAIR sequences were obtained separately. The average tumor SI ($S_{TT1\ FLAIR}$, S_{TT2}, and $SI_{tumor\ enhance}$ [S_{TEN}]) and the pons SI ($S_{PT1\ FLAIR}$, S_{PT2}, $SI_{pons\ enhance}$ [S_{PEN}]) was calculated. Average SI ratios of tumor to pons ($R_{T1\ FLAIR}$, R_{T2}, $Ratio_{enhance}$ [R_{EN}]) were then calculated, and $R_{T1\ FLAIR}$, R_{T2} and R_{EN} were used as the SI ratios of the tumor to the pons in the T1 FLAIR, T2, and enhanced T1 FLAIR sequences, respectively. We used the following formulas:

$$R_{T1\ FLAIR} = S_{TT1\ FLAIR}/S_{PT1\ FLAIR}$$
$$R_{T2} = S_{TT2}/S_{PT2}$$
$$R_{EN} = S_{TEN}/S_{PEN}.$$

Table 1: Continuous variables for patients with SBC[a]

	Minimum	Maximum	Mean	Median	SD
Age (yr)	5	67	36.38	38	14.64
Largest diameter (mm)	15	86	42.04	42	12.75
Blood loss (mL)	100	5500	897.12	700	730.27
R_{T1}[b]	0.11	1.99	0.57	0.54	0.23
R_{T2}[b]	1.10	4.10	2.44	2.40	0.54
R_{EN}[b]	0.21	2.24	1.01	1.01	0.40

[a] Values of minimum and maximum are raw data.
[b] R_{T1}, R_{T2}, and R_{EN} were calculated according to the formula in the text.

Statistical Analysis

Statistical analyses were performed by using SPSS software (SPSS Statistics 20.0; IBM, Armonk, New York). The effects of $R_{T1\ FLAIR}$, R_{T2}, and R_{EN} on overall survival (OS) and progression-free survival (PFS) were analyzed with the Cox model. Significant variables were then selected to establish the SBC MR imaging grading system. Receiver operating characteristic analysis was used to set cutoff values.

Rank sum and *t* tests were used in the analysis of the distributions of continuous variables among different MR imaging subgroups. A χ^2 test was used in analyzing the distributions of categoric variables among different MR imaging subtypes. The Kaplan-Meier test was used in assessing OS and PFS among different MR imaging groups. In the OS and PFS analysis, all factors were first included in univariate analysis separately; then, multivariate analysis was conducted with the inclusion criterion of 0.1. A P value $< .05$ indicated statistical significance.

RESULTS

Of the 242 patients with SBC, 183 individuals underwent a primary operation. For 21 of these patients, pretreatment MR images were not available. For the remaining 162 patients, enhanced T1 FLAIR sequences were not available for 3 patients, and the MR images of another 3 patients were unobtainable for review. Therefore, 156 patients were included in the final analysis.

There were 63 females and 93 males (1:1.5), and the patients' ages ranged from 5 to 67 years (median, 38 ± 14.6 years). No significant differences in age were found between sexes ($P = .18$). The median follow-up time was 42 months (range, 3–122 months); 3 patients were lost to follow-up, and 17 patients died (mortality rate of 11.1%). One died of a brain stem ischemic infarction, 2 died of tumor apoplexy, and the remaining 14 died from complications caused by tumor recurrence. Sixty-five (42.5%) patients experienced tumor progression. Other variables are listed in Tables 1 and 2.

Univariate Cox regression analysis indicated that decreased R_{T2} (hazard ratio = 0.332; 95% CI, 0.201–0.548; $P < .001$) and increased R_{EN} (hazard ratio = 1.836; 95% CI, 1.032–3.264; $P = .04$) were significant adverse variables for PFS. Therefore, R_{T2} and R_{EN} values were included in the MR imaging classification. According to receiver operating characteristic analysis, the cutoff value for

Table 2: Categoric variables for patients with SBC[a]

	No. of Patients	Lost to Follow-Up	Survival		Progression	
			Survival	Death	Y	N
Sex						
Female	62	1	56	6	25	37
Male	91	2	80	11	40	51
Location						
OC	26	0	23	3	15	11
Other	127	3	113	14	50	77
Lobulation						
Y	79	1	70	9	38	41
N	74	2	66	8	27	47
Approach						
Cranial	129	3	114	15	51	78
Nasal	24	0	22	2	14	10
Blood supply						
Abundant	83	2	72	11	45	38
Poor	70	1	64	6	20	50
Texture						
Soft	73	2	62	11	25	48
Hard	80	1	74	6	40	40
Resection grade						
>90%	115	3	103	12	45	70
≤90%	38	0	33	5	20	18
Histopathology						
Conventional	94	1	80	14	46	48
Chondroid	59	2	56	3	19	40
Postradiotherapy						
Y	15	0	13	2	5	10
N	138	3	123	15	60	78
Total	153	3	136	17	65	88

Note:—OC indicates occipitocervical; Y, yes; N, no.
[a] Number of patients is raw data.

Table 3: The distributions of variables of patients with SBC in different MR imaging grades

	Grade I	Grade II	Grade III	*P* Value
Age (yr)	28[a]	39[a]	40[a]	.06[b]
Largest diameter (mm)	45[a]	37[a]	43[a]	.08[b]
Blood loss (mL)	500[a]	800[a]	800[a]	.002[c,d]
Sex				.45[e]
Female	14	25	24	
Male	19	29	45	
Location				.79[e]
OC	7	8	11	
Other	26	46	58	
Lobulation				.42[e]
Y	17	24	39	
N	16	30	30	
Blood supply				.000[d,e]
Abundant	9	28	48	
Poor	24	26	21	
Texture				.05[e]
Soft	22	24	29	
Hard	11	30	40	
Resection grade				.43[e]
>90%	25	44	49	
≤90%	8	10	20	
Histopathology				.56[e]
Conventional	22	30	43	
Chondroid	11	24	26	
Postradiotherapy				.39[e]
Y	4	7	4	
N	29	47	65	

Note:—OC indicates occipitocervical; Y, yes; N, no.
[a] Median value.
[b] Variance analysis (Student–Newman-Keuls).
[c] Wilcoxon rank sum test.
[d] $P < .05$.
[e] χ^2 test.

R_{T2} was 2.49, and it was 0.77 for R_{EN}. The following classification grades were established: MR grade I, $R_{T2} > 2.49$ and $R_{EN} \leq 0.77$; MR grade II, $R_{T2} > 2.49$ and $R_{EN} > 0.77$, or $R_{T2} \leq 2.49$ and $R_{EN} \leq 0.77$; and MR grade III, $R_{T2} \leq 2.49$ and $R_{EN} > 0.77$.

Analysis of the distributions of SBC characteristics among the different MR grades showed that MR grade III tumors had more abundant blood supply than MR grade I tumors ($P < .001$), as well as greater intraoperative blood loss (800 versus 500 mL, $P = .002$). The distribution of SBC pathologic types among the different MR grades was not significantly different ($P = .56$) (Table 3).

Kaplan-Meier analysis of OS showed no significant differences among the different MR grades (Fig 2, left). However, in Kaplan-Meier analysis of tumor progression, MR grade III tumors were associated with shorter PFS than MR grade I ($P < .001$) and MR grade II tumors ($P < .001$) (Fig 2, right). Univariate analysis revealed that tumor blood supply, resection grade, tumor consistency, histopathology, tumor location, surgical approaches, and MR grades were potentially significant risk factors for tumor progression ($P < .001$). After including the above variables in multivariate analysis, tumor blood supply, resection grade, tumor consistency, histopathology, and MR grade were independent variables for PFS and the risk of SBC progression increased by 2.071 times for every single MR grade increase (95% CI: 1.376–3.118, $P < .001$) (Fig 3).

DISCUSSION

In this retrospective study, the MR SI of patients with SBC was incorporated into statistical analyses, and SBCs were classified into 3 MR grades according to R_{T2} and R_{EN} values. It was found that MR grade III tumors had more abundant blood supply than MR grade I tumors. Furthermore, the risk of SBC progression increased by 2.071 times for every single MR grade increase in the MR classification system.

MR imaging is useful not only for diagnosing disease but also in predicting prognosis and tumor classification. The MR SI and SI ratio of a lesion have been considered important indicators in many studies.[18-21] However, chordomas show substantial heterogeneity on MR images, and MR imaging has previously been used only to aid in the diagnosis of SBC. No previous studies have reported the relationships between MR imaging features and SBC outcomes.

In the present study, tumor and pons signal intensities were measured in the PACS with a straightforward measurement process that ensures the acquisition of accurate data.[22] We calculated $R_{T1\ FLAIR}$, R_{T2}, and R_{EN} values to represent the tumor SI in each sequence while eliminating confounding factors caused by MR imaging conditions among different patients. Although there was no evidence that the MR signal ratio is a risk factor for mortality in statistical analysis, our results showed that a higher R_{T2} value predicted diminished tumor progression and that a higher R_{EN} value predicted more rapid tumor progression. We therefore established MR grades on the basis of these values. Multivariate analysis of tumor progression indicated that MR grade was a significant risk factor and that the risk of SBC progression increased as the MR grade increased.

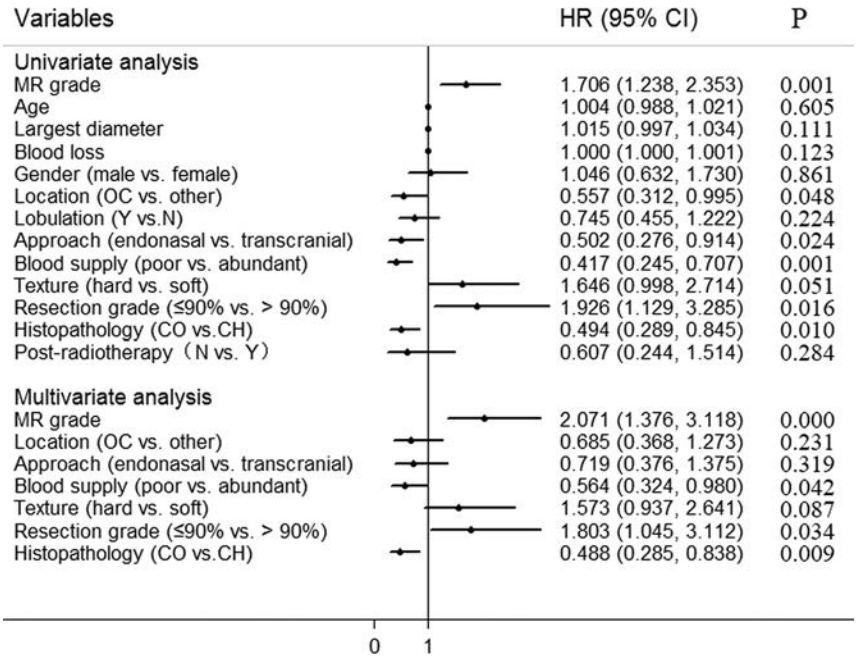

FIG 3. Univariate and multivariate Cox regression models for tumor progression risk. The *black dots* indicate odds ratio, and the *horizontal line* represents 95% confidence intervals. N indicates no; Y, yes; OC, occipitocervical; CO, conventional; CH, chondroid; HR, hazard ratio.

Chordomas can be classified into conventional, chondroid, and dedifferentiated types based on histopathologic manifestations. Conventional chordoma is the most common type, and chondroid and dedifferentiated chordomas exhibit the most favorable and worst outcomes, respectively.[9,23,24] Our results are consistent with those in previous reports. Although pathologic confirmation is the criterion standard for the diagnosis of SBC and pathologic type is an independent variable in the PFS analysis, the MR grading method for SBC was more useful for predicting the prognosis of patients with SBC. This usefulness derived from the following: First, there was a relatively uniform distribution of the 3 MR grades of SBC; second, the MR grade can be immediately determined after an initial MR imaging examination, which is far earlier than a pathologic diagnosis; and third, the grading process is simple because the measurement of SI and the following calculation are both straightforward. This feature makes this technique more accessible to neurosurgeons and radiologists.

Prior studies have discussed the association between MR SI and lesion blood supply.[25] They found that tumors with an abundant blood supply have lower R_{T2} values. We produced similar results in the present study, showing that MR grade III tumors (low R_{T2} and high R_{EN}) had a more abundant blood supply than MR grade I tumors (high R_{T2} and low R_{EN}) and that the former are associated with greater intraoperative blood loss than the latter. This finding is useful for preoperative evaluations of tumor blood supply and is of great significance for clinical practice. Prior knowledge of this factor may alter therapy, such as in preparing adequate quantities of blood, altering a planned operative approach, and in anticipating other measures for potentially significant hemorrhage.

In the present study, chondroid SBCs were associated with a longer PFS than conventional SBCs, and this finding is consistent with those in prior studies. However, SBC pathologic type is not significantly associated with MR grade. Indeed, MR SI did not differ between chondroid and conventional SBCs, and no other studies have reported differences in MR imaging features between different SBC pathologic types. This finding may be because differences in histopathologic levels are not necessarily reflected in imaging modalities. These results need to be confirmed in additional studies.

We enrolled 156 patients with primary SBC in this study, and to the best of our knowledge, this represents the largest primary SBC single-center study. The single-center source avoided the heterogeneity occasionally encountered in multicenter studies. Additionally, we demonstrated the utility of MR SI ratios for SBC grading and confirmed the validity of our MR grading system. We also have demonstrated that the simple ratio of the tumor to the pons allows easy determination of SBC MR grade. This grading system can be widely used. Additionally, the system was useful for predicting the progression of SBC in early tumor stages. Finally, these ratios can also be used to evaluate tumor blood supply, which is of therapeutic significance.

There were limitations to the current study. First, the relatively short follow-up was not sufficient for analyzing long-term outcomes; accordingly, the incidence of terminal events was relatively low for the OS and PFS. Second, the patients were grouped on the basis of retrospective assessments; therefore, further prospective studies are needed to validate the effectiveness of the grading system.

CONCLUSIONS

The tumor-to-pons SI ratio is of diagnostic and potential therapeutic significance for patients with SBC. A higher R_{T2} value predicted slow tumor progression, whereas a higher R_{EN} value was a risk factor for tumor progression. A grading system based on R_{T2} and R_{EN} was useful for predicting tumor blood supply and SBC progression. MR grade III tumors have a more abundant blood supply than MR grade I tumors, and the risk of SBC progression increases with each MR grade increase.

REFERENCES

1. Niu X, Xu H, Inwards CY, et al. **Primary bone tumors: epidemiologic comparison of 9200 patients treated at Beijing Ji Shui Tan hospital, Beijing, China, with 10 165 patients at Mayo Clinic, Rochester, Minnesota.** *Arch Pathol Lab Med* 2015;139:1149–55 CrossRef Medline
2. Salisbury JR. **The pathology of the human notochord.** *J Pathol* 1993; 171:253–55 CrossRef Medline
3. Ho KL. **Ecchordosis physaliphora and chordoma: a comparative ultrastructural study.** *Clin Neuropathol* 1985;4:77–86 Medline
4. Chambers KJ, Lin DT, Meier J, et al. **Incidence and survival patterns**

of cranial chordoma in the United States. *Laryngoscope* 2014;124:1097–102 CrossRef Medline
5. McMaster ML, Goldstein AM, Bromley CM, et al. **Chordoma: incidence and survival patterns in the United States, 1973–1995.** *Cancer Causes Control* 2001;12:1–11 CrossRef Medline
6. Smoll NR, Gautschi OP, Radovanovic I, et al. **Incidence and relative survival of chordomas: the standardized mortality ratio and the impact of chordomas on a population.** *Cancer* 2013;119:2029–37 CrossRef Medline
7. Stüer C, Schramm J, Schaller C. **Skull base chordomas: management and results.** *Neurol Med Chir (Tokyo)* 2006;46:118–24; discussion 124–25 Medline
8. Jian BJ, Bloch OG, Yang I, et al. **Adjuvant radiation therapy and chondroid chordoma subtype are associated with a lower tumor recurrence rate of cranial chordoma.** *J Neurooncol* 2010;98:101–08 CrossRef Medline
9. Amendola BE, Amendola MA, Oliver E, et al. **Chordoma: role of radiation therapy.** *Radiology* 1986;158:839–43 CrossRef Medline
10. Jones PS, Aghi MK, Muzikansky A, et al. **Outcomes and patterns of care in adult skull base chordomas from the Surveillance, Epidemiology, and End Results (SEER) database.** *J Clin Neurosci* 2014;21:1490–96 CrossRef Medline
11. Walcott BP, Nahed BV, Mohyeldin A, et al. **Chordoma: current concepts, management, and future directions.** *Lancet Oncol* 2012;13:e69–76 CrossRef Medline
12. Stacchiotti S, Sommer J. **Building a global consensus approach to chordoma: a position paper from the medical and patient community.** *Lancet Oncol* 2015;16:e71–83 CrossRef Medline
13. Wang L, Tian K, Wang K, et al. **Factors for tumor progression in patients with skull base chordoma.** *Cancer Med* 2016;5:2368–77 CrossRef Medline
14. Tian K, Wang L, Wang K, et al. **Analysis of clinical features and outcomes of skull base chordoma in different age-groups.** *World Neurosurg* 2016;92:407–17 CrossRef Medline
15. Flanagan AM, Yamaguchi T. *World Health Organization (WHO) Classification of Tumors of Soft Tissue and Bone: Notochordal.* Lyon: IARC Press; 2013:328–29
16. Meyer JE, Lepke RA, Lindfors KK, et al. **Chordomas: their CT appearance in the cervical, thoracic and lumbar spine.** *Radiology* 1984;153:693–96 CrossRef Medline
17. Sze G, Uichanco LR 3rd, Brant-Zawadzki MN, et al. **Chordomas: MR imaging.** *Radiology* 1988;166:187–91 CrossRef Medline
18. Nowak J, Seidel C, Pietsch T, et al. **Systematic comparison of MRI findings in pediatric ependymoblastoma with ependymoma and CNS primitive neuroectodermal tumor not otherwise specified.** *Neuro Oncol* 2015;17:1157–65 CrossRef Medline
19. Takashima S, Sone S, Horii A, et al. **Major salivary gland lesions: correlation of MR findings with flow cytometric DNA analysis and prognosis.** *AJR Am J Roentgenol* 1996;167:1297–304 CrossRef Medline
20. Worthley SG, Reis ED, Helft G, et al. **Serial magnetic resonance imaging correlates with neurological outcome in an experimental model of spinal cord ischemia.** *Spinal Cord* 2008;46:222–27 CrossRef Medline
21. Massaro AN, Kadom N, Chang T, et al. **Quantitative analysis of magnetic resonance images and neurological outcome in encephalopathic neonates treated with whole-body hypothermia.** *J Perinatol* 2010;30:596–603 CrossRef Medline
22. El Kady RM, Choudhary AK, Tappouni R**. Accuracy of apparent diffusion coefficient value measurement on PACS workstation: a comparative analysis.** *AJR Am J Roentgenol* 2011;196:W280–84 CrossRef Medline
23. Makhdoomi R, Ramzan A, Khursheed N, et al. **Clinicopathological characteristics of chordoma: an institutional experience and a review of the literature.** *Turk Neurosurg* 2013;23:700–06 Medline
24. Wu Z, Zhang J, Zhang L, et al. **Prognostic factors for long-term outcome of patients with surgical resection of skull base chordomas: 106 cases review in one institution.** *Neurosurg Rev* 2010;33:451–56 CrossRef Medline
25. Shinmura R, Matsui O, Kobayashi S, et al. **Cirrhotic nodules: association between MR imaging signal intensity and intranodular blood supply.** *Radiology* 2005;237:512–19 CrossRef Medline

The Role of MRI in Diagnosing Neurovascular Compression of the Cochlear Nerve Resulting in Typewriter Tinnitus

Y.J. Bae, Y.J. Jeon, B.S. Choi, J.-W. Koo, and J.-J. Song

ABSTRACT

BACKGROUND AND PURPOSE: Typewriter tinnitus, a symptom characterized by paroxysmal attacks of staccato sounds, has been thought to be caused by neurovascular compression of the cochlear nerve, but the correlation between radiologic evidence of neurovascular compression of the cochlear nerve and symptom presentation has not been thoroughly investigated. The purpose of this study was to examine whether radiologic evidence of neurovascular compression of the cochlear nerve is pathognomonic in typewriter tinnitus.

MATERIALS AND METHODS: Fifteen carbamazepine-responding patients with typewriter tinnitus and 8 control subjects were evaluated with a 3D T2-weighted volume isotropic turbo spin-echo acquisition sequence. Groups 1 (16 symptomatic sides), 2 (14 asymptomatic sides), and 3 (16 control sides) were compared with regard to the anatomic relation between the vascular loop and the internal auditory canal and the presence of neurovascular compression of the cochlear nerve with/without angulation/indentation.

RESULTS: The anatomic location of the vascular loop was not significantly different among the 3 groups (all, $P > .05$). Meanwhile, neurovascular compression of the cochlear nerve on MR imaging was significantly higher in group 1 than in group 3 ($P = .032$). However, considerable false-positive (no symptoms with neurovascular compression of the cochlear nerve on MR imaging) and false-negative (typewriter tinnitus without demonstrable neurovascular compression of the cochlear nerve) findings were also observed.

CONCLUSIONS: Neurovascular compression of the cochlear nerve was more frequently detected on the symptomatic side of patients with typewriter tinnitus compared with the asymptomatic side of these patients or on both sides of control subjects on MR imaging. However, considering false-positive and false-negative findings, meticulous history-taking and the response to the initial carbamazepine trial should be regarded as more reliable diagnostic clues than radiologic evidence of neurovascular compression of the cochlear nerve.

ABBREVIATIONS: ABR = abnormal auditory brain stem response; CPA = cerebellopontine angle; IAC = internal acoustic canal; NVC-C = neurovascular compression of the cochlear nerve; T2-VISTA = T2-weighted volume isotropic turbo spin-echo acquisition

Arterial compression of the cochleovestibular nerve complex has been suggested as a potential cause of hearing deficit, typewriter tinnitus, and equilibrium disturbance or vertigo.[1-4] Among these clinical symptoms, typewriter tinnitus, which was first described by a pediatric cardiologist as "ear-clicking tinnitus responding to carbamazepine,"[5] is characterized by paroxysmal attacks. It is either spontaneous or precipitated by positioning or sounds and occurs with staccato sounds described as "Morse code," "machine gun," "coins in a can," "crackling," or "typewriter" sounds.[6-8] Typewriter tinnitus is considered the result of dysmyelination and demyelination of the contact point between the arterial loop and the cochlear nerve that transmits an abnormal signal to the auditory cortex.[9] As in other vascular compression syndromes such as trigeminal neuralgia, typewriter tinnitus is highly responsive to carbamazepine.[6-8,10,11] Complete suppression of tinnitus with carbamazepine treatment, in addition to its paroxysmal character, has led to the hypothesis that typewriter tinnitus results from neurovascular compression of the cochlear nerve (NVC-C), for which microvascular compression would be an effective treatment.[6,7]

However, because typewriter tinnitus is a relatively rare condition and was only recently described, few studies have been performed investigating the relationship between radiologic evi-

Received August 31, 2016; accepted after revision January 25, 2017.

From the Departments of Radiology (Y.J.B., B.S.C.) and Otorhinolaryngology-Head and Neck Surgery (Y.J.J., J.-W.K., J.-J.S.), Seoul National University Bundang Hospital, Seongnam, Korea.

This work was supported by a grant from the Korea Health Technology R&D Project through the Korea Health Industry Development Institute, funded by the Ministry of Health and Welfare, Republic of Korea (grant No. HI14C2264).

The authors declare no conflict of interest related to funding sources or financial holdings that might raise questions about possible sources of bias.

Please address correspondence to Jae-Jin Song, MD, PhD, Department of Otorhinolaryngology-Head & Neck Surgery, Seoul National University Bundang Hospital, 300 Gumi-dong, Bundang-gu, Seongnam, 13620, Republic of Korea; e-mail: jjsong96@snubh.org or jjsong96@gmail.com

Indicates open access to non-subscribers at www.ajnr.org

Indicates article with supplemental on-line photo.

http://dx.doi.org/10.3174/ajnr.A5156

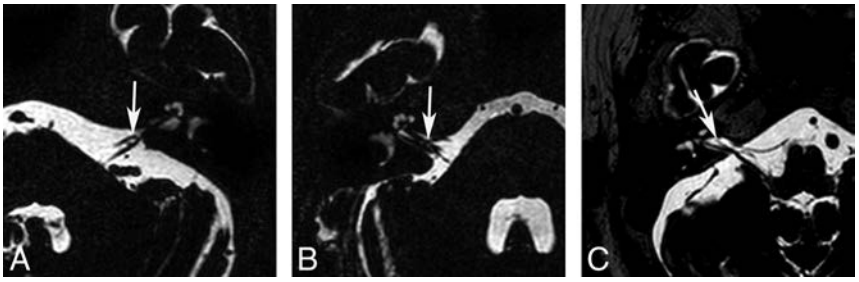

FIG 1. Types of AICA loops. *A*, Type I AICA loops lie within the CPA (*arrow*) but do not enter the IAC. *B*, Type II AICA loops enter the IAC (*arrow*) but do not extend into >50% of the length of the IAC. *C*, Type III AICA loops extend into >50% of the IAC (*arrow*).

dence of cochlear nerve compression on MR imaging and the presence of typewriter tinnitus, to our knowledge. A few previous studies investigating subjects with typewriter tinnitus with carbamazepine responsiveness showed evidence of NVC-C on T2-weighted CISS images; however, the sample sizes were relatively small (4 and 5 subjects, respectively), and no control subjects without tinnitus were included.[6,10] Moreover, signs of neurovascular compression have frequently been detected on MR imaging in asymptomatic patients, which raises questions about the role of MR imaging in the diagnosis of typewriter tinnitus.[7,12]

Thus, in this study, we aimed to evaluate MR imaging findings of subjects with typewriter tinnitus with regard to the presence of radiologic evidence of cochlear nerve compression by performing a 3D T2-weighted volume isotropic turbo spin-echo acquisition (T2-VISTA; Phillips Healthcare, Best, the Netherlands) sequence on 3T MR imaging to effectively visualize neurovascular compression. In other words, the purpose of the current study was to examine whether radiologic evidence of cochlear nerve compression is pathognomonic in subjects with typewriter tinnitus.

MATERIALS AND METHODS

Subjects

This retrospective study was approved by the institutional review board of the Clinical Research Institute of Seoul National Bundang Hospital (B-1608–360-101). From January 2014 to April 2016, 27 patients were initially diagnosed with typewriter tinnitus at our institution. The subjects visited the outpatient clinic of the otorhinolaryngology department with typical symptoms of typewriter tinnitus, which they described as "typewriter," "machine gun," or "crackling" sounds. After we excluded other possible pathologic causes of tinnitus by taking a thorough history and performing neuro-otologic examinations, the patients were prescribed carbamazepine as an initial empiric treatment. Of the 27 subjects, 2 were lost to follow-up and were excluded from further analysis. After a 3-week trial, all 25 patients reported complete resolution or marked improvement of tinnitus.

At the initial visit, MR imaging of the internal acoustic canal (IAC) and the cerebellopontine angle (CPA) was recommended for all patients with typewriter tinnitus. Of the 25 subjects, 15 (5 men and 10 women; age range, 27–84 years; mean age, 54.1 years) underwent MR imaging of the IAC and CPA; thus, these 15 subjects were finally enrolled in the current study. Two neuroradiologists (Y.J.B. and B.S.C, with 7 and 17 years of experience, respectively) evaluated both the IACs and CPAs of all patients separately. Because all patients presented with unilateral tinnitus except for 1 patient who had bilateral tinnitus, 2 groups were included in the analysis as follows: group 1, symptomatic sides ($n = 16$), and group 2, asymptomatic sides ($n = 14$). During the same period, 8 control subjects (4 men and 4 women; age range, 47–74 years; mean age, 60.5 years) who did not have tinnitus but underwent MR imaging for dizziness were also included in our study (16 sides, group 3). No patient had a history of neurologic disease, tumors in the IAC or CPA, or temporal bone trauma.

MR Imaging Protocol

MR imaging was performed by using a 3T instrument (Achieva and Ingenia; Philips Healthcare) with a 32-channel SENSE Head Coil (Philips Healthcare). T2-VISTA imaging of the IAC and CPA was performed with the following parameters: FOV, 160 × 160 mm^2; acquisition matrix size, 228 × 228; section thickness, 0.7 mm; overlapping, 0.35 mm; NEX, 1; TR, 2000 ms; TE, 250 ms; flip angle, 90°. In addition, the following sequences were obtained according to clinical need: axial T2WI of the whole brain (FOV, 185 × 230 mm^2; acquisition matrix size, 420 × 375; section thickness, 5 mm; section gap, 1 mm; NEX, 1; TR, 3000 ms; TE, 80 ms; flip angle, 90°), axial T1WI of the IAC and CPA (FOV, 180 × 180 mm^2; acquisition matrix size, 272 × 217; section thickness, 3 mm; section gap, 0 mm; NEX, 1; TR, 500 ms; TE, 10 ms; flip angle, 50°), and 3D gadolinium-enhancing T1WI of the IAC and CPA (FOV, 200 × 200 mm^2; acquisition matrix size, 256 × 256; section thickness, 1 mm; section gap, 1 mm; NEX, 1; TR, 9.5 ms; TE, 3.3 ms; flip angle, 8°).

Imaging Analysis

Two neuroradiologists blinded to the clinical findings of the subjects evaluated the neurovascular structures of the IAC and CPA on axial 3D T2-VISTA images and sagittal and/or coronal reconstructed images and made final decisions in consensus. First, the type of AICA loop of all study subjects was determined by using the Chavda classification[13] as follows: type I, the AICA loop lying within the CPA but not entering the IAC (Fig 1*A* and On-line Fig 1*A*); type II, the AICA loop entering the IAC but not extending >50% of the length of the IAC (Fig 1*B* and On-line Fig 1*B*); and type III, the AICA loop extending into >50% of the IAC (Fig 1*C* and On-line Fig 1*C*). Second, the type of neurovascular contact was classified into the following 3 categories: type I, no neurovascular contact (Fig 2*A* and On-line Fig 2*A*); type II, neurovascular contact present at the cochleovestibular nerve complex but without angulation/indentation of the nerve (Fig 2*B* and On-line Fig 2*B*); and type III, neurovascular compression causing cochleovestibular nerve angulation/indentation (Fig 2*C* and On-line Fig 2*C*).[12] In addition, the presence of neurovascular contact with arterial structures other than the AICA was assessed.

Statistical Analysis

The type of AICA loop and the type of neurovascular contact on MR imaging in groups 1 and 2 were compared by using the Wilcoxon signed rank test for paired, nonparametric, ordinal data.

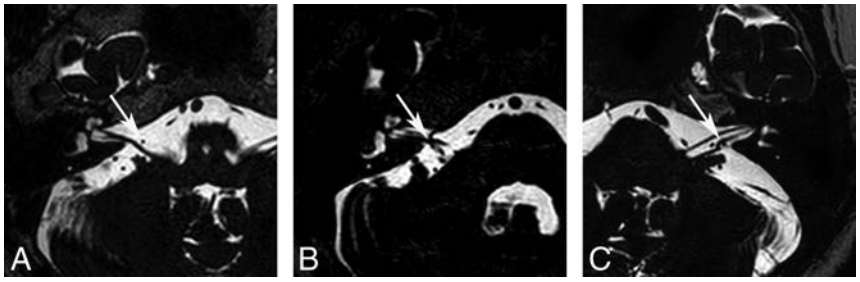

FIG 2. Neurovascular contact types between the AICA and the cochleovestibular nerve. *A*, A type I neurovascular contact shows no neurovascular contact (*arrow*). *B*, A type II neurovascular contact shows contact (*arrow*) between the AICA and the cochleovestibular nerve without angulation/indentation of the nerve. *C*, A type III neurovascular contact shows angulation/indentation (*arrow*) of the cochleovestibular nerve by the AICA loop.

MRI findings according to patient groups

Type	Group 1 (*n* = 16)	Group 2 (*n* = 14)	Group 3 (*n* = 16)	*P* Values
AICA				
I	7 (43.8%)	7 (50.0%)	13 (81.3%)	
II	7 (43.8%)	6 (42.9%)	2 (12.5%)	
III	2 (12.5%)	1 (7.1%)	1 (6.3%)	
				.803[a]/.158[b]/.065[c]
Neurovascular contact				
I	5 (31.3%)	8 (57.1%)	10 (62.5%)	
II	8 (50.0%)	6 (42.9%)	6 (37.5%)	
III	3 (18.8%)	0 (0%)	0 (0%)	
				.130[a]/.769[b]/.032[c,d]

[a] *P* values indicate the results of statistical comparisons between groups 1 and 2 by the Wilcoxon signed rank test.
[b] *P* values indicate the results of statistical comparisons between groups 2 and 3 by the linear association test.
[c] *P* values indicate the results of statistical comparisons between groups 1 and 3 by the linear association test.
[d] *P* values $< .05$.

The comparisons between groups 2 and 3 and between groups 1 and 3 were performed by the linear association test for independent, nonparametric, ordinal data. A *P* value $< .05$ indicated statistical significance. All statistical analyses were performed by using SPSS software (Version 18.0; IBM, Armonk, New York).

RESULTS

The Table summarizes the results of the MR imaging findings of the 3 subject groups.

AICA Loop Type

Group 1 (16 symptomatic sides of subjects with typewriter tinnitus) showed 7 type I (43.8%), 7 type II (43.8%), and 2 type III (12.5%) AICA loops. Group 2 (14 asymptomatic sides of subjects with typewriter tinnitus) showed 7 type I (50.0%), 6 type II (42.9%), and 1 type III (7.1%) AICA loops. Meanwhile, of the 16 AICA loops of group 3, 13 were type I (81.3%), 2 were type II (12.5%), and 1 was type III (6.3%). The comparison of the anatomic location of AICA loops in the IAC and CPA among the 3 groups did not yield statistically significant differences (Table) but showed a trend toward the incidence of a type III AICA loop being higher in group 1 and of a type I AICA loop being higher in group 3.

Types of Neurovascular Contact

Five sides (31.3%) in group 1, 8 sides (57.1%) in group 2, and 10 sides (62.5%) in group 3 showed type I neurovascular contact. Type II neurovascular contact (without nerve angulation/indentation) was shown in 8 sides (50.0%) in group 1, 6 sides (42.9%) in group 2, and 6 sides (37.5%) in group 3. Type III neurovascular contact (compression with nerve angulation/indentation) was demonstrated in 3 of 16 sides (18.8%) in group 1, while no subjects in group 2 or 3 were classified as having type III neurovascular contact. The type of neurovascular contact was significantly different between groups 1 and 3 (Table, $P = .032$). Meanwhile, no vascular structure other than the AICA loop was found to contribute to neurovascular contact of the cochleovestibular nerve.

DISCUSSION

In the current study, we evaluated MR imaging findings of subjects with typewriter tinnitus with regard to the presence of neurovascular cross-compression of the cochlear nerve to investigate whether radiologic evidence of cochlear nerve compression is pathognomonic in typewriter tinnitus. Neurovascular structures are known to be well-visualized on heavily T2-weighted images such as T2-VISTA, FIESTA, or CISS. With T2-VISTA imaging, our results showed that the anatomic location of the AICA loop in the IAC and CPA among the symptomatic and asymptomatic sides of subjects with typewriter tinnitus and controls without tinnitus did not yield statistically significant differences. However, the incidence of neurovascular compression causing angulation/indentation of the cochlear nerve was significantly higher on the symptomatic sides of patients with typewriter tinnitus than in the other groups.

Previous Literature on the Radiologic Findings of Typewriter Tinnitus and the Novelty of the Current Study

The concept of neurovascular compression syndrome of the cochleovestibular nerve has been continuously proposed since Jannetta et al[14,15] first suggested that arterial compression of the cochleovestibular nerve might cause hearing loss, vertigo, and tinnitus.[2,12,16-22] Many studies have advocated this concept by performing microvascular decompression in patients suspected of having cochleovestibular neurovascular compression syndrome and showing favorable clinical outcomes after the operation.[2-4,14,15,17,19,23]

However, there has also been much controversy regarding the relationship between radiologic evidence of neurovascular compression and audiovestibular symptoms. A major concern is that AICA loops are frequently found in the IAC even in asymptomatic healthy subjects.[13,24] Additionally, because heavily T2-weighted high-resolution images such as T2-VISTA, FIESTA, and CISS have been used to provide excellent delineation of the neurovascular structures in the IAC and CPA, many radiologic studies have reported a comparable incidence of neurovascular contact be-

tween the AICA and the cochleovestibular nerve in symptomatic and asymptomatic subjects.[20,25,26] Indeed, several MR imaging studies have claimed that there was no significant association between the presence of tinnitus and AICA configuration or neurovascular compression.[12,21] Gultekin et al[12] compared 58 patients with unexplained tinnitus and 44 controls with regard to the presence of neurovascular contact and the presence of nerve angulation by the vessel with a 3D-FIESTA sequence but concluded that vascular compression of the cochleovestibular nerve could not be a cause of tinnitus.

However, no previous studies have investigated the relationship between MR imaging findings of the AICA loop in the IAC and CPA and the presence of typewriter tinnitus symptoms, to our knowledge. A few studies have enrolled patients with unexplained tinnitus regardless of their symptomatology, but these studies did not perform subgrouping of the subjects with regard to the psychoacoustic characteristics of tinnitus.[12,21] While nonpulsatile subjective tinnitus is thought to be a result of functional changes in auditory or nonauditory brain areas[27-32] and responds very poorly to almost all kinds of medical treatment,[33] typewriter tinnitus is known to have characteristic paroxysmal staccato sounds and is regarded as the result of NVC-C by the AICA loop based on its excellent response to carbamazepine.[6-8,10,11] Two studies have investigated the MR imaging findings of 4 and 5 subjects with typewriter tinnitus, respectively, with regard to vascular compression of the auditory nerve,[6,10] but these studies lacked controls. Therefore, MR imaging findings should be assessed only in patients with typewriter tinnitus who showed a quick response to carbamazepine and should be compared with patients with asymptomatic sides or with healthy controls, as in the current study, to properly evaluate the relationship between neurovascular compression and typewriter tinnitus.

MR Imaging May Help in the Diagnosis of NVC-C Resulting in Typewriter Tinnitus

During 2 years, we enrolled 25 patients diagnosed with typewriter tinnitus and evaluated the types of AICA loops in the IAC and CPA and the types of neurovascular contact by using 3T 3D T2-VISTA imaging in 15 patients. When we compared the symptomatic sides of patients with typewriter tinnitus (group 1) with the asymptomatic sides of those with typewriter tinnitus (group 2) and healthy controls (group 3), the difference was not statistically significant (Table). However, considering that in a previous study, type II and type III AICA loops were observed in 38.0% of 332 patients with ipsilateral auditory symptoms,[13] our results, which demonstrated that 56.3% of group 1 and 18.8% of group 3 had type II and III AICA loops, showed a definite tendency toward type II and III AICA loops on the symptomatic sides of subjects with typewriter tinnitus. Moreover, the 3 groups in this study had significantly different (Table) neurovascular contact types. In group 1, 68.8% of the subjects showed type II or III neurovascular contact, which is comparable with findings in a previous study showing neurovascular contact in 4 of 5 (80%) patients with typewriter tinnitus.[6] In this regard, radiologic evidence of the AICA loop entering the IAC and contact between the AICA loop and the vestibulocochlear nerve may be of additive value in diagnosing NVC-C presenting with typewriter tinnitus.

However, there were considerable false-positive and false-negative radiologic findings in our subjects. Indeed, 43.8% of group 1 showed AICA loops lying within the CPA but not entering the IAC, and 31.3% did not show neurovascular contact with or without nerve angulation/indentation on T2-VISTA (false-negative results). In contrast, of the 30 sides included in groups 2 and 3, 10 subjects (33.3%) had AICA loops entering the IAC and 12 subjects (40.0%) showed neurovascular contact with or without nerve angulation/indentation (false-positive results). Considering that group 1 comprised subjects with characteristic symptoms and excellent responses to carbamazepine and that groups 2 and 3 were nonsymptomatic subjects and healthy controls, respectively, false-positive and false-negative results in up to 40% of the study population may reveal the incomplete role of IAC MR imaging for the diagnosis of typewriter tinnitus. In other words, although previous literature on medical and surgical treatment outcomes has proved that typewriter tinnitus originates from neurovascular contact, the current radiologic imaging modalities cannot completely confirm or rule out the presence of typewriter tinnitus. This situation may be attributed to the following assumptions: First, some neurovascular contact may accompany anatomic proximity, but not direct contact, between the AICA loop and the cochlear nerve. In 2 previous studies investigating subjects with typewriter tinnitus, symptoms were triggered by head position changes or loud sounds. Thus, neurovascular contact between the AICA loop and cochlear nerve is "dynamic" in some patients, meaning that the contact is on and off and that MR imaging may have only captured the "contact-off" status. Second, because false-positive results (ie, evidence of neurovascular contact without any symptoms) existed in a considerable percentage of our subjects, symptoms may be elicited not by direct anatomic contact but by demyelination of the cochlear nerve due to the proximity of the AICA loop, regardless of radiologically demonstrable contact between the 2.

Therefore, we suggest that meticulous history-taking regarding subjectively perceived tinnitus characteristics and their aggravating factors as well as the response to an initial carbamazepine trial should be regarded as more reliable diagnostic clues than radiologic evidence of neurovascular contact in subjects with typewriter tinnitus. However, considering that the symptoms can be cured by microvascular decompression of the cochlear nerve, it may be of value to evaluate all symptomatic patients with typewriter tinnitus with IAC MR imaging, including a heavily T2-weighted sequence, to see whether the anatomic change is severe enough to consider surgical treatment.

Limitations of the Current Study and Proposed Future Studies

To the best of our knowledge, this is the first case-control report to compare the radiologic characteristics of subjects with typewriter tinnitus. However, our case series is limited in several aspects. First, abnormal auditory brain stem response (ABR) findings have been suggested to be diagnostic of NVC-C,[19,34] but ABR was not tested in our series because most of our patients had a relatively short history and previous literature revealed that patients with a short history of NVC-C usually showed intact ABR results.[19,34] However, future studies including ABR for the initial

evaluation of patients should be performed to further evaluate the value of ABR as a diagnostic tool. Second, because we strictly enrolled patients diagnosed with typewriter tinnitus on the basis of their immediate response to a carbamazepine trial, our sample size was relatively small. Therefore, future studies with a larger number of subjects are warranted to further verify our current results. Next, none of the subjects enrolled in the current study underwent microvascular decompression surgery because all subjects reported abated symptoms after carbamazepine treatment. Because decompressing the cochlear nerve and determining symptom relief would be the direct way to confirm the causal relationship between neurovascular contact and typewriter tinnitus, future radiologic studies on subjects treated with microvascular decompression may further reveal the causative relationship, along with evidence from MR imaging findings and the presence of typewriter tinnitus. One subject had bilateral typewriter tinnitus, and some subjects had false-positive findings (ie, radiologic evidence of NVC-C); thus, subjects with unilateral typewriter tinnitus may develop bilateral symptoms in the future. If there are such cases, predicting future symptom development based on radiologic findings will be of further value. Future longitudinal follow-up of the current subjects should be performed to investigate such a possibility.

CONCLUSIONS

Taken together, our results indicate that NVC-C by the AICA loop was more frequently detected on the symptomatic side of subjects with typewriter tinnitus than on the asymptomatic side of these subjects or on both sides of control subjects on MR imaging. However, because all subjects with typewriter tinnitus were strictly enrolled on the basis of their carbamazepine response, some subjects had typewriter tinnitus without NVC-C, and some controls without tinnitus had radiologic evidence of NVC-C, current MR imaging modalities may only be of additive value for the diagnosis of NVC-C resulting in typewriter tinnitus. In other words, meticulous history-taking and the response to the initial carbamazepine trial should be regarded as more reliable diagnostic clues than radiologic evidence of NVC-C.

ACKNOWLEDGMENTS

The English in this document has been checked by at least 2 professional editors, both native speakers of English. Please see http://www.textcheck.com/certificate/eqogwz for a certificate. The authors thank the Medical Research Collaborating Center at Seoul National University Bundang Hospital for consultation on the statistical analyses.

REFERENCES

1. Jannetta PJ. **Cranial nerve vascular compression syndromes (other than tic douloureux and hemifacial spasm).** *Clin Neurosurg* 1981;28:445–56 Medline
2. Yap L, Pothula VB, Lesser T. **Microvascular decompression of cochleovestibular nerve.** *Eur Arch Otorhinolaryngol* 2008;265:861–69 CrossRef Medline
3. Guevara N, Deveze A, Buza V, et al. **Microvascular decompression of cochlear nerve for tinnitus incapacity: pre-surgical data, surgical analyses and long-term follow-up of 15 patients.** *Eur Arch Otorhinolaryngol* 2008;265:397–401 CrossRef Medline
4. Moller MB, Moller AR, Jannetta PJ, et al. **Microvascular decompression of the eighth nerve in patients with disabling positional vertigo: selection criteria and operative results in 207 patients.** *Acta Neurochir (Wien)* 1993;125:75–82 CrossRef Medline
5. Mardini MK. **Ear-clicking "tinnitus" responding to carbamazepine.** *N Engl J Med* 1987;317:1542 Medline
6. Levine RA. **Typewriter tinnitus: a carbamazepine-responsive syndrome related to auditory nerve vascular compression.** *ORL J Otorhinolaryngol Relat Spec* 2006;68:43–46; discussion 46–47 CrossRef Medline
7. Mathiesen T, Brantberg K. **Microvascular decompression for typewriter tinnitus-case report.** *Acta Neurochir (Wien)* 2015;157:333–36 CrossRef Medline
8. Nam EC, Handzel O, Levine RA. **Carbamazepine responsive typewriter tinnitus from basilar invagination.** *J Neurol Neurosurg Psychiatry* 2010;81:456–58 CrossRef Medline
9. De Ridder D, Ryu H, Moller AR, et al. **Functional anatomy of the human cochlear nerve and its role in microvascular decompressions for tinnitus.** *Neurosurgery* 2004;54:381–88; discussion 388–90 CrossRef Medline
10. Brantberg K. **Paroxysmal staccato tinnitus: a carbamazepine responsive hyperactivity dysfunction symptom of the eighth cranial nerve.** *J Neurol Neurosurg Psychiatry* 2010;81:451–55 CrossRef Medline
11. Salvi R, Lobarinas E, Sun W. **Pharmacological treatments for tinnitus: new and old.** *Drugs Future* 2009;34:381–400 CrossRef Medline
12. Gultekin S, Celik H, Akpek S, et al. **Vascular loops at the cerebellopontine angle: is there a correlation with tinnitus?** *AJNR Am J Neuroradiol* 2008;29:1746–49 CrossRef Medline
13. McDermott AL, Dutt SN, Irving RM, et al. **Anterior inferior cerebellar artery syndrome: fact or fiction.** *Clin Otolaryngol Allied Sci* 2003;28:75–80 CrossRef Medline
14. Jannetta PJ. **Neurovascular cross-compression in patients with hyperactive dysfunction symptoms of the eighth cranial nerve.** *Surg Forum* 1975;26:467–69 Medline
15. Jannetta PJ. **Outcome after microvascular decompression for typical trigeminal neuralgia, hemifacial spasm, tinnitus, disabling positional vertigo, and glossopharyngeal neuralgia (honored guest lecture).** *Clin Neurosurg* 1997;44:331–83 Medline
16. Gierek T, Markowski J, Majzel K, et al. **Disabling positional vertigo (DPV): syndrome of vestibulo-cochlear organ impairment during vascular compression of the vestibulo-cochlear nerve (VCS)** [in Polish]. *Otolaryngol Pol* 2005;59:403–07 Medline
17. Brackmann DE, Kesser BW, Day JD. **Microvascular decompression of the vestibulocochlear nerve for disabling positional vertigo: the House Ear Clinic experience.** *Otol Neurotol* 2001;22:882–87 CrossRef Medline
18. Markowski J, Gierek T, Kluczewska E, et al. **Assessment of vestibulocochlear organ function in patients meeting radiologic criteria of vascular compression syndrome of vestibulocochlear nerve–diagnosis of disabling positional vertigo.** *Med Sci Monit* 2011;17:CR169–73 Medline
19. Moller MB. **Results of microvascular decompression of the eighth nerve as treatment for disabling positional vertigo.** *Ann Otol Rhinol Laryngol* 1990;99:724–29 CrossRef Medline
20. Clift JM, Wong RD, Carney GM, et al. **Radiographic analysis of cochlear nerve vascular compression.** *Ann Otol Rhinol Laryngol* 2009;118:356–61 CrossRef Medline
21. Hoekstra CE, Prijs VF, van Zanten GA. **Diagnostic yield of a routine magnetic resonance imaging in tinnitus and clinical relevance of the anterior inferior cerebellar artery loops.** *Otol Neurotol* 2015;36:359–65 CrossRef Medline
22. Kim DH, Kim HJ, Hong SK, et al. **Neurovascular compression syndrome of the eighth cranial nerve: clinical features and medical treatment.** *Korean J Otorhinolaryngol Head Neck Surg* 2014;57:518–25 CrossRef
23. Jannetta PJ, Moller MB, Moller AR. **Disabling positional vertigo.** *N Engl J Med* 1984;310:1700–05 CrossRef Medline

24. Reisser C, Schuknecht HF. **The anterior inferior cerebellar artery in the internal auditory canal.** *Laryngoscope* 1991;101:761–66 Medline
25. Sirikci A, Bayazit Y, Ozer E, et al. **Magnetic resonance imaging based classification of anatomic relationship between the cochleovestibular nerve and anterior inferior cerebellar artery in patients with non-specific neuro-otologic symptoms.** *Surg Radiol Anat* 2005;27:531–35 CrossRef Medline
26. Schick B, Brors D, Koch O, et al. **Magnetic resonance imaging in patients with sudden hearing loss, tinnitus and vertigo.** *Otol Neurotol* 2001;22:808–12 CrossRef Medline
27. Song JJ, Vanneste S, Schlee W, et al. **Onset-related differences in neural substrates of tinnitus-related distress: the anterior cingulate cortex in late-onset tinnitus, and the frontal cortex in early-onset tinnitus.** *Brain Struct Funct* 2015;220:571–84 CrossRef Medline
28. Song JJ, Vanneste S, De Ridder D. **Dysfunctional noise cancelling of the rostral anterior cingulate cortex in tinnitus patients.** *PLoS One* 2015;10:e0123538 CrossRef Medline
29. Song JJ, De Ridder D, Weisz N, et al. **Hyperacusis-associated pathological resting-state brain oscillations in the tinnitus brain: a hyperresponsiveness network with paradoxically inactive auditory cortex.** *Brain Struct Funct* 2014;219:1113–28 CrossRef Medline
30. Song JJ, De Ridder D, Schlee W, et al. **"Distressed aging": the differences in brain activity between early- and late-onset tinnitus.** *Neurobiol Aging* 2013;34:1853–63 CrossRef Medline
31. Song JJ, Punte AK, De Ridder D, et al. **Neural substrates predicting improvement of tinnitus after cochlear implantation in patients with single-sided deafness.** *Hear Res* 2013;299:1–9 CrossRef Medline
32. Kim SH, Jang JH, Lee SY, et al. **Neural substrates predicting short-term improvement of tinnitus loudness and distress after modified tinnitus retraining therapy.** *Sci Rep* 2016;6:29140 CrossRef Medline
33. Elgoyhen AB, Langguth B, Nowak W, et al. **Identifying tinnitus-related genes based on a side-effect network analysis.** *CPT Pharmacometrics Syst Pharmacol* 2014;3:e97 CrossRef Medline
34. De Ridder D, Heijneman K, Haarman B, et al. **Tinnitus in vascular conflict of the eighth cranial nerve: a surgical pathophysiological approach to ABR change.** *Prog Brain Res* 2007;166:401–11 CrossRef Medline

Imaging Manifestations of Pseudoprogression in Metastatic Melanoma Nodes Injected with Talimogene Laherparepvec: Initial Experience

C. Zamora, M. Lopez, F. Cunningham, F. Collichio, and M. Castillo

ABSTRACT

SUMMARY: Talimogene laherparepvec is an oncolytic virus recently approved for targeted treatment of advanced melanoma. Because of an inflammatory reaction, treated lesions may increase in size and develop infiltrative margins that can be construed as disease progression or extracapsular spread. In this report, we describe our initial experience imaging the response of metastatic nodes injected with talimogene laherparepvec. Six of 12 nodes (50%) showed growth from baseline followed by decreased size, 5 of 12 nodes (42%) showed a downward size trend, and 1 node showed continued increase in size. Seven of 9 nodes (78%) developed infiltrative margins at a median of 79 days, and 6 of 9 (67%) nodes became necrotic at a median of 76 days after injection, all showing decreased size at final follow-up. An increase in the size of nodes injected with talimogene laherparepvec does not necessarily indicate progression. Infiltrative margins are also frequently seen and may be confused with extracapsular disease.

ABBREVIATION: T-VEC = talimogene laherparepvec

Talimogene laherparepvec (T-VEC) is a second-generation oncolytic virus that was approved for the treatment of unresectable melanoma in the United States and Europe in 2015. This is the first intralesional immunotherapeutic agent approved by the FDA and the European Commission as well as the first such drug to show an increased durable response rate and overall survival in a Phase III clinical trial in patients with melanoma.[1] T-VEC is a herpes simplex virus type 1 that has been genetically modified to selectively replicate in tumoral tissue. It results in direct lysis of tumor cells, which is followed and enhanced by a systemic immune response against viral and tumoral antigens.[2] Data so far suggest that T-VEC is effective at achieving local control, though treatment of systemic disease may necessitate combination therapy.[3]

Histopathology shows that T-VEC elicits a prominent local inflammatory reaction and, in many cases, an increase in the size of the lesion followed by subsequent response.[4,5] In our institution, in addition to an increase in size, we have noted the development of infiltrative margins and necrosis on CT in several T-VEC–injected nodes that ultimately decreased in size, mimicking extracapsular spread or progression of disease at some point during follow-up. The purpose of this report is to describe the imaging manifestations of nodes injected with T-VEC and correlate these findings with final nodal size and patient outcome.

Case Series

This post hoc analysis was approved by our institutional review board and was derived from a Phase Ib clinical trial assessing the safety of combined intratumoral T-VEC injection and intravenous ipilimumab in adult patients with histologically confirmed stage IIIB/IV melanoma. After the first injection with T-VEC, nodes were re-injected after 4 weeks and then every 2 weeks until complete response, disappearance, or disease progression per the immune response–related criteria.[6] Amenable nodes were injected by using palpation or sonography guidance. The initial dose was 10^6 plaque-forming units/mL followed by 10^8 plaque-forming units/mL thereafter,[4] with injected volumes ranging between 0.5–2 mL. Ipilimumab was administered a total of 4 times, every 3 weeks starting at week 6 from the first T-VEC injection.

We included a total of 12 nodes from 7 patients. The following imaging features were recorded on serial contrast-enhanced CT by a single radiologist and compared with baseline CT before injection: average size (cross-sectional dimensions), margins

Received November 22, 2016; accepted after revision February 25, 2017.

From the Division of Neuroradiology, Department of Radiology (C.Z., M.L., M.C.) and the Division of Hematology and Oncology, Department of Medicine (F. Cunningham, F. Collichio), University of North Carolina School of Medicine, Chapel Hill, North Carolina.

Paper previously presented at: 102nd Scientific Assembly and Annual Meeting of the Radiological Society of North America, November 27–December 2, 2016; Chicago, Illinois.

Please address correspondence to Carlos Zamora, MD, PhD, Division of Neuroradiology, Department of Radiology, University of North Carolina School of Medicine, CB 7510, 3327 Old Infirmary, Chapel Hill, NC 27599-7510; e-mail: carlos_zamora@med.unc.edu

http://dx.doi.org/10.3174/ajnr.A5206

(well circumscribed or infiltrative), and necrosis. The median follow-up was 277 days (interquartile range, 221–348).

Two major growth patterns were observed. Six of 12 nodes (50%) showed an increase in size relative to the baseline followed by decreased size, with the size at final follow-up smaller than baseline (Fig 1*A*). Peak nodal size was reached at a median of 93 days (interquartile range, 79–104) after the first T-VEC injection and ranged from 29%–106% increase in size, with a median of 41%. Five of 12 nodes (42%) showed a downward trend in size (Fig 1*B*). Two of these showed minor increases in size during follow-up, but never larger than baseline. Two of 5 nodes were nonmeasurable at last follow-up CT. The remainder node (1 of 12; 8%) showed an upward trend (Fig 1*A*), but could not be followed after 184 days because the patient was placed under hospice care because of systemic disease progression. Except for this node, the sizes of all other nodes at last follow-up were smaller than baseline.

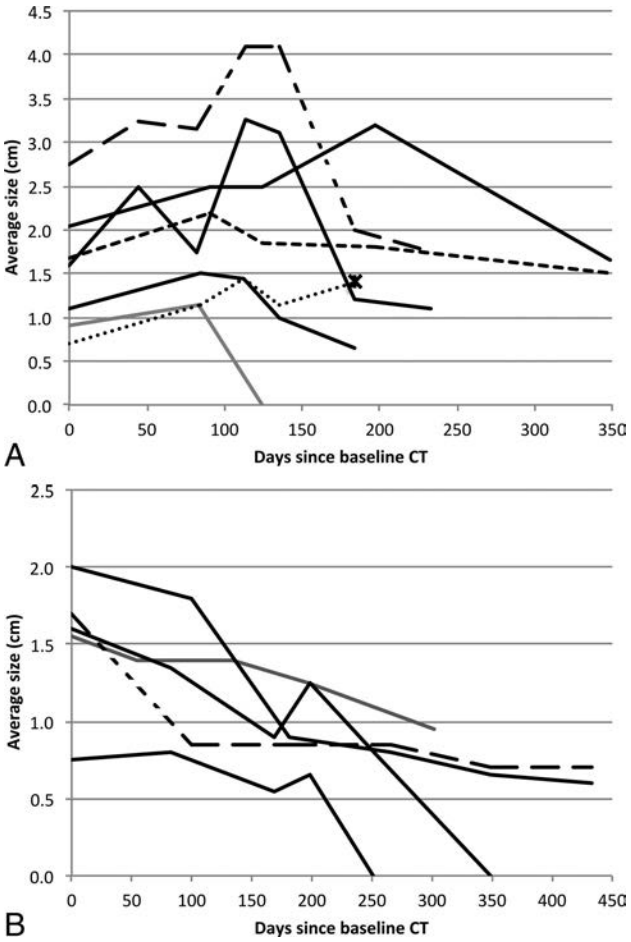

FIG 1. Line graph showing change in size over time relative to baseline CT. *A*, Fifty percent of nodes showed initial growth followed by decreased size. One node (marked with an *asterisk* at last time point) demonstrated a continued increase in size, but could not be followed after 184 days. *B*, Forty-two percent of nodes showed a downward trend in size. The final size was smaller than baseline in all nodes except for the one indicated in *A*.

Regarding margins, these were well circumscribed at baseline in 9 of 12 nodes (75%), and the rest were infiltrative. Seven of the 9 nodes (78%) with initially well-circumscribed margins eventually became infiltrative at a median of 79 days (interquartile range 73–94) after the first T-VEC injection (Fig 2).

Three of 12 nodes (25%) showed necrosis at baseline CT. Necrosis eventually developed in 6 of the remaining 9 nodes (67%) at a median of 76 days (interquartile range, 72–81) since the first T-VEC injection (Figs 2 and 3). All nodes that became infiltrative or developed necrosis during follow-up showed a final size that was smaller than baseline. All nodes that were initially necrotic also showed a decreased final size compared with baseline. Clinical features and patient outcomes are summarized in the Table.

DISCUSSION

The potential antitumoral effects of viral infection have been recognized for many years.[7] Although the affinity of certain viruses for tumor cells has long been established, the main issue until recently has been achieving control of viral replication in normal tissues. Genetic engineering has made it possible to design organisms that will selectively replicate in tumoral tissue while minimizing damage to the host. Deletion of the γ34.5 gene in T-VEC and other oncolytic viruses reduces their pathogenicity by inhibiting replication in normal tissue, whereas inactivation of the α47 gene promotes their replication in cancer cells.[4] In addition, T-VEC has been modified to express granulocyte-macrophage colony-stimulating factor, which amplifies an immune response against the tumor.[5] In essence, T-VEC's mechanism of action is 2-fold: a direct oncolytic effect after viral infection of the tumor and a secondary systemic response mounted by the host. The virus is the treatment agent rather than a drug delivery carrier. Notably, regional and systemic antitumor responses can be delayed for several weeks after the initiation of treatment and are most prominent in injected nodes, but nodes that were not injected are also affected to a lesser extent.[8]

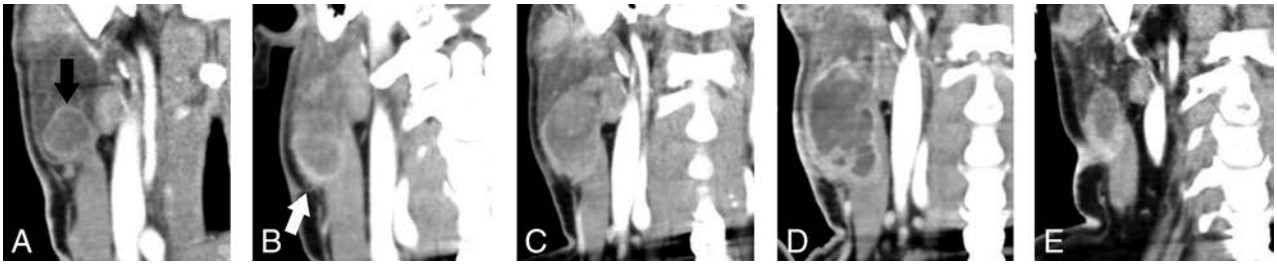

FIG 2. *A*, Coronal contrast-enhanced CT shows a round, well-circumscribed necrotic lesion (*black arrow*) at the inferior aspect of the right parotid gland. *B*, The lesion has increased in size and developed infiltrative margins (*white arrow*) 72 days after injection. Follow-up at 111 days (*C*) and 184 days (*D*) after injection demonstrates further growth and marked increase in central necrosis. *E*, The lesion shows decreased size after 337 days.

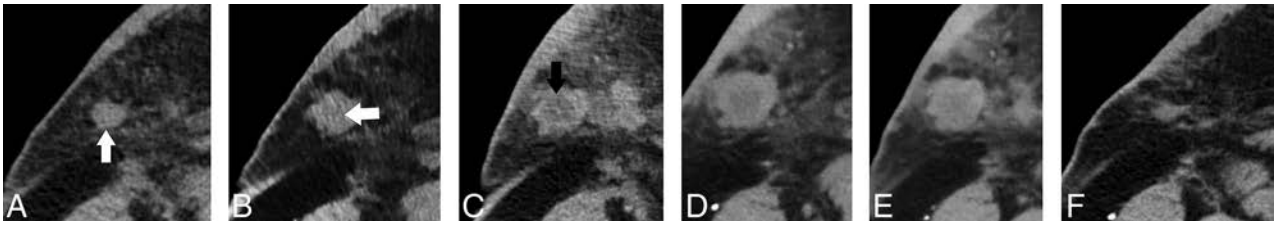

FIG 3. *A*, Axial contrast-enhanced CT shows a small nodule in the deep right breast/axillary region (*white arrow*). The lesion shows slight central hypoattenuation and increased size at 34 days after injection (*white arrow*, *B*) with the development of frank central necrosis after 72 days (*black arrow*, *C*). There is a mild further increase in size at 104 days (*D*), followed by decreased size at 125 days (*E*) and near complete resolution at 174 days (*F*).

Clinical features, disease stage, final nodal size (relative to baseline CT), and patient outcome

Patient No.	Lesion No.	Age, yr	Sex	Stage	*BRAF* Status	Location	Final Lesion Size	Patient Outcome
1	1	63	F	T3bN3M1a	Negative	Left supraclavicular	Decreased	Remission.
2	2	66	M	TxNxM1c	Wild type	Right supraclavicular	Decreased	T-VEC discontinued after disease progression in ribs. Placed on nivolumab with partial response.
	3					Right supraclavicular	Decreased	
3	4	40	M	pT1bN3M1c	Positive	Right preauricular	Decreased	IL-2 followed by *BRAF* and MEK inhibitors after ipilimumab/T-VEC treatment. Deceased.
	5					Right submandibular	Decreased	
4	6	44	M	T3bN3M1b	Positive	Right axillary	Decreased	*BRAF* and MEK inhibitors after ipilimumab/T-VEC treatment, followed by disease progression. Deceased.
	7					Right axillary	Decreased	
5	8	58	F	T3bN2M1a	Wild type	Left upper back	Decreased	Complete response for 21 months, followed by axillary recurrence. Placed on nivolumab.
	9					Left breast	Decreased	
6	10	32	M	T4bN3M1a	Negative	Left retroauricular	Decreased	Partial response for 6 months. Placed on nivolumab.
7	11	63	M	T3aN3M1c	Negative	Right chest wall	Increased	Rapid deterioration after brain metastases.
	12					Right axilla	Decreased	Deceased.

Note:—IL-2 indicates interleukin 2.

On histopathologic analysis, Hu et al[4] showed inflammatory changes in nearly all tumors injected with T-VEC. They found that necrosis was present in most treated tumors and was frequently extensive, with sparing of normal tissue. Although the prognostic significance of necrosis in melanoma nodes injected with T-VEC is established, the development of necrosis in solid tumors is generally accepted as a marker of tumor lysis and cell death.[9] In a Phase II trial of patients with melanoma metastases treated with bevacizumab, the development of marked decreased attenuation or central necrosis (as part of the modified Morphology, Attenuation, Size, and Structure [MASS] criteria) was rare, but constituted a strong predictor of favorable response, with such changes deemed to be secondary to devascularization.[10] A different study where bevacizumab was administered in combination with ipilimumab, an immunotherapeutic agent, also showed that necrosis was rare.[11] In contradistinction to these studies, but consistent with the histopathologic description of T-VEC-injected nodes by Hu and colleagues,[4] the development of necrosis was common in our cohort, and all such nodes showed a subsequent decrease in size. Therefore, it is reasonable to speculate that this phenomenon may be more of a function of the oncolytic properties of the virus rather than a systemic response and, therefore, more likely to be seen in patients injected with T-VEC and similar agents than in those receiving systemic immunotherapies or antiangiogenic drugs.

Most nodes in our study developed infiltrative margins at some point during follow-up, and all of these demonstrated a decreased final size. Although in the appropriate setting, ill-defined nodal margins suggest an inflammatory or infectious process, the imaging appearance of extracapsular tumor spread is indistinguishable. This finding has important treatment implications in a variety of head and neck tumors, where it conveys a poor prognosis.[12,13] In melanoma, extracapsular spread in metastatic nodes also has prognostic implications and has been associated with failure after regional lymphadenectomy and potential benefit from more aggressive therapies.[14,15] Thus, it is critical not to confuse these inflammatory changes with tumor progression because this could lead to the discontinuation of an effective therapy.

In our patients, 50% of all injected nodes showed initial growth before subsequently decreasing in size. This is consistent with the results from a Phase III trial in which more than half of the patients had lesions that initially increased in size or developed new lesions before achieving a response.[1] This phenomenon of pseudoprogression has been described with other immunotherapies and is probably related to a flare reaction in the setting of inflammatory changes with or without edema, whereby established lesions can show a transient increase in size and microscopic disease may become inflamed and detectable as a "new" lesion on posttreatment imaging.[6,16] It is also possible that in at least some of these cases, there is continued tumor growth until a considerable immunologic response is developed.[6] In our study, extensive necrosis accounted for the increase in size of some nodes. Again, transient lesion growth and the development of "new" lesions can lead to patients being classified as having disease progression when some of them may actually benefit from continuation of treatment. Conventional criteria for objective treatment response, such as the Response Evaluation Criteria in

Solid Tumors (RECIST) or the World Health Organization criteria, have inherent limitations in patients receiving immunotherapeutic agents. Prior studies using conventional criteria have documented tumor regression in patients initially thought to have stable or progressive disease.[17] Newer criteria such as the immune response–related criteria are more inclusive of the expected patterns of disease activity in patients receiving these agents and may be better suited to evaluate response in such circumstances.[6]

This study has several limitations, the most notable being the small sample size and the retrospective nature of the analysis. The timing of the development of necrosis and infiltrative margins is a broad estimate because we do not know the exact time point when these changes occurred before the imaging study where they became evident. Depending on individual clinical need, CT studies were performed at different times after injection, and that introduced some variability. In addition, it is difficult to account for effects that ipilimumab may have had on individual nodal response, either by itself or through synergism. It is well established that ipilimumab may incite an inflammatory response and, in some cases, a temporary increase in tumor size can be observed during the first few weeks of treatment.[18] Data from Phase II clinical trials in patients with advanced melanoma treated with ipilimumab show that close to 10% of them would have been misclassified as having progression of disease by World Health Organization criteria based on an increase in lesion size or the development of new lesions alone.[6,19] The greatest increase in nodal size in our study occurred between 9 and 20 weeks after ipilimumab was initiated. We do not know to what extent the presumed inflammatory effects of T-VEC and ipilimumab may have overlapped.

Lastly, although final smaller nodal size may represent successful treatment, the presence of viable disease cannot be excluded because the nodes in our series were not biopsied. In addition, although FDG-PET may have some utility in monitoring the response to T-VEC and other immunotherapies, data from both animal models and patients with cancer suggest that avid uptake could in some cases represent an inflammatory response to the virus and should not be automatically interpreted as progression of disease.[20,21] The patients in our small cohort did not consistently have an FDG-PET scan after T-VEC injection during the time that these nodes were followed, and therefore, correlation with the morphologic changes that we observed was not possible.

CONCLUSIONS

In summary, half of the nodes in our patients showed an initial increase (pseudoprogression) in size after T-VEC injection followed by decreased size and, in some cases, resolution of the lesion. The development of infiltrative margins and necrosis was frequent, and all such nodes showed a final size that was smaller than baseline, a presumed measure of success. These imaging manifestations are concordant with the expected biologic behavior of lesions treated with immunotherapeutic agents, and necrosis appears to be common and prominent after T-VEC injection. Increased size per se is not necessarily indicative of progression or an indication to stop treatment in clinically stable patients. Additional studies with a larger number of patients are needed to fully understand the radiographic progression and magnitude of these changes and the relative contribution of both targeted and systemic immunotherapies. Because the use of targeted agents is a fairly new development and not as of yet widespread, many head and neck radiologists may not be aware of these potential imaging findings. The recognition that a patient may be undergoing such treatments is paramount to avoid diagnostic pitfalls and confusion with extracapsular spread or progression of disease. Our preliminary results highlight the importance of being cognizant of specific treatments before image interpretation.

Disclosures: Frances Collichio—*UNRELATED*: *Consulting Fee or Honorarium*: Amgen*; *Other*: Professional Development Committee of ASCO. *Money paid to the institution.

REFERENCES

1. Andtbacka RH, Kaufman HL, Collichio F, et al. **Talimogene laherparepvec improves durable response rate in patients with advanced melanoma.** *J Clin Oncol* 2015;33:2780–88 CrossRef Medline
2. Ott PA, Hodi FS. **Talimogene laherparepvec for the treatment of advanced melanoma.** *Clin Cancer Res* 2016;22:3127–31 CrossRef Medline
3. Rehman H, Silk AW, Kane MP, et al. **Into the clinic: talimogene laherparepvec (T-VEC), a first-in-class intratumoral oncolytic viral therapy.** *J Immunother Cancer* 2016;4:53 CrossRef Medline
4. Hu JC, Coffin RS, Davis CJ, et al. **A phase I study of OncoVEXGM-CSF, a second-generation oncolytic herpes simplex virus expressing granulocyte macrophage colony-stimulating factor.** *Clin Cancer Res* 2006;12:6737–47 CrossRef Medline
5. Appleton ES, Turnbull S, Ralph C, et al. **Talimogene laherparepvec in the treatment of melanoma.** *Expert Opin Biol Ther* 2015;15:1517–30 CrossRef Medline
6. Wolchok JD, Hoos A, O'Day S, et al. **Guidelines for the evaluation of immune therapy activity in solid tumors: immune-related response criteria.** *Clin Cancer Res* 2009;15:7412–20 CrossRef Medline
7. Fukuhara H, Ino Y, Todo T. **Oncolytic virus therapy: a new era of cancer treatment at dawn.** *Cancer Sci* 2016;107:1373–79 CrossRef Medline
8. Kaufman HL, Amatruda T, Reid T, et al. **Systemic versus local responses in melanoma patients treated with talimogene laherparepvec from a multi-institutional phase II study.** *J Immunother Cancer* 2016;4:12 CrossRef Medline
9. Kaufman HL, Kohlhapp FJ, Zloza A. **Oncolytic viruses: a new class of immunotherapy drugs.** *Nat Rev Drug Discov* 2015;14:642–62 CrossRef Medline
10. Gray MR, Martin del Campo S, Zhang X, et al. **Metastatic melanoma: lactate dehydrogenase levels and CT imaging findings of tumor devascularization allow accurate prediction of survival in patients treated with bevacizumab.** *Radiology* 2014;270:425–34 CrossRef Medline
11. Nishino M, Giobbie-Hurder A, Ramaiya NH, et al. **Response assessment in metastatic melanoma treated with ipilimumab and bevacizumab: CT tumor size and density as markers for response and outcome.** *J Immunother Cancer* 2014;2:40 CrossRef Medline
12. Mermod M, Tolstonog G, Simon C, et al. **Extracapsular spread in head and neck squamous cell carcinoma: a systematic review and meta-analysis.** *Oral Oncol* 2016;62:60–71 CrossRef Medline
13. Maxwell JH, Ferris RL, Gooding W, et al. **Extracapsular spread in head and neck carcinoma: impact of site and human papillomavirus status.** *Cancer* 2013;119:3302–08 CrossRef Medline
14. Bibault JE, Dewas S, Mirabel X, et al. **Adjuvant radiation therapy in metastatic lymph nodes from melanoma.** *Radiat Oncol* 2011;6:12 CrossRef Medline
15. Nathansohn N, Schachter J, Gutman H. **Patterns of recurrence in patients with melanoma after radical lymph node dissection.** *Arch Surg* 2005;140:1172–77 CrossRef Medline
16. Brahmer JR, Tykodi SS, Chow LQ, et al. **Safety and activity of anti-**

PD-L1 antibody in patients with advanced cancer. *N Engl J Med* 2012;366:2455–65 CrossRef Medline
17. van Baren N, Bonnet MC, Dréno B, et al. **Tumoral and immunologic response after vaccination of melanoma patients with an ALVAC virus encoding MAGE antigens recognized by T cells.** *J Clin Oncol* 2005;23:9008–21 CrossRef Medline
18. Saenger YM, Wolchok JD. **The heterogeneity of the kinetics of response to ipilimumab in metastatic melanoma: patient cases.** *Cancer Immun* 2008;8:1 Medline
19. Chiou VL, Burotto M. **Pseudoprogression and immune-related response in solid tumors.** *J Clin Oncol* 2015;33:3541–43 CrossRef Medline
20. Covington MF, Curiel CN, Lattimore L, et al. **FDG-PET/CT for monitoring response of melanoma to the novel oncolytic viral therapy talimogene laherparepvec.** *Clin Nucl Med* 2017;42:114–15 CrossRef Medline
21. Koski A, Ahtinen H, Liljenback H, et al. **[(18)F]-fluorodeoxyglucose positron emission tomography and computed tomography in response evaluation of oncolytic adenovirus treatments of patients with advanced cancer.** *Hum Gene Ther* 2013;24:1029–41 CrossRef Medline

Asymmetric Meckel Cave Enlargement: A Potential Marker of PHACES Syndrome

J.N. Wright and V. Wycoco

ABSTRACT

BACKGROUND AND PURPOSE: PHACES syndrome is a complex of morphologic abnormalities of unknown cause and includes posterior fossa abnormalities; head and neck infantile hemangiomas; arterial, cardiac, and eye anomalies; and sternal or abdominal wall defects. Accurate identification of the syndrome is important for optimal treatment. The purpose of this study was to investigate the incidence of asymmetric Meckel cave enlargement, a potential novel imaging marker, in a population of patients referred for evaluation of possible PHACES syndrome.

MATERIALS AND METHODS: Eighty-five patients referred for neuroimaging evaluation of possible PHACES syndrome were identified and stratified on the basis of their ultimate clinical PHACES diagnosis categorization into PHACES, possible PHACES, or not PHACES. MR imaging studies were subsequently reviewed for the presence or absence of unilateral Meckel cave enlargement, with the reviewer blinded to the ultimate PHACES syndrome categorization.

RESULTS: Twenty-five of 85 patients (29%) were ultimately categorized as having PHACES or possible PHACES according to consensus guidelines. Asymmetric Meckel cave enlargement was present in 76% (19/25) of these patients and in 82% (19/23) of only those patients with definite PHACES. This finding was present in none of the 60 patients determined not to have PHACES syndrome. In 7/19 patients (37%) with this finding, subtle MR imaging abnormalities consistent with PHACES were missed on the initial MR imaging interpretation.

CONCLUSIONS: Asymmetric Meckel cave enlargement was a common feature of patients with PHACES in our cohort and may serve as a novel imaging marker. Increased awareness of this imaging feature has the potential to increase the diagnostic accuracy of PHACES.

ABBREVIATIONS: IAC = internal auditory canal; PHACES = posterior fossa abnormalities; head and neck infantile hemangiomas; arterial, cardiac and eye anomalies; and sternal or abdominal wall defects

PHACES syndrome (Online Mendelian Inheritance in Man No. 606519; omim.org) is a complex of morphologic abnormalities of unknown cause and includes posterior fossa abnormalities; head and neck infantile hemangiomas, often in a segmental distribution; arterial, cardiac, and eye anomalies; and sternal or abdominal wall defects.[1] Accurate recognition of the syndrome is important to identify the potentially increased risk associated with the treatment of infantile hemangiomas in the setting of underlying arterial or cardiac pathology,[2,3] as well as to initiate careful surveillance and aggressive intervention for potential speech and language delays related to posterior fossa anomalies.[4,5] There is increasing consensus that the stigmata of PHACES may be subtler than previously thought, and new diagnostic criteria are being considered. We have observed that asymmetric Meckel cave enlargement is a frequent neuroimaging finding in patients with PHACES syndrome and may serve as an easily recognizable marker that can improve diagnostic sensitivity.

MATERIALS AND METHODS

Following Seattle Children's Hospital institutional review board approval, we retrospectively identified 93 patients referred for MR imaging of the head and neck due to concern for PHACES syndrome between 1994 and 2016, based on the presence or history of large (>5 cm) or segmental head and neck hemangiomas ($n = 92$) or sternal clefting ($n = 1$). Imaging protocols varied but generally included contrast-enhanced MR imaging of the brain and time-of-flight MRA of the head and neck. In all cases, a coronal fluid-sensitive sequence (T2-weighted, STIR, or steady-state free precession [balanced fast-field echo, FIESTA, or CISS]) was included in the protocol. Five patients were excluded due to lesions other

Received October 6, 2016; accepted after revision January 17, 2017.

From the Department of Radiology (J.N.W.), University of Washington and Seattle Children's Hospital, Seattle, Washington; and Department of Neurological Intervention and Imaging (V.W.), Alterna Wellness Center, Nedlands, Western Australia.

Please address correspondence to Jason N. Wright, MD, M/S MA.7.220, Seattle Children's Hospital, PO Box 5371, Seattle, WA 98105; e-mail: jnixon@uw.edu

Indicates article with supplemental on-line table.

http://dx.doi.org/10.3174/ajnr.A5140

Cohort summary data and statistics

	All PHACES	Definite PHACES	Possible PHACES	Not PHACES
No. (% total)	25 (29)	23 (27)	2 (2)	60 (71)
Female (No.) (% category)	21 (84)	19 (82)	2 (100)	50 (83)
Age (mean ± SD)	20 ± 39 mo	22 ± 40 mo	1 ± 0.5 mo	10 ± 17 mo
Age (range) (median)	5 days to 14 yr (4 mo)	5 days to 14 yr (5 mo)	1–2 mo (1.5 mo)	1 mo to 7 yr (4 mo)
Meckel cave enlargement (No.) (% category)	19 (76)	19 (82)	0 (0)	0 (0)
Posterior fossa anomalies (No.) (% category)	15 (60)	15 (65)	0 (0)	0 (0)
Facial hemangioma (No.) (% category)	24 (96)	23 (100)	1 (50)	60 (100)
Arterial anomalies (No.) (% category)	21 (84)	20 (90)	1 (50)	0 (0)
Cardiac anomalies (No.) (% category)	13 (52)	12 (52)	1 (50)	0 (0)
Eye anomalies (No.) (% category)	0 (0)	0 (0)	0 (0)	0 (0)
Sternal or midline abdominal anomalies (No.) (% category)	1 (4)	0 (0)	1 (50)	0 (0)

than hemangiomas identified on MR imaging, and 3 additional patients were excluded due to lack of available clinical records.

We then stratified the remaining 85 patients on the basis of their ultimate clinical PHACES diagnosis categorization within the published 2009 consensus criteria into PHACES, possible PHACES, or not PHACES.[1] Current diagnostic criteria are as previously published by Metry et al.[1] Work-up included a combination of dermatologic evaluation, ophthalmologic examination, cardiology consultation including echocardiography, and structural MR imaging evaluation of the head and neck.

We subsequently reviewed all MR imaging studies for the presence or absence of asymmetric unilateral Meckel cave enlargement, blinded to the ultimate PHACES syndrome categorization. Particular attention was paid to the coronal fluid-sensitive sequences at the level of the sella turcica, which highlighted the comparative volumes of the bilateral Meckel caves. "Presence" was defined as obvious subjective asymmetric enlargement based on visual assessment, with an estimated volume ratio of approximately 1:1.5 used as a cutoff. Our goal was to evaluate the utility of this novel imaging finding in a clinically applicable manner requiring no advanced morphometric analysis for implementation. Minimal asymmetry was not considered sufficient for positivity.

RESULTS

Of the 85 included patients evaluated by MR imaging for suspicion of PHACES syndrome, 25 patients (29%) were ultimately categorized as having PHACES ($n = 23$) or possible PHACES ($n = 2$) according to consensus guidelines. Mean and median ages for the PHACES cohort were 20 and 4 months, respectively. Eighty-four percent were female, in line with prior published reports.[6] Summary statistics for all patients are presented in the Table.

All patients with PHACES presented with large or segmental head or neck hemangiomas, excepting 1 patient (patient 4) categorized as having possible PHACES, who was evaluated for sternal clefting noted at birth and who subsequently developed a left facial segment 3–distribution hemangioma of <5 cm. Additional diagnostic criteria for PHACES present in each patient are provided in the On-line Table.

Asymmetric Meckel cave enlargement was present in 76% (19/25) of all patients with PHACES (Fig 1); the finding was present in 82% (19/23) of patients with definite PHACES. Patients with Meckel cave involvement were more likely to have a facial segment 1 or 2 distribution of facial hemangiomas, while patients without were more likely to have a facial segment 3 or cervicothoracic distribution, though overlap occurred in both directions. Five patients (patients 2, 5, 11, 20, and 23) demonstrated internal auditory canal (IAC) hemangiomas, and 1 patient (patient 23) had a Meckel cave hemangioma, all associated with ipsilateral Meckel cave enlargement.

Of the patients with unilateral Meckel cave enlargement, all enlargements were ipsilateral to the facial or head and neck hemangioma. Sixty-eight percent (13/19) had associated ipsilateral cerebellar hypoplasia, and 58% (11/19) had dysplastic cerebellar clefting associated with the hypoplasia. This finding is compared with 60% (15/25) with ipsilateral cerebellar hypoplasia in all patients with PHACES, and 48% (12/25) with associated dysplastic clefting. In all cases, the cerebellar hemispheric abnormalities were ipsilateral to both the hemangioma and the asymmetrically enlarged Meckel cave.

Eighty-nine percent (17/19) of patients with Meckel cave enlargement had craniocervical vascular anomalies, most with arterial dysplasia. This finding is comparable with 84% (21/25) noted in all patients with PHACES in our cohort. When present, arterial abnormalities were always ipsilateral to the side of the facial hemangioma and Meckel cave enlargement, though additional contralateral abnormalities occurred in a large minority of cases (41%) (Fig 2).

Major cardiac or arch anomalies were present in 21% (4/19) of patients with asymmetric Meckel cave enlargement, compared with a slightly higher 28% (7/25) of all patients with PHACES in our cohort.

Excepting strabismus related to lid or orbital involvement by facial hemangiomas, ocular anomalies described in PHACES were not identified in any patient on imaging or fundoscopic examination.

Of note, in 7 of the 19 patients (37%) with asymmetric Meckel cave enlargement, there were subtle MR imaging abnormalities of the posterior fossa, intracranial vessels, or aortic arch and cervical vessels that were missed on the initial MR imaging interpretation (patients 1, 2, 3, 6, 8, 14, and 17). One of these patients (patient 3) was nevertheless diagnosed with PHACES prospectively on the basis of cardiac abnormalities identified on echocardiography. The 6 additional patients were not prospectively identified and were only retrospectively diagnosed with PHACES during our review. One of these patients (patient 1) was initially imaged before the original description of PHACES by Frieden et al in 1996.[7]

Sixty of the 85 patients (71%) evaluated by MR imaging were

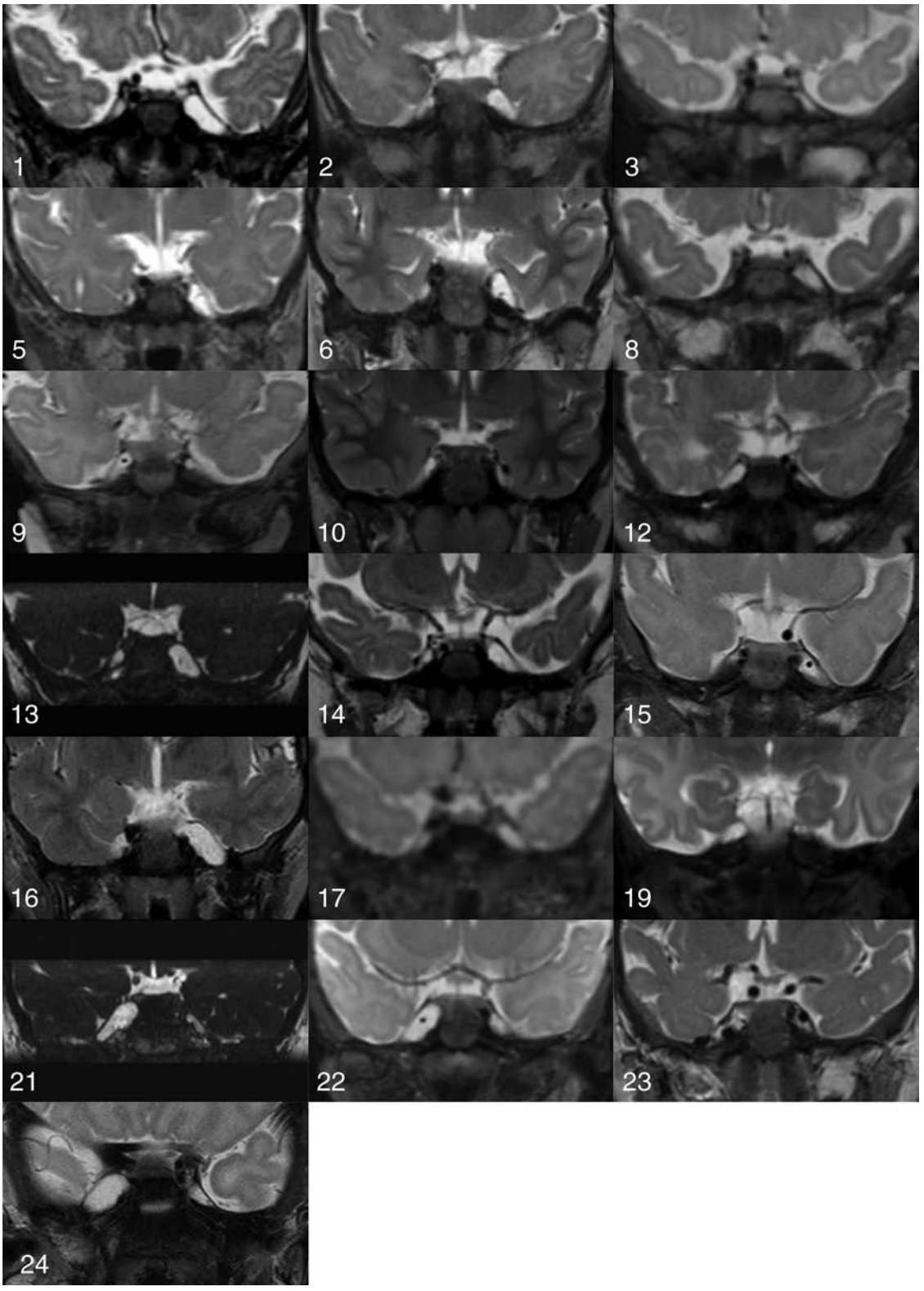

FIG 1. Coronal fluid-sensitive MR images through the bilateral Meckel caves of all patients with asymmetric Meckel cave enlargement. The vascular structure in the enlarged Meckel cave in patients 6, 9, 15, and 22 represents an ipsilateral aberrant ophthalmic artery arising from the basilar artery. The vascular structure in the enlarged right Meckel cave in patient 23 (Fig 2) represents an ectatic persistent trigeminal artery supplying the distal internal carotid artery.

ultimately determined not to have PHACES syndrome. Of these patients, asymmetric ipsilateral Meckel cave enlargement was not identified in any patient.

DISCUSSION

A subset of patients with large or segmental head and neck hemangiomas will have associated morphologic abnormalities that

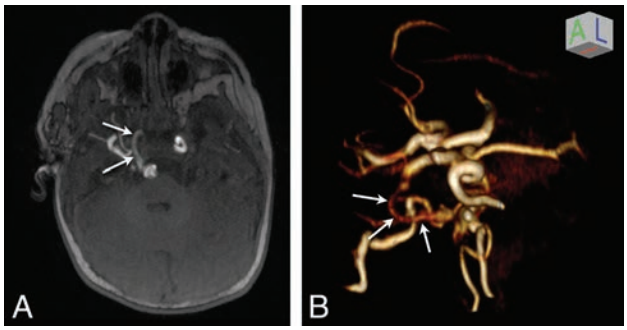

FIG 2. A persistent right trigeminal artery in a 1-year-old girl (patient 23) with PHACES syndrome. *A*, Axial maximum-intensity-projection 3D time-of-flight image demonstrates a persistent right trigeminal artery (*white arrows*). Note that the contralateral left cavernous segment internal carotid artery is tortuous. *B*, Volume-rendered 3D time-of-flight reconstruction demonstrates the persistent trigeminal artery (*white arrows*) connecting the right cavernous segment of the ICA to the tortuous and ectatic basilar artery. Note that the distal right ICA is aplastic proximal to the cavernous segment and is reconstituted via collateral vessels arising from external carotid artery branches.

have fallen under the rubric of PHACES, a neurocutaneous syndrome of uncertain etiology. In our series, 29% of patients referred for MR imaging evaluation for suspicion of PHACES were ultimately diagnosed with PHACES or possible PHACES per consensus guidelines, in line with the overall prevalence reported in prior studies.[1,6]

Thorough and accurate neuroimaging evaluation is one of the mainstays of complete evaluation for such patients, with MR imaging of the brain and MRA of the head and neck recommended in all cases. In addition to evaluating the distribution and extent of proliferative phase infantile hemangiomas, these studies may reveal abnormalities of the posterior fossa, cervicocranial arteries, globes, or aortic arch and great vessels. These findings are important for optimal risk assessment before initiation of β blocker therapy for hemangiomas,[2,3] as well as to cue neurodevelopmental surveillance for possible associated speech and language delays related to posterior fossa anomalies.[4,5]

In this study, we have demonstrated that the finding of asymmetric Meckel cave enlargement ipsilateral to the facial hemangioma is a common feature of PHACES, present in 76% of patients. This imaging finding can serve as a useful and conspicuous marker for the syndrome. When applied as an independent diagnostic criterion to our full patient cohort, the finding demonstrated a sensitivity of 76%, a specificity of 100%, a positive predictive value of 100%, a negative predictive value of 91%, and an accuracy of 93% in predicting a clinical diagnosis of PHACES or possible PHACES syndrome.

In no case was asymmetric Meckel cave enlargement an isolated intracranial finding of PHACES. However, greater than one-third of our patients with Meckel cave enlargement had additional subtle stigmata of PHACES that were missed on the initial evaluation. These may have been more easily or accurately identified with a heightened pretest probability for PHACES associated with asymmetric Meckel cave enlargement. Thus, recognition of this finding could increase the diagnostic sensitivity of neuroimaging for PHACES syndrome. If these additional intracranial findings had been prospectively made in the setting of asymmetric Meckel cave enlargement, the diagnostic sensitivity of MR imaging/MRA for PHACES would have increased by 24% in our cohort.

Meckel cave enlargement as a finding in PHACES syndrome has only rarely been described in the literature to date, to our knowledge, and is not an abnormality that is currently included in the consensus criteria for PHACES. Given the incidence of the finding in our cohort, this omission likely reflects under-reporting. Oza et al[8] described the finding of unilateral Meckel cave prominence in 3 of the 16 patients in their series. The finding was subsequently described in 2 additional case reports.[9,10] Unilateral Meckel cave enlargement is also demonstrated in Figs 6 and 7 in the text *Vascular Lesions of the Head and Neck: Diagnosis and Management* by Persky et al,[11] Figs 1 and 2 from the article by Judd et al,[12] and Fig 5 from the article by Meltzer et al.[13] Furthermore, some authors have described an association of arachnoid cysts and PHACES,[1,2,6,8,12,14] and an asymmetric Meckel cave could conceivably be confused with a middle cranial fossa arachnoid cyst, as was the case in one of our patients (patient 21).

The etiology of unilateral Meckel cave enlargement ipsilateral to the facial hemangioma and posterior fossa anomalies in PHACES syndrome is not definitely known. One plausible explanation derives from the theory that PHACES is caused by aberrant or deficient migration of the cephalic neural crest in a metameric distribution.[15] Neural crest cells and paraxial mesoderm derived from the rhombencephalic metamere contribute to the formation of the skull base; trigeminal nerve ganglia; and facial bones, soft tissues, and blood vessels. Meckel cave enlargement may therefore represent a component of skull base dysplasia secondary to a postzygotic mutation or early prenatal insult in this territory. A similar theory was advanced to explain the relatively high incidence of enlarged IACs seen in PHACES syndrome observed by Meltzer et al.[13]

Alternatively, unilateral enlargement of Meckel cave may be the result of direct expansion secondary to an extant or previously involuted Meckel cave hemangioma. Judd et al[12] reported on the association between PHACES and intracranial hemangiomas. Most commonly described in the cerebellopontine angle or IAC, hemangiomas centered in or extending to Meckel cave both have been described in the literature[12,13] and noted in our series. One of the patients described by Judd et al demonstrated an enlarged Meckel cave containing a hemangioma on initial imaging (Fig 2*C* in Judd et al), which then progressed to isolated Meckel cave enlargement following hemangioma involution (Fig 2*E* in Judd et al), supporting a mechanical etiology of the enlargement.

Metzler et al[13] similarly raised the possibility of a causal association between IAC hemangioma and IAC enlargement. This was based on the increased prevalence of IAC hemangiomas within the enlarged IACs in children when imaged at younger than 1 year of age, compared with children older than 1 year of age at initial imaging, in whom the hemangiomas were presumed to have previously involuted. Given that Meckel cave hemangioma was present in only 1 of 19 patients with Meckel cave enlargement in our cohort, with a median age of 4 months at imaging, it is unlikely that mechanical enlargement can adequately explain the etiology of this finding in all patients in our cohort.

Limitations of our study included the retrospective nature of the analysis and the relatively small sample size. Also, a subset of

patients with PHACES may possibly present without obvious cutaneous stigmata. These patients would likely have been missed by our diagnostic algorithm, and any data regarding the prevalence of asymmetric Meckel cave enlargement may not be applicable to this population of patients.

CONCLUSIONS

Asymmetric Meckel cave enlargement was a common feature of patients with PHACES and possible PHACES in our cohort and may serve as a conspicuous marker for the syndrome. Increased awareness of this imaging feature has the potential to increase the diagnostic accuracy of the neuroimaging evaluation for PHACES in the setting of large or segmental facial hemangiomas.

REFERENCES

1. Metry D, Heyer G, Hess C, et al; PHACE Syndrome Research Conference. **Consensus Statement on Diagnostic Criteria for PHACE Syndrome.** *Pediatrics* 2009;124:1447–56 CrossRef Medline
2. Siegel DH, Tefft KA, Kelly T, et al. **Stroke in children with posterior fossa brain malformations, hemangiomas, arterial anomalies, coarctation of the aorta and cardiac defects, and eye abnormalities (PHACE) syndrome: a systematic review of the literature.** *Stroke* 2012;43:1672–74 CrossRef Medline
3. Metry D, Frieden IJ, Hess C, et al. **Propranolol use in PHACE syndrome with cervical and intracranial arterial anomalies: collective experience in 32 infants.** *Pediatr Dermatol* 2013;30:71–89 CrossRef Medline
4. Tangtiphaiboontana J, Hess CP, Bayer M, et al. **Neurodevelopmental abnormalities in children with PHACE syndrome.** *J Child Neurol* 2013;28:608–14 CrossRef Medline
5. Brosig CL, Siegel DH, Haggstrom AN, et al. **Neurodevelopmental outcomes in children with PHACE syndrome.** *Pediatr Dermatol* 2016;33:415–23 CrossRef Medline
6. Metry DW, Haggstrom AN, Drolet BA, et al. **A prospective study of PHACE syndrome in infantile hemangiomas: demographic features, clinical findings, and complications.** *Am J Med Genet A* 2006; 140:975–86 Medline
7. Frieden IJ, Reese V, Cohen D. **PHACE syndrome: the association of posterior fossa brain malformations, hemangiomas, arterial anomalies, coarctation of the aorta and cardiac defects, and eye abnormalities.** *Arch Dermatol* 1996;132:307–11 Medline
8. Oza VS, Wang E, Berenstein A, et al. **PHACES association: a neuroradiologic review of 17 patients.** *AJNR Am J Neuroradiol* 2008;29: 807–13 CrossRef Medline
9. Arora SS, Plato BM, Sattenberg RJ, et al. **Adult presentation of PHACES syndrome.** *Interv Neuroradiol* 2011;17:137–46 CrossRef Medline
10. Rosmaninho A, Machado S, Bastos-Leite AJ, et al. **PHACE syndrome: a new case report.** *Eur J Dermatol* 2011;21:289–90 CrossRef Medline
11. Persky MS, Waner M, Blei F, et al. *Vascular Lesions of the Head and Neck: Diagnosis and Management.* New York: Thieme; 2015:chap 6
12. Judd CD, Chapman PR, Koch B, et al. **Intracranial infantile hemangiomas associated with PHACE syndrome.** *AJNR Am J Neuroradiol* 2007;28:25–29 Medline
13. Meltzer DE, Robson CD, Blei F, et al. **Enlargement of the internal auditory canal and associated posterior fossa anomalies in PHACES association.** *AJNR Am J Neuroradiol* 2015;36:2159–62 CrossRef Medline
14. Hartemink DA, Chiu YE, Drolet BA, et al. **PHACES syndrome: a review.** *Int J Pediatr Otorhinolaryngol* 2009;73:181–87 CrossRef Medline
15. Krings T, Geibprasert S, Luo CB, et al. **Segmental neurovascular syndromes in children.** *Neuroimaging Clin N Am* 2007;17:245–58 CrossRef Medline

Characterization of Extensive Microstructural Variations Associated with Punctate White Matter Lesions in Preterm Neonates

X. Li, J. Gao, M. Wang, J. Zheng, Y. Li, E.S. Hui, M. Wan, and J. Yang

ABSTRACT

BACKGROUND AND PURPOSE: Punctate white matter lesions are common in preterm neonates. Neurodevelopmental outcomes of the neonates are related to the degree of extension. This study aimed to characterize the extent of microstructural variations for different punctate white matter lesion grades.

MATERIALS AND METHODS: Preterm neonates with punctate white matter lesions were divided into 3 grades (from mild to severe: grades I–III). DTI-derived fractional anisotropy, axial diffusivity, and radial diffusivity between patients with punctate white matter lesions and controls were compared with Tract-Based Spatial Statistics and tract-quantification methods.

RESULTS: Thirty-three preterm neonates with punctate white matter lesions and 33 matched controls were enrolled. There were 15, 9, and 9 patients, respectively, in grades I, II, and III. Punctate white matter lesions were mainly located in white matter adjacent to the lateral ventricles, especially regions lateral to the trigone, posterior horns, and centrum semiovale and/or corona radiata. Extensive microstructural changes were observed in neonates with grade III punctate white matter lesions, while no significant changes in DTI metrics were found for grades I and II. A pattern of increased axial diffusivity, increased radial diffusivity, and reduced/unchanged fractional anisotropy was found in regions adjacent to punctate white matter lesion sites seen on T1WI and T2WI. Unchanged axial diffusivity, increased radial diffusivity, and reduced/unchanged fractional anisotropy were observed in regions distant from punctate white matter lesion sites.

CONCLUSIONS: White matter microstructural variations were different across punctate white matter lesion grades. Extensive change patterns varied according to the distance to the lesion sites in neonates with severe punctate white matter lesions. These findings may help in determining the outcomes of punctate white matter lesions and selecting treatment strategies.

ABBREVIATIONS: AD = axial diffusivity; CST = corticospinal tract; FA = fractional anisotropy; GCC = genu of the corpus callosum; IFO = inferior fronto-occipital fasciculus; OR = optic radiation; PWML = punctate white matter lesion; RD = radial diffusivity; SCC = splenium of corpus callosum

Punctate white matter lesions (PWMLs) are common in neonates and have been found in >20% of preterm neonates (<37 weeks of gestation).[1-5] These lesions may cause severe neurologic disorders, such as cerebral palsy.[2,4] PWMLs can be identified on conventional MR imaging as hyperintensity on T1WI and hypointensity on T2WI.[1-3,6] PWMLs without cystic lesions can be divided into 3 grades.[6] The grading scale ascends in severity on the basis of the number, size, and distribution of cerebral white matter lesions. Extensive microstructural alterations in white matter beyond the PWMLs visible on conventional MR imaging have been observed.[3] The neurodevelopmental outcome of neonates is related to the degree of extension associated with PWMLs.[7,8] However, little is known about the extent of microstructural variations for different PWML grades. More detail is needed regarding the size ranges, shapes, and locations of neonatal/infantile PWMLs, PWML diffusion characteristics, and the distinction between hemorrhagic and nonhemorrhagic PWMLs.[9]

DTI could provide quantitative metrics that reveal microstructural alterations associated with lesions.[10,11] DTI metrics, especially directional diffusivities, are sensitive to underlying histopathologic processes.[12] Several methods for analyzing DTI data

Received July 27, 2016; accepted after revision January 26, 2017.

From the Department of Radiology (X.L., J.G., M. Wang, Y.L., J.Y.) and Clinical Research Center (J.Z.), the First Affiliated Hospital, Xi'an, Shaanxi, China; Department of Biomedical Engineering (X.L., M. Wan, J.Y.), the Key Laboratory of Biomedical Information Engineering of the Ministry of Education, School of Life Science and Technology, Xi'an Jiaotong University, Xi'an, China; and Department of Diagnostic Radiology (E.S.H.), University of Hong Kong, Hong Kong, China.

Xianjun Li and Jie Gao contributed equally to this work.

This work was supported by grants from the National Natural Science Foundation of China (No.81171317, 81471631), the National Key Research and Development Program of China (2016YFC0100300), and the 2011 New Century Excellent Talent Support Plan from the Ministry of Education of China (NCET-11–0438).

Please address correspondence to Jian Yang, PhD, Department of Radiology, The First Affiliated Hospital, Xi'an Jiaotong University, Xi'an, Shaanxi, China; e-mail: cjr.yangjian@vip.163.com

http://dx.doi.org/10.3174/ajnr.A5226

have been proposed. Tract-Based Spatial Statistics (TBSS; http://fsl.fmrib.ox.ac.uk/fsl/fslwiki/TBSS) is an automated approach for assessing alterations on major white matter tracts.[13] The tract quantification method was proposed to characterize the location of alterations in white matter.[14] These automated quantified methods have been used to detect variations due to brain development or injury[3,13-15] and may enable characterization of alterations associated with PWMLs.

The goal of this study was to explore white matter microstructural variations associated with PWMLs of different grades in preterm neonates and to characterize the change in microstructural patterns along white matter tracts.

MATERIALS AND METHODS

This is a cross-sectional and observational study. It was approved by the institutional review board of the First Affiliated Hospital of Xi'an Jiaotong University. The parents of the neonates were informed of the risks of MR imaging and gave written consent.

Subjects

Preterm neonates were enrolled from the neonatal intensive care unit of the First Affiliated Hospital of Xi'an Jiaotong University, from January 2011 to October 2012. During this period, the care, management, MR imaging scanner, and sequences did not change. The inclusion criterion was evidence of punctate lesions in cerebral white matter, which presented as hyperintensity on T1WI and hypointensity on T2WI. Subjects with a clinical diagnosis of congenital malformations of the central nervous system, infections, metabolic disorders, hydrocephalus, gray matter lesions, or major destructive white matter lesions such as cystic degeneration and infarction were excluded. Brain MR imaging was also performed on preterm neonates with comorbid conditions of neonatal asphyxia, hypocalcemia, aspiration pneumonia, and so forth. The preterm neonates without any MR imaging abnormality and matched for sex, gestational age, postnatal age at MR imaging, and birth weight were selected as controls.

MR Imaging Acquisition

The MR imaging datasets used in this study were acquired for clinical examination and diagnosis. To reduce head movement and complete the MR imaging procedure, we sedated patients with a relatively low dose of oral chloral hydrate (25–50 mg/kg).[16] Patient selection, monitoring, and management were performed following the "Guidelines for Monitoring and Management of Pediatric Patients during and after Sedation for Diagnostic and Therapeutic Procedures: An Update."[17] Neonates were laid in a supine position and snugly swaddled in blankets. A pediatrician was present during the MR imaging. Micro earplugs were placed bilaterally in the external acoustic meatuses of the subjects to protect their hearing. The subjects' heads were immobilized by molded foam. Temperature, heart rate, and oxygen saturation were monitored throughout the procedure.

Three-dimensional fast spoiled gradient-recalled echo T1WI, fast spin-echo T2WI, and single-shot echo-planar DTI were performed on a 3T scanner (Signa HDXT; GE Healthcare, Milwaukee, Wisconsin) with an 8-channel head coil. The other parameters for DTI were the following: 35 gradient directions; b-values = 0 and 1000 s/mm^2; TR/TE = 5500/95–105 ms; section thickness = 4 mm without a gap; FOV = 180 × 180 mm^2; matrix size = 128 × 128; and voxel size = 1.41 × 1.41 × 4 mm^3.

MR Imaging Interpretation

To provide clues for the etiology of PWMLs, the comorbid conditions of neonates were recorded by the clinician from the neonatal intensive care unit of the institution. Two radiologists, blinded to the clinical history of the neonates, independently analyzed the MR imaging. Both of the radiologists had >10 years of experience in the interpretation of the neonatal brain MR imaging. Neonates with PWML were grouped into grades I, II, and III (from mild to severe) by using the following MR imaging grading method[6]: grade I: 1 or 2 relatively small lesions (diameter, ≤3 mm); grade II: a) ≥3 lesions, or b) 1 large lesion (diameter, ≥5 mm); and grade III: a) ≥3 lesions, and b) multiple large lesions (diameter, ≥5 mm). The locations of PWMLs were recorded as follows: anterior region (anterior to the frontal horn of the lateral ventricles), central region (between the frontal horn and the trigon of the lateral ventricles), and posterior region (posterior to the trigon of the lateral ventricles).[1] The lesion load in the aforementioned regions was calculated separately. Lesions longer than 5 mm were segmented into subsections in units of 5 mm. Every subsection was counted while we calculated the lesion load.

Preprocessing of DTI Data

DTI data were processed by using the FMRIB software library (FSL; http://www.fmrib.ox.ac.uk/fsl).[18] First, the eddy current correction was performed. Then, brain regions were extracted by using the FSL Brain Extraction Tool (http://fsl.fmrib.ox.ac.uk/fsl/fslwiki/BET). To exclude the influence of artifacts, we rejected artifact-corrupted volumes (directions) automatically before the tensor estimation.[19] The number of rejected volumes varied across subjects (median = 2; range, 0~11). DTI metrics of fractional anisotropy (FA), axial diffusivity (AD), and radial diffusivity (RD) were calculated by using the FMRIB Diffusion Toolbox (http://fsl.fmrib.ox.ac.uk/fsl/fslwiki/FDT).

Image registration was performed by using an optimized protocol.[20,21] First, the group mean FA image in native space was created from the subjects in this study. This method was described in a previous atlas creation study.[22] Second, images of all the subjects were registered to the group mean image. The single-subject FA image with the minimum mean displacement score was selected as the final target.[13,20] Finally, all individual FA images were registered to the target by using a combination of linear and nonlinear registration methods.[20] Other metrics were normalized into the target space by using the deformation parameters of FA.

Voxelwise Analysis of TBSS

The normalized individual FA images were up-sampled to a voxel size of 1 × 1 × 1 mm^3 and then were averaged to create the mean FA.[13] A mean FA skeleton was extracted from the mean FA to represent the center of white matter tracts.[13] The threshold of the FA skeleton was 0.15. DTI metrics were projected onto this skeleton.

Table 1: Demographics of preterm neonates with PWMLs and controls[a]

	PWML Grade I (*n* = 15)	Controls (*n* = 15)	*P* Value	PWML Grade II (*n* = 9)	Controls (*n* = 9)	*P* Value	PWML Grade III (*n* = 9)	Controls (*n* = 9)	*P* Value
GA (wk)	34 + 2 (32 + 0~35 + 6)	34 + 1 (32 + 6~36 + 2)	.21	33 + 6 (30 + 5~34 + 5)	33 + 6 (30 + 1~35 + 0)	.76	33 + 0 (32 + 3~35 + 4)	33 + 2 (32 + 1~35 + 6)	.37
Postnatal age at scan (days)	8 (1~13)	8 (1~13)	.53	10 (6~14)	10 (8~14)	.67	10 (4~13)	9 (1~14)	.80
PMA (wk)	35 + 5 (33 + 1~37 + 2)	36 + 0 (33 + 3~37 + 1)	.32	35 + 3 (32 + 1~36 + 0)	35 + 1 (32 + 1~36 + 4)	.23	34 + 5 (33 + 1~36 + 3)	35 + 2 (32 + 5~36 + 5)	.40
Birth weight (g)	1780 (1470~2360)	1760 (1410~2400)	.22	1950 (1480~2700)	1750 (1460~2360)	.26	1920 (1650~2760)	1700 (1460~2570)	.51
Sex (male/female)	10:5	10:5	–	4:5	4:5	–	3:6	3:6	–

Note:—GA indicates gestational age; PMA, postmenstrual age.

[a] GA, PMA, and birth weight values are medians (ranges). Values in the row of sex are subject numbers. Wilcoxon signed rank tests were used to test the group difference between each grade of PWML and its matched control group due to non-normal distributions of variables. The sex ratios were not tested because they were the same in PWML and the corresponding control groups.

Table 2: Clinical history of subjects

	No. of Subjects (Column-Based Percentage)				
	All Grades (*n* = 33)	Grade I (*n* = 15)	Grade II (*n* = 9)	Grade III (*n* = 9)	Controls (*n* = 33)
Hypoxic-ischemic encephalopathy	20 (61%)	7 (47%)	5 (56%)	8 (89%)	0 (0%)
Neonatal asphyxia	17 (52%)	7 (47%)	3 (33%)	7 (78%)	7 (21%)
Neonatal respiratory distress syndrome	13 (40%)	4 (27%)	3 (33%)	6 (67%)	6 (18%)
Neonatal pneumonia	11 (33%)	6 (40%)	2 (22%)	3 (33%)	2 (6%)
Electrolyte disturbances	10 (30%)	4 (27%)	4 (44%)	2 (22%)	0 (0%)
Neonatal anemia	9 (27%)	4 (27%)	3 (33%)	2 (22%)	4 (12%)
Metabolic acidosis	8 (24%)	3 (20%)	2 (22%)	3 (33%)	7 (21%)
Congenital heart disease	6 (18%)	3 (20%)	0 (0%)	3 (33%)	3 (9%)
Neonatal hypoglycemia	4 (12%)	0 (0%)	2 (22%)	2 (22%)	1 (3%)
Neonatal intracranial hemorrhage	4 (12%)	0 (0%)	2 (22%)	2 (22%)	0 (0%)
Neonatal polycythemia	2 (6%)	0 (0%)	1 (11%)	1 (11%)	0 (0%)
Hyperbilirubinemia	2 (6%)	1 (7%)	1 (11%)	0 (0%)	6 (18%)
Agenesis of bronchus	1 (3%)	0 (0%)	1 (11%)	0 (0%)	0 (0%)
Neonatal hypocalcemia	0 (0%)	0 (0%)	0 (0%)	0 (0%)	9 (27%)
Aspiration pneumonia	0 (0%)	0 (0%)	0 (0%)	0 (0%)	7 (21%)

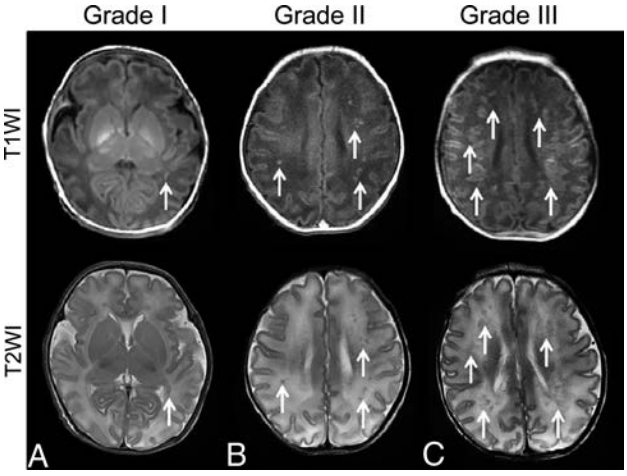

FIG 1. The appearances of 3 PWML grades (*A*, grade I; *B*, grade II; *C*, grade III) on T1WI and T2WI.

Tract-Quantification Analysis

To characterize the change patterns along white matter tracts, we quantified the DTI metrics on the representative tracts: projection fibers of the corticospinal tract (CST) and optic radiation (OR); commissural fibers of the splenium of the corpus callosum (SCC) and genu of the corpus callosum (GCC); and association fibers of the inferior fronto-occipital fasciculus (IFO). First, images of all subjects were normalized to the neonatal template.[22] Second, measurement planes were equally spaced[14] on the tract probabilistic map (cmrm.med.jhmi.edu) for the neonatal template.[22] Measurements were then averaged on each plane.[14] Finally, DTI metrics were measured at 100 equivalent levels.[15] The combination of changes in DTI metrics was used to characterize damage types.[12]

Statistical Analysis

Each case was matched with a control by sex (the same sex in PWML and control groups), gestational age (differences, <1 week), postnatal age at scanning (differences, <5 days), and birth weight (differences, <0.5 kg). Because case and control groups were dependent after matching, Wilcoxon signed rank tests were used for the group difference in demographics between each grade of PWML and its matched control group due to non-normal distributions of variables. κ tests and intraclass correlation coefficients were used to determine intrarater and interrater agreement for the PWML grading and the lesion number respectively. $P < .05$ was significant for the above analyses.

The lesion number was counted repeatedly in anterior, central, and posterior regions for each PWML subject. The Friedman test was used to assess the variation of lesion number across regions. Then pair-wise comparisons among the 3 regions were performed by using Wilcoxon signed rank tests. $P < .017$ (.05/3) was considered significant after the Bonferroni correction. The analyses above were performed by using SPSS (Version 17.0; IBM, Armonk, New York).

The FSL Randomize tool (http://fsl.fmrib.ox.ac.uk/fsl/fslwiki/Randomise/UserGuide) was used for the voxelwise analysis to compare PWML groups and controls. The number of permutations was 10,000. Tests in TBSS were considered significant at $P < .05$ after the threshold-free cluster enhancement and family-wise error rate correction.

In tract-quantification analysis, the Wilcoxon signed rank test in MATLAB (Version 7.11; MathWorks, Natick, Massachusetts) was used to evaluate differences in regional values of DTI metrics between PWML groups and controls. $P < .05$ was considered significant for this analysis.

Table 3: Lesion load of PWMLs in the anterior, central, and posterior regions[a]

Grade	Lesion No. (Median and Range)			*P* Value		
	Anterior	Central	Posterior	Anterior vs Central	Central vs Posterior	Anterior vs Posterior
I	0 (0∼0)	0 (0∼1)	1 (1∼2)	.32	<.001[b,c]	<.001[b,c]
II	0 (0∼6)	1 (0∼9)	5 (3∼12)	.17	.02[b]	<.01[b,c]
III	8 (2∼18)	24 (5∼38)	16 (12∼29)	<.01[b,c]	.37	.01[b,c]

[a] The inter-region comparisons were performed with the Wilcoxon signed rank test after the Friedman test. The anterior region is anterior to the frontal horn of the lateral ventricles. The central region is between the frontal horn and the trigon of the lateral ventricles. The posterior region is posterior to the lateral ventricles.
[b] $P < .05$.
[c] $P < .017$ (.05/3), significant after the Bonferroni correction.

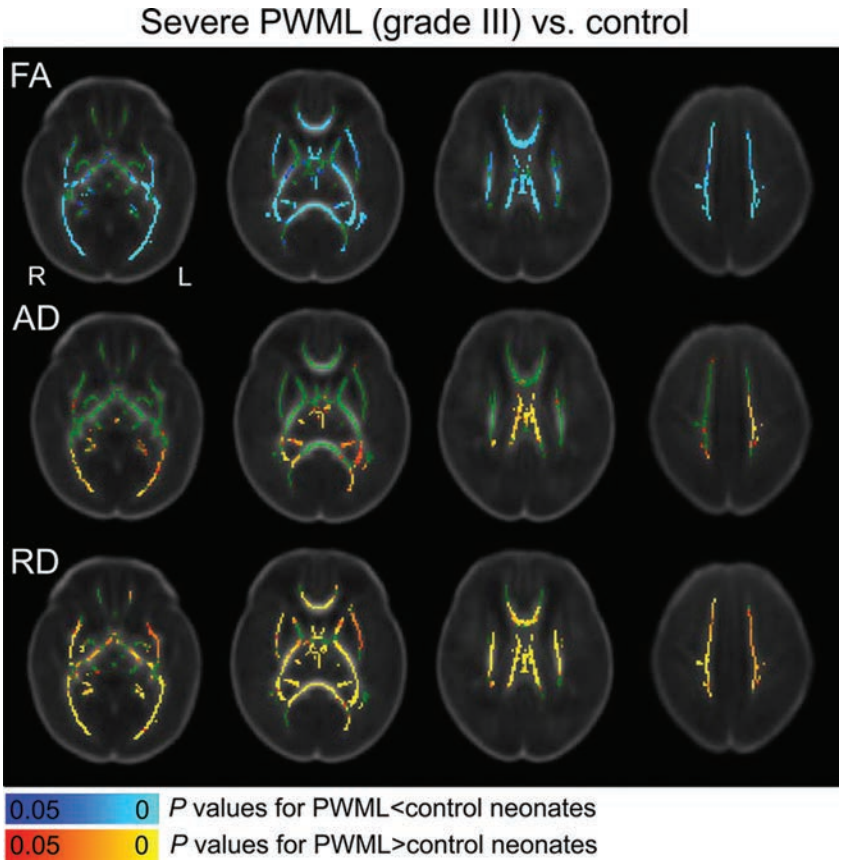

FIG 2. Changes in DTI metrics (FA, AD, and RD) in preterm neonates with severe PWMLs compared with controls revealed by TBSS (there were no significant changes in neonates with PWML grades I and II). Green regions represent the mean FA skeleton without any significant differences. Significant decreases in neonates with PWMLs compared with controls are shown in cool colors (blue and light blue). Significant increases in neonates with PWMLs compared with controls are shown in warm colors (red and yellow).

RESULTS

Demographics

Thirty-three preterm neonates with PWMLs and 33 matched controls were enrolled. The intrarater and interrater agreement for PWML grading was 97% (κ value = 0.953; standard error = 0.906) and 93.3% (κ value = 0.906; standard error = 0.063), respectively. Fifteen, 9, and 9 neonates with PWMLs were classified into grades I, II, and III, respectively. No significant differences in gestational age, postnatal age at MR imaging, postmenstrual age, or birth weight were found between neonates with PWMLs and controls (Table 1). In this study, PWMLs were associated with many comorbid conditions (Table 2). More than half of the neonates with PWMLs had a clinical history of hypoxic-ischemic encephalopathy (61%) and neonatal asphyxia (52%).

PWML Location

PWMLs were mainly located in the white matter adjacent to lateral ventricles, especially the regions lateral to the trigone, posterior horns, and the centrum semiovale and/or corona radiata (Fig 1). The intrarater and interrater correlation coefficients for the lesion number counting were 0.994 (95% confidence interval, 0.989∼0.997) and 0.974 (95% confidence interval, 0. 948∼0. 987), respectively. For grades I and II, most of the lesions were located in the posterior region (Table 3). For grade III, more lesions were located in the central and posterior regions than in the anterior region (Table 3).

Microstructural Alterations in Different PWML Grades

The extent of microstructural alterations was different across PWML grades. There were no significant changes in grades I and II compared with controls ($P \geq .05$). For neonates with PWML grade III, reduced FA, increased AD, and increased RD were observed in the centrum semiovale and/or corona radiata, white matter near the trigone of the lateral ventricles, SCC, and OR (Fig 2). These regions were near PWML sites seen on T1WI and T2WI (Fig 1). Reduced FA, unchanged AD, and increased RD were observed in regions distant from the lesion sites, including the CST in the posterior limb of the internal capsule, more extensive areas in the OR, and the central part of the SCC, GCC, IFO, and the external capsule (Fig 2).

Microstructural Alterations along Tracts

Different patterns of microstructural changes associated with severe PWMLs (grade III) were found along white matter tracts (Fig 3). Increased AD, increased RD, and reduced/unchanged FA were found in the superior part of the CST, the occipital proximal region of the OR, the peripheral regions of the SCC near the lateral ventricles, the anterior and posterior regions of the left IFO, and the anterior region of the right IFO. Unchanged AD, increased RD, and unchanged/reduced FA were observed in the posterior limb of the internal capsule part of the CST, the region of the OR proximal to the thalamus, central regions of the SCC and GCC, the central region of the left IFO, and the central and posterior regions of the right IFO.

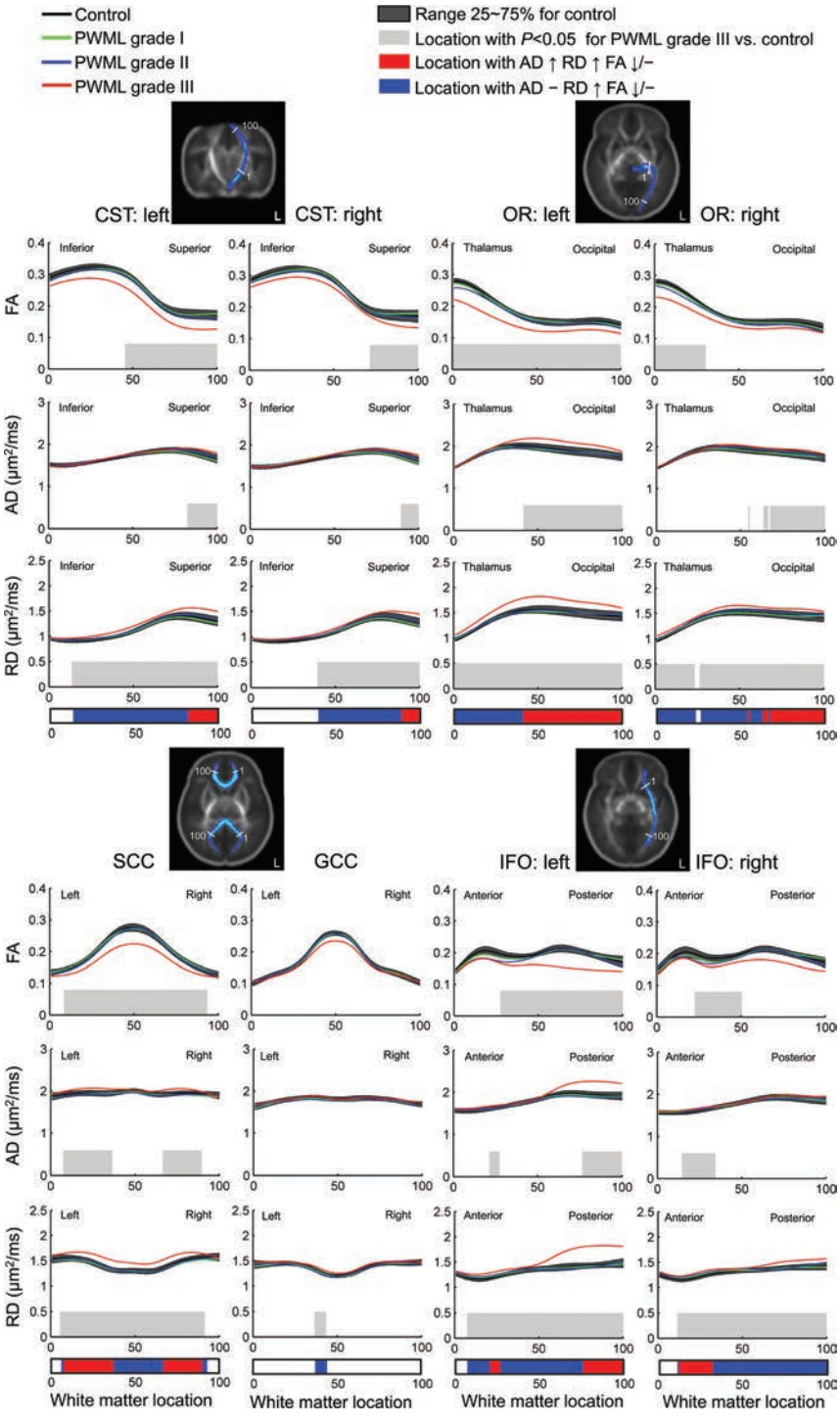

FIG 3. Changes in DTI metrics (FA, AD, and RD) along white matter tracts in preterm neonates with PWML grades I, II, and III compared with controls.

DISCUSSION

The results demonstrated different levels of microstructural alterations across the 3 PWML grades. Extensive white matter alterations were revealed by DTI metrics in neonates with PWML grade III. There were 2 main patterns of alterations found with DTI. The distribution of alterations was related to the distance to lesions visible on the conventional MR imaging.

The etiology of PWMLs is nonspecific.[8] PWMLs were associated with various comorbid conditions in this study (Table 2). Knowledge of the pathogenesis of PWMLs is limited.[7] Evidence has revealed that PWMLs may correspond to vascular congestion with infiltration of activated microglia.[8] Late myelination defects indicate that gliosis and/or loss of oligodendrocytes is possible.[7] Although the etiology and pathogenesis are nonspecific and complex, the location of PWMLs is regular.

PWML Location

PWMLs were common along the corona radiata, in the posterior periventricular white matter, and along the OR. This finding is consistent with previous ones.[7,8,23] The distribution of injury is in agreement with areas of high microglia density and deep medullary venous anatomy.[7,23] Microglia accumulate in restricted laminar bands, most notably around 19–30 gestational weeks, at the axonal crossroads in the centrum semiovale, extending caudally in the immature white matter to the OR.[24] The most vulnerable area is the region of the terminal veins, which is a collection of medullary veins in the posterior frontal, central, and parietal regions.[23] In summary, metabolic demand and regional cerebral blood flow contribute to the distribution of the white matter lesions.[25]

Extensive Microstructural Alterations in Different PWML Grades

The developmental outcome of PWMLs is related to the degree of extension.[7,8] The results in this study reveal that extensive microstructural changes were different across PWML grades. This finding may be due to different pathophysiologic mechanisms[2,6] or different effects on brain development.[2] Rare isolated PWMLs can disappear during brain development and leave no residual abnormality.[3,7,26,27] We found that there were no extensive microstructural alterations associated with PWML grades I and II. Several studies have shown that PWML-related alterations extend beyond the immediate area of injury.[3,28] Extensive microstructural alterations were revealed here in neonates with severe PWMLs. Relatively larger lesions leave areas of hypomyelination, which may relate to focal gliosis, oligodendroglial injury, or axonal swelling in lesion sites.[2,6,7] A cross-talk exists between axons and oligodendrocytes during development.[29] This cross-talk maintains proper metabolic function of axons, trophic support, cytoskeletal arrangement, ion channel organiza-

tion, and axonal transport.[29] Damage to axons or glial cells in PWML sites would affect healthy cross-talk between the axons and the oligodendrocytes along the tract. This may influence the proliferation of oligodendrocyte precursor cells and further myelination, even in areas distant from the lesion sites.

In this study, severe PWML-related alterations were widespread along various white matter tracts, including the CST, OR, SCC, GCC, and IFO. The corticospinal tracts are the major projectional motor fibers of the brain. It has been found that altered structural integrity in the CST may result in delayed psychomotor development,[30] motor impairment,[8] and cerebral palsy.[30,31] High rates of motor impairment or cerebral palsy have been found in subjects with PWMLs.[2,8] Visual function in preterm neonates at term-equivalent age is directly related to the development of white matter in the OR.[32] In agreement with previous findings, PWMLs are often present in the OR and may be associated with impaired visual function.[4,8] The corpus callosum is the primary center for the interhemispheric integration of information.[33] Pictogram test performance,[34] Psychomotor Developmental Index scores,[30] and the speed of bimanual motor coordination[33] are related to the structural integrity of the SCC. The development of the GCC is involved in the maturation of semantic coding,[34] intelligence,[35] and visual learning, possibly through a higher level integration of visual information relayed to the frontal lobes by the IFO.[36] The IFO connects the occipital lobe with the frontal cortex, playing a critical role in neurocognitive maturation of processing speed, visual learning,[36] and semantic processing.[37] The widespread alterations in projection, commissural, and association fibers associated with PWMLs may result in motor, sensory, and cognitive disorders.[4,7,8]

Regional Microstructural Alteration Patterns

Changes in DTI metrics demonstrated a PWML site-related spatial distribution: significantly increased AD, increased RD, and decreased/unchanged FA in regions adjacent to the PWML sites, with unchanged AD, increased RD, and decreased/unchanged FA in regions distant from the PWML sites. These 2 patterns may be related to different mechanisms underlying the effects of PWMLs on brain development, including the delayed oligodendrocyte proliferation or the death of oligodendrocyte progenitors, and the disturbed maturation of oligodendrocytes. During normal brain development, the proliferation of glial cell bodies is linked to decreases in diffusivity indices in all directions. This process would lead to unchanged or increased FA.[38] The disrupted cross-talk between an axon and oligodendrocytes would delay the early process of the oligodendrocyte proliferation or lead to the death of oligodendrocyte progenitors.[29,39] Increases of AD and RD in regions adjacent to PWMLs may reveal this process. The increase in RD without changes in AD could reflect demyelination or dysmyelination.[40,41] In the regions distant from the lesion sites, the change in AD was not significant. This finding suggested that maturation of oligodendrocytes was disturbed without loss of oligodendrocytes in these regions.[39]

According to previous studies[7,8] and one of our ongoing cohort studies, outcomes during infancy and/or preschool age were relevant to the PWML grading and extensive microstructural alterations observed on MR imaging during the neonatal period. Early intervention is associated with improved outcomes.[42] Considering that extensive microstructural alterations were different across PWML grades, patients with different PWML grades should be treated with different approaches. Widespread microstructural changes were observed in neonates with PWML grade III. This finding suggests that early multifaceted treatment strategies (including rehabilitation and interventions associated with motor and cognitive competence, and so forth) might be beneficial to patients.

This study had several limitations. Widespread variations were observed in neonates with severe PWMLs. However, only several representative tracts were selected during the tract-quantification analysis. Besides the selected tracts, other structures (superior fronto-occipital fascicle, tapetum, and so forth) would also be vulnerable. The follow-up work is not finished. We will try to verify outcomes of the enrolled subjects in the future work. The sample size of neonates with PWMLs in each group is relatively small. Furthermore, this work is an in vivo study on the human brain. Pathologic experiments are needed to reveal the exact microstructural changes associated with PWMLs.

CONCLUSIONS

White matter microstructural variations were different across PWML grades. Extensive change patterns varied according to the distance to lesion sites in neonates with severe PWMLs. These findings may help in determining outcomes of PWMLs and selecting appropriate early treatment strategies.

ACKNOWLEDGMENTS

The authors are grateful to Drs Li Liu, Xihui Zhou, and Xiaoquan Li in the neonatology department for preparing and monitoring the neonates before and during imaging.

Disclosures: Jian Yang—*RELATED*: *Grant*: National Natural Science Foundation of China, Ministry of Education of China, Ministry of Science and Technology of China, *Comments*: This work was supported by grants from the National Natural Science Foundation of China (No.81171317, 81471631), the National Key Research and Development Program of China (2016YFC0100300), and the 2011 New Century Excellent Talent Support Plan from the Ministry of Education of China (NCET-11-0438). * *Money paid to the institution.

REFERENCES

1. Tortora D, Panara V, Mattei PA, et al. **Comparing 3T T1-weighted sequences in identifying hyperintense punctate lesions in preterm neonates.** *AJNR Am J Neuroradiol* 2015;36:581–86 CrossRef Medline
2. Kersbergen KJ. **Different patterns of punctate white matter lesions in serially scanned preterm infants.** *PLoS One* 2014;9:e108904 CrossRef Medline
3. Bassi L, Chew A, Merchant N, et al. **Diffusion tensor imaging in preterm infants with punctate white matter lesions.** *Pediatr Res* 2011;69:561–66 CrossRef Medline
4. de Bruïne FT, van den Berg-Huysmans AA, Leijser LM, et al. **Clinical implications of MR imaging findings in the white matter in very preterm infants: a 2-year follow-up study.** *Radiology* 2011;261:899–906 CrossRef Medline
5. Dyet LE, Kennea N, Counsell SJ, et al. **Natural history of brain lesions in extremely preterm infants studied with serial magnetic resonance imaging from birth and neurodevelopmental assessment.** *Pediatrics* 2006;118:536–48 CrossRef Medline
6. Childs AM, Cornette L, Ramenghi LA, et al. **Magnetic resonance and cranial ultrasound characteristics of periventricular white matter**

abnormalities in newborn infants. *Clin Radiol* 2001;56:647–55 CrossRef Medline
7. Raybaud C, Ahmad T, Rastegar N, et al. **The premature brain: developmental and lesional anatomy.** *Neuroradiology* 2013;55:23–40 CrossRef Medline
8. Rutherford MA, Supramaniam V, Ederies A, et al. **Magnetic resonance imaging of white matter diseases of prematurity.** *Neuroradiology* 2010;52:505–21 CrossRef Medline
9. Niwa T, de Vries LS, Benders MJ, et al. **Punctate white matter lesions in infants: new insights using susceptibility-weighted imaging.** *Neuroradiology* 2011;53:669–79 CrossRef Medline
10. Le Bihan D, Iima M. **Diffusion magnetic resonance imaging: what water tells us about biological tissues.** *PLoS Biol* 2015;13:e1002203 CrossRef Medline
11. Hüppi PS, Murphy B, Maier SE, et al. **Microstructural brain development after perinatal cerebral white matter injury assessed by diffusion tensor magnetic resonance imaging.** *Pediatrics* 2001;107:455–60 CrossRef Medline
12. Wang S, Wu EX, Tam CN, et al. **Characterization of white matter injury in a hypoxic-ischemic neonatal rat model by diffusion tensor MRI.** *Stroke* 2008;39:2348–53 CrossRef Medline
13. Smith SM, Jenkinson M, Johansen-Berg H, et al. **Tract-based spatial statistics: voxelwise analysis of multi-subject diffusion data.** *Neuroimage* 2006;31:1487–505 CrossRef Medline
14. Groeschel S, Tournier JD, Northam GB, et al. **Identification and interpretation of microstructural abnormalities in motor pathways in adolescents born preterm.** *Neuroimage* 2014;87:209–19 CrossRef Medline
15. Yeatman JD, Dougherty RF, Myall NJ, et al. **Tract profiles of white matter properties: automating fiber-tract quantification.** *PLoS One* 2012;7:e49790 CrossRef Medline
16. Bracken J, Heaslip I, Ryan S. **Chloral hydrate sedation in radiology: retrospective audit of reduced dose.** *Pediatr Radiol* 2012;42:349–54 CrossRef Medline
17. Coté CJ, Wilson S; American Academy of Pediatrics, American Academy of Pediatric Dentistry, Work Group on Sedation. **Guidelines for monitoring and management of pediatric patients during and after sedation for diagnostic and therapeutic procedures: an update.** *Pediatrics* 2006;118:2587–602 CrossRef Medline
18. Smith SM, Jenkinson M, Woolrich MW, et al. **Advances in functional and structural MR image analysis and implementation as FSL.** *Neuroimage* 2004;23(suppl 1):S208–19 CrossRef Medline
19. Li X, Yang J, Gao J, et al. **A robust post-processing workflow for datasets with motion artifacts in diffusion kurtosis imaging.** *PLoS One* 2014;9:e94592 CrossRef Medline
20. Ball G, Counsell SJ, Anjari M, et al. **An optimised tract-based spatial statistics protocol for neonates: applications to prematurity and chronic lung disease.** *Neuroimage* 2010;53:94–102 CrossRef Medline
21. Li X, Gao J, Wang M, et al. **Rapid and reliable tract-based spatial statistics pipeline for diffusion tensor imaging in the neonatal brain: applications to the white matter development and lesions.** *Magn Reson Imaging* 2016;34:1314–21 CrossRef Medline
22. Oishi K, Mori S, Donohue PK, et al. **Multi-contrast human neonatal brain atlas: application to normal neonate development analysis.** *Neuroimage* 2011;56:8–20 CrossRef Medline
23. Raets M, Dudink J, Raybaud C, et al. **Brain vein disorders in newborn infants.** *Dev Med Child Neurol* 2015;57:229–40 CrossRef Medline
24. Verney C, Monier A, Fallet-Bianco C, et al. **Early microglial colonization of the human forebrain and possible involvement in periventricular white-matter injury of preterm infants.** *J Anat* 2010;217:436–48 CrossRef Medline
25. Takashima S, Itoh M, Oka A. **A history of our understanding of cerebral vascular development and pathogenesis of perinatal brain damage over the past 30 years.** *Semin Pediatr Neurol* 2009;16:226–36 CrossRef Medline
26. Ramenghi LA, Fumagalli M, Righini A, et al. **Magnetic resonance imaging assessment of brain maturation in preterm neonates with punctate white matter lesions.** *Neuroradiology* 2007;49:161–67 CrossRef Medline
27. Cornette L, Tanner S, Ramenghi L, et al. **Magnetic resonance imaging of the infant brain: anatomical characteristics and clinical significance of punctate lesions.** *Arch Dis Child Fetal Neonatal Ed* 2002;86:F171–77 CrossRef Medline
28. Miller SP, Vigneron DB, Henry RG, et al. **Serial quantitative diffusion tensor MRI of the premature brain: development in newborns with and without injury.** *J Magn Reson Imaging* 2002;16:621–32 CrossRef Medline
29. Alizadeh A, Dyck SM, Karimi-Abdolrezaee S. **Myelin damage and repair in pathologic CNS: challenges and prospects.** *Front Mol Neurosci* 2015;8:35 CrossRef Medline
30. Pannek K, Scheck SM, Colditz PB, et al. **Magnetic resonance diffusion tractography of the preterm infant brain: a systematic review.** *Dev Med Child Neurol* 2014;56:113–24 CrossRef Medline
31. Jaspers E, Byblow WD, Feys H, et al. **The corticospinal tract: a biomarker to categorize upper limb functional potential in unilateral cerebral palsy.** *Front Pediatr* 2015;3:112 CrossRef Medline
32. Bassi L, Ricci D, Volzone A, et al. **Probabilistic diffusion tractography of the optic radiations and visual function in preterm infants at term equivalent age.** *Brain* 2008;131:573–82 CrossRef Medline
33. Muetzel RL, Collins PF, Mueller BA, et al. **The development of corpus callosum microstructure and associations with bimanual task performance in healthy adolescents.** *Neuroimage* 2008;39:1918–25 CrossRef Medline
34. Kozlovskiy SA, Vartanov AV, Pyasik MM, et al. **Functional role of corpus callosum regions in human memory functioning.** *Int J Psychophysiol* 2012;85:396–97 CrossRef
35. Kontis D, Catani M, Cuddy M, et al. **Diffusion tensor MRI of the corpus callosum and cognitive function in adults born preterm.** *Neuroreport* 2009;20:424–28 CrossRef Medline
36. Peters BD, Ikuta T, DeRosse P, et al. **Age-related differences in white matter tract microstructure are associated with cognitive performance from childhood to adulthood.** *Biol Psychiatry* 2014;75:248–56 CrossRef Medline
37. Ivanova MV, Isaev DY, Dragoy OV, et al. **Diffusion-tensor imaging of major white matter tracts and their role in language processing in aphasia.** *Cortex* 2016;85:165–81 CrossRef Medline
38. Dubois J, Dehaene-Lambertz G, Kulikova S, et al. **The early development of brain white matter: a review of imaging studies in fetuses, newborns and infants.** *Neuroscience* 2014;276:48–71 CrossRef Medline
39. Back SA, Riddle A, McClure MM. **Maturation-dependent vulnerability of perinatal white matter in premature birth.** *Stroke* 2007;38:724–30 CrossRef Medline
40. Song SK, Yoshino J, Le TQ, et al. **Demyelination increases radial diffusivity in corpus callosum of mouse brain.** *Neuroimage* 2005;26:132–40 CrossRef Medline
41. Song SK, Sun SW, Ramsbottom MJ, et al. **Dysmyelination revealed through MRI as increased radial (but unchanged axial) diffusion of water.** *Neuroimage* 2002;17:1429–36 CrossRef Medline
42. Hadders-Algra M, Boxum AG, Hielkema T, et al. **Effect of early intervention in infants at very high risk of cerebral palsy: a systematic review.** *Dev Med Child Neurol* 2017;59:246–58 CrossRef Medline

Measurable Supratentorial White Matter Volume Changes in Patients with Diffuse Intrinsic Pontine Glioma Treated with an Anti-Vascular Endothelial Growth Factor Agent, Steroids, and Radiation

P. Svolos, W.E. Reddick, A. Edwards, A. Sykes, Y. Li, J.O. Glass, and Z. Patay

ABSTRACT

BACKGROUND AND PURPOSE: Assessing the response to treatment in infiltrative brain tumors by using lesion volume–based response criteria is challenging. We hypothesized that in such tumors, volume measurements alone may not accurately capture changes in actual tumor burden during treatment. We longitudinally evaluated volume changes in both normal-appearing supratentorial white matter and the brain stem lesions in patients treated for diffuse intrinsic pontine glioma to determine to what extent adjuvant systemic therapies may skew the accuracy of tumor response assessments based on volumetric analysis.

MATERIALS AND METHODS: The anatomic MR imaging and diffusion tensor imaging data of 26 patients with diffuse intrinsic pontine glioma were retrospectively analyzed. Treatment included conformal radiation therapy in conjunction with vandetanib and dexamethasone. Volumetric and diffusion data were analyzed with time, and differences between time points were evaluated statistically.

RESULTS: Normalized brain stem lesion volume decreased during combined treatment (slope = −0.222, $P < .001$) and increased shortly after completion of radiation therapy (slope = 0.422, $P < .001$). Supratentorial white matter volume steadily and significantly decreased with time (slope = −0.057, $P < .001$).

CONCLUSIONS: Longitudinal changes in brain stem lesion volume are robust; less pronounced but measurable changes occur in the supratentorial white matter. Volume changes in nonirradiated supratentorial white matter during the disease course reflect the effects of systemic medication on the water homeostasis of normal parenchyma. Our data suggest that adjuvant nontumor–targeted therapies may have a more substantial effect on lesion volume changes than previously thought; hence, an apparent volume decrease in infiltrative tumors receiving combined therapies may lead to overestimation of the actual response and tumor control.

ABBREVIATIONS: BL = baseline; BS-L = brain stem lesion; DIPG = diffuse intrinsic pontine glioma; ePFS = end of PFS; eRT = end of RT; PFS = progression-free survival; RT = radiation therapy; ST-WM = supratentorial white matter; VEGF = vascular endothelial growth factor; W = week

Diffuse intrinsic pontine glioma (DIPG), a diffusely infiltrative high-grade glioma, is the most common brain stem tumor in children. Currently used mainstream therapies for DIPG include conformal radiation and adjuvant steroid therapy, which, in recent years, have been combined with new molecularly targeted agents, including vascular endothelial growth factor (VEGF) inhibitors within the framework of Stage I and/or II clinical trials, but key outcome metrics, such as progression-free survival (PFS) and overall survival, have remained dismal.

As with many other brain tumors, longitudinal evaluation of the response to therapy in clinical trials or care relies heavily on MR imaging. Most clinical trials require 2D or 3D measurements or volumetric evaluation of the tumor to monitor and evaluate the response to treatment with time. Such strategies may be appropriate for discrete tumors, but their adequacy in diffusely infiltrative brain tumors is increasingly questioned because conceptually, the "lesion" seen by imaging does not necessarily correspond to the "tumor within," but with conventional, anatomic imaging, one can measure only the "lesion."

In DIPG, radiation therapy (RT) initially results in reduced lesion volume, which is assumed to indicate some degree of tumor control, albeit temporary. Corticosteroids—potent antiedema agents—reduce tumor-induced edema in brain lesions, in gen-

Received October 2, 2016; accepted after revision January 26, 2017.

From the Departments of Diagnostic Imaging (P.S., W.E.R., A.E., J.O.G., Z.P.) and Biostatistics (A.S., Y.L.), St. Jude Children's Research Hospital, Memphis, Tennessee.

This work was supported by the US National Institutes of Health Cancer Center Support grant (P30 CA21765) and by the American Lebanese Syrian Associated Charities.

Please address correspondence to Zoltan Patay, MD, PhD, Section of Neuroimaging, Department of Diagnostic Imaging, St. Jude Children's Research Hospital, 262 Danny Thomas Place, Mail Stop 220, Memphis, TN 38105-3678; e-mail: zoltan.patay@stjude.org

Indicates open access to non-subscribers at www.ajnr.org
Indicates article with supplemental on-line tables.
Indicates article with supplemental on-line photo.

http://dx.doi.org/10.3174/ajnr.A5159

eral. Anti-VEGF agents may also contribute to apparent volume reduction of tumor lesions by reducing the proportion of angioneogenic, leaky vessels and, hence, interstitial, vasogenic edema.[1] It is conceivable that all of these therapeutic measures affect lesion volume reduction, but their respective contributions are undetermined. In this research, we set out to test our hypothesis that volumetric changes in DIPG during treatment may not accurately reflect changes in tumor burden within the apparent brain stem lesion; hence, volumetric analysis in DIPG (and, perhaps, other infiltrative gliomas) may be inadequate for assessing actual tumor response to treatment.

MATERIALS AND METHODS

Patients

In a prospective Phase I clinical trial (SJBG07, NCT00472017; clinicaltrials.gov) conducted at our institution between June 2007 and August 2009, children with newly diagnosed DIPG were treated with conformal photon radiation therapy and vandetanib (ZD6474, ZACTIMA; AstraZeneca, London, England) in conjunction with adjuvant dexamethasone. The study was approved by our institutional review board. Written, informed consent for participation was obtained from the parents or legal guardians of the patients. Results of this clinical trial have been published.[2] For the current research, we requested that the board allow us to retrospectively evaluate some of the clinical, medication, and imaging data collected within the framework of the aforementioned clinical trial. This request, in conjunction with a waiver of repeat consenting, was granted.

Treatment consisted of 3D conformal RT given in 1.8-Gy fractions 5 days/week for 6 weeks, to a total dose of 54 Gy to the brain stem lesion (BS-L) and orally administered vandetanib. The maximum tolerated dose of vandetanib was evaluated by randomizing patients into 1 of 5 strata, with escalating dosage levels of 50 ($n = 3$), 65 ($n = 3$), 85 ($n = 3$), 110 ($n = 16$), or 145 ($n = 10$) mg/m^2 per day. Vandetanib treatment and RT were started on the same day. Patients were receiving oral dexamethasone as an adjuvant therapy before or on admission to our institution. After admission, dexamethasone was administered as necessary on an individual basis to control neurologic signs and symptoms related to the BS-L, with the goal of reducing or discontinuing use when clinically possible.

As per protocol stipulations, partial response to treatment was defined as ≥50% reduction in the sum of the product of the maximum perpendicular diameters of the BS-L by MR imaging and a stable or decreasing dose of dexamethasone accompanied by stable or improving neurologic examination findings maintained for at least 6 weeks (Fig 1). PFS was defined as the time interval from the start of therapy to disease progression or death. Progressive disease, indicating the end of PFS, was defined in the protocol as the following: 1) neurologic abnormalities or worsening neurologic status not explained by causes unrelated to tumor progression (eg, seizures, anticonvulsant toxicity, electrolyte disturbances, sepsis), or 2) a >25% increase in the product of the maximum perpendicular diameters of the tumor lesion by imaging, or 3) increasing doses of dexamethasone required to maintain a stable neurologic status. Patients received additional dexamethasone as necessary toward the end of PFS. Seven patients underwent shunt placement during the course of their disease: 6 patients before (mean, 19 days) and 1 patient (3 days) after RT initiation. Hydrocephalus requiring shunting did not develop in other patients during the study period.

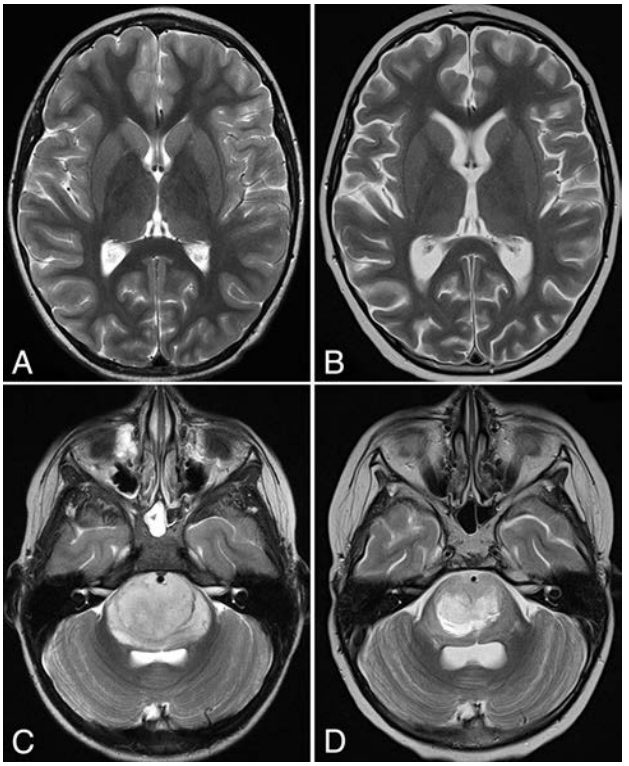

FIG 1. Axial T2-weighted images of the supratentorial brain (*A* and *B*) and brain stem lesions (*C* and *D*) in a patient with DIPG at baseline (*A* and *C*) and after RT (*B* and *D*). *D*, Note the prominent brain stem lesion volume reduction in conjunction with less robust but measurable pseudoatrophic changes within the supratentorial brain parenchyma.

Thirty-five patients with newly diagnosed DIPG were enrolled in the aforementioned therapeutic trial. For the current imaging-based research study, inclusion criteria consisted of the following: 1) patients with newly diagnosed DIPG; 2) participation in the therapeutic protocol and completing RT; 3) a complete dataset of conventional, volumetric, and diffusion data for each patient; and 4) patient follow-up with at least 2 consecutive post-RT imaging studies before the end of PFS (see definition above). Consequently, 3 patients were excluded because they were taken off the trial before the completion of RT because of unacceptable, presumably anti-VEGF–related toxicity. Two patients had no follow-up data: One was taken off protocol at the end of RT because of progressive disease, and the guardian of one withdrew consent on the completion of RT. Another 4 patients survived ≥3 years, suggesting that they may not have had a "classic" DIPG; hence, histopathologic and biologic properties of those tumors might not represent typical DIPG. Overall, 26 patients were eligible for enrollment in our retrospective research (10 boys, 16 girls; mean age at the start of RT, 6.55 ± 3.04 years). Relevant patient data are summarized in On-line Table 1.

MR Imaging

MR imaging was performed on either a 3T system (Magnetom Trio Tim; Siemens, Erlangen, Germany) or a 1.5T platform (Mag-

netom Avanto; Siemens) by using 12-channel matrix head coils. In total, 178 examinations were performed, of which 157 were on the 3T platform. Per protocol requirements, MR imaging examinations were scheduled within 1 week before RT and vandetanib initiation (baseline [BL]); at 1, 3, and 6 weeks (end of RT [eRT]); and every other month (after each vandetanib treatment cycle) until the patient was taken off the study due to progressive disease indicating the end of PFS (ePFS). To maintain consistency between time points of measurements, we considered the initiation of RT as time point zero.

The conventional MR imaging protocol at all time points consisted of whole-brain precontrast sagittal and axial T1W1 gradient-echo and axial T2WI turbo spin-echo sequences. Postcontrast imaging included an axial T1WI gradient-echo sequence and sagittal isotropic 3D MPRAGE and T2WI FLAIR sequences. A section thickness of 4 mm with no gap was used for all 2D acquisitions.

DTI data were acquired by using a double-spin-echo, EPI pulse sequence (TR = 6500–10,000 ms, TE = 100–120 ms, b=0 and 700-1000 s/mm^2) applying bipolar diffusion-encoding gradients to reduce gradient-induced eddy currents. Forty or more 3-mm-thick images were acquired in contiguous axial sections to provide whole-brain coverage with a matrix size of 128 × 128 and an FOV of 192–230 mm^2.

Image Postprocessing

BS-L segmentation was based on T2 hyperintensity and performed by 1 postprocessing specialist supervised by a board-certified, experienced neuroradiologist. T1WI and FLAIR images were aligned to the T2WI from the same examination by using rigid-body registration from the FMRIB Software Library (FSL; http://www.fmrib.ox.ac.uk/fsl). The segmentations were performed manually by drawing an ROI on every T2WI section containing a lesion, and volume was combined across the stack of images. The T1WI and FLAIR coregistered images were used to differentiate lesions from adjacent CSF when necessary (On-line Figure).

For volumetric analysis of supratentorial white matter (ST-WM), T2WI was registered to the T2WI at BL for each patient with the Rigid Body Tools in FSL. The remaining conventional image sets were then aligned to the T2WI for that patient's space by using the same tools. Brain parenchyma masks were computed and then modified to remove the brain stem and cerebellum volume before performing inhomogeneity correction.[3] Finally, the ST-WM volume was segmented by using a Kohonen self-organizing network technique based on T1WI, T2WI, and FLAIR images (On-line Figure).[4,5] Repeated measures of ST-WM demonstrated a predicted variance of approximately 2% with these methods.[5]

DTI data analysis was performed with SPM8 software (http://www.fil.ion.ucl.ac.uk/spm/software/spm12) by using the Diffusion Toolkit (TrackVis; http://www.trackvis.org/dtk) for voxel-wise tensor calculations. Each of the 4 acquisitions was aligned to remove eddy-current drift and patient motion before being averaged. Tensor deconvolution was used to calculate tensors and derive the eigenvectors and eigenvalues. Eigenvalues were combined to acquire ADC parametric maps. The b=0 image, the reference for all tensor calculations, was registered to the T2WI from each examination used for ST-WM segmentation by using the Affine Registration Tools in FSL. The ADC output map was aligned to the same space as the BS-L and ST-WM segmentation data by applying this transformation. These registered maps were used to determine the mean ADC for the segmented BS-L and ST-WM. All output data were normalized to BL.

Volumetric and diffusion measurements of brain stem lesions and supratentorial white matter[a]

	Normalized Volume Mean		Normalized ADC Mean	
Time Points	BS-L	ST-WM	BS-L	ST-WM
Baseline	1.00	1.00	1.00	1.00
eRT	0.65 ± 0.18	0.88 ± 0.11	0.80 ± 0.12	0.98 ± 0.03
W14	0.60 ± 0.17	0.85 ± 0.14	0.76 ± 0.18	0.97 ± 0.06
ePFS	0.99 ± 0.40	0.86 ± 0.11	0.82 ± 0.17	0.95 ± 0.04

[a] All values were normalized to baseline value.

Statistical Analysis

All statistical analyses were conducted by using SAS 9.3 (SAS Institute, Cary, North Carolina). A 2-sided significance level of $P <$ .05 was used for all statistical tests. The changes in volume and ADC measurements between time points were assessed by paired t tests for differences that were normally distributed and by Wilcoxon signed rank tests for differences that were not normally distributed. Normal tests and Q-Q plots were used to assess normality. The false discovery rate method was used to adjust P values for multiple testing.

Linear mixed-effect models were used to describe the patterns of change in volume and ADC measurements with time. The results of pair-wise comparisons between time points, mean response plots with time, and the Akaike information criterion were used to select an optimal mixed-effects model for each measurement. The autoregressive covariance structure was selected to account for the correlation among repeated measurements for all models.

The Wilcoxon rank sum test was used to examine differences in PFS and overall survival between patients with a >50% or ≤50% reduction in volume from baseline.

RESULTS

The mean normalized volume and diffusion values of the BS-Ls and ST-WM are summarized in the Table. In the current study, we longitudinally evaluated volumetric and diffusion changes at 4 distinct clinical time points: at BL, the eRT, 14 weeks (W) from BL (week 14 [W14]), and at the ePFS. The selection of W14 as a time point of measurement was arbitrary, but our data indicated this time as a turning point in the clinical course. Initially, most patients showed clinical and imaging improvement; hence, few patients (2/26) were receiving dexamethasone at that time. Tumor recurrence typically started after W14, and the mean time interval between W14 and ePFS was only 4 ± 3 months.

On the basis of these data, key clinical events, and results of our statistical analysis, we established 3 phases of the evaluation period: Phase I (BL-eRT), Phase II (eRT-W14), and Phase III (W14-ePFS) (Fig 2). Phase I was the combined treatment period (RT, vandetanib for all patients, and dexamethasone for most). The number of patients receiving dexamethasone at baseline and at

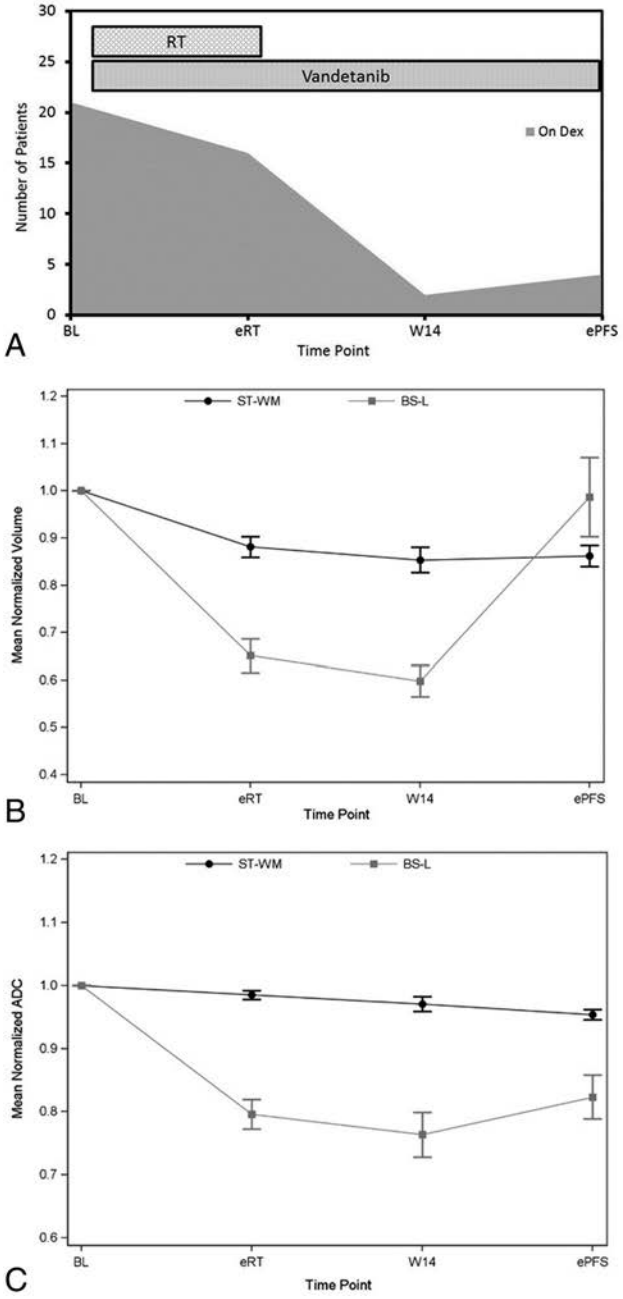

FIG 2. *A*, Treatment duration and number of patients receiving corticosteroids at each time point. Radiation therapy and vandetanib were started on the same date, approximately 1 week from baseline. Longitudinal volumetric (*B*) and diffusion (*C*) changes (mean ± standard error) of the brain stem lesion and supratentorial white matter.

the eRT was 21 and 16, respectively. Phase II indicates the early post-RT period during which patients continued to receive vandetanib and dexamethasone; however, dexamethasone was gradually reduced, and by W14, only 2 patients were still receiving treatment. Phase III was the late post-RT follow-up period leading to the ePFS and patient drop-off from the protocol; it also corresponded to the end of vandetanib administration. Dexamethasone was re-administered as necessary for progressive disease (4/23 patients received dexamethasone by the ePFS time point). Patient medication data at each time point are summarized in On-line Table 2.

In terms of response to treatment, 12/26 patients (46%) had >50% BS-L volume reduction during the therapeutic trial: 5 at the eRT, 3 by W14, and 4 before the ePFS, hence meeting the criterion of partial response as assessed by imaging. However, when we subtracted the volume-reduction percentage of the ST-WM from that of the BS-L for each patient, only 2 had a "net" or "adjusted" volume decrease of the BS-L of >50% (both of those during Phase II) (On-line Table 3).

Volumetric changes of the BS-Ls and ST-WM were analyzed in each phase along with changes in the ADC values. Figure 2 shows longitudinal volumetric and diffusion changes and the treatment scheme applied in each phase.

Overall, the normalized BS-L volume decreased during Phases I and II (slope = −0.222, $P < .001$) and increased in Phase III (slope = 0.422, $P < .001$). The normalized ST-WM volume decreased with time (slope = −0.057, $P < .001$). Similarly, the normalized ST-WM ADC decreased with time (slope = −0.015, $P < .001$), and the normalized BS-L ADC decreased during Phases I and II (slope = −0.125, $P < .001$) and increased in Phase III (slope = 0.069, $P = .02$).

Regarding volumetric and diffusion changes between time points in Phase I, paired *t* test comparisons revealed a statistically significant decrease in BS-L and ST-WM normalized volumes ($P < .001$) and in the normalized BS-L ADC ($P < .001$). No significant changes were observed in either BS-L or ST-WM normalized volumes during Phase II; however, the Wilcoxon signed rank test showed a significant decline in the normalized BS-L ADC ($P = .029$). In Phase III, normalized BS-L volume and ADC increased significantly ($P < .001$ and $P = .029$, respectively). No significant differences were observed in normalized ST-WM volume or ADC between these time points.

We further analyzed our data to determine whether the magnitude of maximal "unadjusted" volume reduction (>50% or <50%) during the monitored course of disease correlated with standard outcome metrics, notably PFS and overall survival. There were no statistically significant differences in PFS and overall survival between patients with a >50% and ≤50% reduction in unadjusted BS-L volume from BL (On-line Table 4).

Our data also showed that at ePFS, only 11 patients had BS-L volumes greater than the corresponding BL volumes and only 4 of those had a volume increase of >25%. In most patients (56%), the BS-L was still smaller at the ePFS than at BL, despite clinical and/or neurologic signs of disease deterioration (On-line Table 5). Altogether, 21 patients (84%) either did not have BS-L volume increases at the ePFS compared with BL or had an increase of <25% (On-line Table 5).

DISCUSSION

According to published data from the Pediatric Brain Tumor Consortium, children with DIPG having >25% decrease in tumor volume (and ADC) after RT have a higher 6-month survival rate than those without such decreases, but the reasons are still unclear.[6] Our data, with >50% volume decrease as the threshold, do not support this observation.

In our cohort, almost half of the patients experienced a volume reduction of >50% of the BS-L sometime during the course of their disease; yet, the ultimate outcome remains uniformly dis-

mal. In this study, we showed that apart from the significant volume changes within the tumor lesion itself, measurable and non-negligible volume changes may also be induced in remote normal brain parenchyma, which is not directly targeted by RT; therefore, those changes likely develop in response to systemic medication used during treatment, particularly corticosteroids, which cause well-known, reversible pseudoatrophic changes in the brain.

In recent years, molecularly targeted treatments for adult high-grade gliomas have generated considerable interest.[7,8] Vandetanib, the anti-VEGF agent used in our clinical trial, is a tyrosine kinase receptor inhibitor that may inhibit VEGF receptor-2 tyrosine kinase activity and shows additional inhibitory activity against the Ret proto-oncogene tyrosine-protein kinase receptor and the epidermal growth factor receptor in isolated enzyme assays.[8] By targeting VEGF, a promoter of angiogenesis that leads to the "haphazard" formation of deficient, new vessels in response to tissue hypoxia, anti-VEGF agents may indirectly decrease fluid leakage into the interstitial space, reducing peritumoral edema in synergy with corticosteroids by reducing the number of defective, leaky vessels.[9,10] The effect of anti-VEGF agents, including vandetanib, on normal vessels (and brain parenchyma) is unclear.

In the present study, the progressive decrease of the normalized ST-WM volume with time was evident. Similarly, although on a larger scale, normalized BS-L volume decreased until approximately 2 months following RT completion, after which BS-L volumes started to increase again, presumably due to commencing tumor recurrence. The BS-L responded well to treatment during Phase I. Normalized ADC values of the lesion decreased during this phase, likely indicating contraction of the intratumoral extracellular water compartments in response to synergistic effects of the various treatments. According to protocol requirements, vandetanib levels were kept constant in each patient stratum, contrary to dexamethasone, which was initially given at higher doses and gradually tapered off as the lesion size decreased and the patient's clinical signs and symptoms improved.[2] Vandetanib may not substantially reduce volume during Phase I because pharmacokinetic studies have shown that therapeutic blood levels of vandetanib are reached after approximately 45 days (6.5 weeks) in adults and, presumably, in pediatric patients as well.[2,11] Hence, by the eRT (6 weeks), vandetanib may not have reached a steady-state blood level that would be sufficient to substantially affect intratumoral edema and, thus, BS-L volume size. Hence, the pronounced volumetric changes in the BS-L during Phase I are likely due to a combination of tumor control by RT and the removal of vasogenic edema by dexamethasone.

Volume changes were also evident in ST-WM as early as Phase I, even though the supratentorial brain was largely outside the radiation field. On the basis of test simulations, approximately 20%–25% of the supratentorial brain (mainly the posterior temporal and the occipital lobes) in patients treated for DIPG receives radiation doses higher than 20 Gy. Therefore, volume decreases of the ST-WM reflect the effect of systemically administered dexamethasone on the normal cerebral parenchyma, especially because no regional differences in pseudoatrophic changes were seen between the "irradiated" and the "nonirradiated" brain regions. For the above-mentioned reasons, vandetanib is not expected to substantially affect ST-WM. The decreasing ADC values in ST-WM may indicate that water is removed, resulting in contraction of the interstitial space in the brain during Phase I. In our patients, no clinical or MR imaging finding suggested that the volume decrease in ST-WM would be indicative of any drug-induced myelinotoxicity.

As expected, the trend toward volume and ADC reduction of the BS-L continued in Phase II after RT completion, most probably due to the sustained effects of RT on the BS-L and the ongoing, potentially synergistic effect of dexamethasone and vandetanib. During this phase, dexamethasone was gradually reduced, and by the end of W14, most patients were taken off therapy. Therefore, the decreased rates may reflect decreasing corticosteroid use, suggesting that the delayed effects of RT and vandetanib may not be sufficient to sustain control of edema. Nevertheless, it is unclear which treatment component has the dominant effect on tumor volume reduction during Phase II. Normalized ST-WM volume also decreased at a slower rate, again, most likely due to weaker dexamethasone effects. The steady decrease of ADC values in ST-WM indicates further contraction of the interstitial water compartments in normal brain parenchyma.

In Phase III, BS-L volume progressively increased despite sustained vandetanib therapy, indicating early signs of tumor recurrence. ADC values gradually increased, suggesting a rebound of edema due to an increasing tumor burden.

Unlike in BS-Ls, volume in ST-WM minimally increased during Phase III at the group level. Because anti-VEGF was continuously given, the only factor inducing this change is probably the discontinuation of dexamethasone for most patients and slow remigration of water back to the ST-WM, leading to a modest re-expansion of the interstitial space. Such reversible brain atrophy due to medication-induced effects has been documented in clinical studies. For example, corticosteroid-induced brain volume changes occur in patients with multiple sclerosis, with researchers showing that brain fractional volumes return to baseline values 1–2 months after treatment.[12,13] Reversible changes in the brain also occurred in a cohort of patients with alcohol dependence under detoxification.[14,15] Similarly, reversal of pseudoatrophic brain changes and cognitive improvement have been associated with discontinuation of drug therapy in epilepsy.[16] All studies accentuated the confounding dynamics of water shifts induced by drugs or other substances in the brain parenchyma, without a concomitant effect on histoarchitectural integrity.

Because the vandetanib dose level was fixed in each stratum, the only robust variable in patients was the presence or absence of dexamethasone. Our results show that corticosteroids may induce measurable volume changes not only in the BS-L but also in the ST-WM volume. This finding is quite remarkable because it clearly indicates that corticosteroids are powerful water-volume regulators not only in pathologic but also in normal tissues. The potential practical implication of this finding is that tumor volume reduction induced by drugs without a direct antitumoral effect (ie, corticosteroids and anti-VEGF drugs in our study) may be potentially misinterpreted as a partial response during treatment or follow-up when volume reduction exceeds 50%. This overestimation occurred in almost 50% of our patients. Hence, observed changes in DIPG "lesion volume" during treatment and the associated T2 normalization may not be reliable indicators of

effective tumor control. Therefore, reliable appreciation of the actual antitumor effect (or lack thereof) of current or future antitumoral drugs in treating DIPG (or other diffusely infiltrative gliomas) in patients who receive corticosteroids may not be possible.

For the whole patient cohort, an overall mean 20% decrease of ST-WM volume was seen, though the ST-WM was largely unexposed to radiation. Assessing how much BS-L volume reduction was induced by RT itself is not feasible, but one may assume that at least 20% of the change is due to concurrent "drug therapy" as seen in the ST-WM. This percentage, however, may be even higher because steroids and anti-VEGF drugs may have a more robust effect on edematous tissue than on normal parenchyma. This notion is supported by our clinical observations suggesting that DIPGs presenting markedly increased T2 signal intensity at diagnosis respond better to therapy, likely due to the presence of more easily "treatable" intratumoral edema. We took advantage of the available data and calculated an "adjusted" volume decrease for the BS-L, after which only 2 patients had a volume reduction of >50%. However, only 4 patients had a volume increase of >25% at the ePFS. These data suggest that both the −50% and the +25% thresholds have poor correlation with clinical reality and are inadequate for partial response and progressive disease determinations. This finding is in keeping with reports showing that advanced MR imaging techniques, such as proton MR spectroscopy, show little, if any, improvement in the metabolic profile of lesions, even during apparent volume reduction of the tumor.[17,18]

In DIPG, the T2 hyperintense area corresponds to the extent of vasogenic edema, which is induced by the tumor within through a mechanism (eg, development of leaky, angioneogenetic vessels) promoting the influx of excess water from the intravascular compartment to the intralesional interstitial compartment. In practical clinical terms, the T2 hyperintense area is likely an inaccurate representation of the actual tumor burden. Consequently, temporal variations of the T2 hyperintense lesion volume during the disease are probably inadequate to monitor therapy- or disease progression–related changes in tumor burden because non-negligible portions of those volume variations may reflect bulk water shifts to and from the lesion area. This situation would be particularly concerning in clinical trials.

The Response Assessment in Neuro-Oncology working group has developed response criteria in adult high-grade gliomas. Although most clinical trials adopt the Response Assessment in Neuro-Oncology criteria,[19] the validity and appropriateness of these schemes for pediatric patients require further studies. Pediatric brain tumors present with unique challenges that may require adjustment of imaging criteria; however, a "one size fits all" strategy may not be the right answer.[19,20] It is unlikely that a universal, standard set of response criteria would be suitable for all types of pediatric brain tumors, including embryonal tumors, infiltrative gliomas, and focal gliomas, due to inherently different histoarchitectural features and tumor-host relationships. Advanced, quantitative MR imaging data may more directly capture key biologic or pathophysiologic tumor properties: indeed, perfusion and spectroscopic data reportedly have potential prognostic value in DIPG.[21,22] A recent study also demonstrated that diffusion measurements could be used as noninvasive biomarkers to differentiate distinct subgroups of DIPG and select patients for clinical trials.[23] Nonetheless, the possibility of incorporating advanced MR imaging techniques (perfusion imaging DTI, MR spectroscopy) in response assessment schemes for childhood brain cancer is still under evaluation.

Overall, shortcomings of anatomic MR imaging in reflecting actual tumor burden in cerebral neoplasms at diagnosis and during treatment are increasingly recognized, especially in cases of diffusely infiltrative high-grade gliomas, such as DIPG. Identifying surrogate biomarkers other than volume-based measures that can accurately predict or measure tumor response to treatment is crucial to effectively managing DIPG or other infiltrative tumors in clinical care and in drug trials.

CONCLUSIONS

Our data suggest that volumetric measurements of the brain stem lesion defined by the T2/FLAIR hyperintense area, which are commonly used in clinical trials for DIPG, may not be appropriate to assess response to treatment. There is an obvious need for robust, standardized, reproducible, and quantitative imaging biomarkers to accurately monitor therapy-induced changes in infiltrative brain tumors, including DIPG.

ACKNOWLEDGMENTS

The authors thank Dr Cherise Guess of the Department of Scientific Editing at St. Jude Children's Research Hospital for editing the manuscript and Edwina Anderson for data management.

Disclosures: Zoltan Patay—*RELATED*: *Grant*: National Institutes of Health, *Comments*: Cancer Center Support grant P30 CA 21765*. *Money paid to the institution.

REFERENCES

1. Pope WB, Young JR, Ellingson BM. **Advances in MRI assessment of gliomas and response to anti-VEGF therapy.** *Curr Neurol Neurosci Rep* 2011;11:336–44 CrossRef Medline
2. Broniscer A, Baker JN, Tagen M, et al. **Phase I study of vandetanib during and after radiotherapy in children with diffuse intrinsic pontine glioma.** *J Clin Oncol* 2010;28:4762–68 CrossRef Medline
3. Ji Q, Glass JO, Reddick WE. **A novel, fast entropy-minimization algorithm for bias field correction in MR images.** *Magn Reson Imaging* 2007;25:259–64 CrossRef Medline
4. Glass JO, Reddick WE, Reeves C, et al. **Improving the segmentation of therapy-induced leukoencephalopathy in children with acute lymphoblastic leukemia using a priori information and a gradient magnitude threshold.** *Magn Reson Med* 2004;52:1336–41 CrossRef Medline
5. Reddick WE, Glass JO, Cook EN, et al. **Automated segmentation and classification of multispectral magnetic resonance images of brain using artificial neural networks.** *IEEE Trans Med Imaging* 1997;16:911–18 CrossRef Medline
6. Poussaint TY, Kocak M, Vajapeyam S, et al. **MRI as a central component of clinical trials analysis in brainstem glioma: a report from the Pediatric Brain Tumor Consortium (PBTC).** *Neuro Oncol* 2011;13:417–27 CrossRef Medline
7. Gagner JP, Law M, Fischer I, et al. **Angiogenesis in gliomas: imaging and experimental therapeutics.** *Brain Pathol* 2005;15:342–63 Medline
8. Rich JN, Sathornsumetee S, Keir ST, et al. **ZD6474, a novel tyrosine kinase inhibitor of vascular endothelial growth factor receptor and epidermal growth factor receptor, inhibits tumor growth of multiple nervous system tumors.** *Clin Cancer Res* 2005;11:8145–57 CrossRef Medline

9. Gerstner ER, Duda DG, di Tomaso E, et al. **VEGF inhibitors in the treatment of cerebral edema in patients with brain cancer.** *Nat Rev Clin Oncol* 2009;6:229–36 CrossRef Medline
10. Dietrich J, Rao K, Pastorino S, et al. **Corticosteroids in brain cancer patients: benefits and pitfalls.** *Expert Rev Clin Pharmacol* 2011;4:233–42 CrossRef Medline
11. Martin P, Oliver S, Kennedy SJ, et al. **Pharmacokinetics of vandetanib: three phase I studies in healthy subjects.** *Clin Ther* 2012;34:221–37 CrossRef Medline
12. Hoogervorst EL, Polman CH, Barkhof F. **Cerebral volume changes in multiple sclerosis patients treated with high-dose intravenous methylprednisolone.** *Mult Scler* 2002;8:415–19 CrossRef Medline
13. Rao AB, Richert N, Howard T, et al. **Methylprednisolone effect on brain volume and enhancing lesions in MS before and during IFN-beta-1b.** *Neurology* 2002;59:688–94 CrossRef Medline
14. Bendszus M, Weijers HG, Wiesbeck G, et al. **Sequential MR imaging and proton MR spectroscopy in patients who underwent recent detoxification for chronic alcoholism: correlation with clinical and neuropsychological data.** *AJNR Am J Neuroradiol* 2001;22:1926–32 Medline
15. Bartsch AJ, Homola G, Biller A, et al. **Manifestations of early brain recovery associated with abstinence from alcoholism.** *Brain* 2007;130(pt 1):36–47 Medline
16. Guerrini R, Belmonte A, Canapicchi R, et al. **Reversible pseudoatrophy of the brain and mental deterioration associated with valproate treatment.** *Epilepsia* 1998;39:27–32 CrossRef Medline
17. Panigrahy A, Nelson MD Jr, Finlay JL, et al. **Metabolism of diffuse intrinsic brainstem gliomas in children.** *Neuro Oncol* 2008;10:32–44 CrossRef Medline
18. Löbel U, Hwang S, Edwards A, et al. **Discrepant longitudinal volumetric and metabolic evolution of diffuse intrinsic pontine gliomas during treatment: implications for current response assessment strategies.** *Neuroradiology* 2016;58:1027–34 CrossRef Medline
19. Wen PY, Macdonald DR, Reardon DA, et al. **Updated response assessment criteria for high-grade gliomas: Response Assessment in Neuro-Oncology working group.** *J Clin Oncol* 2010;28:1963–72 CrossRef Medline
20. Warren KE, Poussaint TY, Vezina G, et al. **Challenges with defining response to antitumor agents in pediatric neuro-oncology: a report from the Response Assessment in Pediatric Neuro-Oncology (RAPNO) working group.** *Pediatr Blood Cancer* 2013;60:1397–401 CrossRef Medline
21. Hipp SJ, Steffen-Smith E, Hammoud D, et al. **Predicting outcome of children with diffuse intrinsic pontine gliomas using multiparametric imaging.** *Neuro Oncol* 2011;13:904–09 CrossRef Medline
22. Sedlacik J, Winchell A, Kocak M, et al. **MR imaging assessment of tumor perfusion and 3D segmented volume at baseline, during treatment, and at tumor progression in children with newly diagnosed diffuse intrinsic pontine glioma.** *AJNR Am J Neuroradiol* 2013;34:1450–55 CrossRef Medline
23. Lober RM, Cho YJ, Tang Y, et al. **Diffusion-weighted MRI derived apparent diffusion coefficient identifies prognostically distinct subgroups of pediatric diffuse intrinsic pontine glioma.** *J Neurooncol* 2014;117:175–82 CrossRef Medline
24. Czock D, Keller F, Rasche FM, et al. **Pharmcokinetics and pharmacodynamics of systemically administered glucocorticoids.** *Clin Pharmacokinet* 2005;44:61–98 CrossRef Medline
25. Yang L, Panetta JC, Cai X, et al. **Asparaginase may influence dexamethasone pharmacokinetics in acute lymphoblastic leukemia.** *J Clin Oncol* 2008;26:1932–39 CrossRef Medline

Differences in Activation and Deactivation in Children with Sickle Cell Disease Compared with Demographically Matched Controls

B. Sun, R.C. Brown, T.G. Burns, D. Murdaugh, S. Palasis, and R.A. Jones

ABSTRACT

BACKGROUND AND PURPOSE: Declines in both functional activation and functional connectivity have been reported in patients with sickle cell disease. In this study, we derived the functional and default mode responses to a word stem paradigm in age-, ethnicity-, and background-matched subjects with sickle cell disease and control groups, with the aim of testing whether both networks were similarly attenuated and whether the changes were related to physiologic parameters that characterize sickle cell disease.

MATERIALS AND METHODS: Both the functional and default mode responses were obtained from age- and background-matched controls and the sickle cell population by using a visually presented word stem paradigm on a 3T scanner.

RESULTS: We observed an attenuated response to both activation and deactivation in the sickle cell disease group. There were no significant differences in the activation response between the 2 groups for the contrast control > sickle cell disease; however, significant differences were observed in the medial parietal cortex, the auditory cortex, and the angular gyrus for the default mode. For the sickle cell group, a significant correlation between the activation *z* scores and the physiologic parameters was observed; for the deactivation, the results were not significant but the trend was similar.

CONCLUSIONS: The results indicate that the physiologic parameters modulate the activation in the expected fashion, but that the effect was weaker for deactivation. Given that significant differences between the 2 groups were only seen for deactivation, additional factors must modulate the deactivation in sickle cell disease.

ABBREVIATIONS: BOLD = blood oxygen level–dependent; DM = default mode; GLM = General Linear Model; SCD = sickle cell disease

Sickle cell disease (SCD) is a hereditary condition that can cause ongoing hemolytic anemia and vaso-occlusion, which can subsequently cause irreversible organ damage. Individuals with SCD are also at an increased risk for ischemic insult to the brain, and both overt[1-4] and silent-type strokes[5-7] have been shown to cause neurocognitive deficits. However, studies involving large numbers of neurologically asymptomatic children and adults with SCD have shown that cognitive impairment occurs even in the absence of structural brain abnormalities on MR imaging.[8-10] Even though the method of neurocognitive assessment varied among these studies, intellectual ability, executive functioning ability, and visual-spatial memory were usually the cognitive areas most likely to be affected.[11] These observations support an emerging consensus that brain injury in SCD is diffuse and insidious[12] and that conventional neuroimaging is prone to underestimating the extent of injury.

Thus, advanced neuroimaging techniques are warranted to better detect differences in SCD. Significant differences in gray matter volumes have been shown in patients with SCD compared with healthy controls.[8] In addition, white matter changes have been discovered in patients with SCD by means of voxel-based morphometry, even in the absence of overt stroke.[10] One article comparing patients with SCD with and without prior stroke demonstrated white matter "density" abnormalities in multiple, anatomic regions.[10] Diffusion-weighted imaging has also been attempted with Tract-Based Spatial Statistics (TBSS; http://fsl.fmrib.ox.ac.uk/fsl/fslwiki/TBSS) to reveal reduced anisotropy and increased diffusivity in subjects with SCD compared with healthy controls, particularly in areas involving the corpus callosum and centrum semiovale.[13]

Received October 6, 2016; accepted after revision February 6, 2017.

From the Departments of Radiology (B.S., S.P., R.A.J.), Hematology (R.C.B.), and Neuropsychology (T.G.B., D.M.), Children's Healthcare of Atlanta, Atlanta, Georgia.

This study was funded by an internal grant from the radiology department at Children's Healthcare of Atlanta.

Paper previously presented, in part, at: Annual Meeting of the American Society of Neuroradiology and the Foundation of the ASNR Symposium, May 21–26, 2016; Washington, DC.

Please address correspondence to Richard A. Jones, PhD, Department of Radiology, Children's Healthcare of Atlanta, 1001 Johnson Ferry Rd, Atlanta, GA 30305; e-mail: Richard.jones@choa.org

http://dx.doi.org/10.3174/ajnr.A5170

In addition to the aforementioned neuroimaging techniques, functional MR imaging seems to be a promising method for studying neurologic changes. Indeed, fMRI can be used to assess not only task-based activation but also deactivation, (ie, rest versus task). One of the most commonly studied networks assessed during rest is the default mode (DM) network. The DM network can be defined with either resting-state[14] or task-driven fMRI.[15]

However, fMRI seems to be underused in SCD because there have been relatively few studies published using this neuroimaging technique, to our knowledge. One possible explanation may be the difficulty in determining whether the changes in the blood oxygen level–dependent (BOLD) effect are due to neurologic differences or possible differences in the hemodynamic properties of SCD. While the hemodynamic properties associated with anemia and SCD have been shown to alter the resting perfusion rate of the brain, the degree to which the changes in perfusion, oxygenation, and blood volume affect the BOLD response is unclear. The studies using fMRI have produced mixed results, depending on whether they were assessing deactivation or activation. One activation study using a visual paradigm for fMRI did find that the BOLD response was attenuated in children with SCD.[16] Resting-state fMRI studies have reported that pain can alter the connectivity between the DM regions and pro- and antinociceptive structures in SCD.[17] Additionally, connectivity of the medial parietal cortex, one of the main elements of the DM network, was shown to be higher in patients with SCD compared with controls.[18]

Given these findings, 1 advantage of using a task-driven approach to define the DM network is that the same paradigm can be used to derive the activation and responses, so that any hemodynamic differences between the patient and control populations will equally affect the activation and deactivation BOLD responses. Because the DM network is implicated in many aspects of brain function[15] and disruption of the DM has been reported to negatively impact attention, working memory, and emotional capacity,[19] an altered DM network in SCD may account for the some of the neurocognitive changes associated with SCD. While the core elements of the DM network are now well-defined, some areas show more variable deactivation, with the presence and/or strength of the deactivation being modulated by the nature of the stimulus.[20,21]

In this study, we used fMRI with a visually presented block word stem paradigm to derive the functional and DM responses from age- and background-matched subjects with SCD and control groups. In the subjects with SCD, we also recorded physiologic parameters that can be used to characterize the BOLD response and correlated these with the functional and DM responses. Our main aim was that with the same task for both activation and deactivation responses, we could better characterize neurologic differences between subjects with SCD and control groups.

MATERIALS AND METHODS

Participants

This prospective study was approved by the institutional review board. The subjects with SCD had the homozygous form of SCD (HbSS), no history of stroke, normal blood velocities on routine screening with transcranial Doppler sonography, and no reported developmental delay. In addition, any prior neuroimaging performed as part of their standard of care had to have normal findings for inclusion in the study. The control group was composed of siblings or demographically matched peers of the prospective SCD group, who had either sickle cell trait or were healthy and had no history of serious illness, brain surgery, or developmental delay, to limit potential confounds. Physiologic variables that were expected to affect the BOLD response, specifically hemoglobin level, mean corpuscular volume, percentage of fetal hemoglobin, and percentage of sickle cell hemoglobin, were recorded for the patients with SCD. For both groups, the lower and upper age limits for this study were 10 and 21 years of age.

Neuropsychology

A number of neuropsychological measures were administered to each subject to determine whether significant differences were observed between the SCD group and the control group in cognitive ability. The measures included the following: measures of intelligence (Wechsler Abbreviated Scales of Intelligence); working memory (Wechsler Intelligence Scale for Children, Fourth Edition, Digit Span subtest); attention/executive functioning (Conners Continuous Performance Test, Second Edition; Delis-Kaplan Executive Function System; Tower of London, Second Edition, Drexel version; and the Behavioral Rating Inventory of Executive Functioning); and memory (Wide Range Assessment of Memory and Learning, Second Edition; and Children's Memory Scale). Scores are reported in standard scores (mean of 100 with a SD of 15), in which ranges that extend 0.6, 1.3, and 2 SDs from the mean are equivalent to the average, low average, and impaired ranges respectively.

Between-group differences were analyzed by using SPSS 22.0 statistical software (IBM, Armonk, New York) with an α level set to .05. Independent-samples t tests were conducted to compare the SCD and control groups across the neuropsychologic measures.

Image Acquisition

MR images from all participants were acquired on a 3T Tim Trio scanner (Siemens, Erlangen, Germany). Standard, noncontrast, clinically diagnostic sequences were performed as follows: T1 3D sagittal MPRAGE (TR/TE/TI = 2300/2.98/900 ms, 1.0 = mm isotropic resolution). 2D T2 and FLAIR images were acquired to screen for disease. MR angiography was performed to screen for large-vessel stenosis. The fMRI sequence used a block-design paradigm of a word stem task in which the participant was visually presented with a set of 3 letters and had to construct a word that starts with those 3 letters.[22] Each word stem could be used to produce at least 3 words that would be within the vocabulary of the patients in this study. Each set of 3 letters was displayed for 3 seconds, and 10 sets were displayed in each block. The patients were instructed to press a button when they found a word that matched the word stem. The fMRI run consisted of 100 dynamic scans with the duration of each dynamic being 3 seconds. There were 5 activation blocks and 5 rest blocks, and the paradigm started with a rest block. During the rest intervals, a crosshair was displayed at the center of the screen and the subject was asked to

focus on the crosshair. The sequence parameters for the fMRI sequence were the following: TR/TE = 3000/35 ms, FOV = 216 × 216 mm, matrix = 72 × 72. Parallel imaging with an acceleration factor of 2 was used in the phase-encoding (anteroposterior) direction.

Diagnostic Imaging Analysis

The clinical diagnostic sequences were reviewed by a board-certified pediatric neuroradiologist. The scans from both patients and volunteers were reviewed for the absence of general pathology; in case of infarcts, these were judged to have normal or abnormal findings. In the latter case, the lesions were then classified as either nonspecific white matter lesions if <3 mm in diameter and visible in 2 planes or focal discreet white matter lesions if >3 mm in 2 planes.[23]

fMRI Processing

fMRI processing of the data was performed by using the software routines in the FSL Software Library (http://www.fmrib.ox.ac.uk/fsl). For each subject, we performed the following steps: motion correction with the MCFLIRT tool of the FSL (https://fsl.fmrib.ox.ac.uk/fsl/fslwiki/MCFLIRT), brain extraction with the FSL Brain Extraction Tool (http://fsl.fmrib.ox.ac.uk/fsl/fslwiki/BET), spatial smoothing with a Gaussian kernel (full width at half maximum = 5 mm), and high-pass temporal filtering. A general linear model (GLM) was then used to generate statistical parametric maps of activation and deactivation for each subject by using the motion parameters as estimated by MCFLIRT for that patient as confounds in the FSL General Linear Model (GLM; http://fsl.fmrib.ox.ac.uk/fsl/fslwiki/GLM). The fMRI data were aligned to a skull-stripped anatomic volume acquired in the same imaging session by using the BBR registration option (https://fsl.fmrib.ox.ac.uk/fsl/fslwiki/FLIRT_BBR) and were subsequently mapped to the standard Montreal Neurological Institute space by using a 12 *df* linear registration. A second-level analysis was performed by using Flame1 (https://fsl.fmrib.ox.ac.uk/fsl/fslwiki/FEAT/UserGuide#Group_Statistics) to generate statistical parametric maps of the group activation, group deactivation, and areas of significant difference between the groups (controls > SCD).

To measure the mean *z* score in areas of activation and deactivation (DM), we thresholded the Z statistical maps corresponding to the group activation and deactivation to create binary ROIs. These ROIs were then projected back from the standard space to the subject space for each individual by using the inverse transform provided by FSL (https://fsl.fmrib.ox.ac.uk/fsl/fslwiki/FLIRT/UserGuide).

RESULTS

Exclusion and Demographic Information

All participants in the current study identified themselves as African Americans. There were initially 17 subjects in the control group and 19 subjects in the SCD group. Three control subjects were excluded due to excessive motion (>3 mm) during the fMRI series, and 1 was excluded due to existing pathology. Four subjects with SCD were excluded due to existing pathology, and 2 were excluded due to excessive motion. Thus, 13 subjects were left in each group. The mean ages were 14.5 ± 3.1 years for the control group and 15.3 ± 2.3 years for the SCD group. The difference in age between the groups was not statistically significant. In the SCD group, 12 subjects were right-handed, and 1 was left-handed. In the control group, 9 were right-handed, 1 was left-handed, and the handedness was not recorded for the other 3 subjects. Nine of the 13 subjects with SCD were taking hydroxyurea to boost their levels of fetal hemoglobin.

Table 1: Summary of the *Z* statistics for the total activated and deactivated (default mode) areas[a]

	Actv (*n* = 13) *Z* Score	Actv (*n* = 10) *Z* Score	DM (*n* = 13) *Z* Score	DM (*n* = 10) *Z* Score
Controls	2.69 ± 0.95	2.76 ± 1.02	2.24 ± 0.55	2.26 ± 0.59
SCD	1.70 ± 1.32	2.38 ± 0.28	1.60 ± 0.67	1.87 ± 0.49

Note:—Actv indicates activation.

[a] For each group, the statistics for the complete group (*n* = 13) and the reduced group (*n* = 10) are presented.

Neuropsychology

Between-group analyses of neuropsychological measures revealed no differences in intelligence, with both groups performing in the average range (Wechsler Abbreviated Scales of Intelligence Full Scale Intelligence Quotient: SCD mean = 97.7, control mean = 106.0, $P = .149$). Differences observed between the 2 groups were found almost exclusively within the cognitive domain of executive functioning. The control group performed significantly higher than the SCD group on a measure of executive functioning that requires sequencing, planning, and inhibition (Delis-Kaplan Executive Function System Color Word Inference Test; SCD mean = 88.1, control mean = 101.9, $P = .022$). Additionally, the control group performed significantly higher on a measure of auditory attention and working memory (Wechsler Intelligence Scale for Children, Fourth Edition, Digit Span; SCD mean = 92.7, control mean = 107.3, $P = .003$).

Functional Imaging

An initial review of the first-level fMRI results revealed 3 subjects with minimal activation but an intact, if attenuated, DM response. Due to the very different responses in these 3 subjects, they were removed from all subsequent analyses. For the controls, the 10 subjects having the best age match to the reduced sickle cell group were chosen so that each group would consist of 10 subjects. Table 1 summarizes the *z* scores for all activated and deactivated voxels, for both the complete ($n = 13$) group and a reduced group ($n = 10$), with the 3 outliers removed. For the activation, the regions seen for both groups were in good agreement with those previously described in the literature (Fig 1).[22] Subjectively, the activation was somewhat more extensive in the SCD group, most notably in the right anterior temporal lobe. However, there were no areas of significant difference in the control > SCD contrast for activation. For the DM analysis, the classic DM regions (medial parietal cortex and medial prefrontal cortex), the auditory cortex bilaterally (left > right), and the angular gyrus bilaterally (right > left) were seen in the controls. The left auditory cortex was absent in the subjects with SCD, and the other areas were subjectively both weaker and less extensive in the SCD group. The control > SCD image for the DM showed areas of significant difference in the medial parietal cortex, the left auditory cortex, and the right angular gyrus (Fig 1).

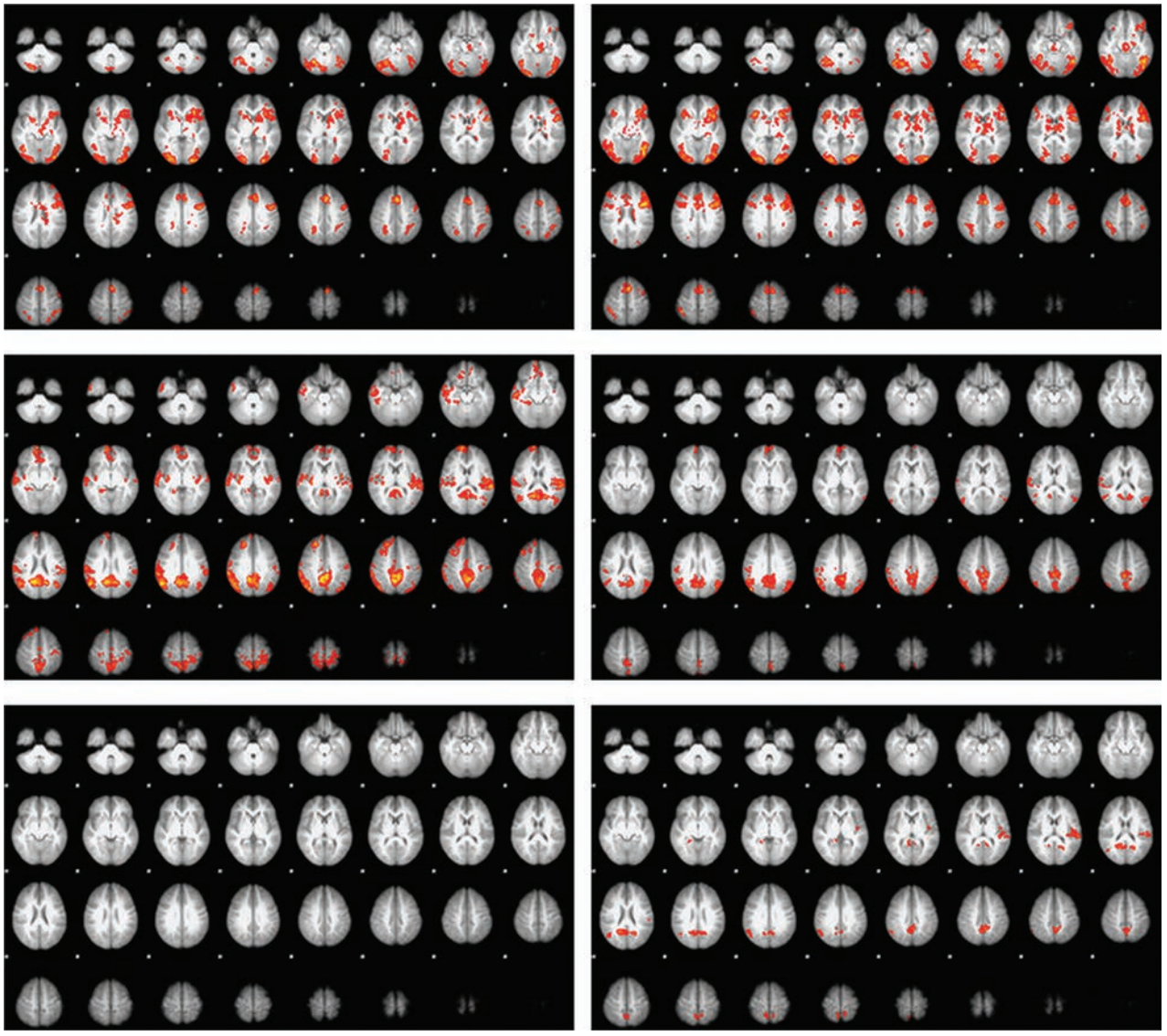

FIG 1. The activation (*top row*) and the default mode (*middle row*) responses to the word stem paradigm in the controls (*left column*) and subjects with SCD (*right column*). The lower row shows the control > SCD contrast for the activation (*left*) and DM (*right*) responses.

Table 2: The results for the GLM modeling of the interaction between the BOLD response as measured by the *Z* score and the physiologic variables[a]

Activation	Hb	MCV	%F	%S
Activation				
Phys. variable (β)	0.173	0.013	0.018	−0.020
Phys. variable (*P* value)	.036[b]	.034[b]	.023[b]	.021[b]
Deactivation				
Phys. variable (β)	0.246	0.013	0.022	−0.023
Phys. variable (*P* value)	.109	.268	.173	.169

Note:—Phys. indicates physiologic; Hb, hemoglobin; MCV, mean corpuscular volume; %F, level of fetal hemoglobin; %S, level of fetal hemoglobin S.

[a] The GLM was run individually for each of the variables in the headers, in each case the patient's age was used as a covariable in the model.

[b] Significant.

A GLM analysis was performed by using age and the physiologic variable as the dependent parameters in the GLM, covarying age, because CBF varies with age in both healthy subjects and those with sickle cell disease.[24] The results are summarized in Table 2. All 4 variables (hemoglobin, percentage of fetal hemoglobin, percentage of sickle cell hemoglobin, and mean corpuscular volume) showed a statistically significant correlation with the *z* score ($P < .05$) for the activation, but none showed a significant correlation with the deactivation *z* score. However, with the exception of hemoglobin, the slopes of the GLM fit were very similar for both the activation and the deactivation.

DISCUSSION

Overall our results provide evidence for attenuated DM network activation in our patients with SCD compared with matched controls. In addition, results revealed decreased volumes of white matter and the globus pallidus in the patients with SCD compared with controls. The lack of differences in the task-based activation is not surprising given the neuropsychological testing, in which the 2 groups were equally matched for intelligence quotient and did not differ in verbal memory measures. In contrast, differences were specifically observed in the DM network activation, with the control group showing significantly greater activation of core DM nodes compared with patients with SCD. Research suggests that the DM network reflects intrinsic organization of a healthy func-

tional organization system that primes the brain for efficiently responding to input from external stimuli.[25] Thus, 1 plausible explanation for our findings is a disruption of the DM network in SCD, causing these patients to work less efficiently to perform a similar task, in this case a word stem task.

Additional results worthy of discussion are that the physiologic variables were significantly correlated with the activation, but not the deactivation *z* scores. Thus in patients with SCD, the activation response reflects the expected effects of variations in the vascular physiology (increases in hemoglobin, mean corpuscular volume, and the percentage of fetal hemoglobin, resulting in higher *z* scores while a higher percentage of sickle cell hemoglobin reduced the *z* score). For the 3 outliers who were excluded after the initial analysis, the physiologic variables were in the same range as in the other patients but did not show any significant correlation with the *z* score. We also investigated other possible reasons for the abnormal activation in these outliers. Of the 3 outliers, 1 was taking hydroxyurea and 2 were not. To investigate the possible effects of pain medications, we acquired the number of emergency department visits during the previous year that required the use of IV pain medications from a review of each subject's medical records. For all 13 subjects, the average number of visits was 1.6, while for the 3 excluded subjects, none of whom had had any such visits in the previous year, the average was 2.0. Thus, neither of these factors appear to explain the lack of activation in these subjects, and other factors, such as changes in cerebrovascular reactivity[26] and/or oxygen extraction fraction,[27] may be responsible for the weak activation and the poor correlation of the physiologic variables with the *z* scores for these subjects. Deriving the activation and DM responses from the same paradigm ensures that the physiologic effects of SCD are common to both responses. The left auditory cortex and the right angular gyrus, while not part of the classic DM network, did exhibit significant deactivation on the difference map (Fig 1). Other groups have previously shown that sensory areas are deactivated when they are not central to task performance,[20,21] so that attention to a single sensory technique (the visually present letters) can result in decreased activity in cortical regions that process information from an unattended sensory technique (the auditory cortex). The deactivation of the auditory cortex has previously been shown to be bilateral; thus, the absence of activation in the left auditory cortex in the subjects with SCD is surprising. Our findings suggest the following: 1) a weaker correlation of the DM with the physiologic variables for subjects with SCD, 2) larger differences in the DM for the control > SCD contrast, and 3) stronger deactivation of the auditory cortex and angular gyrus in the controls. Each of the above may indicate that the deactivation of the DM and associated regions are impaired in the SCD group.

There are some limitations in this work. Many of the DM areas, particularly the medial parietal cortex, are associated with a high resting metabolism and have also been shown to have reduced cortical thickness[26,28] and cerebrovascular reactivity[26] in subjects with SCD. In this study, we were unable to detect any regions of significant cortical thinning; however, the group size used in the other articles was much larger than ours, and they restricted the age range to older than 12 years to minimize age-related effects.[26,28] Applying the same criteria to our already small group size would have reduced the size of the already small control group from 13 to 9 subjects.

CONCLUSIONS

We found significantly decreased volumetric deactivation of the DM network and neuropsychological functioning in patients with SCD compared with controls. These results highlight the effectiveness of using advanced neuroimaging techniques to help inform our understanding of neurocognitive deficits in SCD. Our results lend support to the hypothesis that the deficits seen in executive functioning, which primarily relies on the medial parietal cortex and medial prefrontal cortex, in patients with SCD are shown to have deactivation differences within the DM network. Additionally, these deficits appear to be related to difficulties of patients with SCD in appropriately modulating intrinsic brain activity during a cognitive task. Overall, this study provides support for a more focused examination of the DM network and brain matter differences in patients with SCD.

REFERENCES

1. Cohen MJ, Branch WB, McKie VC, et al. **Neuropsychological impairment in children with sickle cell anemia and cerebrovascular accidents.** *Clin Pediatr (Phila)* 1994;33:517–24 CrossRef Medline
2. Watkins KE, Hewes DK, Connelly A, et al. **Cognitive deficits associated with frontal-lobe infarction in children with sickle cell disease.** *Dev Med Child Neurol* 1998;40:536–43 Medline
3. Wilimas J, Goff JR, Anderson HR Jr, et al. **Efficacy of transfusion therapy for one to two years in patients with sickle cell disease and cerebrovascular accidents.** *J Pediatr* 1980;96:205–08 CrossRef Medline
4. Bernaudin F, Verlhac S, Freard F, et al. **Multicenter prospective study of children with sickle cell disease: radiographic and psychometric correlation.** *J Child Neurol* 2000;15:333–43 CrossRef Medline
5. Schatz J, Finke R, Roberts CW. **Interactions of biomedical and environmental risk factors for cognitive development: a preliminary study of sickle cell disease.** *J Dev Behav Pediatr* 2004;25:303–10 CrossRef Medline
6. Wang W, Enos L, Gallagher D, et al; Cooperative Study of Sickle Cell Disease. **Neuropsychologic performance in school-aged children with sickle cell disease: a report from the Cooperative Study of Sickle Cell Disease.** *J Pediatr* 2001;139:391–97 CrossRef Medline
7. Hijmans CT, Grootenhuis MA, Oosterlaan J, et al. **Neurocognitive deficits in children with sickle cell disease are associated with the severity of anemia.** *Pediatr Blood Cancer* 2011;57:297–302 CrossRef Medline
8. Steen RG, Emudianughe T, Hunte M, et al. **Brain volume in pediatric patients with sickle cell disease: evidence of volumetric growth delay?** *AJNR Am J Neuroradiol* 2005;26:455–62 Medline
9. Steen RG, Langston JW, Ogg RJ, et al. **Diffuse T1 reduction in gray matter of sickle cell disease patients: evidence of selective vulnerability to damage?** *Magn Reson Imaging* 1999;17:503–15 CrossRef Medline
10. Baldeweg T, Hogan AM, Saunders DE, et al. **Detecting white matter injury in sickle cell disease using voxel-based morphometry.** *Ann Neurol* 2006;59:662–72 CrossRef Medline
11. Berkelhammer LD, Williamson AL, Sanford SD, et al. **Neurocognitive sequelae of pediatric sickle cell disease: a review of the literature.** *Child Neuropsychol* 2007;13:120–31 CrossRef Medline
12. Wang WC. **Sickle-cell disease and compromised cognition.** *Pediatr Blood Cancer* 2011;56:705–06 CrossRef Medline
13. Sun B, Brown RC, Hayes L, et al. **White matter damage in asymptomatic patients with sickle cell anemia: screening with diffusion tensor imaging.** *AJNR Am J Neuroradiol* 2012;33:2043–49 CrossRef Medline
14. Smith SM, Fox PT, Miller, KL, et al. **Correspondence of the brain's functional architecture during activation and rest.** *Proc Natl Acad Sci U S A* 2009;106:13040–45 CrossRef Medline

15. Buckner RL, Andrews-Hanna JR, Schacter DL. **The brain's default network: anatomy, function, and relevance to disease.** *Ann N Y Acad Sci* 2008;1124:1–38 CrossRef Medline
16. Zou P, Helton KJ, Smeltzer M, et al. **Hemodynamic responses to visual stimulation in children with sickle cell anemia.** *Brain Imaging Behav* 2011;5:295–306 CrossRef Medline
17. Darbari DS, Hampson JP, Ichesco E, et al. **Frequency of hospitalizations for pain and association with altered brain network connectivity in sickle cell disease.** *J Pain* 2015;16:1077–86 CrossRef Medline
18. Colombatti R, Lucchetta M, Montanaro M, et al. **Cognition and the default mode network in children with sickle cell disease: a resting state functional MRI study.** *PLoS One* 2016;11:e0157090 CrossRef Medline
19. Salgado-Pineda P, Fakra E, Delaveau P, et al. **Correlated structural and functional brain abnormalities in the default mode network in schizophrenia patients.** *Schizophr Res* 2011;125:101–09 CrossRef Medline
20. Laurienti PJ, Burdette JH, Wallace MT, et al. **Deactivation of sensory-specific cortex by cross-modal stimuli.** *J Cogn Neurosci* 2002;14:420–29 CrossRef Medline
21. Humphreys GF, Hoffman P, Visser M, et al. **Establishing task- and modality-dependent dissociations between the semantic and default mode networks.** *Proc Natl Acad Sci U S A* 2015;112:7857–62 CrossRef Medline
22. Ojemann JG, Buckner RL, Akbudak E, et al. **Functional MRI studies of word-stem completion: reliability across laboratories and comparison to blood flow imaging with PET.** *Hum Brain Mapp* 1998;6:203–15 Medline
23. Casella JF, King AA, Barton B, et al. **Design of the silent cerebral infarct transfusion (SIT) trial.** *Pediatr Hematol Oncol* 2010;27:69–89 CrossRef Medline
24. Bush AM, Borzage MT, Choi S, et al. **Determinants of resting cerebral blood flow in sickle cell disease.** *Am J Hematol* 2016;91:912–17 CrossRef Medline
25. Raichle ME, Snyder AZ. **A default mode of brain function: a brief history of an evolving idea.** *Neuroimage* 2007;37:1083–90; discussion 1097–99 CrossRef Medline
26. Kim JA, Leung J, Lerch JP, et al. **Reduced cerebrovascular reserve is regionally associated with cortical thickness reductions in children with sickle cell disease.** *Brain Res* 2016;1642:263–69 CrossRef Medline
27. Jordan LC, Gindville MC, Scott AO, et al. **Non-invasive imaging of oxygen extraction fraction in adults with sickle cell anaemia.** *Brain* 2016;139:738–50 CrossRef Medline
28. Kirk GR, Haynes MR, Palasis S, et al. **Regionally specific cortical thinning in in children with sickle cell disease.** *Cereb Cortex* 2009;19:1549–56 CrossRef Medline

Imaging Findings in Patients with Zoster-Associated Plexopathy

A.S. Zubair, C. Hunt, J. Watson, A. Nelson, and L.K. Jones Jr

ABSTRACT

SUMMARY: Herpes zoster is a reactivation of the latent varicella zoster virus. Among the complications of herpes zoster is zoster-associated limb paresis. The clinical and imaging features of patients with zoster-associated limb paresis due to plexopathies (zoster-associated plexopathy) have had limited description in the literature. The Mayo Clinic patient data base was searched by diagnostic code for patients diagnosed with herpes zoster between January 1, 1996, and September 30, 2012. Patients who met the inclusion criteria for zoster-associated limb paresis or herpes zoster with MRIs obtained were reviewed. Ten patients with zoster-associated plexopathy were identified. Imaging abnormalities were found in 70% of patients. Secondary denervation changes in shoulder girdle muscles and nerve T2 signal hyperintensity were the most frequent abnormalities (50%), followed by nerve enlargement (20%). Enhancement was not evident in any cases despite early imaging in 80% of the cohort. These results demonstrate the clinical utility of MR imaging in confirming the diagnosis of zoster-associated plexopathy.

ABBREVIATIONS: HZ = herpes zoster; ZALP = zoster-associated limb paresis; ZAP = zoster-associated plexopathy

Varicella zoster virus is a DNA virus in the Herpesviridae family, which has been shown to affect only humans. Following initial infection or inoculation by the varicella zoster virus, the virus establishes latency in the sensory ganglia.[1] The latent virus has the potential to reactivate later in a segmental cutaneous eruption known as herpes zoster (HZ) or shingles.[1-3] The incidence of HZ ranges from 1.3 per 1000 person-years among young adults to 10.7 per 1000 person-years among patients older than 80 years of age.[3] The diagnosis of uncomplicated HZ is generally made on clinical grounds without corroborative microbiologic testing.

Complications of HZ include postherpetic neuralgia, varicella zoster virus myelitis, segmental weakness, and delayed ischemic cerebral infarction due to varicella zoster virus–associated granulomatous vasculitis. These neurologic complications can appear simultaneously with the acute eruption of HZ or weeks to months after the rash has subsided.

The most common complication of HZ is postherpetic neuralgia.[4,5] Postherpetic neuralgia is residual neuropathic pain that lasts ≥3 months and is seen in roughly 20% of all patients with HZ and up to one-third of patients with HZ who are older than 80 years of age.[6,7]

Zoster-associated limb paresis (ZALP) is another recognized complication of HZ and consists of segmental weakness in a limb affected by HZ.[8-10] Many questions remain about ZALP, including the precise localization and mechanism of the motor abnormalities and the pathophysiology and imaging findings of the condition.[8,9] The clinical and imaging features of patients with ZALP due to plexopathies (zoster-associated plexopathy [ZAP]) have had limited description in the literature.[11-14] There are few dedicated reports of imaging findings in patients with ZAP despite imaging playing a crucial role in the localization of lesions, excluding other etiologies, and determining the extent of the lesions causing ZAP.[15]

The aim of this study was to identify the specific clinical and imaging features and their frequencies in patients with zoster-associated plexopathy.

MATERIALS AND METHODS

Case Series

This study was approved by the institutional review board and conducted at the Mayo Clinic with a waiver of informed consent being obtained before the study. The Mayo Clinic patient data base was searched by diagnostic code for patients diagnosed with herpes zoster between January 1, 1996, and September 30, 2012. Patients clinically diagnosed with ZAP who had MR imaging of

Received February 4, 2015; accepted after revision January 25, 2017.

From the Mayo Medical School (A.S.Z.); Department of Radiology (C.H.), Division of Neuroradiology; Department of Neurology (J.W., A.N., L.K.J.); and Division of Pain Medicine (J.W.); Mayo Clinic, Rochester, Minnesota.

Please address correspondence to Lyell K. Jones Jr, MD, Mayo Clinic, Department of Neurology, 200 1st St SW, Rochester, MN 55905; e-mail: Jones.Lyell@mayo.edu; @LyellJ

Indicates article with supplemental on-line table.

http://dx.doi.org/10.3174/ajnr.A5149

the affected plexus were included. The case definition for ZAP was the following: 1) documented history of examination evidence of a cutaneous vesicular eruption consistent with HZ; 2) evidence of temporal (within 30 days) and geographic (same limb) associated weakness confirmed on examination by a Mayo Clinic neurologist; and 3) electrodiagnostic evaluation confirming localization to the brachial or lumbosacral plexus during the symptomatic period of weakness. This case definition uses the temporal relationship between the HZ eruption and the limb weakness to establish the ZAP diagnosis; as in prior series, the typically delayed patient presentation limits the utility of virologic or serologic biomarker confirmatory testing.[16] Descriptive statistics were applied to the findings.

Clinical Localization

All patients underwent neurologic examinations administered by a board-certified Mayo Clinic neurologist. The examination findings were reviewed for severity and the distribution of weakness, sensory loss, and changes in muscle stretch reflexes. Plexopathy severity was determined by a standardized scoring of muscle weakness.[8]

Electrodiagnostic Evaluations

Electrodiagnostic studies performed on affected segments were reviewed, and the findings were summarized. Electrodiagnostic studies included nerve-conduction studies performed in standard fashion by using surface-recording electrodes. Needle electromyography was performed with a standard concentric needle electrode and included examination of at least 5 muscles in each affected segment.

Imaging

MR imaging studies of affected areas were reviewed by a board-certified neuroradiologist (C.H.), blinded to the results of the original interpretation, which was performed by a board-certified neuroradiologist or musculoskeletal radiologist, with consensus agreement from the other authors on the imaging findings. While our current brachial plexus imaging protocols have transitioned to 3T imaging, due to the time span of this study, 3 of 8 patients were imaged at only 1.5T. All of the patients with ZAP localized to the lumbosacral plexus were imaged at 1.5T. All studies included both pregadolinium T1- and T2-weighted images in axial, coronal, and sagittal planes. All T2-weighted sequences had either conventional fat saturation or a short tau inversion recovery sequence. Gadolinium-enhanced T1-weighted images (spoiled gradient-recalled acquisition) in at least 2 planes (axial and typically sagittal) were also obtained. Our typical protocol can be completed within 90 minutes from the time the patient enters the MR imaging suite. Root, plexus, or peripheral nerve imaging findings were classified as abnormal when associated with qualitatively prolonged nerve T2 or T2*, nerve enlargement, or postgadolinium nerve enhancement based on comparison with other neural structures within the imaging field. Diffusion sequences were not applied. Contralateral structures were included in the FOV for lumbosacral plexus imaging, but contralateral brachial plexus imaging was not routinely performed. In addition, the proximal shoulder muscles within the FOV were also examined for evidence of abnormal T2 signal.

Clinical features of patients with zoster-associated plexopathy

Features	
Mean age at onset (yr)	74.5 (range, 54–88)
Men	7 of 10 (70%)
Upper limb affected	8 of 10 (80%)
Mean interval between rash and weakness (days)	18
Neuralgia 1 mo after rash	10 of 10 (100%)
Neuralgia 3 mo after rash	7 of 10 (70%)
Corticosteroid treatment	6 of 10 (60%)
Diabetes mellitus	2 of 10 (20%)
Immunosuppression	1 of 10 (10%)

RESULTS

Ten patients satisfying the case definition were identified and reviewed. Patient features are summarized in the Table, and clinical and radiographic details are outlined in the On-line Table. Eight patients (80%) had brachial plexopathies, with the remainder diagnosed with lumbosacral plexopathies. Electrodiagnostic evaluations confirmed the localization to the brachial plexus or lumbosacral plexus in each case (On-line Table). Three patients underwent CSF examination, only 1 of which was performed within 1 month of symptom onset (patient 9, demonstrating an elevated protein level of 159 mg/dL, elevated nucleated cell count of 189 cells/microliter, and a polymerase chain reaction positive for varicella). Six patients (60%) received steroids at some point in the management of their presentation. Five of these patients received short courses of oral prednisone, all >1 month before evaluation, and 1 patient received high-dose IV methylprednisolone for 3 days after imaging was performed, making it unlikely that the imaging findings in this series were influenced by the steroid treatment. There were no reported complications of steroid treatment in these patients such as zoster dissemination.

MR imaging findings were abnormal in 7/10 patients (70%). Five patients (50%) demonstrated increased nerve T2 signal, 2 patients (20%) demonstrated nerve enlargement, and no patients demonstrated nerve enhancement. Denervation changes were noted in 5 patients (50%), primarily in shoulder girdle muscles included in the FOV. All except 1 of the patients with denervation changes also demonstrated abnormal nerve imaging findings; and correspondingly, all except 2 of the patients with abnormal nerve imaging findings also demonstrated denervation changes. The most commonly affected muscles were the infraspinatus (4/5), supraspinatus (3/5), teres minor (1/5), subscapularis (1/5), and the deltoid (1/5). Characteristic imaging abnormalities are shown in Figs 1–3.

DISCUSSION

This study describes the imaging abnormalities in the largest series of patients with ZAP to date.[11-13] ZALP, which may localize to the root, plexus, or more peripheral nerve, is difficult to localize clinically in part because the involved myotomes often do not correspond to the dermatomes affected by the rash.[15] Thus, imaging can be a very useful tool in the identification and localization of the lesions in these patients.

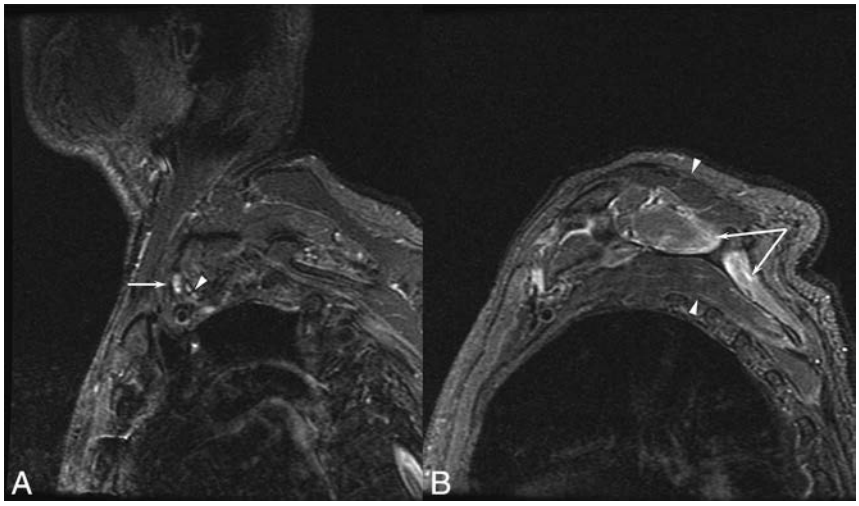

FIG 1. A 77-year-old man with a left brachial zoster-associated plexopathy. *A*, Sagittal inversion recovery image demonstrates increased T2 signal in the upper trunk (*arrow*) compared with the other elements of the plexus (*arrowhead*). *B*, Prolonged T2 is noted in the supraspinatus and infraspinatus (*arrows*), corresponding to denervation resulting from the plexopathy.

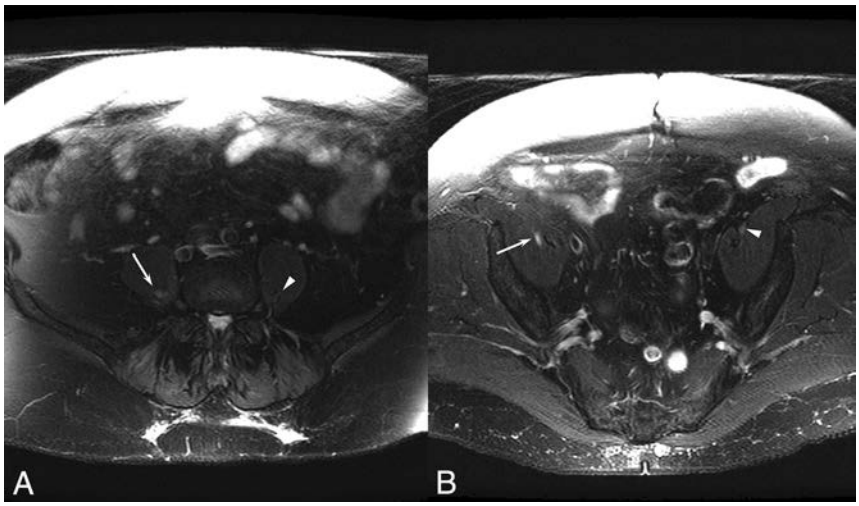

FIG 2. A 70-year-old woman with a right lumbar zoster-associated plexopathy. *A*, Axial T2-weighted image demonstrates increased T2 signal in the right lumbar plexus (*arrow*) compared with the left lumbar plexus (*arrowhead*). *B*, Increased T2 is also noted more distally in the right femoral nerve (*arrow*) compared with the unaffected left side (*arrowhead*).

Prior reports described imaging findings ranging from normal to abnormal, similar to those described in this series. The spectrum of findings in this series ranged from normal to increased T2 signal in the plexus, nerve enlargement, and denervation changes in the muscles innervated by the plexus.

The imaging findings included not only nerve abnormalities but also secondary denervation changes in affected muscles, which were seen in half of all patients. These changes were only present in the shoulder girdle muscles among those patients with brachial ZAP. This constellation of findings can be used clinically to help diagnose patients with ZAP and categorize the severity of their conditions. While no patients with ZAP in this series demonstrated nerve enhancement after administration of gadolinium contrast, postcontrast imaging may still be useful in patients with plexopathy to exclude other potential causes of weakness such as peripheral nerve tumors.

Clinically, patients with ZAP have a high rate of postherpetic neuralgia. At 1 month after the rash, 100% of patients had neuralgia, and at 3 months, 70% of patients had postherpetic neuralgia. This rate exceeds previously reported rates of postherpetic neuralgia in patients with HZ (generally 20%–40%),[3,10] possibly attributable to more severe disease or other unrecognized factors. The rate of postherpetic neuralgia in this series was similar to that reported in all patients with ZALP.[8] In addition to the need to recognize the high rate of postherpetic neuralgia in patients with ZAP, our findings also suggest that these patients are frequently typically treated with short courses of corticosteroids. While the size and structure of this series does not allow comment on efficacy, no patients experienced reported adverse effects related to the steroid treatments, such as zoster dissemination or worsening of neurologic deficits. These findings provide some evidence of safety if future corticosteroid trials are entertained in this group of patients.

The pathophysiology of ZALP due to ZAP is not completely understood. Electrophysiologic and neuropathologic studies have implied viral spread of inflammation from the dorsal root gan-

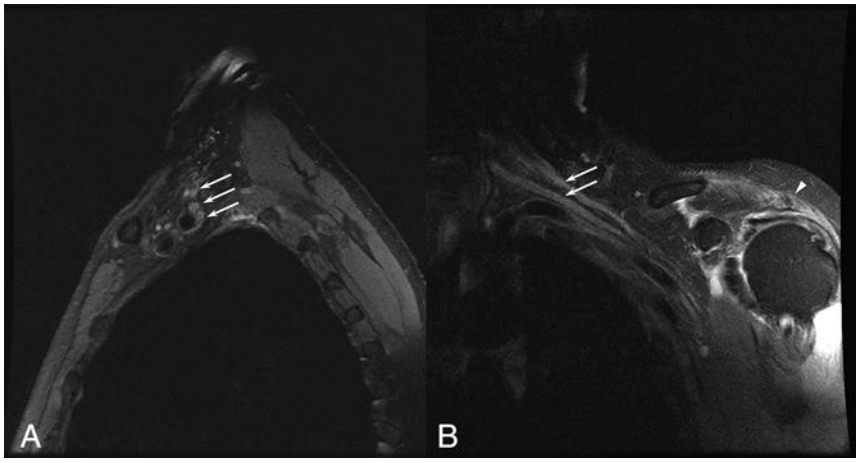

FIG 3. A 75-year-old man with a left brachial zoster-associated plexopathy. *A*, Sagittal T2-weighted image with fat saturation demonstrates diffusely increased T2 in the upper, middle, and lower trunks of the brachial plexus (*arrows*). *B*, Coronal T2-weighted image with fat saturation demonstrates increased T2 in the upper and middle trunks of the brachial plexus (*arrows*). Prolonged T2 associated with denervation is noted in the deltoid (*arrowhead*).

glion to adjacent nervous tissue, including the anterior horn cell and motor roots.[12,16-18] Previous histologic studies of patients with HZ paresis indicated diffuse chronic inflammation of all trunks of the brachial plexus with destruction of myelin and axonal sparing.[12] In practice, the clinical findings in the setting of a history of characteristic rash raise the suspicion of ZALP, and electrodiagnostic abnormalities that localize to the corresponding plexus confirm the presence of a plexopathy. When the diagnosis of ZAP is suspected, imaging can play an important role in supporting the diagnosis and excluding other causes of plexopathy, the primary reason in this series for performing imaging studies. While most of the imaging in this study was performed with 1.5T MR imaging, with the continued transition to 3T scanners, it is anticipated that the sensitivity of plexus MR imaging, especially of small nerves, will increase.

This study is limited by its small size and retrospective design. While our findings suggest that imaging is a useful adjunct in the evaluation of patients with ZAP, corroboration with standardized imaging protocols in larger groups of patients would be helpful, especially in the absence of specific imaging or serologic findings.

CONCLUSIONS

ZALP can result from brachial or lumbosacral plexopathies (ZAP). Patients with ZAP have a high rate of postherpetic neuralgia (100% at 1 month, 70% at 3 months). MR imaging is a useful diagnostic technique in patients with ZAP, with 70% of patients in this series demonstrating radiographic abnormalities attributable to ZAP. Hopefully, these findings and those of future series will be useful in the diagnosis and management of patients with ZAP.

REFERENCES

1. Zerboni L, Sen N, Oliver SL, et al. **Molecular mechanisms of varicella zoster virus pathogenesis.** *Nat Rev Microbiol* 2014;12:197–210 CrossRef Medline
2. Schmidbauer M, Budka H, Pilz P, et al. **Presence, distribution and spread of productive varicella zoster virus infection in nervous tissues.** *Brain* 1992;115(pt 2):383–98 CrossRef Medline
3. Yawn BP, Saddier P, Wollan PC, et al. **A population-based study of the incidence and complication rates of herpes zoster before zoster vaccine introduction.** *Mayo Clin Proc* 2007;82:1341–49 CrossRef Medline
4. Gnann JW Jr, Whitley RJ. **Clinical practice. Herpes zoster.** *N Engl J Med* 2002;347:340–46 CrossRef Medline
5. Jung BF, Johnson RW, Griffin DR, et al. **Risk factors for postherpetic neuralgia in patients with herpes zoster.** *Neurology* 2004;62:1545–51 CrossRef Medline
6. Alshekhlee A, Tay E, Buczek M, et al. **Herpes zoster with motor involvement: discordance between the distribution of skin rash and localization of peripheral nervous system dysfunction.** *J Clin Neuromuscul Dis* 2011;12:153–57 CrossRef Medline
7. Cockerell OC, Ormerod IE. **Focal weakness following herpes zoster.** *J Neurol Neurosurg Psychiatry* 1993;56:1001–03 CrossRef Medline
8. Jones LK Jr, Reda H, Watson JC. **Clinical, electrophysiologic, and imaging features of zoster-associated limb paresis.** *Muscle Nerve* 2014;50:177–85 CrossRef Medline
9. Reda H, Watson JC, Jones LK Jr. **Zoster-associated mononeuropathies (ZAMs): a retrospective series.** *Muscle Nerve* 2012;45:734–39 CrossRef Medline
10. Gilden DH, Kleinschmidt-DeMasters BK, LaGuardia JJ, et al. **Neurologic complications of the reactivation of varicella-zoster virus.** *N Engl J Med* 2000;342:635–45 CrossRef Medline
11. Eyigor S, Durmaz B, Karapolat H. **Monoparesis with complex regional pain syndrome-like symptoms due to brachial plexopathy caused by the varicella zoster virus: a case report.** *Arch Phys Med Rehabil* 2006;87:1653–55 CrossRef Medline
12. Fabian VA, Wood B, Crowley P, et al. **Herpes zoster brachial plexus neuritis.** *Clin Neuropathol* 1997;16:61–64 Medline
13. Mullins GM, O'Sullivan SS, Neligan A, et al. **Non-traumatic brachial plexopathies, clinical, radiological and neurophysiological findings from a tertiary centre.** *Clin Neurol Neurosurg* 2007;109:661–66 CrossRef Medline
14. Yoleri O, Olmez N, Oztura I, et al. **Segmental zoster paresis of the upper extremity: a case report.** *Arch Phys Med Rehabil* 2005;86:1492–94 CrossRef Medline
15. Choi JY, Kang CH, Kim BJ, et al. **Brachial plexopathy following herpes zoster infection: two cases with MRI findings.** *J Neurol Sci* 2009;285:224–26 CrossRef Medline
16. Ismail A, Rao DG, Sharrack B. **Pure motor herpes zoster induced brachial plexopathy.** *J Neurol* 2009;256:1343–45 CrossRef Medline
17. Jeevarethinam A, Ihuoma A, Ahmad N. **Herpes zoster brachial plexopathy with predominant radial nerve palsy.** *Clin Med (Lond)* 2009;9:500–01 CrossRef Medline
18. Ayoub T, Raman V, Chowdhury M. **Brachial neuritis caused by varicella-zoster diagnosed by changes in brachial plexus on MRI.** *J Neurol* 2010;257:1–4 CrossRef Medline

Enhancing the Radiologist-Patient Relationship through Improved Communication: A Quantitative Readability Analysis in Spine Radiology

D.R. Hansberry, A.L. Donovan, A.V. Prabhu, N. Agarwal, M. Cox, and A.E. Flanders

ABSTRACT

BACKGROUND AND PURPOSE: More than 75 million Americans have less than adequate health literacy skills according to the National Center for Education Statistics. Readability scores are used as a measure of how well populations read and understand patient education materials. The purpose of this study was to assess the readability of Web sites dedicated to patient education for radiologic spine imaging and interventions.

MATERIALS AND METHODS: Eleven search terms relevant to radiologic spine imaging were searched on the public Internet, and the top 10 links for each term were collected and analyzed to determine readability scores by using 10 well-validated quantitative readability assessments from patient-centered education Web sites. The search terms included the following: x-ray spine, CT spine, MR imaging spine, lumbar puncture, kyphoplasty, vertebroplasty, discogram, myelogram, cervical spine, thoracic spine, and lumbar spine.

RESULTS: Collectively, the 110 articles were written at an 11.3 grade level (grade range, 7.1–16.9). None of the articles were written at the American Medical Association and National Institutes of Health recommended 3rd-to-7th grade reading levels. The vertebroplasty articles were written at a statistically significant ($P < .05$) more advanced level than the articles for x-ray spine, CT spine, and MR imaging spine.

CONCLUSIONS: Increasing use of the Internet to obtain health information has made it imperative that on-line patient education be written for easy comprehension by the average American. However, given the discordance between readability scores of the articles and the American Medical Association and National Institutes of Health recommended guidelines, it is likely that many patients do not fully benefit from these resources.

ABBREVIATIONS: AMA = American Medical Association; FRE = Flesch Reading Ease; GFI = Gunning Fog Index; NIH = National Institutes of Health

As barriers to on-line access have decreased, the Internet has emerged as a primary resource for Americans desiring greater understanding of their health. According to a June 2015 report by the Pew Research Center,[1] up to 84% of adults access the Internet, and within the past year, 72% of those users have searched for health information.[2] Specifically, 55% wanted to learn more about a disease or medical problem; and 43%, about a medical treatment or procedure.[2] Studies have confirmed that this on-line research impacts decision-making for many patients: the questions they ask, the types of treatment they pursue, and whether they visit a physician.[2-5]

Although more adults are accessing health care information on-line than ever before,[2,4] it is uncertain how much of this information is fully comprehended due to poor health literacy. Health literacy, as defined by the US Department of Health and Human Services, is "the capacity to obtain, process, and understand basic health information and services needed to make appropriate health decisions."[6] In a 2003 assessment commissioned by the US Department of Education, only 12% of adults were found to have proficient health literacy. Proficiency was defined as having the skills necessary to locate, understand, and use information contained within documents commonly encountered in the medical system, such as medication dosing instructions, preventative care documentation, and insurance information. This definition indicates an ability to read, analyze, and synthesize complex content. More than 75 million Americans demonstrated either basic or below basic health literacy and would experience difficulty reading and comprehending health care–related text.[7] The impor-

Received October 7, 2016; accepted after revision January 25, 2017.

From the Department of Radiology (D.R.H., M.C., A.E.F.), Thomas Jefferson University Hospital, Philadelphia, Pennsylvania; Department of Radiation Oncology (A.L.D., A.V.P.), University of Pittsburgh Cancer Institute, Pittsburgh, Pennsylvania; and Department of Neurological Surgery (N.A.), University of Pittsburgh Medical Center, Pittsburgh, Pennsylvania.

Please address correspondence to David R. Hansberry, MD, PhD, Department of Radiology, Thomas Jefferson University Hospitals, 132 South 10th St, Philadelphia, PA 19107; e-mail: david.hansberry@jefferson.edu

Indicates article with supplemental on-line table.

http://dx.doi.org/10.3174/ajnr.A5151

Formulas for the readability assessments

Readability Assessment	Variables	Algorithm
Coleman-Liau Index	L, average number of letters per 100 words S, average number of sentences per 100 words	(0.0588 × L) − (0.296 × S) − 15.8
Flesch Reading Ease	B, average number of syllables W, average number of words per sentence S, average number of sentences	206.835 − (84.6 × [B/W]) − (1.015 × [W/S])
Flesch-Kincaid Grade Level	SY, average number of syllables per word W, average number of words per sentence	(0.39 × W) + (11.8 × SY) − 15.59
FORCAST Formula	SS, number of single-syllable words in a 150-word sample	20 − (SS/10)
Fry Graph	Average number of sentences and syllables per 100 words	1) Extract a 100-word passage 2) Count the number of sentences, counting half a sentence as 0.5 3) Count the number of syllables 4) Find the point on the chart (3 samples recommended)
Gunning Fog Index	S, number of sentences W, number of words C, number of words with ≥3 syllables	0.4 × [W/S + ([C/W] × 100)]
New Dale-Chall	AW, average number of words per sentence U, percentage of unfamiliar words	(0.1579 × U) + (0.0496 × AW)
New Fog Count	C, number of complex words E, number of easy words S, number of sentences	([(E + [3 × C])/S] − 3)/2
Raygor Readability Estimate	Average number of sentences Long words (≥3 characters) per 100 words	1) Extract a 100-word passage 2) Count the number of sentences, estimated to the nearest 10th 3) Count the number of words that are ≥6 letters 4) Find the point on the chart (3 samples recommended)
SMOG	C, average number of words with ±3 syllables S, average number of sentences	1.043 × √([C × (30/S)] + 3.1292)

tance of health literacy cannot be understated because it has a direct influence on both health outcomes and health care expenditures. Studies have linked low health literacy to increased hospitalizations,[8,9] higher mortality rates,[8,10] and an annual cost to the US economy of up to $238 billion.[11] In fact, the American Medical Association (AMA) has identified low health literacy as a strong independent predictor of health status.[12]

Readability, defined as the degree of ease with which a given text can be read and comprehended, is 1 correlative measure of health literacy.[13] The reading level of the average American is between the 7th and 8th grade, while the average Medicaid enrollee reads at just a 5th grade level.[12] Therefore, to maximize the number of individuals benefiting from patient education, the AMA and the National Institutes of Health (NIH) recommend that content be written at a level commensurate with the 3rd-to-7th grade levels.[12,14] However, patient education materials across numerous specialties in medicine do not meet this recommendation. A 2013 readability study published in *Journal of the American Medical Association* analyzed material from 16 different medical specialties and determined that it was too complex for the average patient.[15] Similar conclusions have been drawn regarding the surgical subspecialties.[16]

Readability analyses specific to spine-related patient education have also revealed a failure to meet reading level guidelines.[17-20] However, research to date has only examined surgical procedures and material sourced from professional society Web sites. Three of the 4 studies were also limited by an analysis that incorporated just 1 readability assessment. The purpose of this study was to quantitatively determine the readability of patient education Web sites pertaining to radiologic diagnostic tests and interventions of the spine. We used 10 readability assessments that are well-vetted in the literature to avoid bias from any single test. This analysis does not include patient education materials related to imaging of the brain.

MATERIALS AND METHODS

This study examined publicly available data; thus, institutional review board oversight was not required. In December 2015, Web sites dedicated to patient education relevant to spine imaging were sought on the public Internet by using the Google search engine. Eleven keywords were separately entered as search terms: x-ray spine, CT spine, MR imaging spine, lumbar puncture, kyphoplasty, vertebroplasty, discogram, myelogram, cervical spine, thoracic spine, and lumbar spine. The first 10 articles intended for patients for each term were included in the analysis. Web sites not specifically directed toward patients were excluded. The text of 110 articles was copied, pasted, and saved as individual Microsoft Word (Microsoft, Redmond, Washington) documents. Images, figures, tables, references, and other noneducational text were removed.

Each document was then analyzed, and a readability analysis was performed with Readability Studio Professional Edition (Oleander Software, Vandalia, Ohio). An individual readability score was calculated for each of the 10 following well-validated assessments (Table): the Coleman-Liau Index,[21] Flesch Reading Ease (FRE),[22] Flesch-Kincaid Grade Level,[23] FORCAST,[24] Fry Graph,[25] Gunning Fox Index (GFI),[26] New Dale-Chall,[27] New Fog Count,[23] Raygor Readability Estimate,[28] and SMOG.[29] The FRE reports scores

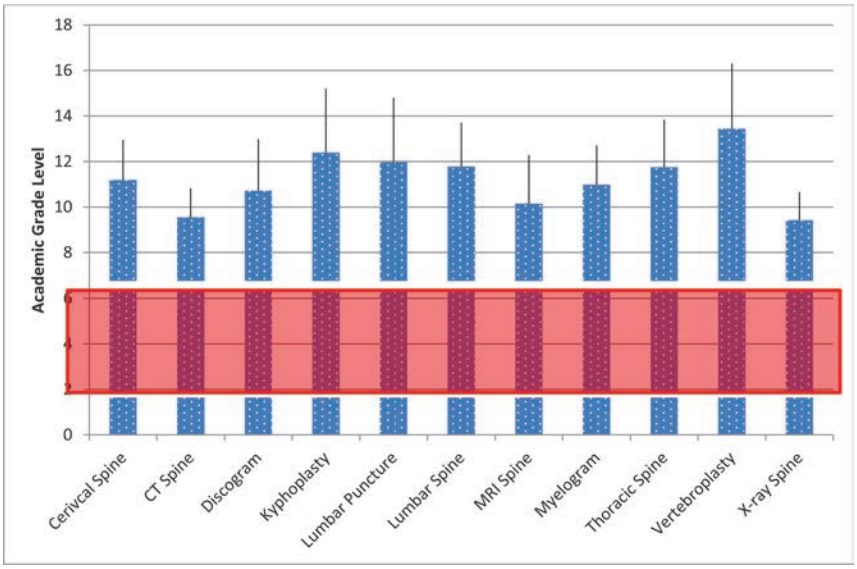

FIG 1. The grade level taken as the mean of all readability scales examined in this study for the 10 top search results for each key term. The *red box* represents the AMA and NIH recommended 3rd-to-7th grade guidelines.

on a 0–100 scale with lower numbers corresponding to more difficult-to-read text. The remaining 9 scales report the readability of the text as a grade level. For instance, a GFI score of 9.0 corresponds to a 9th grade reading level.

Statistical analysis was conducted by using OriginPro (OriginLab, Northamptom, Massachusetts) to compare readability scores among the 11 keywords. A 1-way ANOVA and a Tukey Honestly Significant Difference post hoc analysis were performed with $P < .05$.

RESULTS

Collectively, the 110 articles had a mean FRE score of 51.9, classifying them as fairly difficult on the FRE scale, and an 11.3 mean grade level averaged across the other 9 assessments, scored on the basis of grade level (Fig 1). FRE scores ranged from 74 (fairly easy) to 14 (very difficult), and grade levels ranged from 7.1 to 16.9. None of the articles (0/110) met the recommendations of the AMA and NIH of being written within a 3rd-to-7th grade level. Approximately 35% (39/110) were written at a level that required a high school education or higher (score of ≥12). An additional 50 articles scored between a 9th and 12th grade levels (On-line Table).

The articles consisted of many words characterized as complex, long, or unfamiliar. Words with at least 3 syllables were considered complex and composed 16.1% of the text of the articles, while words with at least 6 characters were considered long and composed 33.7%. More than 28% of words were classified as unfamiliar, as determined by an absence from the Dale-Chall list of simple words, which contains 3000 words known by most 4th grade children.[27] In addition, unfamiliar words made up at least one-third of the text for 19 of the 110 (17.3%) articles. Sentences ranged from 23 to 127 words.

The 1-way ANOVA found a statistical difference among the 11 keywords ($F(10,99) = 3.19$, $P = .001$). Average grade levels for each searched term were as follows: x-ray spine, 9.4; CT spine,9.6; MR imaging spine, 10.2; discogram, 10.7; myelogram, 11.0; cervical spine, 11.2; thoracic spine, 11.8; lumbar spine,11.8; lumbar puncture, 12.0; kyphoplasty, 12.4; and vertebroplasty, 13.4. Tukey Honestly Significant Difference post hoc analysis indicated that the vertebroplasty articles were significantly more advanced than the articles for x-ray spine, CT spine, and MR imaging spine ($P < .05$).

DISCUSSION

Due to the inherently complex nature of spine diagnoses and treatments, patients are apt to seek more information on the Internet. Up to 77% of individuals begin this process with a search engine such as Google.[2] More than 90% do not look beyond the first page of results.[30] Consequently, patients wishing to learn more about radiologic spine imaging and interventions would likely encounter 1 of the 110 articles in this study when searching for these 11 terms. With a mean readability score of 11.3, these articles would be too complex for the average American who reads at a 7th-to-8th grade level. In addition, the abundance of uncommon words and long sentences would make understanding difficult for those classified as having less than proficient health literacy, which indicates an inability to read and synthesize complex health care–related text. Therefore, 62% of the adult population identified by the US Department of Education as having either basic or below basic health literacy would not fully benefit from this information and may be led to uninformed decisions that negatively affect health outcomes.[7]

If on-line patient education resources were written at a 7th grade reading level or lower, more Americans would be able to read and understand the material more thoroughly. Consequently, patients would likely experience increased involvement in their care and improved communication with their physicians. When empowered with knowledge, patients have been shown to ask more questions, communicate concerns with greater confidence, and actively engage in the medical decision-making process.[31-33] Patients have also reported greater satisfaction, particularly with informed consent.[34] In radiology, health literacy has been linked to differing rates of imaging use[35] and patient knowledge of procedure details and radiation use.[36] Complex examinations and interventions, including those of the spine, stand to benefit from the active patient engagement and enhanced patient-provider communication resulting from well-written education materials.

The results of this study are consistent with prior research investigating the readability of on-line patient education. Web sites for both medical and surgical subspecialties are routinely written at a level exceeding the 7th grade.[37-40] Those dedicated to radiology, including radiologyinfo.org sponsored by the American College of Radiology and Radiological Society of North America, are written at a level too advanced for most patients.[41] In addition, patient education materials from professional society Web sites, Wikipedia, WebMD, and hospital Web sites have all

been written above the average comprehension level.[42-45] This study, strengthened by the incorporation of text sourced from multiple Web site types and the use of 10 readability assessments, adds additional support to the conclusions drawn by prior spine imaging readability research. Collectively, these results highlight the need for further action to satisfy AMA and NIH readability recommendations. Authors and editors should use simpler words, construct shorter sentences, reduce abbreviations and acronyms, and eliminate medical jargon.[14] Resources from the NIH,[14] Centers for Disease Control and Prevention,[46] and Center for Medicare and Medicaid Services are available to offer further guidance.[47]

This study is limited by the constraints of the readability assessments. Most important, the algorithms for certain quantitative parameters, such as the number of letters, syllables, words, and sentences used in the text, may lead to inaccurate scores for medical terminology. For instance, words with few syllables that are not necessarily familiar to the average person may lead to inappropriately low scores, while multisyllabic common words would be scored with a higher grade level. The FORCAST formula, which is based solely on the number of single-syllable words, is particularly susceptible to this bias. For example, "pia" would receive a lower rating than "operation," despite being an uncommon term. The other assessments that use syllable counts, including the FRE, Flesch-Kincaid Grade Level, Fry Graph, GFI, and SMOG, may be affected to a somewhat lesser extent due to the use of additional variables. In this study, incorporation of 10 readability assessments reduces the bias of any single algorithm. An additional limitation is that none of the assessments evaluated the nontextual elements of readability, such as style, format, and organization[13] or the use of supplemental material, such as images or diagrams. Further work is needed to determine the effect of these elements on the comprehension of patient education materials, specifically in radiology. Conducting readability and comprehension tests with target prospective patient populations may also be revealing.

CONCLUSIONS

With increasing use of the Internet for patient self-education, there is a growing need for the readability of material to fall within the limits of the average American's comprehension. However, an average reading level is often far exceeded in many disciplines of medicine. Spine imaging and radiologic interventions have not been an exception. It is imperative to broaden awareness of this discrepancy to mitigate the negative outcomes of poor health literacy. By adhering to the AMA and NIH guidelines, physicians, professional societies, and other authors can increase patient comprehension of on-line health care materials.

REFERENCES

1. Perrin A, Duggan M. Americans' Internet Access: 2000–15. Pew Research Center; 2015. http://www.pewinternet.org/2015/06/26/americans-internet-access-2000-2015/. Accessed August 15, 2016
2. Fox S, Duggan M. Health Online 2013. Pew Research Center: Science & Tech. January 15, 2013. http://www.pewinternet.org/2013/01/15/health-online-2013/. Accessed August 15, 2016
3. Pourmand A, Sikka N. **Online health information impacts patients' decisions to seek emergency department care.** *West J Emerg Med* 2011;12:174–77 Medline
4. Rice RE. **Influences, usage, and outcomes of Internet health information searching: multivariate results from the Pew surveys.** *Int J Med Inform* 2006;75:8–28 CrossRef Medline
5. Rainie L, Fox S. The Online Health Care Revolution. Pew Research Center: Internet, Science & Tech. 2000. http://www.pewinternet.org/2000/11/26/the-online-health-care-revolution/. Accessed August 15, 2016
6. Healthy People 2010. U.S. Department of Health and Human Services. Published November 26, 2000. http://www.healthypeople.gov/2010/. Accessed August 15, 2016
7. National Assessment of Adult Literacy: A Nationally Representative and Continuing Assessment of English Language Literary Skills of American Adults. 2003. National Center for Education Statistics. https://nces.ed.gov/naal/fr_skills.asp. Accessed August 15, 2016
8. Berkman ND, Sheridan SL, Donahue KE, et al. **Low health literacy and health outcomes: an updated systematic review.** *Ann Intern Med* 2011;155:97–107 CrossRef Medline
9. Baker DW, Gazmararian JA, Williams MV, et al. **Functional health literacy and the risk of hospital admission among Medicare managed care enrollees.** *Am J Public Health* 2002;92:1278–83 CrossRef Medline
10. Baker DW, Wolf MS, Feinglass J, et al. **Health literacy and mortality among elderly persons.** *Arch Intern Med* 2007;167:1503–09 CrossRef Medline
11. Vernon JA, Trujillo A, Rosenbaum SJ, et al. *Low Health Literacy: Implications for National Health Policy*. Washington, DC: Department of Health Policy, School of Public Health and Health Services, The George Washington University; 2007
12. Weiss BD, Schwartzberg JG; American Medical Association. *Health Literacy and Patient Safety: Help Patients Understand: Manual for Clinicians.* Chicago: AMA Foundation; 2007
13. DuBay WH. *The Principles of Readability.* Costa Mesa: Impact Information; 2004
14. How to Write Easy-to-Read Health Materials. MedlinePLus. https://medlineplus.gov/etr.html. Accessed August 15, 2016
15. Agarwal N, Hansberry DR, Sabourin V, et al. **A comparative analysis of the quality of patient education materials from medical specialties.** *JAMA Intern Med* 2013;173:1257–59 CrossRef Medline
16. Hansberry DR, Agarwal N, Shah R, et al. **Analysis of the readability of patient education materials from surgical subspecialties.** *Laryngoscope* 2014;124:405–12 CrossRef Medline
17. Eltorai AE, Cheatham M, Naqvi SS, et al. **Is the readability of spine-related patient education material improving? An assessment of subspecialty websites.** *Spine (Phila Pa 1976)* 2016;41:1041–48 CrossRef Medline
18. Ryu JH, Yi PH. **Readability of spine-related patient education materials from leading orthopedic academic centers.** *Spine (Phila Pa 1976)* 2016;41:E561–65 CrossRef Medline
19. Agarwal N, Feghhi DP, Gupta R, et al. **A comparative analysis of minimally invasive and open spine surgery patient education resources.** *J Neurosurg Spine* 2014;21:468–74 CrossRef Medline
20. Vives M, Young L, Sabharwal S. **Readability of spine-related patient education materials from subspecialty organization and spine practitioner websites.** *Spine (Phila Pa 1976)* 2009;34:2826–31 CrossRef Medline
21. Coleman ML, Liau TL. **A computer readability formula designed for machine scoring.** *J Appl Psychol* 1975;60:283–84
22. Flesch R. **A new readability yardstick.** *J Appl Psychol* 1948;32:221–33 CrossRef Medline
23. Kincaid JP, Fishburne RP Jr, Rogers RL. *Derivation of New Readability Forumlas (Automated Readability Index, Fog Count and Flesch Reading Ease Formula) For Navy Enlisted Personnel.* Millington: National Technical Information Service; 1975
24. Caylor JS, Sticht TG, Fox LC, et al. *Methodologies for Determining Reading Requirements of Military Occupational Specialties.* Technical Report. Alexandria: Human Resources Research Organization; 1973
25. Fry E. **A readability formula that saves time.** *Journal of Reading* 1968;11:513–78

26. Gunning R. *The Technique of Clear Writing.* New York: McGraw-Hill; 1952
27. Chall JS, Dale E. *Readability Revisited: The New Dale-Chall Readability Formula.* Northampton: Brookline Books Cambridge; 1995
28. Raygor AL. **The Raygor readability estimate: a quick and easy way to determine difficulty**. In: Pearson PD, Hansen J, ed. *Reading: Theory, Research, and Practice: Twenty-Sixth Yearbook of the National Reading Conference.* Clemson: National Reading Conference; 1977
29. McLaughlin GH. **SMOG grading: a new readability formula.** *Journal of Reading* 1969;12:639–46
30. Chitika. The Value of Google Result Positioning. June 7, 2013. https://chitika.com/google-positioning-value. Accessed August 15, 2016
31. Lee CJ, Gray SW, Lewis N. **Internet use leads cancer patients to be active health care consumers.** *Patient Educ Couns* 2010;81(suppl): S63–69 CrossRef Medline
32. Iverson SA, Howard KB, Penney BK. **Impact of internet use on health-related behaviors and the patient-physician relationship: a survey-based study and review.** *J Am Osteopath Assoc* 2008;108:699–711 Medline
33. Hironaka LK, Paasche-Orlow MK. **The implications of health literacy on patient-provider communication.** *Arch Dis Child* 2008;93: 428–32 CrossRef Medline
34. Fraval A, Chandrananth J, Chong YM, et al. **Internet based patient education improves informed consent for elective orthopaedic surgery: a randomized controlled trial.** *BMC Musculoskelet Disord* 2015;16:14 CrossRef Medline
35. Morrison AK, Brousseau DC, Brazauskas R, et al. **Health literacy affects likelihood of radiology testing in the pediatric emergency department.** *J Pediatr* 2015;166:1037–41.e1 CrossRef Medline
36. Gebhard RD, Goske MJ, Salisbury SR, et al. **Improving health literacy: use of an informational brochure improves parents' understanding of their child's fluoroscopic examination.** *AJR Am J Roentgenol* 2015;204:W95–W103 CrossRef Medline
37. Prabhu AV, Hansberry DR Agarwal N, et al. **Radiation oncology and online patient education materials: deviating from NIH and AMA recommendations.** *Int J Radiat Oncol Biol Phys* 2016;96:521–28 CrossRef Medline
38. Prabhu AV, Gupta R, Kim C, et al. **Patient education materials in dermatology: addressing the health literacy needs of patients.** *JAMA Dermatol* 2016;152:946–47 CrossRef Medline
39. Agarwal N, Chaudhari A, Hansberry DR, et al. **A comparative analysis of neurosurgical online education materials to assess patient comprehension.** *J Clin Neurosci* 2013;20:1357–61 CrossRef Medline
40. Kasabwala K, Misra P, Hansberry DR, et al. **Readability assessment of the American Rhinologic Society patient education materials.** *Int Forum Allergy Rhinol* 2013;3:325–33 CrossRef Medline
41. Hansberry DR, John A, John E, et al. **A critical review of the readability of online patient education resources from RadiologyInfo.Org.** *AJR Am J Roentgenol* 2014;202:566–75 CrossRef Medline
42. Hansberry DR, Agarwal N, Baker SR. **Health literacy and online educational resources: an opportunity to educate patients.** *AJR Am J Roentgenol* 2015;204:111–16 CrossRef Medline
43. Hansberry DR, Ramchand T, Patel S, et al. **Are we failing to communicate? Internet-based patient education materials and radiation safety.** *Eur J Radiol* 2014;83:1698–702 CrossRef Medline
44. Hansberry DR, Kraus C, Agarwal N, et al. **Health literacy in vascular and interventional radiology: a comparative analysis of online patient education resources.** *Cardiovasc Intervent Radiol* 2014;37: 1034–40 CrossRef Medline
45. Hansberry DR, Agarwal N, Gonzales SF, et al. **Are we effectively informing patients? A quantitative analysis of on-line patient education resources from the American Society of Neuroradiology.** *AJNR Am J Neuroradiol* 2014;35:1270–75 CrossRef Medline
46. Centers for Disease Control and Prevention. Health Literacy Guidance and Standards. 2015. https://health.gov/communication/literacy/quickguide/quickguide.pdf. Accessed August 15, 2016
47. Toolkit for Making Written Material Clear and Effective. Centers for Medicare and Medicaid Services. https://www.cms.gov/Outreach-and-Education/Outreach/WrittenMaterialsToolkit/index.html. Accessed August 15, 2016

Clinically Feasible Microstructural MRI to Quantify Cervical Spinal Cord Tissue Injury Using DTI, MT, and T2*-Weighted Imaging: Assessment of Normative Data and Reliability

A.R. Martin, B. De Leener, J. Cohen-Adad, D.W. Cadotte, S. Kalsi-Ryan, S.F. Lange, L. Tetreault, A. Nouri, A. Crawley, D.J. Mikulis, H. Ginsberg, and M.G. Fehlings

ABSTRACT

BACKGROUND AND PURPOSE: DTI, magnetization transfer, T2*-weighted imaging, and cross-sectional area can quantify aspects of spinal cord microstructure. However, clinical adoption remains elusive due to complex acquisitions, cumbersome analysis, limited reliability, and wide ranges of normal values. We propose a simple multiparametric protocol with automated analysis and report normative data, analysis of confounding variables, and reliability.

MATERIALS AND METHODS: Forty healthy subjects underwent T2WI, DTI, magnetization transfer, and T2*WI at 3T in <35 minutes using standard hardware and pulse sequences. Cross-sectional area, fractional anisotropy, magnetization transfer ratio, and T2*WI WM/GM signal intensity ratio were calculated. Relationships between MR imaging metrics and age, sex, height, weight, cervical cord length, and rostrocaudal level were analyzed. Test-retest coefficient of variation measured reliability in 24 DTI, 17 magnetization transfer, and 16 T2*WI datasets. DTI with and without cardiac triggering was compared in 10 subjects.

RESULTS: T2*WI WM/GM showed lower intersubject coefficient of variation (3.5%) compared with magnetization transfer ratio (5.8%), fractional anisotropy (6.0%), and cross-sectional area (12.2%). Linear correction of cross-sectional area with cervical cord length, fractional anisotropy with age, and magnetization transfer ratio with age and height led to decreased coefficients of variation (4.8%, 5.4%, and 10.2%, respectively). Acceptable reliability was achieved for all metrics/levels (test-retest coefficient of variation < 5%), with T2*WI WM/GM comparing favorably with fractional anisotropy and magnetization transfer ratio. DTI with and without cardiac triggering showed no significant differences for fractional anisotropy and test-retest coefficient of variation.

CONCLUSIONS: Reliable multiparametric assessment of spinal cord microstructure is possible by using clinically suitable methods. These results establish normalization procedures and pave the way for clinical studies, with the potential for improving diagnostics, objectively monitoring disease progression, and predicting outcomes in spinal pathologies.

ABBREVIATIONS: CSA = cross-sectional area; DCM = degenerative cervical myelopathy; FA = fractional anisotropy; MCL = maximally compressed level; MT = magnetization transfer; MTR = magnetization transfer ratio; SC = spinal cord; TRCOV = test-retest coefficient of variation

The era of quantitative MR imaging has arrived, allowing in vivo measurement of specific physical properties reflecting spinal cord (SC) microstructure and tissue damage.[1,2] Such measures have potential clinical applications, including improved diagnostic tools, objective monitoring for disease progression, and prediction of clinical outcomes.[3] However, technical challenges such as artifacts, image distortion, and achieving acceptable SNR have led to limited reliability. Specialized pulse sequences and custom hardware have advanced the field but incur costs of increased complexity and acquisition time while creating barriers to portability and clinical adoption. Furthermore, quantitative MR imaging metrics often show wide ranges of normal values and confounding relationships with subject characteristics such as age,[4-8] for which most previous studies have not accounted.[3]

Among the most promising SC quantitative MR imaging techniques are DTI and magnetization transfer (MT).[1-3] These provide measures of axonal integrity and myelin quantity that correlate with functional impairment in conditions such as degenerative cervical myelopathy (DCM)[5-7,9] and MS,[3,9] albeit with

Received October 20, 2016; accepted after revision January 28, 2017.

From the Division of Neurosurgery, Department of Surgery (A.R.M., D.W.C., S.K.-R., L.T., A.N., H.G., M.G.F.), and Department of Medical Imaging (A.C., D.J.M.), University of Toronto and the University Health Network, Toronto Western Hospital, Toronto, Ontario, Canada; Polytechnique Montreal (B.D.L., J.C.-A.), Montréal, Quebec, Canada; Functional Neuroimaging Unit (J.C.-A.), Centre de recherche de l'Institut universitaire de gériatrie de Montréal, Université de Montréal, Montréal, Quebec, Canada; and University of Groningen (S.F.L.), Groningen, the Netherlands.

Please address correspondence to Michael G. Fehlings, MD, SCI-CRU, 11th Floor, Toronto Western Hospital, 399 Bathurst St, Toronto, M5T 2S8, ON, Canada; e-mail: michael.fehlings@uhn.on.ca, madeleineoh@gmail.com; @DrFehlings

Indicates open access to non-subscribers at www.ajnr.org

http://dx.doi.org/10.3174/ajnr.A5163

Table 1: Acquisition protocol[a]

Imaging Type	Pulse Sequence; Orientation	Technical Details	Acquisition Time	Metric
T2WI	3D FIESTA-C; sagittal	TR/TE = 5.4/2.6 s, FOV = 200 × 200 mm^2, matrix = 256 × 256, resolution = 0.8 × 0.8 × 0.8 mm^3, NEX = 2, flip angle = 35°	6 min 56 s	CSA
DTI	Spin-echo ssEPI with OVS; axial	TR/TE = 4050/91.2 ms, FOV = 80 × 80 mm^2, matrix = 64 × 64, resolution = 1.25 × 1.25 × 5 mm^3, 25 directions (b=800 s/mm^2), 5 b=0 s/mm^2 images, AP saturation bands, phase encoding = AP, 2nd-order shimming	3 × 2 min 6 s, 1 min 30 s for shimming	FA
MT	2D SPGR with/without prepulse; axial	TR/TE = 32/5.9 ms, FOV = 190 × 190 mm^2, matrix = 192 × 192, resolution = 1 × 1 × 5 mm^3, NEX = 3, flip angle = 6°, flow compensation, phase encoding = AP, prepulse: Gaussian, duration = 9984 μs, offset = 1200 Hz	3 min 45 s each, with and without prepulse	MTR
T2*WI	2D MERGE; axial	TR/TE = 650/5, 10, 15 ms, FOV = 200 × 200 mm^2, matrix = 320 × 320, resolution = 0.6 × 0.6 × 4 mm^3, NEX = 1, flip angle = 20°, BW = 62 kHz per line	3 min 33 s	WM/GM ratio

Note:—AP indicates anteroposterior; BW, bandwidth; FIESTA-C, FIESTA-cycled phases; MERGE, multiecho recombined gradient echo; OVS, outer volume suppression; SPGR, echo-spoiled gradient echo; ssEPI, single-shot echo-planar imaging.

[a] Technical specifications of our multiparametric cervical SC MRI protocol, with an acquisition time of 25 minutes (30–35 minutes, including positioning, section prescription, shimming, and prescans).

limited physiologic specificity (eg, fractional anisotropy [FA] reflects both demyelination and axonal injury).[10,11] SC cross-sectional area (CSA) computed from high-resolution anatomic images can measure atrophy (eg, in MS)[12] or the degree of SC compression in DCM.[13] T2*-weighted imaging at 3T or higher field strengths offers high resolution and sharp contrast between SC WM and GM, allowing segmentation between these structures similar to that in phase-sensitive inversion recovery.[14,15] T2*WI also demonstrates hyperintensity in injured WM,[16-18] reflecting demyelination, gliosis, and increased calcium and nonheme iron concentrations.[19] T2*WI signal intensity is not an absolute quantity, so we normalize its value in WM by the average GM signal intensity in each axial section, creating a novel measure of WM injury: T2*WI WM/GM ratio.[20]

We propose a multiparametric approach to cervical SC quantitative MR imaging with clinically feasible methods, including acceptable acquisition times, standard hardware/pulse sequences, and automated image analysis. Our protocol yields 4 measures of SC tissue injury (CSA, FA, MT ratio [MTR], and T2*WI WM/GM), for which this study establishes normative values in numerous ROIs. We characterize the variation of these metrics with age, sex, height, weight, cervical cord length, and rostrocaudal level and propose normalization methods. Finally, we assess test-retest reliability of FA, MTR, and T2*WI WM/GM and compare our DTI results against those with cardiac triggering.

MATERIALS AND METHODS

Study Design and Subjects

This study received approval from the University Health Network (Toronto, Ontario, Canada), and written informed consent was obtained from all participants. Forty-two subjects were recruited between October 2014 and December 2016 with a broad range of ages and balance between sexes. A physician (A.R.M.) assessed all subjects to rule out symptoms and signs of neurologic dysfunction, and T2WI was screened for abnormalities suggestive of multiple sclerosis, tumor, or severe cord compression. Two subjects were excluded from the study with clinical and imaging findings of DCM, leaving 40 healthy subjects for analysis. Data from 18 patients with DCM were included for analysis of test-retest reliability, and 6 patients with DCM were included in a cardiac-triggering comparison, but subjects with DCM were excluded from other analyses.[20]

MR Imaging Acquisitions

MR images were acquired on a 3T clinical scanner (Signa Excite HDxt; GE Healthcare, Milwaukee, Wisconsin). Peak gradients were 50 mT/m; slew rate, 150 T/m/s with a body coil for transmission and the top 2 elements of a standard 8-element spine coil (Premier III Phased Array CTL; USA Instruments, Aurora, Ohio) for reception. Subjects were positioned head-first and supine with the head tightly padded to prevent movement and the neck flexed to straighten the cervical SC.

The MR imaging protocol was developed on the basis of methods previously used by one of the authors (J.C.-A.).[16,17,21] T2WIs used sagittal FIESTA-cycled phases with 0.8-mm^3 isotropic resolution covering the brain stem to T4. DTI, MT, and T2*WI had 13 axial sections positioned perpendicular to the spinal cord (at C3), covering C1–C7 by using a variable gap, alternating between the mid-vertebral body and the intervertebral disc. Parameters for each sequence are listed in Table 1. DTI used a spin-echo single-shot EPI sequence with an 80 × 80 mm^2 FOV to minimize susceptibility distortions, anterior/posterior saturation bands to achieve outer volume suppression, and no cardiac triggering. Second-order localized shimming was performed before DTI by positioning a VOI encompassing the SC from C1–C7. T2*WIs used the multiecho recombined gradient-echo sequence, with 3 echoes that are magnitude-reconstructed and combined by using a sum-of-squares algorithm.[18] Each session required 30–35 minutes, including subject positioning, section prescription, prescanning, and shimming.

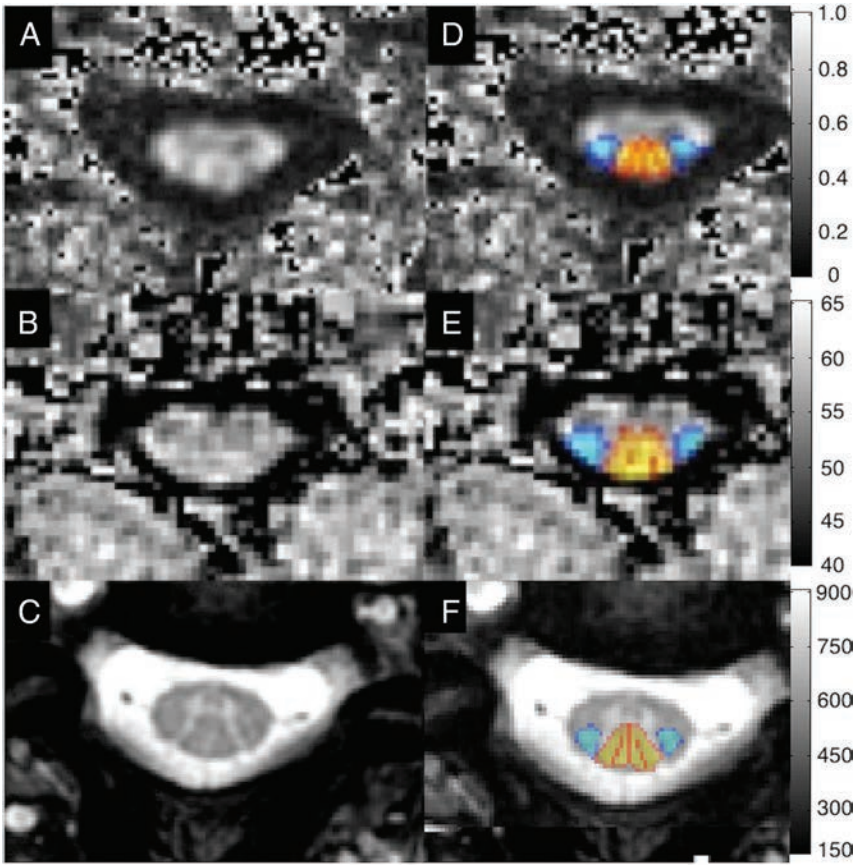

FIG 1. Representative images showing FA maps (*A*), MTR maps (*B*), and T2*WI (*C*) with probabilistic maps of the lateral corticospinal tracts (blue) and dorsal columns (red-yellow) overlaid (*D–F*) following registration to the SCT atlas.

Test-retest reliability was assessed by removing the subject from the scanner and repositioning before rescanning. This was performed in a subset of subjects (DTI: 17 healthy, 9 with DCM; MT: 13 healthy, 4 with DCM; T2*WI: 5 healthy, 11 with DCM) extemporaneously, depending on scanner availability and subject willingness. Reliability was not assessed for SC CSA measurement due to time constraints.

A comparison of DTI with and without cardiac triggering was also performed in 10 subjects (4 healthy, 6 with DCM). Cardiac-triggered DTI was performed with pulse oximetry triggering, trigger delay of 310 ms, window of 250 ms, and TR = 7 R-R interval. Two acquisitions were performed that were analyzed individually for test-retest coefficient of variation (TRCOV) and then concatenated and averaged for comparison with nontriggered DTI.

Image Analysis Techniques

Imaging data were analyzed by using the Spinal Cord Toolbox, Version2.3 (SCT; https://www.nitrc.org/projects/sct/).[22] Each axial image was visually inspected by 1 rater (A.R.M.) and excluded if low signal or artifacts (motion, aliasing) were present. SC segmentation was automatically performed by using native T2WIs and T2*WIs, the mean diffusivity map for DTI, and the MT image with a prepulse. Segmentation errors were resolved by providing seed points for automatic segmentation or manual editing. Images were nonlinearly registered to the MNI-Poly-AMU template/atlas in SCT.[23] T2WIs were used to automatically calculate cervical cord length (from the top of C1 to the bottom of the C7 vertebral levels) and SC CSA. DTI was motion-corrected with regularized registration, and diffusion tensors were calculated with outlier rejection by using the RESTORE (robust estimation of tensors by outlier rejection) method.[24] MT images with and without prepulses were coregistered, and MTR was computed. T2*WI data were further analyzed with automatic segmentation of GM and WM,[25] which was used to refine the registration of T2*WI to the template. FA, MTR, and T2*WI WM/GM ratios were extracted from various ROIs by using the SCT probabilistic atlas with automatic correction for partial volume effects by using the maximum a posteriori method.[26] ROIs included the SC, WM, and GM and the left/right lateral corticospinal tract, fasciculus cuneatus, fasciculus gracilis, and spinal lemniscus in each axial section (Fig 1). Metrics were averaged at rostral (C1–C3), middle (C4–5) or maximally compressed (MCL, subjects with DCM), and caudal (C6–C7) levels.

Statistical Analysis

Statistical analysis was performed with R statistical and computing software, Version 3.3 (http://www.r-project.org/). Normative data were summarized with mean, SD, and intersubject coefficient of variation. Relationships between MR imaging metrics (averaged from C1–C7) and patient characteristics (age, sex, height, weight, cervical cord length) were assessed with Pearson correlation coefficients and backward stepwise linear regression to determine significant independent relationships and their coefficients. Differences by rostrocaudal level were assessed with ANOVA. If differences were found, we calculated Spearman coefficients (between mean values and numbered levels) to identify monotonic relationships. To determine whether nonlinear relationships were present, we performed a likelihood ratio test on linear regression models with and without a 5-knot restricted cubic spline. Paired *t* tests compared WM and GM differences, and ANOVA was used to identify differences among individual WM tracts (averaged bilaterally). Reliability was assessed by using test-retest coefficient of variation, and differences between healthy subjects and those with DCM were assessed with Welch *t* tests, as were pair-wise comparisons between techniques at each rostrocaudal level. Statistical significance was set to $P = .05$ and was not corrected for multiple comparisons due to the exploratory nature of this study.

Table 2: Subject characteristics[a]

Characteristic	Healthy Subjects (*n* = 40)	Subjects with DCM (*n* = 18)
Age (yr)	47.1 ± 15.3 (range, 19–79)	56.4 ± 11.0 (range, 36–76)
Sex	21 men, 19 women	11 men, 7 women
Height (cm)	171.4 ± 8.6	172.8 ± 8.9
Weight (kg)	74.6 ± 11.5	79.0 ± 15.1
Cervical cord length (cm)	10.6 ± 1.0	11.1 ± 0.9

[a] Demographics and characteristics of 40 healthy subjects and 18 with DCM are shown. Data (other than sex) are reported as mean ± SD.

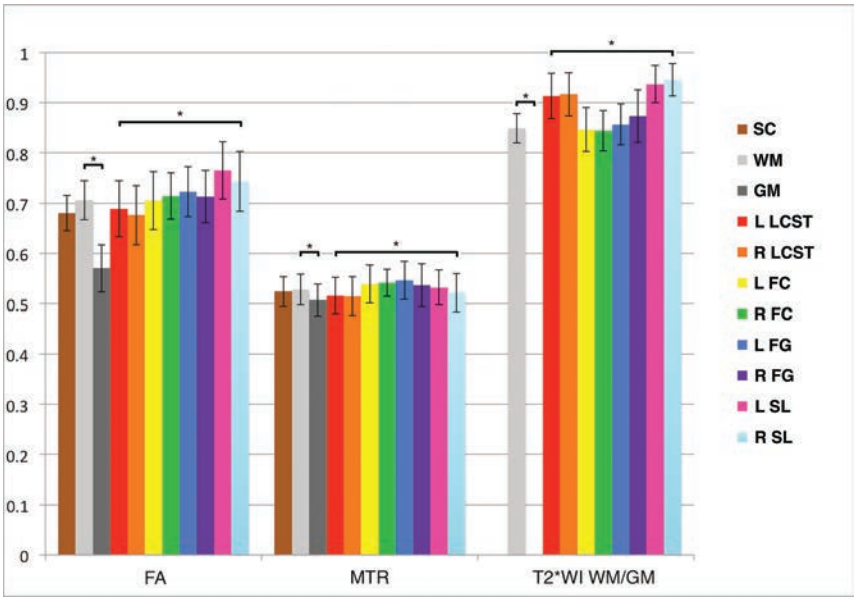

FIG 2. Normative data in the rostral cervical cord for FA, MTR, and T2*WI WM/GM ratios. Metrics are extracted from SC, WM, GM, and key WM tracts averaged over rostral sections (C1–C3). Values are displayed as mean ± intersubject SD (*error bars*). The *asterisk* denotes $P < .05$ with paired *t* tests between WM and GM and ANOVA among WM tracts. L indicates left; R, right; FC, fasciculus cuneatus; FG, fasciculus gracilis; SL, spinal lemniscus; LCST, lateral corticospinal tract.

RESULTS

Subject Characteristics

Characteristics of 40 healthy subjects and 18 with DCM included in this study are listed in Table 2.

Image Acquisition

Acceptable image quality was achieved in all subjects and techniques. For DTI, 27 of 520 axial images (5.2%) were excluded due to artifacts or poor signal. For MT and T2*WI, 6 (1.2%) and 4 (0.8%) sections were excluded due to artifacts, respectively.

Automated Analysis

Automated segmentation was frequently successful, with manual editing required in 8 T2WI datasets (20%), 14 MT datasets (35%), 4 DTI datasets (10%), and 20 T2*WI datasets (50%). Manual segmentation editing was usually restricted to a small number of sections and required <5 minutes per dataset. Automatic registration to the template and data extraction were successful in all cases.

Normative Values for MR Imaging Metrics

Normative data extracted from C1–C3 showed that T2*WI WM/GM had the smallest intersubject coefficient of variation at 3.5% (0.848 ± 0.028), compared with 5.8% for MTR (52.8 ± 3.1%), 6.0% for FA (0.706 ± 0.042), and 12.2% for CSA (78.5 ± 9.6 mm^2) (Fig 2). The strongest contrast between WM and GM was found for T2*WI signal intensity (mean GM-WM difference ± standard error = 83.9 ± 4.72, $P = 3 \times 10^{-20}$), which exceeded that of FA (−0.110 ± 0.0083, $P = 2 \times 10^{-15}$) and MTR (−2.1 ± 0.28, $P = 4 \times 10^{-9}$). Individual WM tracts showed significant variations for T2*WI WM/GM (ANOVA, $P = 2 \times 10^{-9}$), FA ($P = 3 \times 10^{-7}$), and MTR ($P = .01$).

Variations with Subject Characteristics

Univariate relationships between MR imaging metrics and subject characteristics included the following: CSA increased with cervical cord length ($P = 8 \times 10^{-4}$), weight ($P = .03$), and male sex ($P = .03$); FA decreased with age ($P = .009$); and MTR decreased with height ($P = .008$), weight ($P = .01$), and male sex ($P = .006$) (Table 3). Trends were also present for CSA, increasing with height ($P = .06$), and for T2*WI WM/GM, increasing with age ($P = .06$) and weight ($P = .06$). In multivariate analysis, CSA varied only with cervical cord length ($\beta = +5.3690$); FA, with age ($\beta = -0.0012053$); and MTR, with height ($\beta = -0.17410$, $P = .001$) and age ($\beta = -0.074131$, $P = .01$), while T2*WI WM/GM did not require normalization. Following linear corrections, intersubject coefficient of variation decreased to 4.8% for MTR, 5.4% for FA, and 10.2% for CSA.

Metrics by Rostrocaudal Level

ANOVA detected significant differences ($P < .05$) across rostrocaudal levels for all metrics. Monotonic variations were present ($P < .05$) for MTR ($\rho = -0.98$), FA ($\rho = -0.90$), and CSA ($\rho = -0.55$), which all decreased from rostral to caudal levels, whereas T2*WI WM/GM showed a trend toward increasing ($\rho = 0.53$, $P = .06$) (Fig 3). CSA, FA, and T2*WI WM/GM showed nonlinear rostrocaudal variation ($P < .05$), whereas MTR did not ($P = .58$).

Reliability

The T2*WI WM/GM ratio was the most reliable metric (pooled TRCOV: rostral, 0.9%; MCL, 2.9%; caudal, 2.6%), comparing favorably with FA (rostral, 2.6%; MCL, 3.6%; caudal, 3.2%) and MTR (rostral, 2.4%; MCL, 3.7%; caudal: 4.2%), though these differences were only significant for rostral metrics ($P < .05$) (Table 4). Reliability measures were comparable between healthy subjects and those with DCM rostrally (C1–C3), but subjects with DCM trended toward increased TRCOV for MCL MTR (6.1% versus 3.2%, $P = .08$) and caudal FA (4.6% versus 2.2%, $P = .07$). The reliability of data from individual WM tracts was acceptable

Table 3: Univariate relationships of MRI metrics with healthy subject characteristics[a]

Metric	Age	Sex (M vs F)	Height	Weight	Cervical Cord Length
CSA (mm^2)	$r = -0.25$ ($P = .12$)	80.0 ± 11.2 vs 73.5 ± 8.5 ($P = .03$[b])	$r = 0.31$ ($P = .06$[c])	$r = 0.34$ ($P = .03$[b])	$r = 0.51$ ($P < .001$[b])
FA	$r = -0.43$ ($P = .009$[b])	0.658 ± 0.037 vs 0.663 ± 0.034 ($P = .75$)	$r = -0.02$ ($P = .89$)	$r = -0.26$ ($P = .12$)	$r = 0.11$ ($P = .53$)
MTR	$r = -0.25$ ($P = .11$)	48.8 ± 2.5 vs 51.4 ± 2.7 ($P = .006$[b])	$r = -0.41$ ($P = .008$[b])	$r = -0.40$ ($P = .01$)	$r = -0.18$ ($P = .26$)
T2*WI WM/GM	$r = 0.31$ ($P = .06$)	0.863 ± 0.034 vs 0.858 ± 0.031 ($P = .64$)	$r = -0.12$ ($P = .48$)	$r = 0.31$ ($P = .06$[c])	$r = -0.09$ ($P = .55$)

[a] Values for sex are reported as mean ± SD, and other values are Pearson correlation coefficient. FA, MTR, and T2*WI WM/GM ratios are extracted from WM, while CSA of the spinal cord is measured, averaged across C1–C7.
[b] Significance ($P < .05$).
[c] Trends ($P < .10$).

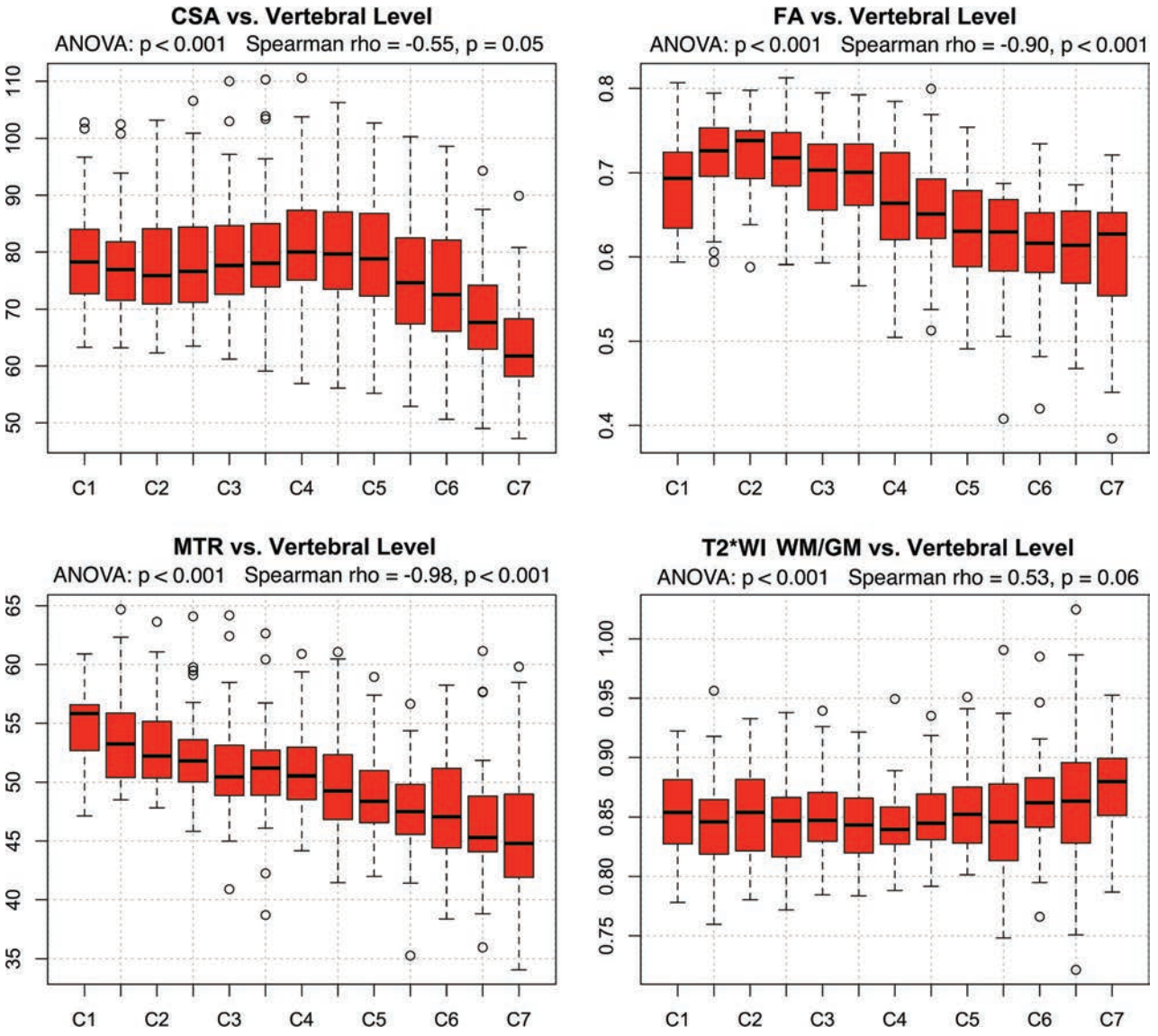

FIG 3. Variations by rostrocaudal level. MR imaging metrics displayed for each vertebral and intervertebral level from C1 to C7. FA, MTR, and T2*WI WM/GM ratios are extracted from WM. ANOVA shows significant differences by level for all metrics. Monotonic variations are present for CSA, FA, and MTR.

(TRCOV < 5%) except for FA of the right and left spinal lemniscus (5.3%, 5.6%, respectively; Fig 4).

Cardiac Triggering in DTI

FA did not differ significantly among DTI acquisitions with and without cardiac triggering, though triggering showed a trend toward higher FA at MCL (0.558 versus 0.514, $P = .06$) and caudal (0.562 versus 0.534, $P = .07$) levels (Table 5). No significant differences in TRCOV were observed, though cardiac-triggered DTI provided approximately 1% lower TRCOV at all levels.

DISCUSSION

Summary of Findings

This study establishes a multiparametric MR imaging protocol and analysis framework to assess the microstructure of the entire cervical SC by using simple methods that are feasible for clinical adoption, requiring only 20 minutes of acquisition

Table 4: Test-retest reliability across rostrocaudal levels[a]

Level	Metric	Healthy	DCM	*P* Value	Pooled
Rostral (C1–C3)	FA	2.5 ± 2.0%	2.8 ± 1.8%	.71	2.6 ± 1.9%
	MTR	2.7 ± 1.9%	1.3 ± 0.5%	.17	2.4 ± 1.9%
	T2*WI WM/GM	0.9 ± 0.6%	1.0 ± 0.7%	.77	0.9 ± 0.7%[b]
Midcervical (C4–C5) or MCL	FA	3.0 ± 2.2%	5.0 ± 5.7%	.21	3.6 ± 3.6%
	MTR	3.2 ± 3.0%	6.1 ± 0.9%	.08[c]	3.7 ± 3.2%
	T2*WI WM/GM	1.4 ± 1.1%	3.5 ± 2.2%	.11	2.9 ± 2.2%
Caudal (C6–C7)	FA	2.2 ± 1.6%	4.6 ± 4.7%	.07[c]	3.2 ± 3.5%
	MTR	4.4 ± 3.8%	3.1 ± 3.9%	.56	4.2 ± 3.7%
	T2*WI WM/GM	3.4 ± 3.0%	2.2 ± 2.1%	.37	2.6 ± 2.4%

[a] TRCOV ± SD is displayed for healthy subjects and those with DCM at rostral (C1–C3), midcervical (C4–5), or maximally compressed levels in subjects with DCM, and caudal (C6–C7) levels. Sample size was 26 subjects (17 healthy, 9 with DCM) for DTI, 17 subjects (13 healthy, 4 with DCM) for MT, and 16 subjects (5 healthy, 11 with DCM) for T2*WI.

[b] Significant differences ($P < .05$) between pooled TRCOV of metrics at each level.

[c] Trends ($P < .10$) in reliability between healthy subjects and those with DCM for each level/metric, and pooled reliability was calculated if no significant differences were found.

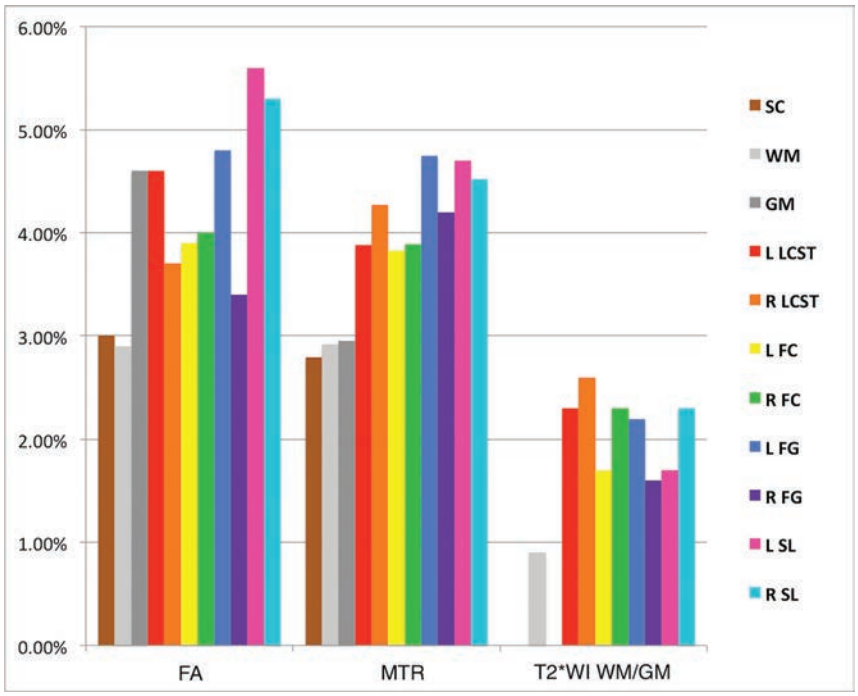

FIG 4. Test-retest coefficients of variation of FA, MTR, and T2*WI WM/GM extracted from SC, WM, GM, and key WM tracts in rostral sections (C1–C3) are displayed. T2*WI WM/GM ratio shows better reliability than FA and MTR. Metrics derived from the SC and WM show TRCOV < 3%, while GM and key WM tracts show TRCOV < 5% except for FA of the spinal lemniscus. FC indicates fasciculus cuneatus; FG, fasciculus gracilis; SL, spinal lemniscus; LCST, lateral corticospinal tract; R, right; L, left.

time in addition to anatomic imaging. Image acquisition was successful in all subjects, and automated analysis provided robust readouts from multiple ROIs, with the results validated by acceptable reliability data. Our results establish normative data for CSA, FA, and MTR that are consistent with previous reports at 3T,[12,21,27-29] in addition to our novel T2*WI WM/GM metric. T2*WI WM/GM, FA, and MTR all showed strong gray-white contrast and differences between individual WM tracts. FA and MTR showed moderate intersubject and test-retest variability, with similar or better reliability than in previous reports despite differences in acquisition and analysis techniques.[8,27-31] T2*WI WM/GM demonstrated low intersubject and test-retest variability, which are favorable statistical properties because they make it more likely that a subject with pathology will show abnormal results (confirmed by encouraging results reported in a companion article[20]). CSA showed greater intersubject variation than other metrics, though this improved slightly following normalization with cervical cord length. Reliability of the CSA measurement was not assessed due to time constraints, but it likely surpasses that of our other measures because it has been previously reported to have TRCOV under 0.5% by using similar techniques.[12] Reliability was greatest in the rostral region for all techniques, where healthy subjects and patients with DCM showed similar results. In contrast, patients with DCM showed trends toward diminished reliability at MCLs and caudal levels, likely related to distorted anatomy, increased partial volume effects, increased susceptibility artifacts, and less accurate registration to the SCT template. However, these differences were not significant, and pooled reliability results were all considered acceptable (TRCOV < 5%). Our clinically feasible multiparametric approach provides 4 unique quantitative measures in multiple ROIs that reflect aspects of macrostructure and microstructure, with the benefit that these measures cross-validate each other to overcome the limitations (reliability, intersubject variability, sensitivity to pathology) of each individual technique. We anticipate that this multivariate approach can accurately characterize tissue injury in various SC pathologies, which could enable quantitative MR imaging of the SC to achieve clinical translation in the near future.

Normalization for Confounding Factors

It is essential that quantitative readouts reflect pathologic changes and eliminate confounding effects as much as possible to move toward clinical use of SC quantitative MR imaging. In keeping with prior reports, significant relationships were found between age and FA[5,7,8] and MTR,[8] but not CSA.[8,23] However, we also identified univariate relationships between MR imaging metrics and sex, height, weight, and cervical cord length, for which we are not aware of previous reports. The relationship between CSA and cervical cord length likely indicates that CSA is related to overall body size because height and weight also showed positive (nonsignificant) correlations. It is unclear why MTR decreases with height, but weak negative trends were also seen with weight and

Table 5: DTI with and without cardiac triggering[a]

Measure	Level	No Triggering	Triggering	*P* Value
FA	Rostral	0.651 ± 0.054	0.664 ± 0.064	.41
	Mid/MCL	0.514 ± 0.068	0.558 ± 0.081	.06[b]
	Caudal	0.534 ± 0.057	0.562 ± 0.044	.07[b]
TRCOV	Rostral	2.6 ± 1.9%	1.5 ± 1.2%	.11
	Mid/MCL	3.6 ± 3.6%	2.2 ± 2.3%	.27
	Caudal	3.2 ± 3.5%	2.4 ± 2.3%	.52

[a] Paired *t* tests were used to compare FA values extracted from WM at rostral (C1–C3), midcervical (C4–5, healthy subjects), or MCL (subjects with DCM), and caudal (C6–C7) levels between no triggering vs triggering in 10 subjects (4 healthy, 6 with DCM). Welch *t* tests were used to compare test-retest coefficient of variation between no triggering ($n = 26$) and triggering ($n = 10$).
[b] Trends ($P < .10$).

cervical cord length, suggesting that MTR (reflecting myelin density) is negatively related to overall body size. However, no relationship was present between MTR and CSA in a post hoc test ($r = 0.01$, $P = .94$). Strong relationships were also found among all 4 metrics and the rostrocaudal level, with the CSA, FA, and MTR showing nonlinearity (Fig 3). CSA increased between the C3 and C6 vertebral levels, reflecting the cervical enlargement that contains increased GM for C5–T1 neurologic levels, and our CSA measurements were highly similar to those in previous reports.[32,33] WM FA peaked at C2 and locally at C7, where the orientations of axons are almost purely rostrocaudal. In contrast, decreases were seen at C1 (likely due to decussation of corticospinal fibers) and in the cervical enlargement (where a fraction of axons turn and form synapses within the GM). The T2*WI WM/GM ratio was nearly invariant from C1 to C6 but increased at C7, likely due to increased susceptibility artifacts from the lungs, decreased SNR, and respiratory motion. We suggest a normalization scheme in which CSA, FA, and MTR are linearly corrected for relationships (cervical cord length, age, and age/height, respectively) and all metrics are converted to *z* scores per rostrocaudal level, as proposed by Uda et al[4] for DTI metrics. Although normalization procedures add complexity to data postprocessing, these methods facilitate fair comparisons, decrease nuisance variability, and produce more accurate biomarkers of SC tissue injury.

Quantitative MR Imaging Techniques: Specificity, Accuracy, Feasibility

The rapidly evolving field of quantitative MR imaging includes a rich array of acquisition techniques, including strict quantitative methods that attempt to measure a specific physical property, such as quantitative MT, longitudinal relaxation rate, and apparent transverse relaxation rate mapping.[27,34,35] However, such techniques are inherently complex and require specialized pulse sequences, while typically requiring lengthy scan times. Furthermore, these methods face challenges in achieving acceptable SNR and reliability, particularly in the SC, which is considerably more difficult to image than the brain due to magnetic field inhomogeneity and physiologic motion. Similarly, reduced FOV DTI has become available, offering increased SNR and reduced distortions but often requiring increased acquisition times and involving proprietary pulse sequences.[31] Our protocol purposefully used standard sequences available from all major MR imaging vendors, making it an attractive approach for multicenter studies and clinical use. A recent study comparing reduced FOV with outer volume suppression for cervical SC DTI found only minimal differences in reliability (intersubject coefficient of variation: reduced FOV = 3.98% versus outer volume suppression = 4.59).[31] Unfortunately, this study did not report *P* values for these comparisons, and it did not assess intrasubject reliability, but the findings suggest that outer volume suppression provides acceptable reliability.

Cardiac-Triggered DTI

Previous research suggests that cardiac triggering reduces variance in diffusion time-series by acquiring data during the quiescent phase of cardiac-related SC motion.[36] However, to our knowledge, no studies have directly compared the test-retest reliability of SC DTI acquisitions with and without cardiac triggering, particularly in the context of multiple acquisitions and outlier rejection during postprocessing. Our pilot data in 10 subjects suggest roughly equivalent results with and without triggering, though trends toward higher FA and lower TRCOV (approximately 1%) were observed with triggering. Further investigation is needed, but the ungated acquisition used in this study is validated by its acceptable reliability. This simpler approach avoids difficulties with triggering such as variable TR and cardiac irregularities (arrhythmias, tachycardia) that are more common in older or critically ill patients.

Limitations

Further studies with larger sample sizes would allow greater accuracy for normative data, influences of confounding variables, and differences in DTI with and without cardiac triggering. The normative data are specific to our methodology, and cross-site and cross-vendor validation is required. Our use of automated analysis aimed to reduce bias, but manual editing of segmentations was frequently required. Other DTI metrics were not analyzed due to an a priori decision to focus on FA, due to its consistent results in previous studies.[3] Our test-retest reliability experiment does not account for scanner drift, but this is unlikely a large source of error because the 2 metrics are ratios rather than absolute signal-intensity values. Neurologically intact subjects with mild SC compression were considered healthy subjects; these changes are evident in 8%–26% of asymptomatic individuals.[32,37] Moreover, we think that the spectrum of "normal" includes this subgroup, but previous studies have excluded such subjects.

CONCLUSIONS

Reliable multiparametric assessment of the SC microstructure is possible with standard hardware, acceptable acquisition times, and automated analysis that provide high-fidelity readouts of tissue injury from numerous ROIs. Normalization procedures can be implemented to mitigate confounding effects such as age, height, cervical cord length, and rostrocaudal level, producing more meaningful quantitative metrics. Our clinically suited approach paves the way for translational studies to evaluate potential uses such as improved diagnostics, monitoring of disease progression, and prediction of outcomes.

ACKNOWLEDGMENTS

This research received funding support from Rick Hansen Institute, as part of the Riluzole in Spinal Cord Injury Study (RISCIS), which is also supported by AOSpine North America, AOSpine International SCI Knowledge Forum, and the North American Clinical Trials Network (NACTN) of the Christopher and Dana Reeve Foundation. This research also received support from the Dezwirek Foundation, the Sherman Clinical Research Unit, and the Gerald and Tootsie Halbert Chair in Spinal Cord Research. Dr. Martin received post-doctoral fellowship support from Canadian Institutes of Health Research.

Disclosures: Allan R. Martin—*RELATED*: *Grant*: Rick Hansen Institute, AOSpine North America, North American Clinical Trials Network of the Christopher and Dana Reeve Foundation, the DeZwirek Foundation, the Sherman Clinical Research Unit, and the Gerald and Tootsie Halbert Chair in Spinal Cord Research*; Dr. Martin received post-doctoral Fellowship funding from Canadian Institutes of Health Research (CIHR) that included $50,000 (CDN) annual salary support and $5,000 annual research allowance that enabled this research. Sukhvinder Kalsi-Ryan—*UNRELATED*: *Consultancy*: Neural Outcomes Consulting; *Royalties*: GRASSP. *Money paid to the institution.

REFERENCES

1. Wheeler-Kingshott CA, Stroman PW, Schwab JM, et al. **The current state-of-the-art of spinal cord: applications.** *Neuroimage* 2014;84:1082–93 CrossRef Medline
2. Stroman PW, Wheeler-Kingshott C, Bacon M, et al. **The current state-of-the-art of spinal cord imaging: methods.** *Neuroimage* 2014;84:1070–81 CrossRef Medline
3. Martin AR, Aleksanderek I, Cohen-Adad J, et al. **Translating state-of-the-art spinal cord MRI techniques to clinical use: a systematic review of clinical studies utilizing DTI, MT, MWF, MRS, and fMRI.** *Neuroimage Clin* 2016;10:192–238 CrossRef Medline
4. Uda T, Takami T, Tsuyuguchi N, et al. **Assessment of cervical spondylotic myelopathy using diffusion tensor magnetic resonance imaging parameter at 3.0 Tesla.** *Spine* 2013;38:407–14 CrossRef Medline
5. Mamata H, Jolesz FA, Maier SE. **Apparent diffusion coefficient and fractional anisotropy in spinal cord: age and cervical spondylosis-related changes.** *J Magn Reson Imaging* 2005;22:38–43 CrossRef Medline
6. Budzik JF, Balbi V, Le Thuc V, et al. **Diffusion tensor imaging and fibre tracking in cervical spondylotic myelopathy.** *Eur Radiol* 2011;21:426–33 CrossRef Medline
7. von Meyenburg J, Wilm BJ, Weck A, et al. **Spinal cord diffusion-tensor imaging and motor-evoked potentials in multiple sclerosis patients: microstructural and functional asymmetry.** *Radiology* 2013;267:869–79 CrossRef Medline
8. Taso M, Girard OM, Duhamel G, et al. **Tract-specific and age-related variations of the spinal cord microstructure: a multi-parametric MRI study using diffusion tensor imaging (DTI) and inhomogeneous magnetization transfer (ihMT).** *NMR Biomed* 2016;29:817–32 CrossRef Medline
9. Oh J, Zackowski K, Chen M, et al. **Multiparametric MRI correlates of sensorimotor function in the spinal cord in multiple sclerosis.** *Mult Scler* 2013;19:427–35 CrossRef Medline
10. Harrison NA, Cooper E, Dowell NG, et al. **Quantitative magnetization transfer imaging as a biomarker for effects of systemic inflammation on the brain.** *Biol Psychiatry* 2015;78:49–57 CrossRef Medline
11. Vavasour IM, Laule C, Li DK, et al. **Is the magnetization transfer ratio a marker for myelin in multiple sclerosis?** *J Magn Reson Imaging* 2011;33:713–18 CrossRef Medline
12. Kearney H, Yiannakas MC, Abdel-Aziz K, et al. **Improved MRI quantification of spinal cord atrophy in multiple sclerosis.** *J Magn Reson Imaging* 2014;39:617–23 CrossRef Medline
13. Nouri A, Tetreault L, Zamorano JJ, et al. **Role of magnetic resonance imaging in predicting surgical outcome in patients with cervical spondylotic myelopathy.** *Spine* 2015;40:171–78 CrossRef Medline
14. Grabher P, Mohammadi S, Trachsler A, et al. **Voxel-based analysis of grey and white matter degeneration in cervical spondylotic myelopathy.** *Sci Rep* 2016;6:24636 CrossRef Medline
15. Datta E, Papinutto N, Schlaeger R, et al. **Gray matter segmentation of the spinal cord with active contours in MR images**. *Neuroimage* 2017;147:788–99 CrossRef Medline
16. Cohen-Adad J, Buchbinder B, Oaklander AL. **Cervical spinal cord injection of epidural corticosteroids: comprehensive longitudinal study including multiparametric magnetic resonance imaging.** *Pain* 2012;153:2292–99 CrossRef Medline
17. Cohen-Adad J, Zhao W, Keil B, et al. **7-T MRI of the spinal cord can detect lateral corticospinal tract abnormality in amyotrophic lateral sclerosis.** *Muscle Nerve* 2013;47:760–62 CrossRef Medline
18. White ML, Zhang Y, Healey K. **Cervical spinal cord multiple sclerosis: evaluation with 2D multi-echo recombined gradient echo MR imaging.** *J Spinal Cord Med* 2011;34:93–98 CrossRef Medline
19. Cohen-Adad J. **What can we learn from T2* maps of the cortex?** *Neuroimage* 2014;93(pt 2):189–200 CrossRef Medline
20. Martin AR, De Leener B, Cohen-Adad J, et al. **A novel MRI biomarker of spinal cord white matter injury: T2*-weighted white matter to gray matter signal intensity ratio.** *AJNR Am J Neuroradiol* 2017 Apr 20. [Epub ahead of print] CrossRef Medline
21. Cohen-Adad J, El Mendili MM, Lehéricy S, et al. **Demyelination and degeneration in the injured human spinal cord detected with diffusion and magnetization transfer MRI.** *Neuroimage* 2011;55:1024–33 CrossRef Medline
22. De Leener B, Lévy S, Dupont SM, et al. **SCT: Spinal Cord Toolbox, an open-source software for processing spinal cord MRI data.** *Neuroimage* 2017;145(pt A):24–43 CrossRef Medline
23. Fonov VS, Le Troter A, Taso M, et al. **Framework for integrated MRI average of the spinal cord white and gray matter: the MNI-Poly-AMU template.** *Neuroimage* 2014;102:817–27 CrossRef Medline
24. Chang LC, Jones DK, Pierpaoli C. **RESTORE: robust estimation of tensors by outlier rejection.** *Magn Reson Med* 2005;53:1088–95 CrossRef Medline
25. Asman AJ, Bryan FW, Smith SA, et al. **Groupwise multi-atlas segmentation of the spinal cord's internal structure.** *Med Image Anal* 2014;18:460–71 CrossRef Medline
26. Lévy S, Benhamou M, Naaman C, et al. **White matter atlas of the human spinal cord with estimation of partial volume effect.** *Neuroimage* 2015;119:262–71 CrossRef Medline
27. Samson RS, Ciccarelli O, Kachramanoglou C, et al. **Tissue- and column-specific measurements from multi-parameter mapping of the human cervical spinal cord at 3 T.** *NMR Biomed* 2013;26:1823–30 CrossRef Medline
28. Smith SA, Jones CK, Gifford A, et al. **Reproducibility of tract-specific magnetization transfer and diffusion tensor imaging in the cervical spinal cord at 3 Tesla.** *NMR Biomed* 2010;23:207–17 CrossRef Medline
29. Ellingson BM, Salamon N, Grinstead JW, et al. **Diffusion tensor imaging predicts functional impairment in mild-to-moderate cervical spondylotic myelopathy.** *Spine J* 2014;14:2589–97 CrossRef Medline
30. Kerkovský M, Bednarik J, Dušek L, et al. **Magnetic resonance diffusion tensor imaging in patients with cervical spondylotic spinal cord compression: correlations between clinical and electrophysiological findings.** *Spine (Phila Pa 1976)* 2012;37:48–56 CrossRef Medline
31. Samson RS, Lévy S, Schneider T, et al. **ZOOM or non-ZOOM? Assessing spinal cord diffusion tensor imaging protocols for multi-centre studies.** *PLoS One* 2016;11:e0155557 CrossRef Medline
32. Cadotte DW, Cadotte A, Cohen-Adad J, et al. **Characterizing the location of spinal and vertebral levels in the human cervical spinal cord.** *AJNR Am J Neuroradiol* 2015;36:803–10 CrossRef Medline
33. Kato F, Yukawa Y, Suda K, et al. **Normal morphology, age-related changes and abnormal findings of the cervical spine, part II: magnetic resonance imaging of over 1,200 asymptomatic subjects.** *Eur Spine J* 2012;21:1499–507 CrossRef Medline

34. Levesque IR, Giacomini PS, Narayanan S, et al. **Quantitative magnetization transfer and myelin water imaging of the evolution of acute multiple sclerosis lesions.** *Magn Reson Med* 2010;63:633–40 CrossRef Medline
35. Freund P, Weiskopf N, Ashburner J, et al. **MRI investigation of the sensorimotor cortex and the corticospinal tract after acute spinal cord injury: a prospective longitudinal study.** *Lancet Neurol* 2013; 12:873–81 CrossRef Medline
36. Summers P, Staempfli P, Jaermann T, et al. **A preliminary study of the effects of trigger timing on diffusion tensor imaging of the human spinal cord.** *AJNR Am J Neuroradiol* 2006;27:1952–61 Medline
37. Wilson JR, Barry S, Fischer DJ, et al. **Frequency, timing, and predictors of neurological dysfunction in the nonmyelopathic patient with cervical spinal cord compression, canal stenosis, and/or ossification of the posterior longitudinal ligament.** *Spine* 2013;38: S37–54 CrossRef Medline

A Novel MRI Biomarker of Spinal Cord White Matter Injury: T2*-Weighted White Matter to Gray Matter Signal Intensity Ratio

A.R. Martin, B. De Leener, J. Cohen-Adad, D.W. Cadotte, S. Kalsi-Ryan, S.F. Lange, L. Tetreault, A. Nouri, A. Crawley, D.J. Mikulis, H. Ginsberg, and M.G. Fehlings

ABSTRACT

BACKGROUND AND PURPOSE: T2*-weighted imaging provides sharp contrast between spinal cord GM and WM, allowing their segmentation and cross-sectional area measurement. Injured WM demonstrates T2*WI hyperintensity but requires normalization for quantitative use. We introduce T2*WI WM/GM signal-intensity ratio and compare it against cross-sectional area, the DTI metric fractional anisotropy, and magnetization transfer ratio in degenerative cervical myelopathy.

MATERIALS AND METHODS: Fifty-eight patients with degenerative cervical myelopathy and 40 healthy subjects underwent 3T MR imaging, covering C1–C7. Metrics were automatically extracted at maximally compressed and uncompressed rostral/caudal levels. Normalized metrics were compared with *t* tests, area under the curve, and logistic regression. Relationships with clinical measures were analyzed by using Pearson correlation and multiple linear regression.

RESULTS: The maximally compressed level cross-sectional area demonstrated superior differences ($P = 1 \times 10^{-13}$), diagnostic accuracy (area under the curve = 0.890), and univariate correlation with the modified Japanese Orthopedic Association score (0.66). T2*WI WM/GM showed strong differences (rostral: $P = 8 \times 10^{-7}$; maximally compressed level: $P = 1 \times 10^{-11}$; caudal: $P = 1 \times 10^{-4}$), correlations (modified Japanese Orthopedic Association score; rostral: −0.52; maximally compressed level: −0.59; caudal: −0.36), and diagnostic accuracy (rostral: 0.775; maximally compressed level: 0.860; caudal: 0.721), outperforming fractional anisotropy and magnetization transfer ratio in most comparisons and cross-sectional area at rostral/caudal levels. Rostral T2*WI WM/GM showed the strongest correlations with focal motor (−0.45) and sensory (−0.49) deficits and was the strongest independent predictor of the modified Japanese Orthopedic Association score ($P = .01$) and diagnosis ($P = .02$) in multivariate models ($R^2 = 0.59$, $P = 8 \times 10^{-13}$; area under the curve = 0.954, respectively).

CONCLUSIONS: T2*WI WM/GM shows promise as a novel biomarker of WM injury. It detects damage in compressed and uncompressed regions and contributes substantially to multivariate models for diagnosis and correlation with impairment. Our multiparametric approach overcomes limitations of individual measures, having the potential to improve diagnostics, monitor progression, and predict outcomes.

ABBREVIATIONS: AUC = area under the curve; CSA = cross-sectional area; DCM = degenerative cervical myelopathy; FA = fractional anisotropy; MCL = maximally compressed level; mJOA = modified Japanese Orthopedic Association; MT = magnetization transfer; MTR = magnetization transfer ratio; qMRI = quantitative MRI; SC = spinal cord; SCI = spinal cord injury; UE = upper extremity

Quantitative MR imaging (qMRI) techniques have the potential to provide in vivo measurement of specific tissue properties, including characterizing aspects of spinal cord (SC) microstructure and tissue injury.[1,2] However, efforts to apply qMRI in clinical studies have thus far achieved only modest success.[3] The strongest results include cross-sectional area (CSA) as a measure of spinal cord atrophy, the DTI metric fractional anisotropy (FA) to evaluate axonal integrity, and the magnetization transfer ratio (MTR) as a measure of demyelination.[3] Spinal cord CSA has shown moderate-to-strong correlation with disability in MS[4-6] but is a nonspecific measure of tissue injury and shows high intersubject variability in healthy subjects,[7,8] somewhat limiting its

Received October 20, 2016; accepted after revision January 29, 2017.

From the Division of Neurosurgery, Department of Surgery (A.R.M., D.W.C., S.K.-R., L.T., A.N., H.G., M.G.F.), and Department of Medical Imaging (A.C., D.J.M.), University of Toronto and the University Health Network, Toronto, Ontario, Canada; Polytechnique Montreal (B.D.L., J.C.-A.), Montreal, Quebec, Canada; Functional Neuroimaging Unit (J.C.-A.), Centre de recherche de l'Institut universitaire de gériatrie de Montréal, Université de Montréal, Montreal, Quebec, Canada; and University of Groningen (S.F.L.), Groningen, the Netherlands.

Please address correspondence to Michael G. Fehlings, MD, SCI-CRU, 11th Floor, Toronto Western Hospital, 399 Bathurst St, Toronto, M5T 2S8, ON, Canada; e-mail: michael.fehlings@uhn.on.ca, madeleineoh@gmail.com; @DrFehlings

Indicates open access to non-subscribers at www.ajnr.org

http://dx.doi.org/10.3174/ajnr.A5162

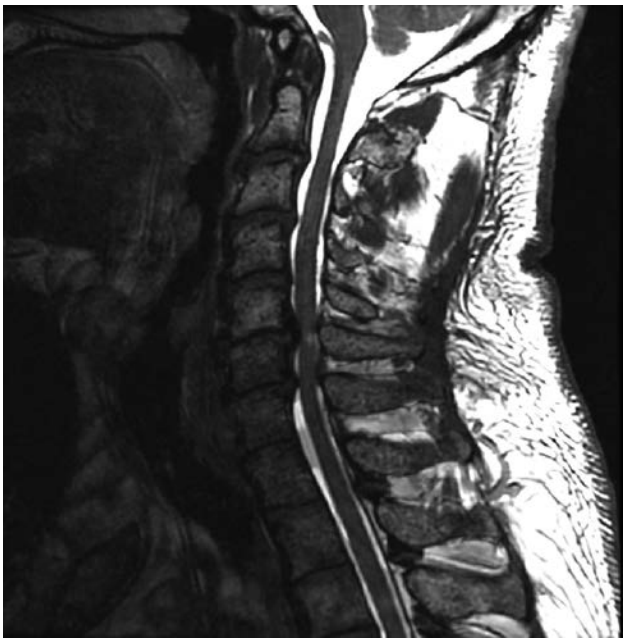

FIG 1. T2WI showing a subject with DCM with spinal cord compression. Sagittal T2WI in a subject with DCM with severe impairment shows multilevel disc degeneration, spondylosis, and spinal cord compression at C5–6 with focal hyperintensity.

utility. FA has demonstrated moderate correlation with global and focal disability in dozens of studies involving various pathologies[3,9-14] but has yet to achieve clinical uptake due to a lack of standardized/portable acquisition methods and cumbersome analysis techniques. MTR has also shown correlation with impairment in MS and spinal cord injury (SCI) studies,[15-17] but results have been inconsistent, in part due to T1 and frequency offset dependencies, and thus insufficient to drive clinical adoption.[3]

At 3T or higher field strengths, T2*-weighted imaging of the SC provides high resolution and strong contrast between GM and WM, allowing segmentation between these structures and calculation of their CSA.[18] It has also been established that T2*WI shows hyperintensity in injured SC WM in various pathologic conditions.[19,20] We hypothesized that T2*WI hyperintensity is a general phenomenon in WM injury, leading to decreased gray-white contrast that can be quantified by normalizing the WM signal intensity within each axial section by that of the GM as a T2*WI WM/GM signal-intensity ratio. Our investigation in 40 healthy subjects established that T2*WI WM/GM has lower intersubject variability compared with CSA, FA, and MTR and superior reliability compared with FA and MTR,[7] though the latter metrics showed acceptable results, in keeping with prior reports.[11,21-25]

These encouraging findings prompted the current study in degenerative cervical myelopathy (DCM), a common condition involving degeneration of the discs, ligaments, and vertebrae, resulting in cervical spinal cord compression and functional impairment (Fig 1).[26,27] We aimed to determine how well T2*WI WM/GM differs between patients with DCM and healthy subjects and correlates with global disability and focal neurologic deficits when extracted from corresponding regions of WM, in comparison with FA, MTR, and CSA of the SC.

MATERIALS AND METHODS

Study Design and Subjects

This study received institutional approval from the University Health Network (Toronto, Ontario, Canada), and all participants provided written informed consent. Fifty-eight patients with DCM were consecutively recruited from the outpatient spine neurosurgery clinic, and 42 healthy subjects were recruited between October 2014 and December 2016. Patients with DCM with confounding neurologic impairment, such as diabetic neuropathy or symptomatic lumbar radiculopathy, were excluded. All subjects were examined by an experienced physician (M.G.F, A.R.M.). Two subjects recruited as healthy volunteers were found to have clinical and imaging evidence of mild DCM and were analyzed as subjects with DCM. Two subjects with DCM failed to complete the MR imaging study due to pain/claustrophobia and were excluded from analysis. Thus, 58 patients with DCM and 40 healthy subjects for analysis remained. DCM severity was categorized on the basis of the modified Japanese Orthopedic Association (mJOA) score (normal = 18 points) into mild (mJOA = 15–17), moderate (mJOA = 12–14), and severe (mJOA < 12).[26] Three patients with DCM had undergone previous cervical operations with metallic implants and had achieved a complete or near-complete recovery (mJOA ≥ 17) followed by new cord compression at another cervical level.

Clinical Assessments

Subjects with DCM were assessed with the following: 1) the mJOA score to determine overall functional impairment; 2) the International Standards for Neurologic Classification of Spinal Cord Injury upper extremity (UE) motor score consisting of power testing (5-point score) in 10 upper extremity muscle groups (maximum score = 50) on both sides[28]; and 3) the UE sensory score consisting of Semmes Weinstein monofilament testing in C6, C7, and C8 dermatomes (4 points each, maximum score = 12). Healthy subjects all had mJOA = 18 and were assumed to have full motor (50/50) and sensory (12/12) scores for analyses.

MR Imaging Acquisitions

Subjects underwent high-resolution isotropic T2WI, DTI with single-shot EPI, spoiled gradient-echo imaging with and without magnetization transfer (MT) prepulse, and T2*WI with multiecho recombined gradient-echo at 3T (Signa Excite HDxt; GE Healthcare, Milwaukee, Wisconsin) as described in a companion article.[7] The multiecho recombined gradient-echo sequence uses 3 echoes that are magnitude-reconstructed and combined with a sum-of-squares algorithm. Total imaging time was approximately 30–35 minutes, including subject positioning, section prescription, and second-order localized shimming.

Image-Analysis Techniques

Template-based analysis was performed by using the Spinal Cord Toolbox, Version 2.3 (https://sourceforge.net/projects/spinalcordtoolbox/),[29] as described in the companion article.[7] Metrics included CSA from T2WI, FA, MTR, and T2*WI WM/GM signal-intensity ratio extracted from the rostral uncompressed SC (C1–C3); the maximally compressed level (MCL); and the caudal un-

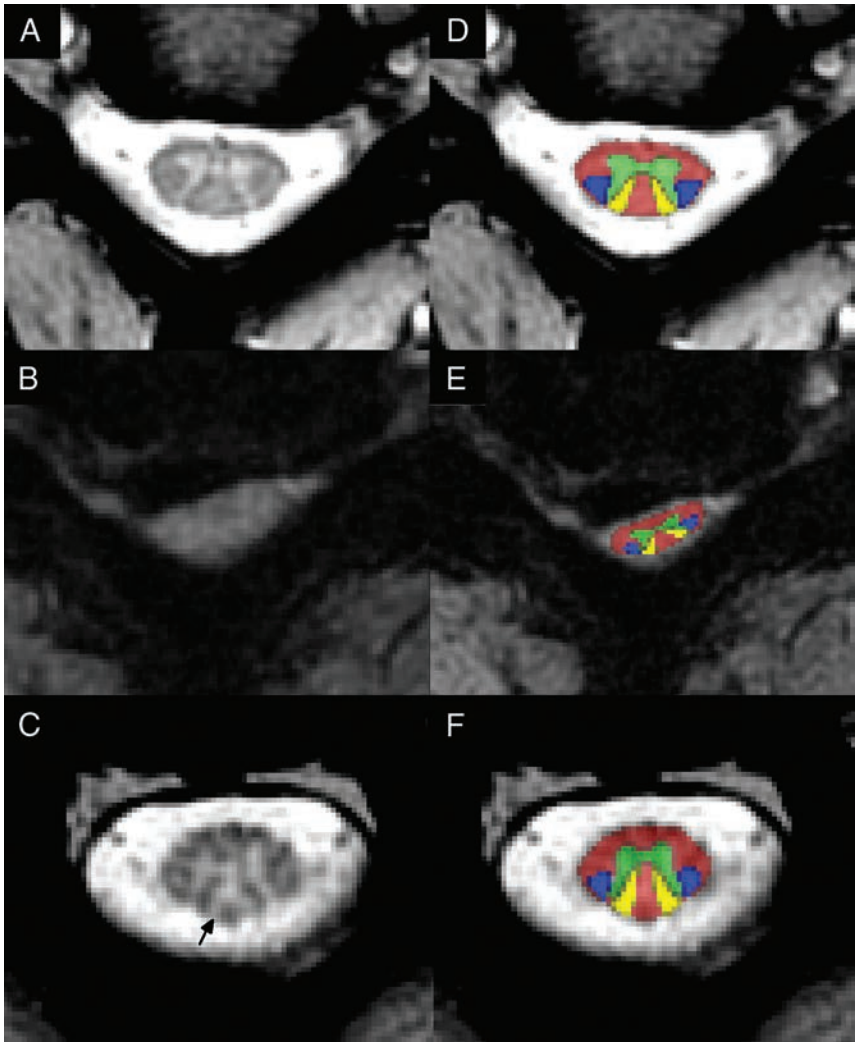

FIG 2. T2*WI demonstrating loss of gray-white contrast and Wallerian degeneration. *A*, Axial T2*WI at C3–4 in a healthy subject shows strong contrast between GM and WM (T2*WI WM/GM = 0.791 for this image). *B*, T2*WI at C5–6 in a subject with severe DCM shows SC compression from a lateral disc herniation, with loss of gray-white contrast (T2*WI WM/GM = 0.967). *C*, T2*WI at C3 in the same subject with DCM shows focal hyperintensity (*arrow*) within the dorsal columns, suggesting Wallerian degeneration (T2*WI WM/GM = 0.923). *D–F*, The same images as in *A–C* with the Spinal Cord Toolbox probabilistic atlas representations of WM (red), GM (green), lateral corticospinal tracts (blue), and fasciculus cuneati (yellow) overlaid.

compressed cord (C6–C7). For MCL metrics, CSA was extracted from a single section, whereas FA, MTR, and T2*WI WM/GM were averaged over 3 sections centered at the compressed level. In subjects with motion artifacts on the T2WI, T2*WI was used to calculate the CSA with correction for the oblique angle. For FA, MTR, and T2*WI, ROIs included total WM, GM (T2*WI only), and the left/right fasciculus cuneatus and lateral corticospinal tract (Fig 2). Sagittal and reformatted axial T2WI were visually assessed for SC hyperintensity by 2 raters (A.R.M., A.N.), with disagreements resolved by discussion.

Statistical Analysis

Statistical analysis was performed with R statistical and computing software, Version 3.3 (http://www.r-project.org). Metrics are reported as mean ± SD. Comparisons between characteristics of healthy subjects and those with DCM were made by using 2-sample *t* tests and χ^2 tests. MR imaging metrics were normalized to correct for confounding relationships according to the following linear equations, developed from data in 40 healthy subjects[7]:

$$1)\ CSA_{corrected} = CSA_{raw} - 5.3690 \times (\text{Cervical Cord Length} - 10.6),$$

$$2)\ FA_{corrected} = FA_{raw} + 0.0012053 \times (\text{Age} - 47.1),$$

$$3)\ MTR_{corrected} = MTR_{raw} + 0.17410 \times (\text{Height} - 171.6) + 0.074131 \times (\text{Age} - 47.1).$$

In Equation 1, CSA is in square millimeters and cervical cord length is in centimeters; in Equation 2, age is in years; and in Equation 3, MTR is expressed as a percentage, height is in centimeters, and age is in years. Metrics were then converted to *z* scores to normalize across rostrocaudal levels (eg, for comparisons at the MCL). Comparisons of normalized MR imaging metrics between DCM and healthy subjects were made by using Welch *t* tests. These tests were also repeated against an age-matched group (by excluding healthy subjects younger than 40 years of age) to confirm the findings. Diagnostic accuracy was assessed with the area under the curve (AUC) and logistic regression, with backward stepwise variable selection. Relationships between normalized MR imaging metrics and clinical measures were assessed by using Pearson correlation coefficients and backward stepwise multiple linear regression. CSA of the SC and other metrics extracted from the total WM were analyzed against the mJOA score, while metrics from each lateral corticospinal tract and fasciculus cuneatus were analyzed against ipsilateral UE motor and sensory scores, respectively. Two-way ANOVA with an interaction term was used to assess how T2*WI WM/GM and T2WI hyperintensity relate to the mJOA score. Results were considered statistically significant at $P < .05$, due to the exploratory nature of this study.

RESULTS

Subject Characteristics

Subjects with DCM showed the following distribution of severity: 33 mild, 15 moderate, and 10 severe. Age differed significantly between healthy subjects and those with DCM (mean, 47.1 ± 15.3 versus 57.0 ± 10.9 years, $P = 3 \times 10^{-4}$; Table 1). When healthy subjects younger than 40 years of age were excluded, age became equivalent ($n = 26$; mean age, 56.3 ± 9.8 years, $P = .76$). Other

demographic variables (sex, height, weight, and neck length) did not vary between groups.

Image Acquisition and Analysis

Four T2WI datasets and 1 T2*WI dataset were excluded due to motion artifacts. Individual sections were excluded due to artifacts as follows: DTI: 5.3%; MT: 0.8%; and T2*WI: 0.7%. Three patients with metallic implants had images excluded at those levels and 2 axial sections above and below them; the remaining images and metrics appeared to be of acceptable quality. Analysis of subjects with DCM required manual editing of segmentation masks in most cases due to deformation of the cord and a lack of contrast with surrounding tissues, requiring <5 minutes per dataset. Automatic registration to the Spinal Cord Toolbox template/atlas was successful in all cases.

MR Imaging Metrics

Significant differences between DCM and healthy subjects were found in 10/12 MR imaging metrics (Table 2), including decreased CSA (rostral: $P = 9 \times 10^{-5}$; MCL: $P = 1 \times 10^{-13}$), increased T2*WI WM/GM (rostral: $P = 8 \times 10^{-7}$; MCL: $P = 1 \times 10^{-11}$; caudal: $P = 1 \times 10^{-4}$), decreased FA (rostral: $P = 2 \times 10^{-4}$; MCL: $P = 2 \times 10^{-9}$; caudal: $P = 2 \times 10^{-4}$), and decreased MTR (rostral: $P = .01$; MCL: $P = .001$). Patients with DCM also showed a trend toward decreased caudal CSA ($P = .08$). All differences remained significant compared with age-matched healthy subjects, and caudal CSA became borderline significant ($P = .05$). The strongest cross-correlations were found between the same metrics at different levels (eg, rostral and caudal CSA: $r = 0.77$) (Fig 3). Cross-correlations were relatively strong between MCL metrics (0.44–0.57) but weaker at rostral and caudal levels.

Table 1: Subject characteristics[a]

Characteristic	Healthy Subjects (n = 40)	Subjects with DCM (n = 58)
Age (yr)	47.1 ± 15.3	57.0 ± 10.9[b]
Sex (M/F)	21:19	36:22
Height (cm)	171.4 ± 8.6	172.4 ± 10.4
Weight (kg)	74.6 ± 11.5	74.9 ± 9.9
Neck length (mm)	106.1 ± 9.6	106.8 ± 9.4
mJOA	18.0 ± 0.0	14.2 ± 2.5[b]
R UE motor	50.0 ± 0.0[c]	46.1 ± 5.2[b]
L UE motor	50.0 ± 0.0[c]	46.5 ± 5.6[b]
R UE sensation	12.0 ± 0.0[c]	10.5 ± 2.5[b]
L UE sensation	12.0 ± 0.0[c]	10.6 ± 2.5[b]

Note:—L indicates left; R, right.
[a] Demographics and clinical measures are reported as mean ± SD.
[b] Significant differences ($P < .05$) between those with DCM and healthy subjects.
[c] Motor and sensory scores for healthy subjects were assumed to be full, on the basis of a screening examination.

Table 2: Summary of MRI metrics[a]

Region and Metrics	Healthy Subjects (n = 40)	Subjects with DCM (n = 58)	P Value	Diagnostic Accuracy (AUC)
Rostral				
CSA (mm^2)	78.5 ± 8.0	70.9 ± 10.4	9×10^{-5}	0.722
FA	0.725 ± 0.036	0.687 ± 0.063	2×10^{-4}	0.692
MTR	52.7 ± 2.4	51.2 ± 3.4	.01	0.648
T2*WI WM/GM	0.848 ± 0.031[b]	0.884 ± 0.034[b]	8×10^{-7}[b]	0.775[b]
MCL/C4–5				
CSA (mm^2)	76.2 ± 10.4[b]	50.8 ± 18.1[b]	1×10^{-13}[b]	0.890[b]
FA	0.652 ± 0.048	0.553 ± 0.094	2×10^{-9}	0.813
MTR	49.9 ± 2.9	47.6 ± 3.8	.001	0.698
T2*WI WM/GM	0.850 ± 0.022	0.899 ± 0.038	1×10^{-11}	0.860
Caudal				
CSA (mm^2)	63.7 ± 9.1	60.1 ± 10.9	.08	0.585
FA	0.599 ± 0.050	0.552 ± 0.060	2×10^{-4}	0.724[b]
MTR	46.2 ± 3.8	46.4 ± 5.1	.85	0.515
T2*WI WM/GM	0.862 ± 0.047[b]	0.903 ± 0.053[b]	1×10^{-4}[b]	0.721

[a] Metrics (mean ± SD) are reported at uncompressed rostral levels (C1–C3), MCL, or C4–5 (healthy subjects) and uncompressed caudal levels (C6–C7). MCL data are converted from z scores to values at C4–5 for ease of interpretation. Diagnostic accuracy is reported as AUC.
[b] Strongest group differences for each region.

Diagnostic Accuracy

MCL CSA showed the highest diagnostic accuracy with AUC = 0.890, outperforming other metrics at MCL: T2*WI WM/GM (0.860), FA (0.813), and MTR (0.698) (Table 2). At the rostral and caudal levels, T2*WI WM/GM showed better discrimination than other metrics with AUC = 0.775 and 0.721, respectively. T2WI hyperintensity was present in 37/58 (64%) of subjects with DCM and 0/40 healthy subjects, with AUC = 0.640. Multivariate analysis with logistic regression achieved AUC = 0.954, retaining rostral T2*WI WM/GM ($P = .02$), MCL FA ($P = .12$), MCL CSA ($P = .14$), and T2WI signal change ($P = .71$).

Correlation with Global and Focal Impairment

The strongest univariate correlate with the mJOA score was MCL CSA ($r = 0.66$) (Table 3). This was stronger than MCL T2*WI WM/GM ($r = -0.59$), FA ($r = 0.54$), and MTR ($r = 0.43$). At the rostral and caudal levels, T2*WI WM/GM showed the strongest correlation with the mJOA score ($r = -0.52, -0.36$, respectively). Multiple linear regression for the mJOA score found a good fit ($R^2 = 0.59$, adjusted $R^2 = 0.55$, $P = 8 \times 10^{-13}$), with rostral T2*WI WM/GM showing the strongest relationship ($P = .01$), followed by rostral MTR ($P = .02$), T2WI signal change ($P = .02$), caudal CSA ($P = .05$), caudal FA ($P = .27$), MCL CSA ($P = .34$), and MCL FA ($P = .44$). The strongest correlate with UE motor and sensory scores was rostral T2*WI WM/GM, extracted from the ipsilateral lateral corticospinal tract ($r = -0.45$, $P = 7 \times 10^{-11}$) and fasciculus cuneatus ($r = -0.49$, $P = 4 \times 10^{-13}$), respectively.

Effects of T2WI Hyperintensity

Subjects with DCM with T2WI with hyperintensity had lower mJOA scores than those with T2WI without hyperintensity (13.6 versus 15.2, $P = .005$) and higher MCL T2*WI WM/GM (0.905 versus 0.886, $P = .07$). When we analyzed all 98 subjects, 2-way ANOVA found significant independent relationships with the mJOA scores for T2*WI WM/GM ($P = .01$) and T2WI signal change ($P = .001$), while the interaction term was nonsignificant ($P = .55$), sug-

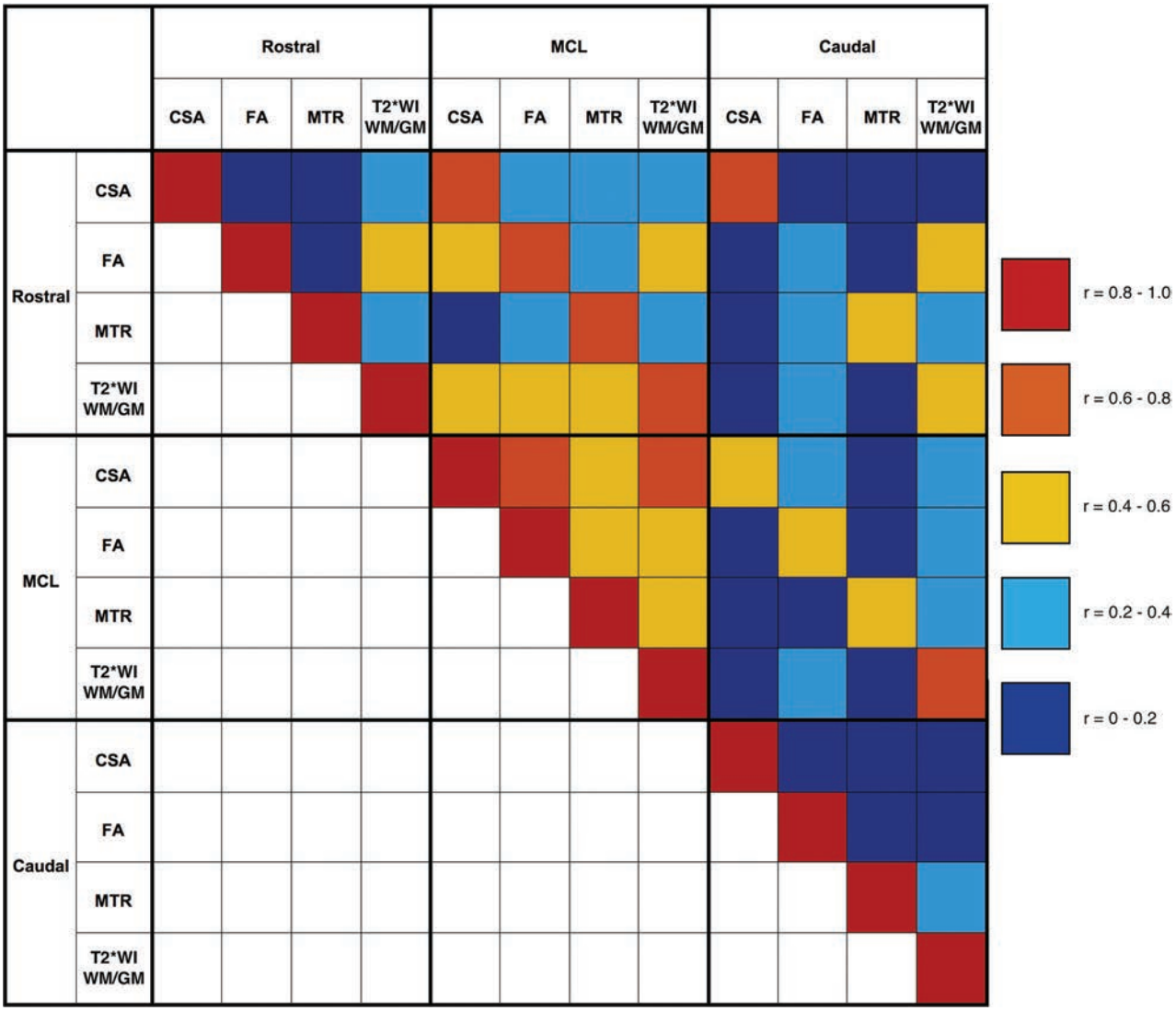

FIG 3. Correlation matrix for MR imaging metrics. Pearson correlation coefficients calculated between MR imaging metrics at rostral (C1–C3), MCL (or C4–5 in healthy subjects), and caudal (C6–7) levels are color-coded to represent the degree of cross-correlation by using data from all 98 subjects.

Table 3: Correlation with clinical measures[a]

Region and MRI Metrics	mJOA Score (n = 98)	UE Motor Score (n = 196)	UE Sensory Score (n = 196)
Rostral			
CSA	0.44 (6×10^{-6})	–	–
FA	0.37 (2×10^{-4})	0.20 (0.006)	0.26 (3×10^{-4})
MTR	0.35 (5×10^{-4})	0.22 (0.002)	0.11 (0.13)
T2*WI WM/GM	−0.52 (5×10^{-8})[b]	−0.45 (7×10^{-11})[b]	−0.49 (4×10^{-13})[b]
MCL/C4–5			
CSA	0.66 (2×10^{-13})[b]	–	–
FA	0.54 (2×10^{-8})	0.36 (5×10^{-7})[b]	0.40 (1×10^{-8})
MTR	0.43 (1×10^{-5})	0.14 (0.04)	0.05 (0.48)
T2*WI WM/GM	−0.59 (7×10^{-10})	−0.33 (3×10^{-6})	−0.43 (8×10^{-10})[b]
Caudal			
CSA	0.27 (0.007)	–	–
FA	0.35 (0.001)	0.09 (0.20)	0.05 (0.49)
MTR	0.02 (0.83)	0.12 (0.11)	0.05 (0.51)
T2*WI WM/GM	−0.36 (3×10^{-4})[b]	−0.17 (0.01)[b]	−0.25 (6×10^{-4})[b]

[a] mJOA is analyzed against FA, MTR, and T2*WI WM/GM extracted from total WM and SC CSA. UE motor score and UE sensory score are analyzed with respect to non-CSA metrics extracted from the ipsilateral, lateral corticospinal tract and fasciculus cuneatus, respectively. Pearson coefficients are shown with P values in parentheses.

[b] Strongest correlations with clinical measures for each region.

gesting that T2WI hyperintensity does not impact the performance of T2*WI WM/GM. The within-group correlation between MCL T2*WI WM/GM and mJOA scores was slightly higher among subjects without hyperintensity (r = −0.43) than among subjects with T2WI hyperintensity (r = −0.36) (Table 4).

DISCUSSION

Summary of Findings

All 4 qMRI metrics analyzed in this study demonstrated significant results in terms of group differences and clinical correlations, which was encouraging given the predominance of subjects with mild DCM in our cohort. MCL CSA outperformed other measures in all univariate analyses; this result is not surprising because this measure of spinal

Table 4: Analysis of T2*WI WM/GM and T2WI signal change[a]

Measure	T2WI− (*n* = 61)	T2WI+ (*n* = 37)	*P* Value
mJOA	17.0 ± 1.6	13.6 ± 2.8	7×10^{-9}
MCL T2*WI WM/GM	0.862 ± 0.033	0.905 ± 0.037	2×10^{-7}
MCL T2*WI WM/GM ~ mJOA	−0.43 (9×10^{-4})	−0.36 (0.03)	

[a] The entire cohort (including subjects with DCM and healthy subjects) is divided into subjects with and without T2WI hyperintensity, denoted T2WI+ and T2WI−, respectively. Mean ± SD are reported. T2*WI WM/GM is extracted from the MCL (subjects with DCM) or C4–5 (healthy subjects), and Pearson correlation coefficients between mJOA and T2*WI WM/GM within each signal change group are shown (*P* values in parentheses).

cord compression reflects the primary mechanism of tissue injury in DCM. Cord compression causes ischemia that often represents partially reversible neurologic impairment,[30] whereas atrophy of the SC (rostral or caudal compression) suggests axonal loss or demyelination, which is more likely to be permanent.[12] MCL CSA has been previously demonstrated to correlate well with severity in DCM,[31] and atrophy measurement has also proved useful in DCM[12] and MS.[4-6] However, MCL CSA does not account for motion-related dynamic injury, which is also believed to be an important mechanism of tissue injury in DCM,[31] suggesting that this metric may be better used in conjunction with other measures that directly interrogate microstructural changes. FA showed strong group differences and moderate correlations with impairment, but diagnostic accuracy was modest. These findings are all consistent with those in the previous literature.[3,9-14] MTR results were relatively weak, which is consistent with findings in prior studies in MS,[16,17] but differ from results seen in chronic SCI.[15]

We are not aware of published reports using MTR in patients with DCM. The T2*WI WM/GM signal ratio showed the strongest results at the rostral and caudal levels, and rostral T2*WI WM/GM was the strongest independent variable in multivariate models for diagnosis and correlation with the mJOA score. T2*WI WM/GM also demonstrated superior performance over FA and MTR in almost every comparison. The encouraging findings for T2*WI WM/GM indicate that this novel biomarker is a relatively accurate measure of WM injury, with particularly strong results in multivariate models. T2*WI WM/GM also shows better reliability, compared with FA and MTR, with our techniques.[7] In comparison with DTI and MT techniques, T2*WI had fewer excluded sections, required less imaging time, and involved less postprocessing, suggesting that this biomarker is well-suited for clinical use.

Unfortunately, all qMRI metrics failed to show diagnostic accuracy (AUC) of >90% and provided only moderate clinical correlations, indicating somewhat limited utility when used individually. However, our protocol produced 10 measures of tissue injury that are relatively independent, enabling multivariate use to strengthen their accuracy. This was evident in the logistic regression model that achieved >95% diagnostic accuracy, and the linear regression model for the mJOA score that had much higher adjusted R^2 than univariate measures. Overall, our results demonstrate that T2*WI WM/GM performs well in comparison with established biomarkers, and our multiparametric approach has the potential to overcome the limitations of individual qMRI measures.

*T2*WI WM/GM: A Novel Biomarker of WM Injury*

T2*WI is available from all major MR imaging vendors, including the GE Healthcare multiecho recombined gradient-echo, Siemens multiecho data image combination, Philips Healthcare multiecho fast-field gradient echo, and Hitachi ADAGE (Additive Arrangement Gradient Echo) sequences, though differences may exist between implementations, and cross-vendor validation is needed.[32] Our investigation of the T2*WI WM/GM signal intensity ratio follows from previous findings that T2*WI detects WM injury by exhibiting hyperintensity. In one study, a pattern consistent with Wallerian degeneration of the fasciculus gracilis could be visualized rostrally following a cervical SC needle injury.[19] Another study found hyperintensity in the bilateral lateral corticospinal tracts in a patient with amyotrophic lateral sclerosis, related to the degeneration of descending upper motor neurons.[20] In our data, a small number of subjects with DCM also exhibited focal T2*WI hyperintensity of the dorsal columns extending through all images rostral to compression, consistent with Wallerian degeneration (Fig 2). However, most patients with DCM showed only loss of gray-white contrast, which is somewhat akin to the diagnosis of acute ischemic stroke on brain CT. However, T2*WI signal intensity is a relative value that varies considerably between subjects, requiring normalization. Although GM may also experience injury in DCM, we found that using GM signal intensity as a reference produced more consistent results than CSF due to variable CSF signal (A.R.M. et al, unpublished data, 2017). Furthermore, T2*WI WM/GM appears to be stable in the context of T2WI hyperintensity; this feature is commonly encountered in DCM, showing no significant interaction (effect modification) and minimal impact on clinical correlations.

The calculation of the WM/GM signal-intensity ratio is easily and accurately performed by using automated template-based analysis.[29] The pathophysiologic processes that underlie T2*WI hyperintensity include demyelination, gliosis, increased calcium concentration, and nonheme iron stored in ferritin, but signal intensity also depends on water content and local concentration of deoxyhemoglobin (used in blood oxygen level–dependent fMRI).[33-37] Thus, T2*WI WM/GM is somewhat nonspecific, reflecting several microstructural features. The moderate cross-correlations observed between T2*WI WM/GM and other metrics did not reveal a clear pattern because these findings may simply be explained by multiple pathologic processes occurring simultaneously. Histopathologic studies are necessary to fully understand exactly what SC microstructural changes are detected by T2*WI WM/GM compared with other measures, and further research is needed to determine its performance in other pathologies. However, its simplicity, sensitivity, and excellent reliability suggest that it could be a very useful imaging biomarker.

ROIs

The strongest results for each metric were found at the MCL in this study, with the exception of rostral T2*WI WM/GM for multivariate analyses and tract-specific correlations. This finding highlights a major challenge to using quantitative MR imaging in

DCM because the compressed region has potential bias related to distorted anatomy (leading to inaccurate registration to the template) and increased susceptibility artifacts. This challenge was partially mitigated by averaging MCL metrics over 3 sections, with sections above and below MCL often showing no compression. However, results from our reliability study showed a trend toward diminished reliability for FA, MTR, and T2*WI WM/GM at the MCL.[7] It was encouraging to also find strong results rostrally for T2*WI WM/GM, which has been previously reported for FA.[14,38] This finding has important clinical implications because this region avoids the aforementioned issues and can be used for postoperative assessment rostral to metallic implants in most patients with DCM. This region is also potentially useful for the prediction of outcomes in acute SCI, with a postoperative scan in the days to weeks following early surgical decompression.[38] The caudal region consistently showed the weakest results, likely due to respiratory motion, susceptibility artifacts from the lungs, and increased partial volume effects due to the angle between sections and the SC (in subjects with irreducible cervical lordosis). Despite these issues, T2*WI WM/GM and FA showed some utility in this region. Metrics extracted from individual WM tracts showed significant correlations with focal neurologic deficits, particularly at the rostral and MCL levels, indicating that our quantitative analysis identifies focal tissue injury. However, correlations with motor/sensory scores were modest, potentially because of the small number of voxels included in metric calculations but also because clinical impairment can also result from GM injury, nerve root compression (radiculopathy), and pain.

Future Directions: Clinical Translation of Quantitative Spinal Cord MR Imaging

At present, SC qMRI has yet to achieve clinical adoption due to challenges with the portability of acquisitions, cumbersome analysis, and modest results in diagnostic accuracy and clinical correlations. However, our multiparametric approach with simple methods and automated analysis is designed to address each of these issues and be suitable for clinical use. We anticipate that the first clinical application of these techniques could be the development of more sensitive diagnostic tools. A diagnostic tool that can directly detect tissue injury could have a major impact in DCM, in which patients sometimes show minimal symptoms that cannot be definitely attributed to the SC by clinical and electrophysiological examinations. Furthermore, many older individuals have spinal cord compression without neurologic dysfunction,[39] indicating that anatomic imaging alone is insufficient. Our approach may also prove useful for monitoring patients with DCM for progression of tissue injury by using serial qMRI examinations. Patients with mild DCM are often managed nonoperatively with periodic clinical assessments, but symptoms are highly subjective and mechanisms of behavioral adaptation and neuroplasticity may mask subtle deterioration. Finally, effort has been made to predict outcomes by using qMRI in DCM and other clinical populations,[3,14] but this effort has yet to show great success, possibly because outcomes depend on factors that extend beyond the current state of tissue injury. However, if qMRI techniques can differentiate between reversible and permanent injury by quantifying specific microstructural changes (eg, demyelination versus axonal loss), enhanced outcome prediction may also be possible. Future studies should be directed at investigating each of these exciting potential applications.

Limitations

Clinical assessments used in this study are somewhat coarse (mJOA score, sensory score) and subjective (mJOA score, motor score), potentially limiting the strength of correlations. T1-weighted imaging was not performed in this study, and the effect of T1WI hypointensity on T2*WI WM/GM has not been characterized. We aimed to minimize bias by using automated analysis, but almost all DCM datasets required manual correction of segmentation. Other DTI metrics were not analyzed due to an a priori decision to focus on FA, due to its consistent results in previous studies.[3] The validity of MR imaging metrics for 3 patients with metallic implants is unknown, but quantitative results distant from the hardware appeared to be consistent with those in other subjects.

CONCLUSIONS

T2*WI WM/GM is a novel biomarker of SC WM degeneration that shows good diagnostic accuracy and correlation with clinical features of DCM, warranting further investigation. This biomarker has strong potential for clinical translation, particularly in multivariate approaches that combine quantitative measures of SC injury. Such measures have the potential to provide more sensitive diagnosis of mild cord injury, monitoring of disease progression or recovery, and prediction of outcomes in DCM and other spinal pathologies.

ACKNOWLEDGMENTS

This research received funding support from Rick Hansen Institute, as part of the Riluzole in Spinal Cord Injury Study (RISCIS), which is also supported by AOSpine North America, AOSpine International SCI Knowledge Forum, and the North American Clinical Trials Network (NACTN) of the Christopher and Dana Reeve Foundation. This research also received support from the Dezwirek Foundation, the Sherman Clinical Research Unit, and the Gerald and Tootsie Halbert Chair in Spinal Cord Research. Dr. Martin received post-doctoral fellowship support from Canadian Institutes of Health Research. We would also like to thank all subjects for their participation and acknowledge MRI Technologists Keith Ta and Eugen Hlasny for their key contributions, and several students, research coordinators, and administrators that assisted with this research.

Disclosures: Allan R. Martin—*RELATED*: *Grant*: Rick Hansen Institute, AOSpine North America, AOSpine International SCI Knowledge Forum, the North American Clinical Trials Network of the Christopher and Dana Reeve Foundation, the DeZwirek Foundation, the Sherman Clinical Research Unit, and the Gerald and Tootsie Halbert Chair in Spinal Cord Research*; Dr. Martin received post-doctoral Fellowship funding from Canadian Institutes of Health Research (CIHR) that included $50,000 (CDN) annual salary support and $5,000 annual research allowance that enabled this research. Sukhvinder Kalsi-Ryan—*UNRELATED*: *Consultancy*: Neural Outcomes; *Royalties*: GRASSP, Version 1.0. *Money paid to the institution.

REFERENCES

1. Stroman PW, Wheeler-Kingshott C, Bacon M, et al. **The current state-of-the-art of spinal cord imaging: methods.** *Neuroimage* 2014; 84:1070–81 CrossRef Medline

2. Wheeler-Kingshott CA, Stroman PW, Schwab JM, et al. **The current state-of-the-art of spinal cord imaging: applications.** *Neuroimage* 2014;84:1082–93 CrossRef Medline
3. Martin AR, Aleksanderek I, Cohen-Adad J, et al. **Translating state-of-the-art spinal cord MRI techniques to clinical use: a systematic review of clinical studies utilizing DTI, MT, MWF, MRS, and fMRI.** *Neuroimage Clin* 2016;10:192–238 CrossRef Medline
4. Oh J, Seigo M, Saidha S, et al. **Spinal cord normalization in multiple sclerosis.** *J Neuroimaging* 2014;24:577–84 CrossRef Medline
5. Kearney H, Yiannakas MC, Abdel-Aziz K, et al. **Improved MRI quantification of spinal cord atrophy in multiple sclerosis.** *J Magn Reson Imaging* 2014;39:617–23 CrossRef Medline
6. Kearney H, Altmann DR, Samson RS, et al. **Cervical cord lesion load is associated with disability independently from atrophy in MS.** *Neurology* 2015;84:367–73 CrossRef Medline
7. Martin AR, De Leener B, Cohen-Adad J, et al. **Clinically feasible microstructural MRI to quantify cervical spinal cord tissue injury using DTI, MT, and T2*-weighted imaging: assessment of normative data and reliability.** *AJNR Am J Neuroradiol* 2017 Apr 20. [Epub ahead of print] CrossRef Medline
8. Kato F, Yukawa Y, Suda K, et al. **Normal morphology, age-related changes and abnormal findings of the cervical spine, part II: magnetic resonance imaging of over 1,200 asymptomatic subjects.** *Eur Spine J* 2012;21:1499–507 CrossRef Medline
9. Uda T, Takami T, Tsuyuguchi N, et al. **Assessment of cervical spondylotic myelopathy using diffusion tensor magnetic resonance imaging parameter at 3.0 Tesla.** *Spine (Phila Pa 1976)* 2013;38:407–14 CrossRef Medline
10. Budzik JF, Balbi V, Le Thuc V, et al. **Diffusion tensor imaging and fibre tracking in cervical spondylotic myelopathy.** *Eur Radiol* 2011;21:426–33 CrossRef Medline
11. Ellingson BM, Salamon N, Grinstead JW, et al. **Diffusion tensor imaging predicts functional impairment in mild-to-moderate cervical spondylotic myelopathy.** *Spine J* 2014;14:2589–97 CrossRef Medline
12. Grabher P, Mohammadi S, Trachsler A, et al. **Voxel-based analysis of grey and white matter degeneration in cervical spondylotic myelopathy.** *Sci Rep* 2016;6:24636 CrossRef Medline
13. Jones JG, Cen SY, Lebel RM, et al. **Diffusion tensor imaging correlates with the clinical assessment of disease severity in cervical spondylotic myelopathy and predicts outcome following surgery.** *AJNR Am J Neuroradiol* 2013;34:471–78 CrossRef Medline
14. Wen CY, Cui JL, Liu HS, et al. **Is diffusion anisotropy a biomarker for disease severity and surgical prognosis of cervical spondylotic myelopathy?** *Radiology* 2014;270:197–204 CrossRef Medline
15. Cohen-Adad J, El Mendili MM, Lehéricy S, et al. **Demyelination and degeneration in the injured human spinal cord detected with diffusion and magnetization transfer MRI.** *Neuroimage* 2011;55:1024–33 CrossRef Medline
16. Oh J, Saidha S, Chen M, et al. **Spinal cord quantitative MRI discriminates between disability levels in multiple sclerosis.** *Neurology* 2013;80:540–47 CrossRef Medline
17. Oh J, Zackowski K, Chen M, et al. **Multiparametric MRI correlates of sensorimotor function in the spinal cord in multiple sclerosis.** *Mult Scler* 2013;19:427–35 CrossRef Medline
18. Yiannakas MC, Kearney H, Samson RS, et al. **Feasibility of grey matter and white matter segmentation of the upper cervical cord in vivo: a pilot study with application to magnetisation transfer measurements.** *Neuroimage* 2012;63:1054–59 CrossRef Medline
19. Cohen-Adad J, Buchbinder B, Oaklander AL. **Cervical spinal cord injection of epidural corticosteroids: comprehensive longitudinal study including multiparametric magnetic resonance imaging.** *Pain* 2012;153:2292–99 CrossRef Medline
20. Cohen-Adad J, Zhao W, Keil B, et al. **7-T MRI of the spinal cord can detect lateral corticospinal tract abnormality in amyotrophic lateral sclerosis.** *Muscle Nerve* 2013;47:760–62 CrossRef Medline
21. Taso M, Girard OM, Duhamel G, et al. **Tract-specific and age-related variations of the spinal cord microstructure: a multi-parametric MRI study using diffusion tensor imaging (DTI) and inhomogeneous magnetization transfer (ihMT).** *NMR Biomed* 2016;29:817–32 CrossRef Medline
22. Samson RS, Levy S, Schneider T, et al. **ZOOM or non-ZOOM? Assessing spinal cord diffusion tensor imaging protocols for multicentre studies.** *PLoS One* 2016;11:e0155557 CrossRef Medline
23. Kerkovsky M, Bednarik J, Dusek L, et al. **Magnetic resonance diffusion tensor imaging in patients with cervical spondylotic spinal cord compression: correlations between clinical and electrophysiological findings.** *Spine (Phila Pa 1976)* 2012;37:48–56 CrossRef Medline
24. Smith SA, Jones CK, Gifford A, et al. **Reproducibility of tract-specific magnetization transfer and diffusion tensor imaging in the cervical spinal cord at 3 Tesla.** *NMR Biomed* 2010;23:207–17 CrossRef Medline
25. Samson RS, Ciccarelli O, Kachramanoglou C, et al. **Tissue- and column-specific measurements from multi-parameter mapping of the human cervical spinal cord at 3 T.** *NMR Biomed* 2013;26:1823–30 CrossRef Medline
26. Fehlings MG, Wilson JR, Kopjar B, et al. **Efficacy and safety of surgical decompression in patients with cervical spondylotic myelopathy: results of the AOSpine North America prospective multi-center study.** *J Bone Joint Surg Am* 2013;95:1651–58 CrossRef Medline
27. Nouri A, Martin AR, Mikulis D, et al. **Magnetic resonance imaging assessment of degenerative cervical myelopathy: a review of structural changes and measurement techniques.** *Neurosurg Focus* 2016;40:E5 CrossRef Medline
28. Kirshblum SC, Burns SP, Biering-Sorensen F, et al. **International standards for neurological classification of spinal cord injury (revised 2011).** *J Spinal Cord Med* 2011;34:535–46 CrossRef Medline
29. De Leener B, Lévy S, Dupont SM, et al. **SCT: Spinal Cord Toolbox, an open-source software for processing spinal cord MRI data.** *Neuroimage* 2017;145(pt A):24–43 CrossRef Medline
30. Tetreault LA, Karpova A, Fehlings MG. **Predictors of outcome in patients with degenerative cervical spondylotic myelopathy undergoing surgical treatment: results of a systematic review.** *Eur Spine J* 2015;24(suppl 2):236–51 CrossRef Medline
31. Nouri A, Tetreault L, Zamorano JJ, et al. **Role of magnetic resonance imaging in predicting surgical outcome in patients with cervical spondylotic myelopathy.** *Spine* 2015;40:171–78 CrossRef Medline
32. White ML, Zhang Y, Healey K. **Cervical spinal cord multiple sclerosis: evaluation with 2D multi-echo recombined gradient echo MR imaging.** *J Spinal Cord Med* 2011;34:93–98 CrossRef Medline
33. Cohen-Adad J. **What can we learn from T2* maps of the cortex?** *Neuroimage* 2014;93(pt 2):189–200 CrossRef Medline
34. Lee J, Shmueli K, Kang BT, et al. **The contribution of myelin to magnetic susceptibility-weighted contrasts in high-field MRI of the brain.** *Neuroimage* 2012;59:3967–75 CrossRef Medline
35. Fukunaga M, Li TQ, van Gelderen P, et al. **Layer-specific variation of iron content in cerebral cortex as a source of MRI contrast.** *Proc Natl Acad Sci U S A* 2010;107:3834–39 CrossRef Medline
36. Haacke EM, Cheng NY, House MJ, et al. **Imaging iron stores in the brain using magnetic resonance imaging.** *Magn Reson Imaging* 2005;23:1–25 CrossRef Medline
37. Marques JP, Maddage R, Mlynarik V, et al. **On the origin of the MR image phase contrast: an in vivo MR microscopy study of the rat brain at 14.1 T.** *Neuroimage* 2009;46:345–52 CrossRef Medline
38. Vedantam A, Eckardt G, Wang MC, et al. **Clinical correlates of high cervical fractional anisotropy in acute cervical spinal cord injury.** *World Neurosurg* 2015;83:824–28 CrossRef Medline
39. Wilson JR, Barry S, Fischer DJ, et al. **Frequency, timing, and predictors of neurological dysfunction in the nonmyelopathic patient with cervical spinal cord compression, canal stenosis, and/or ossification of the posterior longitudinal ligament.** *Spine* 2013;38:S37–54 CrossRef Medline

Regarding "Embolization of Intracranial Dural Arteriovenous Fistulas Using PHIL Liquid Embolic Agent in 26 Patients: A Multicenter Study"

We read the article by Lamin et al[1] with considerable interest. They have highlighted their valuable experience with Precipitating Hydrophobic Injectable Liquid (PHIL; MicroVention, Tustin, California) embolic agent in the management of dural AVFs. We agree with their observations that the use of PHIL is safe and effective for endovascular management of dural AVFs, with outcomes comparable with those of Onyx (Covidien, Irvine, California).

A few points are worth mentioning. The advantages of PHIL over Onyx as they mentioned are the lack of any prior preparation, fewer beam-hardening artifacts, and less adhesiveness, leading to better forward penetration.[1]

Another advantage of PHIL over Onyx is seen when MR imaging is used on follow-up. Onyx causes susceptibility artifacts on gradient and susceptibility-weighted images, which are not seen with PHIL.[2]

Plug formation with PHIL is faster than with Onyx due to fewer layering effects, resulting in reduced fluoroscopy time and consequent radiation dose.[2] There is minimal wastage with PHIL because it comes in a prefilled syringe in contrast to Onyx.

Failed embolization with subsequent requirement of an operation or combined endovascular and surgical management for dural AVFs has also been reported in previous studies. The authors of this study did not experience this failure; however, it has been shown that Onyx forms a continuous smooth-surfaced column within vessels, while PHIL forms a rough-surfaced column interspersed with blood clots. Careful surgical handling of the vessel with low-voltage bipolar cautery to maintain vessel wall integrity is required with the PHIL embolic agent.[2]

We have made similar observations with PHIL at our institution and have found it to be an effective embolic agent in the management of intracranial AVFs as observed in the current study.

http://dx.doi.org/10.3174/ajnr.A5142

REFERENCES

1. Lamin S, Chew HS, Chavda S, et al. **Embolization of intracranial dural arteriovenous fistulas using PHIL liquid embolic agent in 26 patients: a multicenter study.** *AJNR Am J Neuroradiol* 2017;38:127–31 CrossRef Medline
2. Koçer N, Hanımoğlu H, Batur Ş, et al. **Preliminary experience with precipitating hydrophobic injectable liquid in brain arteriovenous malformations.** *Diagn Interv Radiol* 2016;22:184–89 CrossRef Medline

V. Bhatia
A. Kumar
N. Khandelwal
Department of Radiodiagnosis
Postgraduate Institute of Medical Education and Research
Chandigarh, India

Striving for the Best: How Far Should We Go? Regarding "Impact of Modified TICI 3 versus Modified TICI 2b Reperfusion Score to Predict Good Outcome following Endovascular Therapy"

Endovascular thrombectomy has become a valuable part of the treatment of patients with an acute large vessel occlusion in the anterior circulation. High rates of quality reperfusion after endovascular thrombectomy were considered a key element for achieving superior functional outcomes compared with sole medical treatment with IV rtPA.[1] Because a reperfusion grade of TICI 2b or better has been shown to be a precise and reliable predictor of good functional outcomes, TICI 2b and 3 are conventionally considered as "successful reperfusion."[2] In their highly relevant article, Dargazanli et al[3] provided further evidence that the outcomes of patients with "complete" (TICI 3) reperfusions are significantly better as opposed to patients with "near complete" (TICI 2b) reperfusions.[4]

These results not only underscore the need for devices that minimize the occurrence of periprocedural thrombus fragmentation potentially accountable for incomplete reperfusions, but also raise the important question of whether interventionalists should strive to achieve TICI 3 reperfusion in cases where TICI 2b is already achieved ("luxury rescue").

Recent studies have suggested that it is technically feasible to reach and recanalize smaller, distal MCA branches when encountered as the primary occlusion site. However, evidence for a clinical benefit of endovascular thrombectomy versus IV rtPA in treating distal occlusions beyond the proximal M2 level is lacking.

Notwithstanding, risk-benefit ratios might differ in the scenario of already achieved TICI 2b reperfusions. First, catheter placement is already taking place, which, relatively speaking, diminish the general risks of endovascular treatment (eg, groin hematoma). Second, available therapy alternatives are limited when TICI 2b reperfusion has already been achieved because the option of administering IV rtPA is usually no longer available.

The study by Dargazanli et al[3] supports the notion that a more aggressive treatment approach in striving to achieve TICI 3 reperfusions might be of benefit. Because "luxury rescue" maneuvers (eg, using IA lytics or small stent-retrievers) may inherit the risk of jeopardizing the already achieved benefit of a TICI 2b reperfusion, the evaluation of such maneuvers with regard to technical feasibility, safety, and clinical benefit is highly desirable.

Disclosures: Johannes Kaesmacher—*UNRELATED*: *Grants/Grants Pending*: KKF (Technical University Munich)*. *Money paid to the institution.

REFERENCES

1. Manning NW, Chapot R, Meyers PM. **Endovascular stroke management: key elements of success.** *Cerebrovasc Dis* 2016;42:170–77 CrossRef Medline
2. Yoo AJ, Simonsen CZ, Prabhakaran S, et al. **Refining angiographic biomarkers of revascularization: improving outcome prediction after intra-arterial therapy.** *Stroke* 2013;44:2509–12 CrossRef Medline
3. Dargazanli C, Consoli A, Barral M, et al. **Impact of modified TICI 3 versus modified TICI 2b reperfusion score to predict good outcome following endovascular therapy.** *AJNR Am J Neuroradiol* 2017;38:90–96 CrossRef Medline
4. Kleine JF, Wunderlich S, Zimmer C, et al. **Time to redefine success? TICI 3 versus TICI 2b recanalization in middle cerebral artery occlusion treated with thrombectomy.** *J Neurointerv Surg* 2017;9:117–21 CrossRef Medline

J. Kaesmacher
Department of Diagnostic and Interventional Neuroradiology
Klinikum Rechts der Isar
Technical University Munich
Munich, Germany

http://dx.doi.org/10.3174/ajnr.A5154

Caution; Confusion Ahead...

We read with great interest the article entitled "Endovascular Therapy of M2 Occlusion in IMS III: Role of M2 Segment Definition and Location on Clinical and Revascularization Outcomes" by Tomsick et al.[1] This study is a post hoc subgroup analysis of the patients randomized in the endovascular arm of the Interventional Management of Stroke (IMS) III study who underwent a mechanical thrombectomy (MT) for an MCA M2 segment occlusion. This article provides interesting data on distal (ie, M2) occlusions treated by endovascular means. Indeed, the recent randomized controlled trials (RCTs)[2-7] that showed the effectiveness of MT in acute ischemic stroke with large vessel occlusion included very few cases of M2 occlusion (Table). Consequently, the American Heart Association (AHA) guidelines,[8] according to the results of RCTs, suggest that only M1 and more proximal arterial occlusions should be safely treated by MT. Scant data (only nonrandomized, retrospective, monocenter series) on the safety and effectiveness of MT in M2 occlusions are available in the literature.[9-15] Despite the potential interest of this paper, we would like to raise some comments on its methods.

First, we would like to underline the fact that a subgroup analysis, as mentioned in many papers and letters,[16-18] is prone to bias in the statistical analysis. Consequently, the results of such post hoc analyses on small volume subgroups should be interpreted with caution.

Second, we found it very questionable to perform a post hoc analysis of a study[19] that showed such a low recanalization rate, due to the use of obsolete devices like "sonography-assisted thrombolysis" (EKOS system; EKOS, Bothell, Washington) and the "Merci retriever" (Concentric Medical, Mountain View, California), in the era of stent retrievers and aspiration devices. Indeed, the overall recanalization rate of M2 occlusion in this series was only 40%. Recent monocenter retrospective studies using more recent devices showed a recanalization rate over 75%.[9,13,15] Our center's experience with distal artery occlusions treated by endovascular means shows a recanalization rate of 76%.[20]

Third, we would like to report our disagreement with the MCA segmentation used in this paper. Indeed, the MCA segmentation commonly used is the one described in 1938 by Fischer[21] (Fig 1) and further used in anatomic[22] and angiographic[23] descriptive studies. In Fischer's[21] paper (written in the German language), the MCA segments are clearly defined:

Der Verlauf der A. cerebri media zerfällt in folgende Unterabschnitte:

1) *Den horizontalen Anfangsteil (M_1), von der Teilungsstelle der Carotis int. Bis zu dem etwa rechtwinkligen Knie der A. cerebri media reichend,*
2) *Den nach hinten zu ansteigenden Inselabschnitt (M_2), welcher mit 2–3 Hauptästen dem Inselgebiet dicht aufliegt, im Seitenbild in der arteriellen Gefäßachse (Moniz) des Gehirns verläuft und im Vorderbild nahezu vertikal ansteigt,*
3) *Gefäßverzweigungen (M_3) der vorgenannten Hauptäste der Fossa Sylvii mit dem Kandelaber (Foix) und charakteristischen Schleifenbildungen der Aa. Frontales asc. Im Seitenbild. Auf der Vorderaufnahme bilden diese zusammen mit der folgenden Gruppe ein charakteristisches, nach oben zu scharf begrenztes Fächerbild (M_{3-4}), das bei Tumoren der Zentral- oder Parietalregion eine typische Kompression nach unten erfährt,*
4) *Gefäßverzweigungen (M_4) im hintersten Teil der Fissura Sylvii (Gyrus angularis-Gebiet), die im Seitenbild deutlich hervortreten, dagegen auf der Vorderaufnahme mit dem Fächer (M_{3-4}), zusammenfallen,*
5) *Endausbreitungen (M_5) der mittleren hirnarterie, Sie sind zum Teil auf der Vorderaufnahme als feinere und mehr lockere Gefäßmaschen unmittelbar über dem dichteren und etwas gröber gezeichneten Fächerbild sichtbar, besonders klar jedoch im Seitenbild als divergiende Endäste (M_5) zu erkennen (Aa. Parietalis post., angularis und temporalis post.) Bei Tumoren der Hinterhauptlappens können diese Äste von unten her eine Zusammendrängung und Parallelverlagerung nach oben oder aber, bei Entwicklung des Tumors mehr von dorsal her, eine stärkere Auseinanderdrängung in rechtwinkliger bis gerader Form erfahren.*

Our translation of this article reports that:

"The course of the middle cerebral artery is decomposed in the following subsections:

http://dx.doi.org/10.3174/ajnr.A5179

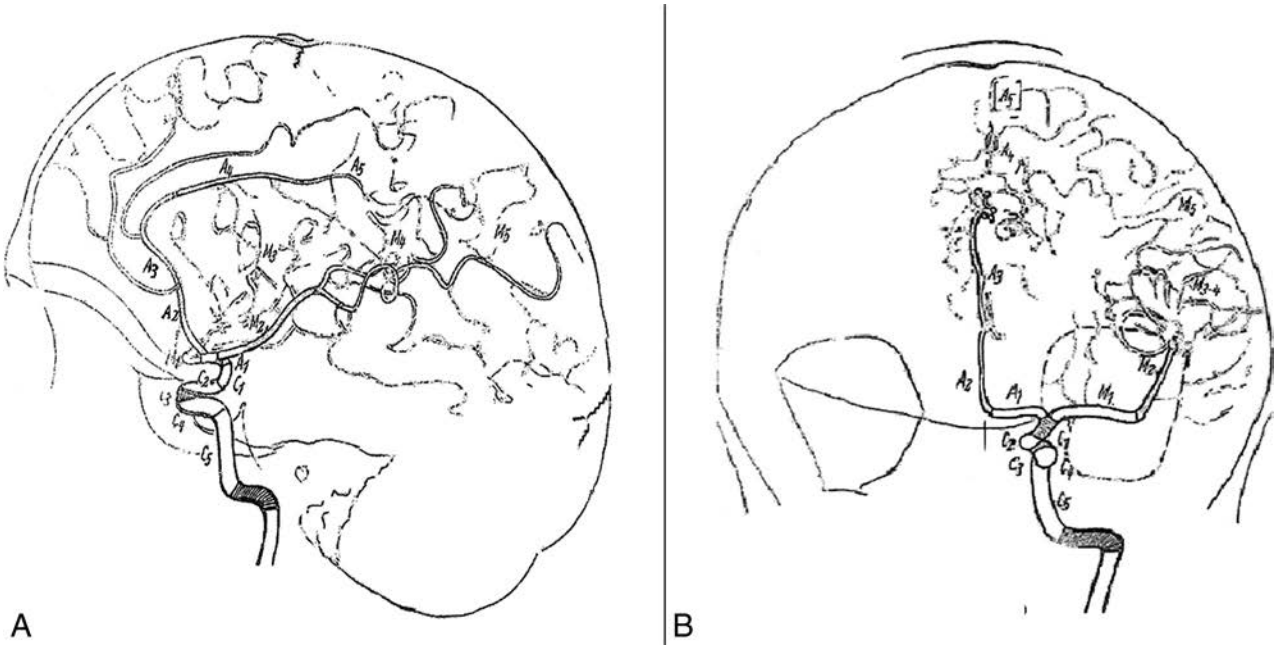

FIG 1. Original drawings of the intracranial arteries by Fischer.[21] *A*, Lateral view; *B*, frontal view. Reprinted with permission from Fischer E. Die Lageabweichungen der vorderen Hirnarterie im Gefässbild. *Zentralbl Neurochir* 1938;3:300–13.

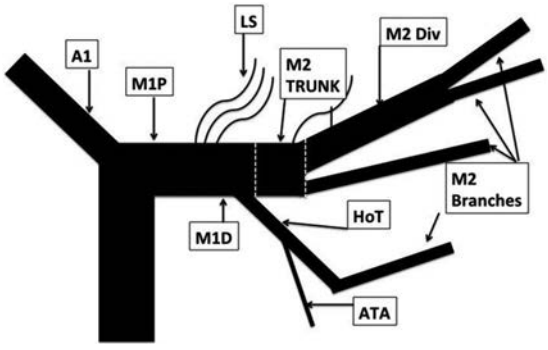

FIG 2. Drawing summarizing the MCA segmentation used in Tomsick et al's[1] article.

Number of patients with M2 occlusion in the recent randomized controlled trials on MT

Study	No. of Patients	Rate of M2 Occlusion (%)
MR CLEAN[2]	39	7.8
SWIFT PRIME[3]	19	10
REVASCAT[4]	18	9
EXTEND-IA[5]	10	14.3
ESCAPE[6]	9	2.9
THRACE[7]	2	1

1) The horizontal initial part (M_1), from the internal carotid bifurcation to the distal *genu* of the middle cerebral artery.
2) On the lateral view, the insular section progresses along the axis of the brain arteries toward the rear and upwardly (M_2) and gives birth to 2–3 main branches lying on the insula, and, on the front view, it is ascending almost vertically.
3) The junction of the above-mentioned main branches of the Sylvian fissure (M_3) with the candelabra (Foix) shows the typical loop aspect of the ascending frontal artery on the lateral view. On the frontal view, these branches form and limit sharply with the following group a typical image of a fan turned upward (M_{3-4}), translated downward in case of a central or parietal lobe tumor.
4) Vessel intersection (M_4) at the rear part of the Sylvian fissure (gyrus angularis), which clearly stands out on the lateral view, whereas they coincide with the fan on the frontal view.
5) At the terminal section (M_5) of the middle cerebral artery, there are, on the frontal view, fine and looser vascular stitches immediately above the attenuated and more visibly marked fan; however, on the lateral view, these appear particularly clear as the segments are divergent (M_5) (posterior parietal, angular, and posterior temporal arteries). With occipital lobe tumors, these branches can be pushed together from downward and be translated upwardly, but with the development of more dorsal tumors, a stronger compression can shift these structures frontally."

We think that using a classification without respecting criteria and landmarks that define these different segments is very confusing. Indeed, in their paper, the authors artificially created what they called an "M2 trunk" (Fig 2)[1] that definitively belongs to the M1 segment according to Fischer's classification (horizontal segment, before the MCA genu). This imprecise interpretation of a segmentation commonly used worldwide may lead to substantial misunderstandings and may render the results published in this series noncomparable with other studies dealing with M2 occlusions. Recently, Goyal et al[24] made an effort to clarify what should be considered as the M1 segment and detailed the M1 and M2 segment anatomic variations. In particular, they proposed to assimilate large anterior temporal artery (ATA) variation (ie, ATA supplying more than the anterior aspect of the temporal lobe) to an M2 segment.

To definitively clarify what is an M1 or M2 occlusion, we suggest using a classification such as the one presented below. In this

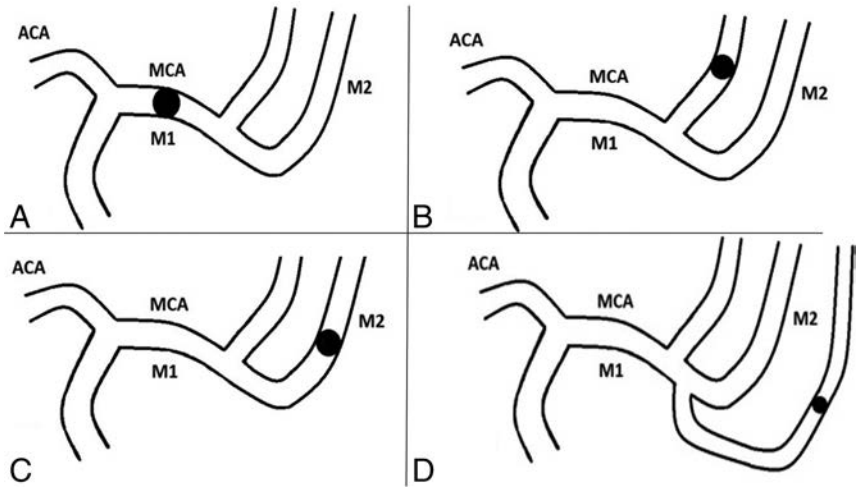

FIG 3. Drawings summarizing true M1 and M2 occlusions. *A*, M1 occlusion; *B*, superior M2 occlusion; *C*, inferior M2 occlusion; *D*, M2 trifurcation occlusion. ACA indicates anterior cerebral artery.

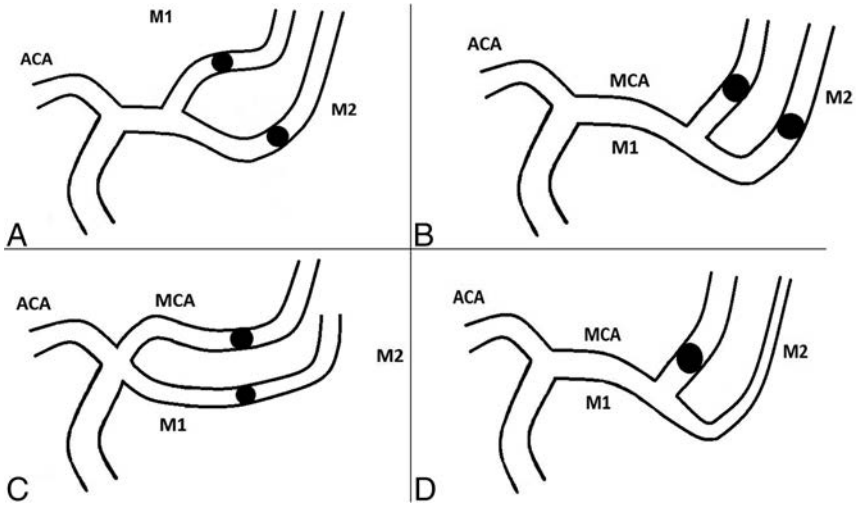

FIG 4. Drawings summarizing "M1-like" occlusions. *A*, Occlusion of both branches after MCA division, short M1 segment; *B*, occlusion of both branches after MCA division, distal to the MCA's genu; *C*, occlusion of both branches of a duplicated or accessory MCA; *D*, occlusion of either the superior or inferior division of the MCA if it is a dominant branch (ie, division branch feeding ≥75% of the MCA's cortical territory). ACA indicates anterior cerebral artery.

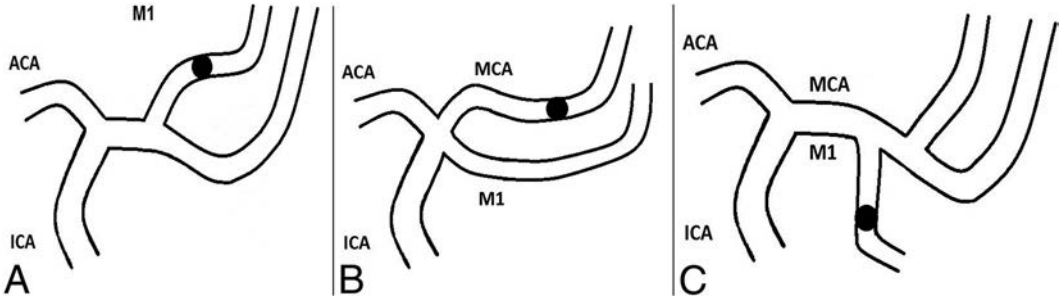

FIG 5. Drawings summarizing "M2-like" occlusions. *A*, Occlusion of 1 branch after MCA division, proximal (short M1 segment) or distal to the MCA's genu; *B*, occlusion of 1 branch of a duplicated or accessory MCA; *C*, occlusion of the anterior temporal artery if its trunk is large (ie, as big as M2). ACA indicates anterior cerebral artery.

classification, in addition to true M1 or M2 occlusions (Fig 3), we describe "M1-like" (Fig 4) occlusions that comprise:

Occlusion of both branches after MCA division, proximal (short M1 segment) (Fig 4*A*) or distal to the MCA's genu (Fig 4*B*);

Occlusion of both branches of a duplicated or accessory MCA (Fig 4*C*); and,

Occlusion of either the superior or inferior division of the MCA, if it is a dominant branch (ie, division branch feeding ≥75% of the MCA's cortical territory) (Fig 4*D*).

We also describe "M2-like" (Fig 5) occlusions that comprise:

Occlusion of 1 branch after MCA division, proximal (short M1 segment) or distal to the MCA's genu (Fig 5*A*);
Occlusion of 1 branch of a duplicated or accessory MCA (Fig 5*B*); and,
Occlusion of the ATA if its trunk is large (ie, as big as M2) (Fig 5*C*).

To conclude, we think that speaking the same language, by using the classifications in a common way, is the only manner to provide comparable results.

Disclosures: Nader Sourour—*UNRELATED*: *Consultancy*: Medtronic; *Payment for Development of Educational Presentations*: Medtronic, *Comments*: workshop; *Stock/Stock Options*: Medina, *Comments*: former investor. Bruno Bartolini—*UNRELATED*: *Consultancy*: Stryker. Frédéric Clarençon—*UNRELATED*: *Consultancy*: Codman, Medtronic.

REFERENCES

1. Tomsick TA, Carrozzella J, Foster L, et al**. Endovascular therapy of M2 occlusion in IMS III: role of M2 segment definition and location on clinical and revascularization outcomes.** *AJNR Am J Neuroradiol* 2017;38:84–89 CrossRef Medline
2. Berkhemer OA, Fransen PS, Beumer D, et al. **A randomized trial of intraarterial treatment for acute ischemic stroke.** *N Engl J Med* 2015; 372:11–20 CrossRef Medline
3. Saver JL, Goyal M, Bonafe A, et al. **Stent-retriever thrombectomy after intravenous t-PA vs. t-PA alone in stroke.** *N Engl J Med* 2015; 372:2285–95 CrossRef Medline
4. Jovin TG, Chamorro A, Cobo E, et al. **Thrombectomy within 8 hours after symptom onset in ischemic stroke.** *N Engl J Med* 2015;372: 2296–306 CrossRef Medline
5. Campbell BC, Mitchell PJ, Kleinig TJ, et al. **Endovascular therapy for ischemic stroke with perfusion-imaging selection.** *N Engl J Med* 2015;372:1009–18 CrossRef Medline
6. Goyal M, Demchuk AM, Menon BK, et al. **Randomized assessment of rapid endovascular treatment of ischemic stroke.** *N Engl J Med* 2015;372:1019–30 CrossRef Medline
7. Bracard S, Ducrocq X, Mas JL, et al. **Mechanical thrombectomy after intravenous alteplase versus alteplase alone after stroke (THRACE): a randomised controlled trial.** *Lancet Neurol* 2016;15:1138–47 CrossRef Medline
8. Powers WJ, Derdeyn CP, Biller J, et al. **2015 AHA/ASA focused update of the 2013 guidelines for the early management of patients with acute ischemic stroke regarding endovascular treatment: a guideline for healthcare professionals from the American Heart Association/American Stroke Association.** *Stroke* 2015;46:3020–35 CrossRef Medline
9. Park JS, Kwak HS. **Manual aspiration thrombectomy using penumbra catheter in patients with acute M2 occlusion: a single-center analysis.** *J Korean Neurosurg Soc* 2016;59:352–56 CrossRef Medline
10. Kim YW, Son S, Kang DH, et al. **Endovascular thrombectomy for M2 occlusions: comparison between forced arterial suction thrombectomy and stent retriever thrombectomy.** *J Neurointerv Surg* 2016 Jul 5. [Epub ahead of print] CrossRef Medline
11. Wong JH, Do HM, Telischak NA, et al. **Initial experience with SOFIA as an intermediate catheter in mechanical thrombectomy for acute ischemic stroke.** *J Neurointerv Surg* 2016 Oct 27. [Epub ahead of print] CrossRef Medline
12. Coutinho JM, Liebeskind DS, Slater LA, et al. **Mechanical thrombectomy for isolated M2 occlusions: a post hoc analysis of the STAR, SWIFT, and SWIFT PRIME studies.** *AJNR Am J Neuroradiol* 2016; 37:667–72 CrossRef Medline
13. Dorn F, Lockau H, Stetefeld H, et al. **Mechanical thrombectomy of M2-occlusion.** *J Stroke Cerebrovasc Dis* 2015;24:1465–70 CrossRef Medline
14. Sung SM, Lee TH, Lee SW, et al. **Emergent intracranial stenting for acute M2 occlusion of middle cerebral artery.** *Clin Neurol Neurosurg* 2014;119:110–15 CrossRef Medline
15. Flores A, Tomasello A, Cardona P, et al. **Endovascular treatment for M2 occlusions in the era of stentrievers: a descriptive multicenter experience.** *J Neurointerventional Surg* 2015;7:234–37 CrossRef Medline
16. Ewald B. **Post hoc choice of cut points introduced bias to diagnostic research.** *J Clin Epidemiol* 2006;59:798–801 CrossRef Medline
17. Kivimäki M, Singh-Manoux A, Ferrie JE, et al. **Post hoc decision-making in observational epidemiology–is there need for better research standards?** *Int J Epidemiol* 2013;42:367–70 CrossRef Medline
18. Post-hoc analysis in clinical trials. Research Supervisor Connect, University of Sydney, Australia. http://sydney.edu.au/research/opportunities/opportunities/2133. Accessed February 2, 2017
19. Broderick JP, Palesch YY, Demchuk AM, et al. **Endovascular therapy after intravenous t-PA versus t-PA alone for stroke.** *N Engl J Med* 2013;368:893–903 CrossRef Medline
20. Premat K, Bartolini B, Di Maria F, et al. **Single-center experience using the 3MAX reperfusion catheter for the treatment of acute ischemic stroke with distal arterial occlusion.** In: *Proceedings of the 29th European Congress of Radiology*, Vienna, Austria. March 1–5, 2017
21. Fischer E. **Die Lageabweichungen der vorderen Hirnarterie im Gefäßbild.** *Zentralbl Neurochir* 1938;3:300–13
22. Gibo H, Carver CC, Rhoton AL Jr, et al. **Microsurgical anatomy of the middle cerebral artery.** *J Neurosurg* 1981;54:151–69 CrossRef Medline
23. Krayenbuhl HA. *Cerebral Angiography (2nd revised edition)*. London: Butterworth & Co; 1968
24. Goyal M, Menon BK, Krings T, et al. **What constitutes the M1 segment of the middle cerebral artery?** *J Neurointerv Surg* 2016 Jan 11. [Epub ahead of print] CrossRef Medline

R. Capocci
Department of Interventional Neuroradiology
Pitié-Salpêtrière Hospital, APHP
Paris, France
E. Shotar
Department of Interventional Neuroradiology
Pitié-Salpêtrière Hospital, APHP
Paris, France
Paris VI University Pierre et Marie Curie
Paris, France
N.-A. Sourour
I. Haffaf
B. Bartolini
Department of Interventional Neuroradiology
Pitié-Salpêtrière Hospital, APHP
Paris, France
F. Clarençon
Department of Interventional Neuroradiology
Pitié-Salpêtrière Hospital, APHP
Paris, France
Paris VI University Pierre et Marie Curie
Paris, France

REPLY:

Thanks to Dr. Capocci and colleagues for their interest in our manuscript. Their comments appear to address: 1) the appropriateness of the manuscript for submission; 2) our departure from a rigid anatomic classification system; and 3) an additional "new" classification of their own.

No strangers to confusion and controversy requiring caution regarding the communication of historical classification constructs,[1] we came to our conclusions after we saw stroke angiograms in studies over 20 years, and ultimately, we were ourselves confused about the best way to analyze and report what we observed.

Regarding the appropriateness, we would have been remiss had we not looked beyond the original published results of the largest randomized interventional stroke treatment study to date with a focus on interventional subgroups.[2] Various issues raised in post hoc analysis should be of value to future investigators planning their own studies.[3-5]

To the correspondents' specific concerns regarding poor recanalization, the Interventional Management of Stroke (IMS) III study showed a recanalization rate of 78.3% for M2 occlusion, with 72.3% modified TICI 2–3 and approximately 40% modified TICI 2b–3 reperfusion rate. However, in IMS III, revascularization (recanalization and reperfusion) had no interobserver agreement for distinction between modified TICI 2–3 and 2b–3 reperfusion versus outcome and did not correlate to good clinical outcome for M2 occlusion. We encourage the stroke community to settle these discrepancies with the correspondents' assumptions in future analyses.

More importantly, however, the correspondents disagree with our departure from strict anatomic categorization of the occlusion site in our manuscript. To be sure, we take no issue with Fischer's and others' anatomic definitions.[6,7] Nothing could be more direct and succinct than "M1, M2, M3, and M4." However, the definitions were derived before angiography and intervention were envisioned and were not designed to specifically meet the need to correlate arterial occlusion branching patterns with clinical outcome after intervention by intravenous or intra-arterial drugs or devices. Reference to Goyal's publication as a resource for the definition of M1–M2 anatomy fails to recognize the prior sharing of a number of emails, images, and documents between us in discussing the M1–M2 issue or his approval as a coauthor of our M2 manuscript after a very long, arduous editing process. Goyal's anatomic recommendation and our functional modifications constitute 2 different reporting models of varying complexity, purpose, and significance, neither perfect for all circumstances.

None of the correspondents' references address any perceived anatomic versus physiologic MCA occlusion concerns before 1994. With no applicable treatments to apply, no controversies of parameters within patient study groups would be anticipated. However, between 1994 and 2014, a concern arose regarding the M1 and M2 definition in the Emergency Management of Stroke (EMS) Study[8,9] and its subsequent IMS I,[10] II,[11] and III[2] successors, culminating in the view that an M1 occlusion would have no M2 segments or distal cortical distribution filling. EMS struggled with the seeming contradiction of terms suggesting that any patent M2 segment, division, branch, artery, or vessel flow should exist with M1 occlusion. M1 occlusion should have 100% of the MCA cortical distribution occluded, save for the classic anterior temporal artery. After all, can, or should, outcome comparisons be made between an M1 occlusion with no distal filling versus an M1 occlusion with distal cortical flow reducing volume at risk, adding collateral circulation, and reducing collateral need from other sources? To compare clinical outcomes, nothing seemed more elemental than defining M1 occlusion as a blockage associated with the absence of arterial filling other than that of a typical anterior temporal artery. Conversely, if 100% of the MCA distribution is not occluded, but rather a branch is patent, coursing into the insular and Sylvian cistern to supply brain beyond, the EMS-IMS functional designation of some form of M2 occlusion becomes operational. The problem of classifying the nature of the M2 occlusion then arises. This conceptual, operational dilemma always lurked in the background of EMS-IMS case evaluation, but returned to the forefront in IMS III, where 83 "M2" occlusions were encountered, with up to 25% exhibiting characteristics easily confused with anatomic M1 occlusion.

Before EMS, no controlled, randomized trial had wrestled with the question of anatomic versus functional occlusion from an endovascular standpoint. PROACT (Prolyse in Acute Cerebral Thromboembolism), conducted concurrently with EMS and reported sequentially from the same podium,[12] did not specifically define M1 and M2 occlusion to address any issue of anatomic concern or to give direction for the future.[13] Having now analyzed the interesting discrepancies subsequently in prospective core-lab analysis of over 100 EMS-IMS M2 occlusions, in addition to many additional trial and nontrial cases, our manuscript hoped to share a succinct method for describing M1, M2, and hybrid cases should such categorization prove of value. With insufficient foresight regarding all the issues that would arise in the final IMS III adjudication, only a post hoc analysis promised to offer clarity regarding our hypotheses and observations.

Even then, to distinguish between M1 and M2 trunk occlusions functionally could have been irrelevant with no significance in doing so, or even erroneous, contributing to another dead wake tailing behind the IMS study. To the contrary, our exploratory analyses suggested that distinctions between distal M1 and M2 trunk occlusion may have relevance, as we very preliminarily reported. A post-post-hoc analysis further exploring unrecognized factors that might contribute to measured numeric differences in the clinical outcome of M1 versus M2 trunk occlusion has been performed. In a presentation at the recent ASNR meeting, we reported a variance in imaging core lab–defined ASPECTS (Alberta Stroke Program Early CT Score) ischemia of the lenticular nucleus (more frequent with M2 trunk occlusion versus distal M1) and insula (less frequent with M2 trunk occlusion versus distal M1). Recognizing that our original post hoc analysis identified at least 30%–40% of M2 trunk occlusions had occluded lateral lenticulostriate arteries arising from them, an associated deep ischemic effect is understandable. In addition, less frequent insular infarction with M2 trunk occlusion further supports our

http://dx.doi.org/10.3174/ajnr.A5200

hypothesis that better collateral flow may indeed be afforded by patent posterior temporal or holotemporal branches. However, these 2 observations would create direct but opposite effects on good clinical outcome, perhaps neutralizing one another in the mRS outcome metric. We would welcome review by the investigators of the smaller recent studies detailed in the letter's table to support or summarily refute our observations.

Finally, the correspondents themselves also appear to find the historical anatomic classification insufficient, suggesting their own new subgroup classification. Their classification addresses issues not directly specific to our manuscript, apart from our simple, general schematic reproduced with their letter. We will not comment on their individual details and depictions. The lack of core lab data and numbers of the varieties of occlusions envisioned provides little perspective on the impact their categorization would provide. However, that "a distal M1 occlusion with a large anterior temporal artery supplying the entire temporal lobe" should not be contracted to "M2 trunk occlusion" seems uneconomical in effort, inflexible in practice, less predictive in comparison of outcomes, and generally less precise in understanding. To use "M1-like" or "M2-like" evades the precision or exactness of what something is in favor of what it seems to be.

Workers interested in greater understanding of less obvious patient-related factors contributing to the clinical outcome after stroke intervention should be open to modifications not envisioned by or on the viewing screens of our predecessors. Perhaps we should ask ourselves, given the advances in the treatment of cerebrovascular disease, where our anatomist ancestors would stand on the issue of splitting or clarifying their anatomic construct. Would they be as flexible as our new clot-removal devices and recognize that new observations on anatomy versus outcome might have sufficient relevance to recommend modifying their construct, or would they be rigid and inflexible, holding to the dictates of their time-honored effort? As a world-renowned empirical observer, radiologist Dr. Benjamin Felson used to summarize, when confronted with controversy and/or disagreement, "My mind's made up. Don't confuse me with the facts."

REFERENCES

1. Tomsick T. **TIMI, TIBI, TICI: I came, I saw, I got confused.** *AJNR Am J Neuroradiol* 2007;28:382–84 Medline
2. Broderick JP, Palesch YY, Demchuk AM, et al. **Endovascular therapy after intravenous t-PA versus t-PA alone for stroke.** *N Engl J Med* 2013;368:893–903 CrossRef Medline
3. Zaidat OO, Yoo AJ, Khatri P, et al. **Recommendations on angiographic revascularization grading standards for acute ischemic stroke: a consensus statement.** *Stroke* 2013;44:2650–63 CrossRef Medline
4. Tomsick TA, Yeatts SD, Liebeskind DS, et al. **Endovascular revascularization results in IMS III: intracranial ICA and M1 occlusions.** *J Neurointerv Surg* 2015;7:795–802 CrossRef Medline
5. Tomsick TA, Foster LD, Liebeskind DS, et al. **Outcome differences between intra-arterial iso- and low-osmolality iodinated radiographic contrast media in the Interventional Management of Stroke III trial.** *AJNR Am J Neuroradiol* 2015;36:2074–81 CrossRef Medline
6. Fischer E. **Die Lageabweichungen der vorderen Hirnarterie im Gefäßbild.** *Zentralbl Neurochir* 1938;3:300–13
7. Goyal M, Menon BK, Krings T, et al. **What constitutes the M1 segment of the middle cerebral artery?** *J Neurointerv Surg* 2016 Jan 11. [Epub ahead of print] CrossRef Medline
8. EMS Study Group. **Emergency management of stroke: IV placebo vs. IV t-PA plus intra-arterial t-PA in stroke treatment.** In: *Proceedings of the 21st International Conference on Stroke and Cerebrovascular Disease,* San Antonio, Texas. January 24, 1996
9. Lewandowski CA, Frankel M, Tomsick TA, et al. **Combined intravenous and intra-arterial r-TPA versus intra-arterial therapy of acute ischemic stroke: Emergency Management of Stroke (EMS) Bridging Trial.** *Stroke* 1999;30:2598–605 CrossRef Medline
10. The IMS Writing Group. **Combined intravenous and intra-arterial recanalization for acute ischemic stroke: the Interventional Management of Stroke Study.** *Stroke* 2004;35:904–11 CrossRef Medline
11. The IMS II Trial Investigators. **The Interventional Management of Stroke (IMS) Study.** *Stroke* 2007;38: 2127–35 CrossRef Medline
12. del Zoppo GJ, Higashida RT, Furlan AJ, et al. **Prolyse in acute cerebral thromboembolism trial (PROACT): results of 6 mf dose tier.** In: *Proceedings of the 21st International Conference on Stroke and Cerebrovascular Disease*, San Antonio, Texas. January 24, 1996
13. Furlan A, Higashida R, Wechsler L, et al. **Intra-arterial prourokinase for acute ischemic stroke. The PROACT II study: a randomized controlled trial. Prolyse in Acute Cerebral Thromboembolism.** *JAMA* 1999;282:2003–11 CrossRef Medline

T.A. Tomsick
Department of Radiology
University of Cincinnati Academic Health Center
University Hospital
Cincinnati, Ohio

D.S. Liebeskind
University of California, Los Angeles Stroke Center
Los Angeles, California

M.D. Hill
Calgary Stroke Program
Department of Clinical Neurosciences, Medicine
Community Health Sciences, Hotchkiss Brain Institute
University of Calgary, Foothills Hospital
Calgary, Alberta, Canada

R. von Kummer
Department of Neuroradiology
Dresden University Stroke Center
Universitätsklinikum Carl Gustav Carusan de Technischen
Universität Dresden
Dresden, Germany

M. Goyal
Department of Radiology and Clinical Neurosciences
University of Calgary
Calgary, Alberta, Canada

J.P. Broderick
Department of Neurology
University of Cincinnati Academic Health Center
Cincinnati, Ohio